A Study of Pulse Shape Discrimination in Scintillator Dark Matter Detectors

Daniel Russell Tovey

University of Sheffield

A thesis submitted for the degree of Doctor of Philosophy in the subject of Physics, October 1998.

To Nan.

Abstract

The existence of 'dark matter' throughout the universe is now well established but its form and origin remain one of the greatest problems for modern cosmology. Particle physics posits a solution to this problem in the form of 'Weakly Interacting Massive Particles' (WIMPs) which are predicted to exist by many theories extending physics beyond the standard model. The discovery of such particles would consequently have profound implications for both disciplines. Many experiments around the world are now endeavouring to achieve this goal but currently the most successful are those using scintillator detectors.

This thesis describes a study of the use of Pulse Shape Discrimination (PSD) techniques to reduce the rate of electron recoil background events in scintillator dark matter experiments. The development of new classes of detector with novel pulse shape properties is described and the results of tests using elastic scattering of monoenergetic neutrons to simulate nuclear recoil signal events are presented. Monte Carlo simulations have been used to assess the performance of CASPAR, a particularly promising new technique, and the results presented here indicate that this has the potential to considerably improve dark matter sensitivity, particularly for spin dependent WIMP interactions. An analysis of 867 kg.days of data from an operational NaI(Tl) detector is described and the resulting evidence for a small population of events with anomalous pulse shape properties discussed.

Acknowledgements

I should like to thank the following (in no particular order) for their advice, assistance and support.

First and foremost my supervisor Neil Spooner and the rest of the members of the Sheffield dark matter group; John Roberts, Vitaly Kudryavtsev, Matt Lehner, Phil Lightfoot, John MacMillan, Jeff Martoff and Christian Peak.

The other members or ex-members of the Sheffield High Energy Physics Group; Craig Buttar, Chris Booth, Susan Cartwright, Fred Combley, Lee Thompson, Mark Lehto, Chris Grigson, Paul Sellin, Andy Beddall, Spyros Manolopoulos, Warrick Newton, Robin Boswell, Sue Walsh, Chris Brew, John Reeve, Mandy Kelly, Debbie Morgan and Paul Hodgson.

Peter Smith and everyone else in the UK Dark Matter Collaboration; Nigel Smith, John Alner, Geoff Arnison, Graham Homer, David Lewin, Igor Liubarsky, Jon Barton, Gareth Jones, Gavin Davies, Colin Lally, David Davidge, Alex Howard, Tim Sumner, Tariq Ali, John Quenby, Arthur Bewick, Harry Vine, Manu Joshi, Ben Ahmed and Rupert Smith.

John Edgington, Ian Blair and Ann Harris from the Karmen group at Q.M.W..

All the technicians in the Physics Department and the University of Sheffield Central Mechanical Workshop; in particular John Newell, Chris Vickers, Trevor Gamble, John Kelly and Richard Nicholson.

Roger Olivant, Alan Bateman, Cathy Haddon and everyone in the Physics Department office.

Alan Yates, Dawn Bussey and everyone in the Chemistry Department and Sorby Centre for Microanalysis who helped with the CaF_2(Eu) synthesis work.

Dave Mowbray for his help with the photoluminescence measurements.

Jim Telfer and Dennis Day at Hilger Analytical Ltd..

The University of Sheffield and Hilger Analytical Ltd. for funding.

And finally Mum, Dad and Caroline.

October 1998

Contents

List of Figures

List of Tables

Abbreviations

The following is a list of some of the abbreviations used in this thesis. The list is not exhaustive but covers those abbreviations which are most commonly used.

CCAL	DM46 Compton CALibration data
CDM	Cold Dark Matter
DAQ	Data AcQuisition system
DATA	DM46 background data
DM	Dark Matter
dof	degrees of freedom
DSF	Data Summary File
DSO	Digital Sampling Oscilloscope
ECAL	Energy CALibration data
ee	electron equivalent
FF	Form Factor
GUT	Grand Unified Theory
HDM	Hot Dark Matter
IC	Information Carrier
LR	Likelihood Ratio
LXe	Liquid Xenon
MT	Mean Time
mV/pe	mV per photoelectron
mwe	metres water equivalent
NCAL	DM46 Neutron CALibration data
pe	photoelectron
pe/keV	photoelectrons per keV
PMT	PhotoMultiplier Tube
PSA	Pulse Shape Analysis
PSD	Pulse Shape Discrimination
SM	Standard Model
SUSY	SUperSYmmetry
TAC	Time to Amplitude Converter
UVIS	Ultra violet VISible detector
WIMP	Weakly Interacting Massive Particle

Chapter 1

The Dark Matter Problem

1.1 Introduction

Dark matter is a problem which arises in astrophysics and cosmology but which potentially has a solution in particle physics. This chapter introduces the problem and then goes on to discuss some of the possible solutions. The chapter begins with a brief description of modern cosmology (§1.2) and then proceeds to discuss some of the theoretical arguments for the existence of dark matter (§1.3). Following this there is a discussion of the cosmological evidence (§1.4) and then an outline of the various dark matter candidates, baryonic and non-baryonic, 'hot' and 'cold', and of the various ways in which their presence might be inferred experimentally (§1.5).

1.2 The Standard Cosmology

Since the discovery by Hubble [1] of a linear relationship between galactic redshift and distance there has been overwhelming observational evidence to suggest that we live in an expanding universe created in a hot Big Bang [2, 3, 4, 5]. The cosmological model of Friedmann, Robertson and Walker (FRW) has proven to be remarkably successful at explaining these observations and has come to be known as the 'standard' cosmology.

In any theory of an expanding universe it is natural to consider a quantity known as the 'scale factor' $S(t)$. This relates the distance r_0 between two objects at time t_0 to the distance $r(t)$ at some subsequent time t:

$$r(t) = r_0 S(t). \tag{1.1}$$

Since it is difficult to measure the absolute size of the universe it is convenient to deal instead with the scale factor, which gives a measure of the relative size.

It is believed that the large scale behaviour of the universe is governed predominantly by the Einstein field equations [6]:

$$G_{\mu\nu} = \frac{8\pi G_N}{c^4} T_{\mu\nu}, \tag{1.2}$$

where $G_{\mu\nu}$ is the Einstein Tensor describing the geometrical properties of spacetime and $T_{\mu\nu}$ is the stress-energy tensor describing the mass-energy distribution of the universe. Now the uniformity of the Cosmic Background Radiation (CBR) to 1 part in 10^4 suggests that on the largest scales the universe is both homogeneous and isotropic. Such a homogeneous isotropic spacetime can be described by the Robertson-Walker metric:

$$ds^2 = c^2dt^2 - S^2(t)\left(\frac{d\sigma^2}{1-k\sigma^2} + \sigma^2 d\theta^2 + \sigma^2 sin^2\theta d\phi^2\right), \tag{1.3}$$

where s is the spacetime distance, σ, θ and ϕ are dimensionless comoving spatial coordinates and k is a parameter related to the Gaussian curvature of spacetime K by $K = k/S^2(t)$, $k = -1, 0$ or $+1$. From this metric one may derive the appropriate forms for $G_{\mu\nu}$ and $T_{\mu\nu}$ and hence solve Eqn. 1.2 to give the Friedmann equations for the evolution of $S(t)$ [7]:

$$\frac{\dot{S}^2(t)}{S^2(t)} = \frac{8\pi G_N}{3}\rho - \frac{kc^2}{S^2(t)} + \frac{\Lambda}{3}, \tag{1.4}$$

$$\frac{2\ddot{S}(t)}{S(t)} + \frac{\dot{S}^2(t)}{S^2(t)} = -\frac{8\pi G_N}{c^2}p - \frac{kc^2}{S^2(t)} + \Lambda, \tag{1.5}$$

where ρ is the matter density, p is the matter pressure and Λ is an integration constant (the 'cosmological constant') corresponding to a non-zero vacuum energy density. For the time being Λ will be assumed to be zero at all times after the Big Bang.

Now the recession velocity of a comoving observer in an expanding universe is given by the Hubble law [1]

$$v = \dot{r} = r_0\dot{S}(t) = rH(t), \tag{1.6}$$

where $H(t)$ is the Hubble parameter

$$H(t) = \frac{\dot{S}(t)}{S(t)}. \tag{1.7}$$

The current value of $H(t)$, H_0, can be determined from Doppler measurements of recession velocities and from knowledge of the distances at which the observed

objects lie. The latter are in general known only imprecisely and so the currently preferred values lie in the broad range

$$H_0 = 100h \ (\mathrm{kms^{-1}Mpc^{-1}}), \qquad 0.65 < h < 0.8. \tag{1.8}$$

One can now define the 'critical' density ρ_{crit} as that density which gives a 'flat' universe of zero curvature, i.e. $k = 0$. From Eqn. 1.4 and 1.7 one then obtains, with Λ set to zero,

$$H^2(t) = \frac{8\pi G_N \rho_{crit}}{3}, \tag{1.9}$$

or

$$\rho_{crit} = \frac{3H^2(t)}{8\pi G_N}. \tag{1.10}$$

It is also convenient to define the density parameter Ω_0 as the ratio of the actual density ρ to the critical density ρ_{crit}:

$$\Omega_0 = \frac{\rho}{\rho_{crit}}, \tag{1.11}$$

whence from Eqn. 1.4 and 1.10

$$kc^2 = H_0^2 S_0^2 (\Omega_0 - 1), \tag{1.12}$$

where S_0 is the current scale factor. Solving Eqn. 1.4, 1.5 and 1.12 for S as a function of t one now finds that the overall evolution of the universe depends critically upon the value of Ω_0. If $\Omega_0 > 1$ ($k = +1$) then the universe is 'closed' and ceases to expand after a time $t_{max} = 2MG_N/3c^3$ (where M is the total mass of the universe), recollapsing after a time $2t_{max}$. If $\Omega_0 = 1$ ($k = 0$) then the universe is 'flat' and ceases to expand only after an infinite amount of time. In the case where $\Omega_0 < 0$ ($k = -1$) the universe does not contain sufficient matter to halt the expansion and it persists indefinitely. These different possibilities are illustrated in Fig. 1.1 (overleaf).

The true value of Ω_0 and hence the fate of the universe are currently unknown. The total mass of luminous matter detectable by conventional (electromagnetic spectrum) astronomy is certainly not sufficient to give $\Omega_0 = 1$. There is good reason to suspect however that not all matter is in this form and that a large fraction of the matter in the universe has yet to be detected. This matter is referred to as 'dark matter'. The observational evidence for its existence will now be discussed.

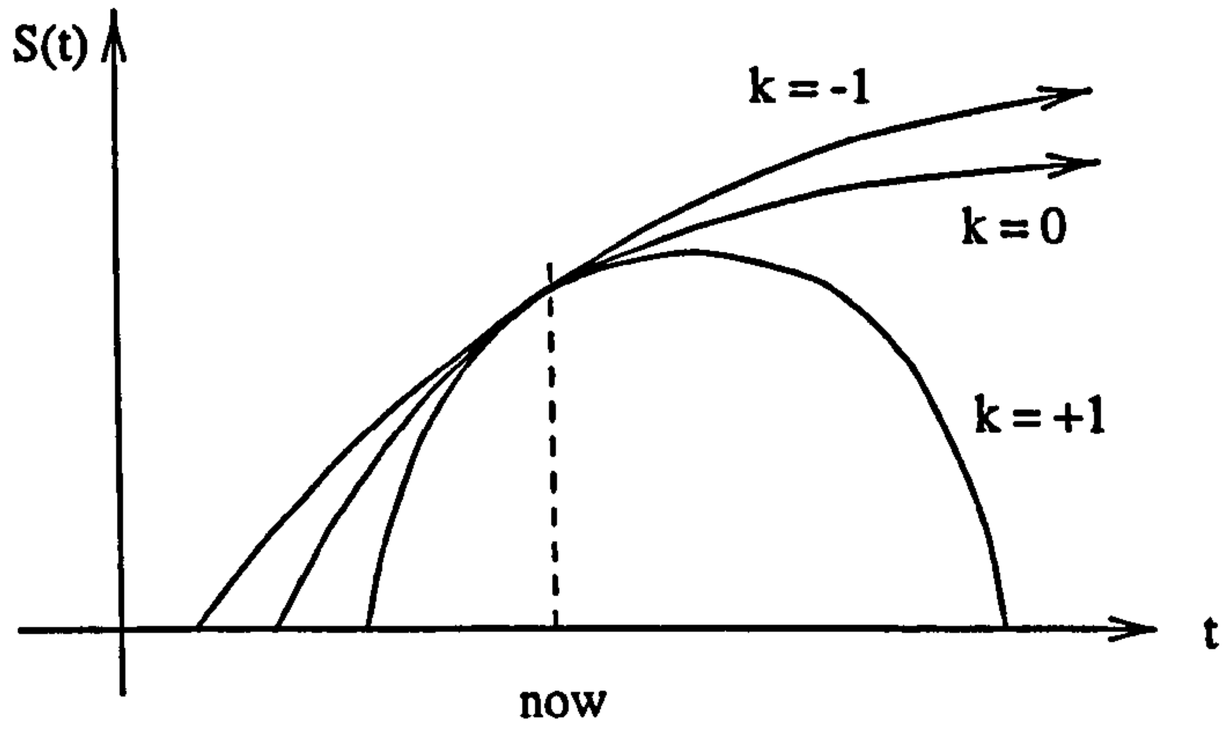

Figure 1.1: *The evolution of the scale factor $S(t)$ with time for negative, zero and positive spacetime curvatures. Adapted from [8].*

1.3 Observational Evidence for Dark Matter

1.3.1 Extragalactic Dark Matter

In recent years there has been an increasing amount of evidence for the existence of dark matter [3]. Its presence has been inferred mainly from the influence it exerts on the visible universe through gravitational interaction. The earliest evidence of this kind came from Doppler measurements of the relative velocities of galaxies in the Coma cluster by Zwicky [9]. The virial theorem relates the distribution of these relative velocities to the escape velocity of the cluster and hence to its gravitational mass M. Combining this with measurements of the luminosity L of the cluster gives a value for the cluster mass to light ratio $(M/L)_{cluster}$. This is in turn directly related to the density parameter for the cluster:

$$(M/L)_{cluster} \propto \Omega_{cluster} h (M/L)_{\odot}. \tag{1.13}$$

In the absence of dark matter $(M/L)_{cluster}$ will be equal to $(M/L)_{lum}$, the value for typical luminous stellar matter (~ 2), while for an appreciable fraction of dark matter $(M/L)_{cluster}$ will be larger, since the dark matter makes no contribution to L. The values of (M/L) for typical clusters (~ 200) are indeed found to be significantly larger than $(M/L)_{lum}$ and from this (and a knowledge of the Hubble parameter) the presence of a large fraction ($\gtrsim 85$ %) of dark matter may be deduced.

This general technique has been applied to systems on many different distance scales, from binary galaxies and clusters to superclusters and large scale flows. In general it is found that the measured value of Ω increases with scale indicating an increase in the observed fraction of dark matter. This is because the power spectrum

of fluctuations in the structure of the dark matter is typically shifted towards larger scales relative to that of luminous matter [5]. Thus by considering larger distance scales one is in effect sensitive to a greater fraction of the overall dark matter density of the universe Ω_{DM}.

It is possible to determine Ω on still larger scales by using Doppler measurements of deviations from the Hubble law for distant objects. The law is assumed to hold statistically for objects at these distances and hence any deviation will be due to peculiar velocities caused by inhomogeneities in the local distribution of matter. This allows an estimate to be made of the matter density Ω from [2]

$$v_{pec} \sim \frac{\Omega^{0.6}\lambda H_0}{b}\left(\frac{\delta n}{n}\right), \tag{1.14}$$

where $\delta n/n$ is the fluctuation in galaxy count at scale λ and b is a bias parameter accounting for differences in the structure power spectra for dark and luminous matter. This technique provides an estimate for Ω of order unity at scales $\gtrsim 100$ MPc [10].

Perhaps the most striking evidence for the existence of dark matter on cosmological distance scales has come from the observation of gravitational lensing of distant objects by clusters of foreground galaxies. By modeling the lensing process Tyson *et al.* [11] have deduced the density distribution of the lensing cluster CL 0024+1654. A map of the cluster density is plotted in Fig. 1.2 and gives a clear indication of the size of the dark halo in comparison with that of the luminous galaxies which it contains.

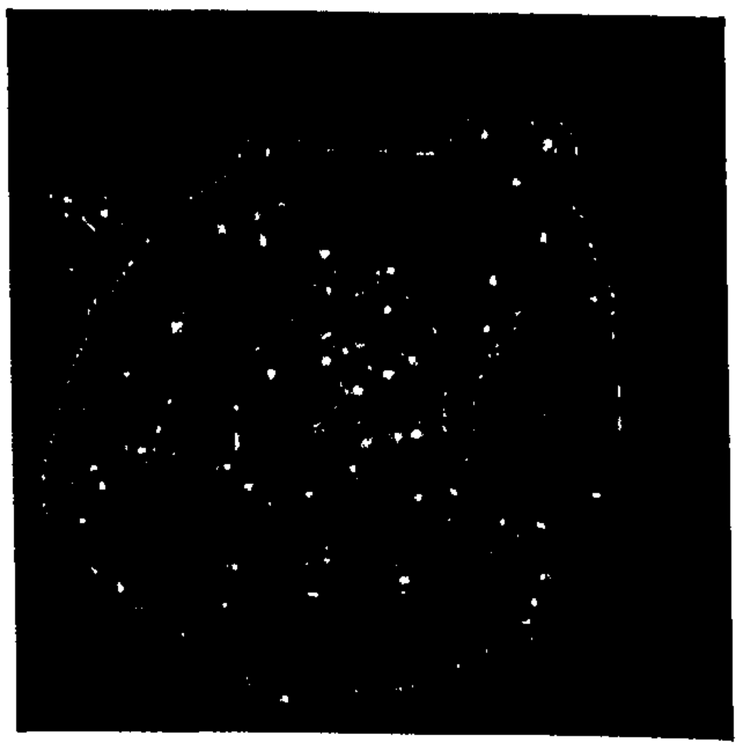

Figure 1.2: *The density profile of CL 0024+1654 obtained through analysis of the macrolensed image of a background galaxy. The light grey shading represents the dark halo while the visible galaxies appear white. The contours represent the lensing density distribution. Taken from [11].*

1.3.2 Galactic Dark Matter

The preceding considerations give no indication of the amount of dark matter which has accumulated within individual galaxies and to measure this one must resort to dynamics on shorter distance scales. Doppler techniques have been used to determine the rotation velocity v of luminous matter (stars, hot gas etc.) within many different spiral galaxies. From Newtonian mechanics the rotation velocity of gravitationally bound matter at radial distance r from the centre of a spherically symmetric galaxy is expected to be given by

$$v = \sqrt{\frac{G_N M(r)}{r}}, \tag{1.15}$$

where $M(r)$ is the total mass enclosed within r. Observations (Fig. 1.3) indicate that typically beyond the galactic bulge v remains approximately constant out to distances in many cases in excess of 100 kpc, and so from Eqn. 1.15

$$M_{total}(r) \propto r, \tag{1.16}$$

or,

$$\rho_{total} \propto r^{-2}. \tag{1.17}$$

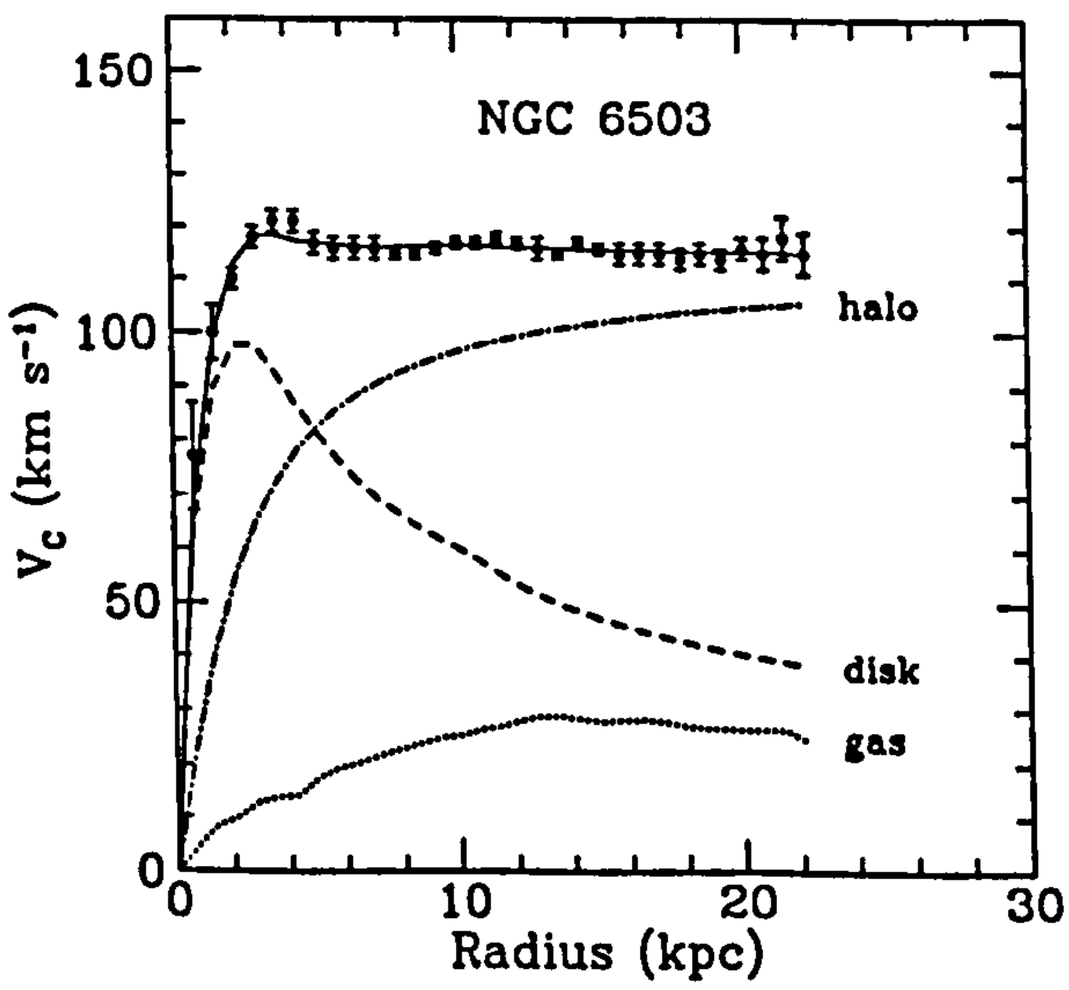

Figure 1.3: *The rotation curve of spiral galaxy NGC 6503. Also plotted is the best fit rotation curve comprising of disk, halo and gas contributions. Taken from [12].*

This is inconsistent with the observed distribution of luminous matter in spiral galaxies, which peaks strongly in the bulge at $r = 0$ and is greatly attenuated at

larger radii. There is thus strong evidence for a significant dark contribution to the total masses of these galaxies ($\Omega_{galaxy} \lesssim 0.2$, $\Omega_{lum} \lesssim 0.04$). Our own galaxy has a typical spiral morphology and here too measurements have shown evidence for a sizeable dark 'halo' out to at least 20 kpc (Fig. 1.4) [13, 14].

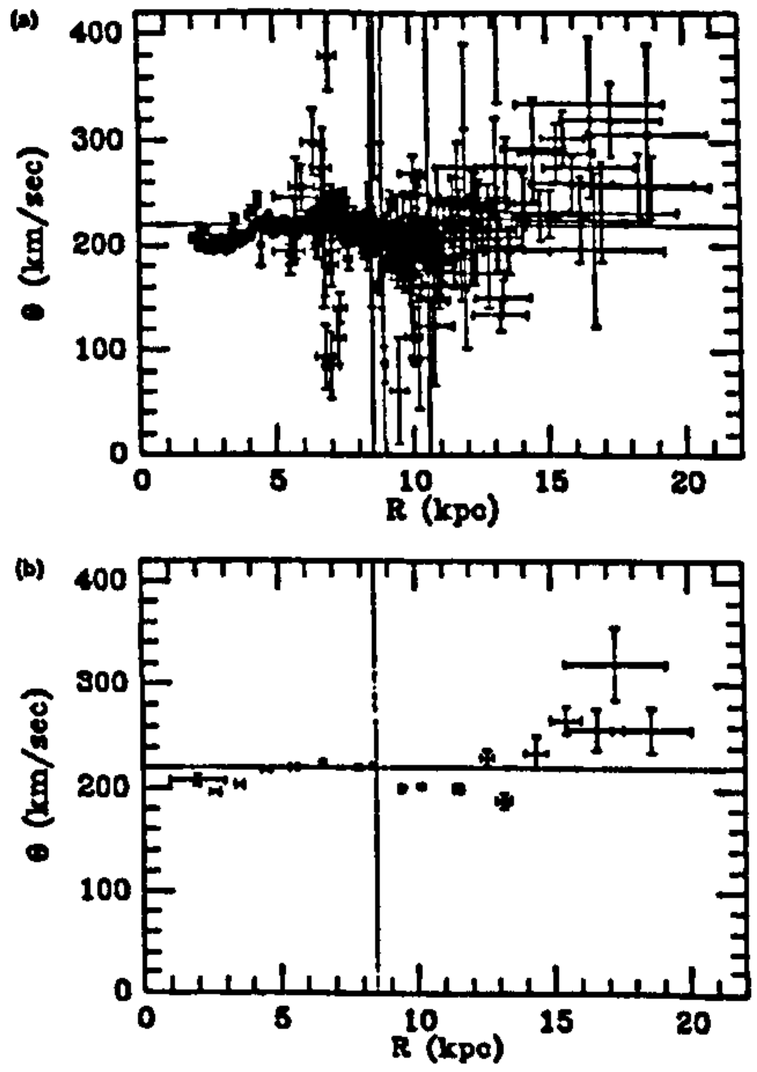

Figure 1.4: *The rotation curve of the Milky Way showing behaviour similar to that in Fig. 1.3. Figure (a) shows raw data and Figure (b) a smoothed data set. θ is the rotation velocity and R is the distance from the galactic centre. Taken from [15]. Data originally from [13].*

1.3.3 Summary of Observational Evidence

Knowledge of the apparent mass density of the universe on different scales, from galaxies to cosmological distances is summarised in Fig. 1.5 (overleaf). The rise in measured Ω with distance scale is apparent, as is the tendency towards $\Omega \sim 1$ at the largest scales.

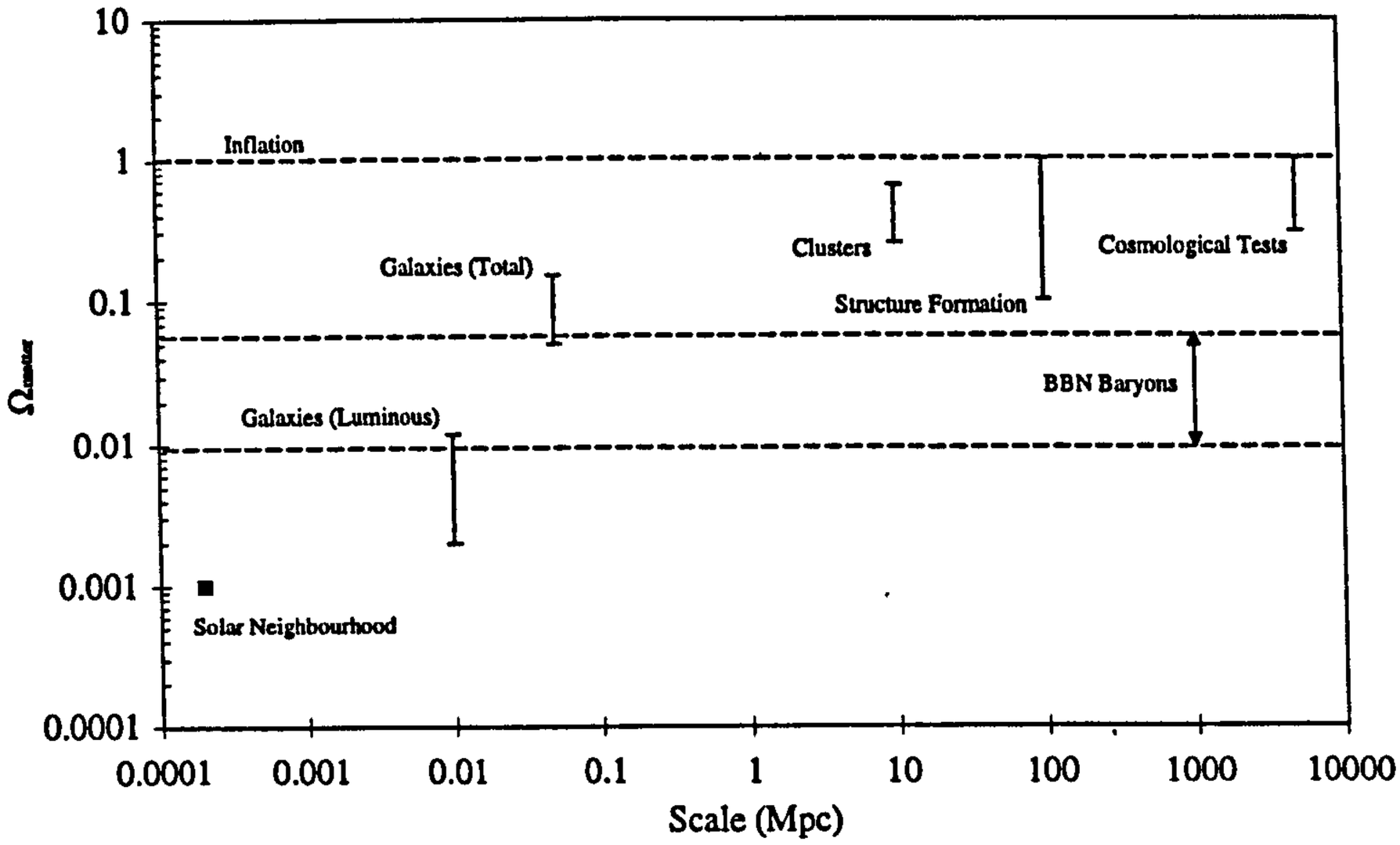

Figure 1.5: *Estimates of Ω at different scales. Based on [10, 16, 17].*

1.4 Theoretical Arguments for Dark Matter

1.4.1 Inflation and the Cosmological Constant

Despite the early successes of the standard cosmological model of FRW there remained a number of problems with the theory [5]:

- The uniformity of the CBR throughout the sky indicates that in the early universe widely spaced regions possessed the same temperature. However since these regions were causally disconnected at this time there is no reason for this to have been so. This apparent paradox is referred to as the 'horizon problem' [2].

- By examining the quantum processes occurring in the early universe one can estimate the current density of topological defects (magnetic monopoles) created as it passed through the GUT (Grand Unified Theory) phase transition. This monopole density ($\sim 1500\ \mathrm{m}^{-3}$) exceeds the limit placed by the survival of galactic magnetic fields (the Parker Bound [2]) by many orders of magnitude and must therefore be incorrect [5]. This paradox is referred to as the 'monopole problem'.

- By using Eqn. 1.12 one can examine the evolution of Ω with time. In the absence of a cosmological constant it is found that any value of $\Omega(t)$ soon after

the Big Bang not equal to 0, 1 or ∞ leads to a universe which either recollapses on itself after the Plank time $t_p = 10^{-43}$ s or rapidly gains a negligible subsequent value for $\Omega(t)$. In particular it is found that to give $\Omega \lesssim 0.01$ as observed for luminous matter in the universe today $\Omega(t_p)$ must have differed from unity by less than $\pm 10^{-60}$. This fine tuning or 'flatness' problem can be solved by setting $\Omega(t_p)$ to 1 in which case $\Omega(t) = 1$ for all time afterwards [5]. This requires the existence of some additional contribution to Ω_0 other than Ω_{lum} and if the present value of Λ is zero then this must come from dark matter.

A solution to these problems was proposed by Guth [18] and Linde [19, 20] in the form of 'inflation'. The standard inflationary model postulates the existence of a non-zero vacuum energy density at times $t < t_{GUT} \simeq 10^{-33}$ s due to the existence of a scalar 'inflaton' field associated with the GUT phase transition. This had the same effect as a large non-zero cosmological constant dominating the righthand side of the Friedmann equations (Eqn. 1.4 and 1.5). Hence one may write

$$\frac{\dot{S}^2(t)}{S^2(t)} \sim \frac{\Lambda}{3} \quad (= H_\Lambda^2), \tag{1.18}$$

giving a solution

$$S(t) \propto e^{H_\Lambda t}. \tag{1.19}$$

This implies that during this phase of its history the universe underwent a period of rapid expansion (inflation) by a factor $> 10^{30}$. At $t = t_{GUT}$ the universe crossed the GUT phase transition and at subsequent times the inflaton field decayed rapidly to zero. Thus for $t >> t_{GUT}$ the behaviour of the universe can be taken to be described by the FRW model with $\Lambda = 0$.

This idea of a rapidly inflating universe has a number of attractive features:

- It drives the Gaussian curvature of spacetime K to zero and thereby drives $\Omega(t)$ to unity (from Eqn. 1.12), hence solving the flatness problem. The standard inflationary theory predicts further that Λ is currently zero and hence supports the above inference of the existence of dark matter from the FRW model.

- It solves the horizon problem since regions of space which were initially in causal contact could have become causally disconnected by the superluminal expansion of spacetime.

- It solves the monopole problem by inflating the mean volume per monopole in the early universe and hence reducing the current monopole density to well below the Parker Bound.

Inflationary models fit well to the recent data from experiments mapping the small scale temperature anisotropies in the CBR [21]. These anisotropies originated as quantum fluctuations in the hot primordial plasma at times $t < t_{GUT}$ and were magnified by inflation to scales where they could provide seeds for structure formation in the later universe. The background photons themselves were originally of energy $E > E_{GUT} \sim 10^{16}$ GeV however the Hubble recession has since redshifted them into the microwave region of the spectrum where they can be detected with conventional astronomical techniques. The power spectrum of the anisotropies is shown in Fig. 1.6 and can be used in particular to constrain models explaining the composition and amount of dark matter in the universe. These constraints will be considered in more detail later in this chapter.

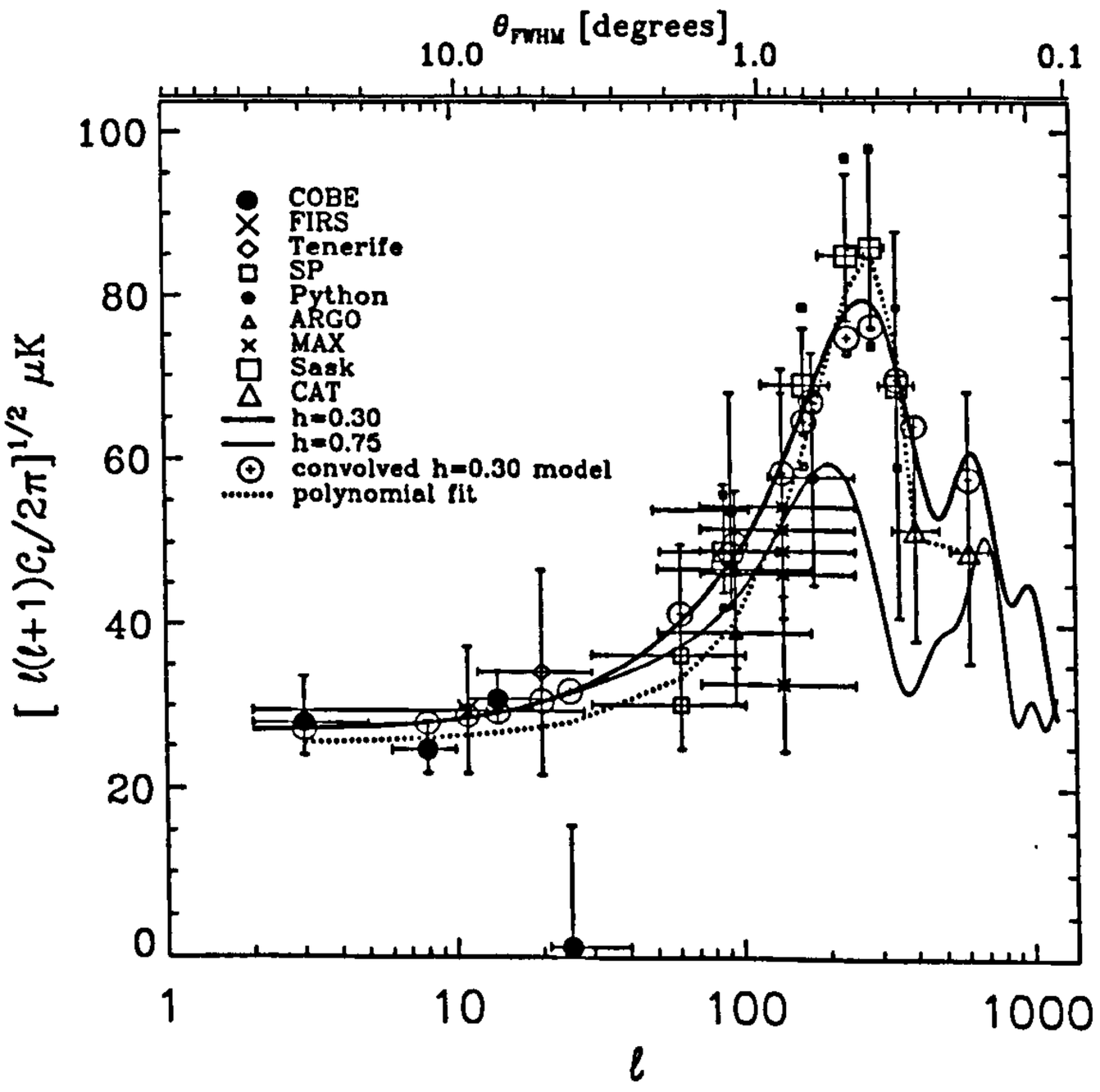

Figure 1.6: *The measured power spectrum of CBR fluctuations plotted as a function of angular scale (top) and wavenumber (bottom). The two full curves are predictions with* $\Omega_B = 0.05$, $h = 0.3$ *(thick) and* $h = 0.75$ *(thin). The dotted line is a polynomial fit. Taken from [22].*

Recently results have been published by the Supernova Cosmology Project suggesting that $\Omega_{matter} < 1$ [23]. By using type Ia supernovae as 'standard candles' the detailed characteristics of the Hubble recession of distant galaxies have been

determined. The results are consistent with $\Omega_{matter} = 0.6 \pm 0.2$ if $\Omega_\Lambda + \Omega_{matter} = 1$ or $\Omega_{matter} = 0.2 \pm 0.4$ if $\Lambda = 0$ (Fig. 1.7). If these results are correct then although Ω_{matter} is inconsistent with a closed or flat universe there is still room for a large amount of dark matter due to the low observed value of Ω_{lum} ($\lesssim 0.01$).

More recent results from the same collaboration using 40 type Ia supernovae appear to show evidence for a large non-zero cosmological constant ($\Omega_\Lambda \gtrsim 0.3$ - Fig. 1.8) however the results are still preliminary [24]. Such findings are certainly controversial [25]. Even with our current understanding of cosmology it is difficult to conceive of a 'natural' theory which is capable of giving a non-zero value for Λ consistent with this observational evidence. In all that follows Λ will therefore be taken to be identically zero, except during the inflationary epoch.

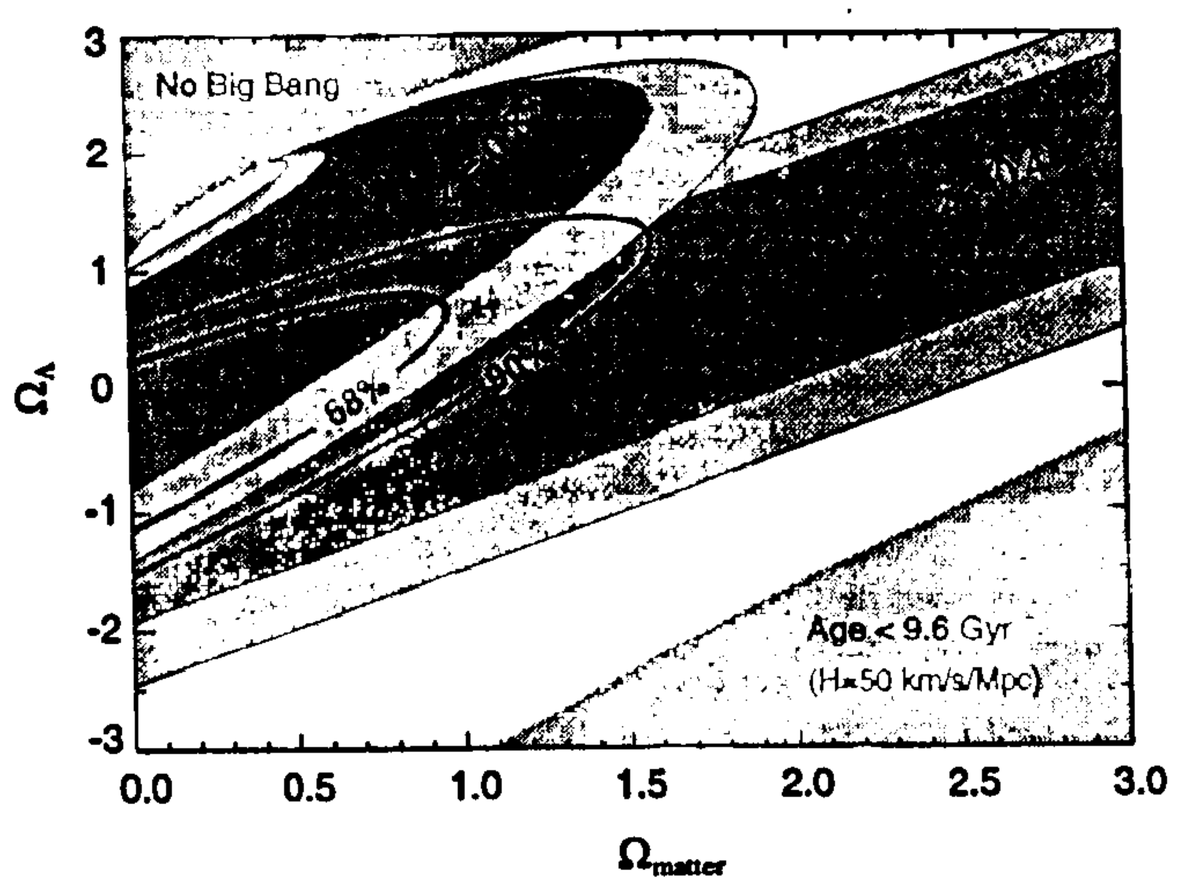

Figure 1.7: *Allowed confidence regions for Ω_Λ and Ω_{matter} from 5 type Ia SNe at $z \sim 0.4$, 1 type Ia SN at $z \sim 0.83$ and from all 6 SNe combined (open contours). Taken from [23].*

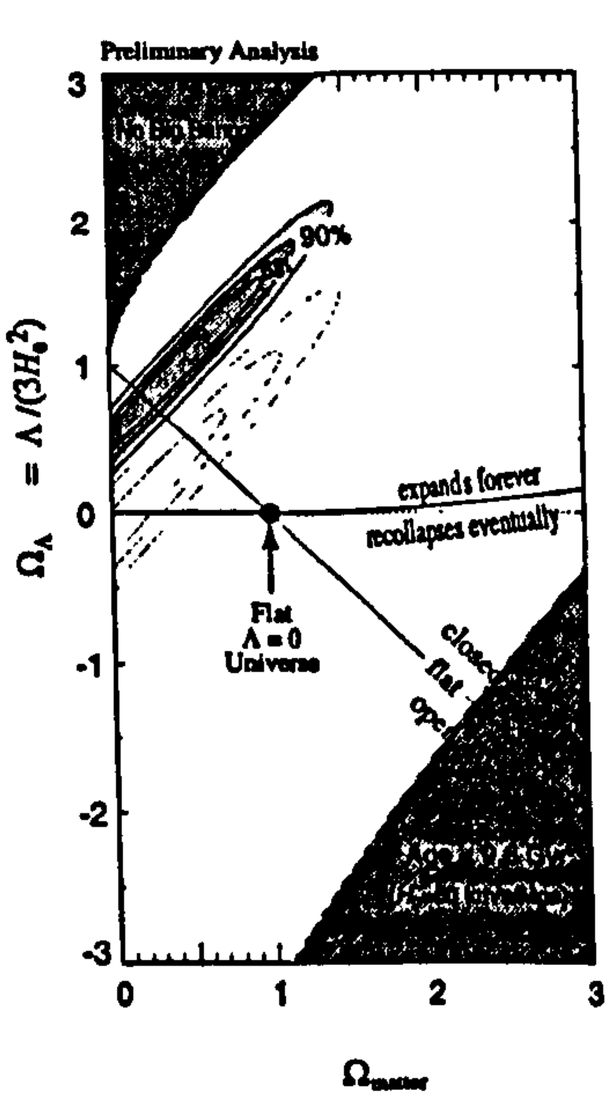

Figure 1.8: *Preliminary allowed confidence regions for Ω_Λ and Ω_{matter} from 40 type Ia SNe. The lower contours show the allowed region given a 0.2 magnitude systematic difference between the luminosities of local (recent) and distant (early) supernovae. Taken from [26].*

1.4.2 Big Bang Nucleosynthesis and Baryonic Dark Matter

Perhaps the earliest recognition of the need for dark matter was in the 19th century when Adams inferred the existence of Neptune from its gravitational effects on the orbit of Uranus. Similarly the simplest solution to the problem currently confronting us would be for the dark matter to be made up of non-luminous baryonic matter in the form of planets, low mass stars or cold gas clouds. This would be attractive in the sense that these objects are already known to exist.

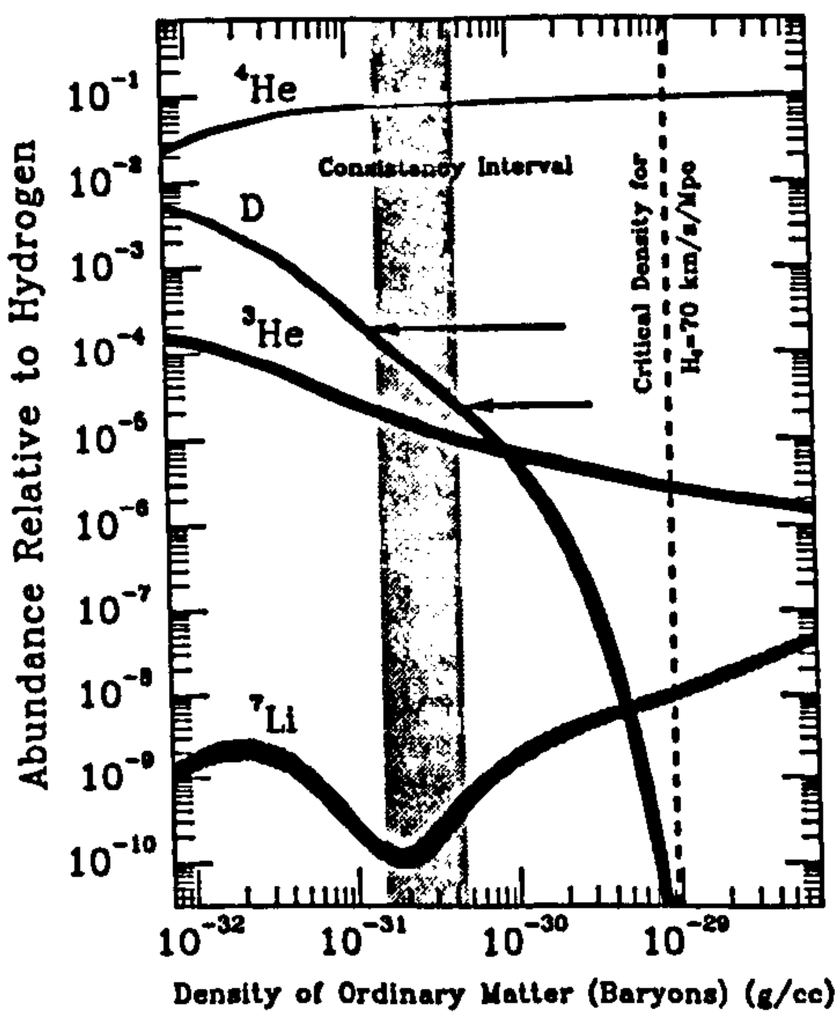

Figure 1.9: *Nucleosynthesis predictions for the abundances of the light elements. The widths of the curves represent the 2-σ uncertainties in the abundances. The predictions are only consistent with observations in the shaded region (equivalent to* $0.008 < \Omega_B h^2 < 0.024$*). Taken from [27].*

A strong constraint on the amount of baryonic material in the universe comes from the theory of Big Bang Nucleosynthesis (BBN). This relates the relative primordial abundances of the light nuclei to the ratio η of the number densities of baryons and photons. η is then related to the baryonic density parameter Ω_B by [28]

$$\eta = 2.72 \times 10^{-8} \Omega_B h^2. \tag{1.20}$$

By measuring the ratio of the abundances of various light nuclei, for example by measuring the intensities of absorption lines in extragalactic gas clouds, one can thus derive a value for $\Omega_B h^2$. Predicted abundances are plotted in Fig. 1.9 and from these the limit $0.008 < \Omega_B h^2 < 0.024$ [27] ($h \sim 0.6$) is derived. Further discussion of BBN constraints can be found in [29].

These considerations indicate that there is indeed a significant amount of baryonic dark matter, given that for galaxies $\Omega_{lum} \lesssim 0.01$. On the other hand there is undoubtedly insufficient baryonic dark matter to explain the large scale measurements of Ω and close the universe as required by FRW and inflation. The nucleosynthesis evidence is supported by the CBR and large scale structure measurements (Fig. 1.6), which appear to be incompatible with a universe dominated by baryonic dark matter. This data can also be used to constrain other models and is considered in more detail in §1.5.2.

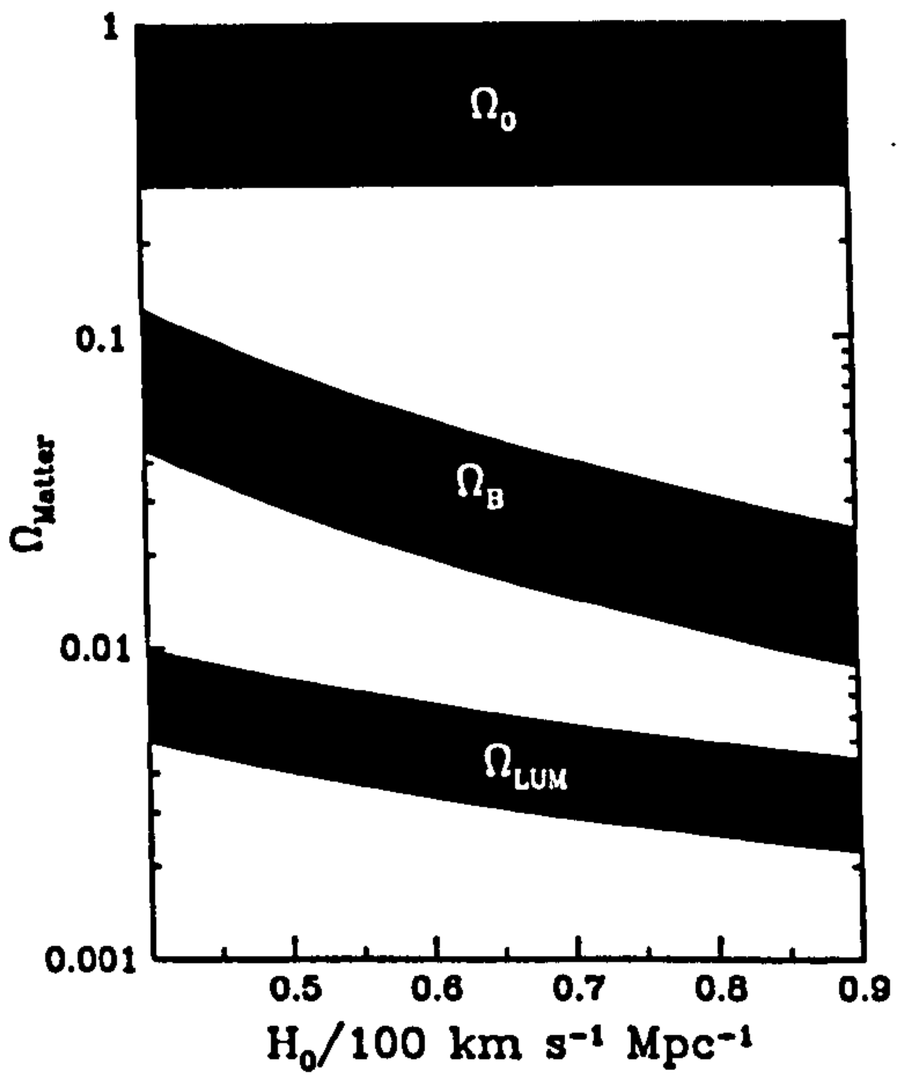

Figure 1.10: *Allowed regions for Ω as a function of H_0. The top band represents Ω_0, the middle band Ω_B (baryonic matter) and the lower band Ω_{lum} (luminous matter). Taken from [27].*

In reality there are thus *two* dark matter problems (Fig. 1.10); a baryonic dark matter problem related to the disagreement between nucleosynthesis constraints and measurements of Ω_{lum}, and a non-baryonic dark matter problem related to the disagreement between Ω_{lum} and measurements of Ω on the largest scales. Nevertheless the dark matter required to explain galactic rotation curves can (just) be explained purely in terms of the baryonic contribution, although there must remain a less densely clustered non-baryonic dark matter background.

1.5 Dark Matter Candidates and Searches

1.5.1 Baryonic Dark Matter

Dark baryons could exist in several forms. A few of these are listed in Table 1.1. There follows a brief description of the candidates based on the review of [30].

Candidate	*Mass* ($\times M_\odot$)
Snowballs	< 0.001
Brown Dwarfs	$0.001 - 0.08$
M-Dwarfs	< 0.1
White Dwarfs	IMF $\sim 0.8 - 8$
Neutron Stars	IMF > 8
Stellar Black Holes	IMF $\sim 20 - 50$
Supermassive Black Holes	$> 10^5$
Gas Clouds (Hot or Cold)	$> 10^8$

Table 1.1: *Baryonic dark matter candidates. 'IMF' stands for Initial Mass Function. Based on [30].*

'Snowballs' are cold objects consisting of condensed hydrogen of atomic density or greater. There are strong theoretical arguments to believe that snowballs cannot have masses below 10^{26} g however and recent results from microlensing (see below) [31] appear to exclude the remaining allowed mass region. Brown dwarfs are stellar objects of insufficient mass to burn hydrogen while M-dwarfs are higher mass stars which burn hydrogen but are nevertheless extremely dim. The former are well motivated theoretically and provide the main motivation for the microlensing searches currently underway. The latter are less favoured as dark matter candidates on account of the absence of significant galactic IR emission. White dwarfs form the end state of most medium mass stars but are most likely too bright to form a significant fraction of Ω_B. Neutron stars are produced by supernovae and form the end state of heavier stellar bodies. The fraction of Ω_B contained within these is also strongly limited. Supermassive black holes form without passing through a nuclear fusion stage and their density is limited by the considerable heating they produce of surrounding matter [30].

Gas clouds can be either 'hot' and atomic, or 'cold' and molecular. Large volumes of hot gas are observable by their X ray emissions and hence are largely excluded [30]. It also now appears unlikely that there is sufficient mass contained within cold

molecular clouds to make the dominant contribution to Ω_B, at least within spiral galaxies [32].

The plausibility of a significant brown dwarf component to the galactic dark matter has led several groups to begin searches for 'MACHOs' or 'MAssive Compact Halo Objects' within our galaxy. 'MACHO' is a blanket term referring to compact dark objects such as snowballs, planets, brown, M- and white dwarfs, neutron stars and stellar black holes.

In order to search for MACHOs one looks for the transient brightening of distant stars located typically in the LMC [33, 31], SMC [31] or galactic bulge [33]. This can be caused by gravitational lensing of the starlight by a dark foreground object passing through the field of view. The lensing process is governed by the Einstein field equations (Eqn. 1.2) and can be parameterised in terms of $u(t) = b/r_E$, where b is the perpendicular distance of the MACHO from the line of sight and r_E, the radius of the Einstein ring, is given by [33]

$$r_E = \sqrt{\frac{4G_N m L x(1-x)}{c^2}}. \tag{1.21}$$

Here m is the MACHO mass, L is the distance between the observer and the lensed star and Lx is the distance between the observer and the lens. If $u(t) > 1$ then a ring image characteristic of macrolensing will be formed however if $u(t) < 1$ then there will be no change in the general shape of a point image and only amplification will be observed. The degree of amplification caused by this 'microlensing' is given by [33]

$$A(t) = \frac{u^2(t)+2}{u(t)\sqrt{u^2(t)+4}}, \tag{1.22}$$

and $u(t)$ can in turn be parameterised as follows:

$$u(t) = \sqrt{u_{min}^2 + \left(\frac{2(t-t_0)}{\tau}\right)^2}, \tag{1.23}$$

where t_0 is the time of maximum amplification, $u_{min} = u(t_0)$ and τ is the event duration. The requirements that the amplification be achromatic, time symmetric and non-repeating allows events due to variable stars, supernovae etc. to be rejected. The duration τ is a linear function of r_E and hence proportional to $\sqrt{m}$. Thus sensitivity to lensing events with a wide range of durations allows limits to be set on the abundance of MACHOs with a wide range of masses.

In Fig. 1.11 are plotted the limits on dark matter halo fraction f set by the EROS collaboration [31, 34] and MACHO collaboration [33], the latter using the lensing events plotted in Fig. 1.12. Although the most probable value for f inferred

from the MACHO events is $\sim 50\%$ ($\sim 70\%$ if two dubious events are included) the errors are such that only the smallest halo fractions are disallowed and no definite statement can be made. In addition there is some suggestion that there may be a tidal flow or small dwarf galaxy in the direction of the LMC thereby biasing the results in favour of high values of Ω [33]. There is consequently still room for a significant non-baryonic contribution to the galactic halo.

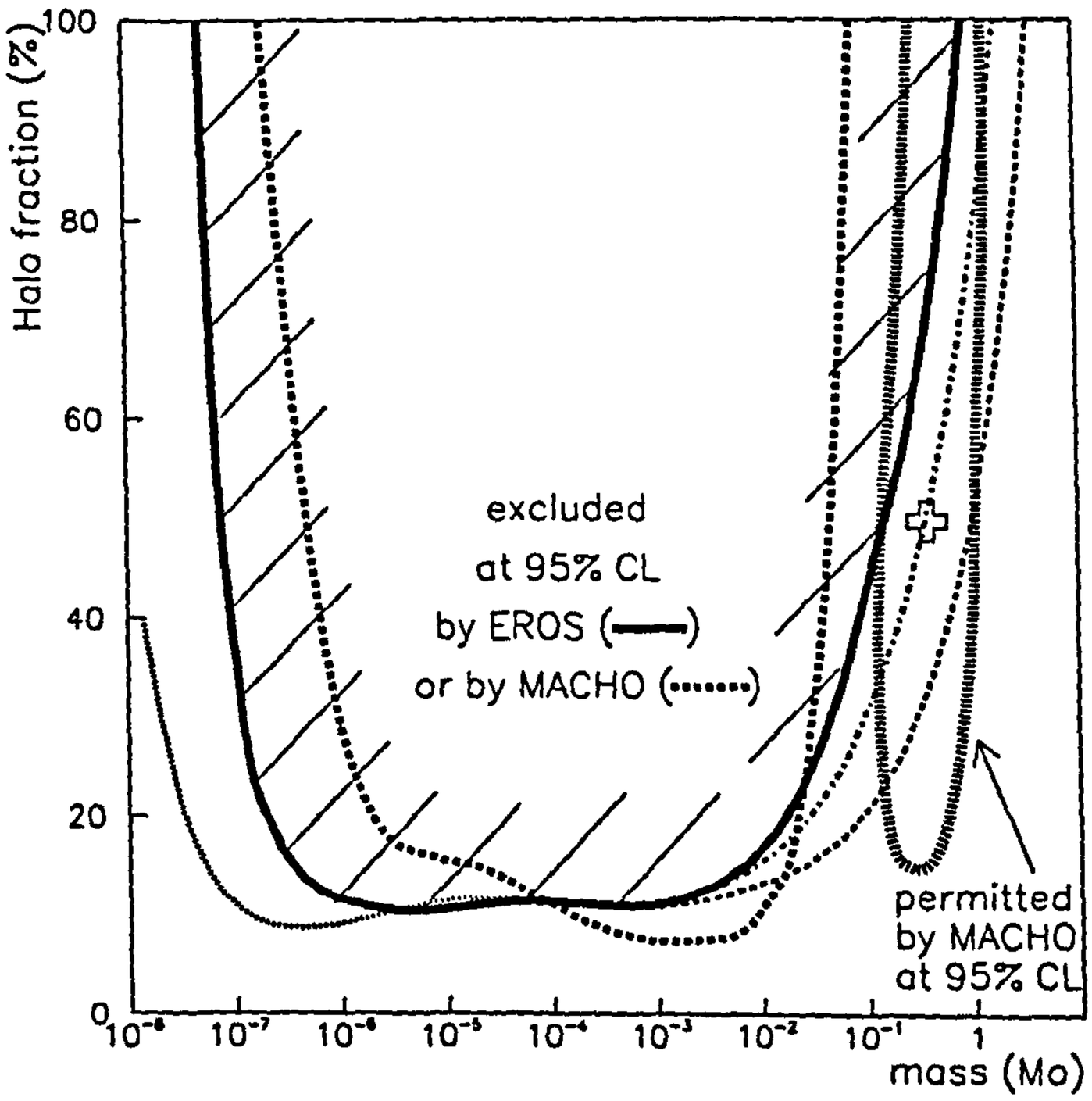

Figure 1.11: *Exclusion diagram for MACHO mass and halo fraction from MACHO and EROS results. The lefthand dotted line is the EROS limit when corrections for systematics are not taken into account. The dotted and dot-dashed lines are the EROS limits assuming that one or two of their candidate events are due to MACHOs. Taken from [34].*

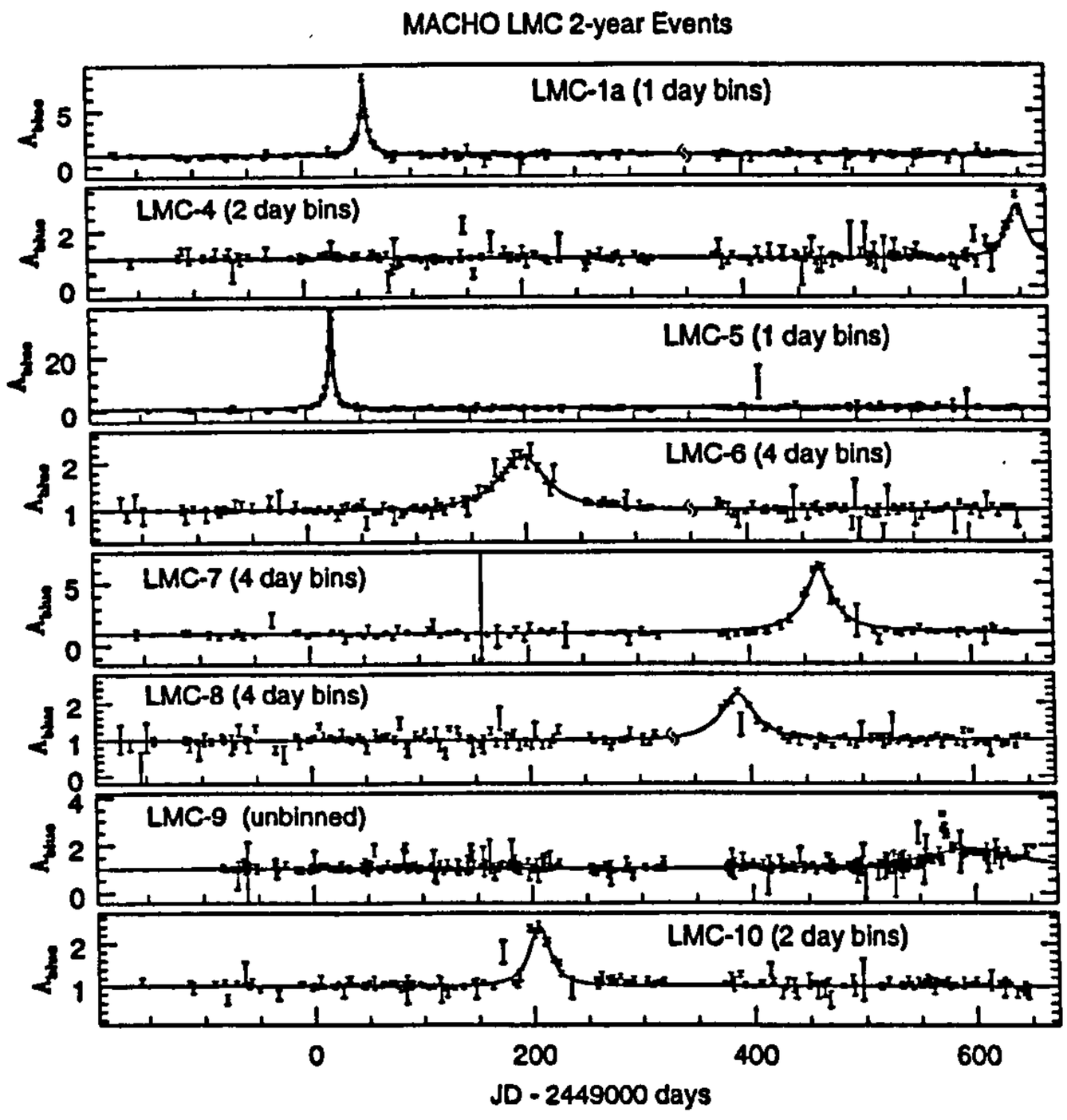

Figure 1.12: *The light curves of the eight MACHO LMC microlensing events. All errors are 1-σ. Taken from [33].*

1.5.2 Non-Baryonic Dark Matter

General Introduction

In most cases non-baryonic dark matter candidates were created in the early universe in thermal equilibrium with the CBR. As the universe expanded the interaction rate of the dark matter particles fell below the expansion rate and thermal equilibrium was lost. If the dark matter particles were relativistic at this point of 'freeze out' then they are referred to as 'Hot Dark Matter' (HDM). HDM particles would have had a high average momentum at freeze out and would therefore have clustered gravitationally only on the largest scales. This HDM density field would initially have washed out any clustering by baryonic matter on small scales and hence would have led to the formation of luminous structure in a 'top down' manner, with small scale structure forming after the structure on larger scales. Computer simulations of the formation of large scale structure in this way [35] are in conflict with the IRAS large scale structure maps (see below). Similarly measurements of the temperature fluctuations in the CBR [21, 36], which in turn map the density perturbations in

the early universe, indicate conflict with the predictions of pure HDM. Finally the phase space occupied by HDM makes it incompatible with the discovery of dark matter on small scales in dwarf spiral galaxies [37]. This evidence makes it unlikely that pure HDM can provide a solution to the non-baryonic dark matter problem.

Dark matter particles which were non-relativistic at freeze out are by contrast referred to as 'Cold Dark Matter' (CDM). On account of their low average momenta they would have clustered much more strongly in the early universe and would have first begun forming structure on small scales, rather like baryonic matter. This provides much better agreement with the IRAS [38] and CBR survey data (Fig. 1.13) than pure HDM. There have also been a number of mixed dark matter scenarios suggested in order to improve this fit [27], most notably 'νCDM' which consists of a mixture of 30% HDM in the form of low mass relic neutrinos (see below) and 70% CDM. A 'tilting' of the initial CBR power spectrum away from the Harrison-Zel'dovich power law model also gives a good fit ('Tilted Dark Matter' or TDM) as does a mixture of CDM and a non-zero cosmological constant (ΛCDM), although it is difficult to reconcile this last possibility with fine tuning arguments (§1.4.1).

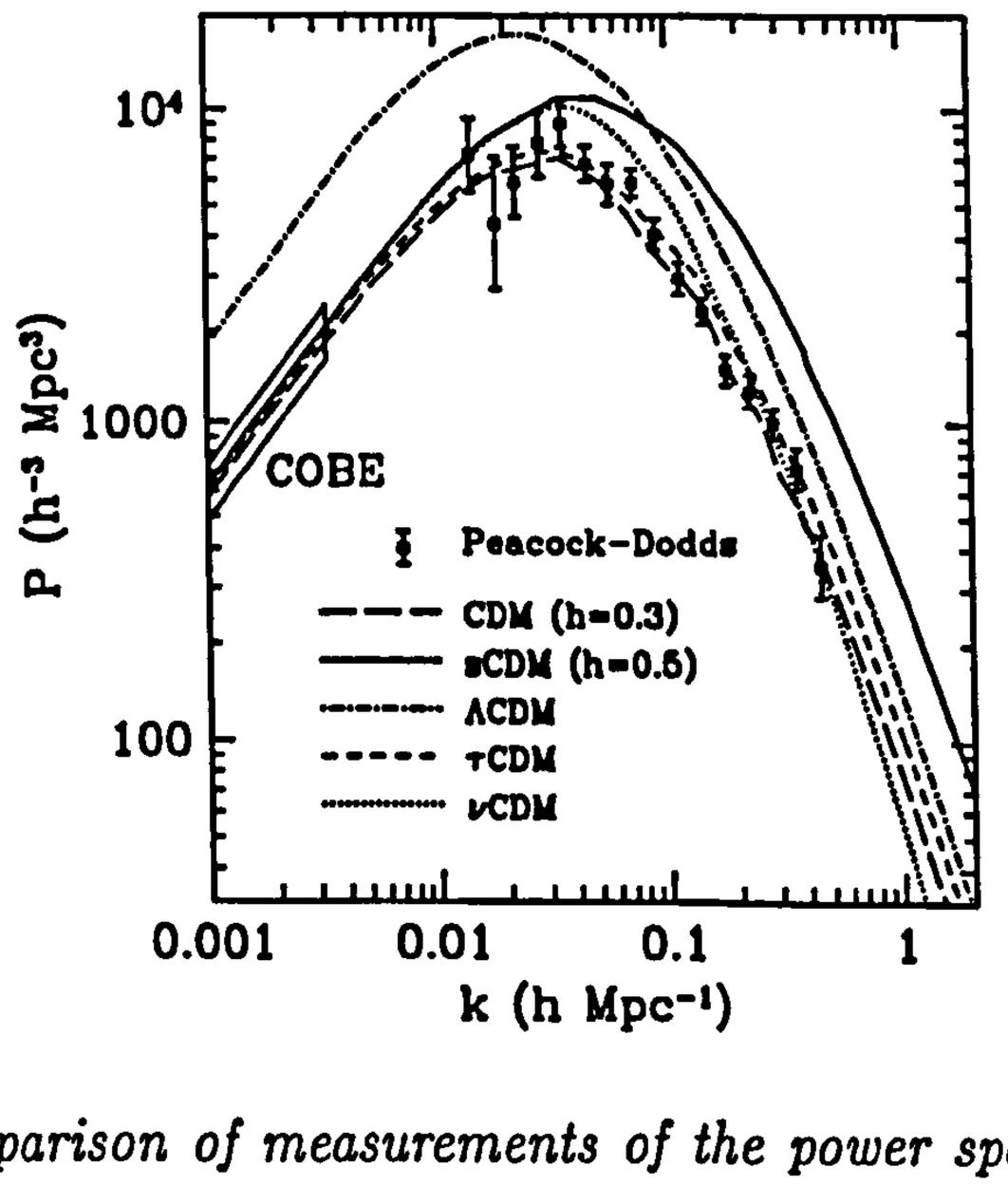

Figure 1.13: *A comparison of measurements of the power spectrum of large scale structure with different dark matter models. The box is from COBE [39] CBR measurements while the data points are from galaxy redshift surveys as analysed in [40]. For the definitions of the models see text. Taken from [41].*

Many potential non-baryonic dark matter candidates have been suggested. A far from exhaustive list is given in Table 1.2. Some of the most promising candidates

will now be considered in more detail.

Candidate	*Mass*	*Abundance* cm^{-3}
Axion	$< 10^{-3}$ eV/c^2	$\sim 10^9$
Light LH Neutrino	< 91.5 eV/c^2	~ 100
Gravitino	$\sim$keV/c^2	~ 10
Neutralino	~ 100 GeV/c^2	10^{-5}
Axino	~ 100 GeV/c^2	10^{-5}
Heavy Neutrino	$\gtrsim 100$ GeV/c^2	$\sim 10^{-5}$
Cryptons etc.	$\sim 10^{12}$ GeV/c^2	$\sim 10^{-18}$
Magnetic Monopole	$\sim 10^{16}$ GeV/c^2	$\sim 10^{-21}$
Quark Nugget	$\sim 10^{15}$ g	$\sim 10^{-44}$
Primordial BH	$\gtrsim 10^{15}$ g	$\lesssim 10^{-44}$

Table 1.2: *Non-baryonic dark matter candidates. Heavy particles interacting with baryonic matter via the electroweak gauge bosons ($W^{\pm}$, Z^0, h) are collectively referred to as 'WIMPs' ('Weakly Interacting Massive Particles'). Neutralinos, axinos and heavy neutrinos fall into this category. This table is based on Table 9.1 in [2].*

Hot Dark Matter and Neutrinos

The leading candidates for HDM are low mass relic neutrinos. All three known species of light lefthanded neutrino were produced abundantly in the Big Bang and consequently at present there is a relic neutrino number density throughout space $\sim 1.12 \times 10^8$ m^{-3} [5]. Should these neutrinos have average mass m_ν this number density contributes an amount [2]

$$\Omega_\nu = \sum_{i=1}^{3} \frac{m_{\nu_i}(\mathrm{eV/c^2})}{91.5h^2} \tag{1.24}$$

to the overall density parameter of the universe Ω_0. The requirement that these neutrinos do not over close the universe consequently places a strict upper bound on any of their masses of $m_\nu < 91.5$ eV/c^2 (the Cowsik-McClelland Bound [42]).

By construction the renormalisation structure of the standard model of particle physics (§2.2) incorporates only mass-less neutrinos and so within the standard model m_ν is identically zero. Within many extensions to the standard model however there are mechanisms for giving the neutrinos mass, most notably the 'see-saw' mechanism [43] embodied within SO(10) GUT models. Here it is the very large

mass of a heavy righthanded Majorana neutrino which generates the very small masses of the known lefthanded neutrinos through virtual loop effects. In these models the neutrinos acquire a mass hierarchy equal to that of the squares of the masses of the corresponding charged leptons or up type quarks [43]:

$$m_\nu = \frac{m_{l/q}^2}{M_R}, \tag{1.25}$$

where $m_{l/q}$ is the appropriate lepton / quark mass and M_R is the righthanded neutrino mass (assumed degenerate for all generations). The electron and muon neutrinos invariably obtain masses too small to be of cosmological interest ($< 10^{-8}$ eV/c^2 and $< 10^{-3}$ eV/c^2 respectively) however the tau neutrino may have a mass as high as 30 eV/c^2 [43]. In this case ν_τ can become a viable candidate for the HDM in models such as νCDM. It is also interesting to note that in this framework the heavy ($M > 10^6$ TeV/c^2) righthanded neutrino generating the lefthanded masses could act as the CDM candidate required to improve the fits to the COBE and IRAS data. The mass of such a relic righthanded neutrino is constrained by over closure arguments only to be greater than 5 GeV/c^2 (2 GeV/c^2 for Dirac neutrinos; the Lee-Weinberg bound [2, 44]). Heavy Majorana or Dirac neutrinos with *standard model* couplings are excluded for almost all masses by a combination of cosmological arguments, constraints from LEP and null results from direct and indirect searches [45, 46].

At present it is impossible to detect relic neutrinos or measure their masses although suggestions for detectors have been made [47]. Instead the masses must be inferred through techniques which use neutrinos produced by sources other than the Big Bang. The principal technique is to search for oscillations between different neutrino flavour eigenstates caused by mixing between different mass eigenstates. The motivation for this has come from an observed deficit in the number of neutrinos coming from production processes occurring both in the sun (β decay and fusion) and in the atmosphere (decay of π and μ secondaries from cosmic ray interactions). It is thought that the underlying cause of this deficit is that neutrinos of one flavour are oscillating into neutrinos of other flavours which are invisible to the detectors [43]. The solar neutrino anomaly could be resolved by oscillations of the form $\bar{\nu}_e - \bar{\nu}_\mu$ and the atmospheric neutrino anomaly by oscillations of the form $\nu_\mu - \nu_\tau$. In each case the probability of oscillation is given by [43]

$$P_{osc} = \sin^2 2\theta . \sin^2 \left(\frac{1.267 \Delta m^2 L}{E} \right), \tag{1.26}$$

where θ is the neutrino mixing angle, L (km) is the oscillation length or 'baseline',

Δm^2 ($(\mathrm{eV/c^2})^2$) is the difference of the squares of the masses of the mass eigenstates and E (GeV) is the neutrino energy.

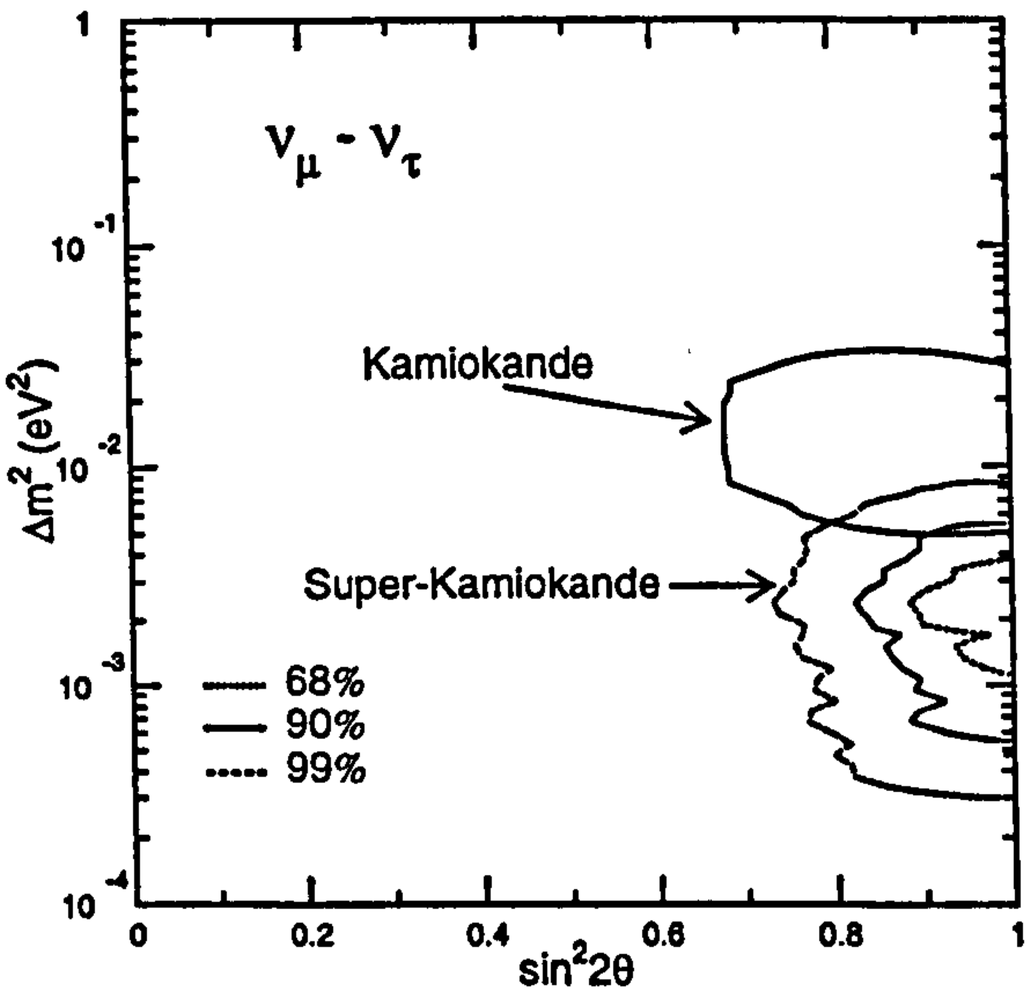

Figure 1.14: *The allowed confidence regions (68%,90%,99%) for* $\sin^2 2\theta$ *and* Δm^2 *for* $\nu_\mu - \nu_\tau$ *oscillations from 33 kt.yrs data from Super-Kamiokande. The thin line is the 90% region from the Kamiokande data. Taken from [48].*

The dependence of the oscillation probability upon $\Delta m^2 L/E$ makes measurements with a specific baseline and neutrino energy sensitive to only a certain range of $\Delta m^2 - \sin^2(2\theta)$ parameter space. The atmospheric neutrino anomaly, recently confirmed by the latest results from the Super-Kamiokande experiment (Fig. 1.14), is most likely due to a muon neutrino / tau neutrino $\Delta m^2 \sim 2.2 \times 10^{-3}$ $(\mathrm{eV/c^2})^2$ with near maximal mixing such that $\sin^2(2\theta) > 0.8$ [48]. The solar neutrino anomaly meanwhile naïvely admits 'vacuum oscillation' solutions with electron antineutrino / muon antineutrino $\Delta m^2 \sim 10^{-10}$ $(\mathrm{eV/c^2})^2$ and once again near maximal mixing. In the solar case there also exists the possibility of a resonant enhancement in the oscillation probability as the neutrinos pass through the electron rich solar plasma. This process is known as the 'Mikheyev-Smirnov-Wolfenstein' (MSW) effect [49, 50] and leads to solutions with electron antineutrino / muon antineutrino $\Delta m^2 \sim 10^{-6}$ $(\mathrm{eV/c^2})^2$ and low mixing angles. These solutions are however disfavoured by the latest data from Super-Kamiokande [48]. Further data on this question should become available in the near future from both the Super-Kamiokande and SNO collaborations [51] but it appears that these results rule out a significant contribution to Ω from standard model neutrinos.

Owing to the low values of Δm^2 and the corresponding long baselines which are required, the allowed region for solar neutrino oscillations is probably inaccessible to experiments using terrestrial sources of neutrinos. In order to understand the atmospheric neutrino anomaly however several terrestrial experiments have been conducted, typically using neutrinos produced by accelerators or commercial fission reactors [43]. The LSND collaboration (baseline $\sim$ 30 m [52]) claims to see neutrino oscillations of the form $\bar{\nu}_\mu - \bar{\nu}_e$ for $\Delta m^2 > 4 \times 10^{-2}$ (eV/c^2)^2 (all mixings) but the claim is disputed by the KARMEN collaboration [53] whose detector is sensitive to roughly the same regions of parameter space. Further work is needed to resolve this question. All other such experiments have reported null results and further progress will probably require the construction of 'long baseline' experiments such as MINOS (baseline 730 km [54]) which are designed to probe directly the regions of parameter space suggested by the atmospheric anomaly [43].

Cold Dark Matter

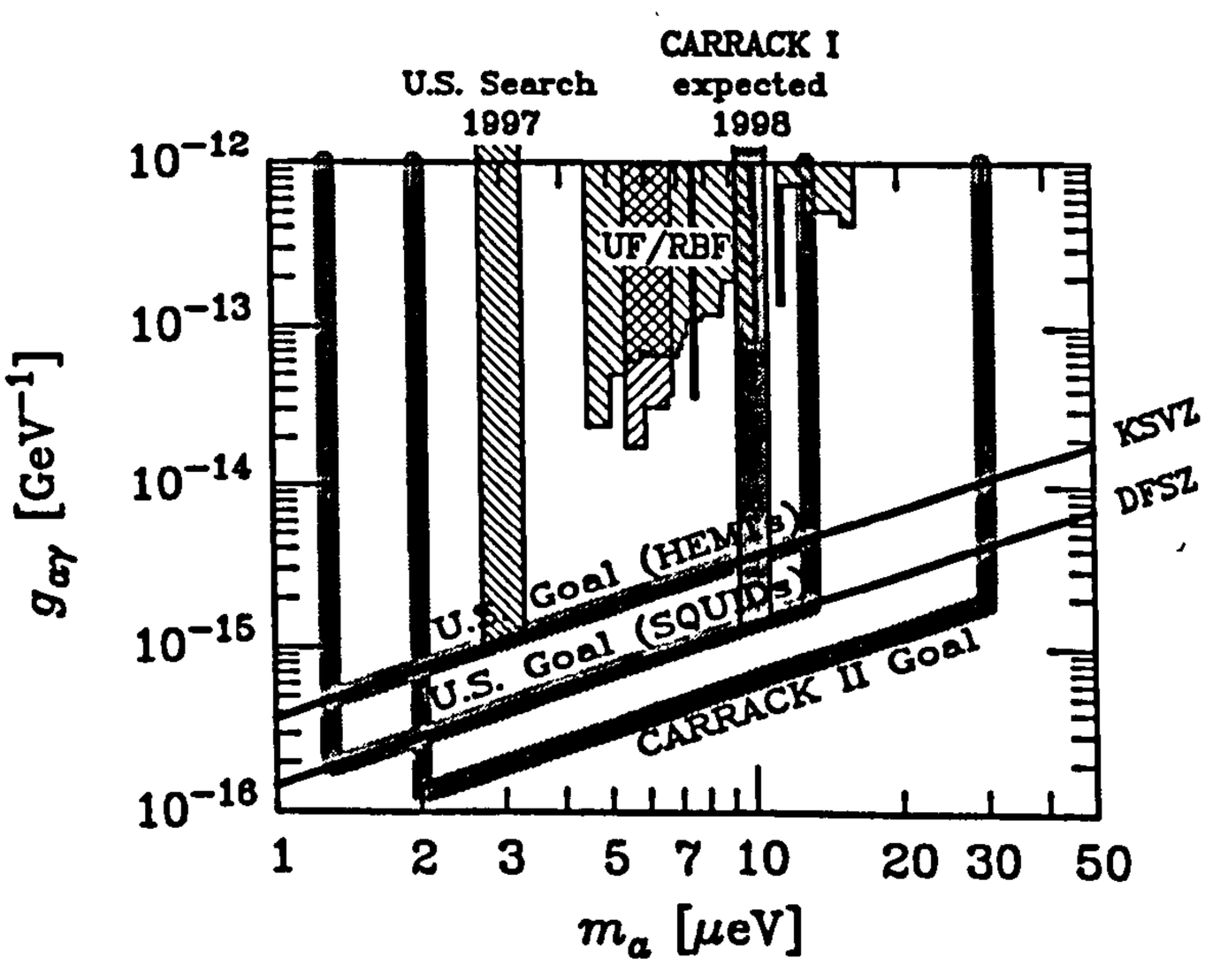

Figure 1.15: *Compilation of experimental limits on axion mass and couplings. Along the x axis is plotted axion mass, and along the y axis the axion-photon coupling. Experiments are University of Florida (UF), Rochester-Brookhaven-Fermilab (RBF), joint U.S. search and Tokyo (Carrack). For references see e.g. [55, 56]. Taken from [56].*

Null results from searches for anomalously heavy protons indicate that stable non-baryonic CDM particles must be colourless and uncharged [57]. There are many

theoretically postulated particles which fall into this category. The leading candidates will now be discussed.

One prominent candidate is the axion, a Higgs like scalar boson proposed to solve the 'strong CP' problem. Generic $SU(3)_C$ QCD models incorporate a phase, θ_{QCD}, which leads to CP violation in strong interactions [55]. Phenomenologically this is unacceptable and so the axion was postulated to dynamically drive this phase to zero. Unlike other CDM candidates the axion would not have been produced in thermal equilibrium with the CBR in the Big Bang and its primary production mechanism would have been through the collapse of topological defects. Its mass is tightly constrained by both accelerator searches and astrophysical arguments, in particular the time spectrum of neutrinos from SN1987a [56]. A small cosmologically interesting mass window (10^{-6} eV/c^2 $< m_a <$ 10^{-3} eV/c^2) remains and this is currently being investigated by several experiments searching for resonant conversion of relic axions to microwave photons in a strong B field (for a review see [55]). No signal has been seen as yet although sensitivity to the axion mass m_a and its coupling to photons $g_{a\gamma}$ is improving rapidly (Fig. 1.15).

Another non-baryonic CDM candidate currently favoured by theorists is the super heavy ($m \sim 10^{12}$ GeV/c^2) 'crypton' derived from certain higher dimensional 'superstring' theories (§2.3). The decay of these particles may explain the observed excess of ultra high energy cosmic rays above the GKZ cut off [58] and hence there is additional motivation to consider them seriously. Indirect detection of these particles will require the use of large extensive air shower arrays [58].

The 'best bet' non-baryonic CDM candidates are generally thought to be 'WIMPs' (Weakly Interacting Massive Particles). These can be defined as heavy relics which interact with baryonic matter via the electroweak gauge bosons. The massive righthanded neutrinos discussed previously fall into this category however the most favoured WIMPs are those predicted to exist by the theory of supersymmetry (SUSY). In many SUSY models the Lightest Supersymmetric Particle (LSP) is absolutely stable and could therefore constitute the dark matter were it to have been produced in sufficient quantities in the Big Bang. Depending upon the model the LSP can be the neutralino (the SUSY partner of the neutral standard model bosons), the axino (the SUSY partner of the axion) the gravitino (the SUSY partner of the graviton) or possibly some other neutral SUSY particle. The neutralino in particular provides a WIMP candidate with just the right properties to solve the non-baryonic dark matter problem [59]. The particle physics underlying SUSY dark matter will be discussed in more detail in the next chapter.

Evidence for WIMP dark matter can be sought in several ways. Direct evidence

could be gained by searching for interactions with baryonic detector materials. Relic WIMPs may occasionally couple to an atomic nucleus in these materials and scatter elastically, causing the nucleus to recoil. If this nuclear recoil can be detected then it is possible to infer the presence of the WIMP and hence the dark matter. Direct searches of this kind for WIMP dark matter form the basis for much of this thesis and the detailed theory underlying the technique will be outlined in §3.

Indirect detection experiments are also possible and these typically look for the products of the coannihilation of WIMPs trapped in the gravitational potentials of the earth, sun or galaxy [46]. These searches are sensitive to all types of WIMP and they have been used in particular to exclude a large region of Dirac masses for relic righthanded neutrinos.

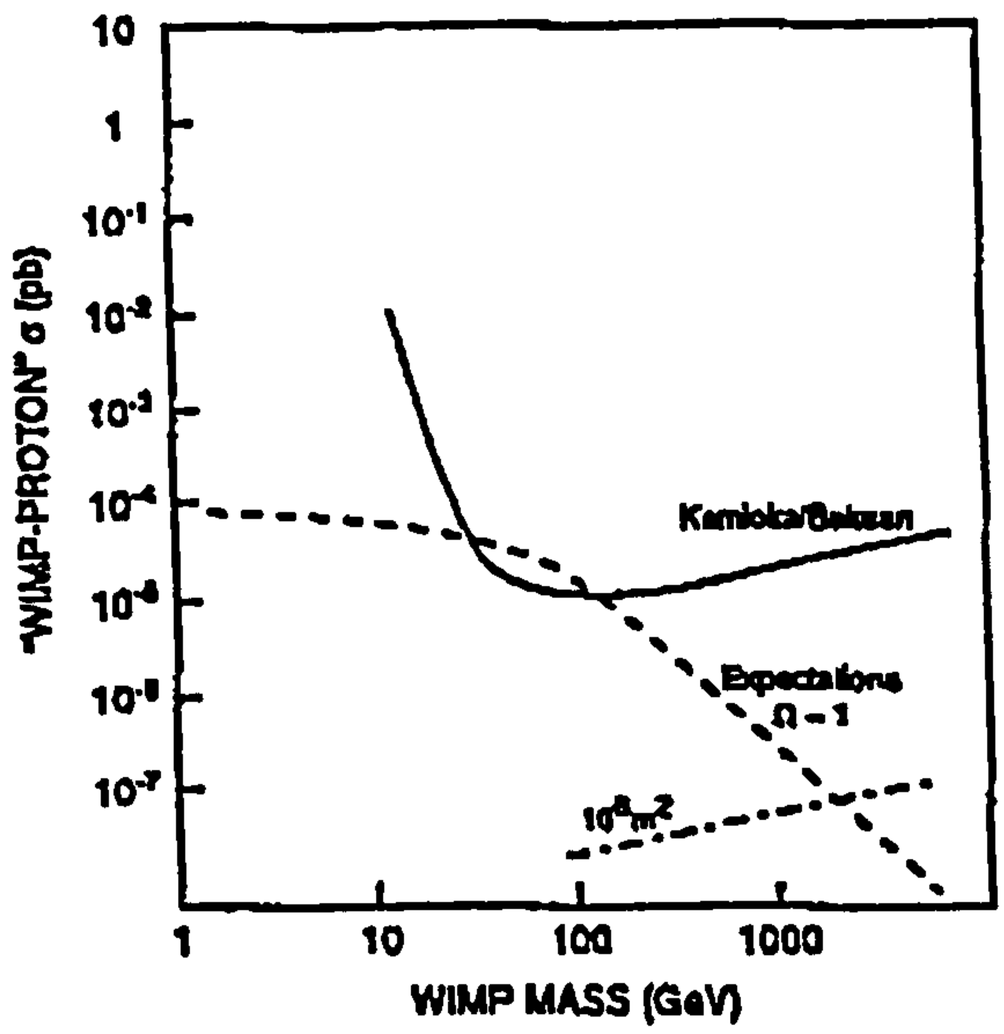

Figure 1.16: *Indirect limits on spin dependent WIMP-nucleon couplings derived from indirect dark matter searches using large volume neutrino detectors. The full line is the combined limit from the Baksan [60] and Kamiokande [61] experiments; the dashed line is an order of magnitude estimate given* Ω *equal to unity. The dot-dashed line is the expected limit from a* 10^6 m^2 *detector. Adapted from [62].*

The most promising indirect technique is to search for neutrinos coming from annihilations within the earth or sun. These searches require the use of large volume, low energy threshold detectors [62]. The detectors are used to look for the up going muons produced when neutrinos interact in the rock beneath the detector. The limits set in this way are extremely stringent and in particular the limits on spin dependent WIMP-nucleon interactions (Fig. 1.16) are similar or superior to the

limits set by direct search experiments [62]. The indirect limits are however more model dependent than the direct search limits and so comparison is difficult.

Indirect searches are also being performed using other techniques. Searches for anomalously large quantities of antimatter in space using balloon or satellite borne spectrometers are sensitive to WIMP annihilation in the galactic halo, since this would be one source of this antimatter [15]. Searches for a diffuse gamma ray background within the galaxy are similarly sensitive to such annihilation processes [15].

1.6 Conclusions

Much theoretical and observational evidence has been discovered for the existence of dark matter throughout the universe. Big bang nucleosynthesis places strong constraints on the fraction of this dark matter which can be baryonic in form and thus non-baryonic scenarios are particularly favoured. The heavy 'cold dark matter' particles which are required in this case are predicted to exist by many theories extending particle physics beyond the 'standard model'. Direct and indirect searches are being carried out for evidence for the existence of these particles.

Chapter 2

Supersymmetric Dark Matter

2.1 Introduction

This chapter gives an overview of the theory underlying models of supersymmetric dark matter. The chapter will begin with a brief account of the standard model of particle physics (§2.2). This is by itself an enormous subject; for a more detailed account see e.g. [63, 64, 65, 66]. The section which follows (§2.3) gives a brief introduction to supersymmetry theory and here again the standard review articles such as [46, 67, 68, 69] should be consulted for more information. There then follows a description of the various dark matter candidates provided by supersymmetry theory (§2.4). The chapter concludes with a discussion of the various constraints placed on the mass of the most favoured candidate, the neutralino, by collider experiments (§2.5).

2.2 The Standard Model

2.2.1 The Standard Model Lagrangian

Our current knowledge of the behaviour of matter on the smallest scales is summarised by the so called 'Standard Model' (SM) of particle physics. This model may be derived by considering the most general symmetries obeyed by the forces of nature and then expressing these symmetries in the language of group theory. Given a force which is invariant under a gauge transformation with symmetry group $\mathcal{G}$ and which describes matter fields transforming under a representation $\mathcal{R}$ of $\mathcal{G}$, it is possible to derive the appropriate Lagrangian density (and hence equations of motion) simply by writing down all those terms which are invariant under $\mathcal{G}$ and satisfy the requirements of perturbative renormalisability [70]. The last requirement

ensures that perturbative calculations are finite and therefore that the model has predictive power. Non-perturbative models may also be constructed but they are in general much more difficult to work with.

All of the small scale physics discovered up to this point (with the possible exception of some neutrino physics - §1.5.2) has been found to possess the symmetries of the group $SU(3)_C \times SU(2)_L \times U(1)_Y$. Of the observed matter fields only the six quarks (u,d,c,s,t,b) couple to the gauge fields described by the $SU(3)_C$ symmetry, transforming as 'colour' triplets of Dirac fermions. The $SU(2)_L$ symmetry describes gauge fields which couple only to the lefthanded fermions (quarks and leptons), which are arranged in weak isospin doublets (e.g. (ν_L, e_L^-) or (u_L, d_L)). The $U(1)_Y$ symmetry describes gauge fields coupling to fermions possessing weak hypercharge Y (the charged fermions), arranged in $SU(2)_Y$ singlets. Righthanded neutrinos do not couple to any of the above fields and so cannot be included within the standard model framework. Some larger symmetry groups containing $SU(3)_C \times SU(2)_L \times U(1)_Y$ as a subgroup contain extra gauge fields coupling to uncharged righthanded fermions and hence these groups can describe the interactions of righthanded neutrinos. Such interactions can lead to non-zero masses for the lefthanded SM neutrinos (§1.5.2).

Consideration of the above symmetry group and matter field representations allows the following standard model Lagrangian (density) to be written down [71]:

$$\begin{aligned}
\mathcal{L}_{SM} \;=\; & -\frac{1}{4}W_{\mu\nu}W^{\mu\nu} - \frac{1}{4}B_{\mu\nu}B^{\mu\nu} \\
& + \bar{L}\gamma^{\mu}\left(i\partial_{\mu} - \frac{1}{2}g\underline{\tau}.\underline{W}_{\mu} - \frac{1}{2}g'YB_{\mu}\right)L + \bar{R}\gamma^{\mu}\left(i\partial_{\mu} - \frac{1}{2}g'YB_{\mu}\right)R \\
& + \left|\left(i\partial_{\mu} - \frac{1}{2}g\underline{\tau}.\underline{W}_{\mu} - \frac{1}{2}g'YB_{\mu}\right)\phi\right|^2 - V(\phi) \\
& - \left(G_1\bar{L}\phi R + G_2\bar{L}\phi_c R + h.c.\right) \\
& - \bar{q}_j\left(i\gamma^{\mu}\partial_{\mu} - m\right)q_j - g''\left(\bar{q}\gamma^{\mu}T_a q\right)G^a_{\mu\nu} - \frac{1}{4}G^a_{\mu\nu}G^{\mu\nu}_a
\end{aligned} \tag{2.1}$$

In this equation the first line contains kinetic terms describing the free motion of the $SU(2)_L \times U(1)_Y$ 'electroweak' gauge bosons; the $W^{\pm}$, the Z^0 and the photon. The second line describes the interactions of these bosons while the third and fourth lines describe the spontaneous symmetry breaking process (the Higgs mechanism) which gives mass to both bosons and fermions. The final line is derived from the $SU(3)_C$ gauge symmetry which describes QCD, the theory of the 'strong' interactions. The term $-\frac{1}{4}G^a_{\mu\nu}G^{\mu\nu}_a$ is a kinetic term describing the free motion of the gluons, the $SU(3)_C$ gauge bosons. A more detailed explanation of the standard model Lagrangian together with definitions of the various parameters and fields can be found in standard text books such as [63, 64, 65, 66].

The $SU(3)_C$ and $SU(2)_L$ symmetry groups described by Eqn. 2.1 are inherently non-Abelian. Terms may be written down in $\mathcal{L}_{SM}$ which are proportional to the commutators of the gauge fields and which consequently describe interactions between these fields. The non-zero values of the commutators of the $SU(3)_C$ and $SU(2)_L$ gauge fields lead in this way to self couplings for the QCD and electroweak gauge bosons. This has a particularly marked effect in the $SU(3)_C$ sector where the QCD coupling strength α_s increases significantly ('runs') towards low energy. This causes low energy QCD interactions between the quarks to be characterised by a web of strongly self coupling gluons. This is believed to be the origin of the 'confinement' which causes all quarks and gluons to be bound in states with no net QCD (colour) charge [66].

The existence of the Higgs sector in Eqn. 2.1 was proposed in order to account for the observed masses of the $W^{\pm}$ and Z^0 gauge bosons. The requirement of perturbative renormalisability forces their masses to be identically zero at tree level, however it was found that by introducing a scalar field (the Higgs field) with non-zero vacuum expectation value (v.e.v.) this problem could be circumvented [64]. The quanta of the Higgs field, the Higgs bosons, couple to the gauge bosons at one loop and higher orders and thereby give them effective masses [59] (Fig. 2.1).

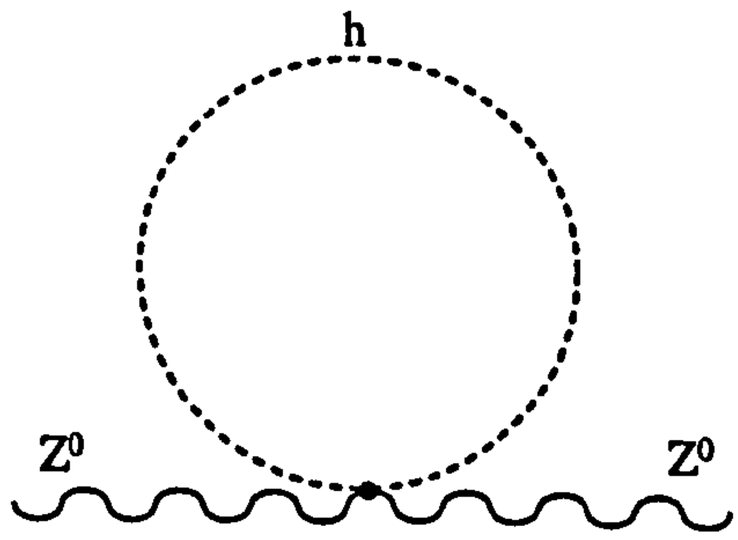

Figure 2.1: *A loop diagram contributing to the Higgs mechanism giving masses to the gauge bosons (in this case the Z^0).*

2.2.2 Deficiencies in the Standard Model

As it stands the standard model of particle physics has been supremely successful at explaining almost everything observed in particle physics experiments. It does contain deficiencies however and must only be regarded as an effective model at the energies currently accessible. In particular it does not explain the origins of the 19

free parameters which appear in the standard model Lagrangian (Eqn. 2.1). One would expect the values of these parameters to be determined by new physics at some higher energy at which the standard model breaks down. Any candidate for a 'Theory of Everything' (TOE) must also include gravity as described by the Einstein field equations (Eqn. 1.2). The standard model clearly does not fulfill this criterion and neither does any other finite renormalisable quantum field theory [66].

One other deficiency found within the standard model is that the mass of the Higgs scalar cannot be protected from large corrections arising from its coupling to virtual fermionic loops (Fig. 2.2). These cause its mass to diverge quadratically as the renormalisation scale of the theory is raised to the point at which new physics comes into play (assumed to be the GUT scale) [59]. This is clearly a problem if one wishes the standard model to be finite and divergence free.

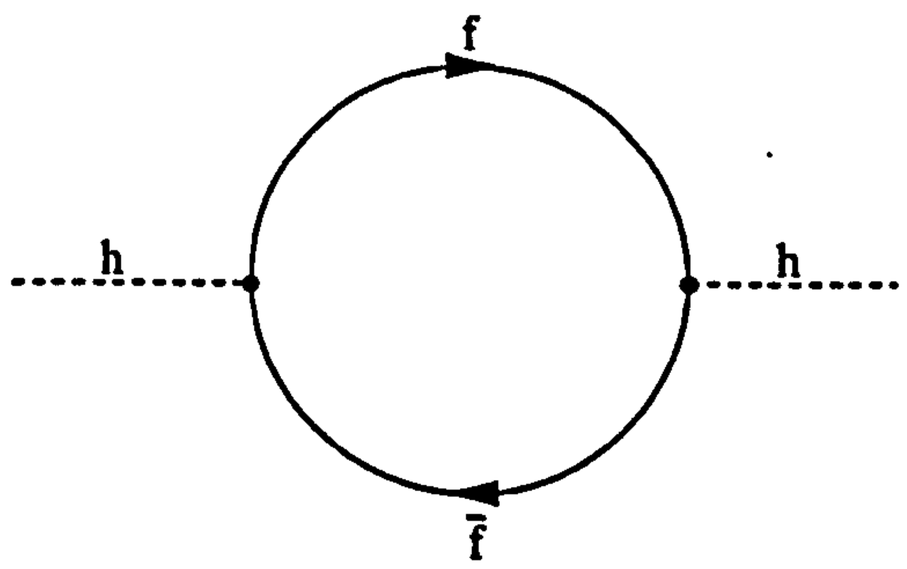

Figure 2.2: *A fermionic loop contributing to the quadratic divergence of the Higgs mass in the standard model.*

This phenomenon of divergent scalar masses is at the heart of the standard model gauge 'hierarchy' problem. This arises from the fact that the energy scale associated with the electroweak interaction is $\mathcal{O}(100\ \text{GeV})$ while the GUT scale is $\mathcal{O}(10^{15}\ \text{GeV})$. Since one expects low energy (electroweak scale) physics to be derivable from physics at higher energies it is desirable for these energy scales to be somehow related. Such a relationship or 'hierarchy' is extremely difficult to establish however, since higher order effects involving scalar fields with divergent masses always conspire to drive the masses of the electroweak bosons to the GUT scale, even if the required electroweak-GUT scale hierarchy is imposed order by order [67]. A grand unified theory avoiding this problem would require impossible degrees of fine tuning of the initial parameters and this is believed to be unphysical [67].

There are several proposals to remove these inconsistencies [59, 72] but the most likely from both an experimental and theoretical point of view is thought to be

supersymmetry.

2.3 Supersymmetry

2.3.1 Motivations for Supersymmetry

Supersymmetry (SUSY) is a symmetry connecting bosons and fermions [46, 67, 68, 69]. The effect of the four Majorana spin 1/2 hermitian generators Q_α of the simplest SUSY transformations is to interchange fermionic (F) and bosonic (B) spin states [67]:

$$Q_\alpha|F>=|B>, \qquad Q_\alpha|B>=|F>. \tag{2.2}$$

Together with Poincaré symmetry (the generalisation of Lorentz symmetry for arbitrary transformations *of* spacetime) and local gauge symmetry (symmetry under arbitrary field transformations at each point *in* spacetime) SUSY forms one of the few possible fundamental continuous symmetries which may be possessed by a Lagrangian. The generators Q_α commute with the four momenta p^μ but satisfy *anti*commutation relations with each other [59]:

$$\{Q_\alpha, \bar{Q}_\beta\} = -2\,(\gamma_\mu)_{\alpha\beta}\,p^\mu, \tag{2.3}$$

where the γ_μ are the Dirac gamma matrices. The dependence of the anticommutator upon the particle momentum has led to SUSY transformations being described as the 'square root' of translations. Herein lies one of the 'miracles' of SUSY since the generators Q_α thus have a direct relationship with the generators of the Lorentz symmetry [59]. This apparently contradicts the Coleman-Mandula theorem [66] forbidding just such a combination of spacetime and internal (here spin) symmetries. The mechanism by which SUSY is able to circumvent the Coleman-Mandula theorem in this way is that the Q_α are Grassmann (anticommuting) variables, whereas in the Lie algebras describing conventional field theories the generators all commute with one another [67].

The circumvention of the Coleman-Mandula theorem opens up the way for the construction of a quantum theory of gravity [66]. If supersymmetry is local, i.e. $Q_\alpha = Q_\alpha(x_\mu)$, then SUSY provides a connection with the generators of the Poincaré algebra describing arbitrary spacetime transformations [67]. Although still divergent, locally supersymmetric quantum field theories ('supergravity' or 'SUGRA' theories) suffer from less serious renormalisation problems than non-supersymmetric quantum gravity models [66]. For this reason most current proposals for finite, non-perturbative quantum theories of gravity based upon non-trivial extended spacetime geometries have local supersymmetry at their heart.

The predominant effect of SUSY on low energy (electroweak scale) physics is to double the number of particles found in nature. In any $N = 1$[1] SUSY model each particle, including the Higgs particles (of which there are two doublets in SUSY), has a partner with the same quantum numbers (except for spin). The partners of the fermions such as the squarks[2] are Majorana scalar bosons while the partners of the bosons such as the photino and Higgsino are spin 1/2 Majorana fermions. Simple SUSY models require the masses of these particles to be identical to those of their SM partners but if this were the case then the SUSY partners would already have been discovered. Resolution of this problem lies in the low energy breaking of supersymmetry such that the partners have much higher masses. The precise mechanism which governs SUSY breaking is currently unknown. It seems likely that it occurs in some 'hidden' sector of the theory which can interact with the SM particles only through gravitational interactions. This hidden sector occurs naturally in some quantum theories of gravity [59].

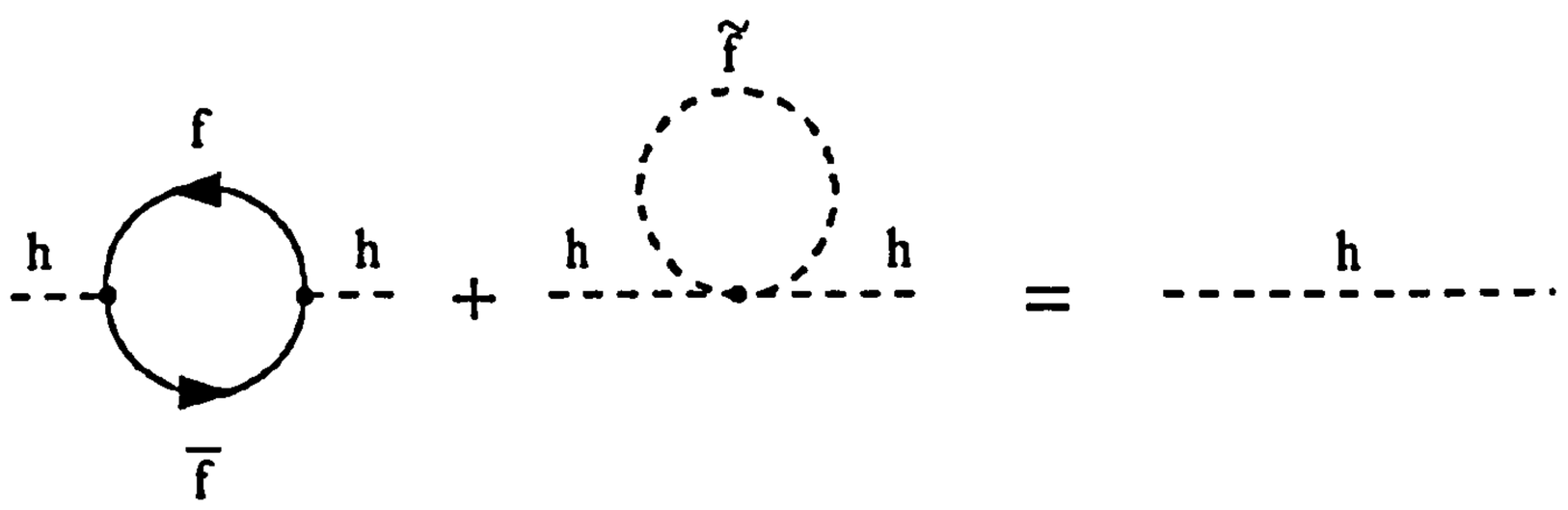

Figure 2.3: *The cancellation of fermionic corrections to the Higgs mass by the scalar fermions ($\tilde{f}$) loops in SUSY.*

Assuming that SUSY is broken at or near the electroweak scale at energies $\mathcal{O}$(TeV) vastly increases the complexity of the standard model Lagrangian (Eqn. 2.1). Many more terms are now permitted by the requirement of perturbative renormalisability. In particular since the SM bosons(fermions) now have fermion(boson) partners these too can participate in loop diagrams. Fermion(boson) contributions to matrix elements have an overall minus sign relative to boson(fermion) contributions and so the overall effect of this is to cancel the SM contributions thus rendering many perturbative calculations divergence free (Fig. 2.3). This solves the gauge hierarchy

[1] N extended SUSY models may be constructed with N sets of generators Q_α^N. Only $N = 1$ global SUSY models are phenomenologically acceptable although $N > 1$ is possible for locally supersymmetric theories [59].

[2] The names of the partners of the SM fermions(bosons) consist of the fermion(boson) names prefixed(suffixed) with 's'('ino').

problem (§2.2.2) and allows a mass to be predicted for the Higgs ($m_h \lesssim 146$ GeV/c^2 [59]) which is broadly consistent with experimental bounds from direct detection and precision electroweak measurements at LEP and elsewhere [73] (Fig. 2.4).

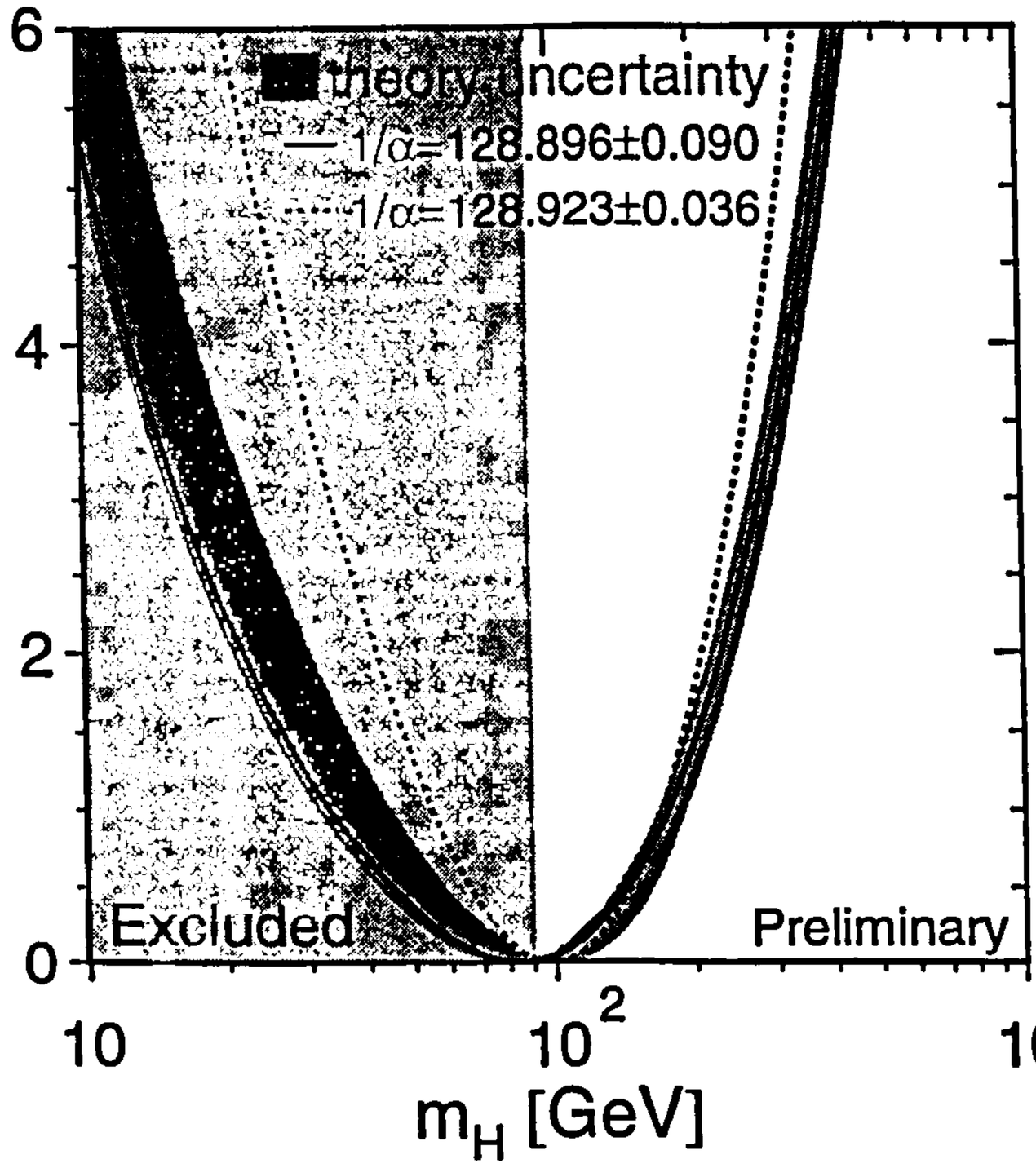

Figure 2.4: *Constraints on the standard model Higgs mass from LEP2 data. The dark grey band is the relative χ^2 of a fit to precision electroweak data plotted as a function of the Higgs mass (requires $m_h < 280$ GeV/c^2 at 95% C.L.). The full and dotted lines are the relative χ^2 curves for different assumed values of α. The grey region is excluded by direct searches. Taken from [73].*

Another consequence of electroweak scale SUSY breaking is that it changes the rate at which the three SM gauge couplings 'run' with energy. If grand unification occurs at some large energy scale then one would expect all three couplings to have the same strength at this energy, signifying that the $SU(3)_C$, $SU(2)_L$ and $U(1)_Y$ groups have been absorbed into a larger GUT group. The renormalisation group equations can be used to evolve the measured values of these couplings at the electroweak scale up to higher energies, however when this is done it is found that they do not meet at a single point [59]. The incorporation of supersymmetry into GUTs changes the running of the couplings by just the right amount to give unification at a *single* higher energy of approximately 10^{16} GeV ([74] Fig. 2.5). This

is a remarkable achievement given that the evolution occurs over a range in energy of some fourteen orders of magnitude.

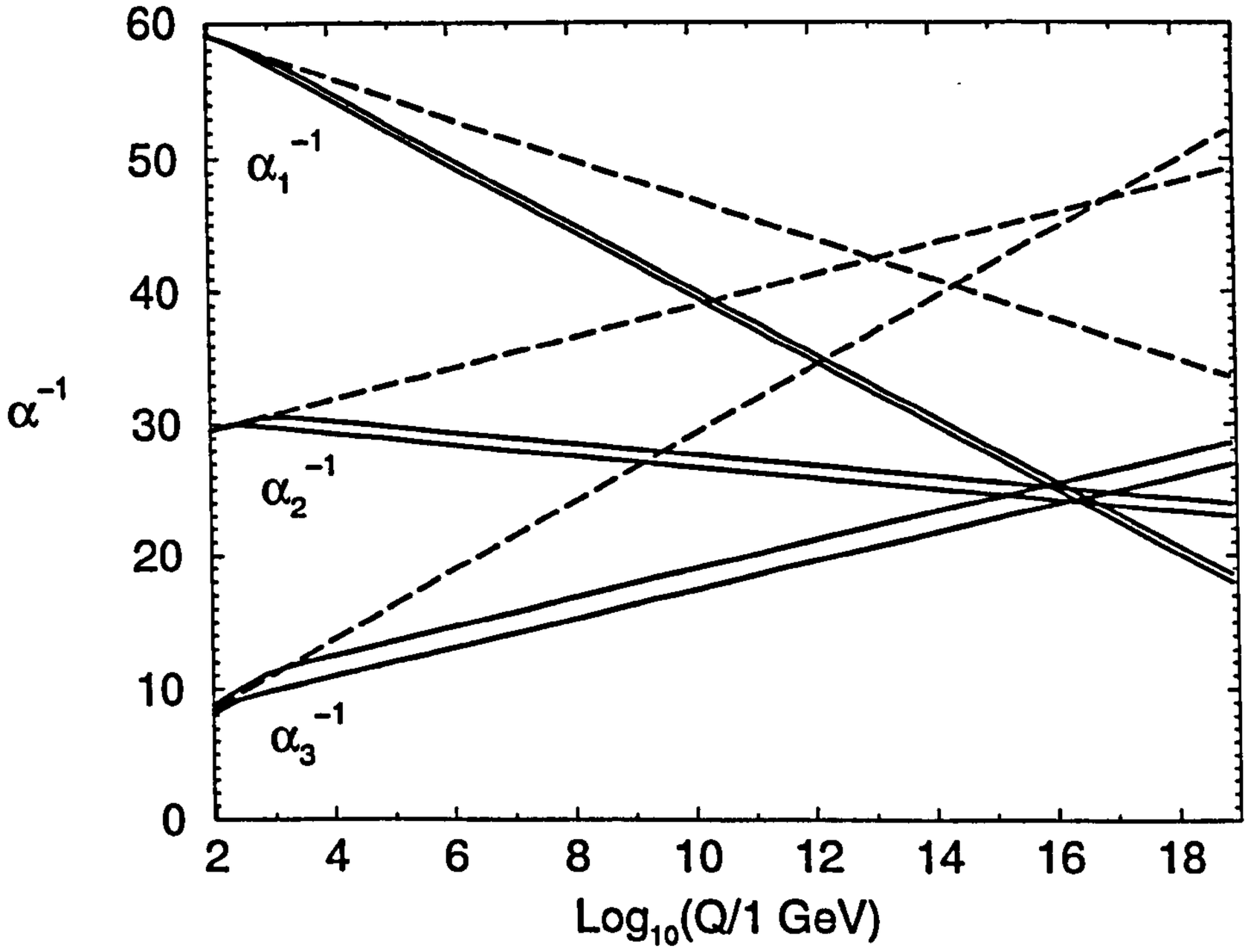

Figure 2.5: *The unification of gauge couplings with (heavy bands) and without (dotted lines) supersymmetry. Inverse couplings (strong, electromagnetic, weak) are plotted as functions of* $\log_{10}(Q)$ *where* Q *is the energy scale. Taken from [74].*

The inclusion of SUSY within the grand unified theories themselves has additional benefits. Generically GUTs predict that the proton has a finite lifetime owing to decay through the exchange of GUT scale baryon number violating X bosons. Owing to the high mass of these bosons the process is extremely rare, with a proton lifetime considerably in excess of the age of the universe. Searches for proton decay therefore typically use a sample of $\gtrsim 10^{33}$ protons in which statistically one may decay in a time $\mathcal{O}$(1 year). Limits on the proton lifetime set in this way are in conflict with many GUT estimates and rule out a large class of models, in particular those based upon the gauge group $SU(5)$ [63]. The situation can be remedied by considering SUSY GUTs, which in general predict a higher unification scale and hence a proton lifetime which is at least a factor of ten greater than the non-SUSY $SU(5)$ expectation and no longer in conflict with experimental bounds [74]. In addition the most probable decay mode is no longer $p \longrightarrow \pi^0 \nu_e e^+$ but $p \longrightarrow K^+ \nu_\tau$, on which

the experimental limits are far less severe [67].

2.3.2 The MSSM

Despite the many successes of supersymmetry there are still problems associated with SUSY extensions of the standard model. A major disadvantage is that the number of parameters required to describe the model is greatly increased. In the most simple model, the Minimal Supersymmetric extension of the Standard Model (MSSM), a further 63 free parameters are required in addition to the 19 appearing within the standard model [46].

Of the 63 extra free parameters 57 arise due to sfermion masses and mixings. In the MSSM the partners of the helicity eigenstates of the charged SM fermions are separate, distinct spin 0 eigenstates of the weak interaction. These states mix to form the physical mass eigenstates with mixing matrices containing angles and masses which are free parameters of the model. In the squark sector mixing also occurs between QCD (colour) eigenstates. The contributions of the these different sfermion components to the mass eigenstates can be determined by diagonalising the mass matrices [46].

The partners of the SM bosons are also mixed to form distinct mass eigenstates of particular charge and quantum number. The partners of the charged Higgs and gauge bosons mix to form four 'charginos' $(\tilde{\chi}^{\pm}_{1,2})$[3] while the partners of the gluons mix to form 'gluinos' and the partners of the uncharged Higgs and gauge bosons (Higgsinos and gauginos) mix to form four 'neutralinos' $(\tilde{\chi}^0_i,\ i = 1,\ldots,4)$:

$$\tilde{\chi}^0_i = f_{i1}\tilde{W}_3 + f_{i2}\tilde{B}^0 + f_{i3}\tilde{H}^0_1 + f_{i4}\tilde{H}^0_2 \tag{2.4}$$

The parameters appearing in the mass matrices (f_{ij} for the neutralinos) include three gaugino mass parameters M_1, M_2 and M_3, a Higgsino mass parameter μ and the ratio of the SUSY Higgs v.e.v.s, $\tan\beta$. A basis is often chosen in which the final free parameter is taken to be the mass of the pseudoscalar SUSY Higgs, m_A. The total number of free parameters is then 63 as required. Sparticle contributions to mass eigenstates can again be determined by diagonalising the appropriate mass matrices [46].

The number of free parameters contained within the MSSM may be reduced slightly by requiring the unification of gaugino masses at the GUT scale. This allows the following relationship between M_1 and M_2 to be derived [46]:

$$M_1 = \frac{5}{3} M_2 \tan^2\theta_w \simeq \frac{1}{2} M_2, \tag{2.5}$$

[3]It is conventional to denote SUSY states with a tilde e.g. $\tilde{\mu}$ for the smuon.

where θ_w is the Weinberg angle. Further reduction comes from the use of relationships derived within SUGRA. The model can then be described by just 5 free parameters. In one particular basis these may be taken to be: $m_{1/2}$ the common gaugino mass, m_0 the common scalar mass, A_0 the common trilinear coupling, $\tan\beta$ and sign(μ). This model is known as the minimal Supergravity model (mSUGRA) [46].

2.3.3 R Parity

Another disadvantage of incorporating SUSY into the standard model is the catastrophic violation of lepton and baryon number by virtual SUSY interactions. It is known from the stringent experimental limits on proton decay mentioned previously (§2.3.1) that baryon number is almost exactly conserved and similar limits exist on lepton number violating processes. In the SUSY version of Eqn. 2.1 there are terms which can lead to violation of these bounds [75]:

$$\mathcal{L}_{R_P} = \lambda_{ijk} L_i L_j \bar{E}_k + \lambda'_{ijk} L_i Q_j \bar{D}_k + \lambda''_{ijk} \bar{U}_i \bar{U}_j \bar{D}_k \tag{2.6}$$

where $L(Q)$ are the lepton(quark) doublet superfields, $\bar{D}$ and $\bar{U}$ are the down like and up like quark superfields, $\bar{E}$ is the lepton singlet superfield, λ, λ' and λ'' are Yukawa couplings and $i, j, k = 1, 2, 3$ are generation indices [75]. The Yukawa couplings can be set to zero, thereby avoiding lepton and baryon number violation, by imposing a new discrete multiplicative symmetry known as R parity which separates particles and sparticles and is defined as

$$R_p = (-1)^{3B+2S+L}, \tag{2.7}$$

where B, L and S are baryon number, lepton number and spin respectively. In alternative scenarios the proton lifetime can be protected by imposing weaker conservation laws on either baryon number or lepton number separately. In these R parity violating models however there are generally processes which act to wash out the matter-antimatter asymmetry created during baryogenesis in the early universe [76]. Thus, unless baryogenesis occurs through some non-standard mechanism, the R parity violating Yukawa couplings in Eqn. 2.6 must be extremely small. Henceforth they will be assumed to be sufficiently small to be cosmologically insignificant.

Phenomenologically one of the key consequences of R parity conservation is that all SUSY particles are created and annihilated in pairs. This in turn leads to the fact that the Lightest Supersymmetric Particle (LSP) is stable and is hence potentially a candidate for the dark matter.

2.4 Supersymmetric Dark Matter Candidates

From the considerations of §1.5.2 the LSP must be colourless and uncharged to form a viable dark matter candidate. In most SUSY models this condition is naturally satisfied. The LSPs appearing in a variety of models will now be discussed.

Gluinos and Sneutrinos

In the MSSM there is a small region of parameter space currently not excluded by experiment where the LSP could be a light gluino (2 GeV/c^2 $\lesssim m_{\tilde{g}} \lesssim$ 4 GeV/c^2). This could evade the constraint from heavy proton searches (§1.5.2) by forming neutral hadrons incapable of binding to conventional baryonic matter. The scenario is being excluded rapidly however by accelerator searches [77]. It is also just possible that the sneutrino could be the LSP but this possibility too is strongly constrained by experiment [46].

Neutralinos

By contrast the lightest neutralino ($\tilde{\chi}_1^0$) forms the LSP over large regions of unconstrained MSSM parameter space. By requiring that SUSY solves the gauge hierarchy problem the mass of this particle is generally found to lie in the range 10 GeV/c^2 $\lesssim m_{\tilde{\chi}_1^0} \lesssim 10^4$ GeV/c^2. This mass range taken together with the predicted $\tilde{\chi}_1^0$ self annihilation cross section leads to relic LSP neutralinos having a density parameter $\Omega_{\tilde{\chi}}$ of order unity [59]. This is a remarkable coincidence, given that SUSY was proposed quite independently of the dark matter problem, and it has led many people to regard the lightest neutralino as the most likely CDM candidate.

Gravitinos

In the MSSM SUSY breaking in the hidden sector (§2.3.1) is communicated to the SM particles via gravitational interactions. Models do exist however where the communication is via the SM gauge bosons. In these 'gauge mediated' models the gravitino, the spin 3/2 partner of the spin 2 graviton appearing in SUGRA, can be extremely light ($m_{3/2} \sim$ keV/c^2) and hence a candidate for the LSP [78]. This scenario has received considerable theoretical attention recently due to the observation of an anomalous event at CDF which could be interpreted as involving gravitino production [79]. There are problems with such an interpretation however [79] and in any case recent experiments at LEP have almost excluded the regions of parameter space required by the event [80]. Gravitino LSPs would couple very weakly to baryonic matter preventing direct detection in any conceivable dark matter

search experiment. Luckily for dark matter experiments however the gravitino in conventional SUSY models has a mass very much greater than that of the partners of the SM particles and thus cannot be the LSP.

Axinos

Still more exotic models incorporating axions into SUSY naturally predict a light axino LSP with $m_{\tilde{a}} \sim 100$ GeV/c^2 [2]. Together with the axion this could provide sufficient dark matter to close the universe. The properties of a relic axino LSP would in general be similar to those of a neutralino LSP [2].

2.5 Collider Neutralino Searches

Given the current theoretical interest in the neutralino in particular as a dark matter candidate the bounds on the neutralino mass and other SUSY parameters which can be set by current and future collider experiments will now be considered.

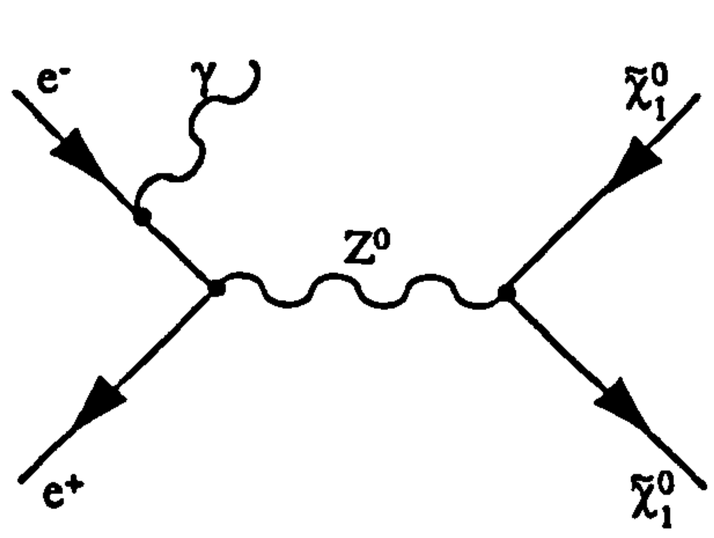

Figure 2.6: *The tree level diagram for the process* $e^+e^- \longrightarrow \tilde{\chi}_1^0\tilde{\chi}_1^0\gamma$.

2.5.1 Neutralino Mass Limits

Limits on the mass of the lightest neutralino are currently being set by experiments at lepton colliders such as LEP. It is not usually possible to search for direct s channel $\tilde{\chi}_1^0$ production as the neutralinos escape from the detector without causing it to trigger. A search is nonetheless possible in the case where initial state radiation is emitted (Fig. 2.6), however the signal is expected to be dwarfed by an irreducible background from the process $e^+e^- \longrightarrow \nu\bar{\nu}\gamma$. Limits must consequently be set by using the null results of searches for other SUSY particles such as the charginos

and the next to lightest neutralino ($\tilde{\chi}_2^0$). These searches exclude various regions of MSSM parameter space and by using model dependent MSSM mass relations the mass of the $\tilde{\chi}_1^0$ can be constrained. Using this technique with LEP2 data acquired at energies $\leqslant$ 183 GeV and taking into account Higgs mass limits, cosmological arguments (over closure of the universe) and radiative corrections, the minimum allowed value of $m_{\tilde{\chi}}$ is 42 GeV/c^2 [81]. This limit can be expected to increase steadily over the next few years as LEP energies are increased. This data also practically rules out a pure Higgsino neutralino, favouring instead states dominated by the gaugino contributions [81].

2.5.2 Discovery Potential

In [82] a survey was performed of mSUGRA parameter space comparing the discovery potentials of collider searches and direct search WIMP dark matter experiments (§1.5.2). The results suggest that in large regions of parameter space the direct detection rates are potentially at observable levels ($> 10^{-3}$ kg^{-1}day^{-1}). For large $\tan\beta$ (> 10) the regions of parameter space accessible to these experiments are greater than those accessible to collider experiments at LEP2 and the Tevatron (Run II) (Fig. 2.7 overleaf). Given the recent evidence from LEP2 Higgs searches that $\tan\beta$ is large (e.g. [83]) it seems likely that direct search WIMP dark matter experiments can set the best limits on mSUGRA parameter space, at least until the LHC comes on line in 2005.

In the event that strongly interacting SUSY particles such as squarks or gluinos are discovered at a collider experiment then subsequent determination of the MSSM parameters could be used to infer the neutralino mass. It is however extremely difficult in such circumstances to determine the masses of any of the SUSY states directly in a model independent manner. This is because all SUSY events contain at least two $\tilde{\chi}_1^0$ in the final state due to the requirement of R parity conservation. This prevents kinematic reconstruction of the masses of the neutralinos which have been produced. In a lepton collider the masses of some of the other sparticles which have been produced may be determined by a dedicated threshold scan but in a hadron collider such as the Tevatron or LHC even this is not possible. Should neutralino dark matter be discovered on the other hand it may be possible to use the results of direct or indirect search experiments to measure the $\tilde{\chi}_1^0$ mass directly, using the results of §3. This is an additional reason to pursue such experiments, even if SUSY is first discovered at a collider.

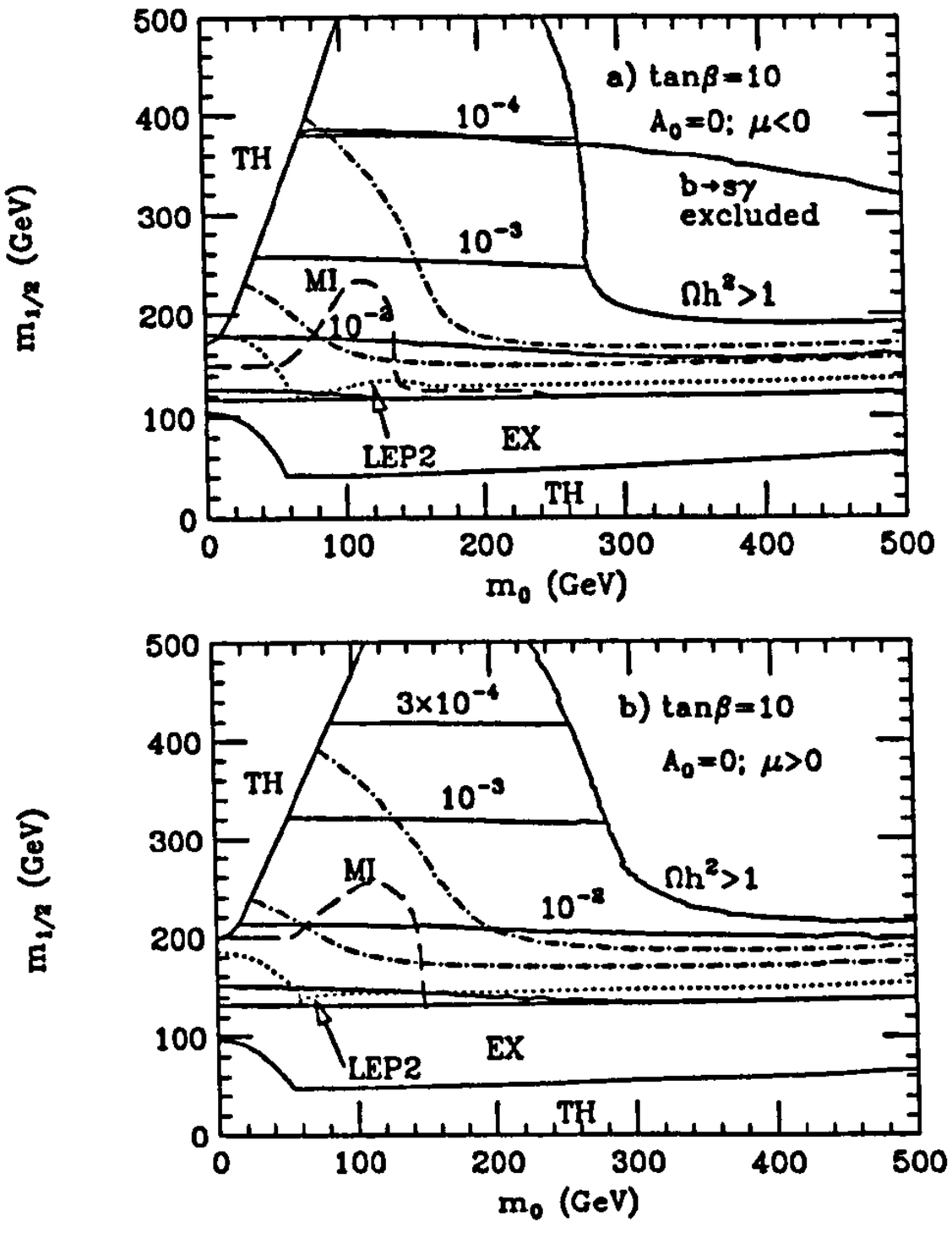

Figure 2.7: *A contour plot of mSUGRA discovery potential in collider experiments and direct search WIMP dark matter experiments for mSUGRA parameters* $A_0 = 0$, $\tan\beta = 10$, *and (a)* $\mu < 0$ *or (b)* $\mu > 0$. *The regions labelled 'TH' and 'EX' are excluded by theory and experiment respectively. The dash-dotted line surrounds the region where* $0.15 < \Omega_\chi < 0.4$ *as required for some mixed dark matter scenarios. 'MI' and 'LEP2' represent the discovery potential of the Tevatron (Run II Main Injector) and LEP2 respectively. Also plotted is the region excluded by the measured* $BR(b \to s\gamma)$. *Taken from [82].*

2.6 Conclusions

The standard model of particle physics has been supremely successful at explaining the observed interactions of matter and energy on the smallest scales. There are inconsistencies contained within it however and these may be resolved through the introduction of the concept of supersymmetry. Many supersymmetric theories naturally contain dark matter candidates, the properties of which can be constrained by current and future collider experiments.

the sensitivity of the experiment. This energy spectrum may be decomposed into a number of factors:

$$\frac{dR}{dE_v} = R_0 . \sum_{E'_v} M(E'_v, E_v) . \sum_{A} f(A) . G_r(A, E_R) . S(A, E_R) . F^2(A, E_R) . I(A). \quad (3.1)$$

Here dR/dE_v is the differential rate of nuclear recoil events of energy E_v observed in the detector and the other factors are as follows:

- A fundamental interaction rate R_0 proportional to the zero momentum transfer WIMP scattering cross section σ_0 (§3.3).
- A detector response matrix element $M(E'_v, E_v)$ taking into account statistical detector effects such as finite energy resolution and event identification efficiency (§3.6).
- A mass fraction $f(A)$ of element A in the target material (§3.5).
- A nuclear recoil relative energy detection efficiency factor $G_r(A, E_R)$ describing the proportion of deposited recoil energy E_R which can be observed by the detector (§3.5).
- A 'spectral' function $S(A, E_R) \sim \exp(-E_R/E_0 r)$ (E_0, r constants) containing the kinematics of the WIMP-nucleus scattering process (§3.4).
- A form factor $F^2(A, E_R)$ accounting for reduction in nuclear coherence due to finite nuclear size (§3.3).
- A coupling enhancement factor $I(A)$ containing model dependent quantities leading to enhancements or reductions in the scattering rate for specific nuclei (§3.3).

Although Eqn. 3.1 describes the expected energy spectrum of signal events in a direct search experiment, the energy spectrum of events which is actually observed also contains another contribution due to background events. Background may be caused by a number of different processes. The principal sources are:

- Nuclear recoil events caused by the scattering of naturally occurring neutrons. For the most part the neutrons come from U and Th chain decays within the detector and its surroundings and from spallation by cosmic ray muons.
- Electron recoils caused by low energy beta or gamma decays within the detector or the Compton scattering of naturally occurring high energy gammas.

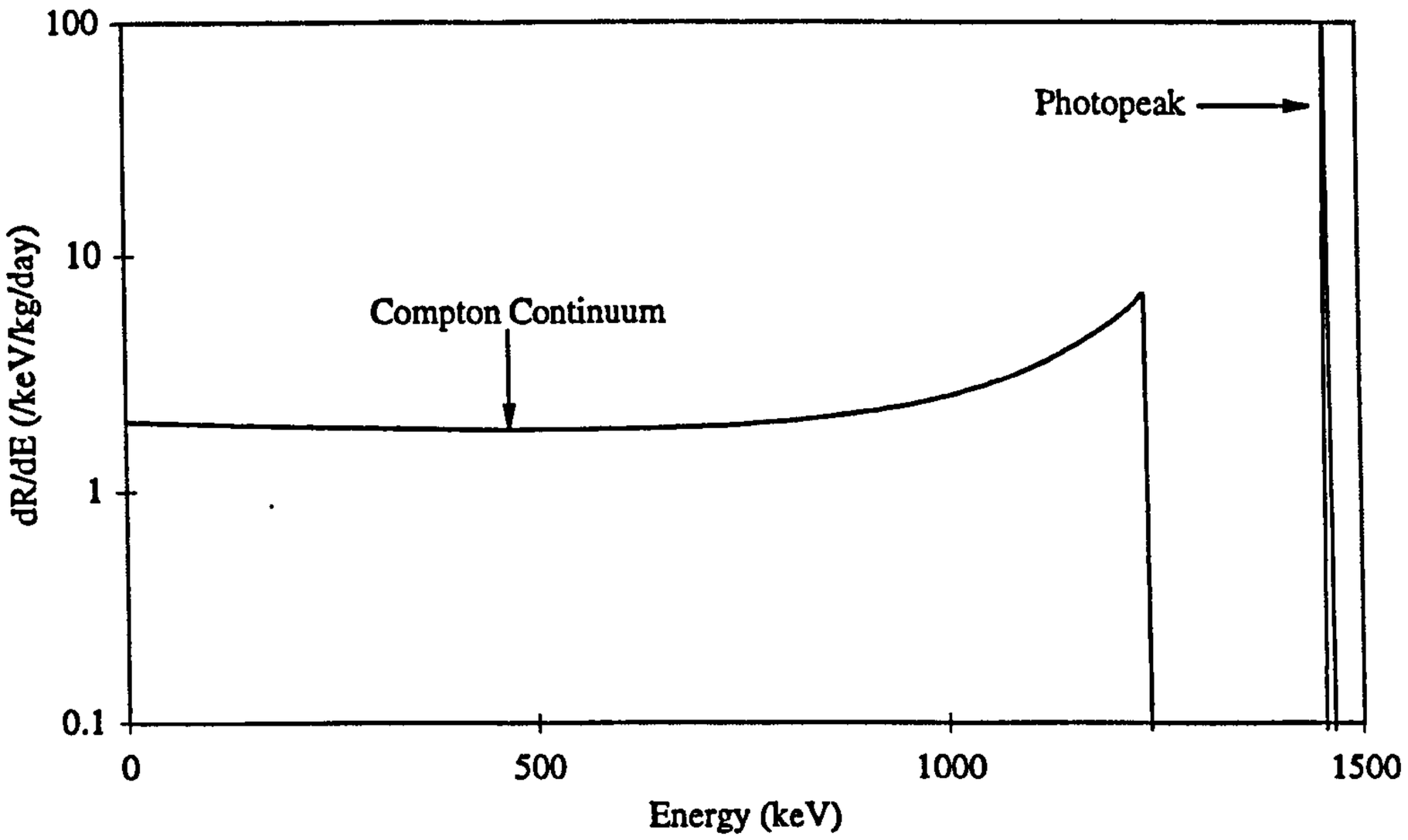

Figure 3.1: *Simulated electron recoil background from the ^{40}K 1460 keV line. The compton continuum was simulated using Eqn. 3.2. Note the Compton 'edge' at 1243 keV as predicted by Eqn 3.3.*

At low energy the Compton process dominates and the electron recoil energy spectrum is given to a good approximation by [85]

$$\frac{dR_e}{dE_v} \propto \frac{1}{E_\gamma^2}\left(2 + \frac{E_v^2 m^2 c^4}{E_\gamma^2 (E_\gamma - E_v)^2} + \frac{E_v (E_v - 2mc^2)}{E_\gamma (E_\gamma - E_v)}\right), \tag{3.2}$$

where E_γ is the energy of the incident photon, E_v is the energy of the recoiling electron and m is the electron mass. This gives a reasonably flat spectrum extending from a maximum energy of

$$E_{vmax} = \frac{2E_\gamma^2}{mc^2 + 2E_\gamma}, \tag{3.3}$$

down to zero energy (Fig. 3.1).

3.2.2 Design Considerations

The need to maximise the signal event rate dR/dE_v drives the design of all direct search dark matter experiments. The main features of Eqn. 3.1 which must then be taken into account when optimising detector design are the following:

- The fundamental WIMP interaction rate R_0 is predicted to be extremely small ($\lesssim 1$ /kg/day), requiring massive, stable detectors capable of running over long periods of time.

- The predicted values of R_0 are also smaller than the rate of background nuclear and electron recoil events in the detector. Consequently these events must be removed by the use of physical shielding (including the installation of experiments deep underground to remove cosmic ray induced nuclear recoils), detector components of high radiopurity and possibly also electron recoil background discrimination techniques. The latter in particular can have an adverse effect on the response matrix M due to a reduction in event identification efficiency. This effect must also be minimised.

- The observed energy spectrum is predicted to be very soft. This is because both $S(A, E_R)$ and $F^2(A, E_R)$ fall rapidly with increasing recoil energy E_R, while $G_r(A, E_R)$ is often small (e.g. < 30 % for most scintillator targets). A high detector visible energy threshold (incorporated within $M(E'_v, E_v)$) can thus prevent a detector from triggering on the majority of signal events. Detectors can be designed which have $G_r(A, E_R)$ of order unity (e.g. bolometers) and which can hence observe more of the signal energy spectrum however these often have poor background discrimination properties. The detector visible energy threshold must therefore be as low as possible.

- The coupling enhancement factor $I(A)$ can vary over several orders of magnitude for different nuclei thereby affecting the total observed event rate. The consequent need to maximise this quantity thus governs the choice of target nucleus and hence target material (via $f(A)$). Depending upon the form of the WIMP-nucleus interaction which is being investigated (spin dependent or spin independent §3.3) either high spin or high A (heavy) nuclei may be favoured.

- The spectral function $S(A, E_R)$ contains a time dependent component due to variation in the velocity of earth borne detectors relative to the galactic WIMP halo. This component causes a small annual modulation ($\lesssim 10\%$) in the observed signal event rate and this can be used to identify the signal against a considerable rate of background events (assuming these are unmodulated). In order to do this however still larger detectors are required so as to minimise the effects of counting statistics.

3.2.3 Direct Detection Techniques

The current world status of direct search WIMP dark matter experiments is summarised in Table 3.1 (overleaf). Some of the more widely used techniques for maximising dR/dE_v and hence sensitivity to WIMPs will now be discussed.

Name	*Location*	*M (kg)*	*Nuclei*	*Disc.*	*Status*
UKDMC-NaI(Tl)	Boulby (UK)	20.0	Na,I	•	R
UKDMC-NaIAD	Boulby (UK)	~100	Na,I	•	P
UKDMC-UVIS	Boulby (UK)	~1	Na,I	•	P
UKDMC-LXe	Boulby (UK)	6.2	Xe	•	F
UKDMC-ZEPLIN	Boulby (UK)	20.0	Xe	•	P
CASPAR	Boulby (UK)	0.12	F,Ca	•	F
DRIFT	Boulby (UK)	<1	Xe	•	P
DAMA-NaI	Gran Sasso (It)	115.5	Na,I	•	R
DAMA-Xe	Gran Sasso (It)	6.5	Xe	•	R
HDMS	Gran Sasso (It)	0.15	Ge		F
GENIUS	Gran Sasso (It)	10^4	Ge		P
CRESST	Gran Sasso (It)	1.0	Al,O		F
Milano	Gran Sasso (It)	1.36	Te,O	•	R
CDMS	SLAC/Soudan (US)	1.0	Ge	•	F
CDMS	SLAC/Soudan (US)	1.0	Si	•	F
EDELWEISS	LSM (Fr)	0.08	Ge	•	F
EDELWEISS	LSM (Fr)	0.024	Al,O		R
Zaragoza	Canfranc (Sp)	32.1	Na,I		R
SALOPARD	Canfranc (Sp)	0.01	Sn	•	F
ELEGANTS V	Kamioka (Jap)	760	Na,I		R
ELEGANTS VI	Kamioka (Jap)	25.9	F,Ca		F
Tokyo	Nokogiriyama (Jap)	0.24	F,Li	•	F
Baksan	Baksan (FSU)	1.7	Ge		R
DEMOS	TANDAR (Ar)	1.0	Ge		R
ORPHEUS	Bern (CH)	1-2	Sn	•	F
Mica	Amherst (US)	$< 10^{-9}$	Si	•	R
SIMPLE	Paris	0.1	F	•	P

Table 3.1: *Current and planned direct detection experiments world wide. 'Disc.' refers to the ability of a detector to discriminate against background. Under 'status', 'R' means running, 'F' means funded and 'P' means proposed. For references on these experiments see e.g. [86] or [87].*

The first limits on WIMP dark matter were set by germanium ionisation detectors originally used for searching for double beta decay. These detectors offer the advantage of low energy threshold and high radiopurity however they provide no electron recoil background discrimination. Other experiments use crystals such as Al_2O_3 operated at cryogenic temperatures as the target and detect the thermal phonons emitted by a recoiling particle using superconducting transition edge thermometers. This technique has the advantage that the recoil energy threshold is still lower than that for ionisation detectors (< 1 keV due to $G_r(A, E_R) \sim 1$) while the detector radiopurity may also be better. On the other hand nuclei such as Al and O possess poor spin dependent and spin independent coupling enhancement factors (§3.3) and again there is little evidence that the technique can provide electron recoil background discrimination.

Several collaborations make use of crystals of Si or Ge operated at cryogenic temperatures. These hybrid devices detect both the ionisation and phonons produced by a recoil. The ratio of signals in the ionisation and phonon channels for a given event depends sensitively on whether the event is due to a nuclear or electron recoil and hence excellent discrimination can be obtained. These experiments are nevertheless extremely difficult and in the past have been plagued by unexpected background problems. The first low background results from these detectors are still awaited.

Of all the detectors currently in operation the most effective are those using scintillators. The recoil of a nucleus or electron through a scintillator causes it to emit light which can then be detected using photomultiplier tubes (§4.3.2) or other sensitive photodetectors. The scintillator itself can be either a solid (e.g. NaI(Tl) or CaF_2(Eu)) or a liquid (e.g. dioxan or Liquid Xenon - LXe). Scintillation materials can easily be purified to reduce the background electron recoil rate and with good light collection they can give a detector energy threshold as low as that of ionisation detectors. They may also contain heavy nuclei such as iodine or xenon with large spin independent coupling enhancement factors I_{si} or nuclei such as fluorine with large spin dependent coupling enhancements factors I_{sd} (§3.3). Furthermore, in some scintillators it is possible to discriminate signal from electron recoil background by examining the precise time spectrum of the pulse of scintillation light from an event ('Pulse Shape Discrimination'). The pulse shape differences required may be intrinsic to the scintillator, as in the case of NaI(Tl) (§4.2.2 and §8), or alternatively engineered into it, as in the case of the CASPAR detector (§4.2.4 and §7). The U.K. Dark Matter Collaboration (UKDMC) currently operates NaI(Tl) WIMP dark matter detectors, and is also involved in developing several other types

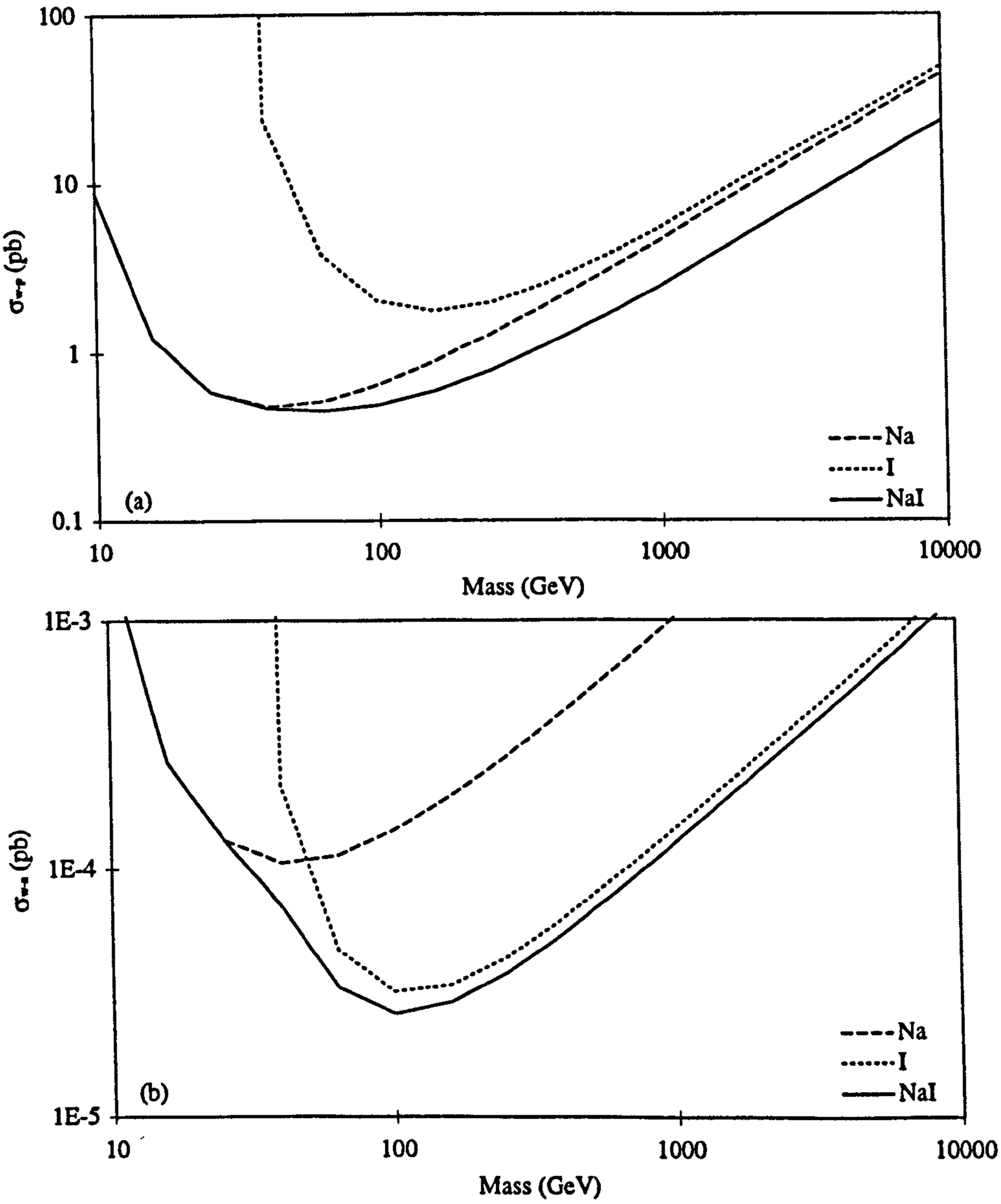

Figure 3.2: *Cross section limits from a 6.2 kg UKDMC NaI(Tl) detector. Figure (a) shows the limits on spin dependent cross section and WIMP mass, Figure (b) the limits on spin independent cross section and WIMP mass. In both cases the dashed and dotted curves represent the contributions from individual nuclei, and the full curves the combined limits. The regions above the curves are excluded. The characteristic minima in the single element curves lie at WIMP masses determined by the mass of the target nuclei (through kinematics) and the finite detector visible energy threshold (which decreases the sensitivity to light WIMPs). The curves have been calculated using the data of [88] and form factors and coherence factors described in §3.3. The curves have been normalised to WIMP-nucleon cross sections as described in §3.7.*

of scintillator detector. The most recent limits on WIMP mass and cross section set by an operational UKDMC NaI(Tl) detector are plotted in Fig. 3.2.

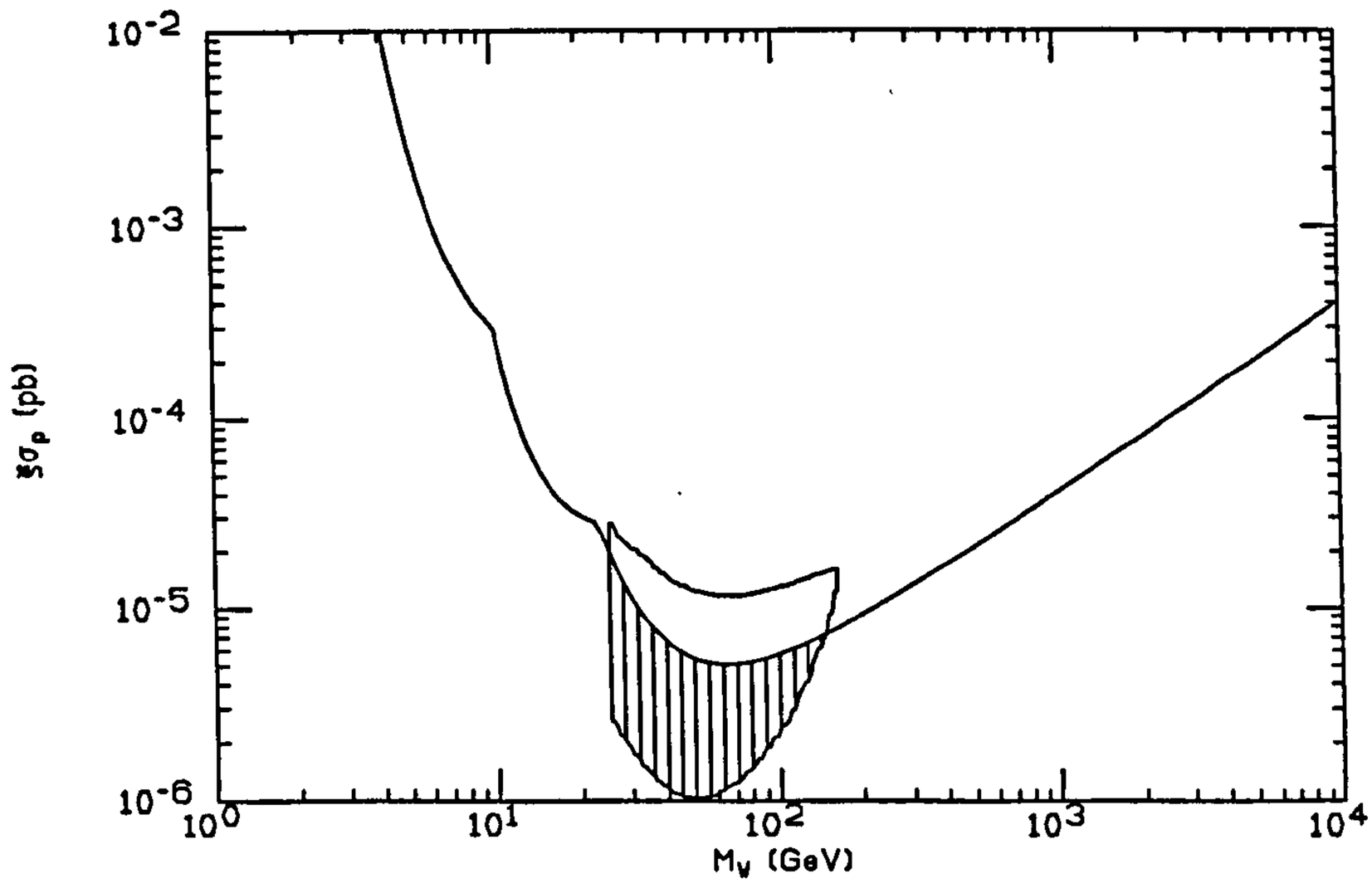

Figure 3.3: *Spin independent cross section data from the DAMA-NaI0 experiment. The curve is the best previous limit from DAMA-NaI0 and DAMA-Xe0 data while the hatched area is the allowed region from an annual modulation analysis of 4549 kg.days of NaI(Tl) data. The lefthand edge of the shaded region is excluded by accelerator SUSY searches (§2.5). Taken from [89].*

Bulk NaI(Tl) crystal scintillator detectors are also operated by the DAMA collaboration at Gran Sasso (Italy) [89]. 4590 kg.days of data from an array of nine 9.7 kg crystals have been analysed to search for the annual modulation expected in the signal rate. The observation of a small modulation in data from some of the crystals has been taken as evidence for a WIMP signal consistent with the hatched region of parameter space in Fig. 3.3. Critics of DAMA however point out that the data was collected over just two short summer and winter periods (1185.2 kg.days and 3363.8 kg.days respectively) and therefore cannot be used to demonstrate that the modulation is *annual*. Furthermore the modulation is only seen in three of the nine crystals in the array [90]. Without the use of pulse shape discrimination it is uncertain whether the 'signal' is caused by a modulation in noise, background events or detector performance rather than in a population of nuclear recoils. More work is needed.

The limits from all direct search experiments, including those plotted in Fig. 3.2

and Fig. 3.3, are calculated from observed visible energy spectra using Eqn. 3.1. It is appropriate therefore that the different terms in this equation now be investigated in more detail.

3.3 Couplings, Cross Sections and Form Factors

At the most fundamental level the magnitude of an observed nuclear recoil energy spectrum is related to the total event rate and hence to the WIMP scattering cross section σ. This cross section may be calculated to high accuracy by considering the full set of tree level and in some cases one loop diagrams responsible [46]. In the MSSM (§2.3.2) the cross section may include terms due to Z^0, Higgs or squark exchange, with the relative magnitudes of these terms depending upon the precise constituents of the WIMP (here assumed to be the neutralino).

The relative magnitudes of the different scattering diagrams determine whether the interaction is predominantly with the spin of the nucleus or its mass. This feature of WIMP scattering spectra is in general quantified by dealing with two separate cross sections due to the spin dependent (axial vector) and spin independent (scalar) contributions. When calculating the limits set by a particular experiment it is usual to quote limits on both spin dependent and spin independent cross sections, taking into account the different sensitivities of the target nuclei to the different interactions. If a signal is observed then the situation is somewhat different and the fractional contribution of the two interactions to the total cross section may be considered a free parameter to be determined from the data.

3.3.1 Spin Dependent Neutralino Interactions

Zero Momentum Transfer

In the MSSM the spin dependent neutralino scattering cross section is characterised by axial vector couplings arising at tree level from t channel Z^0 exchange and s channel squark exchange (Fig. 3.4 overleaf). The appropriate Feynman rules give the following matrix element $\mathcal{M}_{i,j}$ for the scattering of quark species i from neutralino component sparticle j [46]:

$$\mathcal{M}_{i,j} = d_{i,j}\bar{\tilde{p}}_j\gamma_\mu\gamma_5\tilde{p}_j\bar{q}_i\gamma^\mu\gamma_5 q_i. \tag{3.4}$$

for an effective coupling $d_{i,j}$ and quark and sparticle fields q_i and $\tilde{p}_j$ respectively. In the non-relativistic limit the sparticle term $\bar{\tilde{p}}_j\gamma_\mu\gamma_5\tilde{p}_j$ reduces to $2\mathbf{S}_j$ for sparticle spin vector $\mathbf{S}_j$ [91] and likewise the quark term $\bar{q}_i\gamma^\mu\gamma^5 q_i$ reduces to $2\mathbf{S}_i$ for quark spin

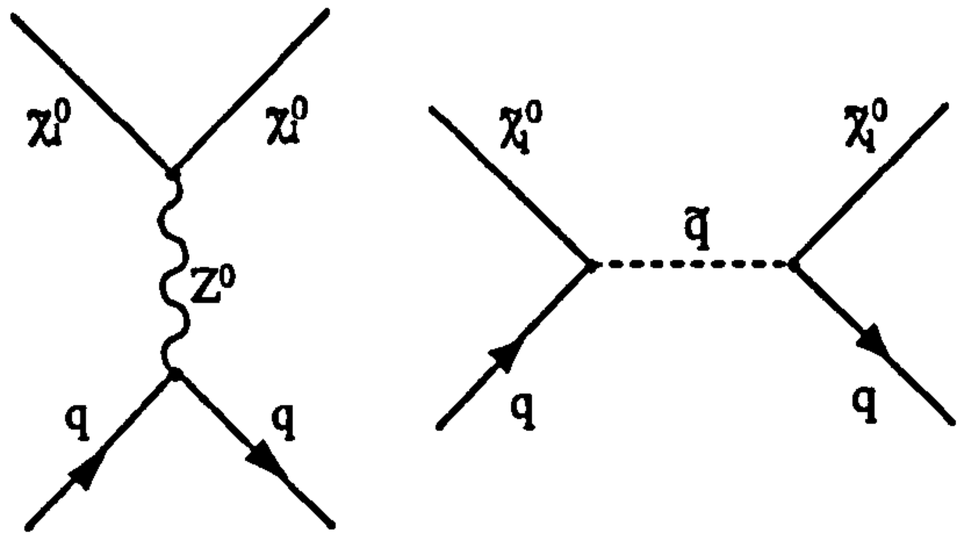

Figure 3.4: *Tree level diagrams contributing to spin dependent neutralino-nucleus scattering.*

vector $\mathbf{S}_i$. The expectation value of $\mathbf{S}_i$ within the nucleon may be approximated by $\mathbf{S}_n.\Delta q_i$ [92] where Δq_i is the fraction of nucleon spin carried by quark i (determined from DIS data and nuclear theory).

In order to proceed further an explicit sparticle composition of the neutralino must be assumed, as this governs the form of $d_{i,j}$. In the case of a pure photino neutralino the propagator is predominantly a squark and $d_{i,j} \propto Q_i^2$ $(= D_{i,\tilde{\gamma}})$ for quark charge Q_i. In the pure Higgsino case on the other hand the propagator is mainly a Z^0 and $d_{i,j} \propto T_i^3$ $(= D_{i,\tilde{h}})$ where T_i^3 is the third component of quark isospin. Denoting the constants of proportionality by d'_j the following may be written quite generally (in analogy to [92]):

$$< nucleon|\mathcal{M}_{i,j}|nucleon >= 4d'_j\mathbf{S}_j.\mathbf{S}_n \sum_i D_{i,j}\Delta q_i. \tag{3.5}$$

The Wigner-Eckardt theorem can now be used to relate this expression to the equivalent nuclear matrix element [91]. The theorem states that the expectation value of the *nucleon* spin $\mathbf{S}_n$ over the nucleus is equal to the expectation value of the *nuclear* spin $\mathbf{J}$ multiplied by some constant λ. This expression must be determined from a suitable nuclear model, with the early single unpaired nucleon estimates now superceded by more sophisticated odd group model calculations. Using this result, taking the square of the expectation value and summing over initial and averaging over final spin states the following cross section is obtained [92]:

$$\begin{aligned} \sigma &= \frac{4}{\pi}\mu^2\lambda^2 J(J+1)d_j'^2\left(\sum_i D_{i,j}\Delta q_i\right)^2 \\ &= \sigma_0.I_{sd}. \end{aligned} \tag{3.6}$$

Here I_{sd} is a spin dependent coupling enhancement factor containing all the spin dependence of the cross section, σ_0 is a 'raw' cross section and μ is the reduced mass of the neutralino-nucleus system given by

$$\mu = \frac{M_D M_T}{(M_D + M_T)}, \tag{3.7}$$

for target nucleus mass M_T and neutralino (WIMP) mass M_D. The proportionality of σ to μ^2 is a general feature of all WIMP-nucleon cross sections, coming from the kinematics of the interaction.

It is usual to treat the sum in Eqn. 3.6 as a single constant C. Hence by assuming a particular neutralino composition all model dependent differences in cross section between target nuclei are contained within the spin dependent coupling enhancement factor $I_{sd} = C^2\lambda^2 J(J+1))$. When evaluating C^2 the calculation can be simplified considerably by assuming that only the unpaired nucleon in the nucleus participates in the interaction (as in the single unpaired nucleon model). Experimental limits for a particular nuclear target are generally normalised to the equivalent WIMP-nucleon cross section rather than expressed in terms of the fundamental MSSM parameters and so only the ratios of the C^2 and the $\lambda^2 J(J+1)$ for nuclei and nucleons are required. This has the additional benefit of removing the need to know $d_{i,j}$ explicitly.

Non-Zero Momentum Transfer

In extrapolating from a neutralino-quark matrix element to a neutralino-nucleus matrix element the above argument implicitly assumes that the scattering is coherent. This is true in the limit of zero momentum transfer q, as in this case the propagator has insufficient momentum to resolve the nucleons or quarks contained within the nucleus. At higher values of q however this is no longer true and the cross section should be multiplied by a form factor correction $F^2(q) < 1$:

$$\sigma = \sigma_0 . I_{sd} . F^2(q). \tag{3.8}$$

At the Born level the form factor is merely the Fourier transform of the nuclear density distribution $\rho(r)$, reflecting the probability of scattering from a particular point, i.e. [84]

$$\begin{aligned} F^2(q) &= \left(\int \rho(r) e^{i\vec{q}.\vec{r}} d^3r \right)^2 \\ &= \left(\frac{4\pi}{q} \int_0^\infty r \sin(qr) \rho(r) dr \right)^2, \end{aligned} \tag{3.9}$$

for a spherically symmetric density distribution. In the simple case of an interaction with a single unpaired nucleon the appropriate density distribution is a thin shell of nuclear radius $r_n = 1.0A^{1/3}$ fm. The form factor is then [84]

$$\begin{aligned} F^2(q) &= j_0^2(qr_n) \\ &= \left(\frac{\sin(qr_n)}{qr_n}\right)^2. \end{aligned} \tag{3.10}$$

In the more realistic case of an odd group nucleus, calculations indicate that at least the first zero in the Bessel function is filled [88, 84] giving an empirical form factor of

$$\begin{aligned} F^2(q) &= j_0^2(qr_n) \\ &= \left(\frac{\sin(qr_n)}{qr_n}\right)^2 \qquad (qr_n < 2.55, qr_n > 4.5), \\ F^2(q) &= 0.047 \qquad (2.55 < qr_n < 4.5). \end{aligned} \tag{3.11}$$

When calculating nuclear recoil energy spectra it is often convenient to express the form factor as a function of recoil energy E_R rather than momentum transfer q, using the relation

$$q = \frac{\sqrt{2M_T E_R}}{\hbar c}, \tag{3.12}$$

for a target of mass M_T.

Unified Treatment

The above treatment of the spin dependent scattering cross section relies to a large extent upon considerably simplified models of the nucleus. This approach is useful for illustrating the underlying physics and estimating detector sensitivity when more detailed calculations are not available. Cross section calculations have recently reached a much higher degree of sophistication however and it is now possible to avoid many of the approximations required previously. The calculations generally proceed in three steps [46] relating to the calculation of the neutralino-quark matrix elements in terms of the MSSM parameters, the extrapolation to neutralino-nucleon matrix elements using DIS data and quark models, and the derivation of the neutralino-nucleus cross section using a detailed nuclear shell model calculation. These treatments take into account couplings to both protons and neutrons [46], and the effects of the mixture of sparticles within the neutralino. The result is that although the calculated cross sections retain the same general form as Eqn. 3.6 the quantity $I_{sd}.F^2(q) = C^2\lambda^2 J(J+1)F^2(q)$ no longer factorises to give a form factor

$F^2(q)$ which is independent of MSSM parameters. This makes the publication of completely model independent limits impossible. It is nevertheless still possible to define a form factor in which the SUSY model dependency is small thus enabling meaningful calculations to be performed [93].

In these detailed calculations the explicit form of I_{sd} is [46]

$$I_{sd} \equiv (C_{wp} < N|S_p|N > + C_{wn} < N|S_n|N >)^2 \frac{J+1}{J}, \tag{3.13}$$

where $< N|S_i|N >$ is the expectation value of nucleon i over the nucleus and C_{wn} and C_{wp} represent the sum in Eqn. 3.6 for neutron and proton scattering respectively. The corresponding point like nuclear scattering cross section is then [46]

$$\sigma = \frac{32 G_F^2 \mu^2}{\pi} I_{sd}. \tag{3.14}$$

For non-zero momentum transfer $F^2(q)$ is parameterised by [84]

$$F^2(q) = \frac{S(q)}{S(0)}, \tag{3.15}$$

where [94]

$$S(q) = a_0^2 S_{00}(q) + a_1^2 S_{11}(q) + a_0 a_1 S_{01}(q). \tag{3.16}$$

The isovector and isoscalar coefficients a_1 and a_0 are proportional to the $d_{i,j}$ or alternatively the nucleon C^2 factors and are hence dependent upon the neutralino composition and MSSM parameters. σ_0 may be derived from Eqn. 3.14 through the use of Eqn. 3.6.

In this detailed framework an *effective* $\lambda^2 J(J+1)$ may be defined using the following expression [93]

$$\lambda^2 J(J+1)_{eff} = \left(< N|S_p|N > + \frac{C_{wn}}{C_{wp}} < N|S_n|N > \right)^2 \frac{J+1}{J}. \tag{3.17}$$

The squares of the C_{wi} parameters used in these calculations are listed in Table 3.2 while the resulting $\lambda^2 J(J+1)_{eff}$ are listed in Table 3.3. Form factors derived from Eqn. 3.15 for iodine and sodium nuclei are plotted as functions of recoil energy E_R in Fig. 3.5(a). Conversion from q to E_R has been performed using Eqn. 3.12.

Interaction (wi)	C^2_{wi}
$\tilde{\gamma}p$	$0.096 \pm .009$
$\tilde{\gamma}n$	0.012 ± 0.003
$\tilde{H}p$	0.46 ± 0.04
$\tilde{H}n$	0.34 ± 0.03
$\tilde{B}p$	0.10 ± 0.01
$\tilde{B}n$	0.010 ± 0.003
$\tilde{Z}p$	0.9 ± 0.1
$\tilde{Z}n$	0.002 ± 0.006

Table 3.2: *C^2 factors estimated from Eqn. 3.6 for different neutralino compositions w and nucleon targets i. Adapted from Table 4 in [84].*

Isotope	*Odd Nucleon*	J	$\lambda^2 J(J+1)_{eff}$			
			$\tilde{\gamma}$	$\tilde{H}$	$\tilde{B}$	$\tilde{Z}$
^{1}H	p	1/2	0.750	0.750	0.750	0.750
^{19}F	p	1/2	0.685	0.696	0.684	0.676
^{23}Na	p	3/2	0.097	0.089	0.097	0.103
^{27}Al	p	5/2	0.155	0.142	0.156	0.166
^{29}Si	n	1/2	0.053	0.053	0.053	0.053
^{73}Ge	n	9/2	0.103	0.141	0.096	1.400
^{127}I	p	5/2	0.112	0.084	0.114	0.136
^{125}Te	n	1/2	0.248	0.248	0.248	0.248
^{129}Xe	n	1/2	0.231	0.316	0.216	3.200
^{131}Xe	n	3/2	0.067	0.078	0.065	0.34

Table 3.3: *$\lambda^2 J(J+1)_{eff}$ for different nuclei and neutralino compositions. From [93].*

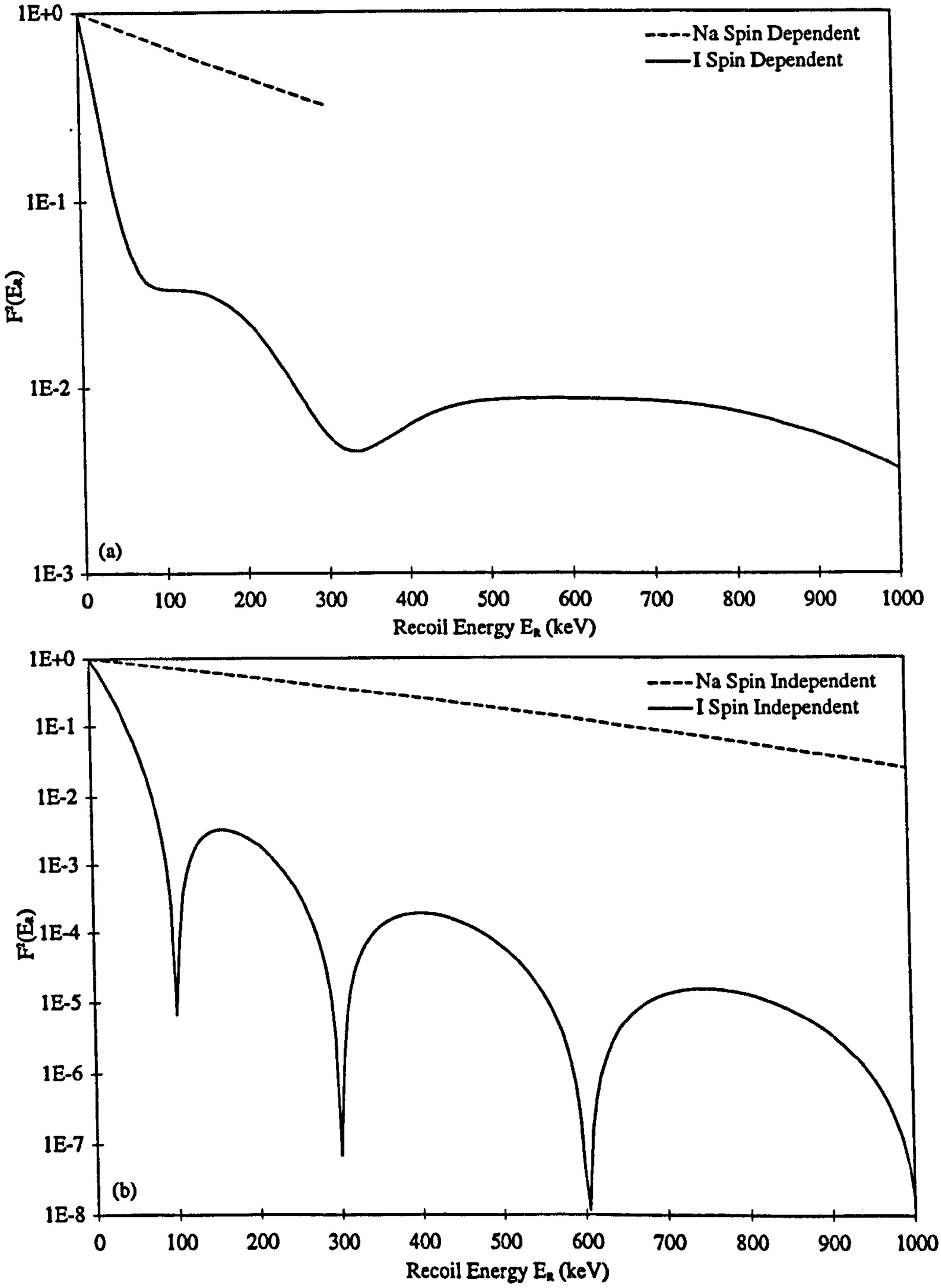

Figure 3.5: *Form factors for Na and I plotted as functions of recoil energy E_R. Figure (a) shows the spin dependent form factors from [93] using calculations in [94]. Figure (b) shows the spin independent form factors calculated using Eqn. 3.20 with c parameters determined from fits to muon-nucleus scattering data [84].*

3.3.2 Spin Independent Neutralino Interactions

In the case of spin independent cross sections the route from elementary matrix element to neutralino-nucleus cross section is similar to that outlined above. Here however the calculation is complicated by the contribution to the cross section made by scalar neutralino-gluon scattering via squark and Higgs exchange at the one loop level [46]. This may be similar in magnitude to the scalar neutralino-quark contribution due to tree level t channel Higgs exchange and s channel squark exchange (Fig. 3.6). Vector interactions do not occur due to the Majorana character of the neutralino [46].

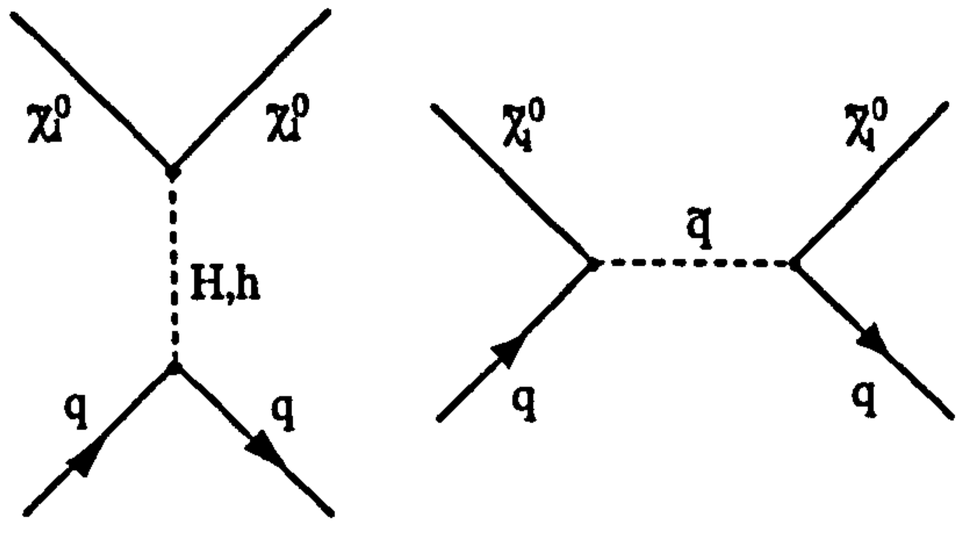

Figure 3.6: *Tree level diagrams contributing to spin independent neutralino-nucleus scattering.*

The scalar interaction responsible for spin independent interactions traces the mass distribution of the nucleus. The expectation value of the overall neutralino-nucleus matrix element is thus proportional to the total nuclear mass due to coherence effects. The cross section for a point like nucleus of atomic mass A is then proportional to a spin independent coupling enhancement factor $I_{si} = A^2$ [46]:

$$\begin{aligned} \sigma &= \frac{4\mu^2 f^2}{\pi} I_{si} \\ &= \sigma_0 I_{si}, \end{aligned} \tag{3.18}$$

for generic nucleon coupling parameters f. The spin independent coupling enhancement factor must be modified by a form factor at finite momentum transfer just as before, however since the coherence is now governed by the nuclear mass rather than spin distribution the Fourier transform of the mass distribution provides a rather accurate estimate for $F^2(q)$. The simplest approximation is to assume a solid sphere nucleus of radius $r_n = 1.1A^{1/3}$ fm (given constant nuclear mass density), in which

case [84]:

$$F^2(q) = \left(\frac{3j_1(qr_n)}{qr_n}\right)^2 = \frac{9\left(\sin(qr_n) - qr_n\cos(qr_n)\right)^2}{(qr_n)^6}. \quad (3.19)$$

A better fit to experimental fixed target elastic lepton-nucleon scattering data [95] is provided by multiplying this expression by an additional term accounting for a smeared out nuclear density at large radius [96]:

$$F^2(q) = \left(\frac{3j_1(qr_n)}{qr_n}\right)^2 e^{-qs^2}, \quad (3.20)$$

where s is determined by the fit and is generally $\sim$ 0.9 fm. This form factor is plotted for iodine and sodium (again using Eqn. 3.12) in Fig. 3.5(b).

Detailed calculations of spin independent cross sections including one loop effects are now available [46] but unlike in the spin dependent case the MSSM model dependency does still seem to be confined to the neutralino-quark coupling and model independent limits can still be set. The spin independent cross section is found to vanish for pure gaugino or Higgsino states [84] but is nevertheless significant and comparable to the spin dependent cross section in large regions of the MSSM parameter space.

3.3.3 Other WIMPs

Direct detection experiments searching for elastic nuclear recoils are sensitive to WIMPs other than neutralinos. Some consideration must therefore also be given to the cross sections for the scattering of these particles. One general model encountered previously is that incorporating a heavy neutrino (§1.5.2). If this is a Majorana particle then it has a spin dependent total point like cross section given by [84]

$$\sigma = \frac{2G_F^2}{\pi\hbar^4}\mu^2 I_{sd}, \quad (3.21)$$

where the I_{sd} and $F^2(q)$ are those derived for Higgsino scattering (Z^0 exchange). The spin independent cross section is similar to that for neutralinos (Eqn. 3.18) but with different generic nucleon couplings f.

For a Dirac neutrino the spin dependent cross section is one quarter of that for a Majorana neutrino [84]. The spin independent scattering of heavy Dirac neutrinos is governed by vector Z^0 exchange and traces the nuclear *charge* distribution [46].

The point like cross section is given by [84]

$$\sigma = \frac{G_F^2}{8\pi\hbar^4}\mu^2 I_{si}. \tag{3.22}$$

where the spin independent coupling enhancement factor I_{si} is

$$\begin{aligned} I_{si} &= \left((A-Z) + \left(1 - 4\sin^2\theta_W\right) Z\right)^2 \\ &\simeq (A-Z)^2 . \end{aligned} \tag{3.23}$$

The distribution of nuclear charge is similar to that of nuclear mass [46] and so the form factor $F^2(q)$ may be approximated by that due to a smeared solid sphere distribution (Eqn. 3.20), as in the case of neutralino scattering.

In limited regions of MSSM parameter space the LSP is the sneutrino (§2.4) and in this case owing to the predominance of Z^0 exchange the sneutrino scattering cross sections are merely those for the heavy Dirac neutrino multiplied by a factor of four [84]. All cross sections above may be converted to σ_0 through the use of Eqn. 3.6 or Eqn. 3.18.

3.4 Nuclear Recoil Kinematics

In order to calculate the *shape* of the nuclear recoil energy spectrum, nuclear recoil kinematics as well as form factor effects must be taken into account. In the former case it is the direction of scatter and the magnitude and direction of the WIMP velocity vector which fix the recoil energy while in the latter it is the magnitude of the momentum transfer q. Having already derived expressions for $F^2(E_R)$ the kinematic contribution will now be discussed. The reader is referred to Appendix A of [84] for a more detailed derivation of the formulae used.

3.4.1 Halo Models

When considering nuclear kinematics a WIMP phase space distribution must first be assumed as this determines the energies of the incoming WIMPs prior to scattering. It is generally assumed that the WIMP halo has had sufficient time to virialise in the potential well of the galaxy [97], although less conventional models are also possible [98]. In the virial case the distribution is Maxwellian with velocity dispersion v_0 determined from the specific dark matter halo model being used. Due to uncertainties in observational parameters and the halo models themselves v_0 is known only imprecisely, lying in the range $\sim 270 \pm 70$ km s^{-1} for the simplest isothermal sphere models [97]. More complicated models assume a flattened halo which may or

may not be corotating with the luminous disc, however estimates of v_0 are generally similar within errors.

The halo model also permits the local WIMP density ρ_{DM} to be calculated from observed galactic rotation curves (§1.3.2). Depending on the model this density is typically in the range 0.3 GeV/c^2 cm^{-3} to 0.7 GeV/c^2 cm^{-3} in the absence of any baryonic component [84]. Recent microlensing results (§1.5.1) indicate that there may in fact be a significant baryonic MACHO component to the halo and taking this into account gives a conservative estimate of 0.4 GeV/c^2 m^{-3} [88].

The velocity $\vec{v}_w$ of any WIMP relative to the rest frame of the halo is given by the vector sum of its velocity in the earth's frame of reference $\vec{v}$ and the velocity of the earth through the halo (assumed to be non-rotating) given by $\vec{v}_E$. Thus the Maxwell-Boltzmann phase space distribution discussed above may be written

$$f(\vec{v}, \vec{v}_E) = e^{-\frac{(\vec{v}+\vec{v}_E)^2}{v_0^2}}. \tag{3.24}$$

The WIMP density distribution is then given by

$$dn = \frac{n_0}{k} f(\vec{v}, \vec{v}_E) d^3\vec{v}. \tag{3.25}$$

Here n_0 is the mean WIMP number density ($= \rho_{DM}/M_D$) for WIMP mass M_D and k is a normalisation factor given by [84]

$$k = \int_0^{2\pi} d\phi \int_{-1}^{+1} d(\cos\theta) \int_0^{v_{esc}} f(\vec{v}, \vec{v}_E) v^2 dv, \tag{3.26}$$

where v_{esc} is the galactic escape velocity. Performing the integrals in Eqn. 3.26 then gives [84]

$$k = k_0 \left(\mathrm{erf}\left(\frac{v_{esc}}{v_0}\right) - \frac{2}{\pi^{1/2}} \left(\frac{v_{esc}}{v_0}\right) e^{\frac{-v_{esc}^2}{v_0^2}} \right), \tag{3.27}$$

where

$$k_0 = \left(\pi v_0^2\right)^{3/2}. \tag{3.28}$$

3.4.2 The Scattering Process

The WIMP event rate per unit mass for a target of atomic mass A is given by (following [84] throughout this section)

$$dR = \frac{N_A}{A} \sigma v dn, \tag{3.29}$$

where N_A is the Avogadro number and σ is the scattering cross section from §3.3. The total event rate is the integral of this expression,

$$R = \frac{N_A}{A} \sigma \int v dn. \tag{3.30}$$

Defining R_q as the total rate for a target at rest w.r.t. an infinite halo ($v_E = 0$ and $v_{esc} = \infty$), i.e.

$$R_q = \frac{2}{\pi^{1/2}} \frac{N_A}{A} \frac{\rho_{DM}}{M_D} \sigma v_0, \tag{3.31}$$

the following total event rate is obtained

$$R = R_q \frac{k_0}{k} \frac{1}{2\pi v_0^4} \int v f(\vec{v}, \vec{v}_E) d^3v. \tag{3.32}$$

This expression may be used more usefully in its differential form

$$dR = R_q \frac{k_0}{k} \frac{1}{2\pi v_0^4} v f(\vec{v}, \vec{v}_E) d^3v. \tag{3.33}$$

Now a non-relativistic WIMP of mass M_D and speed v has kinetic energy $E(v)$ given by

$$E(v) = \frac{1}{2} M_D v^2, \tag{3.34}$$

The kinetic energy E_R in the lab. of a recoiling nucleus struck by such a particle is

$$E_R = \frac{Er}{2\,(1 - \cos\theta)}, \tag{3.35}$$

where θ is the CMS scattering angle and r is given by

$$r = \frac{4 M_D M_T}{(M_D + M_T)^2}. \tag{3.36}$$

Assuming isotropic scattering in $\cos\theta$ and hence a uniform distribution of $E_R < Er$,

$$\begin{aligned} \frac{dR}{dE_R} &= \int_{E_{min}}^{E_{max}} \frac{1}{Er} dR(E) \\ &= \frac{1}{E_0 r} \int_{v_{min}}^{v_{max}} \frac{v_0^2}{v^2} dR(v), \end{aligned} \tag{3.37}$$

where $E_{min} = E_R/r$, $E_0 = E(v_0)$ and

$$v_{min} = \sqrt{\frac{2E_{min}}{M_D}}. \tag{3.38}$$

Hence from Eqn. 3.33

$$\frac{dR}{dE_R} = \frac{R_q}{E_0 r} \frac{k_0}{k} \frac{1}{2\pi v_0^2} \int_{v_{min}}^{v_{max}} \frac{1}{v} f(\vec{v}, \vec{v}_E) d^3v. \tag{3.39}$$

For a target at rest w.r.t. an infinite halo this expression integrates to give

$$\frac{dR(0,\infty)}{dE_R} = \frac{R_q}{E_0 r} e^{-\frac{E_R}{E_0 r}}. \tag{3.40}$$

In fact $v_{esc} \sim 600$ km s^{-1} [99] and the earth orbits the sun in a plane at angle 60^o to the sun's galactic velocity leading to [84]

$$v_E \simeq 244 + 15\sin(2\pi t)\text{kms}^{-1}, \tag{3.41}$$

for time t (in years) from 2^{nd} March. In this case

$$\frac{dR(v_E,\infty)}{dE_R} = \frac{R_q}{E_0 r}\frac{\pi^{1/2}}{4}\frac{v_0}{v_E}\left(\text{erf}\left(\frac{v_{min}+v_E}{v_0}\right) - \text{erf}\left(\frac{v_{min}-v_E}{v_0}\right)\right), \tag{3.42}$$

and

$$\frac{dR(v_E,v_{esc})}{dE_R} = \frac{k_0}{k}\left(\frac{dR(v_E,\infty)}{dE_R} - \frac{R_q}{E_0 r}e^{-\frac{v_{esc}^2}{v_0^2}}\right). \tag{3.43}$$

In all that follows this equation will be written in abbreviated form:

$$\begin{aligned}\frac{dR}{dE_R} &= \frac{R_q}{E_0 r}.\frac{k_0}{k}.\left(\frac{E_0 r}{R_q}\frac{dR(v_E,\infty)}{dE_R} - e^{-\frac{v_{esc}^2}{v_0^2}}\right)\\ &= R_0.S(E_R).F^2(E_R),\end{aligned} \tag{3.44}$$

where R_0 is the raw point like rate given by

$$R_0 = \frac{R_q}{F^2(E_R)}, \tag{3.45}$$

and $S(E_R)$ is the 'spectral' function. This is the differential recoil energy spectrum of WIMP scattering events from nuclei. Ignoring the form factor dependence of σ, the spectrum is seen to closely resemble an exponential function (Fig. 3.7 overleaf), as would be expected from the form of the approximate spectrum given by Eqn. 3.40. The time dependence of Eqn. 3.44 is also illustrated in Fig. 3.7.

The normalisation of Eqn. 3.44 is expressed in terms of the raw point like rate R_0 however this may be converted quite simply into a normalisation in terms of σ_0 by using Eqn. 3.30, Eqn. 3.45, Eqn. 3.8 and the trivial relation

$$\mu^2 = \frac{rM_D M_T}{4}. \tag{3.46}$$

It is then found that R_0 is directly related to σ_0 by

$$\frac{R_0}{r} = \frac{m_N \rho_{DM} N_A v_0}{2\pi^{1/2}}.\frac{\sigma_0}{\mu^2}. \tag{3.47}$$

In convenient units this gives

$$\frac{R_0}{r} \simeq 1.37\rho_{DM}v_0.\frac{\sigma_0}{\mu^2}, \tag{3.48}$$

with ρ_{DM} in GeV/c^2 cm^{-3}, v_0 in km s^{-1}, R_0/r in kg^{-1} day^{-1} and σ_0 in pb (μ is dimensionless).

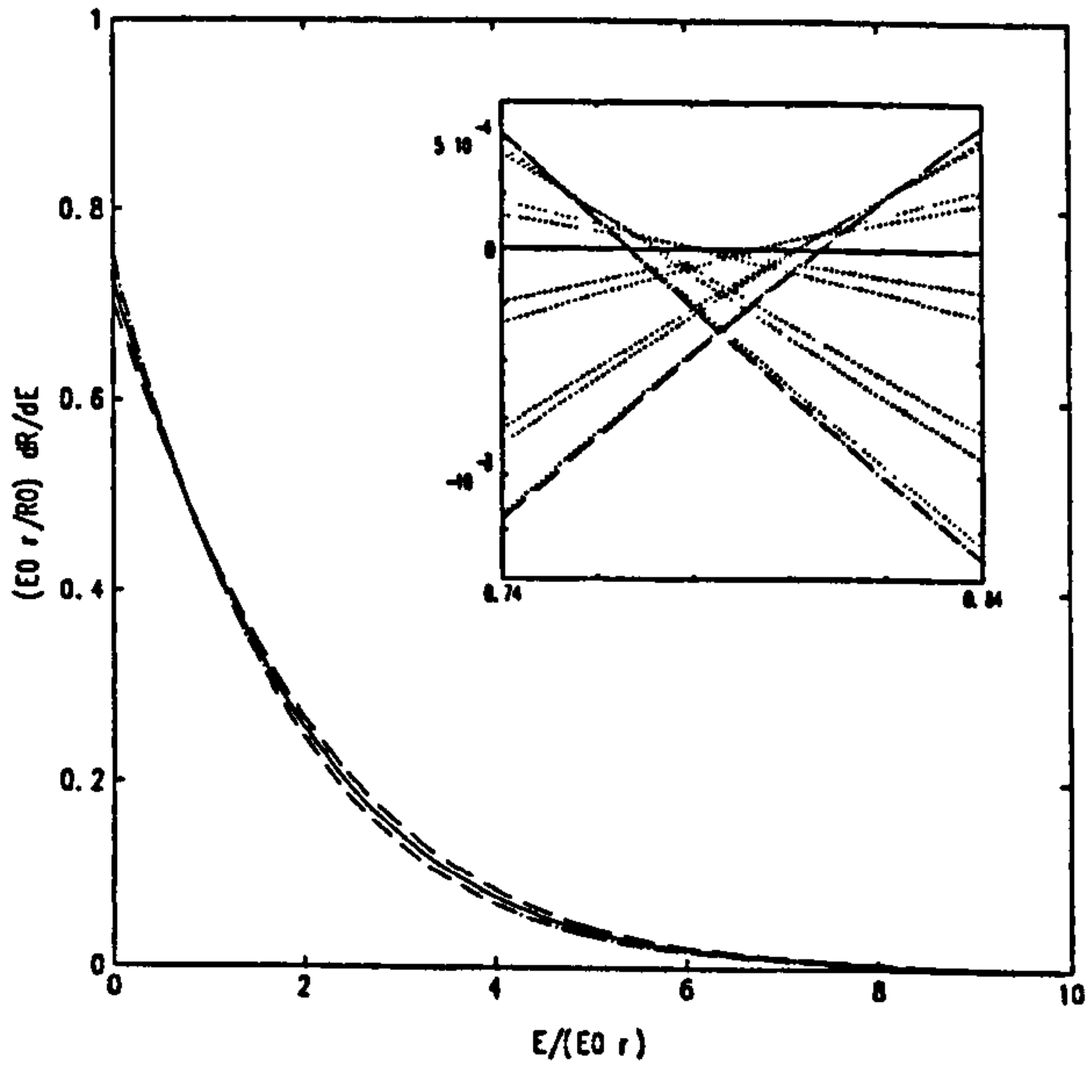

Figure 3.7: *Raw differential nuclear recoil energy spectrum of WIMP scattering events from Eqn. 3.44. The full line is the time averaged spectrum over the course of one year. The dashed and dash-dotted lines are summer and winter spectra. Inset is a detail of the cross over region showing monthly spectra after the subtraction of the yearly mean spectrum. Taken from [84].*

3.5 Target Specific Factors

Having established the form of the raw WIMP induced recoil energy spectrum of individual nuclei (Eqn. 3.44) the total spectrum of such events within a target material of given elemental composition must now be calculated. This must also take into account the fact that within a given target the physics of the energy transfer process limits the amount of deposited energy which can be directly observed. This behaviour is independent of the design of the detector itself and is referred to as the energy detection efficiency.

3.5.1 Target Composition

The target at the heart of a particular detector may contain more than one species of target nucleus. In this case the total energy spectrum is given merely by the sum of the spectra of the constituent nuclei weighted by the appropriate mass fraction $f(A)$.

If data from the detector is being used to set limits however, such as was done in Fig. 3.2, then a different approach can be used. The target material (of mass m)

contains a total mass $m.f(A)$ of each target nucleus and so cross section limits can be calculated using the results of this chapter for each nucleus separately. Examples of these single nucleus limits are plotted in Fig. 3.2. By considering Eqn. 3.44 the total raw cross section limit σ_0 is then related to the raw cross section limits $\sigma_0(A)$ from individual nuclei by

$$\begin{aligned}\frac{1}{\sigma_0} &= \frac{a}{dR/dE_R}\sum_A f(A).S(A,E_R).F^2(A,E_R) \\ &= \sum_A \left(\frac{a.f(A).S(A,E_R).F^2(A,E_R)}{dR/dE_R}\right) \\ &= \sum_A \frac{1}{\sigma_0(A)}, \end{aligned} \tag{3.49}$$

where a is the $R_0 - \sigma_0$ conversion factor from Eqn. 3.48.

3.5.2 Energy Detection Efficiency

In many classes of detector the amount of energy detected for a particular recoil is dependent not only on the recoil energy but also on the type of particle recoiling. This causes problems because *in situ* calibration of operational detectors is generally performed using monoenergetic gamma sources, which produce only electron recoils. This means that any experimentally observed energy spectrum is equivalent to the true recoil energy spectrum *iff* all the events are due to electrons. The spectrum of nuclear recoils in terms of E_R (Eqn. 3.44) may be converted to a spectrum in terms of the electron equivalent or 'visible' energy E_v by means of an absolute energy detection efficiency $g_a(A,E_R) = E_v/E_R$. This efficiency is a property of the specific target nucleus and of the target material through which it is travelling.

In practice $g_a(A,E_R)$ can be determined by performing nuclear recoil calibrations for each nucleus in each target material using a monoenergetic neutron beam, as described in §6.4. Because operational detectors are calibrated with high energy gamma sources rather than at low energies the efficiency is in fact calculated relative to this high energy point. This relative efficiency $g_r(A,E_R)$ is clearly only an approximation to the absolute efficiency since it neglects the effects of non-linearities in the electron recoil response at low energy. Nevertheless $g_r(A,E_R)$ may still be used to convert nuclear recoil energy to visible energy just so long as $g_a(A,E_R)$ is constant at the energies used for gamma calibration during data taking and neutron beam tests.

In some circumstances $g_r(A,E_R)$ can be evaluated theoretically. One approach used with crystal scintillators is to assume Birks' formula for the visible energy

emitted by a recoil per unit path length x [100]

$$\frac{dE_v}{dx} = \frac{SdE'_R/dx}{1 + kBdE'_R/dx}, \tag{3.50}$$

for constant S and kB. Rearranging this expression gives

$$E_v = \int_{E_R}^{0} \frac{S}{1 + kBdE'_R/dx}.dE'_R, \tag{3.51}$$

and so

$$g_r(A, E_R) = \frac{E_v}{E_R} = \frac{1}{E_R}.\int_{E_R}^{0} \frac{S}{1 + kBdE'_R/dx}.dE'_R. \tag{3.52}$$

Due to the pick up of electrons the value of dE_R/dx for nuclei is expected to fall at energies below [101]

$$E_c = \frac{M_T}{4m_e}\left((T_e + E_g)^{1/2} - T_e^{1/2}\right)^2, \tag{3.53}$$

for electron binding energy E_g and kinetic energy T_e. Thus Eqn. 3.52 leads to a rise in $g_r(A, E_R)$ for nuclei at low energy (§6.4).

Another approach, valid for ionisation detectors, is to use Lindhard theory [101]. This parameterises $g_r(A, E_R)$ at energies greater than E_c in terms of the recoil energy directly:

$$g_r(A, E_R) = \frac{g'(E_R)}{1 + g'(E_R)}, \tag{3.54}$$

where the function $g'(E_R)$ is defined by

$$g(E_R) = 0.6E_1^{\frac{1}{6}} + 0.2E_1^{\frac{2}{3}} + 0.8E_1, \tag{3.55}$$

and

$$E_1 = \frac{Z^{\frac{5}{3}}}{A^3}E_R. \tag{3.56}$$

The onset of electron pick up at energies $\sim E_c$ can be taken into account by the multiplication of Eqn. 3.54 by an exponential term [101]:

$$g_r(E_R) = \frac{g'(E_R)}{1 + g'(E_R)}\left(1 - e^{-E_R/E_c}\right). \tag{3.57}$$

Values for the relative energy detection efficiency calculated using the above formulae are generally rather imprecise and so it is preferable to use the results of experimental neutron beam calibrations. Given a value for $g_r(A, E_R)$ for the specific

nucleus and target being considered the observed energy spectrum of nuclear recoils can be calculated from:

$$\begin{aligned}\frac{dR}{dE_v} &= \frac{dR}{d(g_r E_R)} \\ &= \frac{1}{g_r}\left(1+\frac{E_R}{g_r}\frac{dg_r}{dE_R}\right)^{-1}\frac{dR}{dE_R} \\ &= G_r\frac{dR}{dE_R}. \end{aligned} \tag{3.58}$$

The overall effect of the energy detection efficiency (which is usually $\leqslant 1$) is to soften the visible energy spectrum with respect to the recoil energy spectrum in Eqn. 3.44. This softening has the undesirable effect of causing any non-zero detector visible energy threshold (§3.6) to cut out considerably more of the nuclear recoil spectrum, reducing the sensitivity of the detector. This is of particular importance for scintillator detectors where g_r, referred to as the relative scintillation efficiency, is generally $\lesssim 30$ %.

3.6 Detector Specific Factors

The above considerations apply to any experiment searching for direct evidence of WIMPs via elastic nuclear recoil. There are other contributions to the recoil energy spectrum however which depend specifically on the physical design of the detector. In this section the statistical character of these effects will be investigated before discussing how to account for them when considering the observed WIMP induced nuclear recoil energy spectrum.

3.6.1 Statistical Effects

At the simplest level all detectors have a finite visible energy threshold E_{thresh} and this prevents all nuclear recoil events with $E_v < E_{thresh}$ from being observed. In noisy detectors the threshold should be set at a level below which irreducible background noise dominates the spectrum. For large numbers of noise events this threshold is then sufficiently high to give a sudden cut off in the energy spectrum (e.g. Fig. 8.21). If the threshold is low however then it may approach the minimum energy physically observable within the detector E_{lo}. One example of this is in scintillator detectors using photomultiplier tubes (§4.3.2), where the scintillation pulse consists of a finite number of photons. An event cannot be registered if it contains less than one photon and so this sets the value of E_{lo}. Generally for $E_{thresh} \sim E_{lo}$ the statistics of the

system come into play and there is no longer a hard cut off in the energy spectrum at E_{thresh}.

These statistical processes also modify the energy spectrum in other ways. Most importantly they lead to a finite detector energy resolution which must be convolved with the theoretical energy spectrum (Eqn. 3.44) to obtain the observed spectrum. Furthermore, the use of noise rejection cuts (§8) introduces an energy dependent event identification efficiency which can lead to further statistical variation into the energy spectrum. When calculating the observed energy spectrum it is often possible to model these effects analytically however for simplicity it is generally preferable to use Monte Carlo techniques (§7).

All the statistical processes at work within a given detector contribute to the fluctuations in the measured energy spectrum. Very often however most of these processes can be neglected, since by far the greatest variability arises from the statistics of that one part of the detector in which the number of discrete 'Information Carriers' (ICs) such as photons, electrons or phonons is at a minimum.

To prove this statement the physics of the detector itself must be examined [102]. In any given event the recoil energy of an electron or nucleus is absorbed by the material through which it is travelling. This energy is shared between a finite number n_0 of ICs, each with probability p_0 of emission. The probability of n_1 ICs being emitted is given by the binomial distribution:

$$P(n_1) = \frac{n_0!}{(n_0 - n_1)!n_1!} p_0^{n_1} (1 - p_0)^{n_0 - n_1}, \tag{3.59}$$

with the expected number of emitted ICs $\bar{n}_1$ being given by $n_0 p_0$ and its variance $V(n_1)$ by $n_0 p_0 (1 - p_0)$. In most detectors the probability p_0 is small and so the binomial distribution may be approximated by the Poisson distribution:

$$P(n_1) = \bar{n}_1^{n_1} \frac{e^{-\bar{n}_1}}{n_1!}, \tag{3.60}$$

with expectation and variance given by $\bar{n}_1$.

Each emitted IC can be absorbed or cause secondary emission thus giving n_2 total ICs at some arbitrary subsequent point. This process may be repeated many times before the event is registered in the detector Data Acquisition (DAQ) electronics. If there are n_i ICs at point i then the relative variance in n_i is given by $V(n_i)/n_i^2$. If zero signal fluctuations for all previous points are assumed then the relative variance at point i is $1/n_i$ by the properties of Poisson statistics. These idealised relative variances can now be summed in quadrature to obtain the total relative variance at

point i taking into account the fluctuations at all previous points:

$$\frac{V(n_i)}{n_i^2} = \sum_{i'=0}^{i} \frac{1}{n_{i'}}. \tag{3.61}$$

Thus the variance and hence the fluctuation in the number of ICs recorded by the DAQ system (n_∞) is dominated by the contribution from that point at which n_i is smallest [102]. This means that in many cases the standard deviation $\sigma(n_\infty)$ in n_∞ is approximately $n_\infty/\sqrt{n_{min}}$ for n_{min} minimal ICs. Since $E_v \propto n_\infty$ the detector energy resolution is then:

$$R = 2.35\frac{\sigma(E_v)}{E_v} = 2.35\sqrt{\frac{k}{E_v}}, \tag{3.62}$$

where k is the visible energy per minimal IC. The resolution may contain additional contributions independent of the physics of the detector itself, e.g. due to poor signal digitisation in the DAQ system, however in an optimised detector these should be small.

A further approximation to the energy resolution may also be made. From the preceding discussion the distribution of observed energies from a line source is in general Poissonian with mean $\bar{E}_v$ and width $\sigma(\bar{E}_v)$. For a large number of ICs the Poisson distribution tends to a normal distribution:

$$P(E_v)dE_v = \frac{1}{\sigma(\bar{E}_v)\sqrt{2\pi}} e^{-\frac{(E_v-\bar{E}_v)^2}{2\sigma^2(\bar{E})}} dE_v. \tag{3.63}$$

This is much simpler to evaluate than the Poisson distribution and so is generally preferred in Monte Carlo calculations convolving the energy response of a detector (here Eqn. 3.63) with the raw recoil energy spectrum (Eqn. 3.44).

The binomial distribution is also of use when considering multichannel detectors. These detectors have the great advantage of incorporating significant noise rejection since such noise may be expected to be generated only within one channel at any given time (e.g. thermal photoelectrons in a photomultiplier tube - §4.3.2). Thus by requiring a coincidence between two or more such channels these noise events can be rejected on line. This does of course raise the detector energy threshold by a factor equal to the number of channels required to be in coincidence. This is generally not a problem however as without a coincidence requirement the threshold must still be raised to provide equivalent noise rejection. If channel j of a k channel detector has a probability p_j of receiving each IC that is generated in an event then the probability of receiving n_j ICs in j is given by a multinomial distribution:

$$P(n_1, n_2, \ldots, n_k) = \frac{N!}{\prod_j n_j!} \prod_j p_j^{n_j}. \tag{3.64}$$

Here N is the mean total number of ICs generated. In the case of a two channel detector this then reduces to the binomial distribution (not the Poisson distribution as stated in [84]).

Additional cuts on event parameters can be performed on data off line, particularly in the case of multichannel detectors. In particular parameters such as individual channel pulse heights should be similar to within a few standard deviations of their governing distributions for a balanced detector. In the pulse height case this is equivalent to performing a more stringent cut on the tails of the multinomial distribution discussed above. Similar consistency cuts can also be performed on event start time and background discrimination parameters. These cuts will be discussed in more detail in §8.

3.6.2 Event Identification Efficiency

The overall effect of all these cuts, including the finite detector energy threshold, is to reduce the efficiency ϵ with which valid events can be identified. ϵ is energy dependent and may be quantified by Monte Carlo simulation. ϵ also takes into account modification of the energy spectrum due to finite detector energy resolution and so may be expressed in the form of a response matrix M with elements $M(E'_v, E_v)$ for raw and observed visible energies E'_v and E_v respectively. For either a spin dependent or a spin independent interaction the final expression for the observed differential nuclear recoil visible energy spectrum given in §3.2.1 is then obtained:

$$\frac{dR}{dE_v} = R_0 . \sum_{E'_v} M(E'_v, E_v) . \sum_{A} f(A) . G_r(A, E_R) . S(A, E_R) . F^2(A, E_R) . I(A). \quad (3.65)$$

This function is plotted in Fig. 3.8 for illustrative WIMP masses of 20 GeV/c^2 and 10 TeV/c^2. In the presence of both spin dependent and spin independent interactions the total energy spectrum is given by the sum of the separate contributions from each.

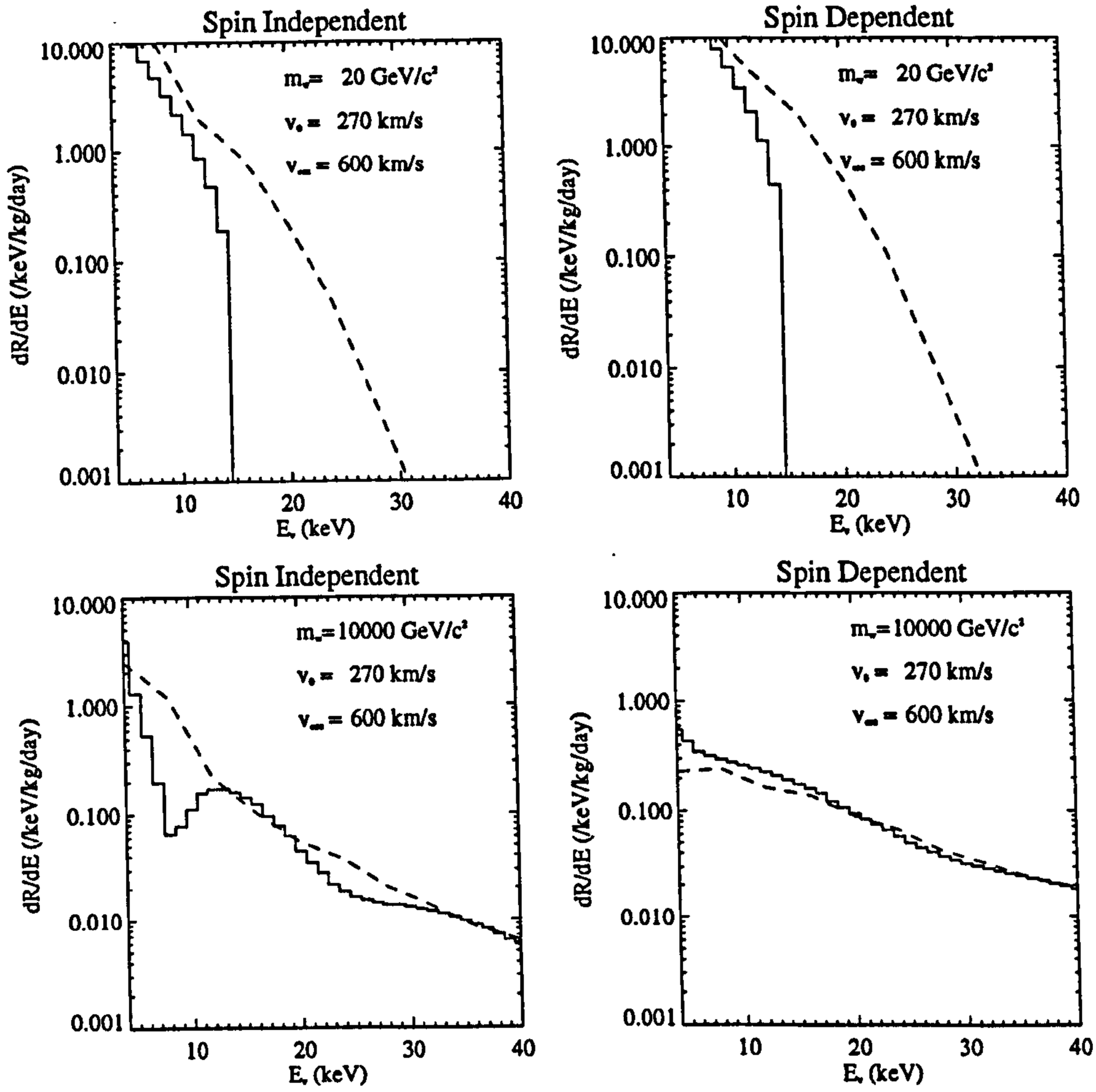

Figure 3.8: *Simulated WIMP signal spectra in a NaI(Tl) scintillator detector. The upper and lower plots are respectively for 20 GeV/c^2 and 10 TeV/c^2 WIMPs. The full histograms are raw spectra from Eqn. 3.44 converted to visible energy with Eqn. 3.58 and the dashed lines are the same spectra convolved with a realistic detector response (Eqn. 3.65). The simulation is that used in §8.*

3.7 Calculating Dark Matter Limits

The means by which limits on the properties of WIMP dark matter may be set will now be considered. The first step is to calculate the number of potential signal events which are contained within each visible energy bin. A further binning may also be performed in terms of the Julian date d_j of the event if the detector has been running for $\gtrsim$ 6 months. This enables a search for an annual modulation of the signal event rate caused by the variation of v_E over the year (Eqn. 3.41). Throughout the following discussion such a time binning will be assumed for the

purposes of generality. In practice however, and particularly in the absence of any discernible signal, the analysis of data can be performed without this time binning so as to improve the statistics in each energy bin.

The next step depends upon the capabilities of the detector. In non-discriminating detectors only an upper limit on the number of signal events in each $E_v - d_j$ bin can be set. For this reason it may be said that such detectors can only set limits on the properties of WIMP dark matter and cannot actually discover it. Experimentalists using electron recoil discriminating detectors on the other hand make use of the extra information which they provide to determine the number of signal events within the bin, as opposed to the number of signal + (electron recoil) background events. The discrimination process may proceed in one of a number of ways depending upon the quality of the detector and data. In all cases the starting point is the value of a discriminating variable r_c calculated for each event. This variable can be extracted directly or in more complicated cases can be derived from an optimised combination of a number of other such variables.

3.7.1 High Discrimination Efficiency

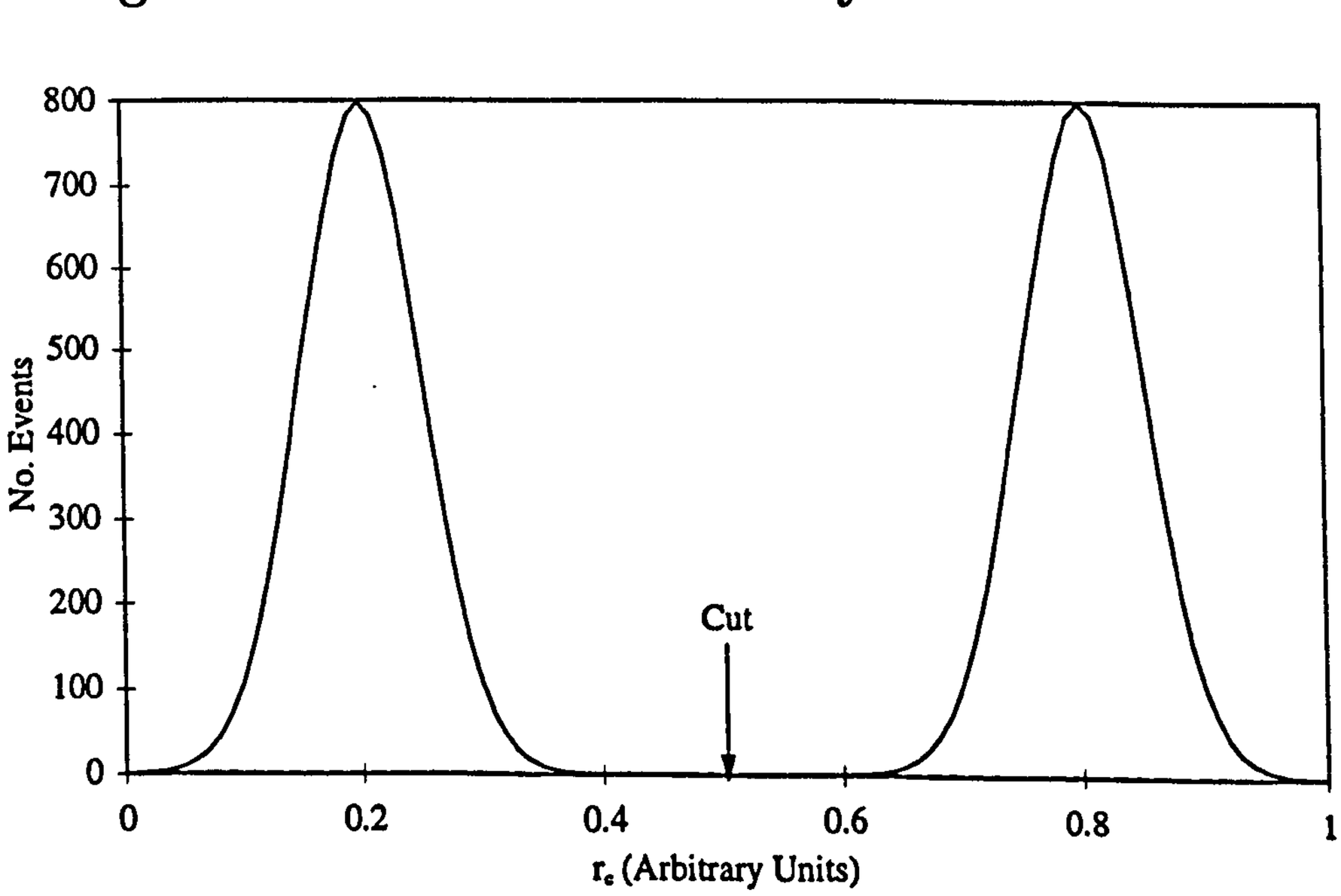

Figure 3.9: *A possible distribution of r_c for high discrimination efficiency. The dashed lines (barely visible) represent the contributions from signal and background. The full line is the sum.*

In the case of detectors with high discrimination efficiency the values of r_c for signal events in a given $E_v - d_j$ bin are well separated from those for background events

(Fig. 3.9). In this case it is appropriate to make a cut on r_c at a value $r_{cut}(E_v, d_j)$ in each bin to reject the majority of background events. The mean remaining number of background events passing the cut in each bin $\mu_B(E_v, d_j)$ may be estimated from the number of events failing the cut $n_<(E_v, d_j)$ and the detector background discrimination efficiency $D(E_v, d_j)$ (100% for complete discrimination):

$$\mu_B = n_< \frac{(1-D)}{D}. \tag{3.66}$$

The position of r_{cut} in each bin should be optimised prior to running on actual data through the use of calibrations or simulations. In this way the values of μ_B may be minimised while maximising ϵ for signal events. A suitable minimisation variable useful for determining r_{cut} in this way is the nuclear recoil signal limit $R_n(E_v, d_j)$ determined from [103]:

$$1 - c = 1 - \frac{e^{-(\mu_B - R_n)} \sum_{n=0}^{n_0} \frac{(\mu_B + R_n)^n}{n!}}{e^{-\mu_B} \sum_{n=0}^{n_0} \frac{\mu_B^n}{n!}}, \tag{3.67}$$

where $100(1-c)$ is the desired percentage confidence limit and n_0 is the observed number of events passing the cut.

A log-likelihood fit may now be made to the observed number of events passing the cuts in all bins using a sum of $\mu_B(E_v, d_j)$ and the expected signal spectrum (Eqn. 3.65 multiplied by bin width and detector exposure), with the normalisation of the latter ($R_0/r(m_w)$ or $\sigma_0(m_w)$) the free parameter. The fit should be performed several times for different assumed WIMP masses m_w and WIMP interactions.

If the calculated values of $R_0/r(m_w)$ or $\sigma_0(m_w)$ are inconsistent with zero for some m_w bins then the fits should be reperformed using m_w and any other unknown variables as free parameters. This permits an allowed region of parameter space to be delimited for the potential signal. This should then enable comparison with results from other detectors and subsequent investigations.

If however the fits give values of $R_0/r(m_w)$ or $\sigma_0(m_w)$ which are consistent with zero within errors then conservative confidence limits may be set on these parameters using Monte Carlo simulation or (in the case of Gaussian errors) the standard deviations $\sigma(R_0/r(m_w))$ or $\sigma(\sigma_0(m_w))$ (i.e. using 1.28σ for 90% C.L.). $R_0/r(m_w)$ limits are often expressed relative to the equivalent rate in a Ge detector by multiplying the limit by a factor $I(\mathrm{Ge})$ equivalent to the appropriate spin dependent or spin independent coupling enhancement factor of germanium. Cross section limits are by contrast often normalised to the WIMP-nucleon cross section σ_{w-N} by multiplying by $I(\mathrm{nucleon})$ (proton for spin dependent interactions and neutron for spin independent interactions). The curves in $R_0/r - m_w$ space or equivalently $\sigma_{w-N} - m_w$

space connecting the calculated limits for different WIMP masses m_w constitute 'limit curves' and it is these which all experiments quote in their published results. Crucially the curves can be compared with, and used to constrain, the predictions of theories such as the MSSM.

3.7.2 Moderate Discrimination Efficiency

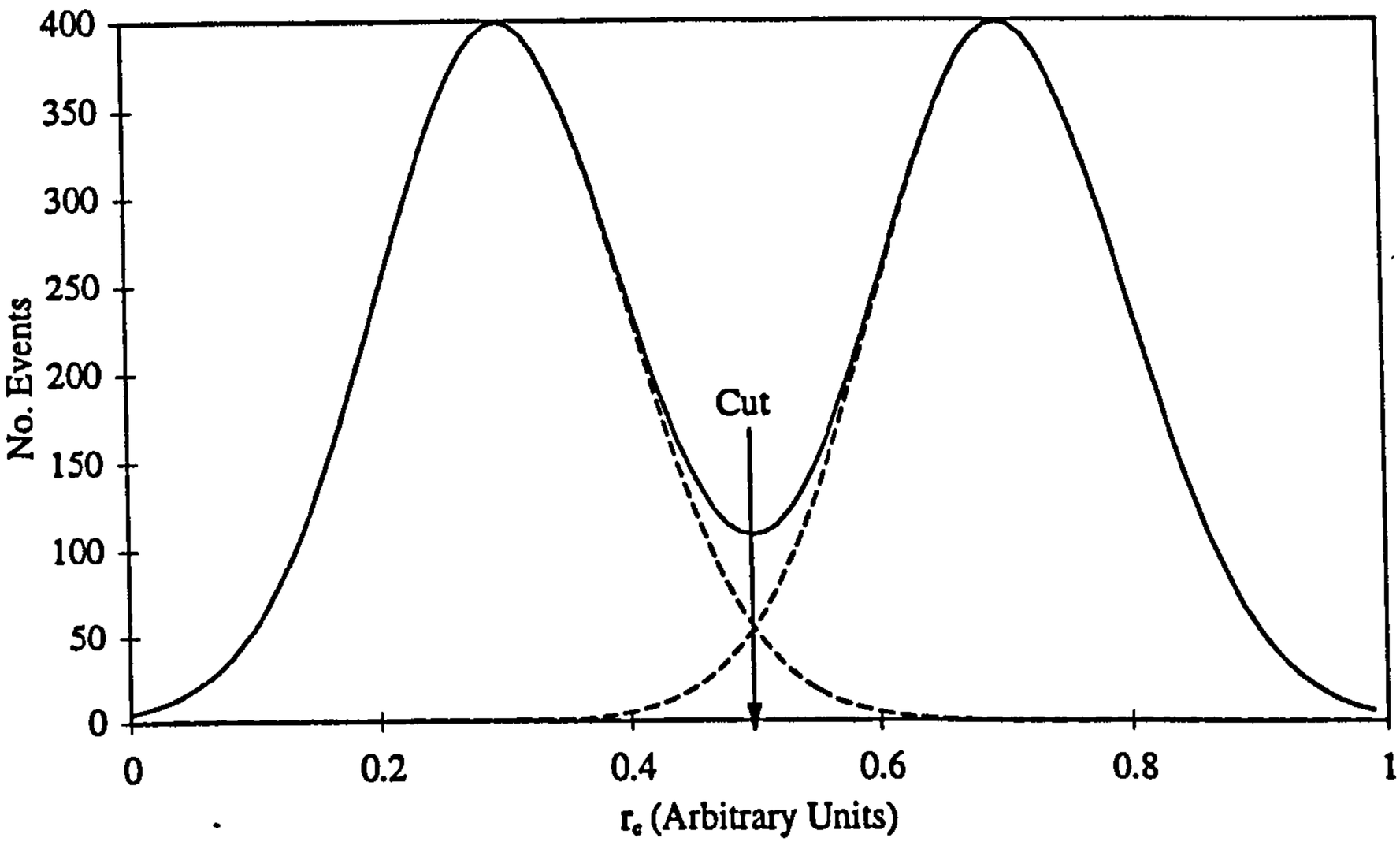

Figure 3.10: *A possible distribution of r_c for moderate discrimination efficiency. The dashed lines represent the contributions from signal and background. The full line is the sum.*

If the discrimination provided by a detector is not sufficiently good to give a probability of background rejection $D \sim 1$ (Fig. 3.10) then another cut based treatment may be used [104]. If there is a statistically significant excess of events above background (Eqn. 3.66) after the application of the cuts then a fit to the data using a sum of signal and background distributions should be used as in the previous section. In the absence of a signal however the analysis may be simplified by first calculating a limit on nuclear recoil signal events in each bin, irrespective of the shape or normalisation of the expected WIMP signal spectrum.

The analysis proceeds as follows. If there is a large total number of background events then the Poissonian fluctuations in this number may be neglected and only binomial fluctuations in the number of events passing the cut need be considered. Consider a total number of events $N(E_v, d_j)$ in a given $E_v - d_j$ bin and an associated background discrimination efficiency $D(E_v, d_j)$ and signal efficiency $\epsilon(E_v, d_j)$ (100%

for complete acceptance). For a total number of signal events $R_n(E_v, d_j)$ the mean number of events passing the cut $n_0(E_v, d_j)$ is the sum of the mean number of background events $\mu_B = (N - R_n).(1 - D)$ and the mean number of signal events ϵR_n:

$$n_0 = (N - R_n).(1 - D) + \epsilon.R_n. \tag{3.68}$$

Under the null hypothesis the assumption is that the data contains no signal events. Hence n_0 must be the sum of the mean expected number of background events $\sim N.(1-D)$ and a number of events due to binomial statistical fluctuations. From the properties of the binomial distribution the one sided 90% C.L. on these fluctuations is approximately $1.28\sqrt{D(1-D)N}$. Hence under the null hypothesis:

$$n_0 = (1 - D)N + 1.28\sqrt{D(1-D)N}. \tag{3.69}$$

Neglecting fluctuations in the number of signal events and equating Eqn. 3.68 and Eqn. 3.69 the limit on the number of signal events is given by:

$$R_n = 1.28\frac{\sqrt{D(1-D)}}{(\epsilon + D - 1)}\sqrt{N}. \tag{3.70}$$

This process should be carried out initially with simulated or calibration data in order to optimise r_{cut} by minimising R_n for each bin.

The next step is to set R_0 to unity and calculate Eqn. 3.65 for different choices of WIMP mass and interaction. The 90% signal rate limit $S_n(E_v, d_j)$ must also be calculated for each bin by dividing the signal limit $R_n(E_v, d_j)$ by the energy bin width and the detector exposure. Dividing $S_n(E_v, d_j)$ by the predicted rate from Eqn. 3.65 for each taget nucleus then gives R_0 limits $R_0(E_v, d_j, m_w, A)$ as functions of WIMP mass and interaction for each energy and d_j bin. Dividing by r converts these to limits on R_0/r.

The limits from the different bins should now be combined. The limits are standard deviation like quantities and the following formula may be used to combine the limits from different energy and d_j bins [84]:

$$\frac{1}{(R_0/r(m_w, A))^2} = \sum_{E_v, d_j} \frac{1}{(R_0/r(E_v, d_j, m_w, A))^2}. \tag{3.71}$$

The combined limit curves are then given by $R_0/r(m_w, A)$ for each WIMP interaction and nucleus. Limits from individual nuclei can now be combined using Eqn. 3.48, 3.7 and 3.49. Limits on $R_0/r(m_w)$ may be converted to limits on $\sigma_0(m_w)$ using Eqn. 3.48. Suitable normalisations should be applied to limit curves as described in the previous section.

3.7.3 Poor Discrimination Efficiency

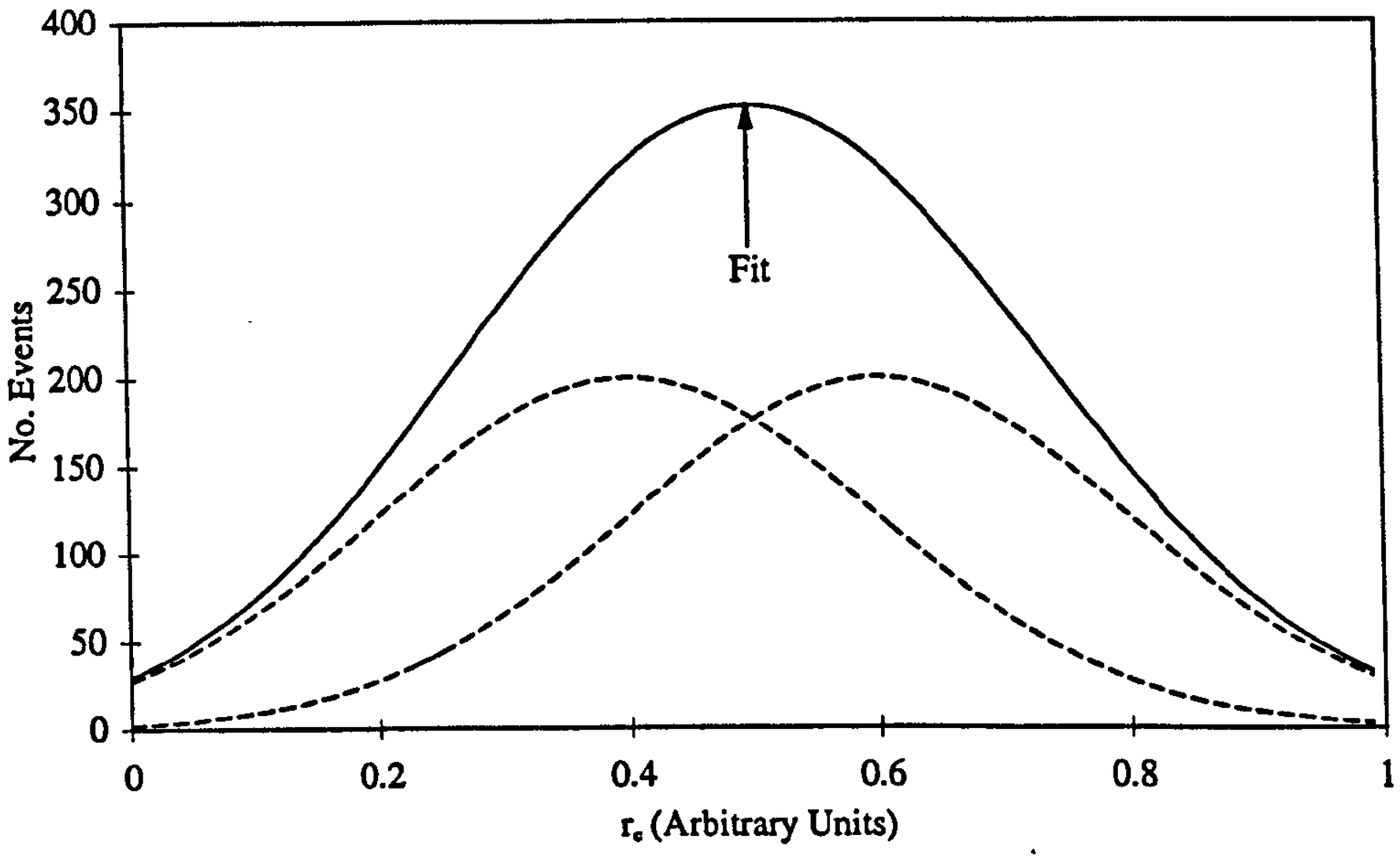

Figure 3.11: *A possible distribution of r_c for poor discrimination efficiency. The dashed lines represent the contributions from signal and background. The full line is the sum.*

If the discrimination provided by a detector is poor (Fig. 3.11) then a third technique should be used (as for Fig. 3.2). In this case the signal and background distributions in r_c may overlap completely and differ only in their shape. One possible approach is to fit a sum of these distributions to the data using the absolute numbers or rates of signal and background events as free parameters. Alternatively if these distributions can be quantified simply in terms of analytical functions (e.g. log-normal distributions as in §4.2.2) then the fit may use the sum of these two functions. The type of fit used depends upon personal preference although if the number of events is large a binned technique is more efficient. In this case a χ^2 fit is simplest and there are many fast algorithms available for speeding up the fitting process. Other possibilities include the binned Kolmogornov-Smirnov test and the Cramer-von Mises test, although in the latter case the errors on fitted parameters for arbitrary data distributions may need to be determined by Monte Carlo simulation [105].

If the fitted rate of signal events $S_f(E_v, d_j)$ for some bins is statistically inconsistent with zero then a fit of Eqn. 3.65 to the data for different assumed WIMP masses and interactions can again be used to delimit an allowed signal region in parameter space. Otherwise S_f may be set to zero in all bins (the null hypothesis)

and a conservative 90% nuclear recoil signal rate limit $S_n(E_v, d_j)$ derived from

$$S_n = 1.28\sigma(S_f) \tag{3.72}$$

Appropriately normalised limit curves may then be derived using the method described in the previous section.

3.8 Conclusions

WIMPs interact weakly with baryonic matter, scattering elastically from atomic nuclei. WIMP dark matter may thus be detected directly by searching for evidence of anomalous sources of nuclear recoils in low background detectors. In this chapter the energy spectrum of these signal events has been investigated and the design of running and planned experiments searching for these events reviewed. Techniques have also been developed with which to disentangle such events from background due to recoiling electrons of low energy.

Chapter 4

Scintillator Detectors and the UKDMC Programme

4.1 Introduction

The current programme of the UK Dark Matter Collaboration (Imperial College London, Rutherford Appleton Laboratory, University of Sheffield) is based on the use of scintillator detectors for WIMP dark matter. As outlined in §3.2.2 these combine the advantages of low energy threshold, high radiopurity and spin dependent or spin independent coupling enhanced constituent nuclei with an ability to discriminate signal from electron recoil background. This chapter discusses the use of scintillator detectors for WIMP dark matter in more detail, with emphasis placed on the UKDMC program. The chapter begins with a brief description of each of the different scintillator targets employed by the UKDMC (§4.2). Techniques for collecting and detecting scintillation light are then described under the general heading of detector design (§4.3). Measures aimed at assuring the lowest possible background count rate in such detectors are then discussed, namely detector shielding (§4.4) and detector radiopurity (§4.5). The chapter finishes with an outline of the long term 'future' of dark matter detection, which may lie with so called directional detectors (§4.6). Much of the material describing pulse shape discrimination in NaI(Tl) (§4.2.2) and novel data acquisition systems (§4.3.3) is the result of work performed by this author.

4.2 Scintillator Detectors

4.2.1 Crystal Scintillator Theory

Most current scintillator WIMP dark matter detectors rely on the use of inorganic crystal scintillator targets. The theoretical mechanism thought to be responsible for scintillation in these materials will now be described.

In an inorganic scintillation crystal energy deposited by a recoiling particle is converted into light. A simplified mechanism [105] is presented in Fig. 4.1. A recoil event creates many electron hole pairs along the length of its track (1). Each electron(hole) can propagate independently through the crystal lattice until it meets another hole(electron). At this point it is energetically more favourable for the electron and hole to form a bound state (2). This 'exciton' continues to propagate until it decays (3) or is absorbed by a dopant atom (4).

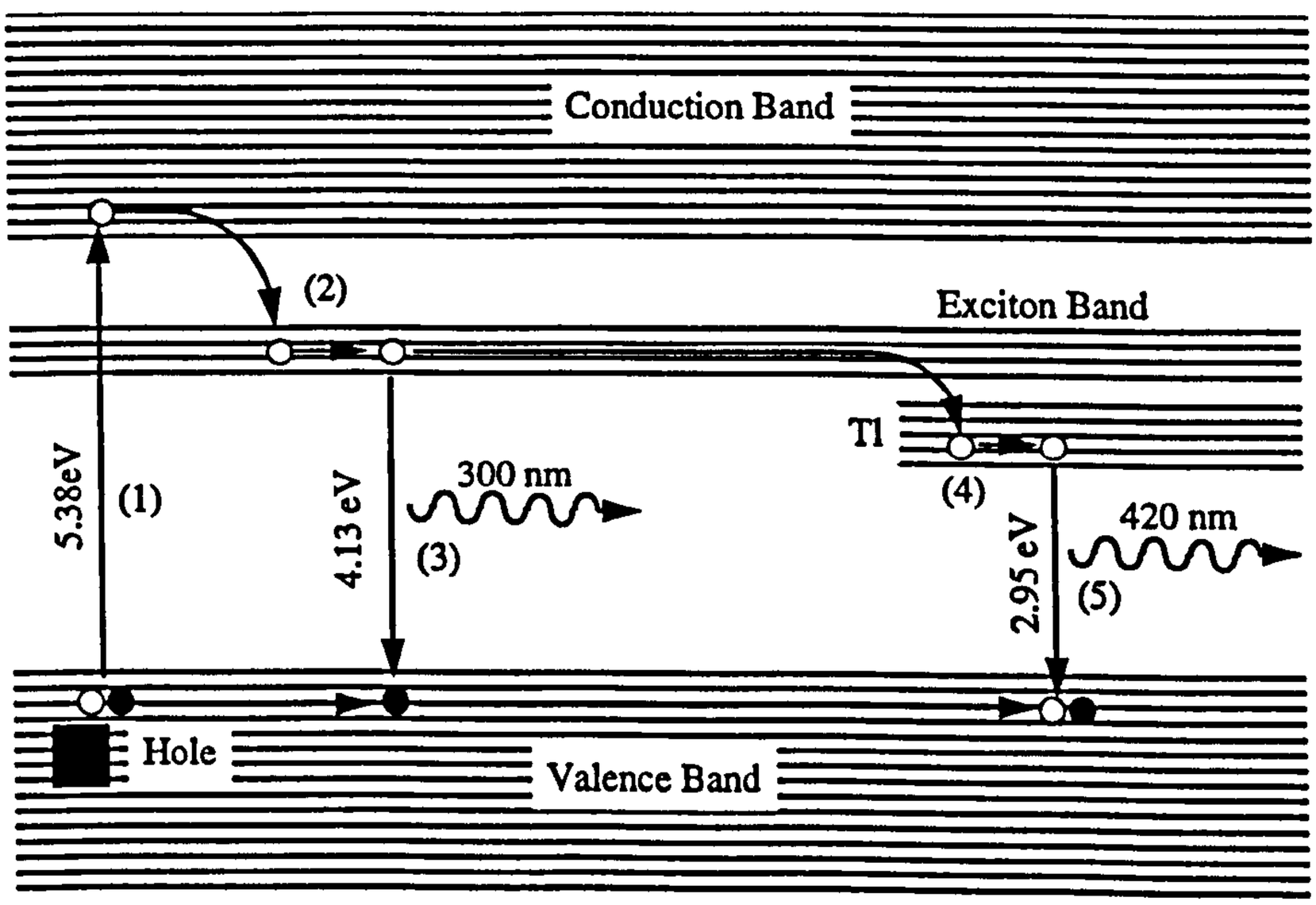

Figure 4.1: *A schematic diagram of the scintillation mechanism in a crystal scintillator (here NaI(Tl)). Adapted from [105].*

The decay process predominates in the case of zero or lightly doped crystals and involves the recombination of the electron and hole to produce a single photon of a wavelength characteristic of the crystal lattice. This photon may then escape

from the crystal and be observed as (intrinsic) scintillation. The time spectrum of photons emitted in this way depends upon the life time of the exciton and is well represented by an exponential decay.

In the case of heavily doped crystals the majority of excitons are absorbed directly by the dopant atoms as are any intrinsic photons created by excitons which escape. The absorption process excites the dopant atoms which then decay radiatively to the ground state through the emission of a scintillation photon of a wavelength characteristic of the dopant (5). The time spectrum of these photons depends upon the life time of the excited dopant state and is again well represented by an exponential decay. The precise choice of dopant depends upon both the desired wavelength of this extrinsic photon and the efficiency with which it is emitted. This efficiency is related to the ease with which energy is transferred to the dopant and hence to the quality of the crystal lattice. Dopant atoms occupy substitutional sites within this lattice and those dopants with ionic radii similar to those of the atoms which they replace consequently give the best quality crystals with the highest light output.

In addition to the above radiative processes there are also competing processes which do not lead to the emission of photons. At any point energy may be lost to phonons which subsequently disperse the energy as heat. In most scintillator experiments this energy cannot be detected and so the total amount of energy observed in an event does not equal the total amount of energy deposited. Furthermore the fraction of energy dispersed by phonons and other non-radiative processes depends upon the density of ionisation along the recoil track, since there is a limit to the amount of energy per unit volume which can be used to create electron hole pairs. Thus heavily ionising particles such as nuclei disperse more of their energy as phonons than do less ionising electrons. Hence comparatively more energy is observed for electrons than for nuclei of the same recoil energy. This is the origin of the energy detection efficiency for scintillators ('scintillation efficiency') discussed in §3.5.2.

4.2.2 NaI(Tl) Detectors

The mainstay of the UKDMC programme is the NaI(Tl) crystal scintillator. The physical and pulse shape properties of this material will now be discussed, followed by the 'discriminating variables' most appropriate for performing NaI(Tl) pulse shape discrimination.

Physical Properties

NaI has an intrinsic emission wavelength of 300 nm (UV) which is poorly matched to the absorption characteristics of most photodetectors. The extrinsic emission provided by thallium doping however has a wavelength of 410 nm (blue), well matched to the response of the bialkali photocathodes used in photomultiplier tubes (PMTs - §4.3.2). Furthermore the ionic radii [106] of thallium (0.95 Å) and sodium (0.97 Å) are similar and so NaI(Tl) is an efficient scintillator at this wavelength ($\sim$ 40 photons/keV [100]). The level of thallium doping is governed by a desire to maximise the crystal light output while avoiding self absorption caused by over doping. The relative light output for various dopings is plotted in Fig. 4.2 and peaks at a dopant concentration of around 0.1% M. Most UKDMC crystals contain approximately this dopant concentration.

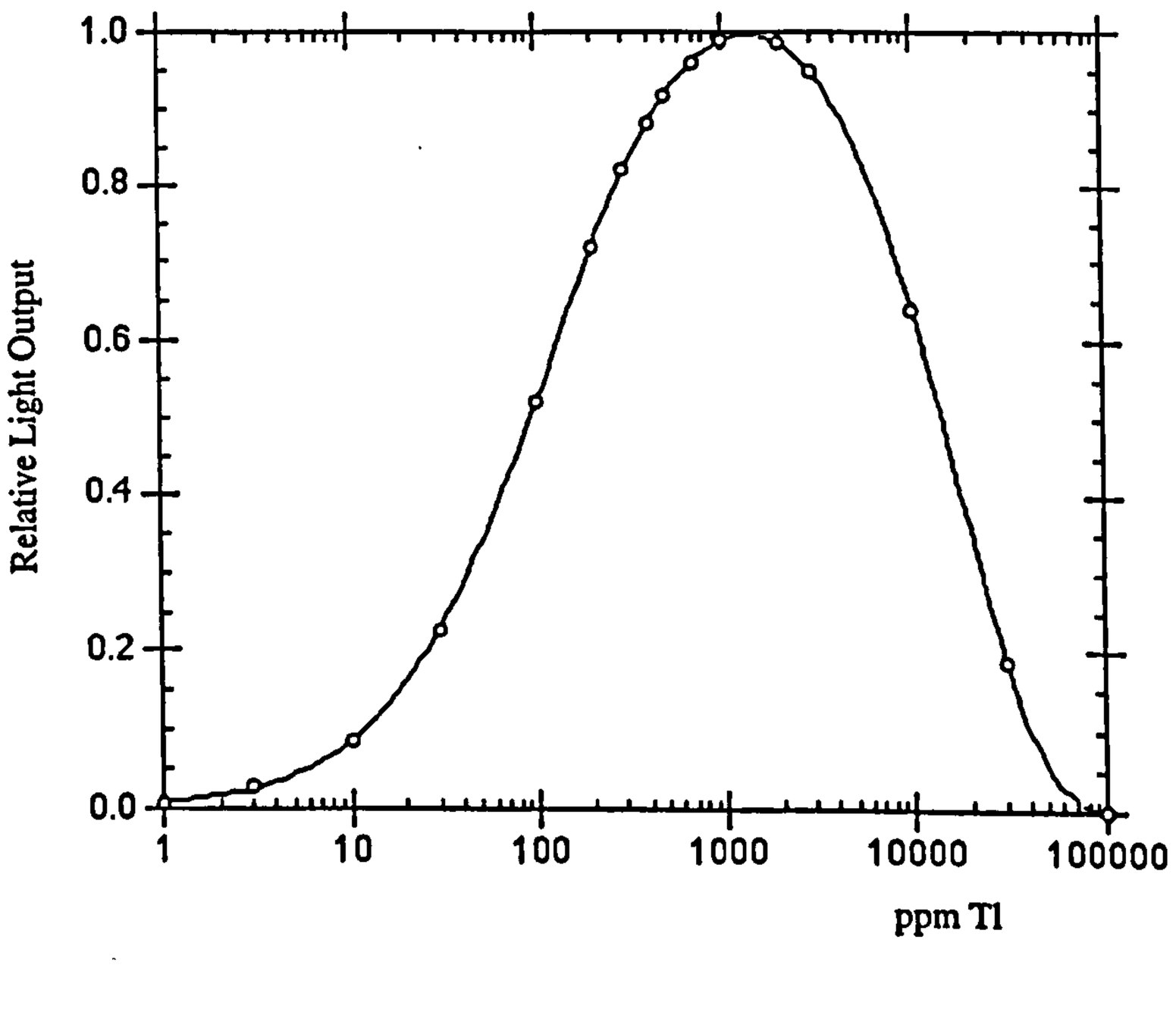

Figure 4.2: *The variation of NaI(Tl) light output with Tl doping. Diagram from [107]. Data from [100].*

The physical properties of NaI(Tl) are listed in Table 4.1, along with those of some other scintillators relevant to WIMP searches. The intrinsic spin of Na nuclei and the high mass of I nuclei give NaI(Tl) detectors sensitivity to both spin dependent and spin independent WIMP interactions with large coupling enhancement

Scintillator	*Nuclei*	ρ *(g/cm^3)*	r_i	λ_{max} *(nm)*	τ_γ *(ns)*	*Rel. LO*
			Inorganic			
NaI(Tl)	Na,I	3.67	1.775	410	~350	100
NaI	Na,I	3.67	1.775	300/410	30/1000	190
CaF_2	Ca,F	3.17	1.443	380	900	~7
CaF_2(Eu)	Ca,F	3.17	1.443	435	900	48
Liquid Xenon	Xe	3.06	1.603	175	2.2/27	<175
			Organic			
Anthracene	C,H	1.25	1.62	447	30	44
Stilbene	C,H	1.16	1.626	410	4.5	22
NE221 (Dioxan)	C,H,O	1.08	1.44	425	4.0	24
NE224	C,H	0.88	1.504	425	2.6	35
NE213	C,H	0.87	1.508	425	3.7	34
BC533	C,H	0.80	1.45	424	3.0	22

Table 4.1: *The physical properties of some scintillators of use in WIMP direct search experiments. λ_{max} is the wavelength of maximum emission and τ_γ is the scintillation decay time constant for electron recoils. The last column is the percentage light output relative to NaI(Tl). All quantities are measured at the optimum operating temperature. For further information see e.g. [109].*

factors (§3.3). The high density of the material enables the construction of compact, massive detectors, while the high light output gives a low detector visible energy threshold. The raw NaI powder used in the crystal growing process is of high radiopurity and the process itself (§5.2.1) acts to concentrate impurities in the bottom half of the boule from which the crystal is cut. Thus by discarding the bottom halves of two boules and regrowing a third boule from the remaining material a crystal can be cut which is of still greater radiopurity [108]. This double growth technique is used to produce all UKDMC low background crystals. Further improvements in radiopurity can arise as a result of prepurifying the raw NaI powder by passing it through a DIPHONIX ion exchange column to remove U and Th impurities (§5.3.2).

NaI(Tl) is extremely hygroscopic and so must normally be encapsulated in a dry atmosphere to prevent exposure to moisture. This has the disadvantage of decreasing the efficiency with which light can be collected from the crystal because scintillation photons must pass through a window (usually quartz) before entering

the detector. Photons can be internally reflected back into the crystal and absorbed when crossing any refractive index boundary. Thus by adding four such boundaries through encapsulation the probability of detecting a particular photon is reduced significantly thereby raising the visible energy threshold. Photon trapping of this kind is especially important in NaI(Tl) as the refractive index (1.78 [110]) is significantly higher than that of most suitable window materials such as quartz ($\sim$ 1.5 [110]). The Collaboration is investigating techniques for removing the need for encapsulated crystals and these should significantly improve the light collection efficiency (§4.3.1).

Pulse Shape Properties

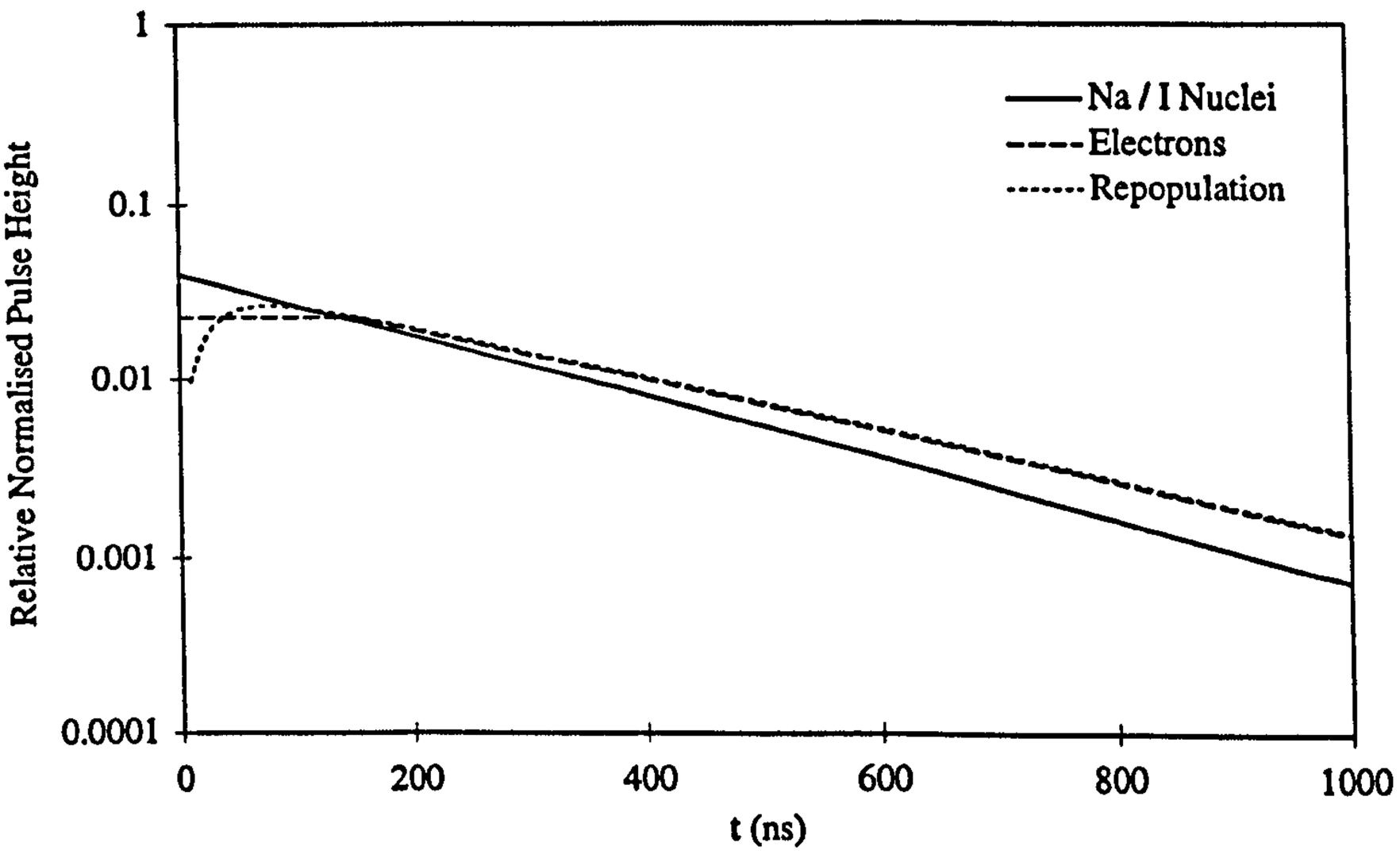

Figure 4.3: *Theoretical NaI(Tl) pulse shapes showing the pulse shape differences between nuclear and electron recoils. The dotted line is the prediction from Eqn. 4.2 with* $t_0 = 0$, $\tau_1 = 30$ *ns and* $\tau_2 = 300$ *ns.*

Background discrimination in scintillator detectors can be provided by analysis of the scintillation pulse shape (§8). In NaI(Tl) pulse shape differences between nuclear and electron recoils occur naturally as a useful by product of the scintillation process. The scintillation pulse shape for nuclear recoils, consisting mainly of extrinsic photons, is well represented by a single exponential decay of time constant $\tau \sim 250$ ns (Fig. 4.3). For electrons on the other hand there is evidence [100] for additional pulse shape components leading to a flattening of the pulse for the first $\sim$ 150 ns, followed by a slower exponential decay than for nuclei ($\tau \sim 300$ ns Fig. 4.3).

This flattening of the beginning of the pulse may arise from a finite lifetime for the repopulation of the radiative Tl states from the NaI valence band (Fig. 4.1), leading to a finite pulse rise time. Assume that the valence band contains N_2 electrons, the Tl levels N_1 and the conduction band N_0. Further assume that the non-radiative transition (4) has a decay time constant τ_2 and the radiative transition (5) a decay time constant τ_1. The time spectrum of scintillation light may now be derived by considering the following differential equations:

$$\begin{aligned} \frac{dN_2}{dt} &= -\frac{N_2}{\tau_2}, \\ \frac{dN_1}{dt} &= -\frac{N_1}{\tau_1} + \frac{N_2}{\tau_2}, \\ \frac{dN_0}{dt} &= \frac{N_1}{\tau_1}, \end{aligned} \tag{4.1}$$

where the scintillation pulse shape is given by dN_0/dt. The solution to these equations for this quantity is

$$\frac{dN_0}{dt} = \frac{A}{\tau_1 - \tau_2}\left(e^{-(t-t_0)/\tau_2} - e^{-(t-t_0)/\tau_1}\right), \tag{4.2}$$

where t_0 is the observed arrival time of the first photon relative to the start of the pulse. This function is also plotted in Fig. 4.3.

Decay Time Constant Discrimination

Elementary pulse shape discrimination can be performed with NaI(Tl) by assuming that the scintillation pulse shape is well represented by a gamma distribution offset from the true pulse start time by a time t_0:

$$P(t_i).dt = \frac{1}{\Gamma(b)}\left(\frac{b(t_i - t_0)}{\tau}\right)^b \frac{1}{(t_i - t_0)} e^{-b(t_i - t_0)/\tau}.dt, \tag{4.3}$$

where $P(t_i)$ is the Poisson probability of photon arrival time t_i. This function tends to an exponential decay in the limit $b \to 1$, thus describing the nuclear recoil pulse shape, and approximates well the electron recoil pulse shape for $b \sim 1.25$ (§6.4.2).

Assume now that most pulse shape differences are due to differing values of τ for nuclear and electron recoils. Consequently the discriminating variable (§3.7) of most use is an estimator T of the decay time constant. This estimator may be calculated by fitting to a time integrated pulse height / pulse time spectrum as is currently done with all UKDMC data. This technique suffers from the disadvantage that measurement errors on the raw pulse height at different times become correlated through integration thereby complicating the fitting process. A pure exponential

pulse shape must also be assumed in order to fit to low energy events. An alternative approach giving an unbiased estimator considers the unbinned log-likelihood of the photon arrival times [101]:

$$\ln \mathcal{L} = \sum_{i=1}^{n} \ln P(t_i), \tag{4.4}$$

where $P(t_i)$ is given by Eqn. 4.3. Maximising the log-likelihood as a function of τ gives

$$\begin{aligned} \tau &\equiv T \\ &= \frac{1}{n}\sum_{i=1}^{n}(t_i - t_0) \\ &\approx \frac{1}{n}\sum_{i=1}^{n} t_i, \end{aligned} \tag{4.5}$$

which is equivalent to using the mean photon arrival time as the discriminating variable T. This gives a more accurate representation of τ without introducing interdependent measurement errors. This technique is known as the Mean Time (MT) technique.

Owing to the relatively small pulse shape differences provided by NaI(Tl), event by event discrimination (§3.7.1) cannot be performed. Thus it is the *distribution* of pulse mean times which must be used, as described in §3.7.3. The form of this distribution may be calculated by using the characteristic function of the gamma distribution [111]:

$$\phi(k) = \frac{1}{(1 - ik\tau)^b}. \tag{4.6}$$

Using the convolution theorem the probability of observing a mean value T of t_i for a given event consisting of n photons is then given by the inverse Fourier transform of the product of n of these characteristic functions [112]:

$$P(T).dT = \frac{1}{2\pi}\int_{-\infty}^{\infty} \frac{e^{-iknT}}{(1 - ik\tau)^{nb}}.dk.dT. \tag{4.7}$$

This integral may be computed in the complex plane using the residue theorem [112] to give:

$$P(T).dT = \frac{1}{\Gamma(nb)}\left(\frac{nbT}{\tau}\right)^{nb}\frac{1}{T}e^{-nbT/\tau}.dT. \tag{4.8}$$

A more accurate representation of this distribution is to replace T with $T + \bar{t}_0$ throughout where $\bar{t}_0$ is a mean time difference between the start of the pulse and the arrival of the first photon (equal to τ/n for an exponential pulse). This technique partially compensates for lack of direct knowledge of the pulse start time.

Eqn. 4.8 is often approximated by a log-normal distribution

$$P(T).dT = \frac{1}{\sigma\sqrt{2\pi}}\frac{1}{T}e^{-(\ln(T)-\ln(T_0))^2/2\sigma^2}.dT, \tag{4.9}$$

where σ is a width parameter and the quantity T_0 is an effective mean T approximately equal to τ. This distribution is compared with Eqn. 4.8 in Fig. 4.4.

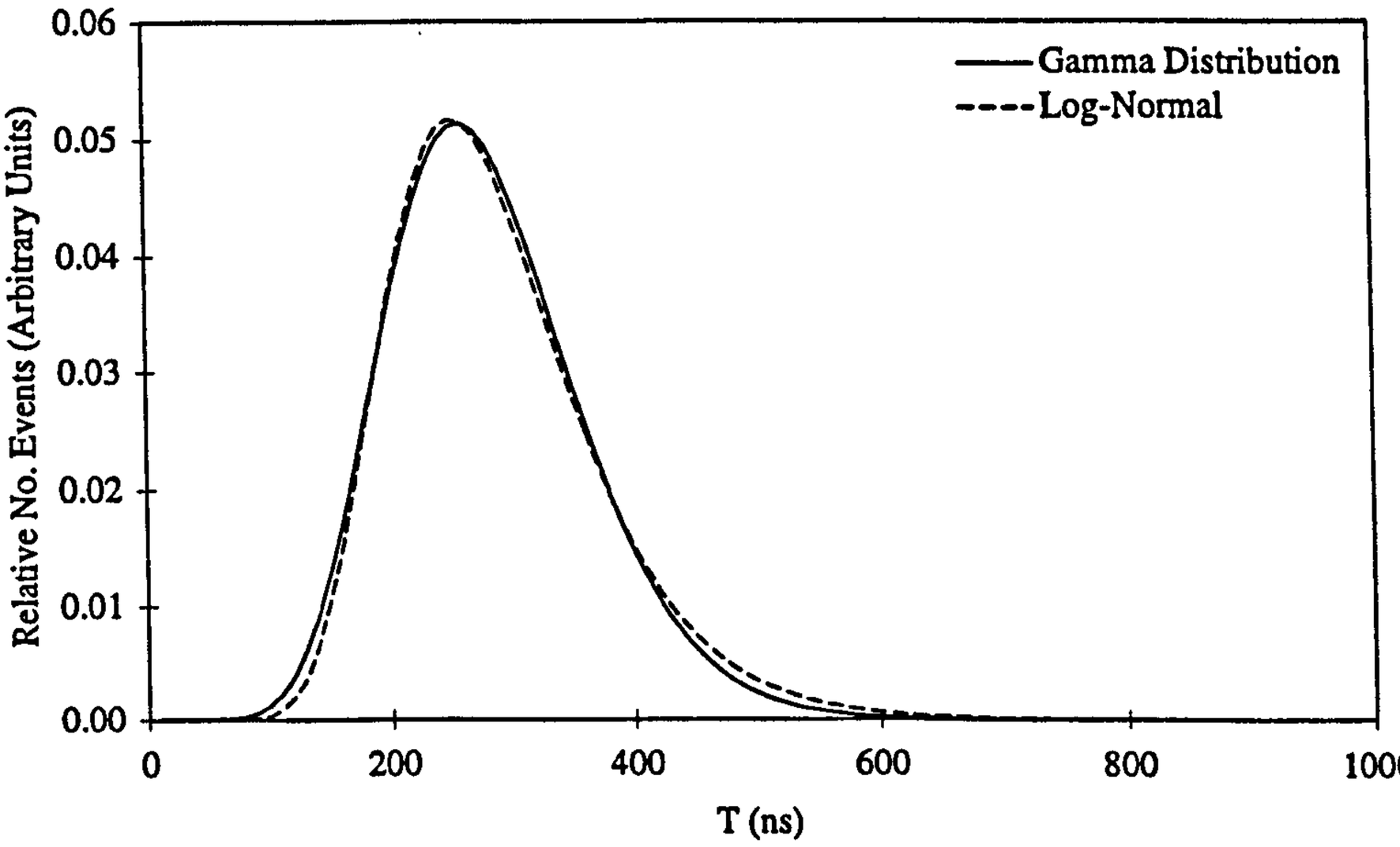

Figure 4.4: *A comparison of Eqn. 4.8 with a log-normal distribution.*

This log-normal approximation can be used in conjunction with some additional assumptions to extract nuclear recoil signal limits from data either by fitting (§3.7.3) or using other techniques [88]. Data from an operational UKDMC NaI(Tl) detector and fitted log-normal curves are plotted in Fig. 4.5 (overleaf). The means of the distributions ($\sim \tau$) rise with increasing crystal temperature at a rate $\sim$ 3.0 ns/°C [88]. Consequently current UKDMC detectors are temperature stabilised at $\sim$ 10°C in order to avoid systematic shifts in τ over the course of data taking (§8). The data from Fig. 4.5 was used to set the limits plotted in Fig. 3.2.

The Likelihood Ratio Technique

A potentially more efficient technique for pulse shape discrimination is to make use of differences in both b and τ for nuclear and electron recoils. This can be achieved throught the use of the Likelihood Ratio (LR) technique [101]. The likelihood ratio is defined as the difference of the maximum log-likelihood error estimators (Eqn. 4.4), with the $P(t_i)$ calculated using Eqn. 4.3 or mean calibration nuclear and electron

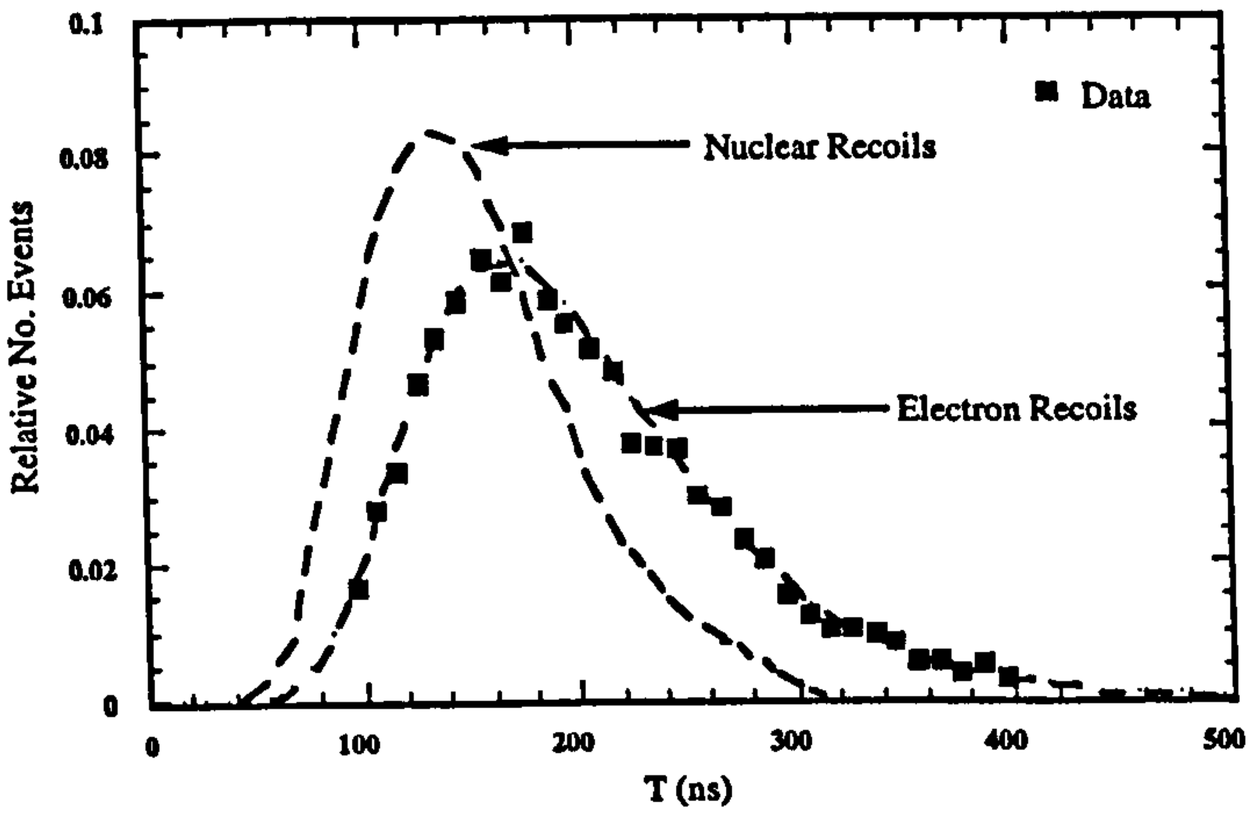

Figure 4.5: *A comparison of data from a 6 kg NaI(Tl) detector with the nuclear and electron recoil log-normal distributions. Adapted from [88].*

recoil pulse shapes. The likelihood ratio $\Re$ is then written as

$$\Re = \ln\left(\frac{\mathcal{L}_e}{\mathcal{L}_n}\right), \tag{4.10}$$

for nuclear and electron recoil likelihoods $\mathcal{L}_n$ and $\mathcal{L}_e$ respectively.

This method has the advantage that it makes use of all available pulse shape information for discrimination. It is also applicable to any pulse shape and so may be of use when analysing data from detectors using scintillators other than NaI(Tl). The disadvantage of the technique however is that it is often difficult or impossible to quantify the distribution of likelihood ratios for a particular class of event. The only exception is in the case of a pure exponential pulse shape. Here $\Re$ is proportional to T and thus follows a similar distribution:

$$P(\Re_p).d\Re = \frac{1}{\Gamma(n)}\left(\frac{\tau_e\tau_n(\Re_p-\alpha)}{(\tau_e-\tau_n)\tau_p}\right)^n \frac{1}{(\Re_p-\alpha)} e^{-((\Re_p-\alpha)\tau_e\tau_n)/(\tau_p(\tau_e-\tau_n))}.d\Re, \tag{4.11}$$

where the n and e subscripts refer to nuclear and electron recoils respectively and p indicates the particular recoil being considered. α is a parameter defined by

$$\alpha = n\ln\left(\frac{\tau_n}{\tau_e}\right). \tag{4.12}$$

The distributions of $\Re$ for nuclear and electron recoils given by Eqn. 4.11 are plotted in Fig. 4.6.

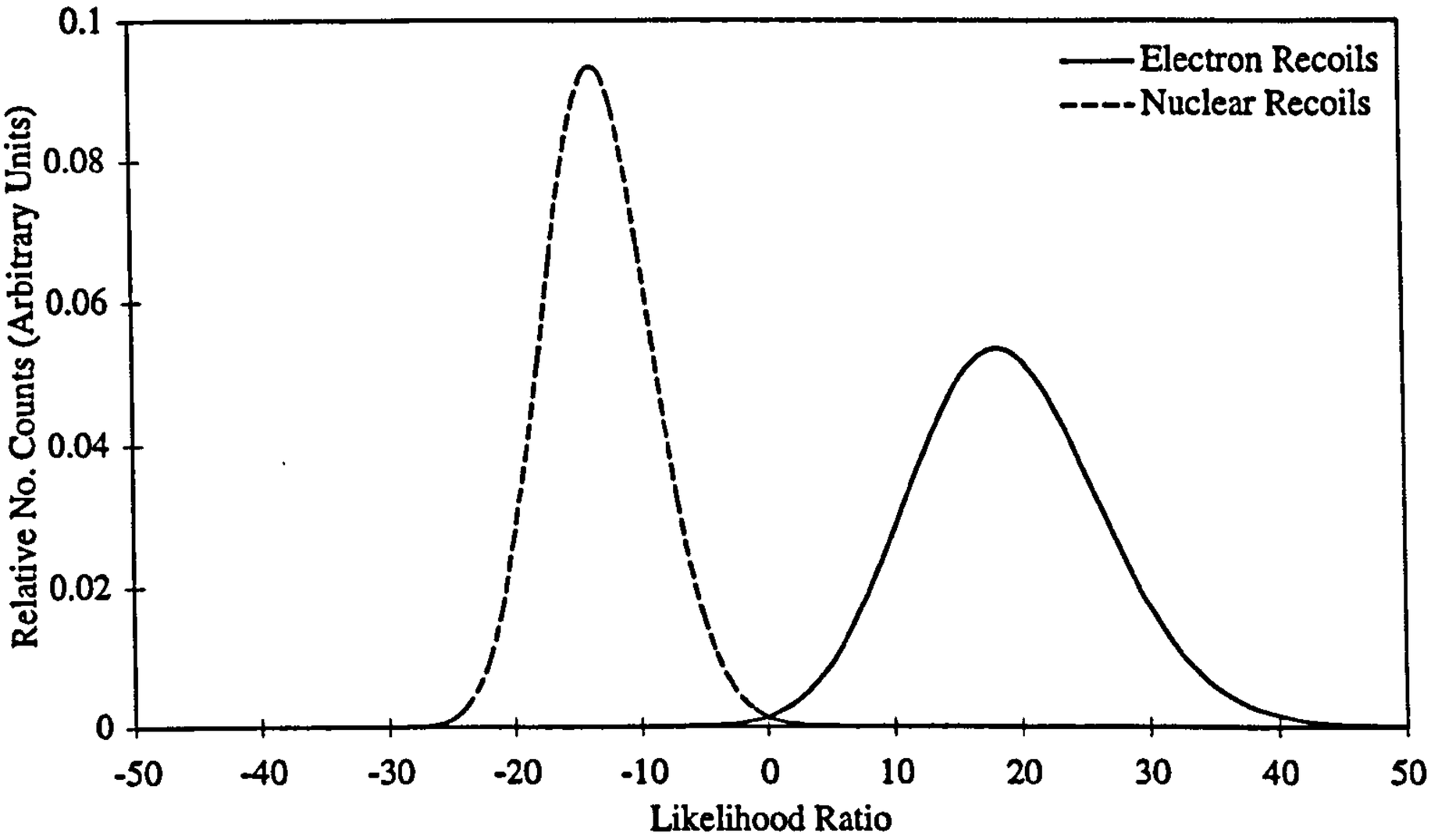

Figure 4.6: *Likelihood ratio distributions derived from Eqn. 4.11.*

The use of both the likelihood ratio technique and that using the mean time of the pulse are examined in more detail in §8 with a view to optimising discrimination in an operational NaI(Tl) detector.

4.2.3 The UVIS NaI Detector

Physical Properties

Another material currently being studied by the UKDMC is undoped NaI. At room temperature this is rather a poor scintillator with an emission wavelength of 300 nm (Table 4.1) situated well into the UV where most photodetectors have low sensitivity. Coupled with the problems associated with collecting light from NaI due to its hygroscopicity and high refractive index this would seem to be an unwise choice for a dark matter target. There is evidence however that at low temperatures ($\sim$ 160 K) undoped NaI has a light output almost as high as that of NaI(Tl) at room temperature [100]. Furthermore at these temperatures it displays remarkably large pulse shape differences between nuclear and electron recoils [104]. These differences arise from the presence of a strong 410 nm component to the scintillation light in addition to that at 300 nm. The relative strength of these two components depends strongly on the type of recoil and since they have vastly differing decay time constants ($\sim$ 1 μs and $\sim$ 30 ns respectively), this leads to large pulse shape differences [113] (Fig. 4.7).

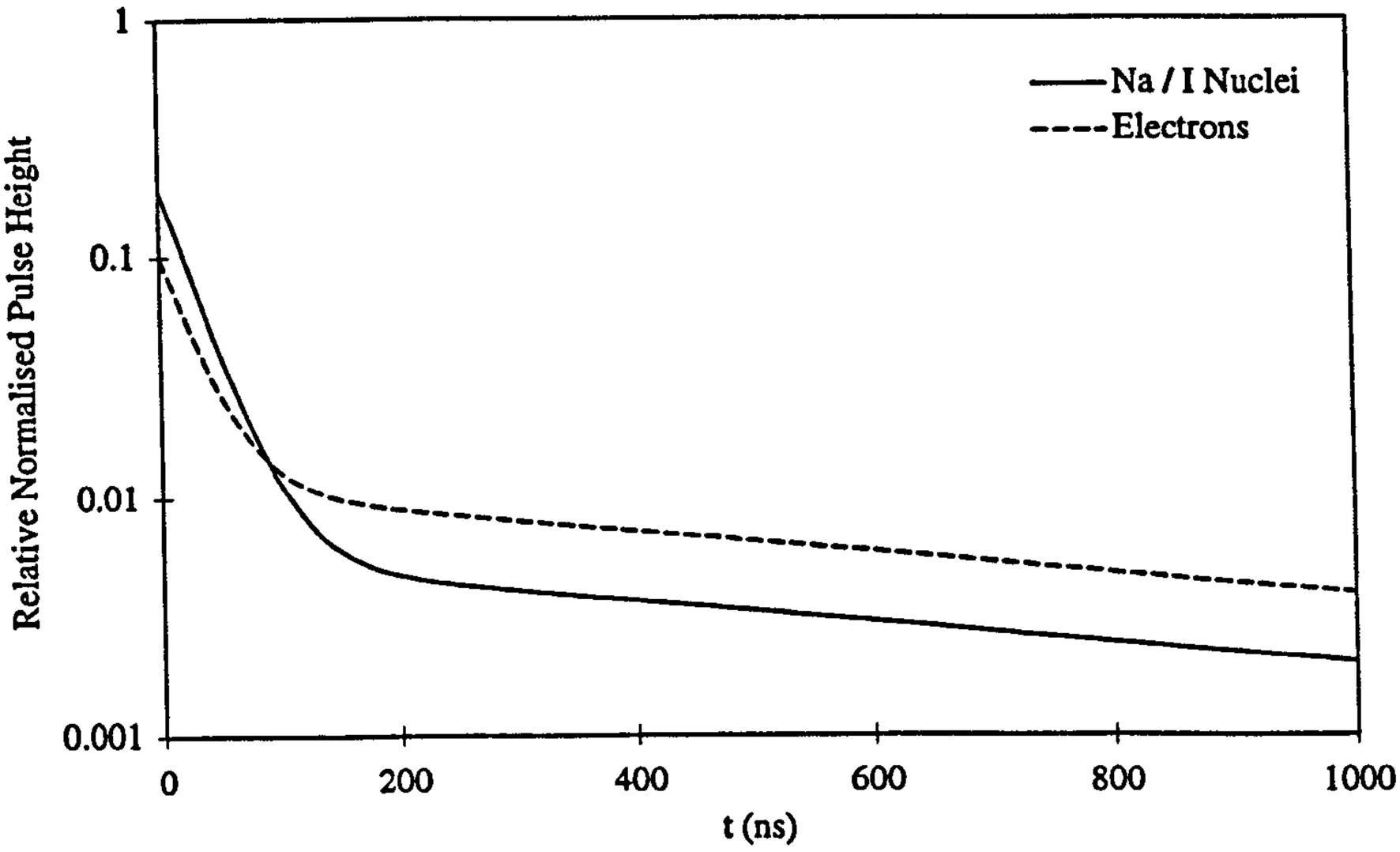

Figure 4.7: *Theoretical UVIS NaI pulse shapes showing the pulse shape differences between nuclear and electron recoils.*

The precise origin of the 410 nm component or the reason as to why its strength relative to the UV component varies in this way are uncertain. The naïve theory presented in §4.2.1 predicts that in the absence of any dopant only one intrinsic decay component should be present in the scintillation pulse. The extra component may be due to exciton absorption by iodine vacancies or to defects or impurities in the crystal lattice [105], however these explanations are by no means widely accepted. What is clear is that the potential for discrimination provided by the 410 nm component makes low temperature NaI crystals promising dark matter targets.

The UKDMC has proposed an experiment based upon the discrimination properties of undoped NaI [114]. This 'UVIS' (Ultraviolet VISible) detector can use wavelength shifting materials to convert the UV emission into visible light which can be detected by conventional PMTs [105]. Alternatively UV sensitive PMTs (§4.3.2) may be used to detect the 300 nm scintillation directly. With the latter technique an additional possibility is to place absorption edge filters in front of each of the two PMTs observing the crystal such that each PMT detects light of only one wavelength. This decreases the energy detection efficiency of the system but allows discrimination both through pulse shape analysis and through measurement of the relative pulse heights in the two tubes [105].

Pulse Shape Discrimination

The UVIS scintillation pulse shape consists of at least two exponential components. Pulse shape discrimination can be performed with the likelihood ratio technique described in §4.2.2. Alternatively a fit can be performed using the fraction of the total pulse height contained within one of the two components as the free parameter. The decay time constants of the two components are less sensitive to the type of recoil (§5.2.3) however these too may be used as fitting parameters, in which case three discriminating variables are available. Neural network or other techniques can then be used to reduce these three variables to a single optimised discriminating variable. The UVIS technique is discussed in more detail in §5.2.

4.2.4 The CASPAR Detector

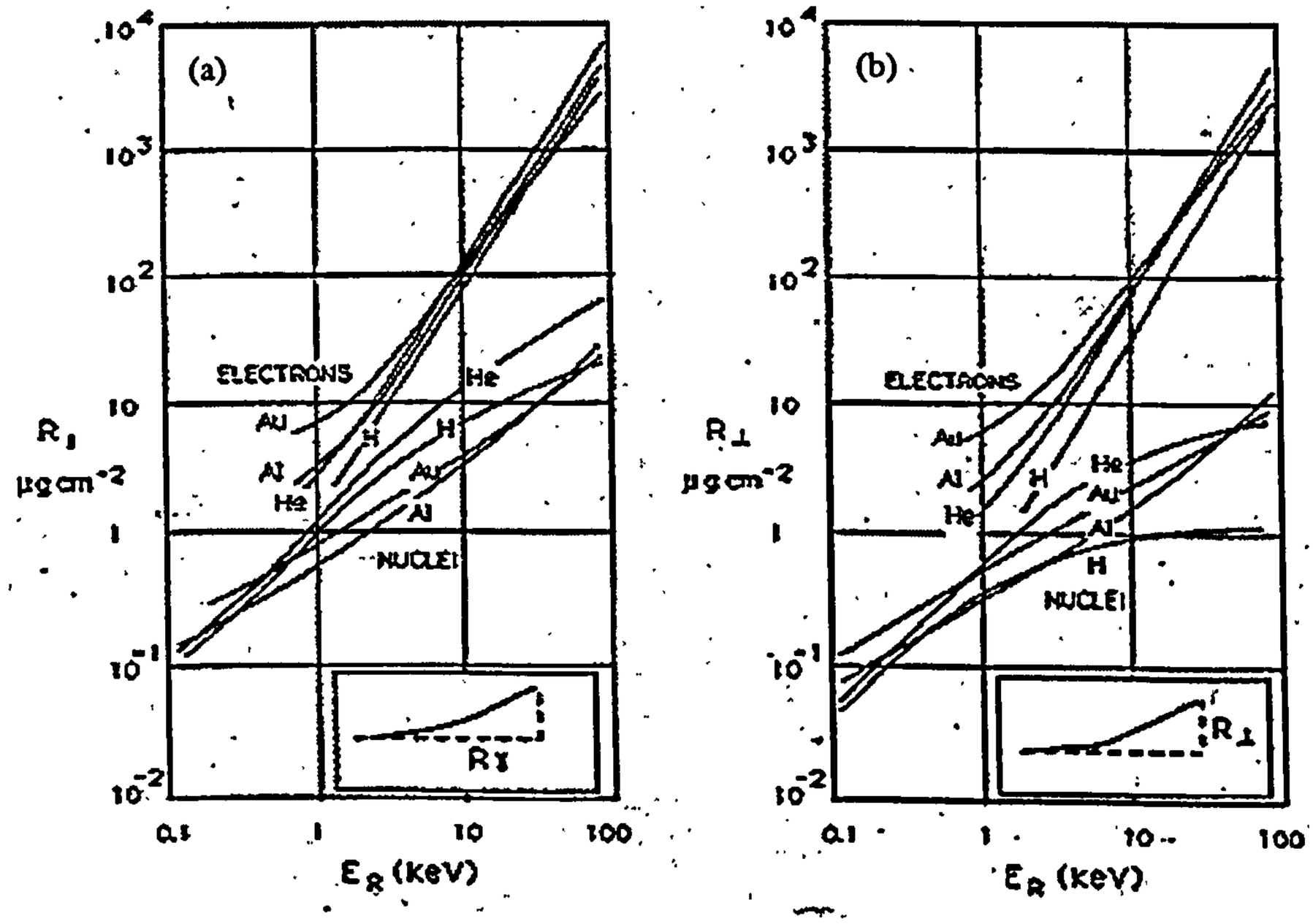

Figure 4.8: *The recoil ranges of nuclei and electrons (a) parallel and (b) perpendicular to the initial velocity vector. From [47].*

The optimum target nucleus for searching for spin dependent WIMP-nucleon couplings is fluorine due to its large spin dependent coupling enhancement factor (Table 3.3). The only scintillator crystal containing fluorine which has both high light

output and low intrinsic radioactivity is europium doped calcium fluoride CaF_2(Eu) (Table 4.1). Unlike NaI(Tl) there is no evidence to suggest that CaF_2(Eu) exhibits any intrinsic differences in pulse shape between nuclear and electron recoils (§6). Nevertheless several collaborations are currently using CaF_2(Eu) detectors to search for WIMPs and are succeeding in setting competitive spin dependent cross section limits even without the use of PSD [115]. It would clearly be of considerable benefit however if a CaF_2(Eu) detector could be designed which incorporated PSD properties.

In order to perform discrimination in a dark matter detector use must be made of the differing dE/dx of recoiling electrons and nuclei [47]. One consequence of this difference is that the ionisation density along the track also differs in the two cases and it is this which forms the basis for Pulse Shape Discrimination (PSD) in NaI (§4.2.3) and NaI(Tl) (§4.2.2). Another consequence is that for a given recoil energy the total range of electrons is very much greater than that of nuclei, as shown in Fig. 4.8. The theory governing the energy loss of low energy charged particles is based upon that developed by Lindhard (§3.5.2) and has now been incorporated into sophisticated numerical codes [93]. Much of the interest in these energy loss processes has come from the semiconductor industry where ion implantation doping of Si and other materials often involves the use of beams of low energy nuclei.

The 'CASPAR' (Cocktail with Alkali halide Scintillating PARticles) concept seeks to use recoil range differences to 'engineer' PSD properties into a detector containing CaF_2(Eu) [116, 117, 118]. The technique relies on two useful properties of CaF_2(Eu), namely:

- It is chemically inert.
- The refractive index r_i is extremely low for an alkali halide (1.44).

The former property allows CaF_2(Eu) crystals to be immersed in almost any liquid without decomposing. The latter property permits the liquid (refractive index higher(lower) than that of CaF_2(Eu)) to be refractive index matched to the crystals by adding another liquid with refractive index lower(higher) than CaF_2(Eu) in the correct proportion. This procedure causes all internal reflection of light at the liquid / crystal interface to vanish thus permitting the observation of the CaF_2(Eu) scintillation light by external photodetectors.

The next consideration is to arrange for the mean linear dimension of the CaF_2(Eu) crystals to be greater than that of low energy nuclear recoil tracks ($\sim$ 100 nm) but less than that of low energy electron recoil tracks ($\sim$ 1μm). This ensures that if WIMPs couple to Ca or F nuclei within the crystals then these nuclei can never

recoil sufficiently far to enter the surrounding liquid. Electrons however, originating both from within the crystals and from within the liquid recoil through both media. Consider now the result of using as the liquid an organic scintillator. Liquid scintillators typically possess decay time constants $\lesssim 10$ ns while CaF_2(Eu) has an equivalent decay time constant ~ 900 ns (Table 4.1). Thus the nuclear recoil pulse shape consists entirely of the long decay characteristic of CaF_2(Eu) while the electron pulse shape contains in addition a fast component characteristic of the liquid scintillator (Fig. 4.9). Hence by analysing the pulse shape, discrimination against electron recoil events may be obtained. The technique is equivalent to using a microscopic Compton veto shield providing a fast component to the scintillation pulse shape with which to tag electron recoil events. The PSD technique itself is essentially identical to that described for the UVIS detector (§4.2.3). In both cases the scintillation pulse consists of two exponential components and the ratio of the amplitudes of these provides the discriminating variable.

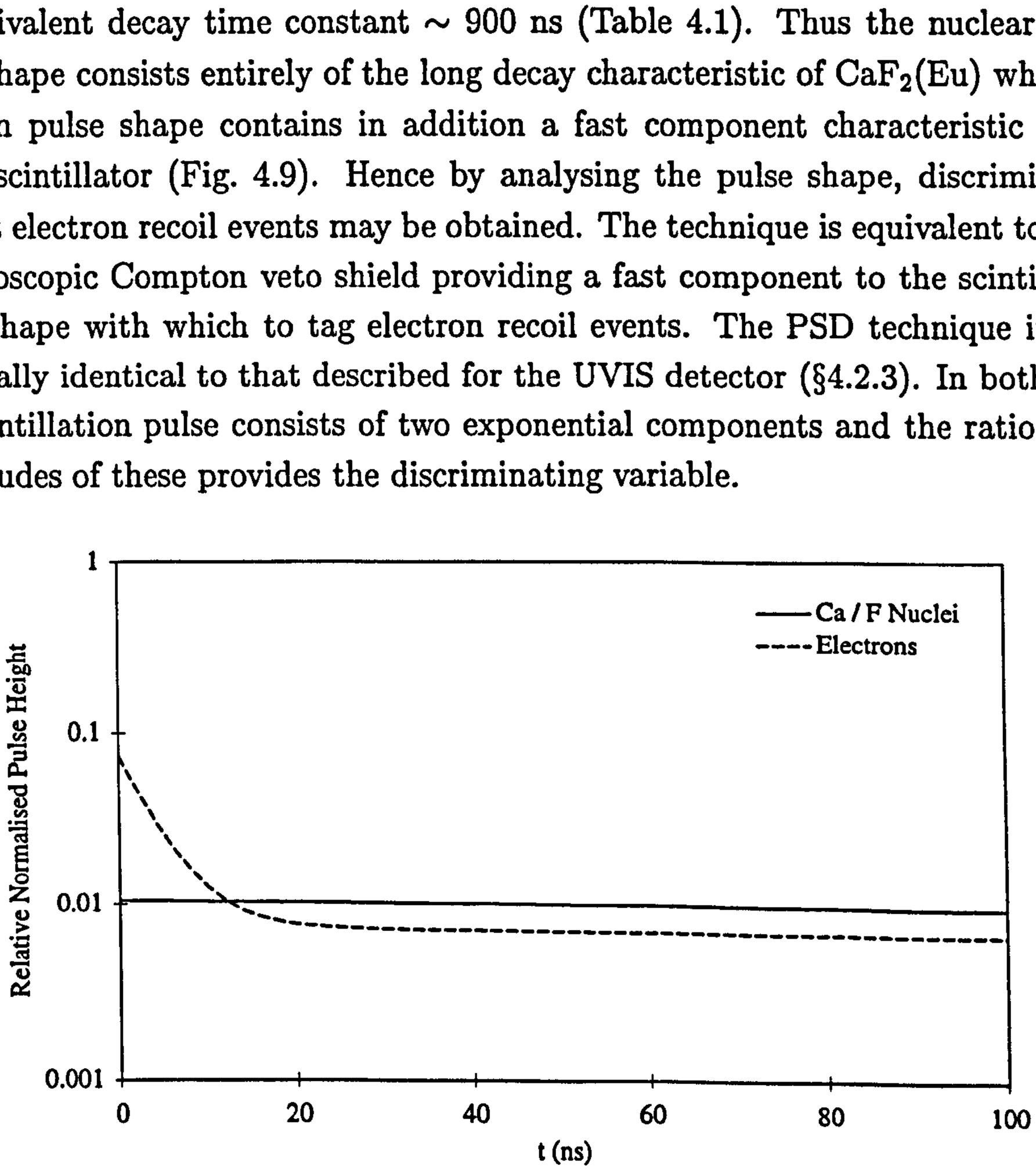

Figure 4.9: *Theoretical CASPAR pulse shapes showing the pulse shape differences between nuclear and electron recoils.*

A further advantage of this technique is that it is relatively inexpensive. The required size of the CaF_2(Eu) crystals is similar to that of the CaF_2 precipitate grains produced during chemical synthesis. Consequently if a method can be found to dope these grains with europium then the expensive process of bulk crystal growth is no longer required. This makes the construction of a large ($\sim$ tonnes) detector conceivable, possibly performing a dual role as a liquid scintillator supernova

neutrino observatory, as in the OMNIS proposal [119]. Other possibilities include the construction of a NaI(Tl) based CASPAR detector, although in this case more work is needed addressing the questions of minimum achievable grain size, of grain hygroscopicity and of obtaining liquids with refractive index > 1.78.

Before even a CaF_2(Eu) CASPAR dark matter detector can be built a number of key points must first be addressed:

- Most important is the doping of the grains of CaF_2 with europium, since this considerably improves the light output of the material (Table. 4.1) and hence reduces the detector energy threshold.
- Techniques for controlling the grain size of the precipitate must be found so as to ensure that optimum discrimination is obtained.
- Issues of radiopurity of detector materials must be addressed, as CaF_2 naturally contains a rather high level of U and Th contamination.
- Various other parameters such as the choice of liquid scintillator, grain packing fraction, and grain suspension technique must be optimised.

These issues are considered in §5.3.

4.2.5 Xenon Detectors

Liquid Xenon Detectors

Another nucleus of considerable interest for dark matter experiments is Xe. Its high atomic number ($\sim$ 131) makes it sensitive to spin independent WIMP interactions, while its spin dependent coupling enhancement factor is also large (Table 3.3). The radiopurity of Xe gas is poor owing to contamination by ^{85}Kr however this can be largely removed through the use of a centrifuge. In the absence of quenching impurities such as water or oxygen liquid xenon is an excellent scintillator with a light output potentially in excess of that of NaI(Tl) (Table 4.1). Two mechanisms, involving direct excitation and charge recombination, lead to excited Xe states, while there are two decay channels, via singlet ($\tau \sim 3$ ns) and triplet ($\tau \sim 27$ ns) excimer states, which can lead to the emission of scintillation light ($\lambda = 175$ nm). These processes give a complicated pulse shape exhibiting large differences between nuclear and electron recoils [101] (Fig. 4.10). Combined with fast, UV sensitive photodetectors liquid xenon has the potential to set WIMP-nucleon cross section limits two orders of magnitude lower than current limits [120]. Prior to this however a considerable amount of development work is required to resolve difficulties

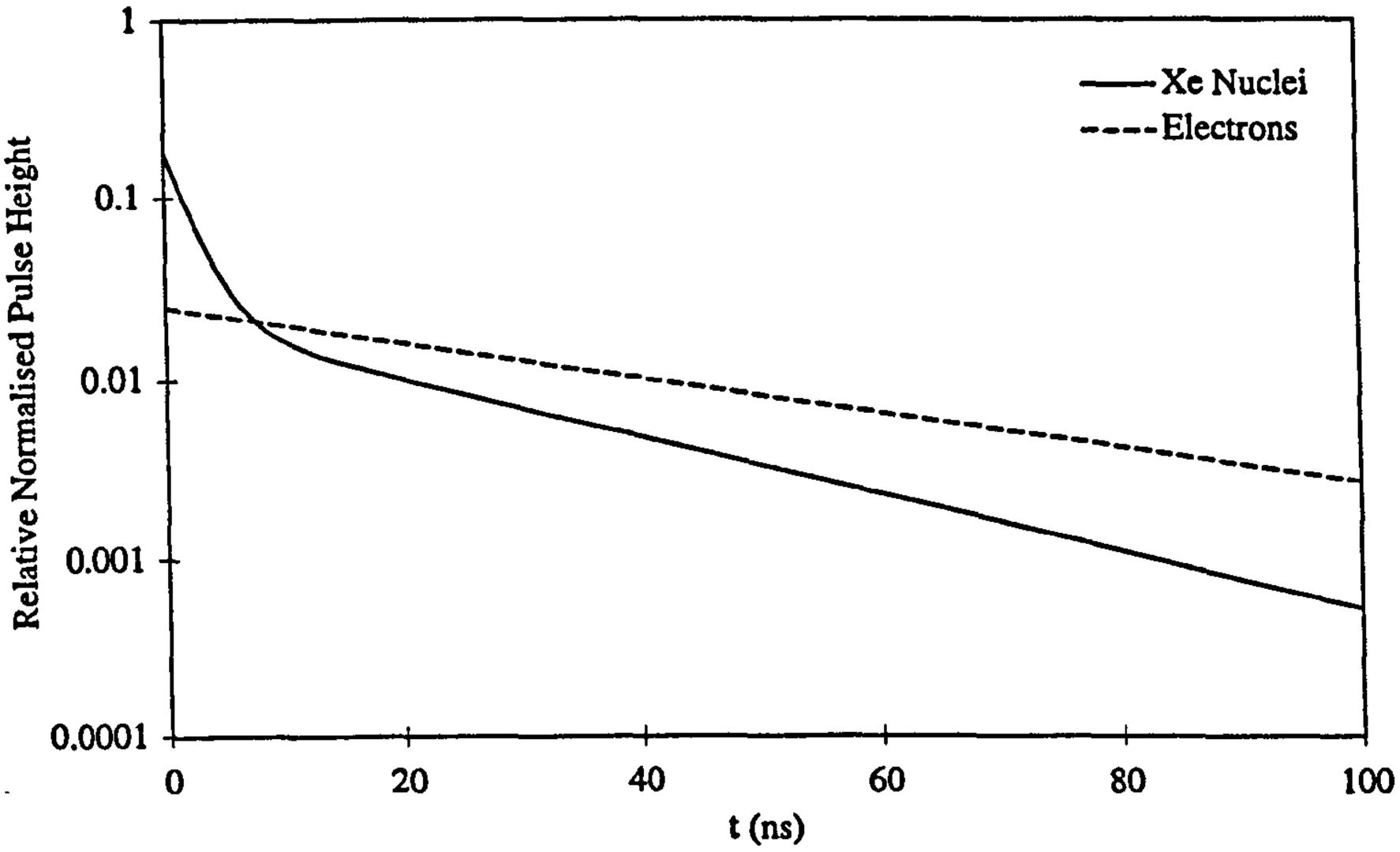

Figure 4.10: *Theoretical liquid xenon pulse shapes showing the pulse shape differences between nuclear and electron recoils.*

associated with the removal of quenching impurities and the collection and detection of the VUV scintillation light.

The DAMA collaboration has had experience with operating a 6 kg liquid xenon dark matter experiment but has not so far made use of PSD [121]. Consequently the WIMP sensitivity of this experiment is similar to that of current NaI(Tl) experiments. The UKDMC is in the process of building a 6.2 kg liquid xenon detector and it is hoped that this will be sufficiently sensitive to the pulse shape to enable PSD to be used to set improved limits. On account of the complicated pulse shape the optimum PSD technique for use with data from this detector may be a likelihood ratio technique similar to that described in [101] or §4.2.2.

Double Phase Xenon Detectors

A development of the liquid xenon scintillator detector is the double phase detector proposed by the ICARUS-WIMP collaboration (UCLA / Torino) [122]. By passing a strong E field through a liquid xenon chamber the charge generated by an event can be prevented from recombining and drifted into a read out region. The scintillation produced by direct excitation of Xe atoms is not affected by this process and can be read out with photodetectors. Nuclear recoils do not create intrinsic ionisation unlike electron recoils and so by using the ratio of ionisation to excitation as a discriminating variable > 97 % discrimination may be obtained for events of 10 keV

recoil energy [123].

Unfortunately inefficient 'dead' regions within the detector volume may lead to electron recoil events for which no ionisation is detected thereby faking nuclear recoils. Furthermore detection of the VUV scintillation light is extremely difficult. One solution to these problems is to use a double phase (liquid / gas) chamber containing Xe doped with 10^{-6} M TriEthyl Amine (TEA). The TEA converts the scintillation photons into a diffuse charge cloud which is drifted alongside the intrinsic ionisation into a gas avalanche read out region [122]. Nuclear recoil events generating mostly scintillation are characterised by the presence of the charge cloud only, while electron recoil events contain in addition a delta function of intrinsic ionisation at the centre of the cloud. These charge distributions can be imaged in three dimensions ($x - y - z(t)$) either electrically or optically and their shapes used to perform discrimination [122]. An additional advantage of this technique is that the high efficiency of the system leads to a large number of minimal Information Carriers (electrons), thereby allowing low threshold operation and excellent discrimination through high electron statistics. The UKDMC proposes to develop a double phase detector in conjunction with UCLA and Torino and when operational it should be capable of setting limits at least three orders of magnitude lower than those currently set by NaI(Tl) detectors [123].

4.3 Detector Design

4.3.1 Light Collection

Given the importance of good photon statistics and a low detector energy threshold for scintillator WIMP searches it is extremely important that for each event the maximum number of scintillation photons reach the photodetector. In any detector there is a non-zero probability per unit path length of absorption in every material through which the photons travel. In particular most scintillators have a relatively short photon absorption length and so it is most important that scintillation light is efficiently extracted from the target material and delivered to the photodetector. This task is complicated in NaI(Tl) by its high refractive index and the need for encapsulation, leading to internal reflection at crystal boundaries. A further factor is that the only photodetectors currently available with response time sufficiently rapid to permit PSD are photomultiplier tubes (PMTs) containing photocathodes of poor radiopurity. The scintillator target must be shielded from the radiation generated by the photocathodes and thus cannot be directly coupled to the PMT. UVIS and liquid xenon targets present the additional problem that much of the scintillation light is

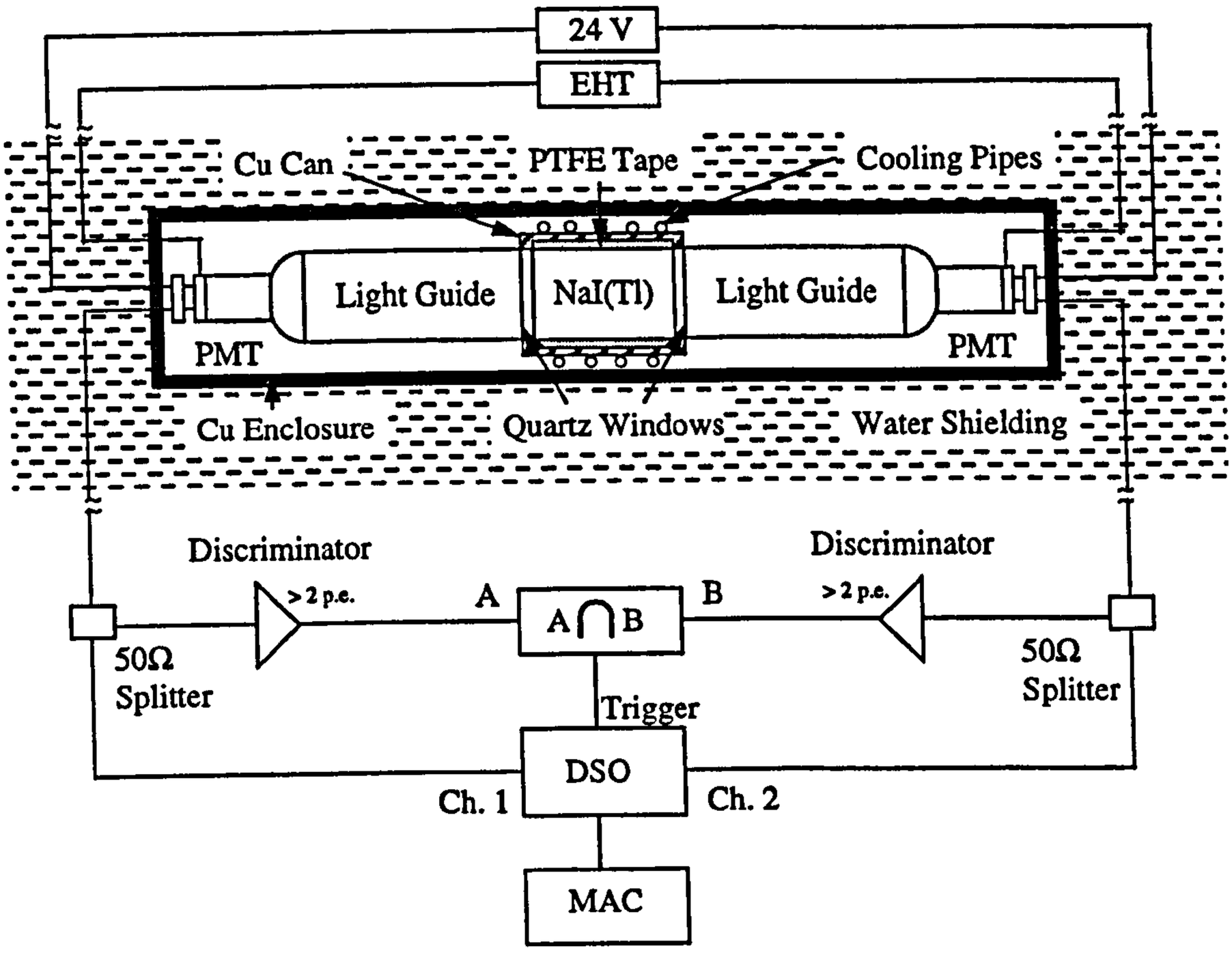

Figure 4.11: *A schematic diagram of a UKDMC NaI(Tl) rig showing the detector itself, water shielding and the DAQ system. Detectors may alternatively be shielded with Pb and Cu castles (§4.5).*

in the VUV and hence is absorbed rapidly by otherwise transparent materials.

Most UKDMC experiments (excluding those using Xe) have a layout similar to that sketched in Fig. 4.11. Two photomultiplier tubes used in coincidence view the target from some distance through long quartz light guides. The separation of the PMTs from the target provides a $1/r^2$ reduction in the background count rate due to photocathode gammas. The quartz ('Spectrasil B' grade) is extremely radiopure and its high density also provides some additional shielding from photocathode radioactivity. Light collection tests and Monte Carlo simulations indicate that the optimum geometry for this system is cylindrical, as this prevents light from becoming trapped in the corners of the target or light guide [124].

The target itself is covered on its cylindrical surface by PTFE, which is an efficient diffuse reflector of light (reflectivity $\gtrsim$ 98 % [125]) and has the further advantage of being of high radiopurity. At either end of the target is a quartz window in the encapsulating can (NaI and NaI(Tl)) or liquid scintillator cell (CASPAR). In NaI(Tl) targets this window is directly attached to the crystal however for UVIS

a N_2 gap must be left in order to allow for crystal expansion during cooling. This has a detrimental effect on the light collection in the UVIS system since the vastly differing refractive indices of N_2 gas (1.0) and NaI (1.78) lead to internal reflection and absorption within the scintillator.

The quartz windows are coupled to the light guides with optical grease. This has a refractive index very similar to that of quartz ($\sim$ 1.5 [110]) and acts to fill any air gaps thus preventing internal reflection at this boundary. The light guides channel light to the PMTs using internal reflection at the cylindrical quartz / air boundary. Coupling to the end windows of the PMTs is again improved by the use of optical grease.

Tests are being performed of alternative PMT-target coupling arrangements in order to investigate how the light collection may be improved. Given the particularly severe problems associated with UVIS crystals it may be beneficial to use unencapsulated NaI directly coupled to the light guides. Problems of hygroscopic degradation of the crystal surface are avoided since the crystal is run in an evacuated cryostat so as to thermally isolate it from its surroundings. The problem of ensuring that the crystal remains unblemished during pumping down has still to be solved however [126].

Simulations indicate that light collection from NaI(Tl) can also be improved by using an unencapsulated crystal, but this time immersed in paraffin (Fig. 4.12 overleaf) [124]. The paraffin is continuously dehydrated using scrap NaI fragments and therefore does not attack the crystal surface. The paraffin also acts as an efficient light guide collecting light from all surfaces of the crystal. With the judicious use of specular and diffuse reflectors around the sides of the detector vessel this light can be delivered efficiently to three large PMTs immersed in the liquid above the crystal. The three fold coincidence technique permitted by this setup should significantly reduce the rate of noise events, as discussed in §3.6.1.

The light collection problems associated with liquid xenon scintillator detectors are still more severe than those of UVIS. The solution which has been adopted is to use a detector geometry similar to that in use in the liquid coupled NaI(Tl) system (Fig. 4.13 overleaf). A central vessel of liquid xenon is viewed by three PMTs situated at the end of cylindrical light guide tubes also containing liquid xenon. Since xenon only weakly absorbs its own scintillation this arrangement maximises the light collection efficiency. Electron recoil events occurring within the light guides are vetoed with a three fold coincidence requirement.

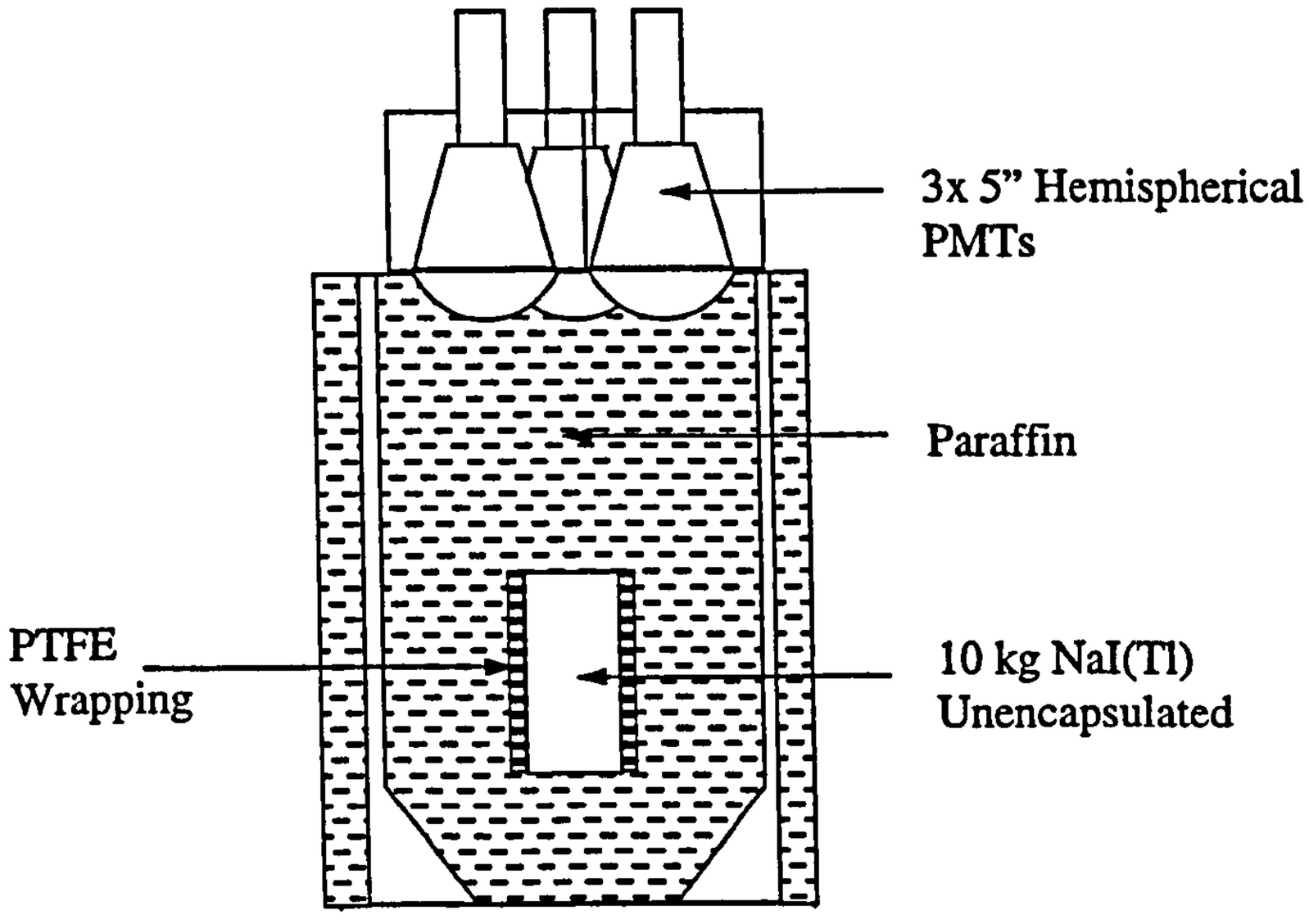

Figure 4.12: *A schematic diagram of a liquid coupled NaI(Tl) detector.*

Figure 4.13: *A schematic diagram of a UKDMC 6.2 kg LXe Detector. The third PMT (facing out of the page) has been cut away for clarity. From [123].*

4.3.2 Photodetection

Any photodetector suitable for use in a UKDMC experiment must satisfy three main criteria.

- It must be sensitive to single scintillation photons without generating excessive numbers of noise events so as to give the lowest detector energy threshold and best PSD properties (through high IC statistics).
- The measurement error associated with the arrival times of those photons must be significantly less than the decay time constant of the scintillator so as to avoid distorting the pulse shape.
- The detector must have a sufficiently large photosensitive area to cover the entire surface of the end of the light guide.

At present the only devices fulfilling all three of these criteria are photomultiplier tubes (PMTs). The characteristics of three PMTs commonly used by the UKDMC are listed in Table 4.2. All are supplied by Electron Tubes Ltd. [127].

PMT	9265 3"	9266 2"	9821 3"
Photocathode	Bialk	Bialk	Bialk
Dynodes	9LF CsSb	10LF CsSb	12LF BeCu
Eff. Diameter (mm)	67	45	60
Typical Gain $\times 10^6$	0.83	0.6	6.7
t_t *(ns)*	42	37	38
σ_{tt} *(ns)*	4.68	2.51	0.94
σ_{pe} *(ns)*	6.38	2.34	1.36

Table 4.2: *The properties of three PMTs commonly used by the UKDMC. All the quantities are defined in the text. Information from [128].*

The internal structure of a typical PMT is sketched in Fig. 4.14(a) (overleaf). Incident photons pass through a transparent window into a vacuum envelope where they strike a photocathode and generate free electrons via the photoelectric effect. The material from which the photocathode is constructed is chosen so as to give optimum sensitivity to photons of the wavelength emitted by the scintillator target. For the blue emission from NaI(Tl) and CASPAR targets the optimum material is 'bialkali', an alloy of tin, potassium and caesium or tin, rubidium and caesium [128]. Reasonable UV sensitivity is also achieved when used in conjunction with quartz or MgF_2 entrance windows.

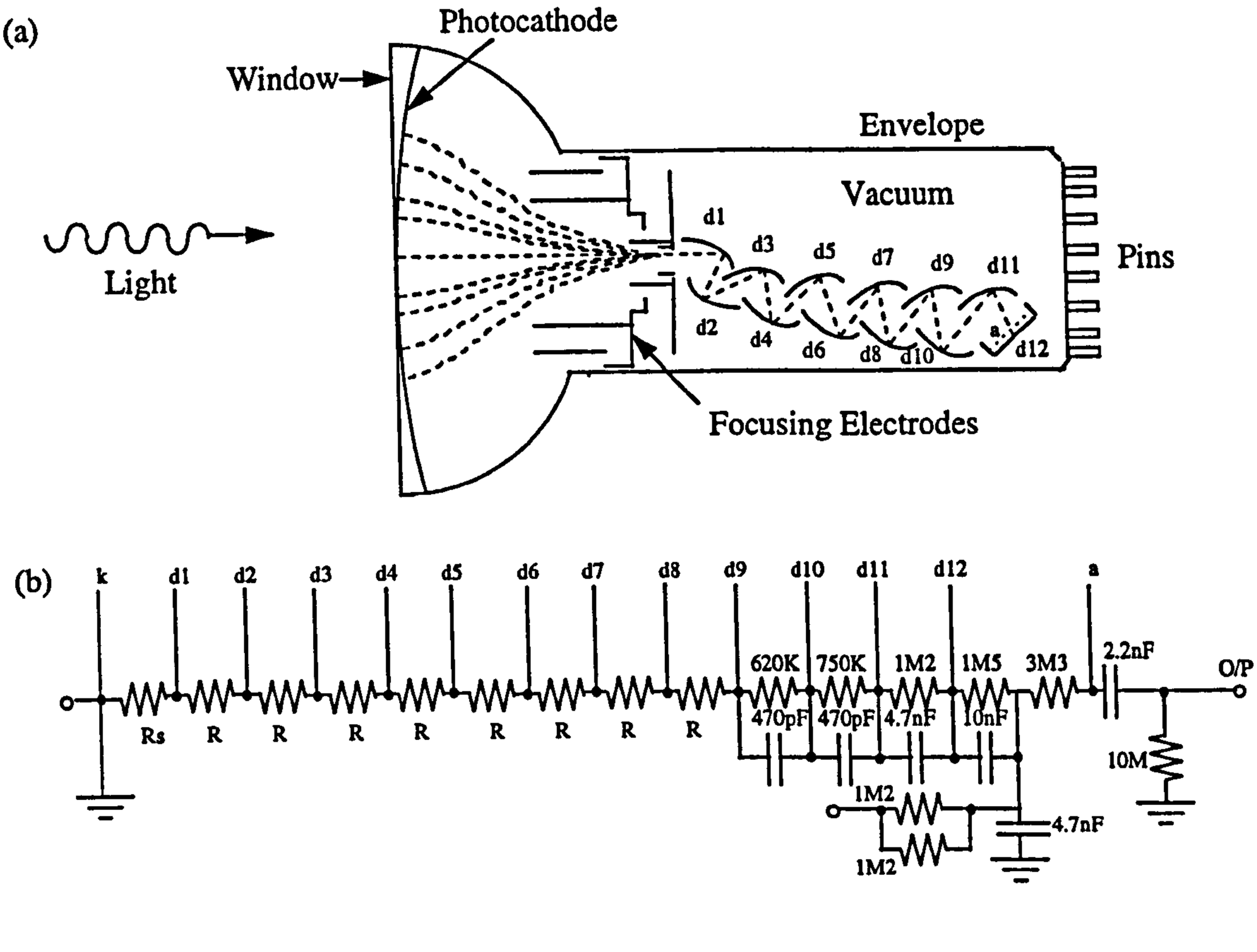

Figure 4.14: *Schematic diagrams of (a) a PMT and (b) a dynode chain. In the figure 'd'i refers to the i^{th} stage of the dynode chain and 'a' refers to the anode. Figure (a) was adapted from [128]. Figure (b) was adapted from information supplied by [129].*

The absolute sensitivity of photocathode materials is referred to as the 'quantum efficiency' ($\eta(\lambda)$) and is defined as the average number of photoelectrons emitted for each incident photon. The quantum efficiency of bialkali photocathodes never exceeds $\sim$ 25 % and this is one significant disadvantage of their use in dark matter experiments [128]. The radiant sensitivity of a PMT $E(\lambda)$ is related to the quantum efficiency by $E(\lambda) = 0.81.\lambda.\eta(\lambda)$ mA/W [128]. Radiant sensitivities of several popular photocathode materials are plotted in Fig. 4.15 (overleaf).

Photoelectrons expelled from the photocathode are accelerated towards a 'dynode' by a large positive potential difference. The magnitude of this potential difference is governed by the values of resistors in an external voltage divider (the 'dynode chain', Fig. 4.14(b)) and is generally chosen to be as low as possible. This reduces the rate of emission of thermal noise photoelectrons which can contribute to the

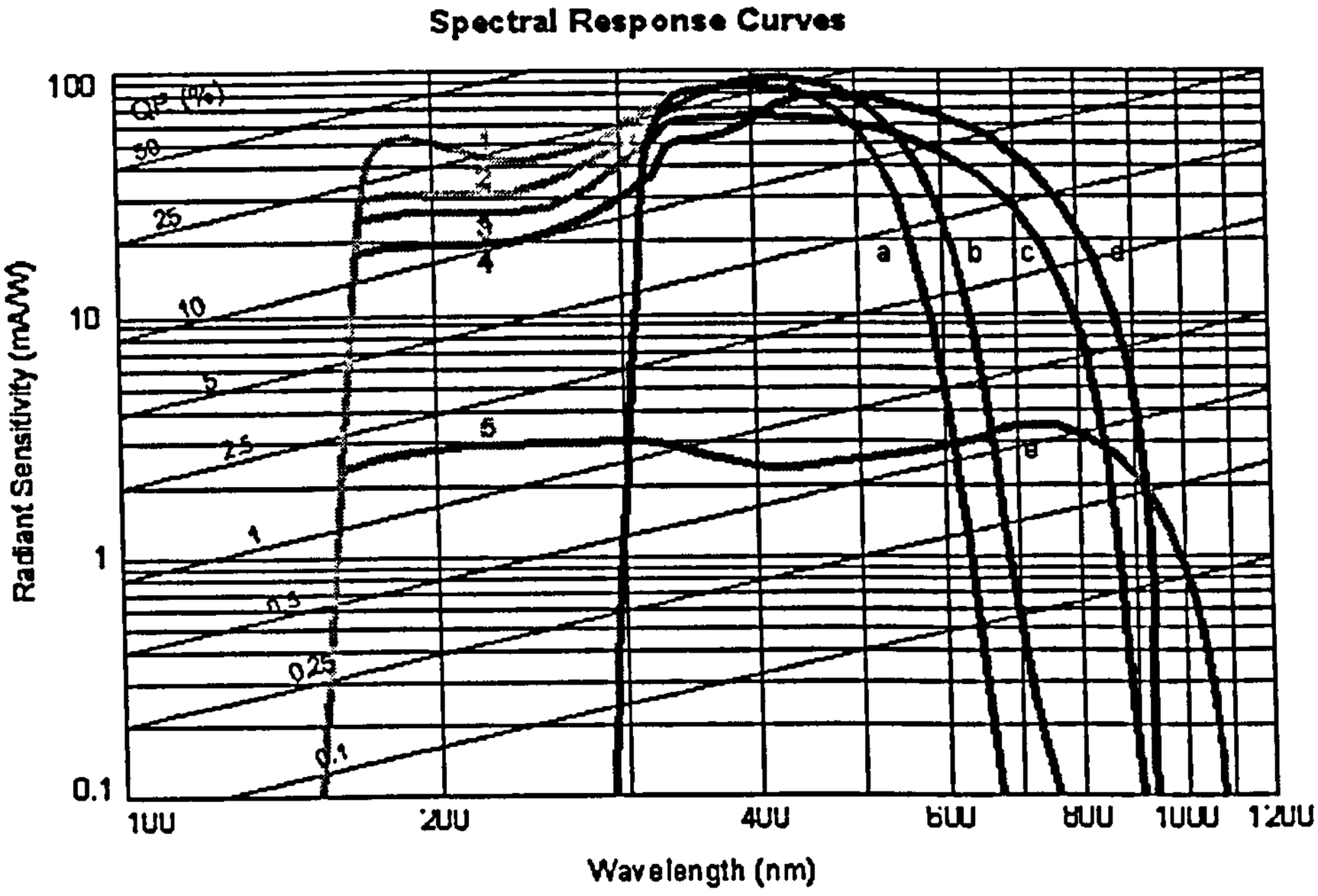

Figure 4.15: *Radiant sensitivity plotted against wavelength for different photocathode materials. The curves are for (a) bialkali, (b) S11, (c) and (d) S20, and (e) S1 photocathodes. The heavier curves are for PMTs with borosilicate glass windows while the lighter curves show the improved UV response of tubes with quartz windows. Taken from [128].*

background 'dark current' in the tube.

Upon being struck by the initial photoelectron the dynode expels δ secondary electrons which are accelerated towards a second dynode. This too emits δ additional electrons for every electron incident and thus the total number of electrons increases geometrically. The process is repeated at each dynode stage until finally the electrons strike an anode connected to the DAQ electronics. The overall charge amplification or 'gain' provided by the PMT is given by $\alpha\delta^N$, where α is the fraction of photoelectrons captured by the dynode structure and N is the number of dynode stages in the tube [102]. For typical dynode materials such as SbCs $\delta \sim 5$ and for modern tubes $\alpha \sim 1$ [102]. Thus a ten stage tube can easily have a gain in excess of 10^6. Low gains are often used in PMTs capable of operating at much higher gains as this increases the dynamic range by reducing space charge saturation problems.

The energy resolution of a given PMT is predominantly a function of the properties of its dynodes. The resolution can be determined by considering the Poissonian statistics (§3.6.1) governing the dynode electron emission process [102]. For a single photoelectron incident upon the first dynode stage the total number of electrons emitted is δ and for a Poissonian process the standard deviation of this quantity is $\sqrt{\delta}$ and the relative variance $1/\delta$. Summing relative variances at each stage in quadrature the total relative variance is found to tend to $1/(\delta - 1)$ for an N stage device with $N >> 1$. Thus for $\delta >> 1$ the single photon energy resolution, proportional to the square root of the relative variance, is dominated by the statistics of the emission from the first stage of the dynode chain, where the number of Information Carriers (electrons) is smallest. This is in accordance with the discussion of §3.6.1.

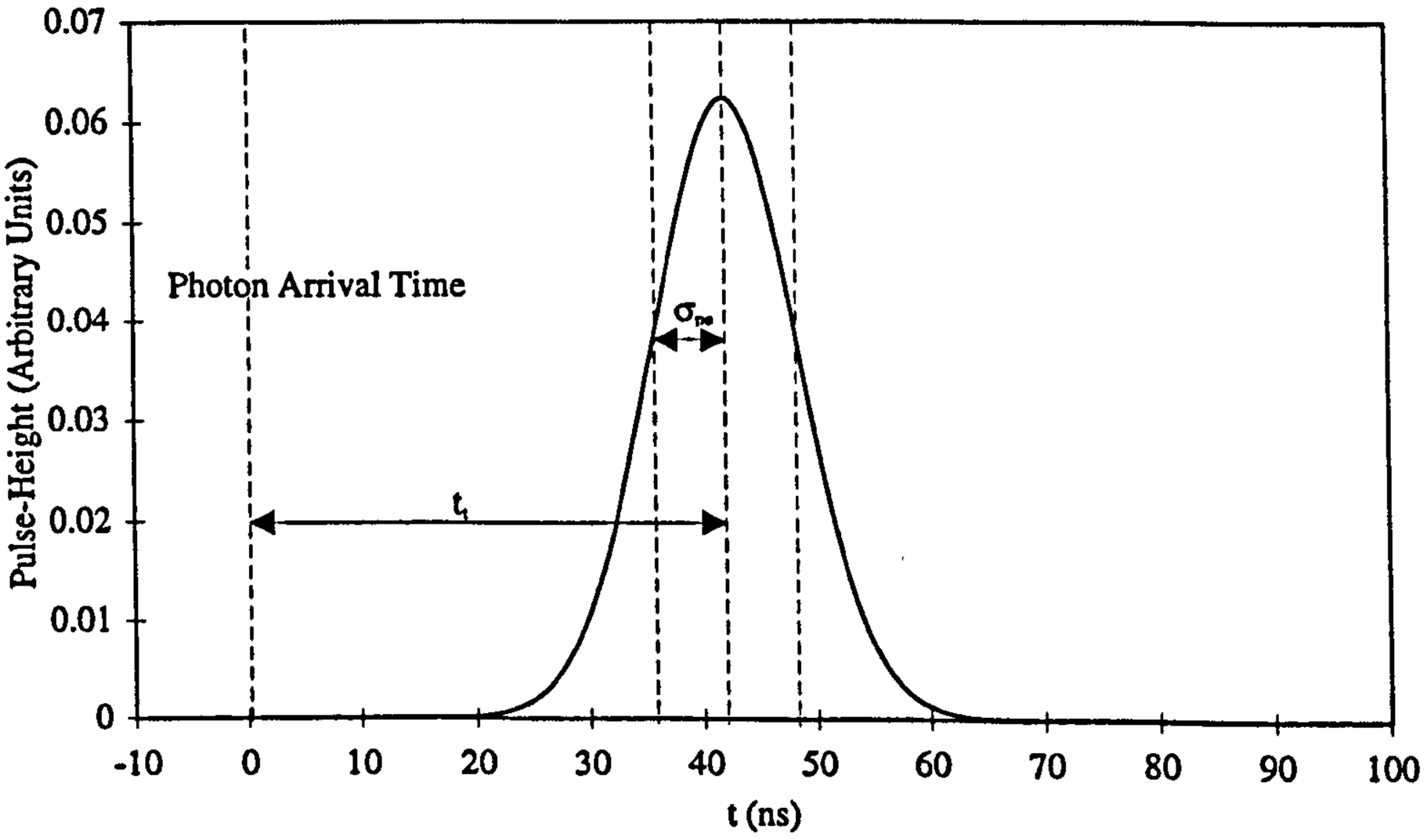

Figure 4.16: *A timing diagram for a single photoelectron pulse in a PMT. From [128].*

The timing characteristics of a PMT are functions of both the tube geometry and dynode chain. A charge pulse is collected by the anode a finite time after the absorption of the incident photon by the photocathode (Fig. 4.16). This mean transit time t_t occurs because of the finite time taken for charge to propagate through the dynode structure. The larger the potential difference between the photocathode and the anode the greater the acceleration of electrons between dynode stages and the smaller the mean transit time. There is also variability in the lengths of the paths taken by the individual electrons and this may be affected by the relative positions and shapes of the dynodes and the voltages between them. The path length

variability leads to a spread in the transit time distribution for the individual electrons generated by a single photoelectron. This distribution is roughly normal with a width σ_{pe} unique to the tube and dynode chain. The finite single photoelectron width limits the PMT time resolution and hence the minimum measurable scintillation decay time constant. For PSD it is important to have tubes with the minimum possible σ_{pe}, especially if the target generates pulses with very fast components, as is the case for liquid xenon, UVIS and CASPAR detectors.

The transit time of charge through a PMT is also a function of the position of incidence of the initial photon on the photocathode. Thus in addition to an intrinsic width to the charge arrival time distribution for each photoelectron, the distribution of the means of these distributions t_t for many photoelectrons also has a finite width. This width, the 'transit time spread' σ_{tt}, is generally of a similar magnitude to σ_{pe}.

A major disadvantage of blue sensitive PMTs is that bialkali photocathodes are both radioactive and of low quantum efficiency. The vacuum envelopes containing the dynode structure are also slightly radioactive, being made of glass containing a significant amount of ^{40}K. For UVIS and xenon detectors quartz PMT windows must be used in order to detect the UV scintillation photons (Fig. 4.15) and in these tubes ^{40}K contamination is still poorer on account of the need for mixed glass graded seals between windows and envelopes. For conventional NaI(Tl) detectors the UKDMC uses low background PMTs from Electron Tubes Ltd. [128] containing glass windows. The problem of photocathode activity remains however and as described in §4.3.1 elaborate steps must be taken to shield the target from its effects.

An alternative approach to this problem is to abandon the use of PMTs altogether and use Avalanche PhotoDiodes (APDs) in their place. These solid state devices are of far higher quantum efficiency and radiopurity than PMTs, allowing them to be directly coupled to the target resulting in an improvement in light collection efficiency [130]. Their surface area is generally small ($\lesssim 1$ cm^2) however this can be used to advantage by segmenting the target into individual cells each read out by a single APD. Multisite Compton events can then be rejected electronically using anticoincidence techniques. The major disadvantage with APDs is that their poor timing characteristics prevents their use in systems incorporating PSD. UKDMC members at Imperial College are currently working on improving both the active areas and time resolutions of these devices and it is hoped that this will permit their use in future detectors. The time resolution and noise associated with APDs are strongly temperature dependent and so they must be operated at cryogenic temperatures. This rules out their use with NaI(Tl) crystals however other targets, in particular UVIS NaI crystals, are suitable. It is believed that CASPAR detectors

may be operated with liquid scintillators such as BC533 (Table 4.1) with freezing points as low as -50 °C and so this technique is also an option for use with APDs.

4.3.3 Data Acquisition Systems

The DAQ system used by most UKDMC detectors is sketched in Fig. 4.11 while a typical dynode chain layout can be found in Fig. 4.14(b). Each PMT is operated such that the photocathode is grounded and the final stage of the dynode structure is at a large positive potential. The high voltage decoupling capacitor (2.2 nF) allows the anode signal to be read out at ground potential, to which the read out electronics are anchored by the large resistor (10 MΩ).

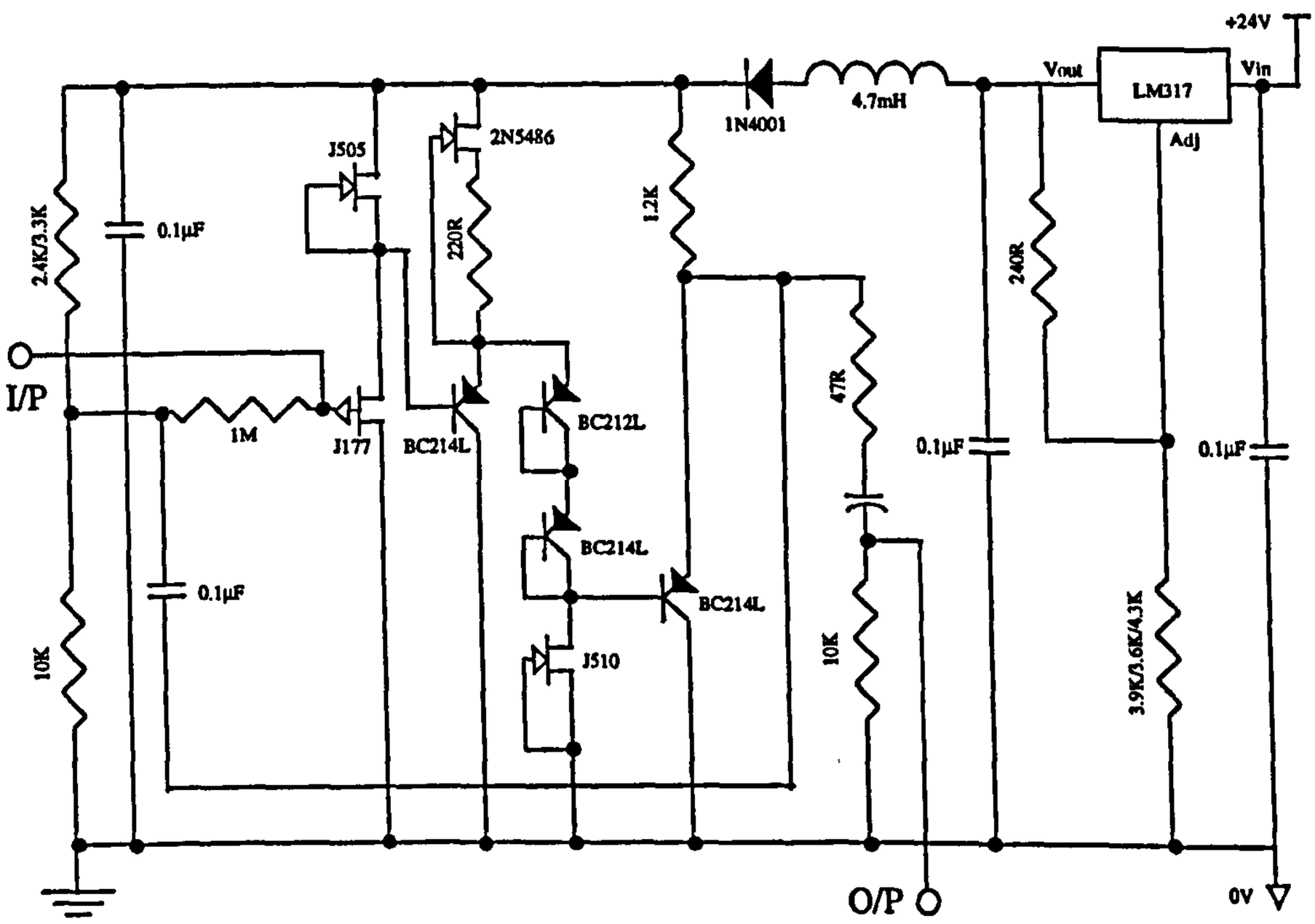

Figure 4.17: *A circuit diagram of the UKDMC pulse shape buffer. Layout from [129].*

The read out system for each PMT consists of a unity gain buffer amplifier (Fig. 4.17) which is situated on top of the dynode chain so as to minimise noise pick up. The purpose of this buffer is to integrate the signal from the PMT so that it can be used for triggering purposes and is less sensitive to noise. One disadvantage of the technique is that stray capacitance causes the read out to have a minimum rise time

$\tau_r \sim 30$ ns [131] which further limits the PSD efficiency of detectors with fast time constants. Another disadvantage is a consequence of the fact that the buffer output must be reset to ground before the arrival of the next event. This is accomplished by a continuous exponential decay of the buffer output voltage with capacitative time constant $\tau_B \sim 40$ μs. This alters the shape of the integrated pulse and must be removed during off line data analysis. Furthermore the slow time constant of this decay means that the DAQ system is unable to operate in a high rate environment such as that encountered during calibration.

The outputs from the two buffer amplifiers in the detector (channels 1 and 2) pass down standard 50 Ω coaxial cables to trigger electronics situated in a NIM crate. Before entering the trigger system each channel is split in two with one output being passed to the 50 Ω input of a LeCroy DSO [132]. The second output for each channel is used to trigger a low threshold discriminator usually set at the 2 photoelectron level. Coincidence logic determines whether all channels have triggered within a 1 μs window and if this is the case then a signal is passed to the external trigger of the DSO. Once triggered the DSO digitises the output waveform from each PMT with a 10 or 20 ns sampling interval. The digitised waveforms are then passed via a GPIB connection to an Apple Macintosh computer running custom written DAQ software. This performs elementary on line analysis of the data (pulse height, pulse mean time) and records the waveforms on disk for more sophisticated off line analysis.

The off line analysis will be described in more detail in §8 and makes use of the pulse analysis techniques described in §3. Before the analysis can take place corrections must be made for alteration of the pulse shapes by the 40 μs buffer recovery. At present this is performed by simply dividing the digitised time dependent integrated pulse height $v(t_i)$ by a function $v(t_i)\exp(-(t-t_0)/\tau_B)$ equivalent to the observed integrated pulse height decay for a delta function anode pulse. For pulses with long decay time constants such as those from NaI(Tl) however a more rigorous approximation should be used and this will now be presented.

Consider a true integrated digitised pulse $f(t_i)$ and an observed buffer integrated digitised pulse $v(t_i)$. The anode pulse is given by

$$f'(t_i) = \frac{(f(t_i) - f(t_{i-1}))}{\Delta t}, \tag{4.13}$$

where Δt is the digitisation interval of the DSO. Now we may consider the anode pulse to consist of a series of delta functions at the times t_i, each with an amplitude given by $f'(t_i)$. The buffer recovery causes the integrals of these delta functions to be exponential functions of decay time constant τ_B rather than true step functions.

The observed integrated pulse at time $t_n > t_i$ is then the sum of contributions from all the preceding exponentials. Thus

$$v(t_{n-1}) = \sum_{i=1}^{n-1} f'(t_i)\Delta t e^{-(t_{n-1}-t_i)/\tau_B}, \tag{4.14}$$

and

$$\begin{aligned} v(t_n) &= \sum_{i=1}^{n} f'(t_i)\Delta t e^{-(t_n-t_i)/\tau_B} \\ &= \sum_{i=1}^{n-1} f'(t_i)\Delta t e^{-(t_{n-1}-t_i)/\tau_B} e^{-\Delta t/\tau_B} + f'(t_n)\Delta t \\ &= e^{-\Delta t/\tau_B} v(t_{n-1}) + f'(t_n)\Delta t. \end{aligned} \tag{4.15}$$

Hence

$$f'(t_n) = \frac{1}{\Delta t}\left(v(t_n) - e^{-\Delta t/\tau_B} v(t_{n-1})\right), \tag{4.16}$$

and integrating we obtain

$$\begin{aligned} f(t_n) &= \sum_{i=1}^{n} f'(t_i)\Delta t \\ &= \sum_{i=1}^{n} \left(v(t_i) - e^{-\Delta t/\tau_B} v(t_{i-1})\right) \\ &\approx \sum_{i=1}^{n} \left(v(t_i) - \left(1 - \frac{\Delta t}{\tau_B}\right) v(t_{i-1})\right), \end{aligned} \tag{4.17}$$

for $\Delta t/\tau_B << 1$. Rearranging and cancelling terms we obtain

$$\begin{aligned} f(t_n) &= \sum_{i=1}^{n} \left(v(t_i) - v(t_{i-1}) + \frac{\Delta t}{\tau_B} v(t_{i-1})\right) \\ &= v(t_n) - v(t_0) + \frac{\Delta t}{\tau_B} \sum_{i=1}^{n} v(t_{i-1}). \end{aligned} \tag{4.18}$$

This fast algorithm can be implemented simply within the analysis code and permits an accurate correction to be made for the buffer recovery characteristics.

One aspect of any dark matter experiment which the DAQ system must be capable of handling is calibration. In addition to energy calibration with monoenergetic gamma sources such as ^{137}Cs, samples of low energy nuclear and electron recoil events must be generated in order to use and test PSD techniques. The electron recoils can be generated by Compton scattering of high energy gammas from a ^{60}Co source while nuclear recoils are created by exposure to neutrons from a ^{252}Cf fission

or Am-Be source. An unfortunate feature of the buffer circuit however is that the raw detector event rate must be kept sufficiently low to avoid saturation. Further, if the trigger rate is too high the rate at which events can be recorded becomes limited by the dead time introduced by the speed of the GPIB interface between the DSO and the Macintosh. Thus the sources must be either weak or well shielded / remote from the detector. PSD calibration is therefore typically a lengthy process.

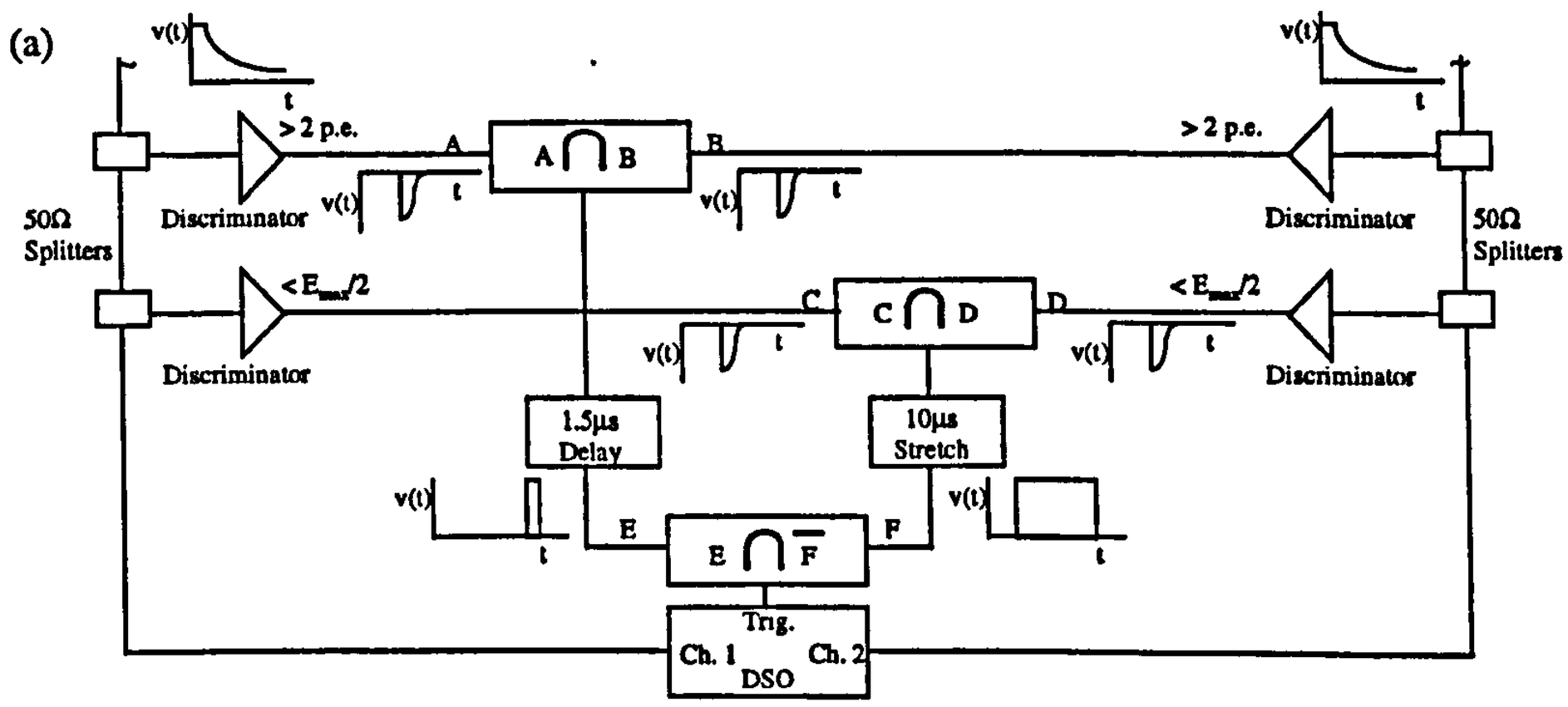

Figure 4.18: *The layout and operation of the new high energy cut DAQ system. Figure (a) shows the circuit layout while Figure (b) shows the delay between low energy and high energy triggers and the need for delaying and stretching the trigger pulses.*

When using these sources the majority of triggers are due to unwanted high energy electron recoils from Compton scattering. The GPIB saturation problem may thus be solved by rejecting these events. An additional high energy trigger has been developed to accomplish this and is sketched in Fig. 4.18(a). With this system the buffer outputs are split into three before entering the trigger electronics. Once again one output from each channel goes to the DSO and another goes to a discriminator with a two photoelectron threshold. The third output is passed to another discriminator with a high threshold equal to V_{max}/N where V_{max} is the

maximum desired total pulse height and N is the number of channels. The outputs from all the low threshold discriminators are added in coincidence as are those from the discriminators with the high threshold. A DSO trigger pulse is then constructed by requiring anticoincidence between low threshold and high threshold triggers. In the case of pulses with a long decay time constant the high threshold trigger is delayed by a varying amount (due to photon statistics) relative to the low threshold trigger. Thus the former trigger pulse must be stretched and the latter delayed in order to ensure the efficient rejection of large pulses (Fig. 4.18(b)).

Owing to the rate limitations and pulse shape damage associated with the buffers the need for their use should be reassessed. The pulse heights of the raw PMT anode signals are typically small ($\sim$ mVs) and are often considered to be too sensitive to noise pick up to be of direct use for DAQ purposes. A further consideration is that some form of integration is essential in order for the DAQ system to trigger on small amplitude ($\sim$ 2 photoelectron) pulses with long decay time constants. Some inherent signal integration is provided by the non-zero σ_{pe} of the PMTs however for slow pulses this is negligible. In response to these considerations a new DAQ system has been designed which can be implemented in two stages so as to minimise any interference with detector operation.

The first stage of the new system involves the use of the raw anode signals for PSD, with the buffer being retained for triggering purposes only (Fig. 4.19(a) overleaf). This removes some buffer pulse shape damage but potentially introduces serious noise problems. These are minimised by splitting the anode signals before they enter the decoupling capacitors. One anode output passes once again to the buffer through the capacitor and thence to either of the trigger systems described above. The other output passes through a second capacitor and thence directly to the 50 Ω input of the DSO via a 50 Ω screened coaxial cable. The low voltage side of this capacitor is tethered to ground by two 100 Ω resistors connected in parallel, whose total resistance is 50 Ω. The use of 50 Ω resistances and impedances throughout prevents signal reflections at impedance boundaries. High frequency noise propagating from the trigger line through the decoupling capacitors and into the signal line is minimised by connecting a 10 μF tantalum capacitor and a 10 nF ceramic capacitor in parallel across the 24 V DC supply to the buffer. Noise is further reduced by limiting the bandwidth of the DSO to $<$ 50 MHz so as to filter out the higher noise frequencies. This has the unfortunate additional effect of increasing the minimum measurable pulse decay time constant to a level similar to τ_r. The buffer recovery time problem is nevertheless removed by this technique.

The second stage of the new system involves replacing the buffer with a resettable

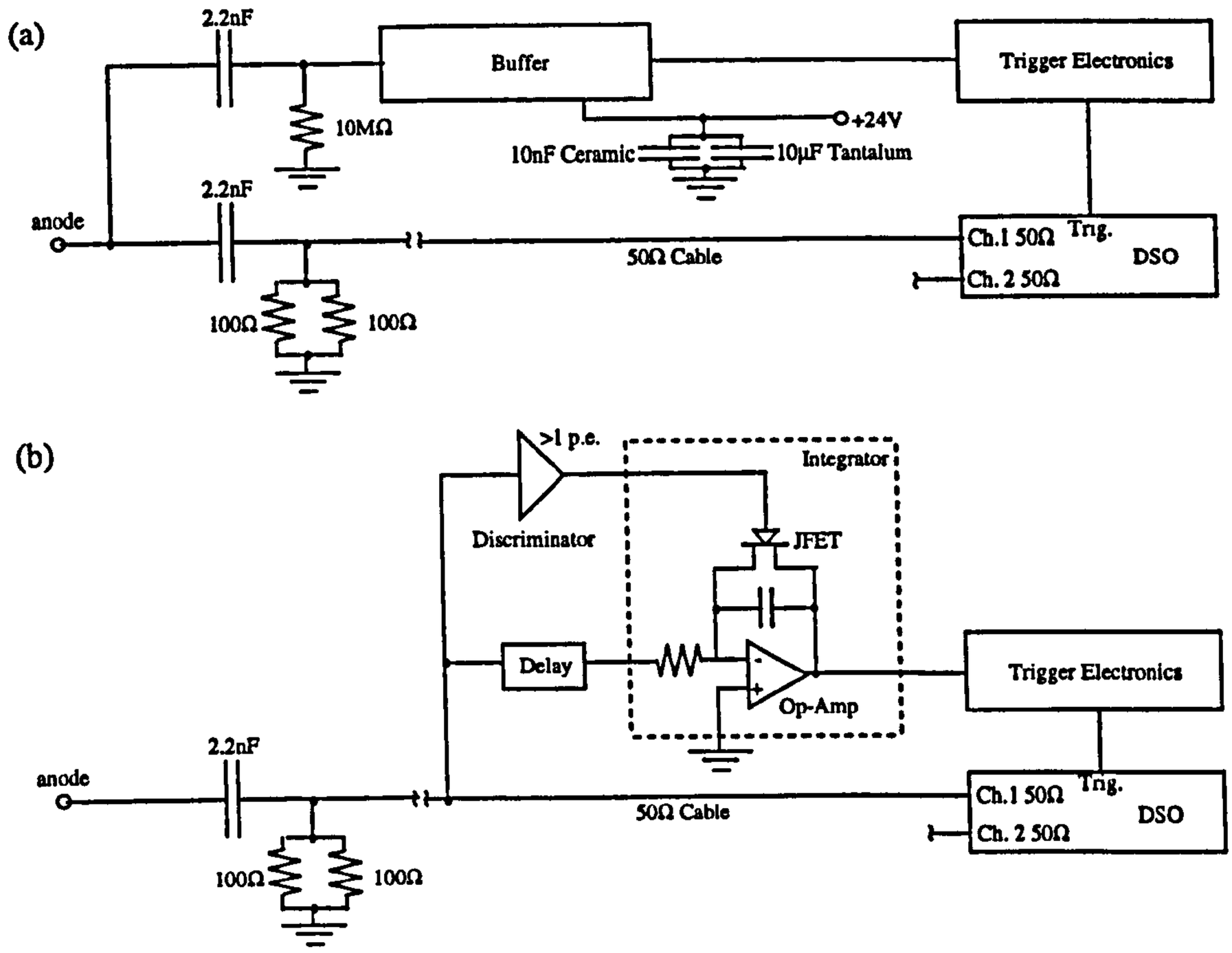

Figure 4.19: *Circuit diagrams for the proposed new DAQ system. Figure (a) shows the first stage retaining the pulse shape buffer for trigger purposes only. Figure (b) shows the complete system incorporating a resettable op-amp integrator for low threshold triggering on slow pulses.*

op-amp integrator (Fig. 4.19(b)) [133]. This device integrates the pulse for a set period of time determined by the width of an external gate input. As currently envisaged its implementation would involve removing the trigger line from the PMT altogether and splitting it from the signal line at the input to the DSO. A low threshold discriminator set to the anode single photoelectron level triggers the device which then integrates for the predetermined period and passes the result to the trigger systems previously described (Fig. 4.11). The integrator need not have a fast rise time as its output is not used for PSD. It does have a fast recovery time however since this is just the period over which the integration takes place. Thus the use of such a system should considerably increase the rate at which calibration data can be acquired. Trials of this system are awaited in the near future.

4.4 Detector Shielding

Radioactive background events in a dark matter experiment can originate from a number of sources both internal and external to the detector. Although PSD can reduce background significantly its use is strictly limited to discriminating against electron recoils and even then cannot compensate for an extremely high event rate. The most important way to remove background then is to ensure that the raw event rate is as low as possible. The crudest way to accomplish this is to shield the detector from external sources of radiation.

Any detector situated on the surface of the earth is exposed to radiation from many sources. At sea level cosmic ray air showers contain predominantly muons, electrons (positrons) and photons and these can interact directly with the detector. The muons also interact with nuclei outside the detector via spallation and capture to create neutrons which give low energy nuclear recoils inside. Unstable isotopes present in the environment such as ^{40}K and those from the U and Th chains decay to give monoenergetic gamma radiation. These high energy photons are Compton scattered to give a large continuum gamma background capable of causing electron recoils within the detector through the Compton and photoelectric effects. U and Th nuclei themselves also give neutrons via fission, again leading to background nuclear recoils. A further hazard of the U / Th chain is presented by the daughter isotope ^{222}Rn. This is a naturally occurring gas which is widespread in the atmosphere and decays to give ^{210}Pb. This is a radioactive solid with a half life of 22 years and can plate detector components which have previously been cleaned thoroughly. Other unstable isotopes ('cosmogenics') can also be created within the detector by cosmic ray transmutation.

The exterior gamma background can be attenuated with a large surface density of shielding material. One approach is to surround the detector with heavy metal blocks arranged to form a shielding 'castle'. Alternatively the detector can be lowered into a large tank containing many tonnes of water. These arrangements also reduce the rate of nuclear recoil background events by scattering or thermalising and absorbing a large proportion of incident neutrons. Further neutron shielding can be provided by surrounding detectors with hydrogenous materials such as polyethene.

At sea level shielding also attenuates the flux of cosmic ray electrons, positrons and photons. Cosmic ray muons are far harder to shield against however and can penetrate most materials to depths of several hundred metres before being absorbed. The simplest solution is to situate the detector under a large volume of rock so as to provide passive muon shielding. To this end the UKDMC has established an underground laboratory at the Boulby Mine operated by Cleveland Potash Ltd..

This is a working potash mine with an extensive network of tunnels situated in a halite (NaCl) seam some 1100 m (3600 mwe) beneath the coast of North Yorkshire (UK). The considerable rock overburden reduces the muon flux by a factor 10^4 relative to that at the surface. This corresponds to an absolute flux comparable with that at other underground facilities situated elsewhere in the world (Fig. 4.20).

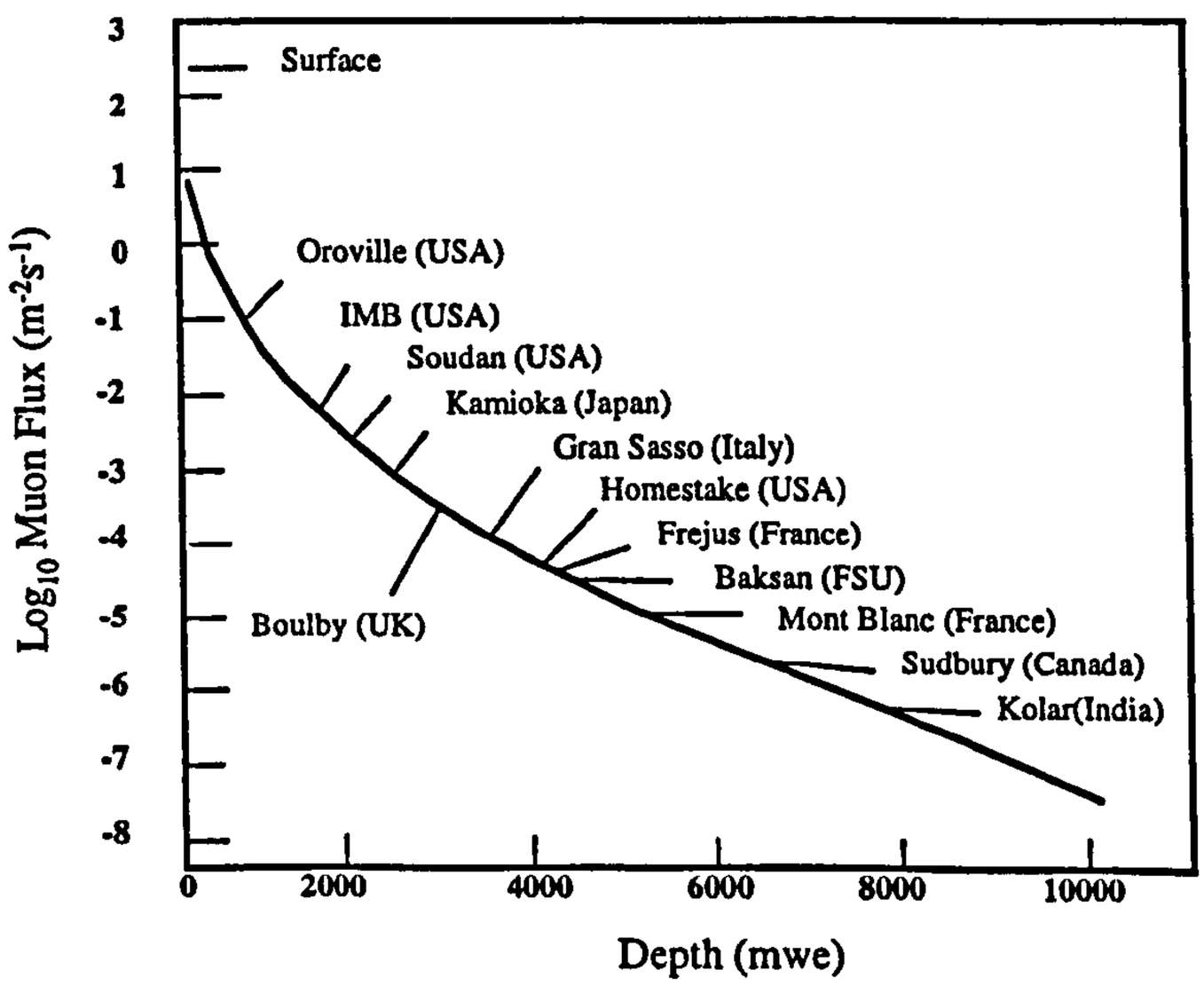

Figure 4.20: *The muon flux as a function of depth for major underground laboratories. Adapted from [47].*

The halite rock at Boulby is sufficiently radiopure to give a reduced external gamma and fission neutron background relative to the surface. Another consequence of this is that ^{222}Rn levels in the atmosphere are also low thus reducing problems of plate out. A significant reduction in the remaining background is achieved using shielding castles or a 200 tonne water tank as outlined previously. The resulting background rate is sufficiently low to permit an active liquid scintillator veto to be operated without introducing dead time problems. This can be used to veto both through going muons and a large proportion of Compton events. Such a veto system is currently under construction at Boulby.

4.5 Detector Radiopurity

The reduction in the total background rate provided by external shielding is strictly limited by the radiopurity of both the detector and the shielding itself. Reasonable gamma background rates $\lesssim 1$ /keV/kg/day require impurity levels of $\lesssim$ ppm K and $\lesssim$ ppb U and Th in the shielding and levels an order of magnitude lower in the detector itself. Both the removal and assay of impurities at these concentrations is highly non-trivial and sophisticated techniques must be developed.

Of greatest concern is the radiopurity of the scintillator target. This must contain a low level of not only gamma and neutron emitting isotopes but also those isotopes which emit short range alpha and beta particles. Radiopure NaI or NaI(Tl) crystals are double grown in low potassium quartz crucibles, possibly using raw NaI powder which has been prepurified with the DIPHONIX ion exchange resin (§5.3.2). The chemical precursors of the CaF_2(Eu) powder used in CASPAR can also be purified with DIPHONIX while the liquid scintillators which are required already possess low levels of contaminants through distillation. In xenon targets ^{85}Kr contamination can be removed through the use of a centrifuge.

The radiopurity of the detector and target housing must also be addressed. PMT photocathodes and envelopes typically contain large amounts of ^{40}K and the UKDMC is involved in a collaboration with Electron Tubes Ltd. aimed at reducing this. Careful detector design also helps to minimise the effects of this source of background (§4.3.1). Much of the physical structure of the detector and in particular the encapsulation surrounding NaI and NaI(Tl) crystals is made from high purity materials such as PTFE, quartz or electroformed copper. The radiopurity of all raw detector materials is measured through mass spectrometry, neutron activation analysis or gamma spectrometry, the last of which is performed using a low background Ge detector installed underground for this purpose. Any additional short lived cosmogenic activation is limited by the prestorage of components and materials for long periods at Boulby.

The radiopurity of shielding materials is less critical than that of the detector but harder to achieve in practice. The approach of using heavy metal castles allows the shielding for a particular detector to be compact however the potential for U and Th chain contamination in such an arrangement is large. Pb is most commonly used for castle construction as it is extremely dense and can be refined with relative ease on account of its low melting temperature. The refining process cannot remove the ^{210}Pb produced by U decay however and so it is of considerable benefit to use 'old' refined Pb in which this isotope has had time to decay away. The difficulty of obtaining Pb shielding of sufficient radiopurity has led the UKDMC to construct

castles consisting of a 6" thick outer layer of Pb bricks surrounding an inner layer of electroformed Cu blocks of much higher purity. The detectors then rest inside a cavity in the Cu.

The alternative shielding arrangement using water presents less of a radiopurity problem. Hydrogen and oxygen are immune to cosmogenic activation and do not have isotopes which emit high energy gammas or neutrons. Impurity atoms dissolved within the water can be removed with conventional purification and demineralisation processes. The disadvantages of this technique are that a much larger volume of shielding is required, and detectors must be water proof.

A combination of both shielding and radiopurification techniques leads to a total background event rate ~ 4 /keV/kg/day in the energy range of interest (< 100 keV visible energy). By far the majority of these events are due to electron recoils and so can be removed by PSD. Most background neutrons present within the shielding are due to U and Th fission processes in the rock, shielding or detector. These processes also produce copious amounts gammas and Monte Carlo simulations indicate that the fission neutron induced nuclear recoil rate within the target should be at least a factor 10^5 lower than the gamma induced electron recoil rate [120]. Muon induced neutrons are predicted to produce a background nuclear recoil rate $\lesssim 0.01$ /kg/day after passive shielding [120] and the use of an active veto should reduce this by at least two orders of magnitude.

4.6 The Future: Directional Detectors?

The detectors described in this chapter can search for rudimentary evidence for the existence of WIMP dark matter by using PSD to isolate an anomalous nuclear recoil signal. With sufficient statistics it should then be possible to find evidence for an annual modulation in that signal, as is predicted by the theory outlined in §3. Incontrovertible proof of the cosmological origin of this signal can only come from an observation that the *direction* of these recoils is diurnally modulated however. Such a directional modulation could only be explained by the presence of WIMPs and would arise from the changing orientation of the detector relative to the effective WIMP flow caused by the rotation of the earth. Consequently there is considerable interest in the development of direction sensitive dark matter detectors. The absolute (unmodulated) dark matter sensitivity of these detectors is often less than that of the detectors described previously and so it is likely that they would be of most use only after positive evidence for a nuclear recoil signal has been seen by other detectors.

A number of organic crystal scintillators display crude direction sensitivity. This typically arises from a highly anisotropic crystal structure in which the scintillation efficiency for nuclei varies strongly with orientation [134]. This leads to a diurnal modulation in the shape of the visible energy spectrum of any WIMP signal. The UKDMC is investigating the use of stilbene crystals [134] while anthracene is another possibility. These materials offer the additional advantages of excellent intrinsic PSD properties and reasonable light output (Table 4.1). On the other hand both crystals are hydrocarbons and therefore are of low density and contain nuclei with poor spin dependent and spin independent coupling enhancement factors. A large array of these detectors would therefore be needed to achieve an unmodulated nuclear recoil sensitivity similar to that of the planned double phase Xe chambers.

Another proposal ('DRIFT' - 'Directional Recoil Identification From Tracks') is to use an array of large drift chambers containing Xe gas at low pressure [135]. In these devices the length of electron recoil tracks is sufficiently great to allow them to be imaged. Discrimination can thus be performed on the basis of recoil range, while the recoil direction can be measured directly. Track imaging is limited in large (length $\gtrsim$ 1 m) detectors by the diffusion of charge in a plane transverse to the drift direction. One solution to this problem is to place the chamber in a large superconducting solenoid producing an axial B field [136] however a scale up of this technique to large target masses is rather expensive. An alternative solution currently under investigation is to dope the Xe with molecules such as CS_2. These absorb the charge to create heavy negative ions which can drift long distances into the read out region without diffusion [135].

One further technique worthy of note is the directional variant of CASPAR. This makes use of anisotropic CaF_2(Eu) 'needles' or 'plates' in place of the cubes which are currently produced during synthesis (§5.3). These crystals are aligned through the application of a strong electric or magnetic field, the latter coupling to the large paramagnetic moment of Eu atoms. The crystals must be of sufficiently small a size in at least one linear dimension to allow nuclear recoils in this (these) directions to escape into the liquid scintillator. If the other linear dimension(s) is (are) the same as those of the crystals used in the conventional CASPAR technique then the PSD provided by this detector is direction sensitive. The total (energy integrated) rate of a WIMP induced nuclear recoil signal then obtains an additional diurnal modulation. It is unclear as to how the required needles or plates of CaF_2(Eu) could be grown however there is a suggestion that fabrication from $CaCO_3$ microfibres may be possible [137].

4.7 Conclusions

Scintillator detectors provide a range of different techniques with which to discriminate nuclear recoil signal from electron recoil background events in searches for WIMP dark matter. The UK Dark Matter Collaboration operates or is developing a number of such detectors for use at its low background underground site at the Boulby Mine. These detectors and their associated DAQ electronics have been optimised to obtain the greatest possible sensitivity to potential signal events, both through design and through radiopurification and shielding.

Chapter 5

Detector Development

5.1 Introduction

UKDMC effort to improve the recoil discrimination provided by crystal scintillators centres around UVIS (§4.2.3) and CASPAR (§4.2.4). In the following chapter these techniques are described in more detail and results presented of work carried out by this author investigating possible enhancements to the light output and discrimination which they provide. In §5.2 studies of the performance of UVIS detectors containing NaI crystals grown by different techniques is investigated while in §5.3 optimisation of the inorganic crystal, organic liquid and gelling agent components of the CASPAR detector is discussed.

5.2 UVIS

5.2.1 Crystal Growth

The UKDMC has conducted numerous tests of undoped NaI UVIS crystals. Studies have been performed at various temperatures of the total light output and the strengths and decay time constants of the UV and visible scintillation components [105]. The results (Fig. 5.1 overleaf) indicate that optimum discrimination and light output are obtained at operating temperatures of around 160 K. Unfortunately however the maximum light output obtained in these tests ($\sim$ 1.25 pe/keV [105]) was rather poor in comparison with that obtained from NaI(Tl) crystals operated at room temperature ($\sim$ 3 pe/keV - §8). This is in marked contrast to earlier results obtained by other workers [100] which suggest similar performance in the two cases. With the observed light output the threshold in such detectors is too high to provide WIMP sensitivity comparable to that of NaI(Tl) experiments despite the enhanced

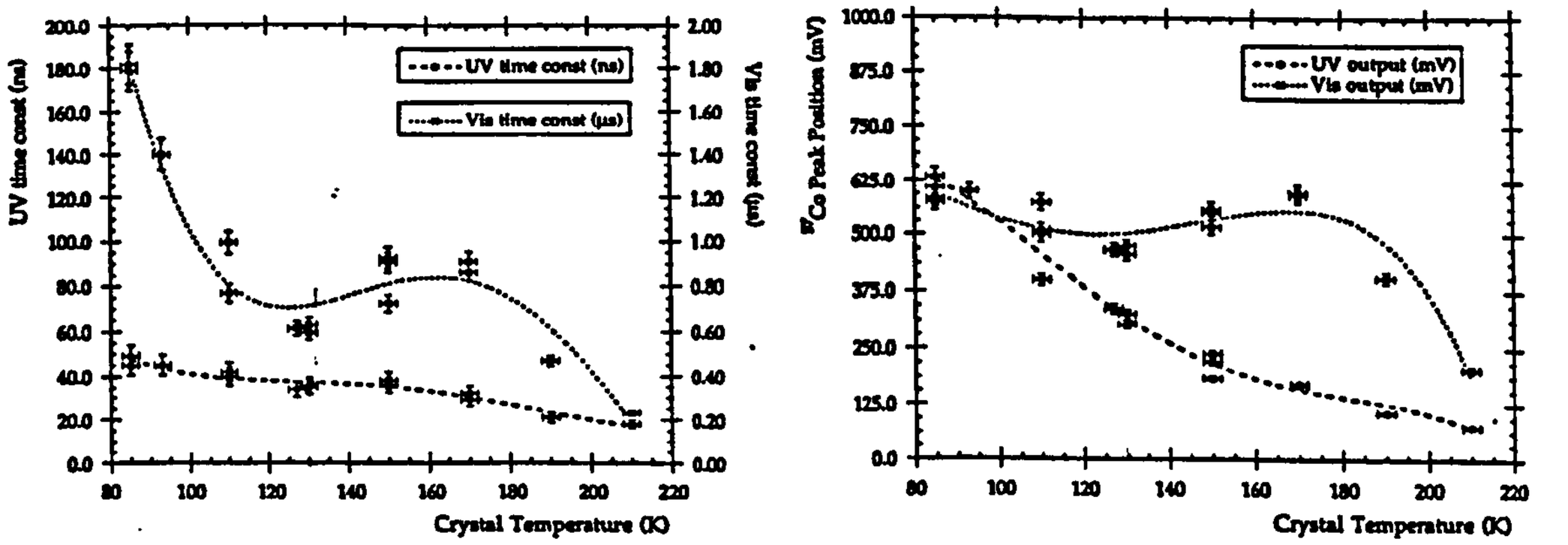

Figure 5.1: *The pulse shape properties of a Kyropoulos UVIS NaI crystal. The lefthand figure shows the estimator of the UV and visible component decay time constants (T_0). The lefthand axis on this figure refers to the UV component T_0 and the righthand axis the visible component T_0. The righthand figure shows the UV and visible component pulse amplitudes. Taken from [105].*

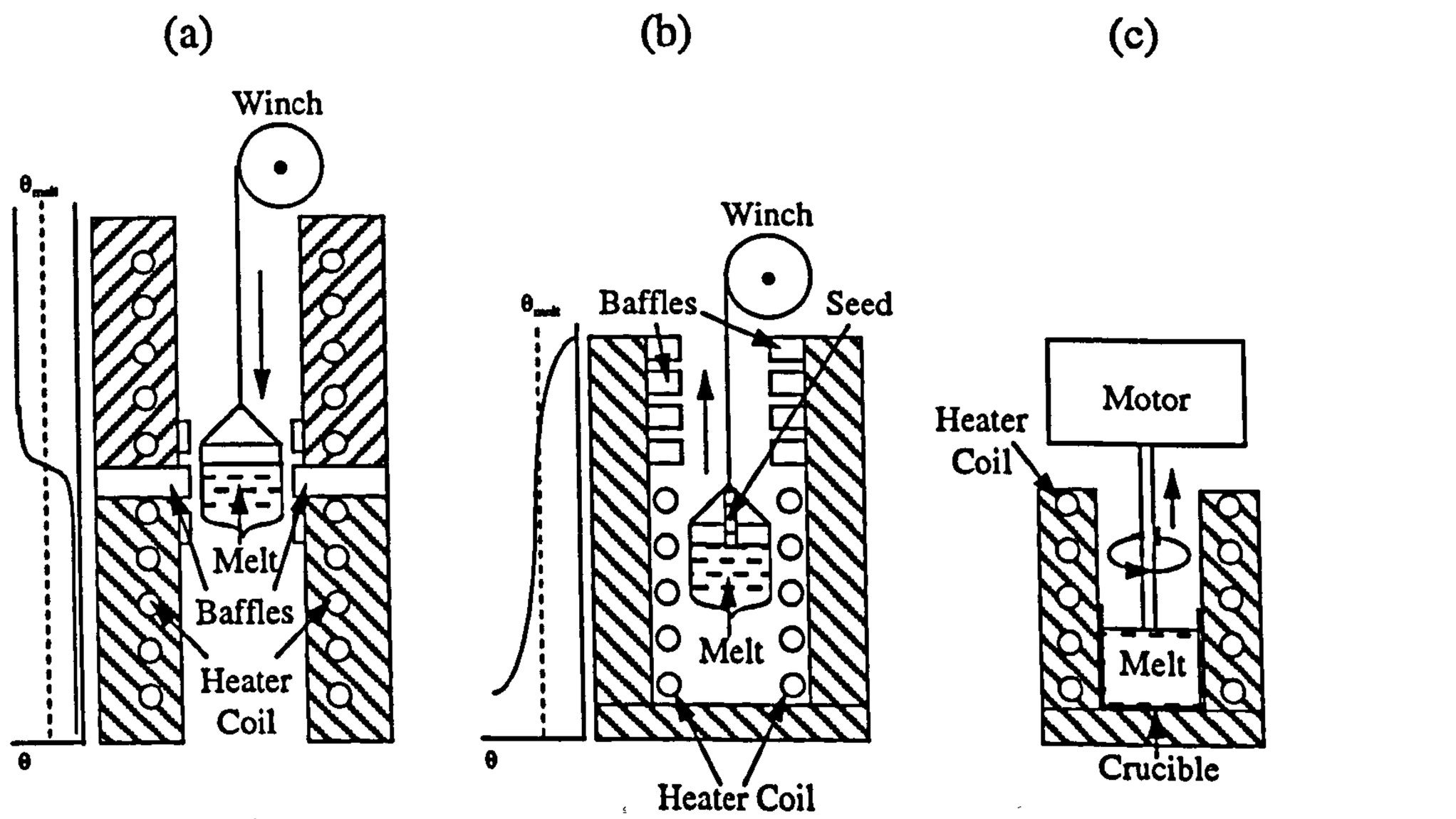

Figure 5.2: *Alternative crystal growth techniques. Technique (a) is Bridgeman-Stockbarger, technique (b) is Kyropoulos and technique (c) is Czochralski. Adapted from [138].*

discrimination provided by the UVIS technique [105]. Thus it is of paramount importance that the light output be improved.

One consideration which has not been investigated by the Collaboration with a view to improving light output is the crystal growth technique. The best original results [100] were obtained from crystals grown by the Bridgeman-Stockbarger process [138] illustrated in Fig. 5.2(a). The crucible containing the NaI melt is slowly lowered from a hot zone through a region of carefully controlled temperature gradient into a cooler zone. The upper and lower temperatures are chosen to be respectively just higher and just lower than the melting temperature of NaI. As the shaped tip of the crucible passes through the intermediate region it acts as a 'seed' for nucleation within the melt and a crystal begins to form inside. This crystal becomes progressively larger as the crucible is lowered until finally it consumes the entire melt. The crystal must then be annealed slowly at an elevated temperature in order to remove stresses within the lattice due to the differing thermal expansion coefficients of crystal and crucible.

The Bridgeman-Stockbarger process produces good quality crystals of potentially great size ($\sim$ 1 m ϕ [109]). It is not the only process which can be used however and most UKDMC NaI(Tl) crystals are grown using an alternative technique known as the Kyropoulos process [138] (Fig. 5.2(b)). Kyropoulos involves placing a high quality seed crystal in the melt and then slowly decreasing the temperature of the melt to a point below that at which crystallization begins to occur. The bulk crystal or 'boule' forms around the seed crystal until it occupies the entire crucible. Scintillation crystals are then cut from the centre of the upper half of the boule [108] so as to remove radiocontaminants, which are concentrated in the surface and lower half. Further purification can be achieved using double growth (§4.2.2). One advantage of this technique is that the crystal is never in contact with the crucible while forming and therefore does not become stressed through differential thermal contraction. A disadvantage is that large boules cannot be grown as the narrow seed crystal is unable to support a large weight without becoming stressed and cracking.

A third commonly used technique is the Czochralski process [138] (Fig. 5.2(c)). This is similar to the Kyropoulos process but involves pulling the seed crystal from the melt while rotating it about a vertical axis. The melt crystallises at the surface of the cooled seed and forms a boule which steadily increases in size as it is pulled. The rotation of the seed enables large boules to be grown.

The light output of a scintillation crystal depends strongly upon its quality and hence upon the growth technique used. Defects, impurities and stresses within the crystal lattice can absorb excitons and cause them to decay non-radiatively. It was

thought that one reason for the poor performance of the original Kyropoulos UVIS NaI crystals may have been that the growth technique led to their being of poor quality thus compromising their light output. It was therefore decided that further tests should be performed with Czochralski and Bridgeman-Stockbarger crystals.

5.2.2 Experimental Apparatus and Procedure

Tests were performed using the apparatus sketched in Fig. 5.3. The double sided crystals were encapsulated by the manufacturers (Hilger Analytical Ltd. [139]), first by wrapping the cylindrical surfaces in reflective PTFE tape and then by mounting the wrapped crystals in cylindrical Cu cans with quartz end windows. Due to differing rates of thermal expansion gaps containing dry N_2 gas were left between the crystals and windows. These gaps were maintained by using three small stand offs of epoxy resin on each window, arranged in the form of a tripod (Fig. 5.4 overleaf).

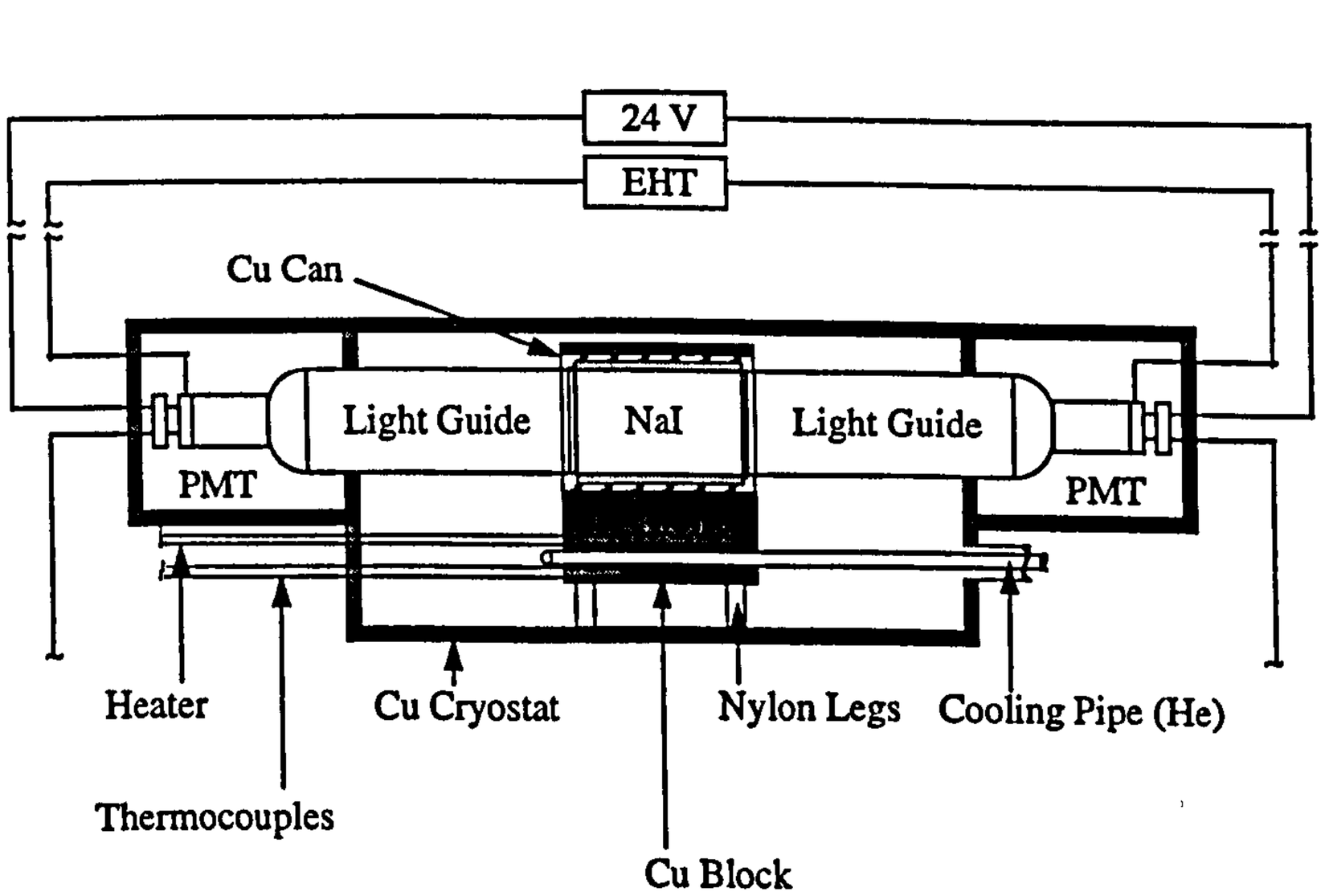

Figure 5.3: *A schematic diagram of the experimental apparatus used for UVIS tests.*

For each test the encapsulated crystal was mounted in a copper block in thermal contact with cooling pipes through which flowed He exchange gas. The crystal,

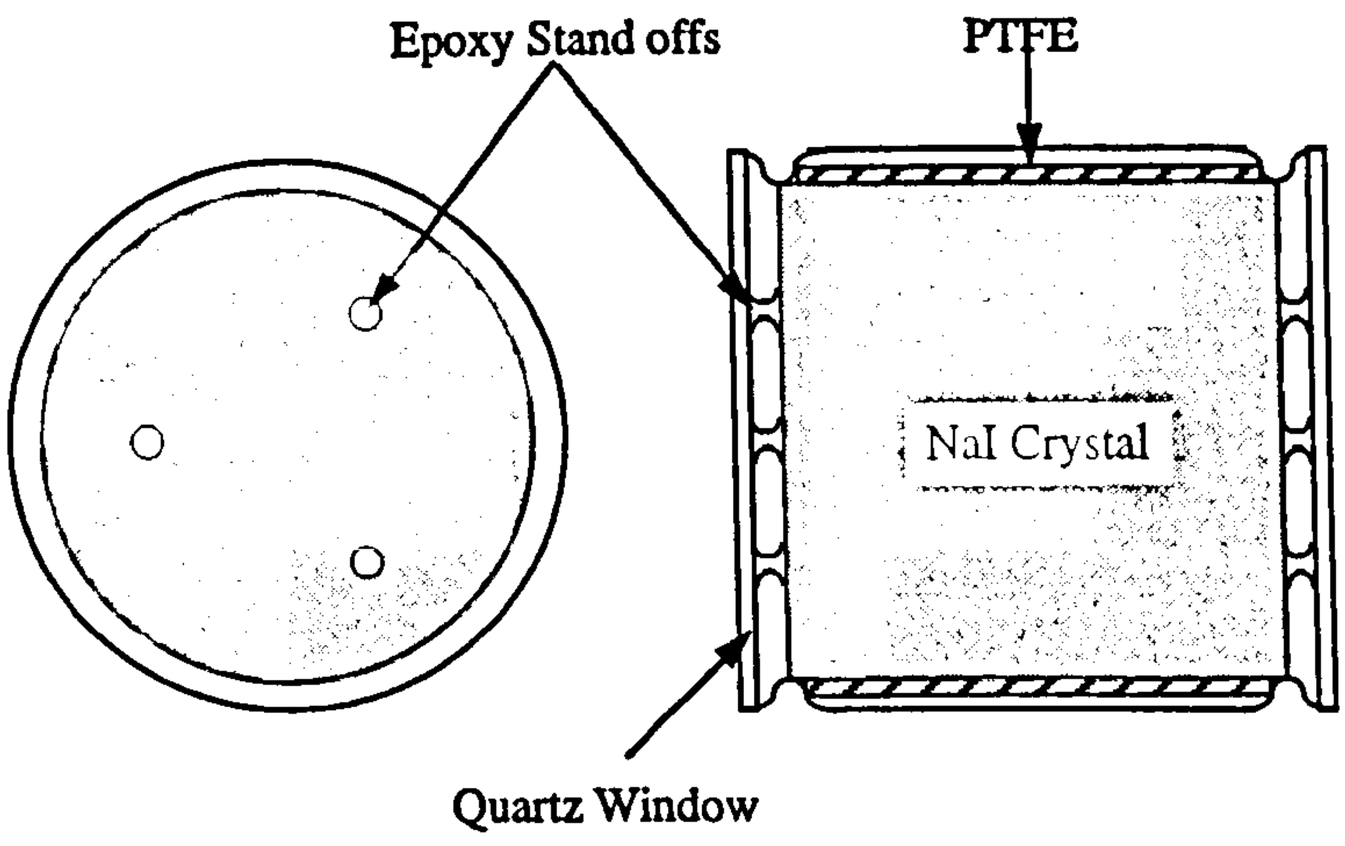

Figure 5.4: *A schematic diagram of a UVIS NaI crystal showing the epoxy stand offs.*

block and pipes rested inside an evacuated copper cryostat on thermally insulating nylon legs. Thermocouples and an electrical heating element were attached to the block and connected to a heating system incorporating an OMEGA CN76000 programmable temperature controller [140]. Cooling was provided by an Edwards Cryodrive 3.0 mechanical device [141].

Light collection was performed using a variation on the standard UKDMC system described in §4.3.1, with light guides extending outside the cryostat (Fig. 5.3). A thin layer of Dow-Corning Q2-3067 (packaged under licence by BDH [142]) was used to couple the windows to the light guides and the light guides to the PMTs. The entire system was inspected visually at 130 K and no deterioration in the quality of coupling was observed. The PMTs, dynode chains and buffers were mounted outside the cryostat in light tight copper tubes. The DAQ system described in §4.3.3 incorporating a high energy cut was used. The cut was not used during energy calibrations and was switched out at the final coincidence unit of Fig. 4.18. During pulse shape calibrations the cut was set to reject all events with visible energy greater than 30 keV.

Each experiment consisted of slowly ramping the temperature of the crystal down to the lowest value possible while performing frequent energy calibrations with the 122 keV line from a 1μCi ^{57}Co source situated above the cryostat at a distance $\sim$ 0.3 m. NaI is prone to cracking as a result of thermal stress and so the rate of change of crystal temperature was intended never to exceed 4 K/hr. Once the lowest possible crystal temperature had been obtained it was slowly raised once more while performing energy and nuclear and electron recoil pulse shape calibrations. 0 - 30 keV electron recoil calibrations were performed with Compton events from a 1 μCi ^{60}Co source situated $\sim$ 0.5 m from the crystal, while 0 - 30 keV nuclear recoils were generated through the scattering of neutrons from a 50 mCi ^{252}Cf source. This was situated inside a 15 mm thick steel pot placed $\sim$ 0.5 m from the crystal inside a cave constructed from 100 mm of Pb bricks surrounded by $\sim$ 0.3 m of wax. Due to the large number of background gammas and hence electron recoil events also produced by this source it would have been preferable to use a monoenergetic neutron beam (§6) to perform these measurements. Such apparatus was not available at the time these experiments were carried out however.

Data was analysed using a χ^2 fitting routine ('Curvefit') implemented in IDL [143]. The buffer integrated ^{57}Co event pulse shapes were fitted using a sum of two exponential functions with free parameters pulse start time, UV and visible component decay time constant estimators T and pulse height amplitude ratio R_A (the ratio of the slow (visible) component pulse height to the total pulse height - §4.2.3). The total pulse height was taken to be the absolute normalisation of the pulse. UV and visible component pulse heights were deduced from the total pulse height and amplitude ratio values and are therefore not independent of these other parameters. The ^{60}Co and ^{252}Cf event pulse shapes were fitted with double exponential functions with all decay time constant estimators set to the mean values from the ^{57}Co data and all total pulse heights set to the absolute pulse height normalisations. Free parameters were then the pulse start time and pulse amplitude ratio. Owing to the low statistics (numbers of photoelectrons) of these pulses it proved impractical to fit them with functions with freely varying time constants.

Normal curves were fitted to the pulse height and amplitude ratio histograms with a χ^2 minimisation routine in order to determine the mean values and errors. Log-normal curves (§4.2.2) were fitted in the same way to the histograms of component decay time constant estimators T. Typical histograms from ^{57}Co data of total pulse height, UV and visible component decay time constant estimators T and pulse heights and amplitude ratio R_A are plotted in Fig. 5.5. Typical amplitude ratio histograms from ^{60}Co and ^{252}Cf data are plotted in Fig. 5.6.

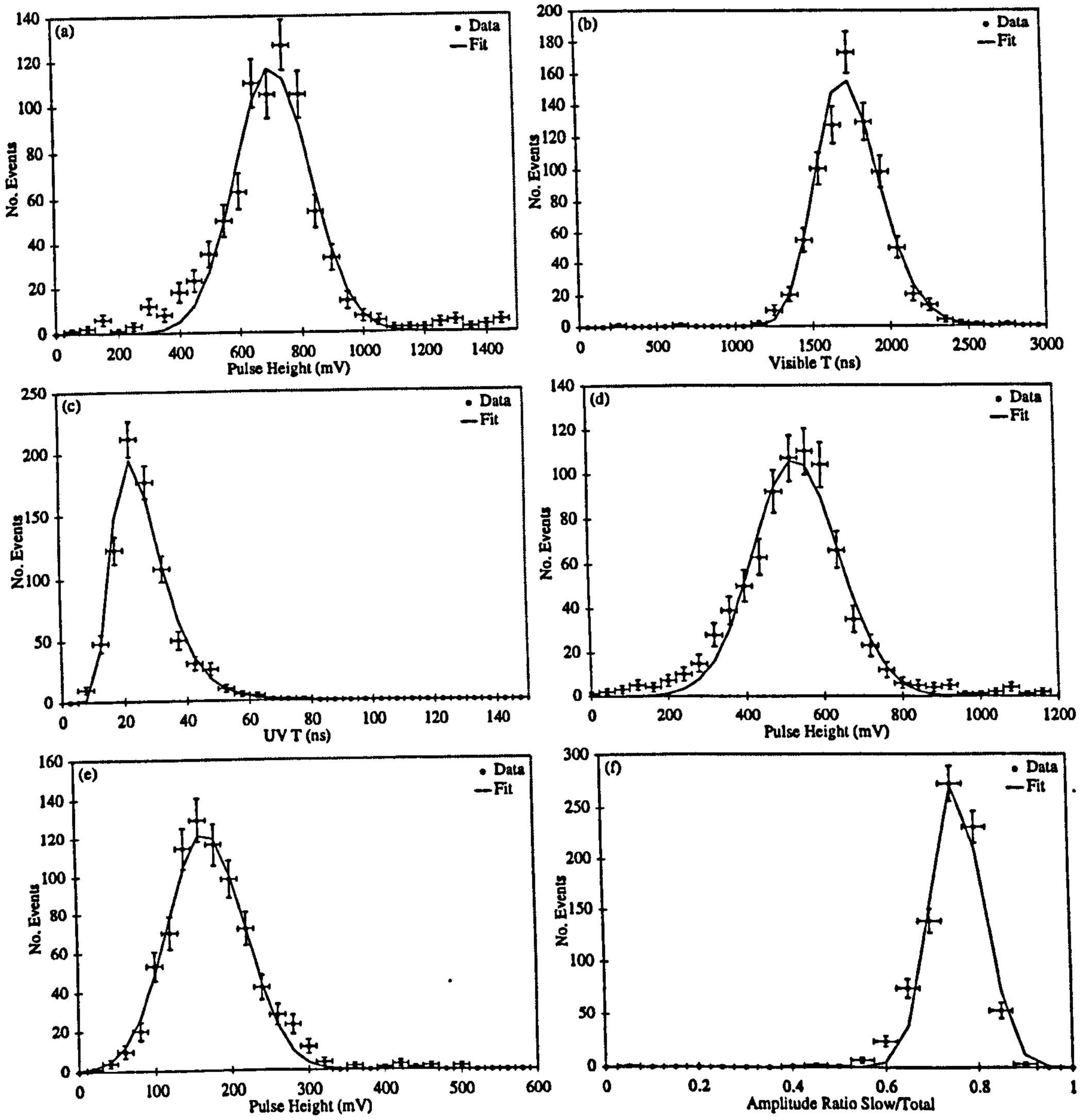

Figure 5.5: *Example ^{57}Co pulse parameter distributions from data taken with the Bridgeman-Stockbarger crystal running at 150 K. Figure (a) shows the total pulse height distribution, Figures (b) and (c) show the T distributions for the visible and UV components respectively, Figures (d) and (e) show the individual pulse height distributions for the visible and UV components respectively and Figure (f) shows the distribution of pulse amplitude ratios (defined in the text). The curves are fits to the data; log-normal curves for T in Figure (b) and Figure (c) and normal curves in all other figures.*

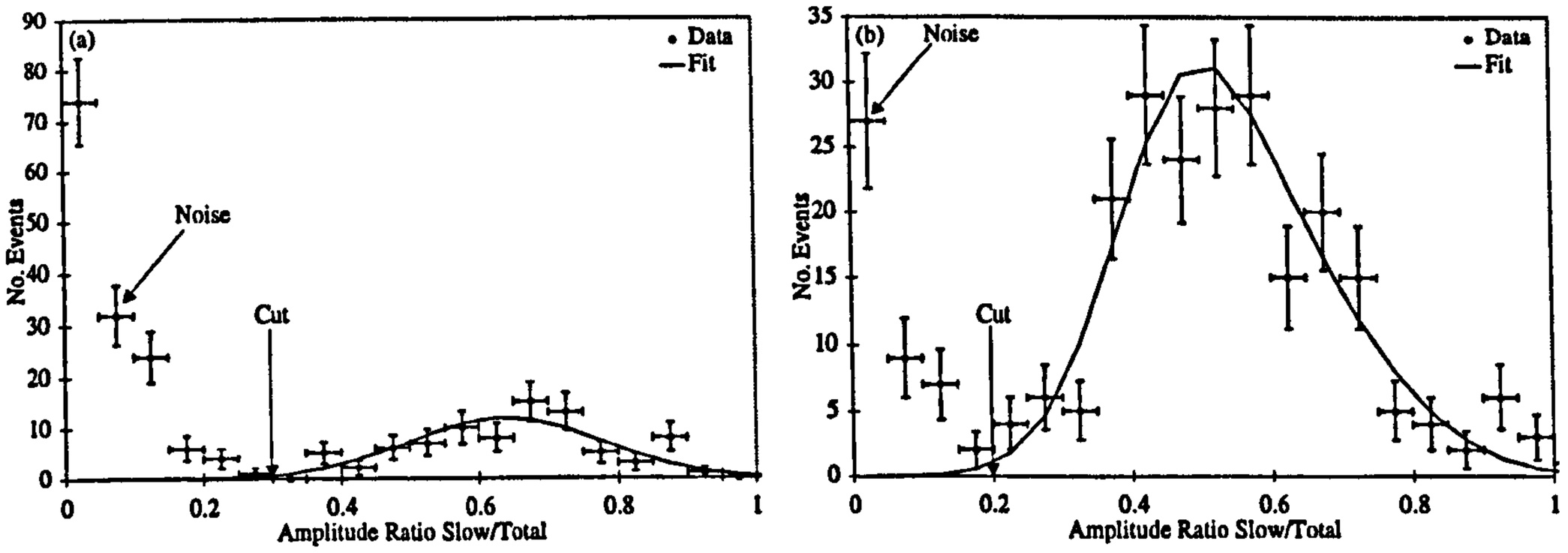

Figure 5.6: *Example low energy (0 - 30 keV) UVIS pulse parameter distributions from data taken with the Bridgeman-Stockbarger crystal running at 150 K. Figure (a) shows the distribution of pulse amplitude ratios for ^{60}Co data (electron recoils) while Figure (b) shows the distribution of pulse amplitude ratios for ^{252}Cf data (nuclear and electron recoils). The lines are fits of normal curves to the data.*

5.2.3 Results and Interpretation

With the cooling system described above it should have been possible to take data at temperatures as low as 80 K [131]. Unfortunately however poor thermal contact between the cooling pipes and crystal limited the minimum temperature to $\sim$ 130 K. Following these experiments the system was dismantled and the pipes brazed to the block, allowing significantly lower temperatures to be obtained.

One problem which had been noticed with earlier UVIS crystals was that following temperature cycling the surfaces of the NaI beneath the windows became covered with an opaque white crazing. This appeared to emanate from the epoxy stand offs, spreading out with repeated cycling until it covered the entire face of the crystal, appreciably reducing the light collection efficiency. It was suggested [108] that this may be due to the differing thermal expansion coefficients of NaI and epoxy stressing the crystal surface during cooling thereby causing it to crack. Outward propagation of these cracks would then cause the observed crazing. During the tests described here no crazing was observed initially and the crystals remained perfectly transparent. At one point however a short circuit in the temperature controller caused the temperature of the crystal to decrease more rapidly than intended and following this significant crazing was observed to have formed. This supports the above hypothesis and indicates that the problem may be avoided in future by more careful temperature control.

The results from the ^{57}Co energy calibrations are plotted in Fig. 5.7 as functions

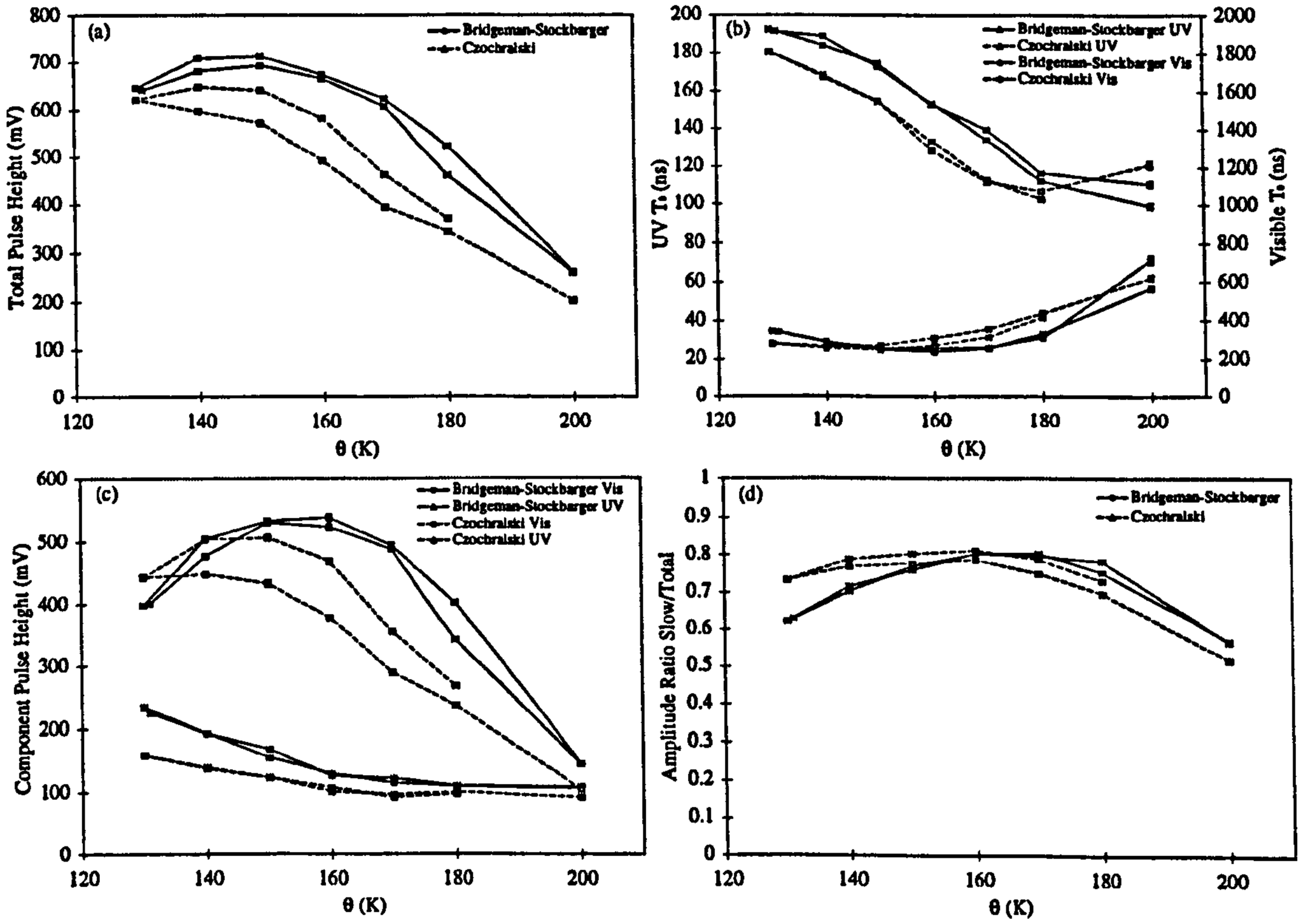

Figure 5.7: *The evolution of ^{57}Co UVIS pulse parameters with crystal temperature θ. Figure (a) shows the total pulse height, Figure (b) shows the individual UV and visible component decay time constant estimators T, Figure (c) shows the individual UV and visible component pulse heights and Figure (d) shows the pulse amplitude ratio. The data in Figure (b) is deliberately plotted on two axes so as to aid comparison with Fig. 5.1.*

Crystal	*Threshold*			*Discrimination*		
	θ (K)	*S*	*pe/keV*	*θ (K)*	*S*	*pe/keV*
Bridgeman-Stockbarger	150	0.6	1.17	140	0.9	1.16
Czochralski	140	0.3	1.06	130	0.7	1.02

Table 5.1: *The optimum operating temperatures for UVIS NaI crystals with the best discrimination properties or lowest energy threshold. The separation variable S is defined below.*

of crystal temperature. The overall behaviour is broadly in agreement with the results of [105]. The amplitude of the fast UV component falls monotonically with increasing temperature while the amplitude of the slow visible component peaks for

both crystals in the temperature range 150 - 160 K. In both cases the estimator T_{0UV} of the decay time constant of the UV component is approximately constant at $\sim$ 30 ns. For both crystals the estimator T_{0vis} of the decay time constant of the visible component appears to continue rising below the lowest achievable temperature ($\sim$ 130 K). The overall light output from the Bridgeman-Stockbarger crystal reached a maximum value of 1.17 $\pm$ 0.07 pe/keV at temperatures $\sim$ 150 K. The light output from the Czochralski crystal showed evidence for a maximum at a value of 1.06 $\pm$ 0.01 pe/keV at temperatures $\sim$ 140 K. The optimum light output of the crystals was no better than that of previously tested Kyropoulos crystals [105]. The results are summarised in Table 5.1.

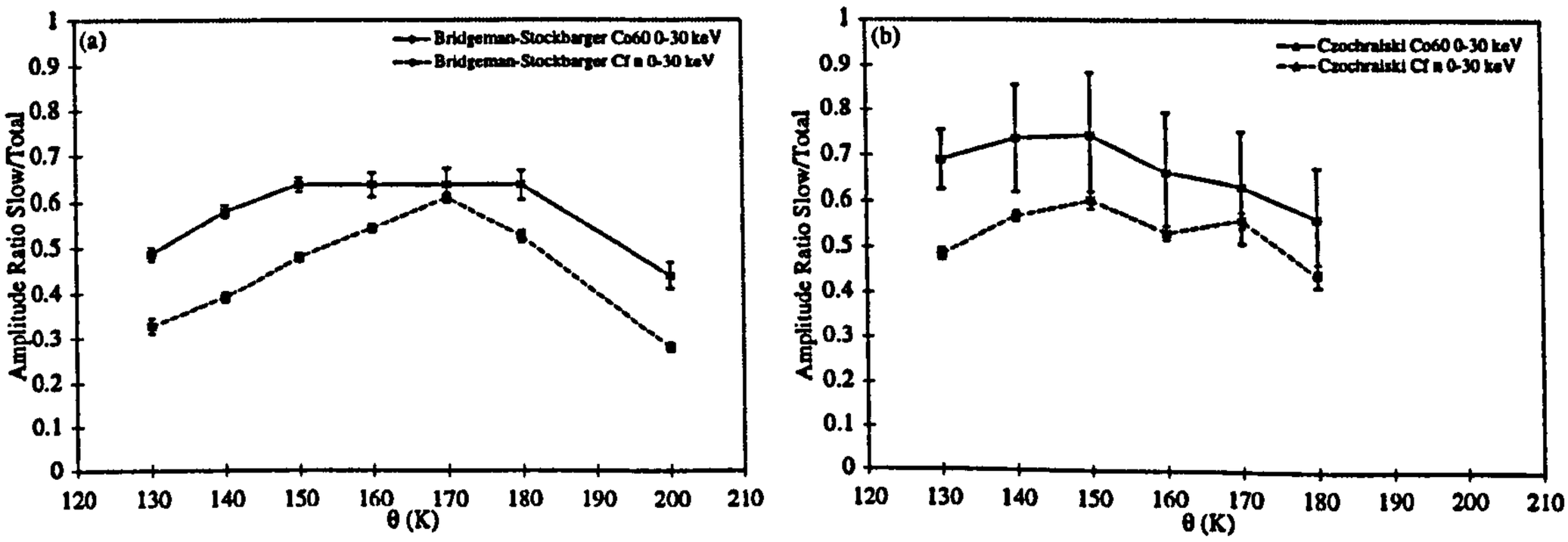

Figure 5.8: *The evolution of low energy (0 - 30 keV) UVIS pulse parameters with crystal temperature θ. Figure (a) compares the evolution of nuclear and electron recoil amplitude ratios for the Bridgeman-Stockbarger crystal while Figure (b) compares the evolution of nuclear and electron recoil amplitude ratios for the Czochralski crystal. The error bars in Figure (b) are larger than those in Figure (a) due to poorer event statistics.*

Discrimination properties were determined from the nuclear and electron recoil calibrations performed at each temperature. The pulse amplitude ratio R_A was used as the discriminating variable (§3.7) and the R_A histograms were integrated over the 0 - 30 keV visible energy range so as to maximise statistics. Significant populations of noise events were observed at values of $R_A \sim 0$ and ~ 1 (Fig. 5.6) but these were reduced by rejecting events with PMT asymmetry cuts, as described in §8. The electron recoil data (e.g. Fig. 5.6(a)) was χ^2 fitted with three parameter (mean value $\bar{R}_{Ae}$, width σ_e and normalisation N) normal functions. The ^{252}Cf data (e.g. Fig. 5.6(b)) was fitted with sums of two similar normal functions representing the expected nuclear and electron recoil populations. The electron recoil normal distributions were assumed to have means and widths identical to those determined

using the ^{60}Co data. Four free parameters were therefore used: the mean of the nuclear recoil normal $\bar{R}_{An}$, the width of the nuclear recoil normal σ_n, the nuclear recoil normalisation N_n and the electron recoil normalisation N_e.

The observed values of $\bar{R}_A$ for nuclear and electron recoils are plotted in Fig. 5.8 (previous page). Discrimination ability was assessed by using the following function of the $\bar{R}_A$ and σ, which measures the mean separation of the means of the distributions from their common mean:

$$S = \frac{\bar{R}_{An} - \bar{R}_{Ae}}{\sigma_n + \sigma_e}. \tag{5.1}$$

The Bridgeman-Stockbarger crystal provided optimum discrimination at $\sim$ 140 K ($S \sim 0.9$) while the Czochralski crystal provided optimum discrimination at $\lesssim$ 130 K ($S \sim 0.7$), although in this latter case the temperature was the lowest obtainable with the apparatus. These results and the light outputs at these temperatures are also summarised in Table 5.1. The values of S at the temperatures where maximum light output were obtained are also listed in this table.

These results suggest that the use of NaI UVIS crystals grown using alternative techniques to Kyropoulos gives no significant improvements in light output or discrimination. The optimum operating temperature was $\sim$ 140 - 150 K for the Bridgeman-Stockbarger crystal and $\lesssim$ 140 K for the Czochralski crystal. In order for UVIS to form the basis for an operational dark matter experiment it is clear that other techniques (e.g. unencapsulated crystals) must be investigated so as to increase light output and decrease energy threshold.

5.3 CASPAR

5.3.1 Introduction

The scintillating target upon which the CASPAR detector (§4.2.4) is based must contain three main ingredients:

- A radiopure, highly efficient inorganic scintillator powder of sub-micron grain size.
- An efficient liquid scintillator of identical refractive index to that of the powder.
- A gelling agent mixed in with the liquid scintillator which is capable of holding the powder in suspension over the lifetime of an experiment ($\sim$ years).

These three components will now be considered in more detail and the results of work attempting to optimise their properties described.

5.3.2 The CASPAR Inorganic Scintillator

Synthesis

As outlined in §4.2.4 the optimum choice for the inorganic scintillator in CASPAR is CaF_2(Eu) on account of its low refractive index, its low hygroscopicity, its high light output and the excellent spin coupling characteristics of its constituent F nuclei. There remain three questions regarding its use however:

- Is it possible for CaF_2 powder to be doped with Eu ions so as to give superior light output?
- Is it possible to ensure that the powder has a grain size sufficiently small ($\lesssim$ 1 μm) and uniform for range discrimination to take place?
- Is it possible to obtain powder of sufficient radiopurity for use in a low background dark matter experiment?

Initially it was thought that suitable CaF_2(Eu) powder could be obtained by grinding bulk scintillation crystals with a planetary ball mill. This is however an expensive and time consuming technique which tends to produce grains with a broad range of sizes (Fig. 5.9(a) overleaf) and poor light output [144]. Coupled to the poor radiopurity of bulk CaF_2(Eu) crystals ($\gtrsim$ 80 ppb U, $\gtrsim$ 1200 ppb Th [145]), and the radioimpurities introduced during milling, this seems to preclude the use of this technique.

A simpler approach and one which offers several additional benefits is to synthesise the powder chemically. The synthesis procedure used to produce CaF_2 powder industrially involves adding $CaCO_3$ powder to a concentrated solution of hydrofluoric acid (HF). The following reaction takes place:

$$CaCO_3 + 2HF \longrightarrow CaF_2 + H_2CO_3, \tag{5.2}$$

and the CaF_2 precipitates out of solution due to its insolubility in water. The CaF_2 grain size is typically small ($\sim$ 500 nm) and uniform (Fig. 5.9(b) overleaf) however there are disadvantages. Since the $CaCO_3$ feed stock is not initially in aqueous solution its radiopurification would seem difficult and hence the radiopurity of the resulting CaF_2 is likely to be poor. For the same reason doping of the CaF_2 precipitate with europium is also likely to be difficult as the Eu ions are unable to mix fully with the Ca^{+2} ions.

For these reasons synthesis procedures involving only aqueous precursors were adopted. Due to the hazards associated with working with HF initial experiments

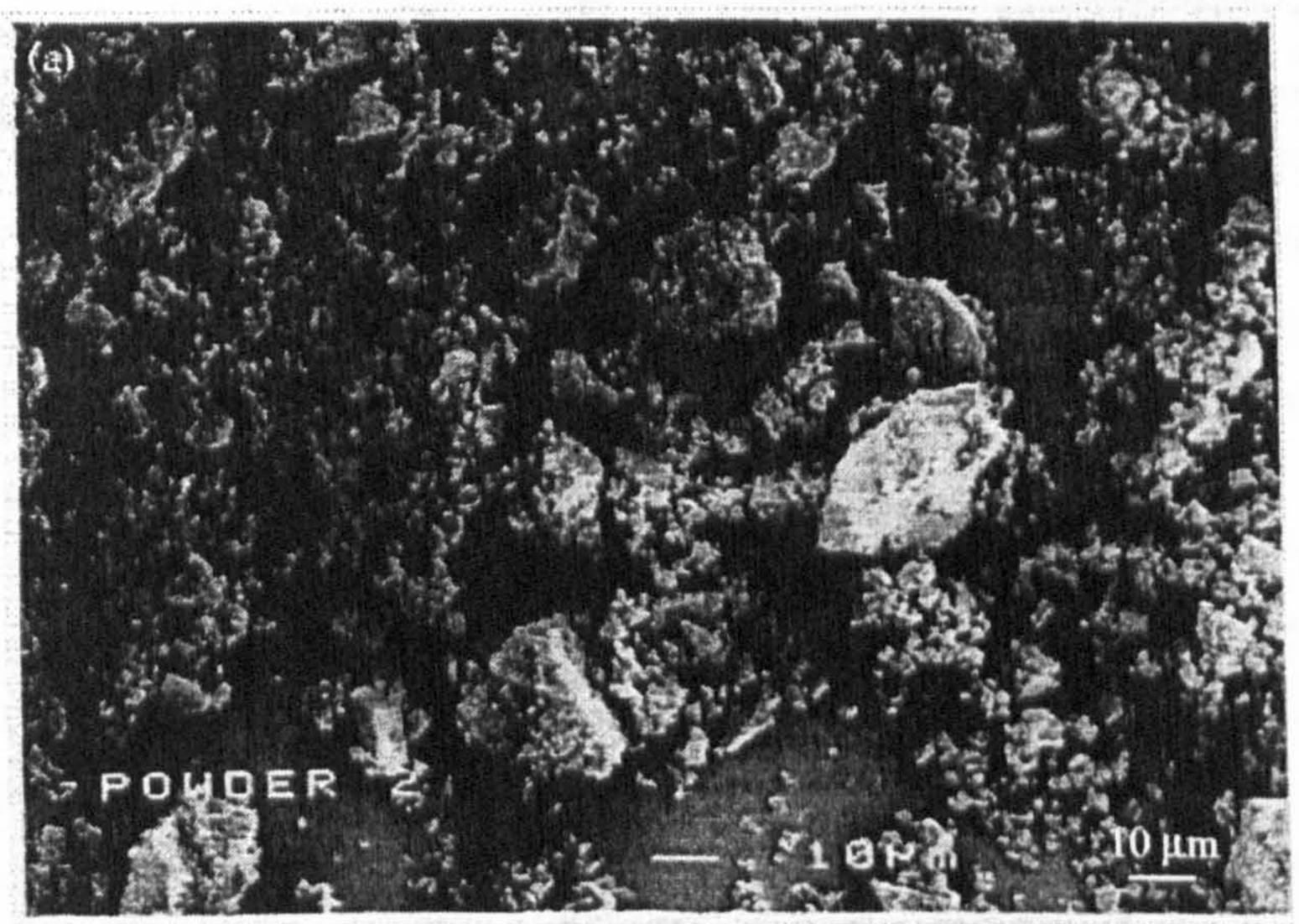

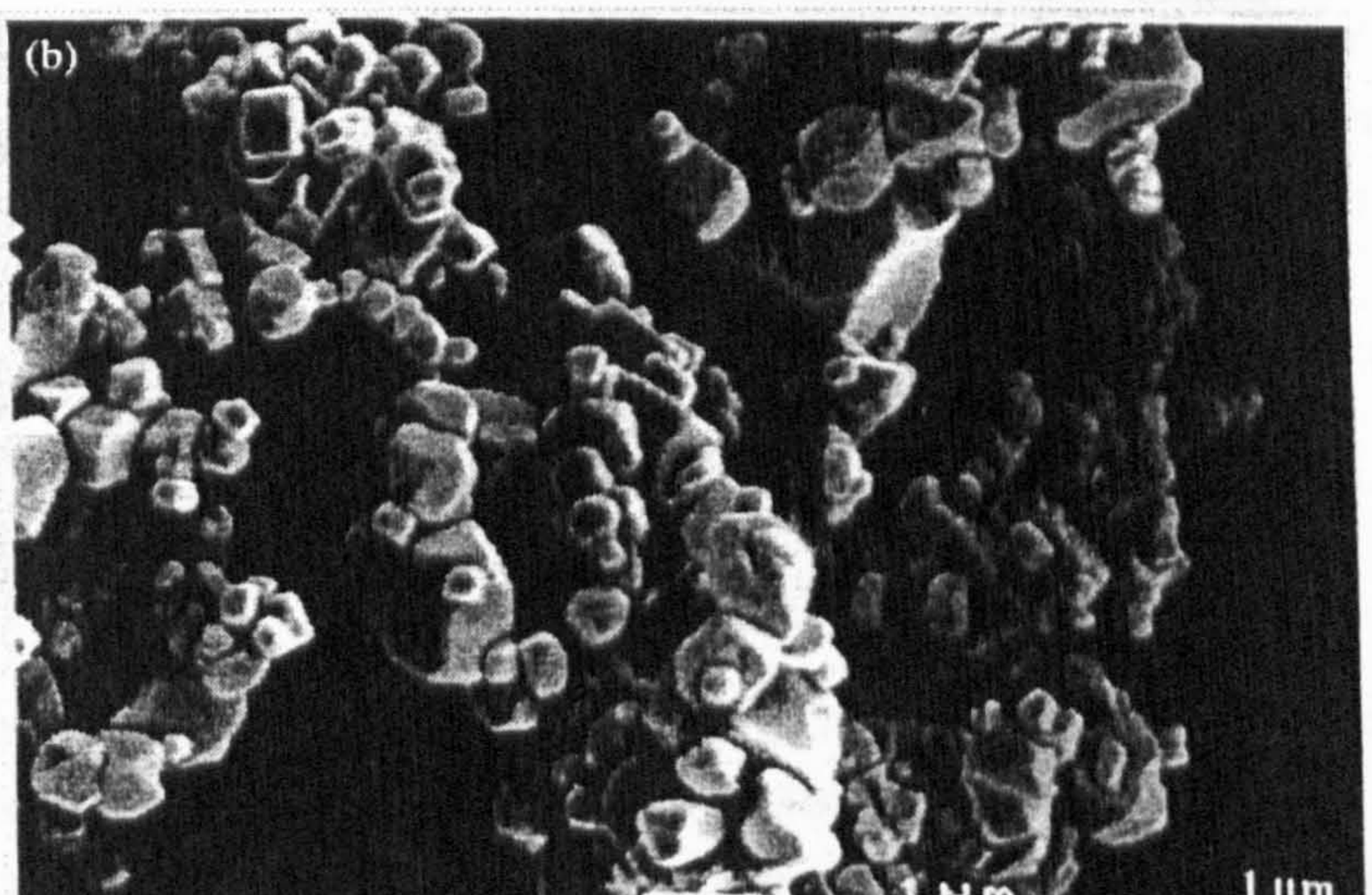

Figure 5.9: *Electron micrographs of CaF_2 powder. Figure (a) shows powder made from crushed bulk $CaF_2(Eu)$ crystal while Figure (b) shows commercial undoped powder with a mean grain size $\sim$ 500 nm. The micrographs were obtained using equipment at the Sorby Centre for Electron Microscopy and Microanalysis [145].*

were conducted using aqueous $Ca(NO_3)_2$ and NH_4F:

$$Ca(NO_3)_2 + 2NH_4F \longrightarrow CaF_2 + 2NH_4NO_3. \quad (5.3)$$

Owing to the small grain size of the CaF_2 precipitate produced in this way it forms a gelatinous mass which is impossible to filter [147]. Thus drying of the powder was performed at an elevated temperature in an oven. Amorphous NH_4NO_3 remained however, even after baking at temperatures greater than that at which NH_4NO_3 sublimes (210 °C). This caused the powder to agglomerate into a dense cake preventing subsequent dispersion in liquid scintillator, even after grinding. For this reason the use of NH_4F was rejected in favour of HF.

Bulk grown CaF_2(Eu) crystals are doped with Eu^{+2} ions and the resulting 435 nm scintillation is well matched to bialkali PMTs. It was hoped that doping of CaF_2 powder with these ions could be performed in aqueous solution by adding an aqueous Eu^{+2} salt prior to reaction. It was soon appreciated however that the instability of Eu^{+2} to oxidation and the strong oxidation potential of NO_3^- ions causes Eu^{+3} to be formed at the instant the salt is added. Although this development is of interest for other applications (see below) it is unlikely to be of use in a dark matter detector due to the predominant $\sim$ 610 nm red emission of $CaF_2(Eu^{+3})$ which is poorly matched to the response of most PMT photocathodes (Fig. 4.15). Hence the use of $Ca(NO_3)_2$ was also rejected.

The synthesis which was found to give the best results involves the following reaction between $CaCl_2$ and HF:

$$CaCl_2 + 2HF \longrightarrow CaF_2 + 2HCl. \quad (5.4)$$

The synthesis is described in detail in Appendix A. Aqueous $CaCl_2$ is only a weak oxidising agent and $CaCl_2.6H_2O$ powder (solubility 279 g/100cc H_2O [110]) of high purity ($<$ 0.0005 % Pb) can be purchased cheaply from many manufacturers (e.g. Fluka [148]). Because it is used in aqueous solution the $CaCl_2$ can be purified still further by passing it through a chromatography column containing the DIPHONIX ion exchange resin which removes U and Th [149, 150] (Appendix A). Commercially available HF is generally of high purity ($<$ 0.000005 % Pb from Fluka) due to the use of distillation techniques by the manufacturers. The grain size of the CaF_2 powder produced during the synthesis can be controlled by varying the rate of reaction, either by varying the speed with which HF is added to the $CaCl_2$ solution or by performing the reaction in an ultrasonic bath. Ultrasound at cavitation levels creates nuclei for rapid crystal growth while even at lower levels it increases rates of ion transport and hence crystal growth [151]. Grain sizes in the range 10 nm - 20 μm

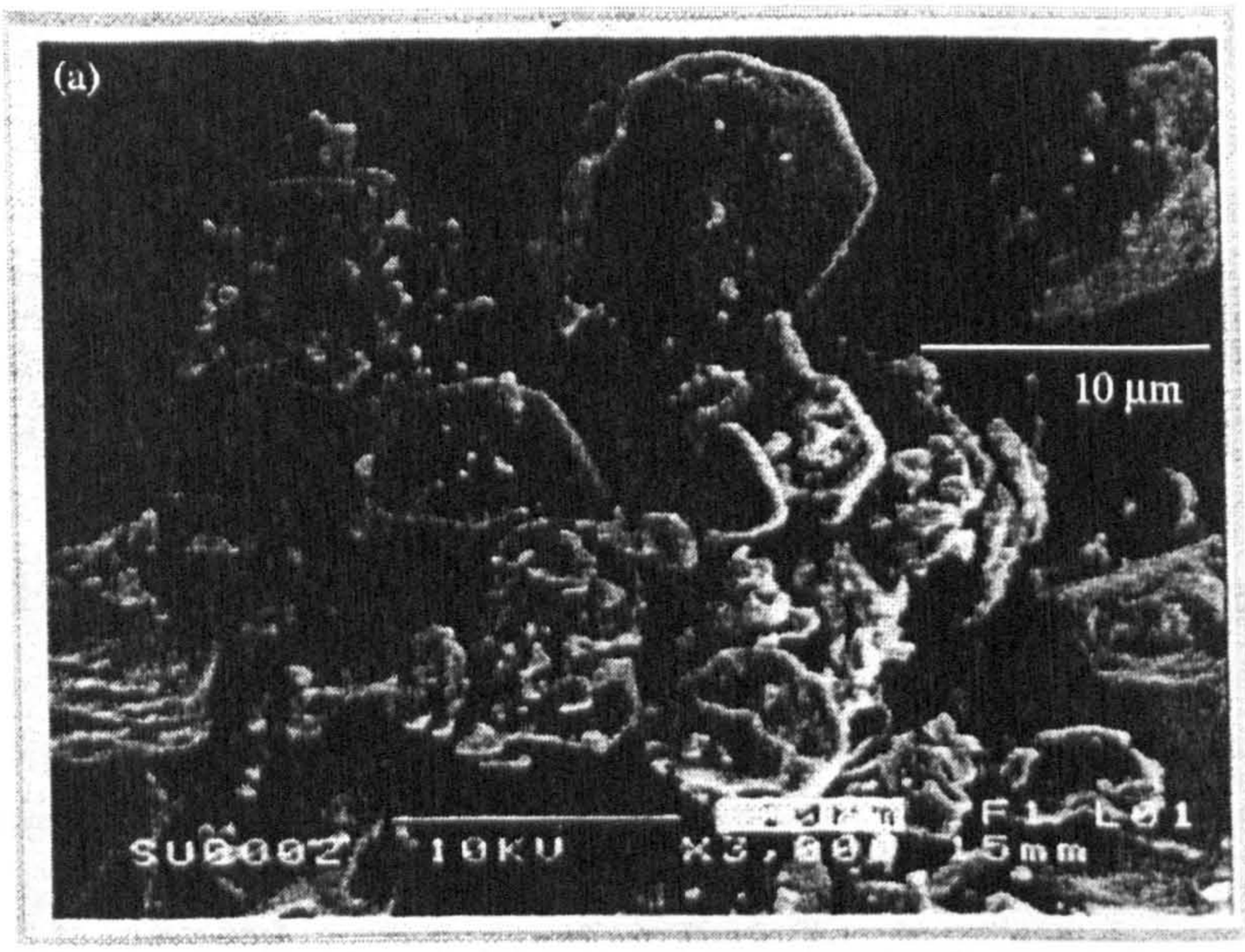

Figure 5.10: *Electron micrographs of synthesised $CaF_2(Eu^{+2})$ powder. Figure (a) shows the original powder with large grain size, Figure (b) the powder produced using acetic acid to maintain a solution of $EuCl_2$ and Figure (c) the same powder after annealing, showing sintering of small grains. The micrographs were obtained using equipment at the Sorby Centre for Electron Microscopy and Microanalysis [145].*

can be produced with these techniques hence satisfying the grain size requirement of CASPAR (§4.2.4).

By initially adding aqueous $EuCl_x$ ($x = 2$ or 3) to the $CaCl_2$ solution and annealing the resulting CaF_2 powder under vacuum (Appendix A), doping with either divalent or trivalent Eu ions can be performed. The amount of $EuCl_x$ is determined

by the required doping level of the powder; 0.1 % M to 1 % M dopings are used for commercial bulk grown crystals [108] and here it was assumed that all Eu was incorporated into the CaF_2. The annealing process helps to incorporate the Eu ions into the crystal lattice in substitutional Ca sites. The annealing parameters (temperature, time and atmosphere) were chosen by reference to the extensive literature which exists on the annealing of CaF_2 deposited on silicon substrates (e.g. [152]). An annealing temperature of $\sim$ 800 - 1000 °C held for $\sim$ 10 minutes is sufficient to activate the Eu, and a slow quench $\sim$ 300°C/hour, obtained by simply turning off the furnace, appears not to harm the scintillation properties. As short an annealing period as possible is preferable since after long periods the powder tends to form a cake which must subsequently be broken back into powder form (see below).

Electron micrographs of $CaF_2(Eu^{+2})$ powder produced using this technique can be found in Fig. 5.10. During initial synthesis trials it proved to be impossible to maintain $EuCl_2$ in solution when mixed with $CaCl_2$ solution before the addition of HF. The small grains of $EuCl_2$ possibly acted as seed nuclei for CaF_2 growth and consequently the size of the CaF_2(Eu) grains was very large ($\sim$ 20 μm : Fig. 5.10(a)). Further work by C.J. Martoff indicated that the addition of a small amount of glacial acetic acid to the solution keeps the $EuCl_2$ in solution and the resulting grain size is found to be much smaller ($\sim$ 40 nm : Fig. 5.10(b)). During annealing these small grains sinter together owing to their large surface area (Fig. 5.10(c)) giving grains of diameter $\sim$ 250 nm. The same sintering process possibly induces planar defects (visible as fringes in Fig. 5.10(c)) which may lead to undesirable optical properties for the powder (see below).

Assay

The CaF_2(Eu) powder obtained with this technique can be assayed using PhotoLuminescence (PL) measurements. The apparatus used is sketched in Fig. 5.11. A 325 nm He-Cd UV laser was used to excite the powder, which was held in a small silica test tube. Luminescence was focused by means of a lens onto the entrance slit of a grating spectrometer read out by a broad band (S20 photocathode) PMT [127].

The first object to be tested was an empty quartz test tube. The small amount of scattered light gave the spectrum of Fig. 5.12. This scattered laser emission was fitted with a power law curve:

$$I(\lambda) = A(\lambda - 348\text{nm})^{-0.577}, \tag{5.5}$$

and this function, with a suitable normalisation A, was subtracted from all subsequent spectra.

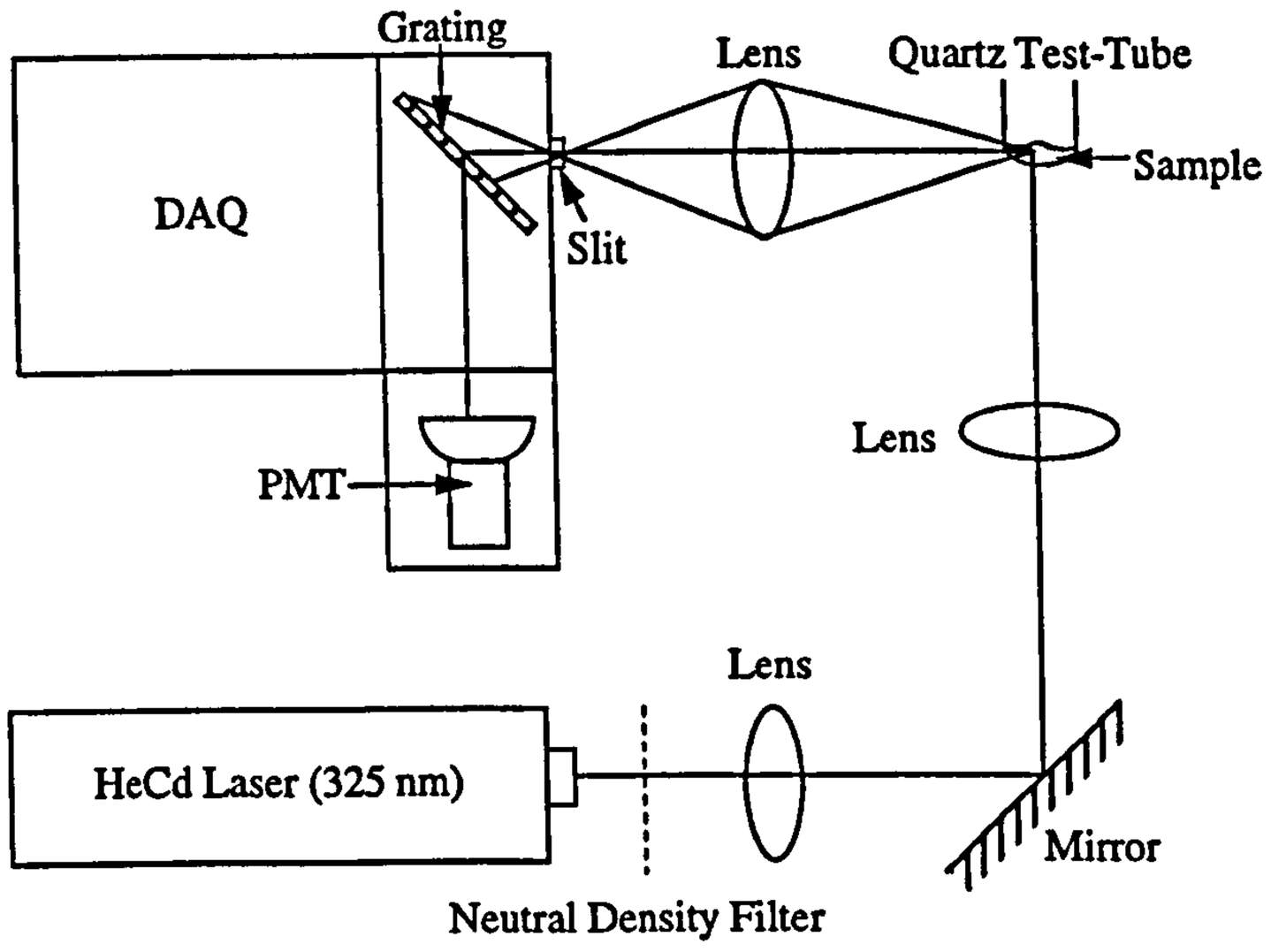

Figure 5.11: *A schematic diagram of the photoluminescence apparatus used to test $CaF_2(Eu)$ powders.*

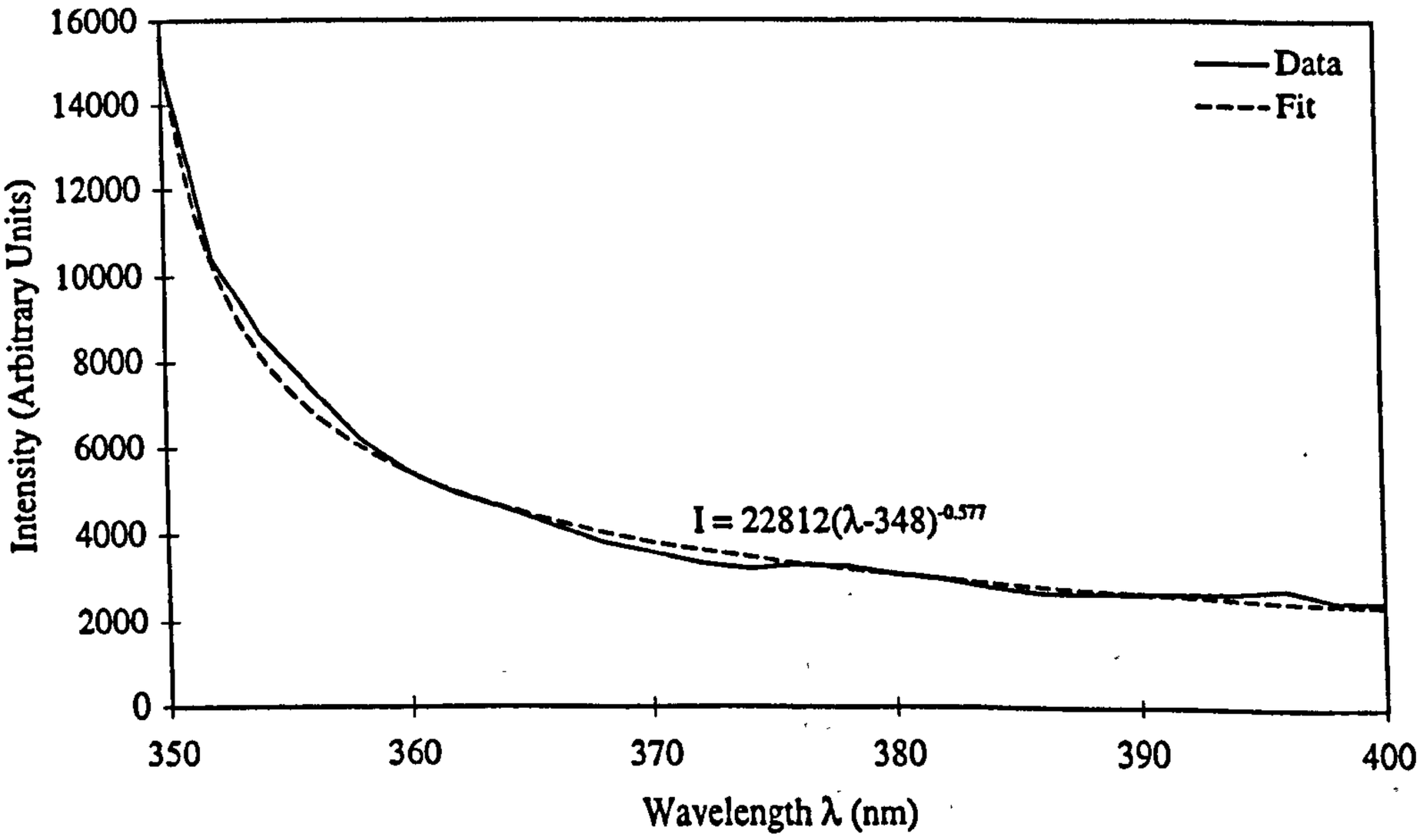

Figure 5.12: *The HeCd laser emission spectrum. The full line is the data and the dashed line is a fit to the power law* $I(\lambda) = A(\lambda - 348\text{nm})^{-B}$.

The emission spectrum of commercial undoped CaF_2 powder obtained from Aldrich [153] is plotted in Fig. 5.13, both with and without the laser correction. There is a faint peak at $\sim$ 380 nm just visible as a shoulder on the uncorrected curve. The position of this peak is consistent with that of the intrinsic CaF_2 emission reported by other workers [154].

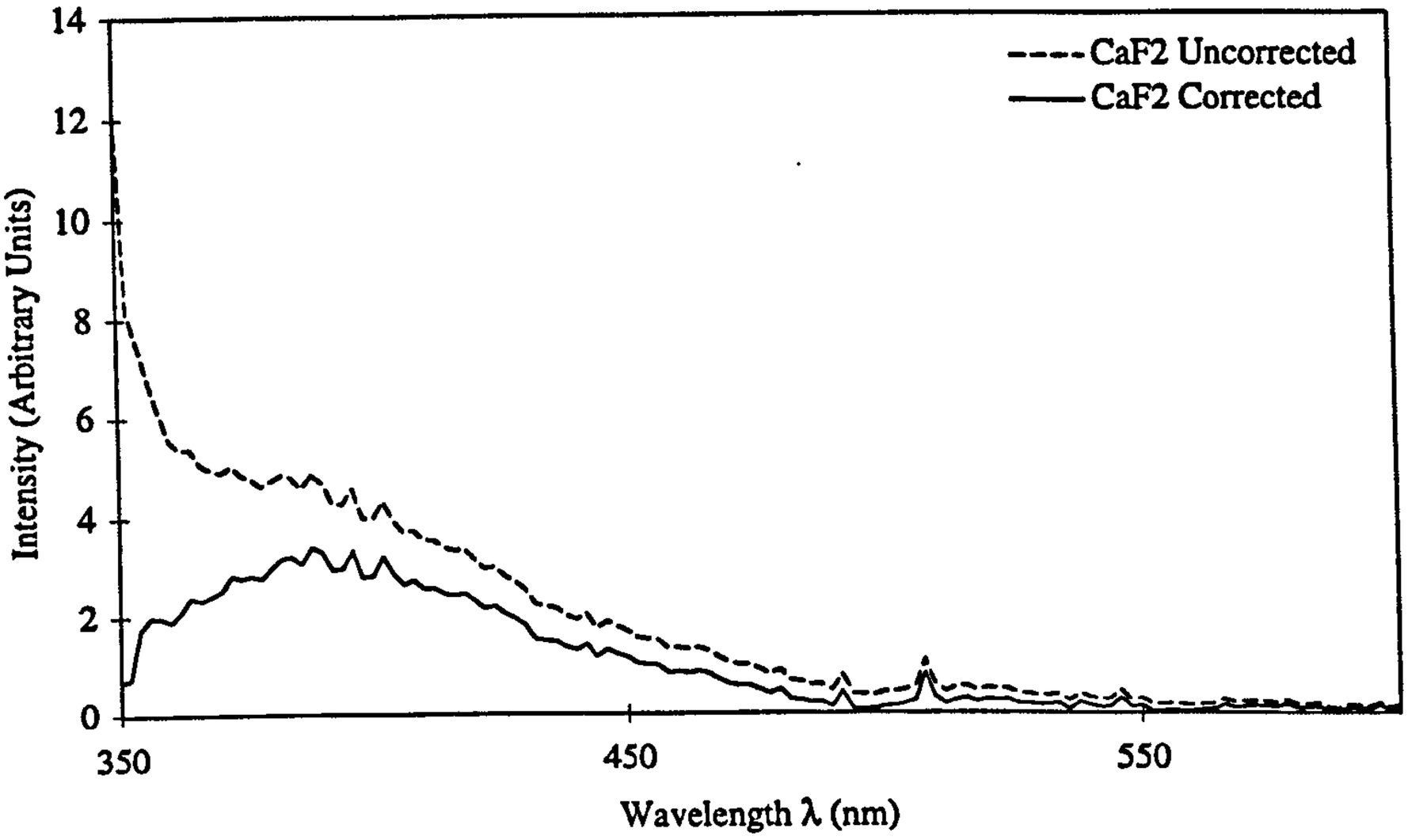

Figure 5.13: *The photoluminescence spectrum from undoped CaF_2 powder. The dashed line is the raw data and the full line is the same data with the laser emission (Eqn. 5.5) subtracted. The peak in the laser corrected data corresponds to the intrinsic CaF_2 emission.*

Emission spectra obtained from synthesised Eu^{+2} doped powder are plotted in Fig. 5.14 (overleaf) for samples both before and after annealing. In both cases a single broad extrinsic line is observed at $\sim$ 435 nm in agreement with the results of [154]. Due to variations in light collection in the apparatus it was difficult to obtain a quantitative comparison between the light outputs of different samples however by performing the measurements sequentially qualitative comparison was possible. It is apparent from the size of the peak in the annealed sample spectrum in Fig. 5.14 that annealing has a beneficial effect on luminescence intensity and hence powder light output. This is possibly because synthesis causes Eu ions to be trapped within the CaF_2 lattice and it is then only during the annealing period that these ions are actually incorporated substitutionally *into* the lattice.

A comparison between sequential spectra from undoped, crushed bulk Eu^{+2} doped and annealed synthesised Eu^{+2} doped CaF_2 powders is presented in Fig. 5.15.

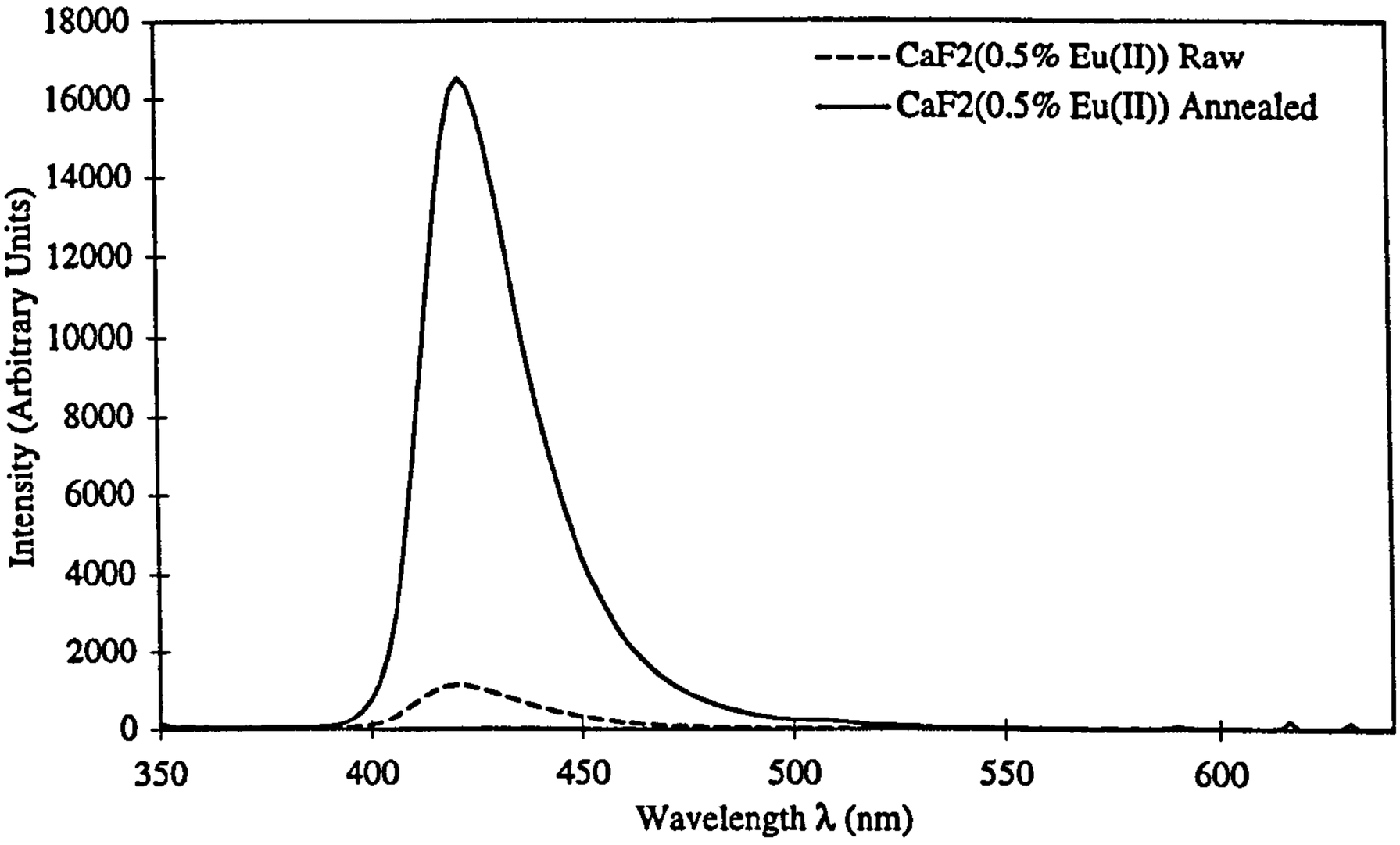

Figure 5.14: *Photoluminescence spectra from synthesised $CaF_2(0.5\%\ M\ Eu^{+2})$ powder showing the strong 435 nm emission. The dashed line is data from the raw powder and the full line is data from annealed powder from the same batch.*

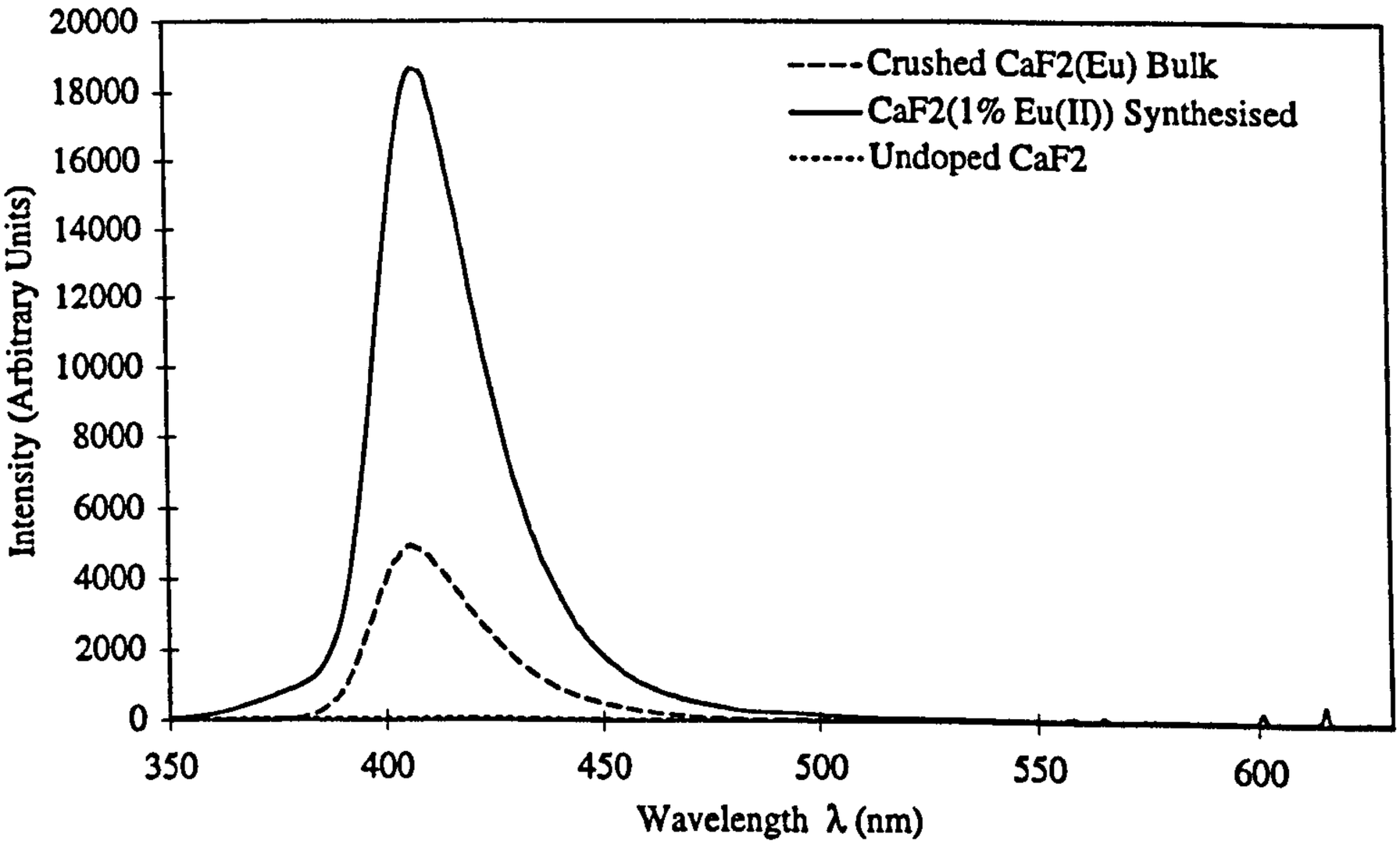

Figure 5.15: *Photoluminescence spectra from $CaF_2(Eu^{+2})$ powder showing the 435 nm emission. The dashed line is data from crushed bulk crystals, the full line is data from synthesised annealed $CaF_2(1\%\ M\ Eu^{+2})$ powder and the dotted line (just visible above the λ axis) is data from undoped powder from Aldrich [153].*

Again only qualitative comparison is possible however the significantly improved light output of the synthesised powder is once more apparent, even when compared with the crushed scintillation crystal. This may be because the rapid formation of the synthesised powder causes it to be free from the quenching defects which are more prevalent in the bulk grown material.

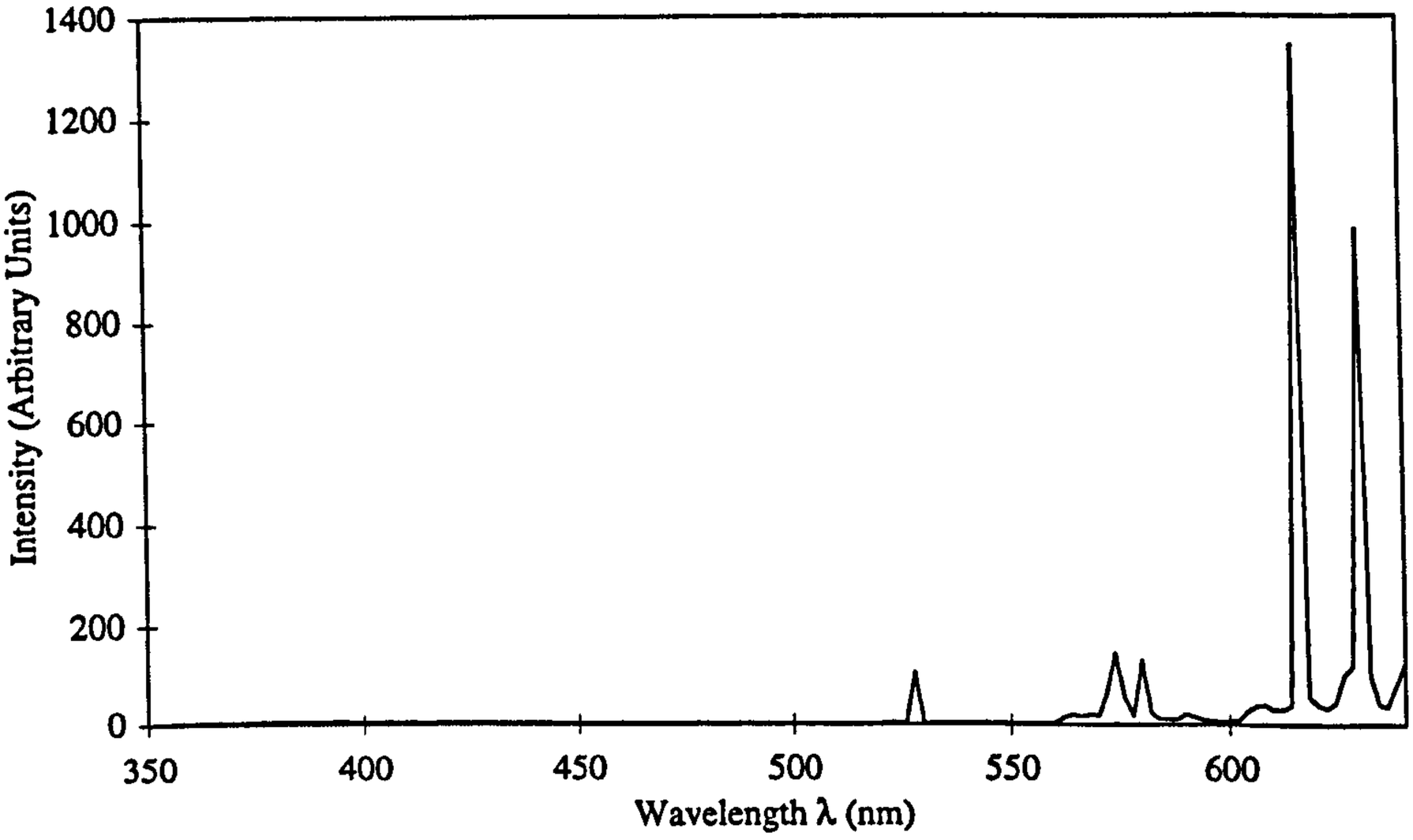

Figure 5.16: *The photoluminescence spectrum from synthesised annealed $CaF_2(Eu^{+3})$ powder showing the strong 610 nm emission.*

In Fig. 5.16 is plotted a spectrum obtained from a Eu^{+3} doped synthesised annealed CaF_2 powder sample. The emission spectrum is very different from those in Fig. 5.15 and demonstrates the dominance of the red emission around 610 nm. When the same powder is baked at 1000 °C for three days some of the Eu^{+3} ions are reduced to Eu^{+2}, as occurs during bulk crystal growth (where trivalent ions from Eu_2O_3 are reduced to divalent dopant ions). The resulting emission spectrum is plotted in Fig. 5.17 and clearly displays the emergent Eu^{+2} emission. This material is much more strongly agglomerated than powder which has only been annealed for a short period of time.

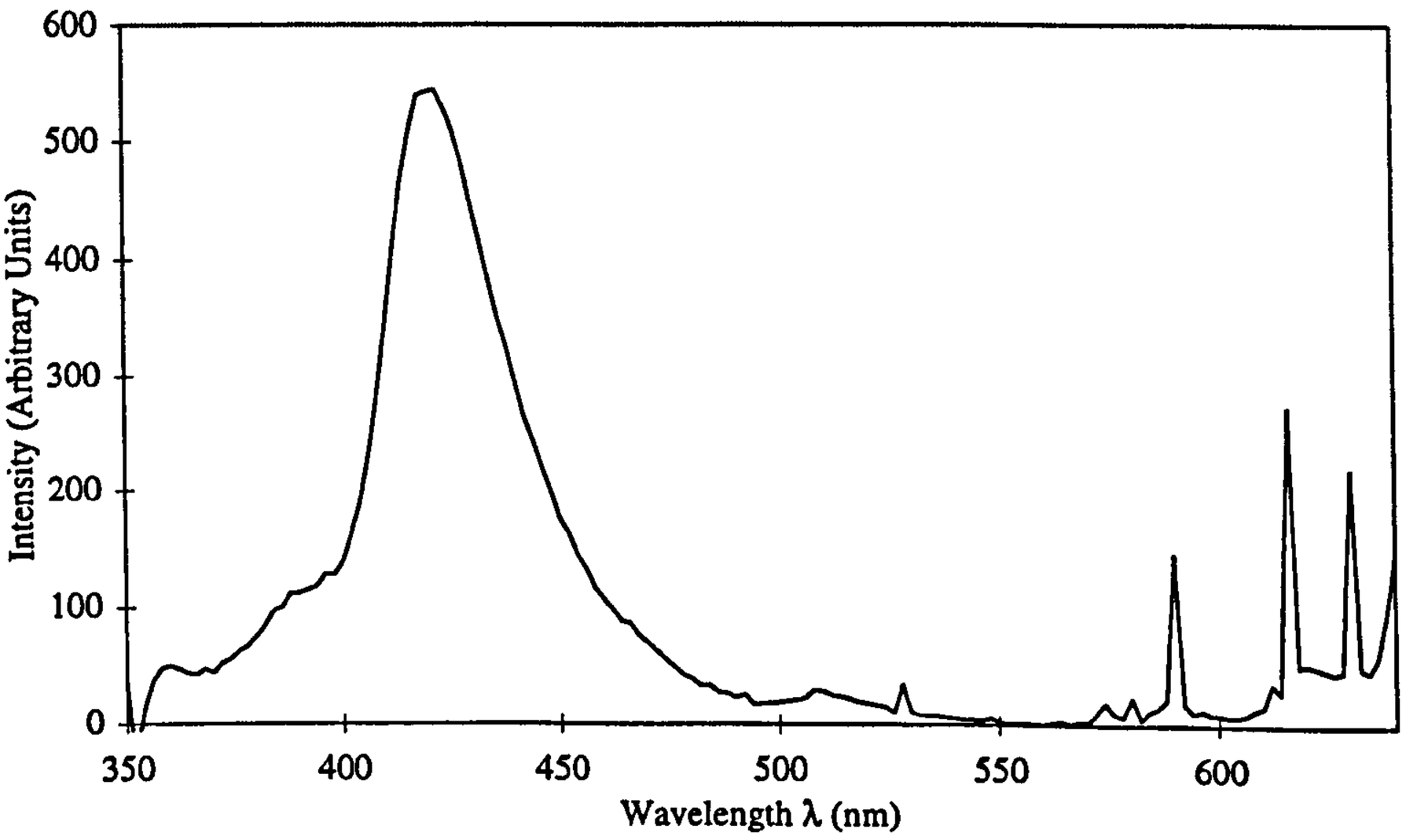

Figure 5.17: *The photoluminescence spectrum from synthesised sintered $CaF_2(Eu^{+3})$ powder. The heights of the 610 nm (Eu^{+2}) peaks have decreased while the height of the 435 nm (Eu^{+2}) peak has increased dramatically from zero.*

The emission wavelengths of the different CaF_2 powders tested are summarised in Table 5.2. The powder doped with trivalent Eu may find application in industry, where it has previously been impossible to create large amounts of $CaF_2(Eu^{+3})$ powder phosphor. Bulk crystals can only be doped with the divalent state due to the reducing environment present in the crucible. Previously only costly small scale production has been possible using solid state reactions [155] or ion implantation [154]. Being based upon simple chemical procedures the process described here should be more suitable for scale up. Add to this the possibility of doping with Eu^{+2} and Tb ions ($\lambda \sim 545$ nm [154]) in the same way and the technique gives a route to producing large amounts of cheap, highly efficient white light phosphor

powder for the lighting, CRT and medical industries. A patent is pending on this technique.

Doping	*Wavelength (nm)*
undoped	~ 380
Eu^{+2}	~ 435
Eu^{+3}	~ 610

Table 5.2: *The emission wavelengths of differently doped CaF_2 powders.*

Dispersal

Once dryed and annealed CASPAR CaF_2(Eu) powder must be redispersed in liquid scintillator. In order for this to occur the individual grains must be mechanically separated from one another. With unannealed powder this can be performed simply by vigorous shaking of the powder-liquid mixture. Annealed powders on the other hand tend to be stuck together more strongly with the bonding between grains increasing in strength with increasing annealing time. The bonding may be caused by the loss of protective water molecules from the surfaces of the grains allowing weak chemical bonds to form between them [156]. Over long periods of annealing the increased mobilities of ions at high temperature may allow the grains to physically amalgamate creating an even more strongly bound powder (Fig. 5.10(c)). This phenomenon can occur even at temperatures well below the melting temperature of CaF_2 (1423 °C [110]) [156].

The breaking of these bonds to disperse the powder can be performed by grinding however in this case the minimum powder size achievable is probably larger than that of the individual CaF_2(Eu) crystals. This implies that polycrystalline grains remain and if there are microscopic inclusions within these grains then the viscosity of the liquid scintillator may prevent them from being filled thereby making refractive index matching impossible.

Another technique involves placing the annealed powder in water and applying high power ultrasound (e.g. 500 W, 20 kHz frequency) at cavitation levels for several days using an ultrasonic probe (Fig. 5.18) such as the VC500 from Sonic and Materials Inc. [157]. The cavitation bubbles created by the probe form around the CaF_2(Eu) grains and implode violently breaking the powder apart at the 100 nm scale. The technique is particularly effective with brittle materials such as CaF_2 [151] and can even be used to break apart individual crystals which are initially too

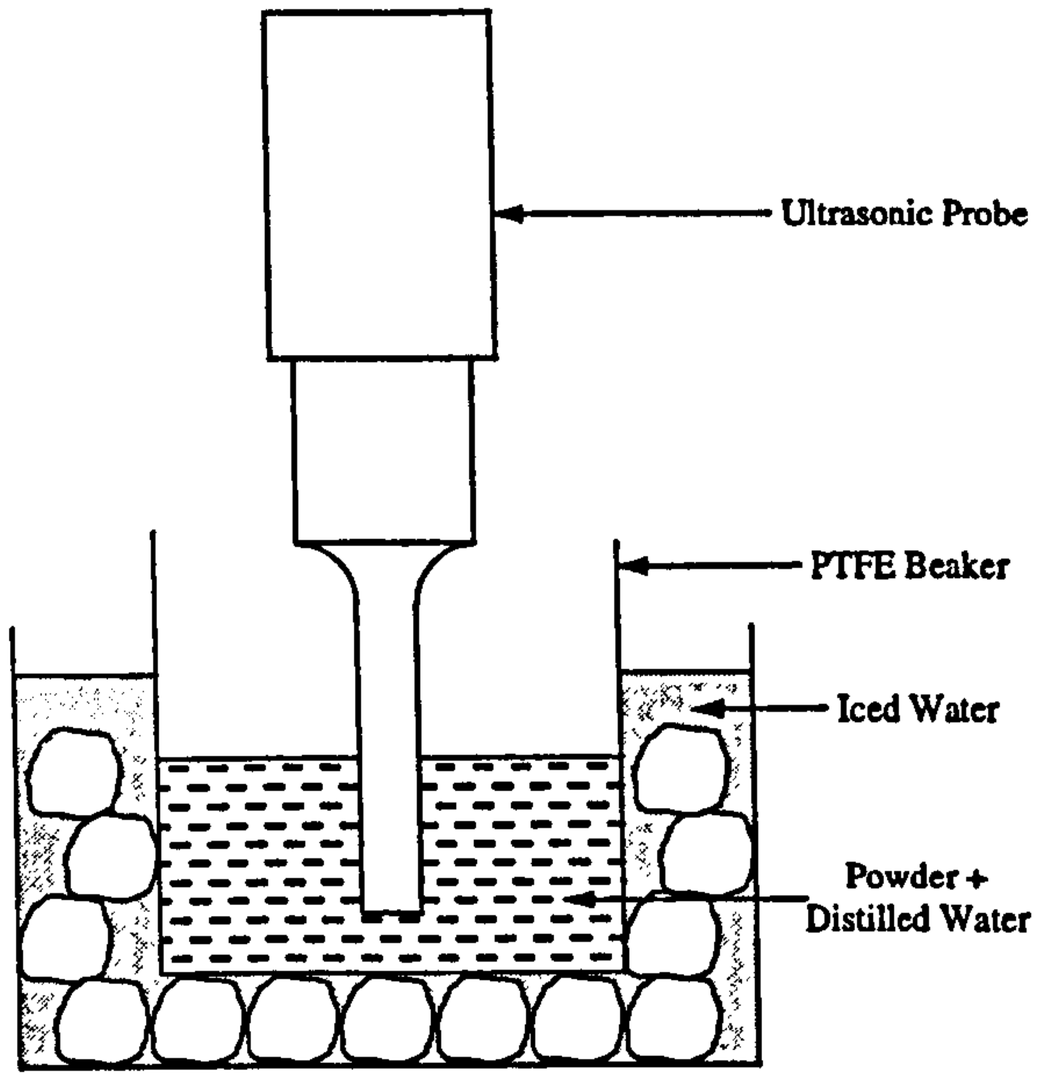

Figure 5.18: *A schematic diagram of the ultrasonic processing apparatus used with CaF_2 powders.*

large to be of use in CASPAR. Following ultrasonic processing the powder must be dried thoroughly under vacuum before it can be redispersed in the liquid scintillator.

Optical Properties

There remains one problem with the chemical production of CaF_2(Eu) scintillator; following the annealing and dispersal stages the resultant powder is invariably dark grey in colour. The powder is an excellent phosphor when used in thin layers but this colour indicates that it strongly absorbs its own emission when used in bulk in an index matched solution. The reasons for the colouration of the powder are at present unknown. Undoped powder treated with power ultrasound displays no colouration while crushed bulk CaF_2(Eu) powder does. Synthesised CaF_2(Eu) powder of both divalent and trivalent dopings displays colouration either after annealing or after ultrasonic processing. It thus appears that one contributory factor is the presence of Eu of either valence state. Another factor may be the presence of high temperatures during annealing and processing [1]. The extreme conditions present during annealing have been observed to cause F^- ions to be lost from the powder by reacting with the water molecules coating the surfaces of the grains to form HF:

$$2H_2O + CaF_2 \longrightarrow 2HF + Ca(OH)_2. \tag{5.6}$$

[1] temperatures may be $\gtrsim$ 5000 K during cavitation collapse [151]

The same process may occur in aqueous solution during processing and the resulting deficiency of F^- ions may alter the electronic structure of the CaF_2(Eu) crystals sufficiently to open up an optical band gap. Further work is needed to understand this process but it is hoped that improvements to the annealing and processing procedures may ameliorate the problem.

5.3.3 The CASPAR Liquid Scintillator

Choice of Liquid

The choice of liquid scintillator for CASPAR is governed by the choice of inorganic powder. The liquid must have a high light output and short scintillation decay time constant but a low refractive index similar to that of CaF_2(Eu).

One possibility to be considered was NE224 (Table 4.1), a pseudocumene (1,2,4 - trimethylbenzene) based scintillator supplied by Nuclear Enterprises [158]. This has a refractive index of 1.505 and the highest light output of any liquid scintillator (80 % of anthracene). Because the refractive index is considerably higher than that of CaF_2(Eu) it requires a 2:1 dilution with methanol in order to match refractive indices. Methanol was chosen as a diluter as it has a low refractive index (r_i = 1.3288 [110]) and is only a weak quencher of scintillation [159]. Even in the absence of quenching however the act of dilution reduces the scintillation efficiency by $\sim 1/3$ to a level at which the material produces no more light than many other commercial liquid scintillators. In addition to this pseudocumene is not miscible with water and forms instead an opaque white emulsion offering poor light collection. The ability to use water to clean the CASPAR scintillation cell is desirable and so this is a definite disadvantage. Immiscibility with water is also probably the cause of the poor light collection observed when attempting to gel the scintillator (§5.3.4). Taken together these facts led to NE224 being rejected for this purpose.

Another possibility is BC533 (Table 4.1), a petroleum based liquid scintillator of refractive index 1.45 supplied by Bicron Corp. [160]. This has the advantage that it has an extremely high flash point ($\sim$ 65 °C), making it safe for use in the elevated temperatures found at Boulby. It also has an extremely low freezing point ($\lesssim$ -50°C) and could hence be used in the future with a cooled APD read out (§4.3.2). The light output is less than that of NE224 (51 % anthracene) however the lower refractive index means that less methanol is required in order to match the refractive index to that of CaF_2(Eu). As with NE224, BC533 is not miscible with water and therefore care must be taken to ensure that the two do not come into contact.

The final liquid scintillator which was considered was a cocktail based upon

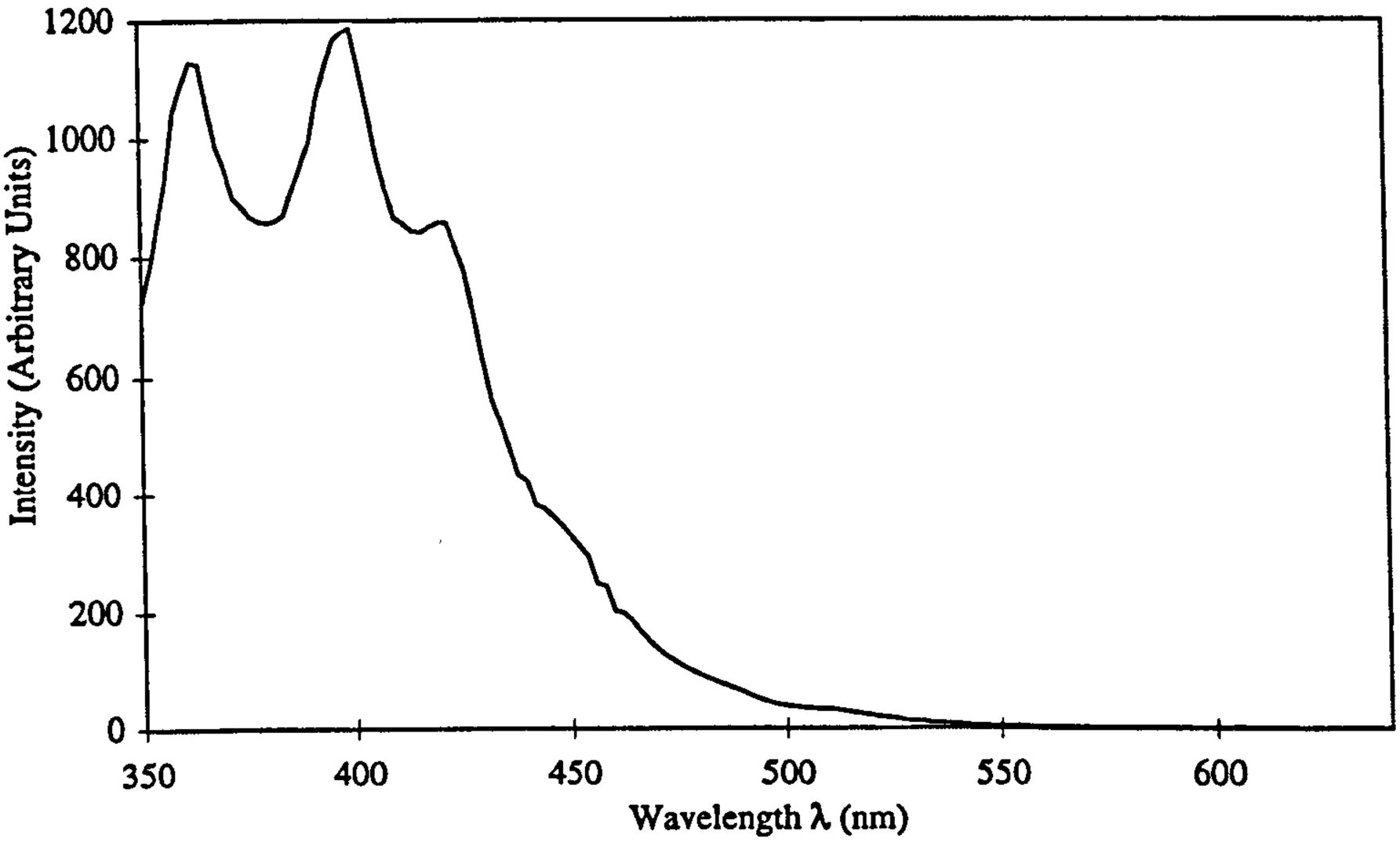

Figure 5.19: *The photoluminescence spectrum from dioxan scintillator showing the predominantly blue emission at wavelengths $\lesssim$ 450 nm. The spectrum was obtained using the apparatus sketched in Fig. 5.11.*

dioxan ($C_4H_8O_2$) previously available from Nuclear Enterprises (NE221 [158], Table 4.1) and now available from Zinsser Analytic (UK) Ltd. [161]. Dioxan itself has a low refractive index ($r_i = 1.4165$ [110]) and is a poor scintillator, however upon the addition of 150 g/l naphthalene (plus < 12 g/l bis-MSB and PPO) it gains a light output $\sim$ 55 % anthracene from an emission centred in the blue region of the spectrum (Fig. 5.19). The addition of the naphthalene ($r_i = 1.5898$ [110]) causes the overall refractive index of dioxan scintillator to rise to $\sim$ 1.44. Furthermore, by reducing the amount of naphthalene used to $\sim$ 80 g/l it was found that it was possible to refractive index match to CaF_2(Eu) without harming the light output through quenching or dilution effects from the addition of methanol. In practice some methanol is needed in order to match the refractive indices precisely, primarily because naphthalene is a solid at rtp and is therefore harder to work with. The amount of methanol required is however small. Another advantage of dioxan scintillator is that it is miscible with water and can therefore be handled and gelled with ease. The one disadvantage is that dioxan has an extremely low flash point ($\sim$ 35 °C) and may therefore be hazardous to use at Boulby. The safety precautions associated with the running of an operational CASPAR detector containing dioxan scintillator must therefore be stringent.

Assay

Tests were performed on BC533 and dioxan scintillators refractive index matched to CaF_2(Eu) in order to determine their relative light outputs. The raw dioxan scintillator was a naphthalene free custom cocktail supplied by Zinsser Analytic (UK) Ltd. [161] and coarse index matching was performed by adding $\sim$ 80g/l naphthalene. Prior to use dry N_2 gas was bubbled through both raw scintillators at a rate $\sim$ 1 cm^3/s for $\sim$ 4 hours so as to remove absorbed O_2 (which quenches scintillation [159]). It was found that N_2 could not be bubbled through the dioxan scintillator after refractive index matching as the naphthalene tended to sublime into and block the narrow Cu gas nozzle.

In the case of BC533 refractive index matching was performed by progressively increasing the fraction of methanol in the cocktail while taking test samples to which CaF_2 powder was added. When the BC533 / CaF_2 mixture became perfectly transparent the addition of methanol to the cocktail was ceased. A similar procedure using naphthalene and methanol was used to fine tune the refractive index of the dioxan scintillator, the testing technique being based upon that described in step (4) of Appendix B.

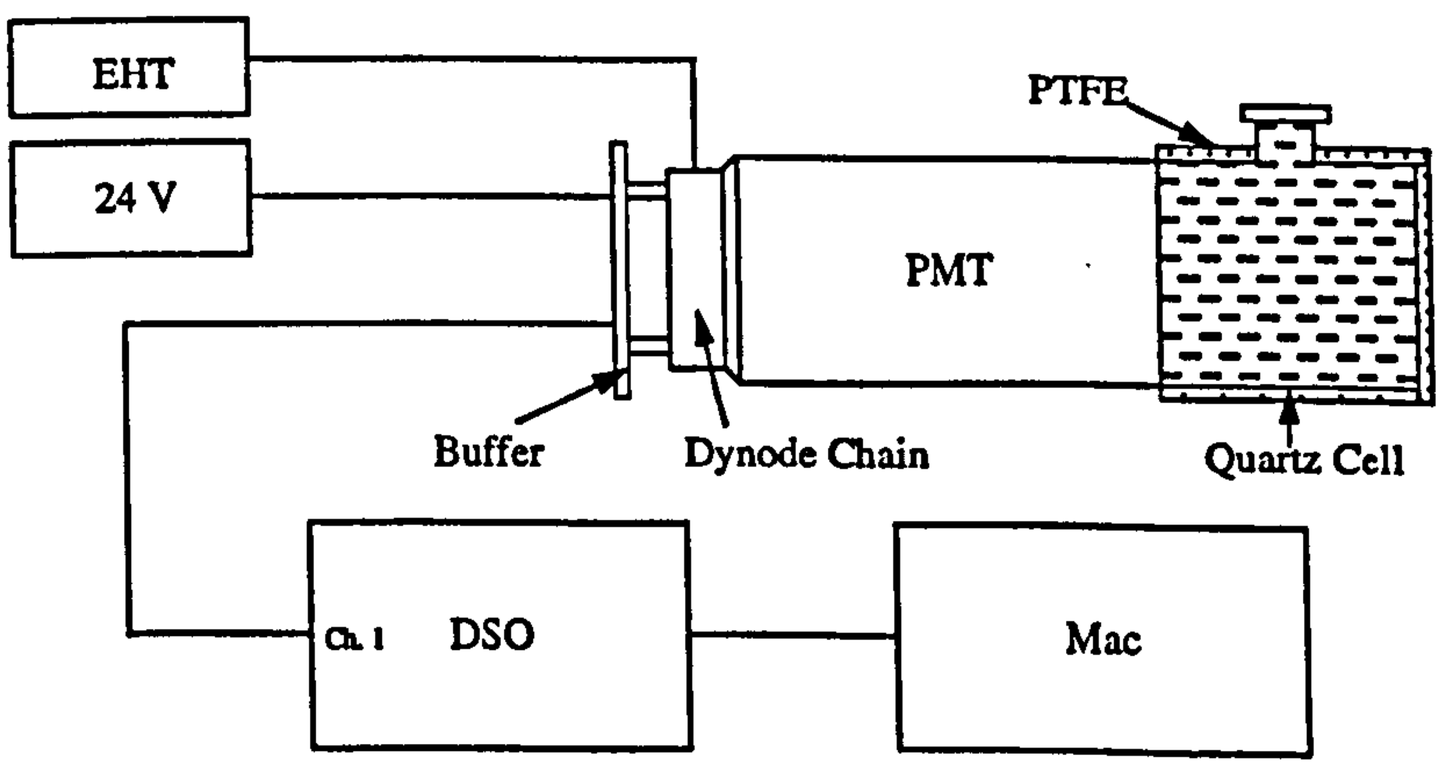

Figure 5.20: *A schematic diagram of the apparatus used to measure the light output of liquid scintillators.*

The test rig is sketched in Fig. 5.20. The scintillation cocktails were held in a

50 mm ϕ × 50 mm long cylindrical quartz cell supplied by Lightpath Optical Ltd. [162]. The cylindrical surface and one end face of the cell were wrapped in diffuse reflecting PTFE tape. An Electron Tubes [127] 9266A 2" PMT (Table 4.2) with a bialkali photocathode was directly coupled to the other face with Dow-Corning Q2-3067 optical grease [142]. The cell and PMT were then placed under a light tight black blanket. The buffer integrated output from the PMT was passed to a LeCroy 9430 DSO [132] connected to an Apple Macintosh running Labview [163] DAQ software.

Data was taken with 22 keV X rays generated by an ^{108}Ag foil source illuminated by 60 keV gammas from an ^{241}Am source. Photopeaks were clearly visible (Fig. 5.21) and were fitted using a χ^2 routine. The results are summarised in Table 5.3 and show the dioxan cocktail to be superior. Given this data and the other advantages of the dioxan cocktail it was decided that dioxan scintillator should be used for CASPAR. The use of BC533 will be reserved for CASPAR detectors with cooled APD read out (§4.3.2).

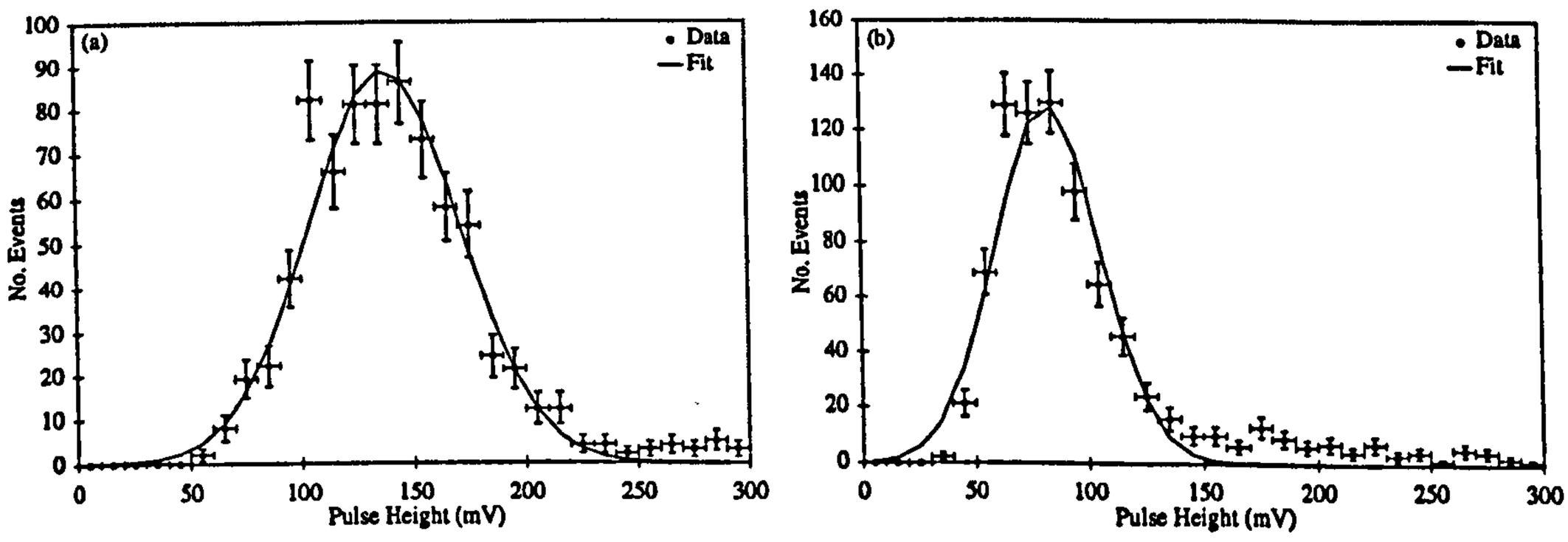

Figure 5.21: *The photopeaks observed in liquid scintillators illuminated with 22 keV X rays. Figure (a) shows data taken with dioxan scintillator while Figure (b) shows data taken with BC533.*

Scintillator	*Light Output (pe/keV)*
Dioxan	1.4 ± 0.3
BC533	0.9 ± 0.2

Table 5.3: *The results of the liquid scintillator light output tests.*

5.3.4 The CASPAR Gelling Agent

In order for range discrimination (§4.2.4) in CASPAR to be successful some technique must be employed for maintaining the CaF_2(Eu) grains in suspension over long periods of time. If the grains lie in permanent contact with one another at the bottom of the cell then low energy electron recoils leaving the grains can enter other grains without passing through a significant amount of liquid. In this case the electron recoil events resemble slow nuclear recoil events and PSD is rendered impossible.

A number of techniques for grain suspension were considered. Initially it was thought that natural convection currents would be sufficient to support the grains however following tests it was realised that owing to their density and the high viscosity of the liquid scintillator they tended to settle out from suspension within minutes of vigorous stirring. This phenomenon in fact provides a useful measure of the grain size of CaF_2(Eu) powders because larger grains settle out considerably more rapidly than smaller grains. Thus a rapidly settling 'sand' can be deduced to have a larger mean grain size than a slowly settling 'clay'. Further details are given in [110].

One suspension technique which was considered was to use a standing wave ultrasonic field. With this technique the grains would be concentrated in the displacement minima of the field, suspended within the liquid. It was soon appreciated however that the ultrasonic power required for this technique would be so great as to cause cavitation in the liquid (§5.3.2), possibly damaging its scintillation properties.

A better approach would be to use a gelling agent to solidify the liquid scintillator while the CaF_2 grains are still in suspension following stirring. This technique is commonly used in medicine and environmental monitoring to assay beta emitting contaminants in emulsions or sludges [164]. Initially a polymer gel was tested (PolyEthylene Oxide PEO) and this had the advantage of requiring only a minute amount of material to ensure a solid gel. The resulting gel was slightly less than water white transparent however and so its use was rejected.

The conventional gelling material used with scintillators is fumed silica (SiO_2), manufactured under the trade name 'CAB-O-SIL' by Cabot corp. [165]. The raw material is an extremely fine low density white powder and upon addition to dioxan scintillator forms a water white, perfectly transparent gel. The powder consists of $\sim$ 10 nm wide fibres of silica which disperse and interlock when added to the liquid to form the gel. The width of the fibres is sufficiently small to prevent the mismatch in refractive indices between the silica and the scintillator from scattering light. The CaF_2(Eu) grains sit in the lattice formed by the fibres and hence are prevented

from precipitating; an early CASPAR detector containing CAB-O-SIL has survived for two years without significant degradation in powder suspension. A volume of powder equal to that of the liquid scintillator cell is required in order to form a rigid gel, however owing to its low density ($\sim$ 40 g/l) the total mass of powder is no greater than that of the amount of PEO required to provide the same level of gelling. A further advantage of CAB-O-SIL gels is that they are thixotropic and can therefore be poured easily after vigorous stirring, simplifying the process of filling liquid scintillator cells. The gel should also be of high radiopurity due to the high purity of silica and the small mass of powder required to form the gel.

One problem associated with the use of fumed silica with liquid scintillators is that in most cases the resultant gel is white and partially opaque. It appears that dioxan scintillator is the only liquid in which this does not occur. This is unlikely to be a refractive index effect as opaque gels are even formed with index matched NE224. It is more likely that the cause is water vapour adsorbed onto the vast surface area of silica contained within even a small volume of CAB-O-SIL. Upon addition of CAB-O-SIL to liquid scintillator this water disperses and if the liquid is not miscible with water then it forms an opaque emulsion. Dioxan is one of the few liquid scintillator bases which is miscible with water and so it may be that this is why only dioxan scintillation cocktails form transparent gels. Extensive baking of the powder under vacuum may alleviate the problem for other scintillators, however this (and the hypothesis in general) have yet to be tested.

An alternative to the technique of gelling the liquid scintillator used in CASPAR would be to replace the liquid altogether with a thermosoftening plastic scintillator. By melting this material, mixing in the CaF_2(Eu) powder and allowing the mixture to set a solid CASPAR detector could be made. Unfortunately most plastic scintillators are based upon PolyStyrene (PS) or PolyVinylToluene (PVT), both of which are cyclic polymers and therefore have high refractive indices [100]. Index matching through the addition of other materials to the polymer melt would appear to be difficult or impossible and so this technique may be impractical. Advances in polymer and scintillator technology may improve the situation in the future and from a commercial point of view it may be possible to mix the powder with non-scintillating PolyChloroTriFluoroEthylene (PCTFE) ($r_i \sim 1.44$ [110]) to form an almost perfectly matched solid. Although PCTFE has a short absorption length for visible light [2] this material may find application as an efficient, cheap, high density scintillating plastic coating for use in medicine, the nuclear industry or academia.

[2] PCTFE is described as 'translucent' in [110].

5.4 Conclusions

Detector development work has been performed aimed at optimising the performance of UVIS and CASPAR detectors. For UVIS tests have been performed of light output and PSD properties as functions of crystal growth technique and operating temperature and these indicate similar performance to that of the Kyropoulos crystals tested previously.

Work on CASPAR has been aimed at optimising light output from both inorganic powder and organic liquid scintillators. CaF_2 powder has been successfully doped with Eu ions through a modified chemical synthesis procedure and the powder has been observed to be extremely luminous when stimulated with 325 nm laser light. Dioxan scintillator has been chosen as a suitable liquid scintillator for CASPAR and tests have quantified its light output properties. CAB-O-SIL has been chosen as the optimum compound for gelling the liquid scintillator due to its high transparency and radiopurity.

Chapter 6

Neutron Beam Tests

6.1 Introduction

Scintillator dark matter detectors can be accurately calibrated with nuclear recoils by performing neutron scattering experiments with a monoenergetic neutron beam. In this chapter the results of such tests carried out by this author on several different targets are presented. The chapter begins with a discussion of the theory underlying the technique (§6.2) and then moves onto an account of CASPAR pulse shape tests conducted using a 5.5 MeV neutron beam at the University of Birmingham Dynamitron facility (§6.3). Nuclear recoil pulse shape and scintillation efficiency tests on NaI(Tl) and CaF_2(Eu) crystal scintillator targets using a new University of Sheffield 2.85 MeV beam are then described (§6.4).

6.2 Theory

The response of UKDMC scintillator dark matter detectors to nuclear recoils is very different from that to electron recoils, both in terms of pulse shape and recoil relative energy detection / scintillation efficiency (§3.5.2). These differences must be quantified before data from a given detector can be used to search for a dark matter signal. Pulse shape differences between nuclear and electron recoils can be determined crudely using Am-Be or ^{252}Cf fission neutron sources as described in §5.2. Data taken with these sources is however contaminated with electron recoil events caused by Compton scattering of gamma radiation emitted during the fission process. Furthermore the energy distribution of the emitted neutrons is in general broad [166] and so the use of these sources is not suitable for energy response or nuclear recoil scintillation efficiency measurements.

An alternative technique is to use elastic scattering of nuclei by neutrons from

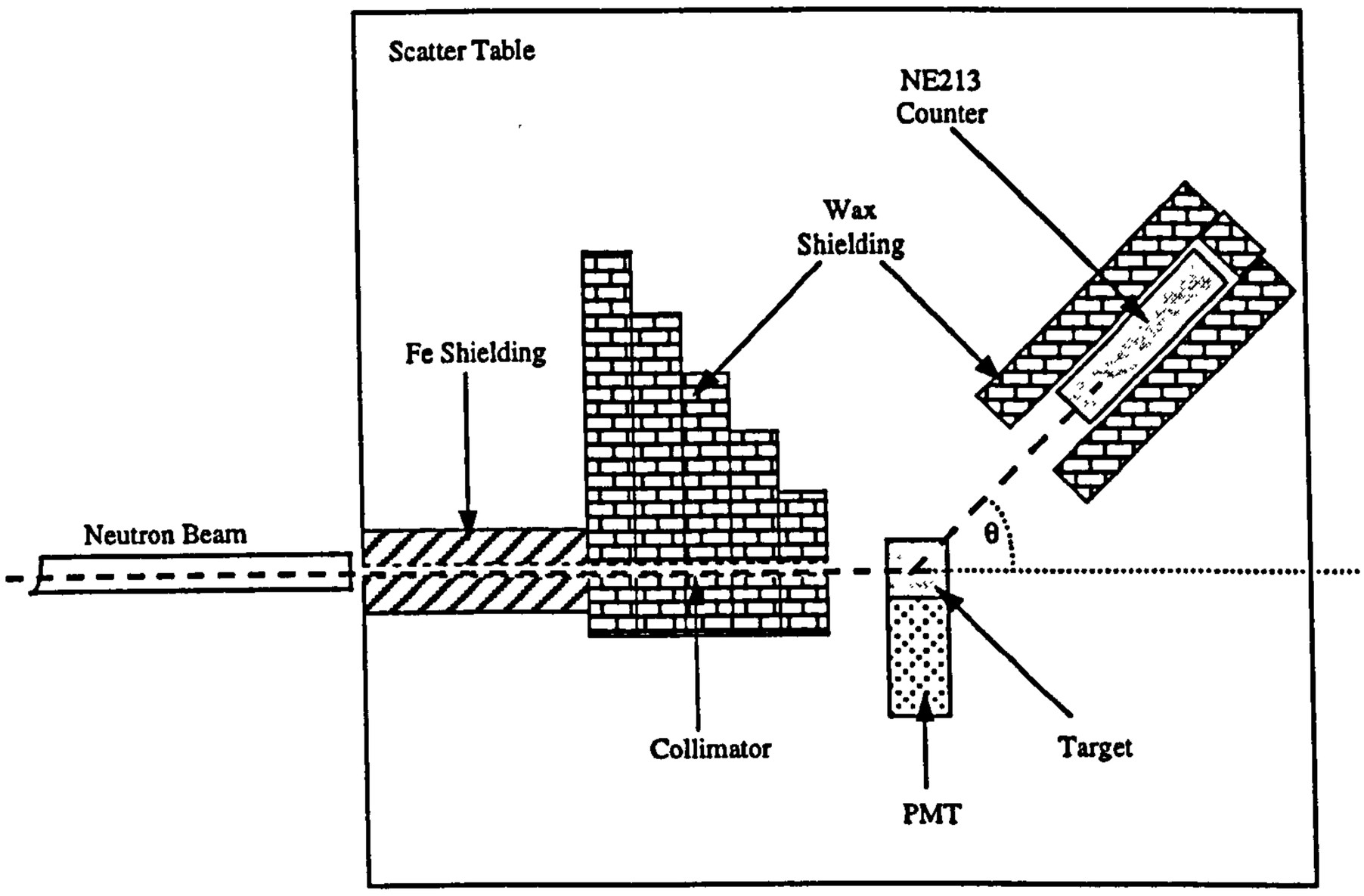

Figure 6.1: *A schematic diagram of apparatus used for neutron beam scattering tests.*

a high intensity beam [167, 168, 104]. The beam is produced via fusion rather than fission processes and as a consequence of the two body fusion final states (e.g. ^{3}He, n or ^{4}He, n) the neutrons are monoenergetic. The large flux enables nuclear recoils to be tagged by detecting the scattered neutrons as coincident events in neutron / gamma discriminating counters situated some distance from the target detector (Fig. 6.1). This reduces the number of electron recoil background events to negligible levels in most cases. This in turn enables precise PSD studies to be carried out while at the same time permitting a sample of monoenergetic nuclear recoils to be obtained for nuclear recoil scintillation efficiency measurements (§3.5.2).

The nuclear recoil energy may be calculated by considering a coincidence counter situated at an angle θ to the beam direction as in Fig. 6.1. Using the vector sum of momenta shown in Fig. 6.2 (overleaf) the recoil momentum of the nucleus p_2 is obtained from

$$p_2^2 = p_1^2 + {p_1}'^2 - 2\vec{p}_1.\vec{p}_1' cos\theta, \tag{6.1}$$

where p_1 and p_1' are respectively the initial and final state neutron momenta. Using conservation of kinetic energy the dependence upon p_1' may be removed to give

$$E_2^2(m_1+m_2)^2 - 4m_1E_1E_2(m_1(1-cos^2\theta)+m_2) + 4m_1^2E_1^2(1-cos\theta) = 0, \tag{6.2}$$

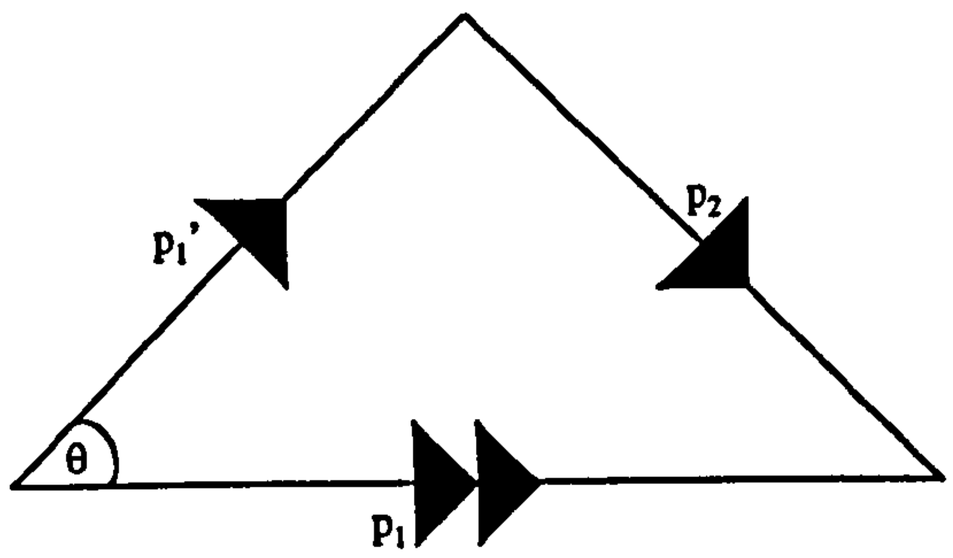

Figure 6.2: *The vector sum of neutron and nucleus momenta.*

where E and m are kinetic energy and rest mass respectively and the subscripts 1 and 2 refer to the neutron and nucleus as before. This quadratic equation in E_2 may be solved to give

$$E_2 = \frac{2m_1E_1}{(m_1+m_2)^2}\left(m_1(1-cos^2\theta)+m_2 \pm \sqrt{m_1^2cos^4\theta - m_1^2cos^2\theta + m_2^2cos^2\theta}\right). \quad (6.3)$$

In the case of heavy nuclei of mass $A >> 1$ this may be approximated by

$$E_2 = \frac{2AE_1}{(A+1)^2}(1-cos\theta), \quad (6.4)$$

assuming neutrons to have A equal to unity. This expression for E_2 allows energy calibrations to be performed with nuclear recoils from neutron beam scattering in much the same way as is done with monoenergetic gamma sources. Nuclear recoil relative scintillation efficiencies $g_r(A, E_R) = E_v/E_R$ (§3.5.2) for a given target can thus be determined and used with Eqns. 3.58 and 3.65 to calculate predicted WIMP induced nuclear recoil energy spectra.

6.3 CASPAR Neutron Beam Tests

6.3.1 Experimental Apparatus and Procedure

In order to measure the discrimination provided by the CASPAR technique neutron beam pulse shape tests were performed on a small prototype detector. A neutron beam at the University of Birmingham Dynamitron facility was used, providing neutrons of energy 5.5 MeV from the reaction d(d,^{3}He)n at a rate of $\sim 10^9$ sr^{-1} s^{-1}. Nuclear recoil energies for specific neutron scattering angles θ calculated from Eqn. 6.4 for the Dynamitron source are listed in Table 6.1.

θ	Ca	F	C
120	392.62	783.75	1171.60
105	329.49	657.73	983.22
90	261.75	522.50	781.06
75	194.00	387.27	578.91
60	130.87	261.25	390.53
45	76.66	153.04	228.77
30	35.07	70.00	104.64
15	8.92	17.80	26.61

Table 6.1: *Nuclear recoil energies at the Dynamitron (5.5 MeV) from Eqn. 6.4.*

Experiments were conducted in the Low Scatter Cell, a 10 m × 10 m × 10 m chamber with a false floor at half height to enable the target to be positioned away from scattering surfaces. The beam passed through a 20 mm ϕ double wedged collimator surrounded by iron shielding and then borated wax (Fig. 6.1). This arrangement produced a well collimated beam free from significant numbers of stray neutrons and gammas, thereby reducing beam related background. Further details of the general shielding arrangements are given in [167, 101].

The detector itself consisted of a 50 mm ϕ x 50 mm long PTFE wrapped cylindrical quartz cell from Lightpath Optical Ltd. [162] filled with a CASPAR mixture consisting of CAB-O-SIL gel [165], dioxan scintillator and 10 % by volume undoped CaF_2 powder of mean grain size $\sim$ 500 nm purchased from Aldrich Ltd. [153] (§5.3.2). Undoped CaF_2 was used because at that time Eu^{+2} doped powder was not available. Refractive index matching was performed using the procedure outlined in Appendix B and the cell was shaken immediately prior to use in order to ensure that the CaF_2 was held in suspension. One face of the cell was optically coupled with Dow-Corning Q2-3067 grease [142] to a 2"ϕ ET 9266A bialkali PMT (§4.3.2), while the opposite face was optically sealed with PTFE tape. The PMT output was integrated using a standard UKDMC buffer circuit (§4.3.3) and passed to DAQ electronics situated in the counting room. Low beam currents ($\sim$ 1 μA) were used because the slow recovery time of the buffer severely limited the rate at which data could be taken. The detector was positioned in the beam directly in front of the collimator, resting on top of a large scattering table. Two 75 mm ϕ Nuclear Enterprises [158] NE213 neutron / gamma discriminating liquid scintillation counters were stacked on the scattering table $\sim$ 0.7 m from the target detector at an angle θ to the beam for coincidence purposes. These counters were surrounded by bo-

rax blocks on all sides except those facing the target in order to thermalise stray neutrons reflected from the walls of the chamber (Fig. 6.1).

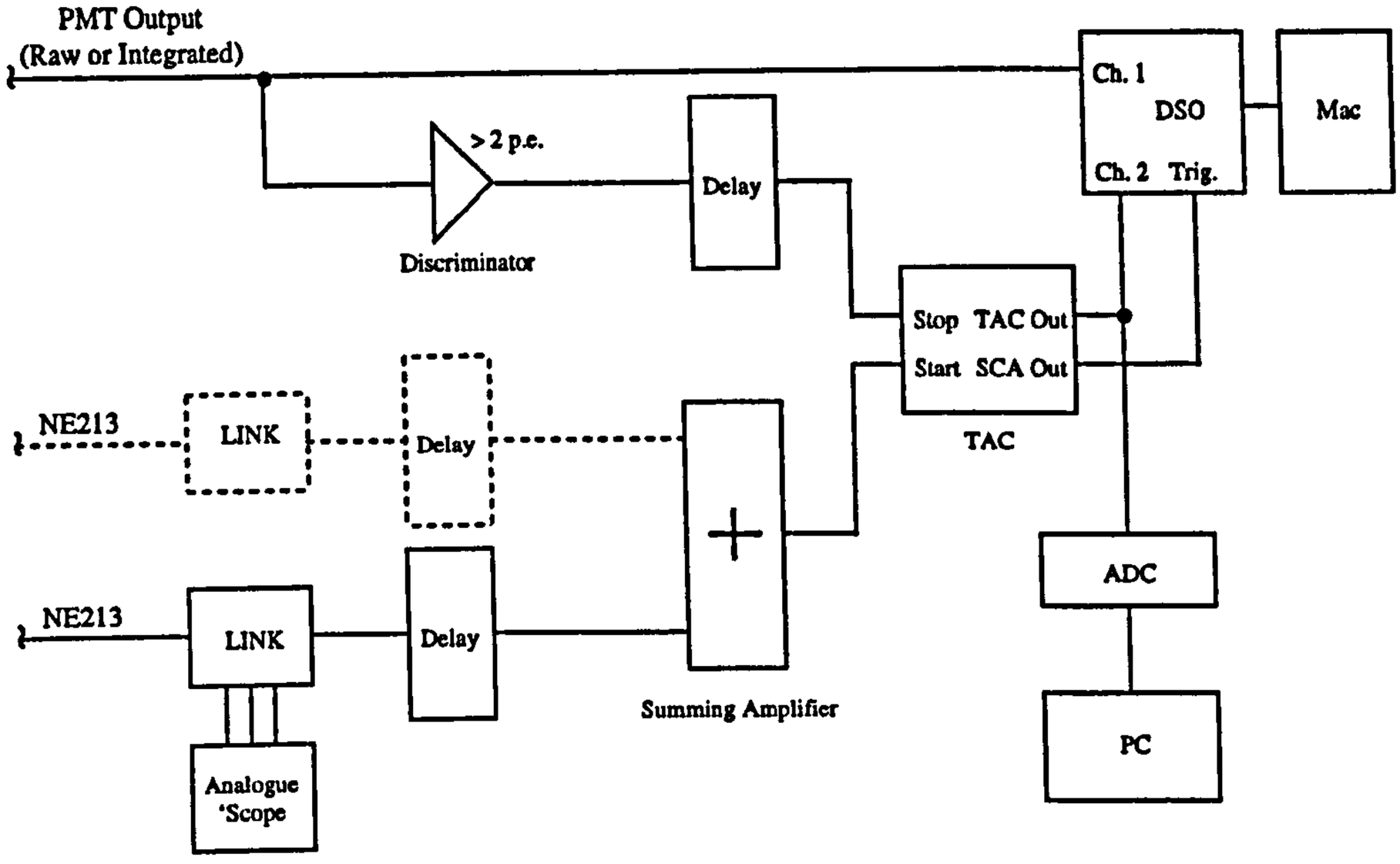

Figure 6.3: *The DAQ system used in the neutron beam scattering tests. The second NE213 unit, LINK module and summing amplifier were used only during the tests with the Dynamitron source.*

Fig. 6.3 shows the DAQ system which was used in these tests. A 10 mV threshold (2 pe) discriminator was used to produce trigger signals from the detector with which to start a TAC unit. In parallel with this the outputs from the NE213 counters were fed into two LINK Systems 5020 PSD units. The NE213 pulse shape consists of three components of differing decay time constant ($\sim$ 3 ns, 32 ns and 270 ns respectively), the relative amplitudes of which depend strongly upon whether the event is due to a neutron generated H recoil or background gamma generated electron recoil. The LINK units integrate this pulse shape over two periods of time, one very much greater than the decay time constant of the 270 ns component to the pulse and one very much less. The magnitudes of these two integrals crudely represent the total pulse height and fast component pulse height respectively. Thus these quantities can be used by the LINKs to discriminate neutron events from gamma events on an event by event basis. The LINK units can also discriminate against low energy

multiple wall scattered neutrons by rejecting low energy events with an internal threshold trigger.

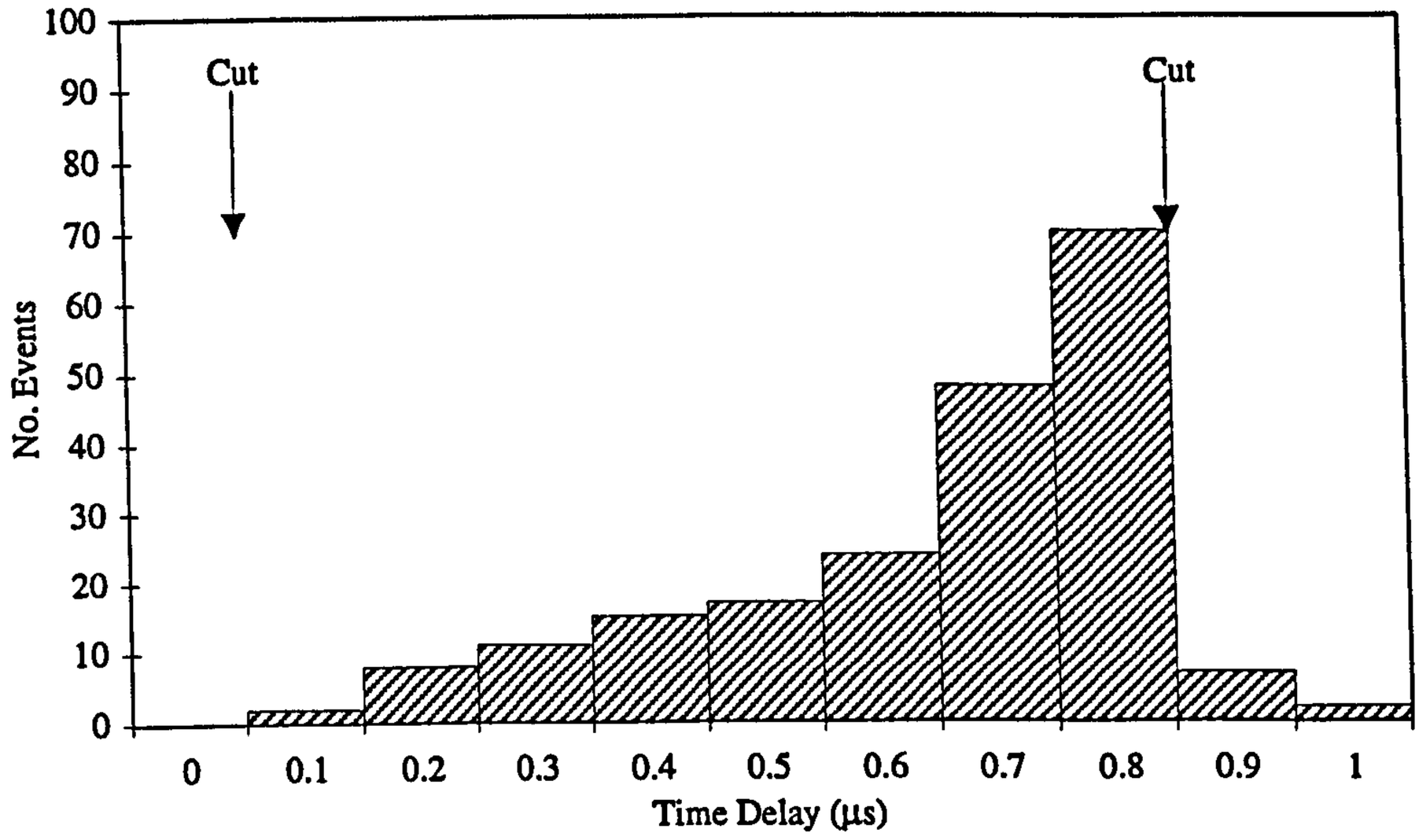

Figure 6.4: *An example TAC peak from the Dynamitron CASPAR neutron beam tests ($\theta = 120^o$). The long tail at times $t < 0.8$ μs is caused by photoelectron statistics combined with the long decay time constant of the CaF_2 pulse shape.*

The neutron trigger signals produced by the LINKs were combined with a summing amplifier and then passed to the stop input on the TAC. The TAC range was set to 1 μs and the system was configured such that valid coincidences would have a TAC arrival time separation of around half this value. This was done by calibrating the system with the back to back 511 keV gammas from a ^{22}Na source situated between the detector and NE213 counters and using delay / gate generators to achieve the desired time difference between the output signals. Valid events within the 1 μs window were digitised with a Lecroy 9430 DSO [132] triggering on the SCA output, while the TAC output was fed into channel 2 of the DSO for digitisation purposes. The digitised detector and TAC pulses were fed via GPIB link to an Apple Macintosh computer running custom Labview [163] DAQ software written especially for these tests. This software enabled the distribution of TAC amplitudes to be inspected and further cuts to be made. The absence of beam related background in the experiment was confirmed by the sharp TAC peaks (width < 50 ns) which were observed (Fig. 6.4). Both detector and TAC pulses were stored on disk for later off line analysis.

6.3.2 Data Analysis and Results

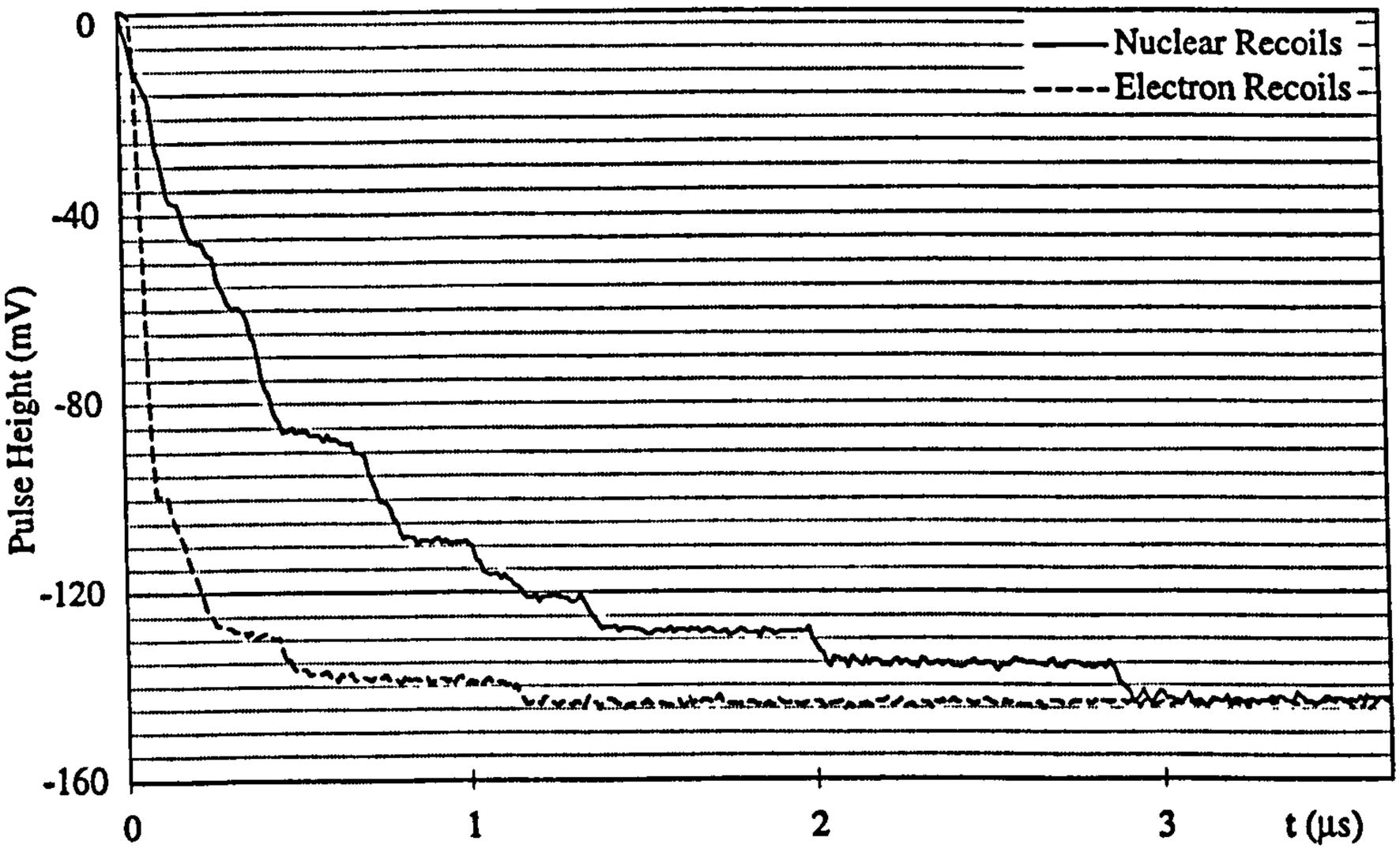

Figure 6.5: *Typical buffer integrated CASPAR pulses showing single photoelectron 'steps'. The horizontal lines represent the assumed photoelectron levels* $(i + 0.5)V$ *(*$V = 5\ mV$*). Photoelectron arrival times were determined from the points at which the time integrated pulse shapes crossed these levels.*

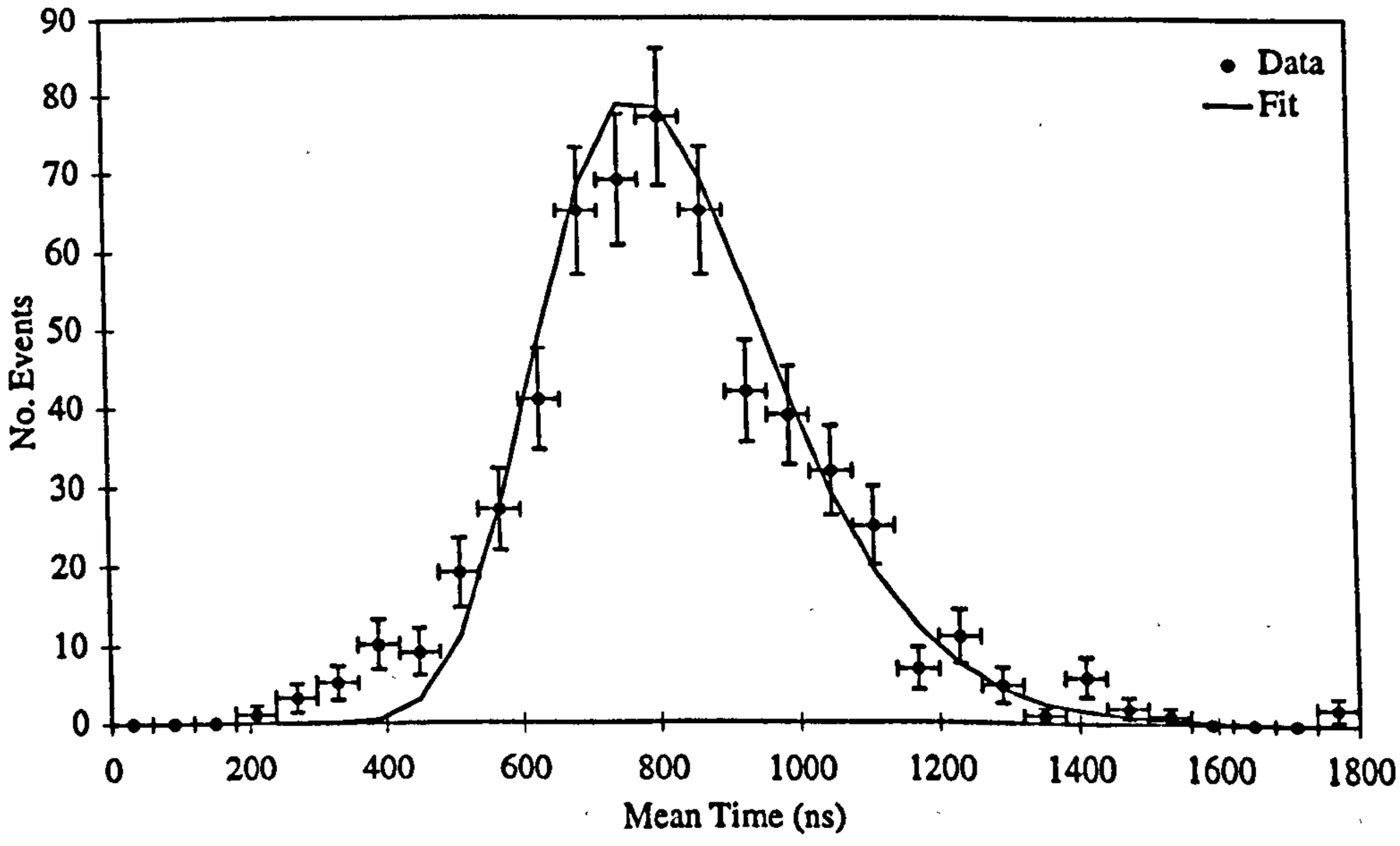

Figure 6.6: *The mean time distribution of 60 keV electron recoil events in* CaF_2 *(points). The line is a log-normal (Eqn. 4.9) fit to the data.*

The data were analysed by cutting on the TAC amplitude and then performing a log-likelihood fit to the arrival times of the photoelectrons in valid events with a double exponential pulse shape (§4.2.4). Typical valid events are plotted in Fig. 6.5. The photoelectron arrival times were determined by measuring the times at which each time integrated pulse passed below the levels $(0.5+i)V$ (Fig. 6.5) where i is the photoelectron number and V is the measured mV/pe ($\sim$ 5.0 mV during these tests). The decay time constants of the two components to the pulse were assumed to be 22 ns and 813 ns respectively. The former was the measured minimum rise time of the buffer and PMT while the latter was the decay time constant of electron recoil events in CaF_2 measured with a 10 μCi ^{241}Am 60 keV gamma source (Fig. 6.6). The amplitude ratio R_A (§5.2.2) of the 813 ns component pulse height to the total pulse height was used as the discriminating variable.

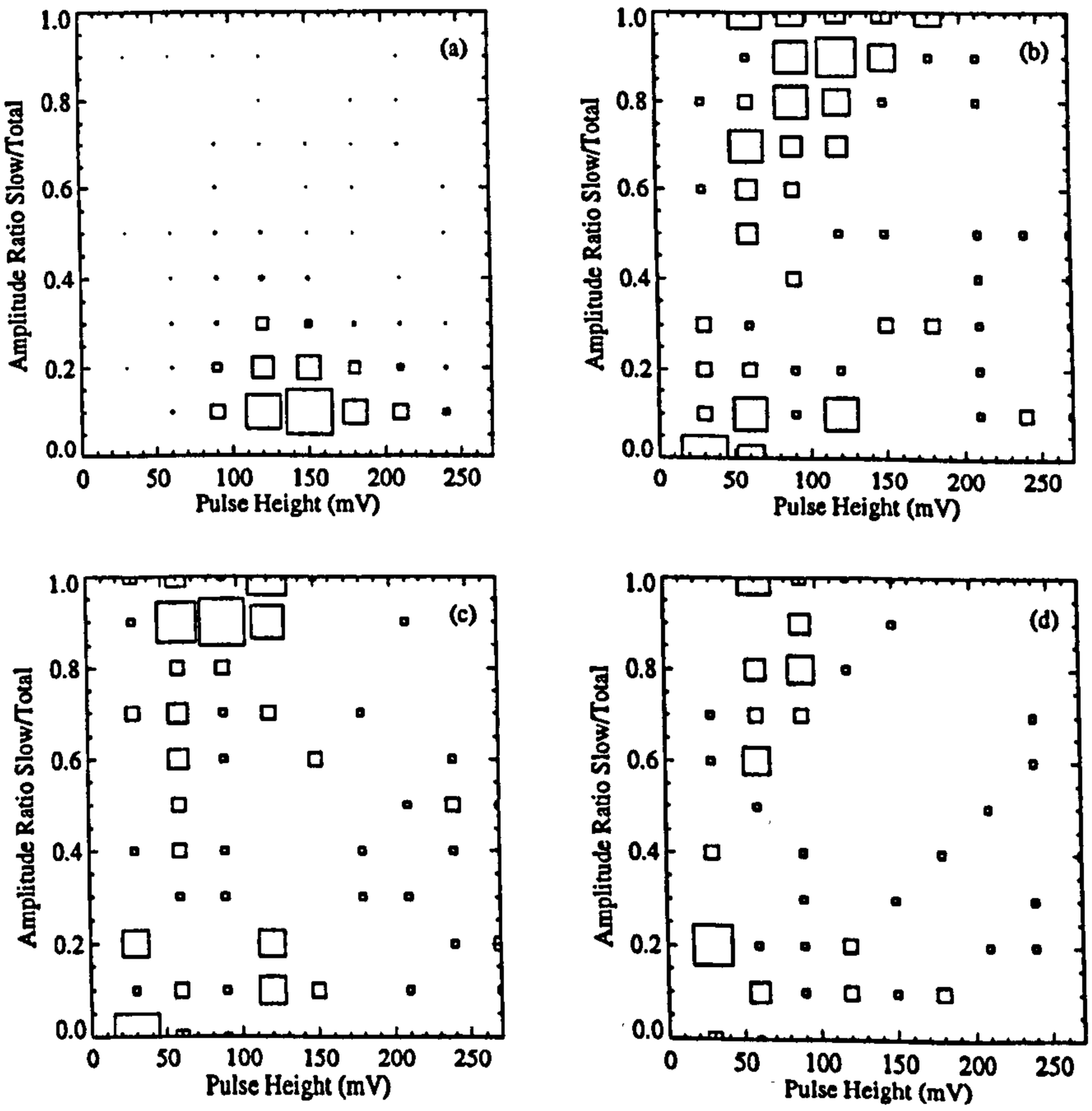

Figure 6.7: *The pulse height / amplitude ratio distribution of CASPAR events. Figure (a) shows data taken with an ^{241}Am 60 keV gamma source. Figures (b), (c) and (d) show neutron beam data taken at NE213 angles $\theta = 120^o$, 90^o and 60^o respectively.*

Distributions of events in terms of R_A and total pulse height for nuclear and electron recoil events are plotted in Fig. 6.7. Electron recoils generated with 60 keV gammas from a 10 μCi ^{241}Am source produced predominantly fast events (Fig. 6.5) with $R_A \lesssim 0.2$ (Fig. 6.7(a)). This is consistent with only a small fraction of each electron recoil track having passed through the CaF_2, as expected from the discussion of §4.2.4. The position of the photopeak suggests an electron equivalent light output from the liquid of 0.5 $\pm$ 0.1 pe/keV.

In Fig. 6.5 is also plotted the pulse shape of a typical candidate nuclear recoil event acquired with the beam on. The pulse is entirely composed of the slow decay component and hence originates from the CaF_2. The R_A - pulse height distributions of such data taken at coincidence angles of 120^o, 90^o and 60^o are shown in Figs. 6.7(b), 6.7(c) and 6.7(d) respectively.

Considering Fig. 6.7(b), it can be seen that the distribution is very different from that for electron recoil events. The cluster of events at a pulse height $\sim$ 50 mV and $R_A \lesssim 0.2$ is consistent with C recoils, which occur entirely within the liquid and hence have low R_A. Given the measured nuclear recoil relative scintillation efficiencies of Ca and F ($\sim$ 8% and $\sim$ 12% respectively from [168]) and C ($\sim$ 2% from [168]), it is proposed that the cluster of events with $R_A \gtrsim 0.6$ and pulse height between 50 mV and 200 mV is due to Ca and F nuclei recoiling within the grains. It is events with this R_A signature which would constitute a dark matter signal in an operational detector and it is clear that they are well separated from the electron recoils indicating excellent discrimination at this energy i.e. $\gtrsim$ 90% for $\lesssim$ 5% loss of signal events at 60 keV electron equivalent energy in the liquid (electron liquid equivalent - ele).

At smaller scattering angles one expects from Eqn. 6.4 to see the pulse heights of nuclear recoil events to be reduced. This behaviour is indeed seen in Figs. 6.7(c) and (d). The abundant H recoils produced by the beam lie well off the pulse height scale in these plots on account of the efficient n-p energy transfer and the large H recoil relative scintillation efficiency [168].

From the results plotted in Fig. 6.7(a) it appears to be impossible to calibrate the light output of the CASPAR grains using electron recoils, since these events rarely produce entirely slow CaF_2 pulses. Instead calibration could be performed using monoenergetic Ca or F recoils produced by a neutron beam. In these tests the energy resolution was too poor to separate the Ca and F recoil peaks and so all that can be said is that the grain light output was in the range 0.3 - 0.5 pe/keV. It is expected however that more precise calibrations could in future be performed given Eu^{+2} doped powder and improved light output.

6.4 NaI(Tl) and CaF_2(Eu) Neutron Beam Tests

Neutron beam tests were also performed on bulk crystals of NaI(Tl) and CaF_2(Eu). Tests of nuclear recoil scintillation efficiencies in these crystals had already been performed during earlier work at the Dynamitron [167, 168]. In these tests however the high beam energy prevented data from being taken at recoil energies sufficiently low to simulate the majority of WIMP induced recoils. By decreasing θ in Eqn. 6.1 it is theoretically possible to tag recoils of arbitrarily low energy however the proximity of the NE213 counters to the unscattered beam in practice limits θ to $\gtrsim 15^o$ in a realistically sized scatter chamber. Thus to observe low energy nuclear recoils a low energy beam is required.

6.4.1 Experimental Apparatus and Procedure

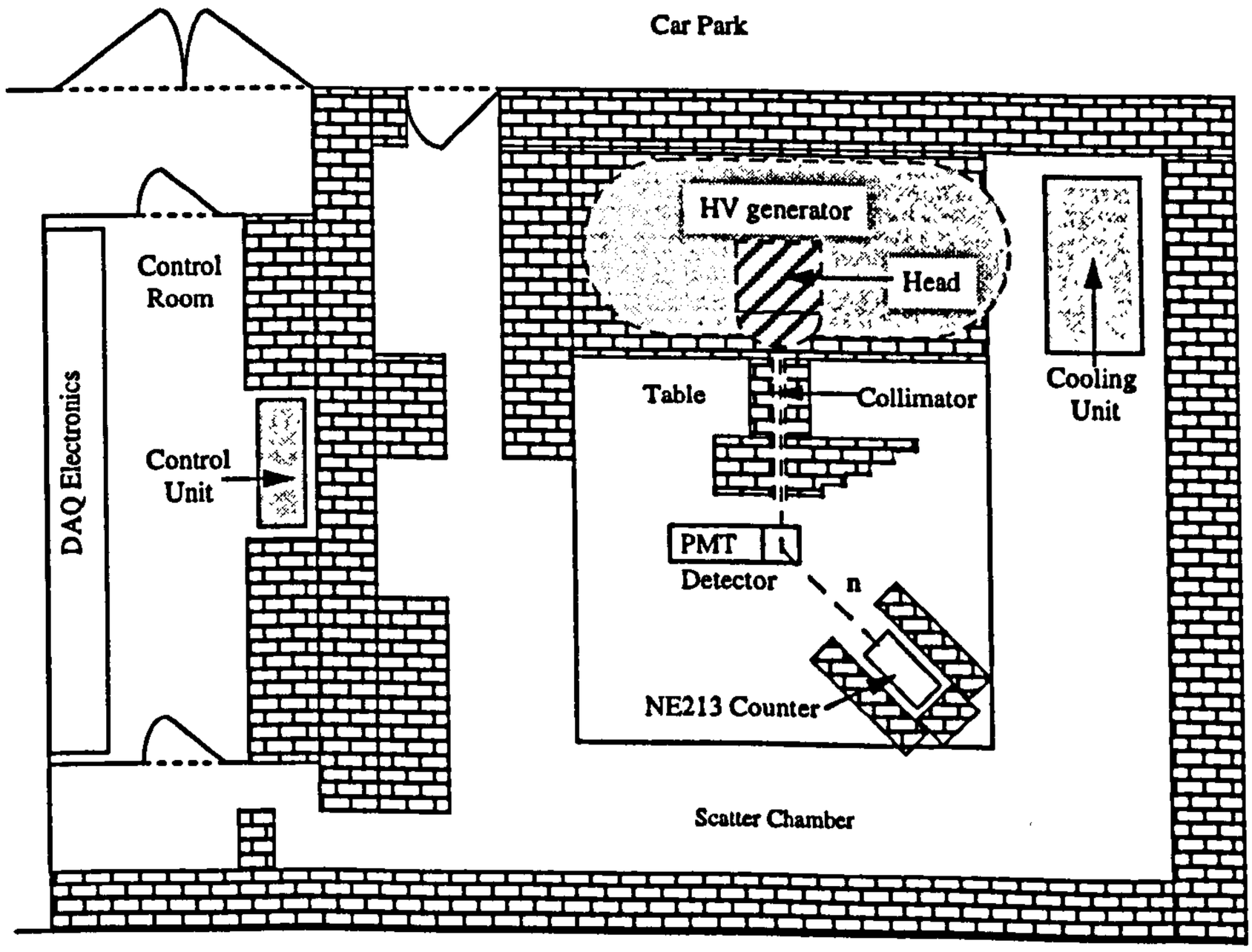

Figure 6.8: *A schematic diagram of the Sheffield 2.85 MeV neutron beam facility (not to scale).*

The installation at the University of Sheffield of a new Kaman Sciences A-711 [169] 2.85 MeV d(d,^{3}He)n device producing up to 10^9 neutrons s^{-1} (isotropic) allowed low energy tests to be performed. The beam head was mounted in concrete and

wax shielding in a 6 m x 5 m x 4 m high chamber lined with concrete blocks to a depth of $\sim$ 0.5 m (Fig. 6.8). In order to collimate the beam the same collimator and iron / borax shielding arrangements were used as those at the Dynamitron. Owing to the proximity of the deuterium target to the detector the neutron and gamma backgrounds present with this arrangement were considerably higher than those in the Dynamitron tests and so extra shielding was also required. The side of the beam head cavity which faced the target detector was lined with 100 mm of Pb followed by 1 m of borax blocks in order to absorb more of the off axis radiation. Gammas passing down the collimator and into the target detector were removed by shielding the collimator from the beam head with 5 - 15 mm of Pb sheet. Before this shielding was put in place Compton scattering of these gammas contributed significantly to the background random coincidence event rate. The shielding was not observed to cause any degradation in the beam neutron energy spectrum (Fig. 6.9).

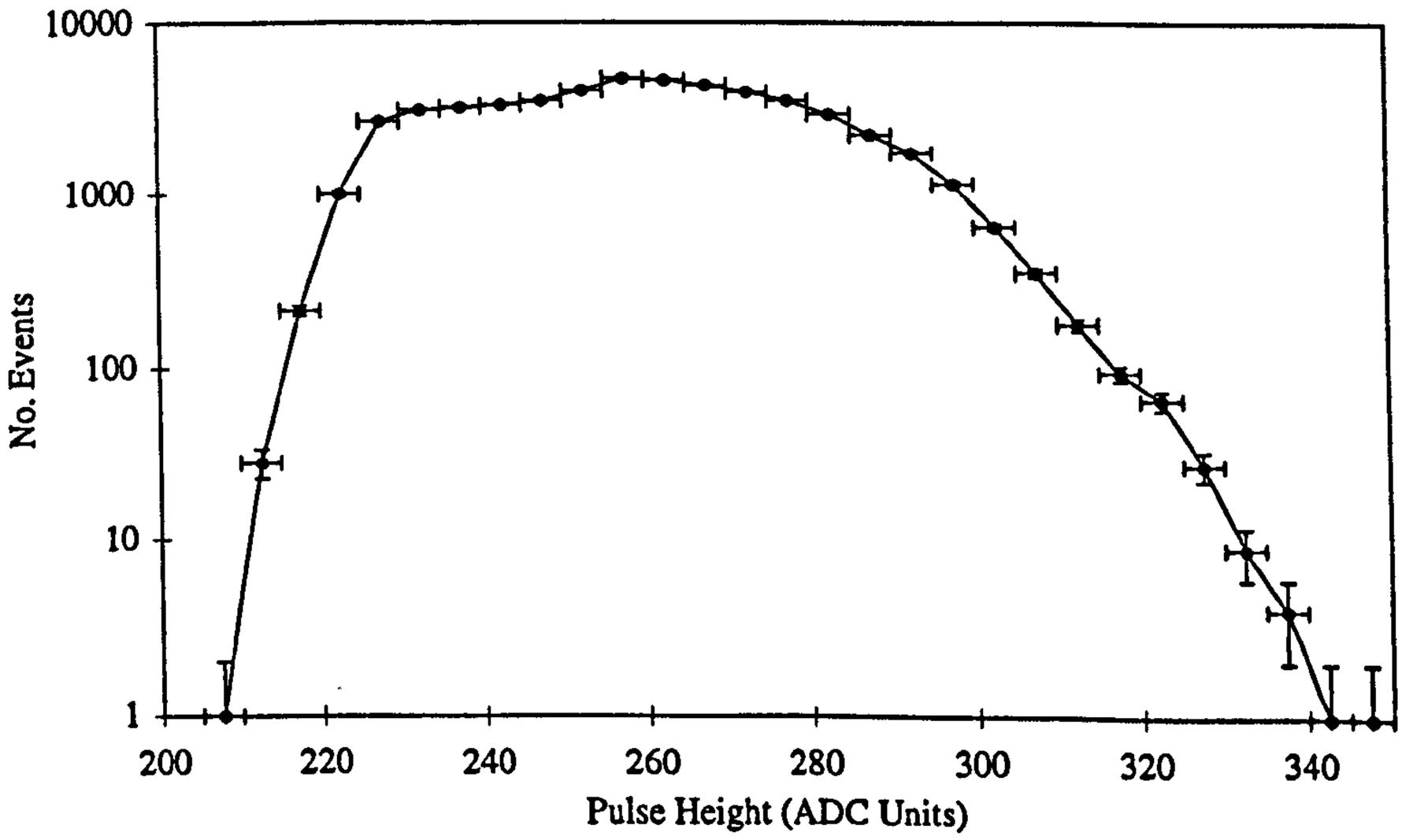

Figure 6.9: *The pulse height spectrum of neutron events in a discriminating NE213 counter placed on the beam axis. The clean 'edge' (note log scale) occurs at the maximum proton recoil energy and indicates that the beam is approximately monoenergetic.*

Cylindrical 25 mm ϕ x 25 mm long target crystals were used in the tests. The small size of the crystals reduced the probability of double scattering of neutrons from the beam, which could affect the scintillation pulse shape and pulse height leading to erroneous results. For the NaI(Tl) tests a Hilger Analytical Ltd. [139] encapsulated crystal with 1000 ppm Tl doping was used while for the CaF_2(Eu)

tests the crystal was unencapsulated and of doping 0.5% M Eu^{+2}. Both crystals were wrapped in PTFE tape in order to optimise light collection. Neither crystal had been used in previous tests. The crystals were directly coupled to an ET 9266A bialkali PMT (§4.3.2) with Dow-Corning Q2-3067 grease [142] and then placed in the beam at the end of the collimator. Excellent light collection was observed from both crystals, being 7.41 ± 0.04 pe/keV for the NaI(Tl) and 5.28 ± 0.09 pe/keV for the CaF_2(Eu). This enabled data to be taken at low visible energies ($\gtrsim$ 2 keV).

The DAQ system used in these tests was identical to that used at the Dynamitron (Fig. 6.3) but for the use of the raw PMT anode signal for both triggering and pulse shape purposes as outlined in §4.3.3. This development allowed the beam to be run at a high current ($\sim$ 2 - 3 mA) because the target event rate was no longer limited by the buffer recovery time. Slow pulses containing small numbers of photoelectrons generate raw pulse shapes which never exceed the pulse height of a single photoelectron and so this technique necessitated the use of a 1 pe discriminator threshold for low energy events. Due to the low noise rate in the PMT however it was felt that the additional thermal photoelectron background generated by this threshold could be tolerated. The use in future of a resettable integrator similar to that sketched in Fig. 4.19 would allow the discriminator to be operated once more at the 2 pe level.

The previous NaI(Tl) and CaF_2(Eu) tests performed with the Dynamitron [167, 168] used a less sophisticated DAQ system which, while capable of operating at high event rates was unable to acquire pulse shape information. By contrast the buffer-less system used for the tests described here did permit pulse shape acquisition at high event rates. Thus studies could be performed of both nuclear recoil scintillation efficiencies and pulse shapes for the target crystals.

One other minor difference between this system and that used in the Dynamitron CASPAR tests was that only one NE213 coincidence counter was used. This counter was mounted closer to the target detector than in the CASPAR tests ($\sim$ 0.5 m). This increased the signal to noise (neutron / gamma) ratio in the counter and was necessary because of the higher gamma background rate in these tests caused by the close proximity of the beam head. The resulting TAC peaks (Fig. 6.10 overleaf) were sharp for both NaI(Tl) and CaF_2(Eu) tests, although in the former case some degradation was observed at high beam currents, possibly due to long lived phosphorescence in the crystal.

Data was taken at a variety of neutron scattering angles between 105° and 15°, and in addition a 1 μCi ^{60}Co source was used to produce low energy electron recoils for comparison with the nuclear recoil data. Typical visible energy spectra for

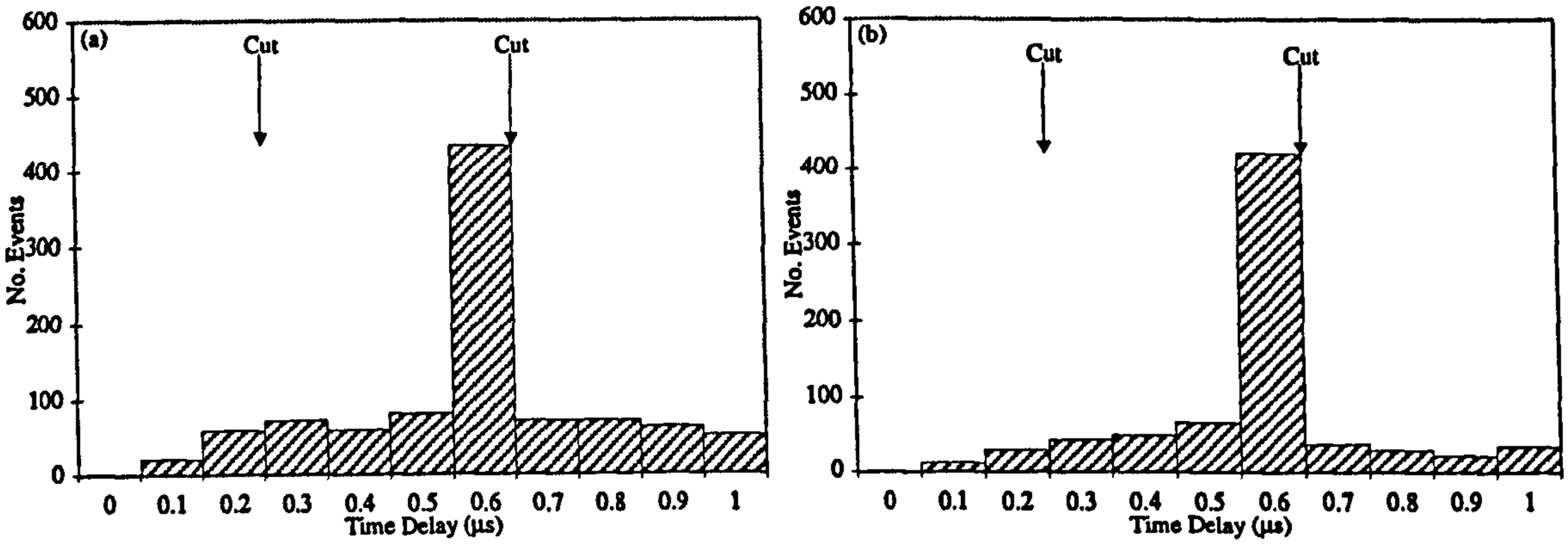

Figure 6.10: *Typical TAC peaks from the Sheffield neutron beam tests. Figure (a) shows the TAC peak from typical NaI(Tl) data while Figure (b) shows the TAC peak from typical $CaF_2(Eu)$ data. The data was taken at $\theta = 90°$.*

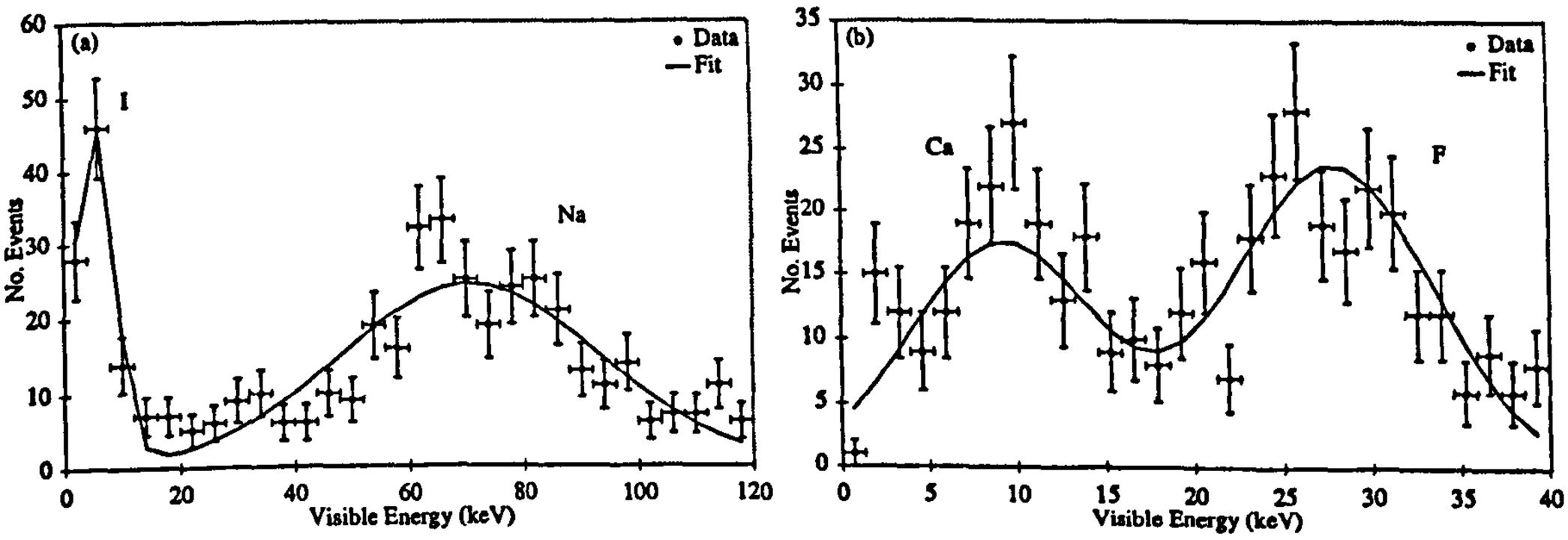

Figure 6.11: *Typical pulse height spectra from the Sheffield neutron beam tests. Figure (a) shows data taken with the NaI(Tl) crystal while Figure (b) shows data taken with the $CaF_2(Eu)$ crystal. The data was taken at $\theta = 90°$, giving Na, I, Ca and F recoil energies of 228 keV, 44 keV, 136 keV and 271 keV respectively.*

NaI(Tl) and CaF_2(Eu) events are plotted in Fig. 6.11. The nuclear recoil energy depends upon the nuclear mass through Eqn. 6.4 (Table 6.2 overleaf) and hence nuclei with different masses give events clustered in peaks in the visible energy spectra. The mean visible energies of the nuclear recoils at each scattering angle were determined with χ^2 fits of normal distributions to the energy peaks observed in the data recorded at that angle. Calibration of the detectors in terms of visible (electron equivalent) energy was performed with the 60 keV gamma line from a 10 μCi ^{241}Am source (Fig. 6.12 overleaf).

θ	Ca	F	Na	I	Xe
120	203.45	406.12	341.41	66.27	64.28
105	170.74	340.82	286.51	55.62	63.95
90	135.63	270.75	227.60	44.18	42.85
75	100.53	200.67	168.70	32.75	31.76
60	67.82	135.37	113.80	22.09	21.43
45	39.73	79.30	66.66	12.94	12.55
30	18.17	36.27	30.49	5.92	5.74
15	4.62	9.23	7.76	1.51	1.46

Table 6.2: *Nuclear recoil energies at the Sheffield neutron beam (2.85 MeV) from Eqn. 6.4.*

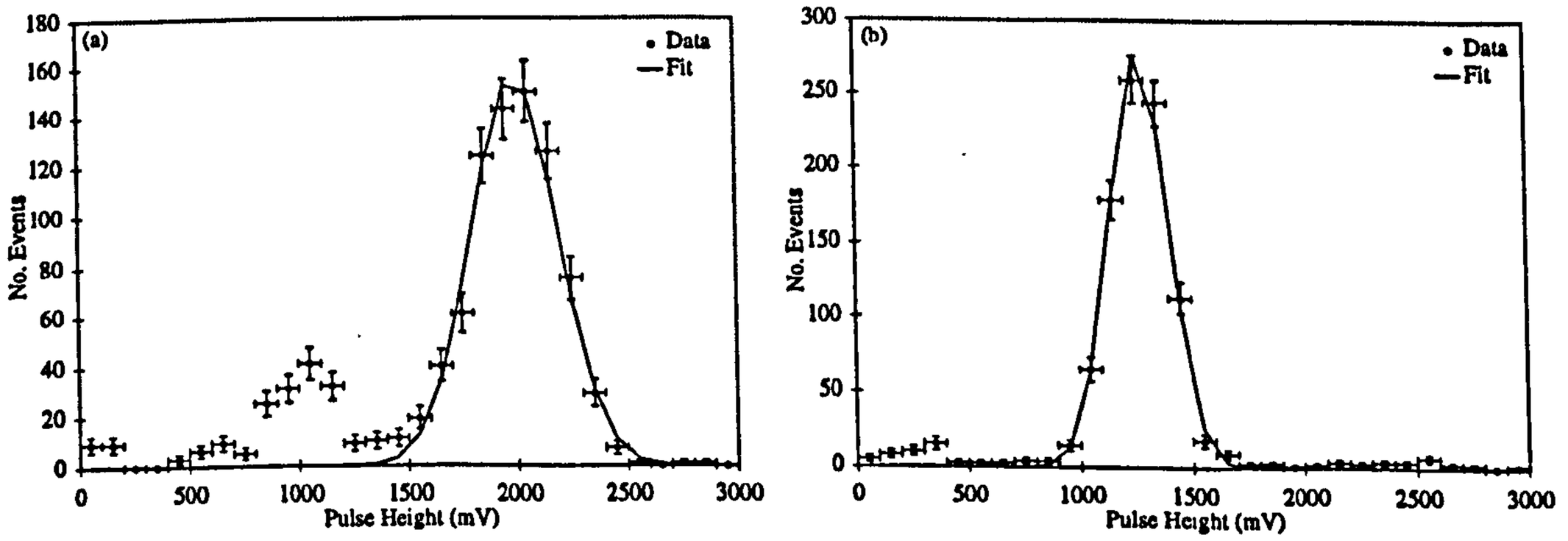

Figure 6.12: *Pulse height spectra from ^{241}Am calibrations. Figure (a) shows data taken with the NaI(Tl) crystal while Figure (b) shows data taken with the $CaF_2(Eu)$ crystal. The small peaks to the left of the main peaks are believed to be due to the weak 26 keV ^{241}Am line.*

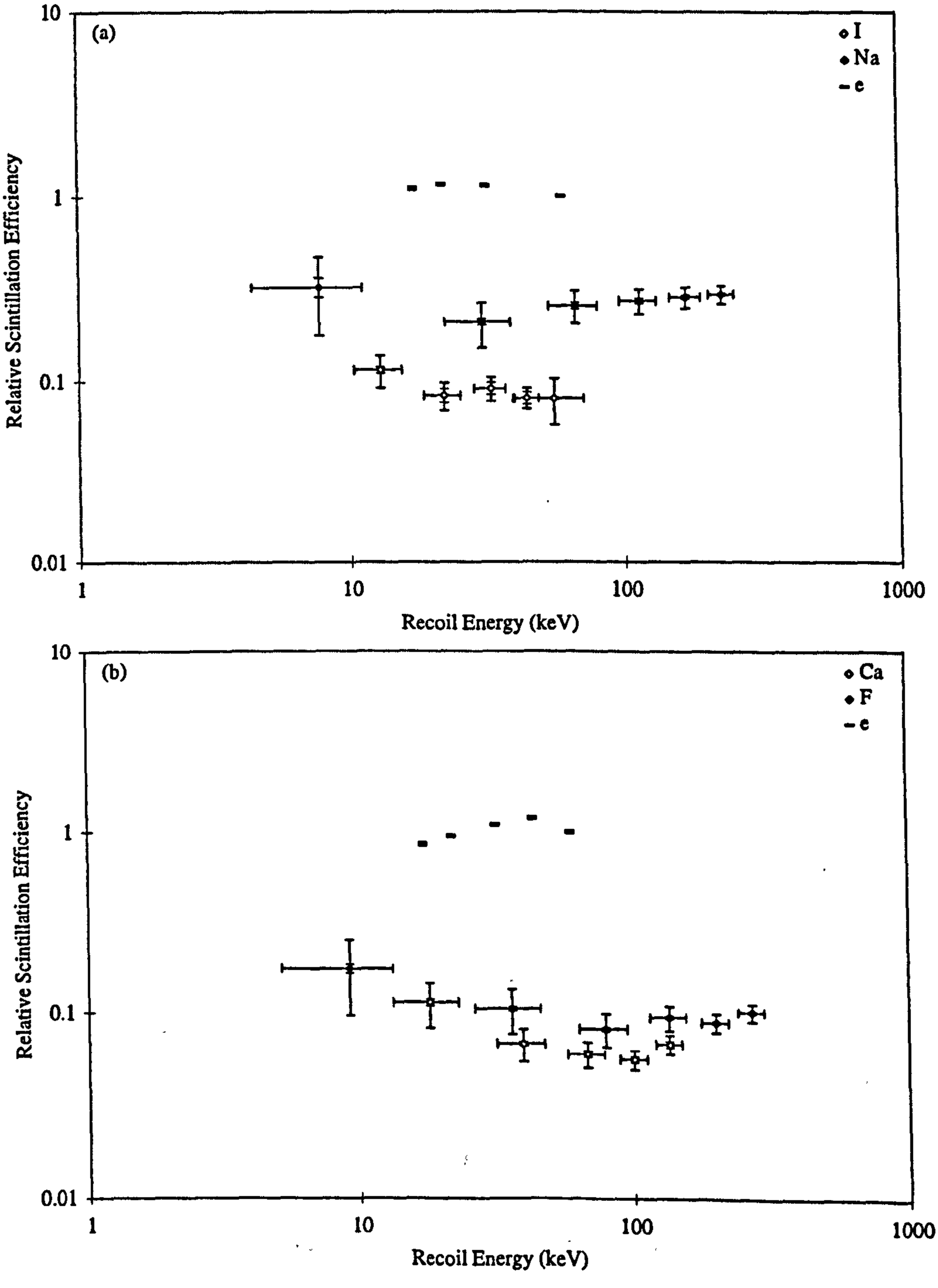

Figure 6.13: *The evolution of nuclear recoil relative scintillation efficiencies with recoil energy. Figure (a) shows data taken with the NaI(Tl) crystal (Na, I and electron recoils) while Figure (b) shows data taken with the $CaF_2(Eu)$ crystal (Ca, F and electron recoils).*

6.4.2 Data Analysis and Results

Relative Scintillation Efficiencies

The results of the measurements of relative scintillation efficiencies for nuclear recoils in NaI(Tl) and CaF_2(Eu) are plotted in Fig. 6.13. All scintillation efficiencies were calculated relative to the high energy calibration point provided by the ^{241}Am source. Non-linearities in the response to low energy gamma events have no effect on the *relative* nuclear recoil scintillation efficiencies at these energies (§3.5.2). Such behaviour was nevertheless investigated with the use of foil X ray sources and these results are also presented in Fig. 6.13.

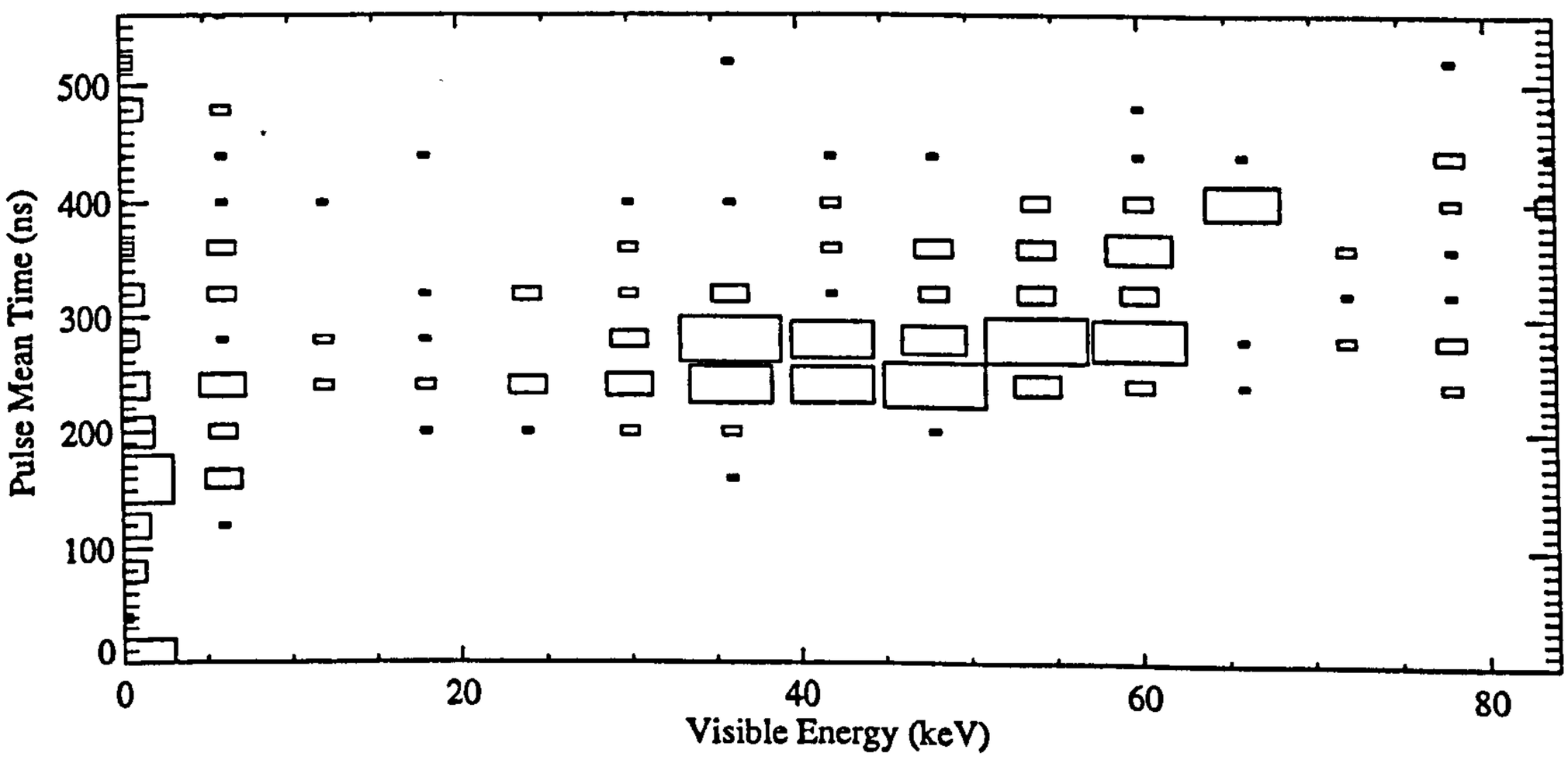

Figure 6.14: *The distribution of 75° NaI(Tl) events as a function of visible energy and pulse mean time. The events with visible energy < 5 keV and T < 50 ns are noise while those with visible energy < 10 keV and T > 100 ns are I recoil events. The events in the cluster with visible energy ~ 30 - 60 keV and T ~ 200 - 300 ns are Na recoil events while the events nearby clustered around E_v ~ 60 keV and T ~ 350 ns are electron recoils from the I 57 keV inelastic peak.*

In all cases the total error in the relative scintillation efficiency is dominated by systematic effects due to the finite sizes of the target crystals and NE213 coincidence counter. The beam energy was monitored throughout with the NE213 counter and was found to be stable to within errors. Any error in beam energy of this magnitude ($\lesssim$ 50 keV) has a negligible effect. A potential source of error in the Na recoil data at recoil energies $\gtrsim$ 100 keV was due to contamination with < 20 % electron

recoil events due to Compton scattering of gammas from the prominent 57 keV inelastic I peak (Fig. 6.14). The double recoil in these events leads to a significant fast component to the scintillation pulse and hence PSD can be used to remove them. This was a further advantage of the non-integrated DAQ system which was employed, since such a procedure would have been impossible during the earlier scintillation efficiency measurements [167]. For comparison both statistical errors and total errors are displayed on data points in Fig. 6.13.

The results for NaI(Tl) are consistent with the previous measurements at higher energies [167] and indicate average Na and I relative scintillation efficiencies of 27.5 $\pm$ 1.8 % and 8.6 $\pm$ 0.7 % in the recoil energy ranges 4 - 252 keV and 10 - 71 keV respectively. The CaF_2(Eu) results on the other hand show some evidence for a fall in the relative scintillation efficiencies for Ca and F in the recoil energy range 10 - 100 keV. The low values at higher energies are consistent with the earlier published results [168]. This behaviour is in agreement with other recent results [170] and may be explained by the inverse dependence of the relative scintillation efficiency upon the dE/dx of the recoiling nucleus in Eqn. 3.52 (§3.5.2). Such a rise in the values for Ca and F recoils in CaF_2(Eu) at low energies would have important consequences for CASPAR. It would imply lower recoil energy thresholds and hence sensitivity to a greater fraction of the total WIMP induced nuclear recoil energy spectrum.

Decay Time Constants

Pulse shape analysis of nuclear recoil events was performed by considering the arrival times of pulse photoelectrons. These were determined by integrating each pulse numerically in software and then measuring the times at which the integrated pulse passed below the level $(0.5 + i)V$ (§6.3.2) where i is the photoelectron number and V is the measured mV/pe ($\sim$ 4.5 mV during these tests). A pulse shape consisting of a single exponential component was assumed initially and measurement of the pulse decay time constant τ consisted of taking the mean arrival time T of the photoelectrons relative to the pulse start time (§4.2.2). This start time is not known *a priori* and so was approximated by the arrival time of the first photoelectron, valid for large numbers of photoelectrons. This leads to a systematic shift in the value of this quantity away from the actual decay time constant of order τ/n, where n is the total number of photoelectrons. It was decided however that correcting for this shift could introduce additional errors and so no correction was made. The uncorrected T values can be compared with data from operational NaI(Tl) detectors (§8) if no correction is applied to that data either.

At each scattering angle the distribution of the T for a particular nucleus is

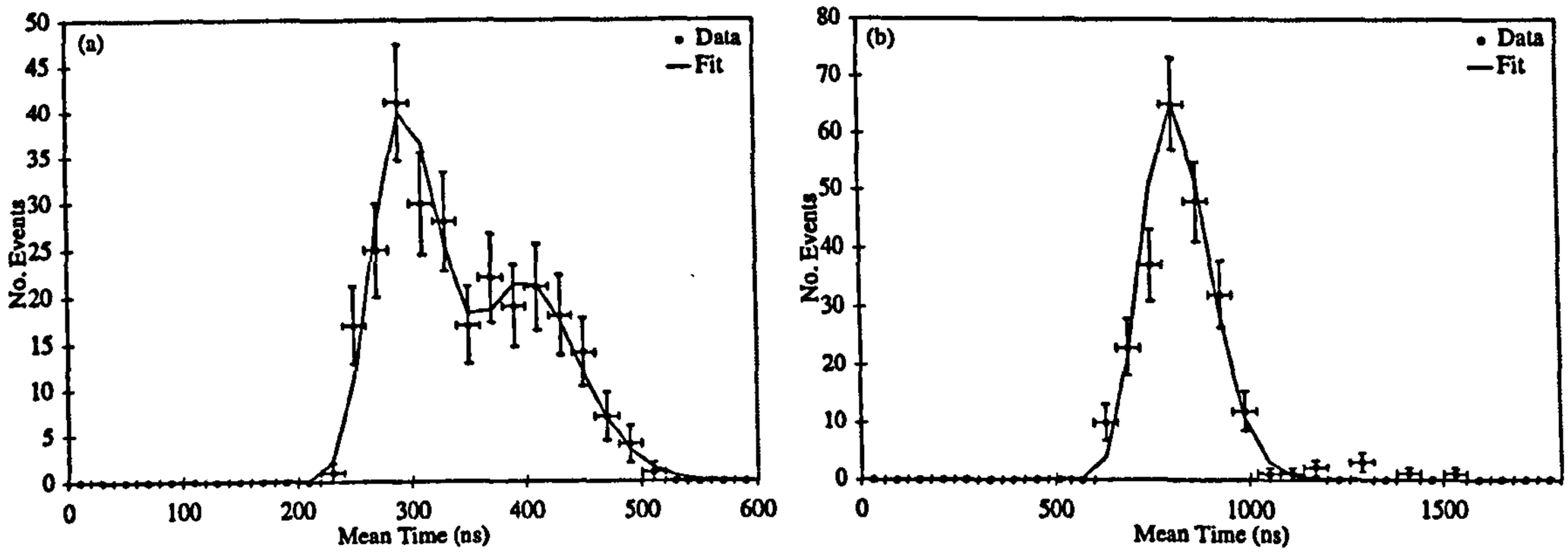

Figure 6.15: *Typical pulse mean time distributions with χ^2 fits to log-normal curves. Figure (a) shows Na recoil data taken with the NaI(Tl) crystal while Figure (b) shows F recoil data taken with the $CaF_2(Eu)$ crystal. Figure (a) also shows evidence for electron recoil contamination from the I 57 keV line and the log-normal fit takes this into account. Data was taken at $\theta = 90^o$.*

approximately log-normal (§4.2.2). In order to measure the T_0 parameters of these distributions events in 1σ energy regions about the recoil peaks were selected. Log-normal functions were then fitted to the distributions (Fig. 6.15) and values for the T_0 extracted, as in [88]. The results are presented in Fig. 6.16 (overleaf) for both NaI(Tl) and CaF_2(Eu). The errors on the T_0 include statistical fluctuations in the T_0 distributions and systematic effects due to the variation in temperature of the crystals over the course of the experiments. This temperature was monitored continually and was found to vary from a mean of 11°C by no more than ± 3 °C. A 1 °C temperature change leads to a 3 ns shift in decay time constant for NaI(Tl) [88] and consequently gives a contribution to the error of ± 9 ns. For CaF_2(Eu) the effect is smaller and leads to an additional error of conservatively no more than ± 5 ns. Also presented in Fig. 6.16 are the T_0 for electron recoils generated by the ^{60}Co source.

The overall mean T_0 for nuclear recoil events in NaI(Tl) was found to be 281.0 ± 5.1 ns, while the values for electron recoil events rose rapidly with energy from ~ 320 ns (visible energy $E_v \sim 7$ keV) to ~ 440 ns ($E_v \sim 52$ keV). The mean T_0 for Na events (2 keV $< E_v <$ 8 keV) and I events (2 keV $< E_v <$ 5 keV) were found to be 263 ± 15 ns and 272 ± 10 ns respectively and hence in this energy range there is no evidence for significant pulse shape differences between them. This supports the premise that coherent I scattering events in dark matter detectors can be simulated with Na recoil events induced by exposure to neutrons from a fission source ([88], §8). This is important because it is the recoil of I nuclei in particular which is expected to

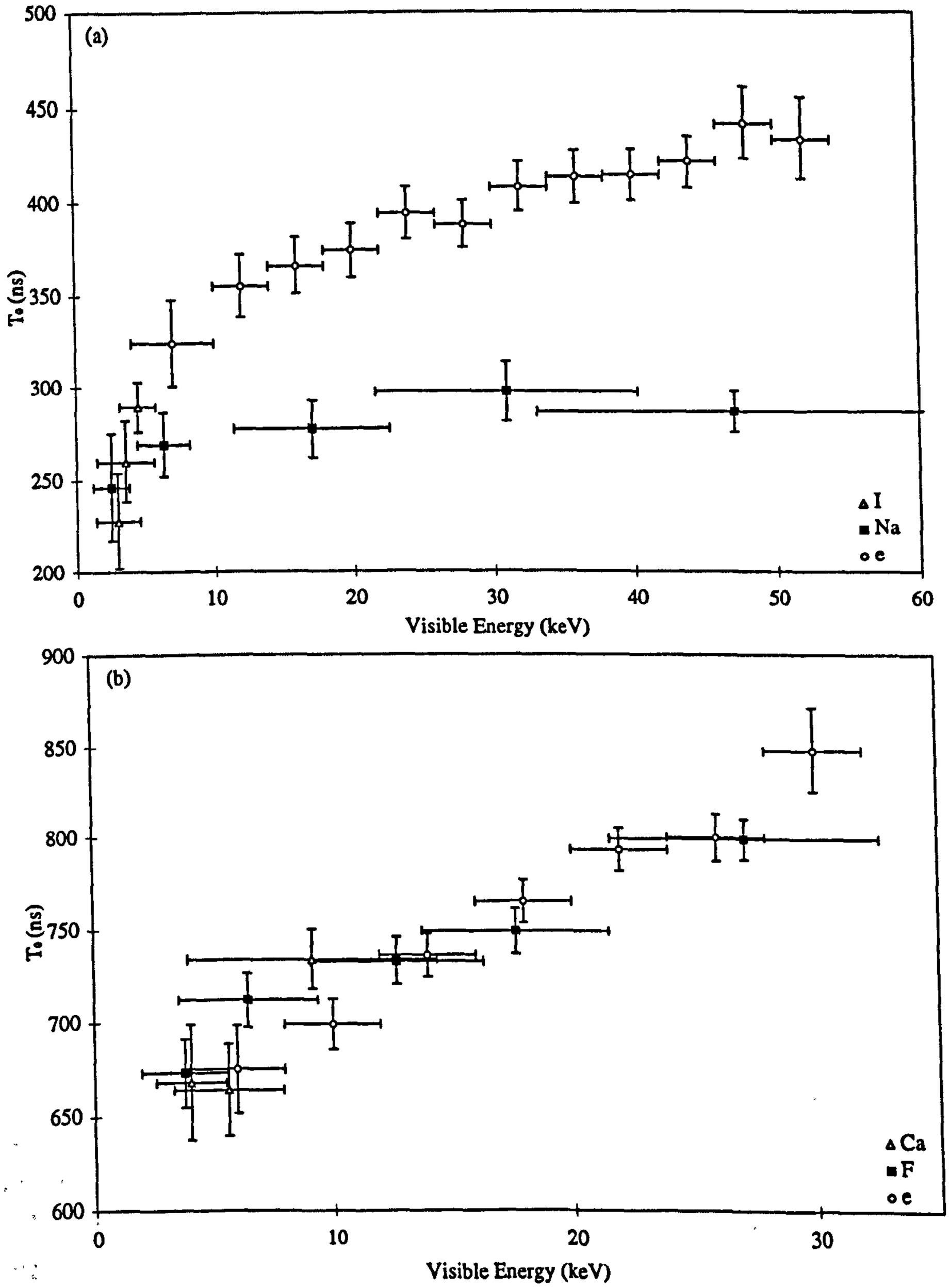

Figure 6.16: *The evolution of recoil mean times with visible energy. Figure (a) shows data taken with the NaI(Tl) crystal (Na, I and electron recoils) while Figure (b) shows data taken with the $CaF_2(Eu)$ crystal (Ca, F and electron recoils).*

provide the first indication of spin independent WIMP-nucleon interactions (§3.3.2).

In CaF_2(Eu) the T_0 for both nuclei and electrons rose from $\sim$ 660 ns ($E_v \sim 6$ keV) to $\sim$ 850 ns ($E_v \sim 30$ keV). In this case no evidence was seen for significant differences in T_0 for electron, Ca or F events. This implies that PSD in CASPAR must be performed using purely the amplitude ratio R_A as there is no additional discrimination power to be obtained from the use of the CaF_2(Eu) (slow component) decay time constant.

Explicit Pulse Shape Analysis

The lack of electron contamination in the event samples obtained with this technique allows direct examination of the scintillation pulse shapes in order to investigate deviations from pure exponentials. The photoelectron arrival time distributions for 10 keV $< E_v <$ 25 keV F and electron recoil events in CaF_2(Eu) are plotted in Fig. 6.17(b) and show no differences within errors. These can be compared with the equivalent distributions for 10 keV $< E_v <$ 20 keV Na and electron recoil events in NaI(Tl) plotted in Fig. 6.17(a).

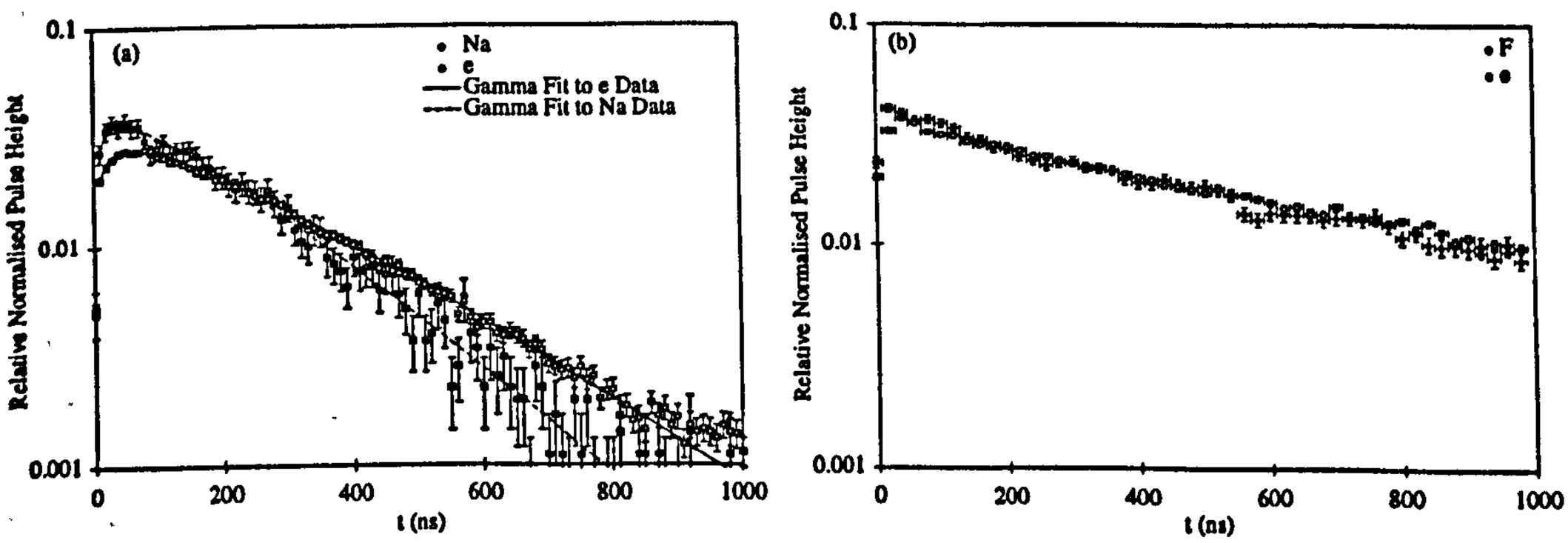

Figure 6.17: *Example photoelectron arrival time distributions. Figure (a) shows Na data taken with the NaI(Tl) crystal and $\theta = 45^o$ (10 keV $< E_v <$ 20 keV) while Figure (b) shows F data taken with the CaF_2(Eu) crystal and $\theta = 75^o$ (10 keV $< E_v <$ 25 keV). Both plots also include electron recoil data in the same energy ranges generated by Compton scattering of gammas from the ^{60}Co source. Also presented in Figure (a) are the results of pulse shape fits using gamma distributions (see text).*

Although the Na recoil pulse shape in NaI(Tl) is well approximated by a single exponential the electron recoil pulse shape appears to display a more pronounced flattening at the beginning of the pulse, as reported in [100, 171] and discussed in §4.2.2. Fits of gamma distributions (Eqn. 4.3) to both pulse shapes are plotted in

Parameter	*Electrons*	*Nuclei*
t_0(ns)	3 ± 2	5 ± 6
τ(ns)	281 ± 2	213 ± 4
b	1.25 ± 0.02	1.22 ± 0.06
χ^2/dof	0.437	0.647

Table 6.3: *Results of gamma distribution fits to the mean pulse shapes for electron and nuclear recoil events.*

Fig. 6.17(a) and these yield the parameterisations listed in Table 6.3. In both cases the fit is good (χ^2/dof 0.437 and 0.647 respectively) however few additional pulse shape differences beyond the exponential decay are highlighted by this technique (i.e. there are only small differences in the pulse shape parameter b).

6.5 Conclusions

Measurements have been performed with a prototype CASPAR detector of nuclear and electron recoil pulse shapes. The results indicate that the CASPAR technique has the potential to provide significant background discrimination in searches for WIMP dark matter.

Measurements have also been performed at low energy of relative scintillation efficiency and pulse shape for nuclear and electron recoils in NaI(Tl) and CaF_2(Eu). It is concluded that while the relative scintillation efficiencies of Na and I in NaI(Tl) remain constant with energy at 27.5 $\pm$ 1.8 % ($E_R > 4$ keV) and 8.6 $\pm$ 0.7 % ($E_R >$ 10 keV) respectively, those of Ca and F in CaF_2(Eu) show some evidence for a rise towards lower energy ($E_R < 100$ keV). Significant pulse shape differences between Na and electron recoil events were found in NaI(Tl), beyond those assumed in current UKDMC experiments. No differences in pulse MT between Na and I recoil events for $E_v < 5$ keV were seen however. No pulse shape differences of any kind were found in CaF_2(Eu).

Chapter 7

CASPAR WIMP Sensitivity

7.1 Introduction

Having determined the scintillation properties of a given dark matter target using neutron beam tests the results can be used to predict the energy spectrum of nuclear recoils due to WIMPs possessing different masses and nuclear interactions (Eqn. 3.65). With this data the WIMP sensitivity of the detector can then be determined. In this chapter this process is performed with simulated data from a prototype CASPAR detector. The chapter begins with a description of the IDL [143] Monte Carlo program which was written to simulate CASPAR (§7.2). There follows a description of the pulse shape analysis technique which was used to analyse the Monte Carlo data, and which will also be suitable for use with data from an operational detector (§7.3). Following on from this the results of a preliminary study aimed at optimising detector parameters are presented (§7.3.1) and then finally the results of a more detailed study of detector performance are discussed (§7.4).

7.2 The CASPAR Monte Carlo Simulation

7.2.1 The Grain Environment

Most of the results which will be presented in this chapter are based to a large extent upon the use of a crude Monte Carlo simulation of the nuclear and electron recoil response of the CASPAR detector. This simulation will now be described.

A significant portion of the Monte Carlo is devoted to modelling the morphology and spatial distribution of $CaF_2(Eu)$ grains in CASPAR. For simplicity the grains are assumed to be spherical in shape, although in practice a cubic morphology would be more accurate. The diameters d_i of the spheres are chosen from a normal

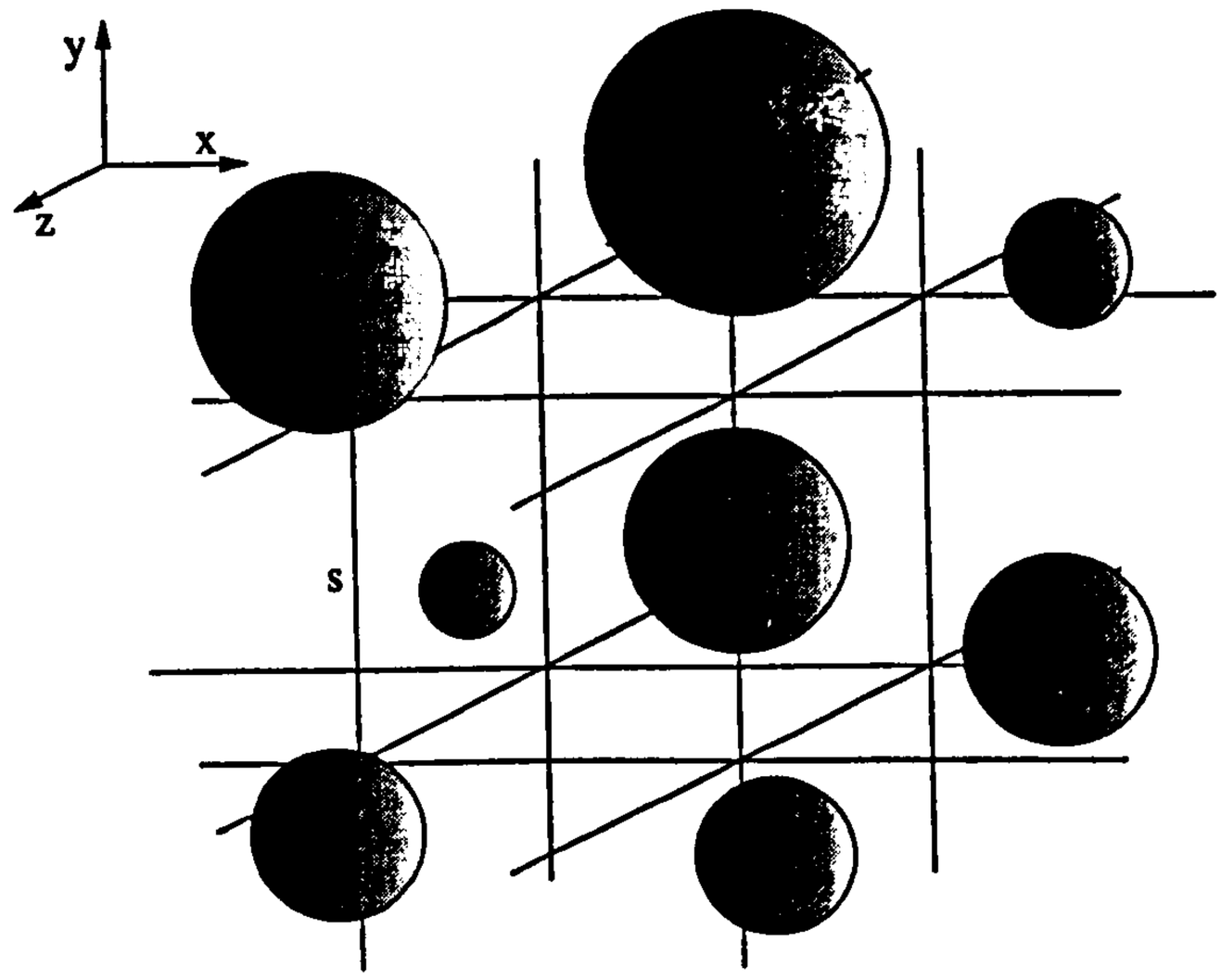

Figure 7.1: *A schematic diagram of the grid used in the CASPAR simulation. d_i is the diameter of grain i and s is the spacing of lattice. The centres of the grains are perturbed from the lattice centres so as to avoid equispacing.*

distribution of mean $\bar{d}$ and width $\sigma(d)$. The arrangement of the grains in the liquid scintillator (dioxan) is approximated by a uniform lattice of spacing $s = \sqrt[3]{\pi \bar{d}^3/6 f_p}$ determined from $\bar{d}$ and the grain volume packing fraction f_p. The positions of the grains are then perturbed such that their centres lie randomly within cubes of side $s - d_i$ centred upon each lattice point. The grain environment modelled in this way is sketched in Fig. 7.1.

Nuclear recoils are allowed to originate from any point within the grains but never from within the liquid scintillator, reflecting the poor spin dependent and spin independent coupling enhancement factors (§3.3) of C and H. Electron recoils are assumed to originate from Compton scattering of high energy gammas and hence to originate at the same rate per unit mass in both grains and liquid. This assumption is motivated by the proportionality of the atomic Compton scattering cross section to the number of atomic electrons [102]. In neutral atoms this is equal to the number of protons and consequently the bulk scattering rate for an absorber consisting of such atoms is proportional to the total mass of material, independent of the properties of the constituent nuclei.

7.2.2 Recoil Simulation

Once a recoil has been initiated it is tracked through the CASPAR medium. Straggling is assumed to be negligible on scales smaller than the grain diameter and each recoil is allowed to proceed in a straight line, losing energy at a rate determined by input dE_R/dx data, until it crosses a grain boundary. At this point a new velocity vector is chosen using a normal distribution of straggling angles θ. The entire process is then repeated until the recoil loses all energy. The technique is crude but fast and allows a large number (thousands) of recoils to be simulated in a matter of hours. In future work it may be preferable to replace this stage of the simulation with more accurate molecular dynamics code.

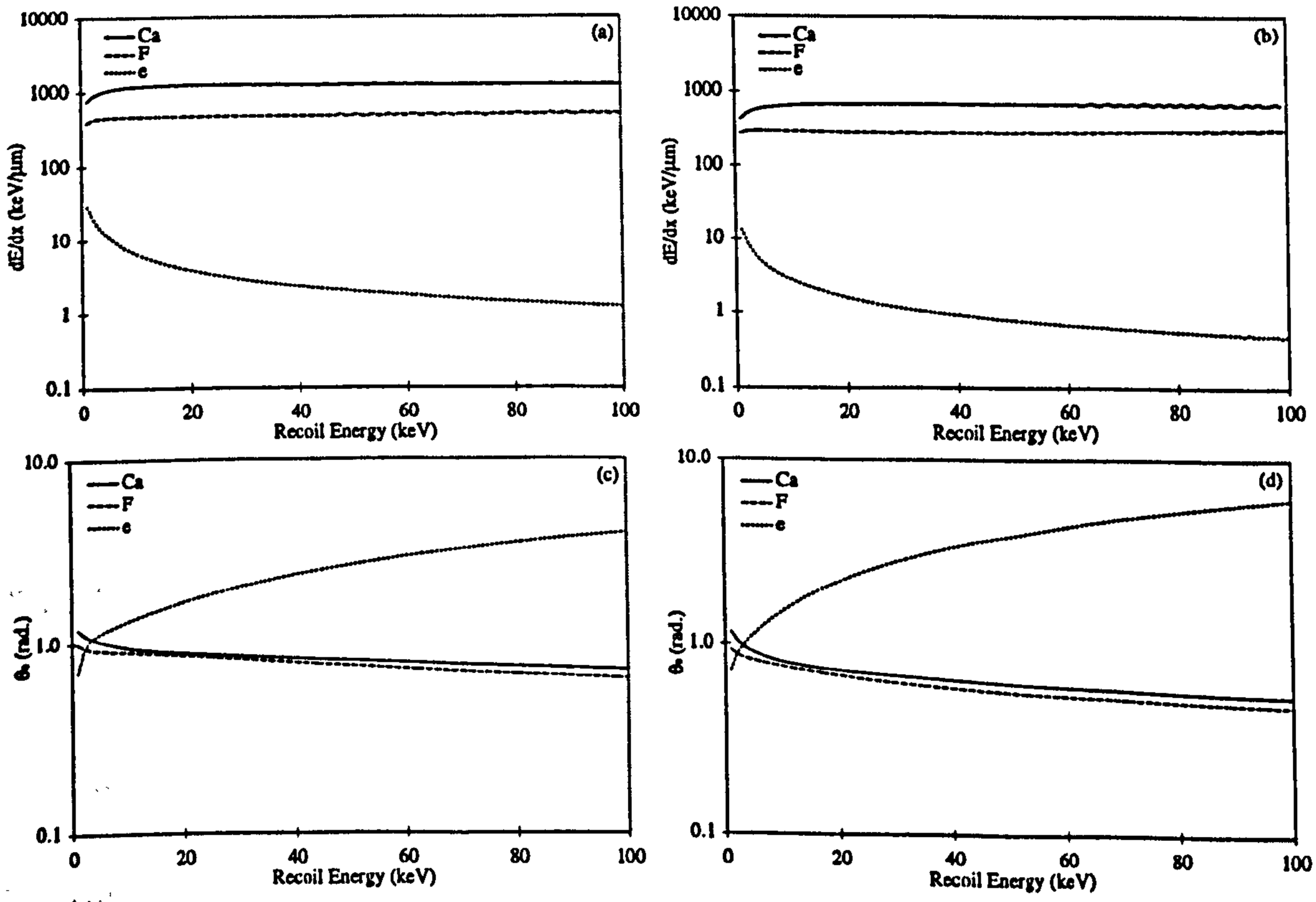

Figure 7.2: *The kinematic data used in the CASPAR simulation. Figures (a) and (b) show the dE_R/dx data for CaF_2 and Dioxan. Figures (c) and (d) show the θ_0 data for CaF_2 and Dioxan. Data from [93].*

Values for dE_R/dx and the rms straggling angle θ_0 used in this simulation must be input by hand. The data was supplied by a program developed by J.D. Lewin for a search for hypothetical heavy charged particles [172]. The data which was used is plotted in Fig. 7.2 for nuclear and electron recoils in CaF_2 and dioxan. Analytical functions (polynomials, logarithmic curves or power laws) were fitted to all data

used in the simulation in order to speed calculations. The data for nuclear recoils are in general similar but the electron data differs considerably both in magnitude and form. This reflects the differing energy loss processes at work, which lead the electron dE_R/dx to increase at low energies while that for nuclei decreases due to the gradual screening of nuclear charge (§3.5.2).

In the simulation the energy deposits in each nuclear path length interval are converted to visible energies using the nuclear recoil relative scintillation efficiencies $g_r(A, E_R)$. The values for Ca and F in CaF_2(Eu) are known from the results of §6.4 and are fitted analytically with a function

$$g_r(A, E_R) = \alpha(A)e^{\beta(A)/E_R}. \tag{7.1}$$

The fitted values of the constants α and β are listed in Table 7.1. The electron liquid equivalent (ele) energy deposited per unit path length is calculated using

$$dE_v = \left(1 - \frac{\beta}{E_R}\right) g_r dE_R, \tag{7.2}$$

for a given recoil energy deposit dE_R.

	Ca	*F*
α	0.047	0.087
β	15.64	6.182

Table 7.1: *The relative scintillation efficiency parameter values assumed in the CASPAR simulation.*

The nuclear recoil relative scintillation efficiencies of Ca and F in dioxan are not known and are difficult to measure directly[1]. The relative scintillation efficiency for C recoils in a similar liquid scintillator (NE224) has been measured in previous work however [168] and this value ($\sim$ 0.7 %) is here assumed for Ca and F on account of the similar energy loss characteristics of these nuclei. These relative scintillation efficiencies are assumed to be independent of energy and hence $dE_v = g_r(A)dE_R$.

The dE_v are summed to give the visible energy deposited by a recoil in each scintillator medium. Using the decay time constants of CaF_2(Eu) and dioxan scintillator a mean pulse shape is then constructed for the event. The former is assumed to be given by a fit to the data in Fig. 6.16(b) resulting in

$$\tau_{CaF2} = (6.95E_v + 634)\text{ns}. \tag{7.3}$$

[1]such measurements would probably require the use of a high energy ion beam

The dioxan scintillator decay time constant is assumed to be 4 ns (Table 4.1).

From the treatment of §3.6.1 it will be appreciated that the statistics of each scintillation pulse are predominantly those of the photoelectrons emitted from the photocathodes of the PMTs (the 'minimal information carriers'). Hence the physics of the light collection process can to a good approximation be modelled by considering only the mean numbers of photoelectrons detected in each PMT per keV of visible energy (pe/keV). The actual numbers of photoelectrons seen by each PMT are then determined through the use of a Poisson distribution to calculate the total number of photoelectrons and a binomial distribution to calculate the proportion of these observed in each PMT.

For each event the pulse shapes observed in each tube are calculated by normalising the mean pulse shape to unity and using it as a probability distribution from which to select photoelectron arrival times. Noise photoelectrons from thermal excitation of the photocathodes of the PMTs are also added at this stage by selecting small numbers of photoelectrons from a uniform time distribution. The two pulse shapes are then convolved with the PMT photoelectron response, assumed to be normal with width given by $\sigma_{pe} = 6.38$ ns [2]. Random electronic noise is then added to the signal to simulate pick up on long signal cables and the two pulse shapes digitised and passed to the analysis software. In this way the simulated data can be analysed in exactly the same manner as genuine data, with the Monte Carlo program merely replacing the code which reads in genuine data from disk.

7.3 CASPAR Pulse Shape Analysis

A pulse shape analysis procedure similar to that used in §6.3.2 was adopted for use with Monte Carlo CASPAR data in the studies described here. The assumption was made here of a buffer-less data acquisition system, with the data consisting of the digitised raw output pulses from the PMT anodes (Fig. 4.19). The pulses were thus integrated numerically in software prior to analysis. The high frequency components to the simulated random electronic noise were cancelled during this integration however the low frequency components caused a systematic drift in the integrated pulse height. This was eliminated by setting all raw digitisation points of absolute pulse height less than some value to zero before integration. This value (the 'zeroing level') was chosen such that it was several standard deviations greater than the amplitude of the noise fluctuations ($\sim$ 0.02 mV or 0.004 pe).

The energy of each event was extracted by summing the maximum pulse heights

[2] the value for an ETL 9265 PMT in Table 4.2

of the time integrated pulses in each PMT and then converting to energy using the assumed pe/keV value (1 /keV). The amplitude ratio defined in §6.3.2 was used as the discriminating variable and was determined through the use of a log-likelihood fit to the photoelectron arrival times (relative to the first photoelectron). The photoelectron arrival times were determined by calculating the times at which the integrated PMT pulses crossed the equivalent integrated photoelectron levels given by $(i+0.5)V$ $(i=0,\ldots,n-1)$ for n photoelectrons of integrated pulse height V ($V=5$mV). This procedure is identical to that described in §6.3.2 and §6.4.2.

In an operational detector genuine scintillation pulses are mixed in with noise events. These can arise from sources such as event pile up, thermal photoelectrons, PMT breakdown and Čerenkov light in the light guides and PMTs from through going muons or electrons [173]. Such noise events can be removed by considering the properties of the pulses in the two PMTs. Noise pulses are in general highly asymmetric and by cutting on the difference or ratio of pulse parameters (mean photoelectron arrival time T, number of photoelectrons, arrival time of first photoelectron etc.) the noise pulses can be removed with high efficiency for little loss of scintillation events. This is discussed in more detail in §8.3.2. In the analysis of simulated CASPAR data the same noise cuts were applied as were developed for use with NaI(Tl) data so as to simulate the small resultant reduction in event identification efficiency. The noise events themselves could not be simulated as their origins are not yet fully understood. Given the high efficiency with which these events can be removed from NaI(Tl) data however (§8.3.2) it was assumed here that the cuts are $\sim$ 100% efficient.

7.3.1 Optimisation of Detector Parameters

7.3.2 Technique

Before investigating the WIMP sensitivity of CASPAR the optimum values of the parameters $\bar{d}$ and f_p were determined. A series of nuclear and electron recoil detector simulations were performed with different assumed grain diameters and volume packing fractions. Monoenergetic low energy recoils were used ($\sim$ 10 keV visible energy) and the events were binned coarsely in amplitude ratio to minimise the statistics required. One hundred events of each class (nuclear and electron recoil) were generated for each parameter combination and the amplitude ratio histograms analysed using the binomial technique (§3.7.2) to extract nuclear recoil signal limits S_n. These limits were then scaled by $1/\sqrt{t}$ to give the limits expected from 1 year's data from a 400 cm^3 prototype CaF_2(Eu) detector with a background event rate of

2 /keV/kg/day.

7.3.3 Origin of Electron Recoils

The electron recoils used in this study were assumed to originate entirely from within the CaF_2(Eu) grains. This assumption is the most pessimistic possible and was used because at large grain diameters the simulation of data events becomes inaccurate owing to differences in origin between these and Compton recoil events (used for the reference distributions). This point will now be discussed in more detail.

At large grain diameters electron recoils originating in the grains may be expected to generate similar pulse shapes to nuclear recoils, which are hence impossible to reject using PSD. Electron recoils originating in the liquid scintillator however generate pulses consisting of a single fast component which can be rejected with almost 100 % efficiency. Thus the simulation of a detector with large grain diameters is equivalent to a simulation of two detectors, one sensitive to WIMP scattering and one not, which are exposed to the same background and which produce a nuclear recoil signal limit from the difference in detector count rates. While this may be reasonable in principle, in practice the background within such a detector cannot be adequately modelled by Compton scattering alone owing to the presence of low energy internal beta and gamma decays. Thus the reference R_A distributions for a real detector containing large grains, generated by Compton calibration, do not match the R_A distributions of background events, even in the absence of a signal. Consequently when simulations are performed assuming large grain diameters and background events modelled by Compton scattering, the nuclear recoil signal limits obtained are too optimistic.

In this preliminary study the sensitivity of detectors containing large grains was explicitly investigated. Therefore the pessimistic scenario of electron recoils originating entirely from within grains was assumed in order to provide a meaningful comparison with the results for small grain diameters. The critical diameter at which the Compton simulation begins to fail to adequately model data from a realistic detector depends upon the origins of the actual background events and the magnitude of the nuclear recoil signal limit which is set. In all subsequent simulations (with relatively small grain diameters) this critical diameter was assumed to be large compared with the actual grain diameter and thus background modelling with Compton events was used.

7.3.4 Results

The S_n values obtained using the technique described above are plotted in Fig. 7.3 as functions of $\bar{d}$ and f_p. The errors on the data points are Poissonian simulation errors coming from the limited event statistics. Optimum performance was obtained with $\bar{d}$ in the range $\sim$ 0.3 - 1.0 μm, which represents a compromise between poor nuclear recoil identification efficiency ϵ for small grain diameters (nuclear recoils escaping from grains) and poor electron recoil rejection for large grain diameters (electron recoils entirely within grains). Similarly the optimum packing fraction was $f_p \gtrsim 0.1$, although realistically the detrimental effect of a large grain volume packing fraction on light collection makes smaller values preferable.

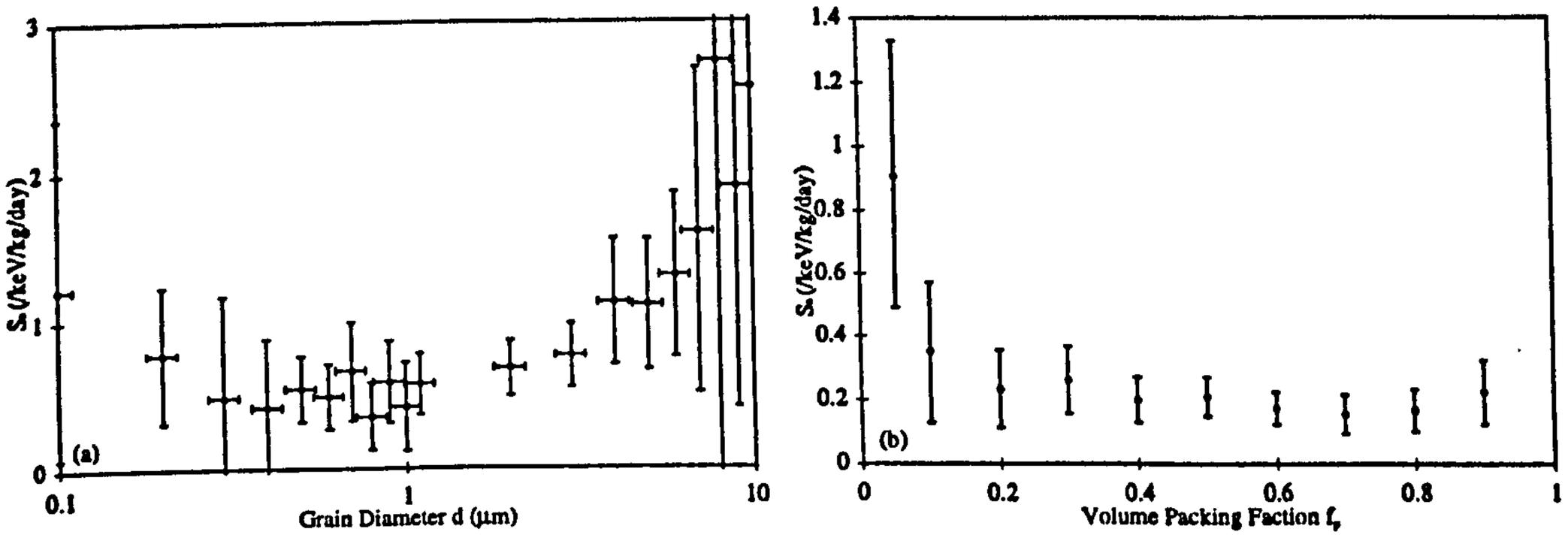

Figure 7.3: *The evolution of the nuclear recoil signal limit S_n as a function of detector parameters. Figure (a) shows the evolution with mean grain diameter $\bar{d}$ while Figure (b) shows the evolution with grain volume packing fraction f_p. The nuclear recoil signal limit is minimised when most nuclear recoils remain inside the grains while most electron recoils pass through the liquid. The error bars on the points (statistical) become larger at extreme parameter values because of poor event identification efficiencies for nuclear or electron recoils.*

7.4 Detector Sensitivity

7.4.1 Nuclear Recoil Signal Rate

The detector simulation was used to generate large statistics event samples with which to assess the sensitivity of CASPAR to WIMPs. Parameter values of $\bar{d} = 0.8$ μm and $f_p = 0.1$ were chosen in accordance with the findings of the previous section. In contrast to the previous study, electron recoils were generated in both grains and

liquid scintillator at the same rate per unit mass and at all visible energies in the range 0 - 25 keV. As before a small 400 cm^3 detector volume was assumed along with a live time of one year leading to a total target mass of 120 g $CaF_2(Eu)$ and a detector exposure $\sim$ 44 kg.days. The assumed visible energy threshold was 5 keV (5 pe).

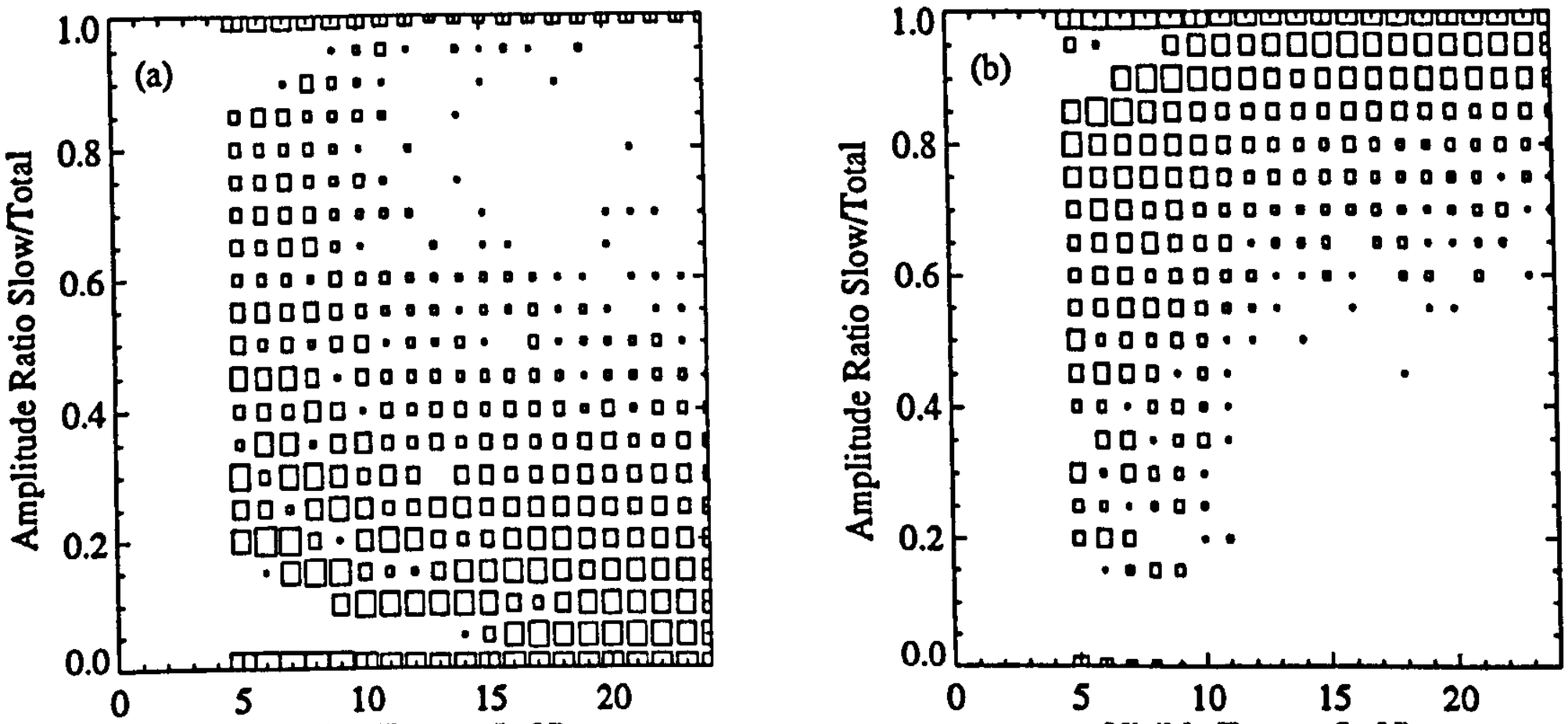

Figure 7.4: *Predicted amplitude ratio / visible energy distributions from the CASPAR simulation. Figure (a) shows electron recoil events while Figure (b) shows nuclear recoil events. For electron recoils the distribution of events is concentrated in the region* $R_A < 0.5$ *while for nuclear recoils the distribution is concentrated in the region* $R_A > 0.5$ *(c.f. Fig. 6.7). At low visible energies the distributions become quantised due to photoelectron statistics. In both figures the z axis (box size) is logarithmic.*

The χ^2 fitting technique was used for the discrimination analysis (§3.7.3). Nuclear and electron recoil reference distributions each containing 10000 events were generated from uniform energy distributions (Fig. 7.4). 4000 background electron recoil events were then generated, also with a uniform energy distribution (matching the background spectrum seen in NaI(Tl) [88]). A χ^2 fit to the background with the weighted sum of the normalised reference distributions (§3.7.3) was then performed. The measured numbers of nuclear recoil events in each energy bin (Fig. 7.5) were assumed to be consistent with zero and the errors were converted into the nuclear recoil sensitivities expected after one year of operation. This conversion was performed by assuming an electron recoil rate of 2 /keV/kg/day and a Poissonian

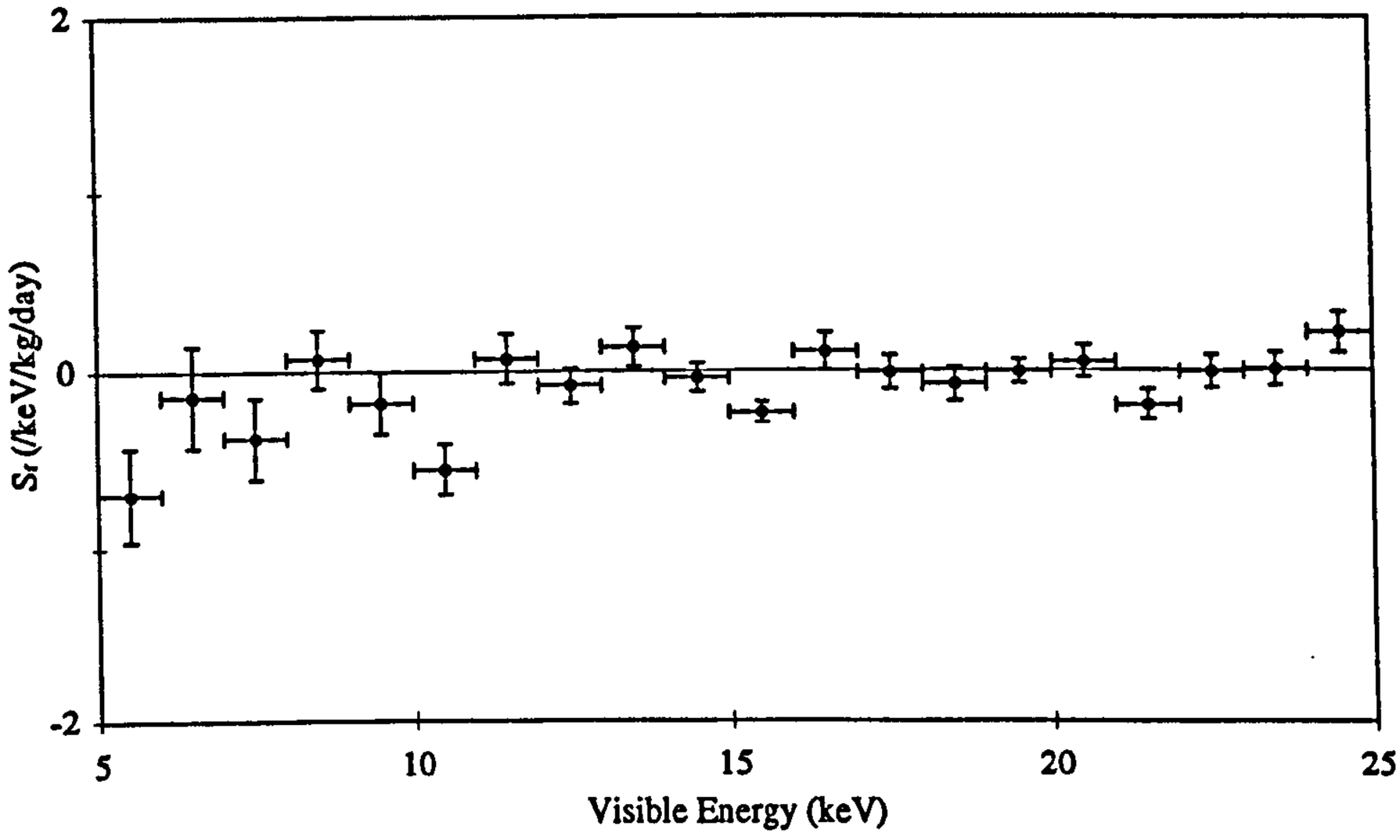

Figure 7.5: *Predicted measured nuclear recoil rates in the absence of a signal from the CASPAR simulation.*

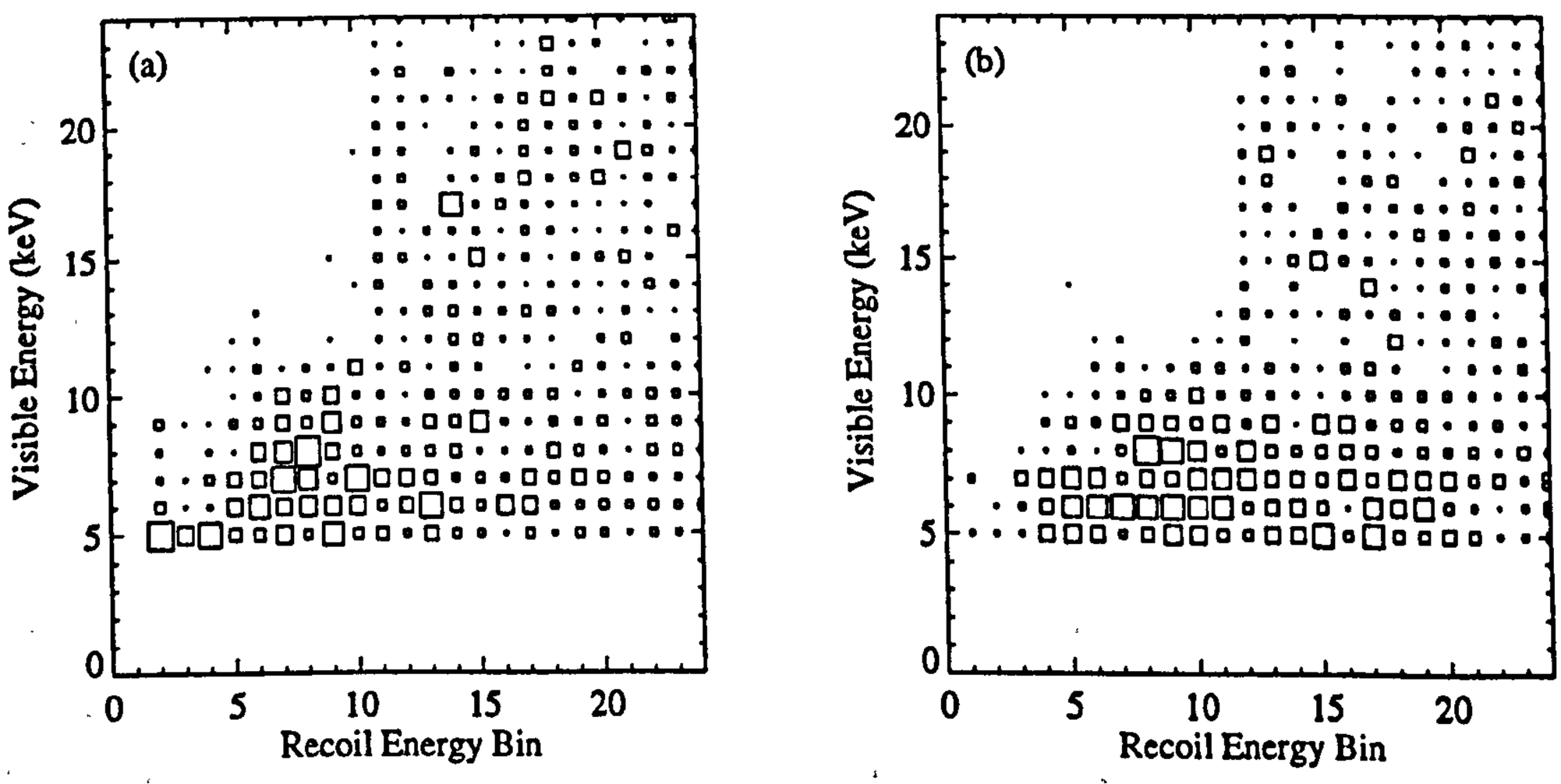

Figure 7.6: *CASPAR nuclear recoil response matrices. Figure (a) shows the response matrix for Ca recoils while Figure (b) shows the response matrix for F recoils. The nuclear recoil energy bins are of equal width (1 keV) in visible energy in CaF_2. This simplifies the process of calculating the WIMP induced nuclear recoil visible energy spectrum.*

improvement in sensitivity (rate) proportional to $1/\sqrt{t}$.

7.4.2 Nuclear Recoil Response Matrix

The previous results were now used to estimate the sensitivity of CASPAR to a nuclear recoil WIMP signal. To simplify this process a detector response matrix was constructed by generating 100 nuclear recoil events for each recoil energy bin (Fig. 7.6). The visible energy distribution of events passing the trigger threshold and noise cuts for each recoil energy was calculated and then normalised to 1 % of the total number of accepted events for that recoil energy to account for finite event identification efficiency. The ensemble of these distributions (the response matrix M) was then used to convolve the WIMP induced nuclear recoil energy spectrum with the detector and target response to give the observed visible energy spectrum:

$$\frac{dR}{dE_v} = \sum_{E_R} M(E_v, E_R).G_r(A, E_R).\frac{dR}{dE_R}. \tag{7.4}$$

The calculated response matrices for Ca and F recoils are plotted in Fig. 7.6. The depletion in events at low visible energies is due to the trigger threshold while the spread in visible energies is due to Poissonian photoelectron statistics and variations in light emission caused by recoils passing into the liquid scintillator, where g_r is small. One disadvantage of this general approach is that it cannot take into account systematic losses of nuclear recoil events due to the fitting process however these are expected to be small (§8.5.2).

7.4.3 Analysis and Results

Nuclear recoil energy spectra were calculated for WIMPs with twelve different masses interacting with both Ca and F nuclei via both spin dependent and spin independent interactions. The energy spectra were next convolved with the detector and target responses using the response matrices derived above. This data was then used with the nuclear recoil signal limit of Fig. 7.5 and the technique of §3.7.3 to determine the total WIMP nucleon cross section sensitivity. A flow chart of the entire process, from Monte Carlo event generation to the calculation of the detector sensitivity can be found in Fig. 7.7.

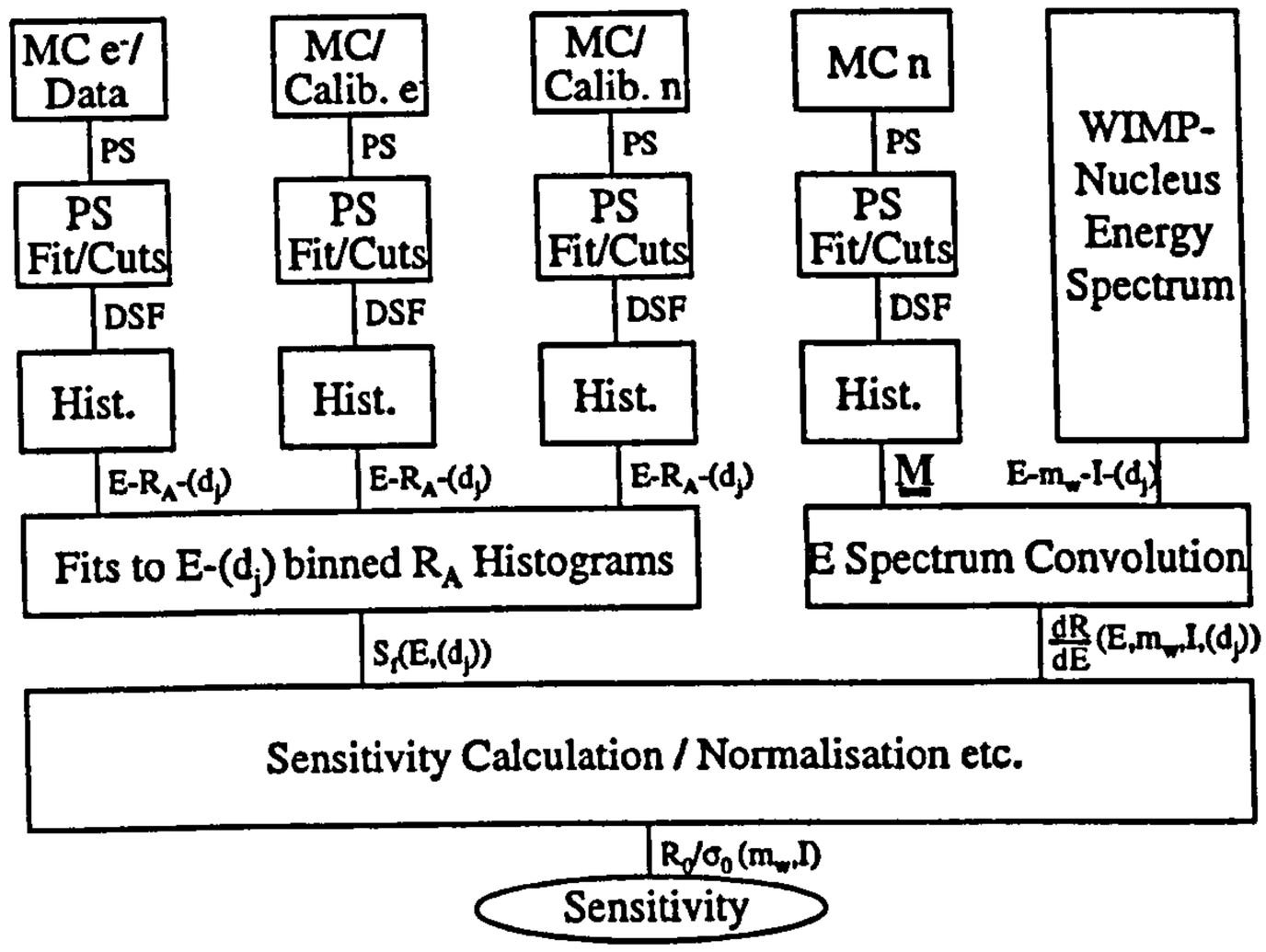

Figure 7.7: *A flow chart of the analysis procedure.*

The results are shown in Fig. 7.8 (overleaf). The normalisations of Fig. 5 in [88] are largely used save for the spin independent nuclear coupling enhancement factors I_{si} which are here assumed to be given by A^2, as is appropriate for SUSY neutralino WIMPs. Results from a UKDMC NaI detector ([88] and Fig. 3.2) are also plotted in Fig. 7.8, having been recalculated with the new form factors and spin dependent coupling enhancement factors discussed in §3.3.1 and §3.3.2.

Fig. 7.8(a) shows the raw R_0/r sensitivity curve of CASPAR without taking into account spin dependent coupling enhancement factors. Due to the modest mass of the CASPAR detector its performance is predicted to be poorer than that of the 6kg NaI(Tl) detector used to obtain the results of [88]. Fig. 7.8(c) shows the same results calculated in terms of cross section and plotted taking into account the spin dependent coupling enhancement factors of the different nuclei. The large enhancement factor for F nuclei (Table 3.3) causes even the sensitivity of a small CASPAR detector to be superior to that of the 6 kg NaI(Tl) crystal (1003.4 kg.days).

Figs. 7.8(b) and 7.8(d) show the SUSY normalised sensitivity curves of CASPAR to WIMPs coupling via spin independent interactions. These curves demonstrate that for these interactions the performance of CASPAR is no better than that of the 6 kg NaI(Tl) detector for the small CaF_2 mass assumed. This is due to the absence of high A nuclei in CaF_2(Eu), although this effect is partially ameliorated by the superior discrimination provided by CASPAR at low visible energies.

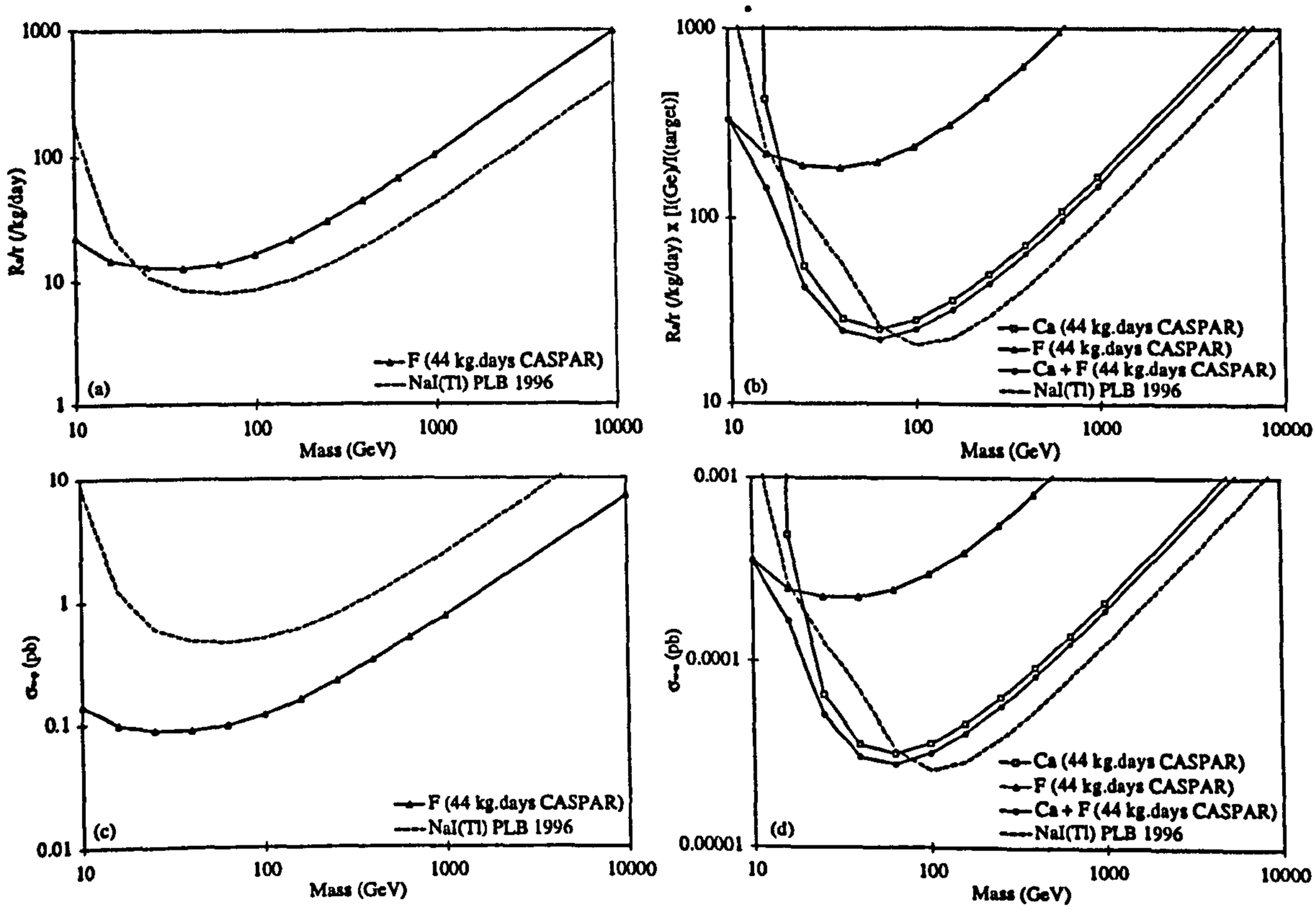

Figure 7.8: *Predicted WIMP-nucleon sensitivities from the CASPAR simulation. The normalisations are similar to those used in Fig. 5 of [88]. Figure (a) shows the 'raw' sensitivity to R_0/r for spin dependent interactions not including the coupling enhancement factor I_{sd}. Figure (b) shows the sensitivity to R_0/r for spin independent interactions normalised to the value for a Ge target and assuming $I_{si} = A^2$ (SUSY neutralino). Figure (c) shows the sensitivity to the spin dependent WIMP-proton cross section σ_{w-p} including model dependent SUSY coupling enhancement factors. Figure (d) shows the sensitivity to the spin independent WIMP-neutron cross section σ_{w-n}. Also plotted are the suitably normalised results from [88] (dotted lines).*

7.5 Conclusions

A Monte Carlo simulation of the CASPAR detector has been used to optimise several detector parameters. The results suggest that the optimum grain diameter lies in the range 0.3 - 1.0 μm and that the optimum grain volume packing fraction lies in the range $f_p > 0.1$. Small values of f_p are however favoured by light collection considerations.

The performance of an optimised prototype CASPAR detector has been assessed by making reasonable assumptions about electron recoil background rate (2 /keV/kg/day) and light collection (1 pe/keV). The results suggest that the WIMP-nucleon cross section sensitivity of a 400 cm^3 detector running for 1 year with 120 g CaF_2(Eu) ($f_p = 0.1$) should be superior to that of a large 6 kg NaI(Tl) detector for spin dependent interactions. The sensitivity to spin independent interactions is less good owing to the low A of Ca and F nuclei.

Chapter 8

NaI(Tl) Analysis

8.1 Introduction

The simulation and analysis techniques described in §3, §4, §6 and §7 have been applied by this author to data from the operational UKDMC NaI(Tl) dark matter detector referred to as DM46. A comparative study was performed of the relative merits of the mean time (MT) and likelihood ratio (LR) techniques (§4.2.2), and the results used to investigate the properties of a population of anomalous nuclear recoil like events which had previously been discovered within the data [174]. In this chapter the DM46 detector is described (§8.2) followed by details of the analysis beginning with corrections to the raw digitised scintillation pulses and preselection cuts used to remove spurious noise events (§8.3). The MT and LR analysis techniques themselves are then described in detail (§8.4). The results of these analyses are presented and error analysis using Monte Carlo techniques outlined (§8.5). Annual modulation in the rate of residual anomalous events is then investigated (§8.6). Finally different interpretations of these anomalous events in terms of background or signal are discussed in §8.7.

8.2 The DM46 Detector

The DM46 detector is mounted in a water shielding tank (§4.4) and contains a 5.2 kg 1000 ppm Tl Hilger crystal viewed by two buffered ETL 9390 5" PMTs arranged as in Fig. 4.11. The data acquisition system used is also that sketched in Fig. 4.11. Data from this crystal was used to set the limits published in [88]. Since that time the detector has been completely overhauled to improve light collection to an estimated 3.04 pe/keV. Running with the improved system commenced in October 1996 and apart from brief breaks in operation for maintenance and power outage continued

until August 1997, when the failure of a PMT caused the run to be aborted. The replacement of the PMT caused the properties of the detector to change and hence data taken after this date is not considered here.

The detector enclosure was temperature stabilised to avoid systematic drifts in the effective mean of the decay time constant estimator (T_0 - §4.2.2). The temperature was monitored continually with thermocouples attached to the Cu can encapsulating the crystal and during the course of normal data taking was found to vary by no more than $\pm$ 0.1 ^{o}C from the target temperature. Mean operating temperatures in the range 8^{o}C - 12^{o}C were chosen as a result of extensive tests [174] in order to maximise the intrinsic PSD and light output of the NaI(Tl). Data taken around the time of maintenance and power outages, when the crystal temperature was not under control, was not used in this analysis.

During data taking regular calibrations were performed using an automatic slow control system. This operated motorised source droppers which lowered calibration sources into the water tank down to the level of the detector. For electron recoil pulse shape calibration a 1 μCi ^{60}Co source was lowered for 5 hours per day, while for energy calibration a 1 μCi ^{137}Cs source was exposed to the detector for 1 hour per week. Events taken at the time of these automatic calibrations were stamped **CCAL** ('Compton CALibration') and **ECAL** ('Energy CALibration') as appropriate, while background data was stamped **DATA**. These stamps were used later to separate the different classes of data. The DAQ system automatically changed the gain of the DSO for high energy (662 keV) **ECAL** events so that they could be digitised correctly. The pulse heights of these events were subsequently analysed and the distributions fitted with normal functions in order to determine the detector energy response as a function of time [175].

Nuclear recoil pulse shape calibration was also performed, although less frequently than the electron recoil calibration. During the course of the acquisition of the data analysed here one calibration was performed in June 1997. A 1 mCi ^{252}Cf fission source was suspended next to the detector in the tank and data acquired over the course of 2 days. A further neutron calibration was performed in March 1998, however by this stage the detector characteristics had changed as a result of the replacement of the PMT. That data is consequently also not considered here.

371126 valid **DATA** events lying in the visible energy range 2 - 80 keV were collected over the course of 166.8 days live time (867 kg.days). The **CCAL** data lay in the same energy range and consisted of 588043 valid events. The neutron calibration data (hereafter referred to as **NCAL** data) again lay in this energy range and consisted of a total of 6500 valid events. The small number of **NCAL**

events presented problems when attempting to identify the nature of non-electron recoil events in the DATA sample however this was not a problem in the initial stages of the analysis where only a deviation from the electron recoil pulse shape distribution was sought.

8.3 Preliminaries

8.3.1 Pulse Shape Correction

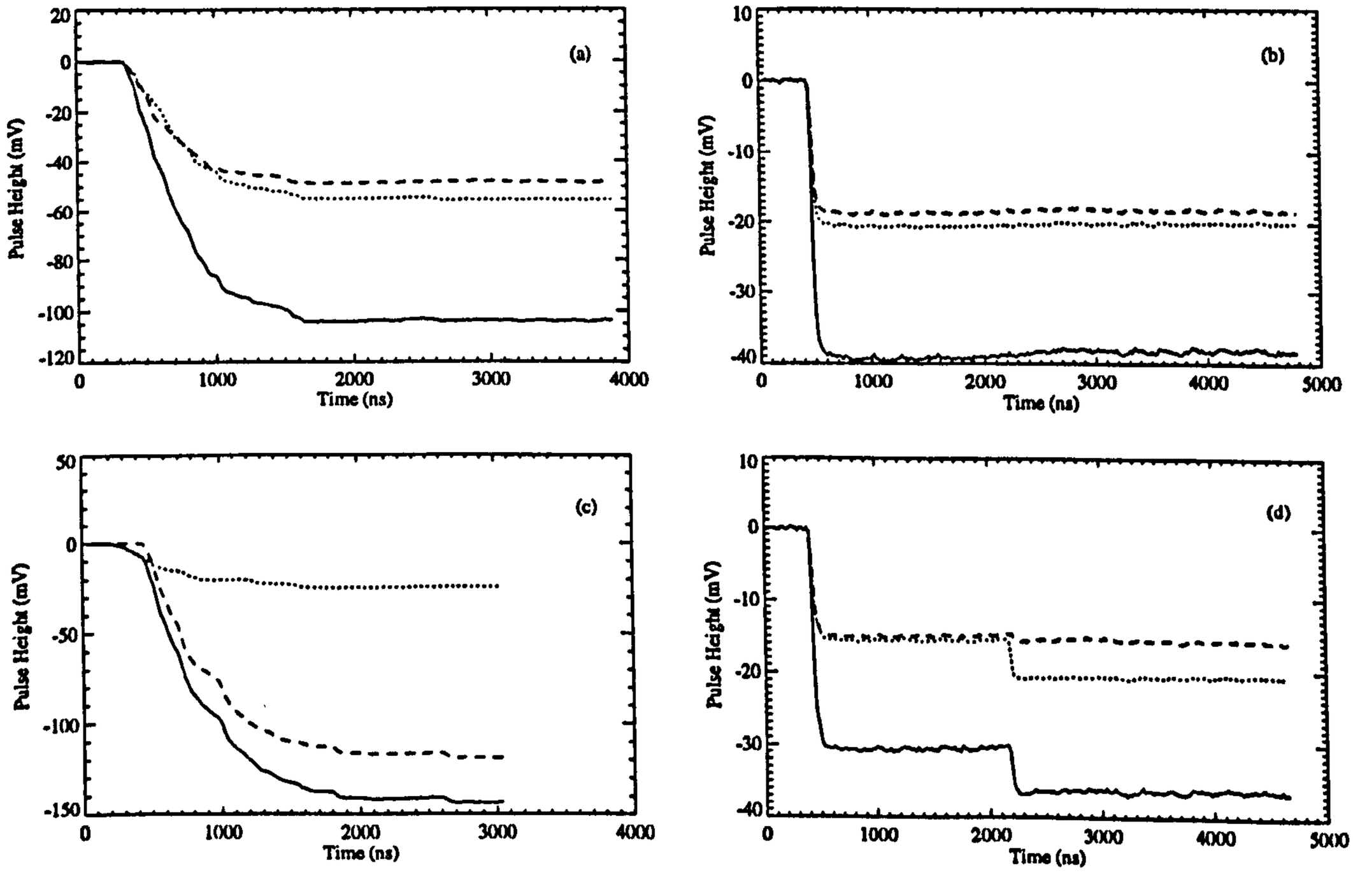

Figure 8.1: *Typical DM46 events. Figure (a) shows a candidate scintillation pulse which passes all noise cuts. Figure (b) shows a fast noise pulse of the type used to calibrate the recovery time of the buffer. Figure (c) shows a typical noise pulse displaying asymmetry in pulse start time, pulse mean time and pulse height between PMT channels. Figure (d) shows a typical 'stepped' noise pulse. All these noise events were successfully rejected by preselection cuts. In all cases dashed and dotted lines represent buffer corrected signals from individual PMTs while full lines represent total buffer corrected signals.*

In order to properly correct for the finite recovery time of the buffers used on the DM46 detector (τ_B - §4.3.3) this quantity was measured as accurately as possible for both PMTs. Typical NaI(Tl) scintillation pulses (Fig. 8.1(a)) prevent the buffer recovery behaviour from being seen clearly and so fast step function pulses were used. This was done by selecting raw noise (Čerenkov, breakdown etc.) events with pulse shapes with mean time $T < 20$ ns (Fig. 8.1(b)).

If a pulse in a particular PMT satisfied the selection criterion then it was fitted using a χ^2 routine with a function

$$v(t) = -Ae^{-(t-t_0)/\tau_B} \tag{8.1}$$

with free parameters A, t_0 and τ_B. In this way the mean τ_B of a large number of such pulses was determined. The results are presented in Table 8.1 and are consistent for the two PMTs to within errors.

Channel	τ_B (μs)
1	43 ± 16
2	41 ± 12

Table 8.1: *The results of the calibration of the buffer recovery time using fast noise pulses ($T < 20$ ns).*

8.3.2 Event Selection

Preselection cuts were devised aimed at removing the majority of non-scintillation noise events. These cuts will now be described in detail.

Cut C1: Absolute Pulse Mean Time

Noise events similar to those used in the previous section to determine τ_B were removed from the data during analysis. The simplest method of doing this was to cut on the pulse mean time in each PMT thus removing fast events (Fig. 8.1(a)), here defined as having $T < 100$ ns.

Cut C2: Absolute Pulse Amplitude

A further simple cut was used to strengthen the on line trigger requirement of ≥ 2 pe in each channel. There is a non-zero Poisson probability P given by

$$P = (1 - P(0) - P(1))^2$$

$$\approx \frac{(RT_{win})^4}{4} \tag{8.2}$$

that in a coincidence time window of width T_{win} (here ~ 5 μs) two PMTs with dark count rates R will each observe ≥ 2 photoelectrons. Additional non-Poissonian effects such as NaI(Tl) phosphorescence can also create photoelectrons which satisfy this requirement. Because the governing distributions (Poisson or otherwise) are strongly peaked at low numbers of photoelectrons many of these single photoelectron pile up pulses were removed by simply requiring ≥ 3 pe (~ 1 keV E_v) in each channel. This requirement was subsequently found to be too loose and a further cut requiring events to possess total visible energy ≥ 6 keV was employed.

Cut C3: Relative Pulse Amplitude

Noise events typically have structures quite unlike those of scintillation pulses when examined in detail. In the case of 'physical' events (Čerenkov and breakdown) the origin of the event is quite asymmetric in the detector and hence a large signal may be seen in one PMT while only a small signal is seen in the other. This indicates that a cut should be made on the relative numbers of photoelectrons detected by the two tubes.

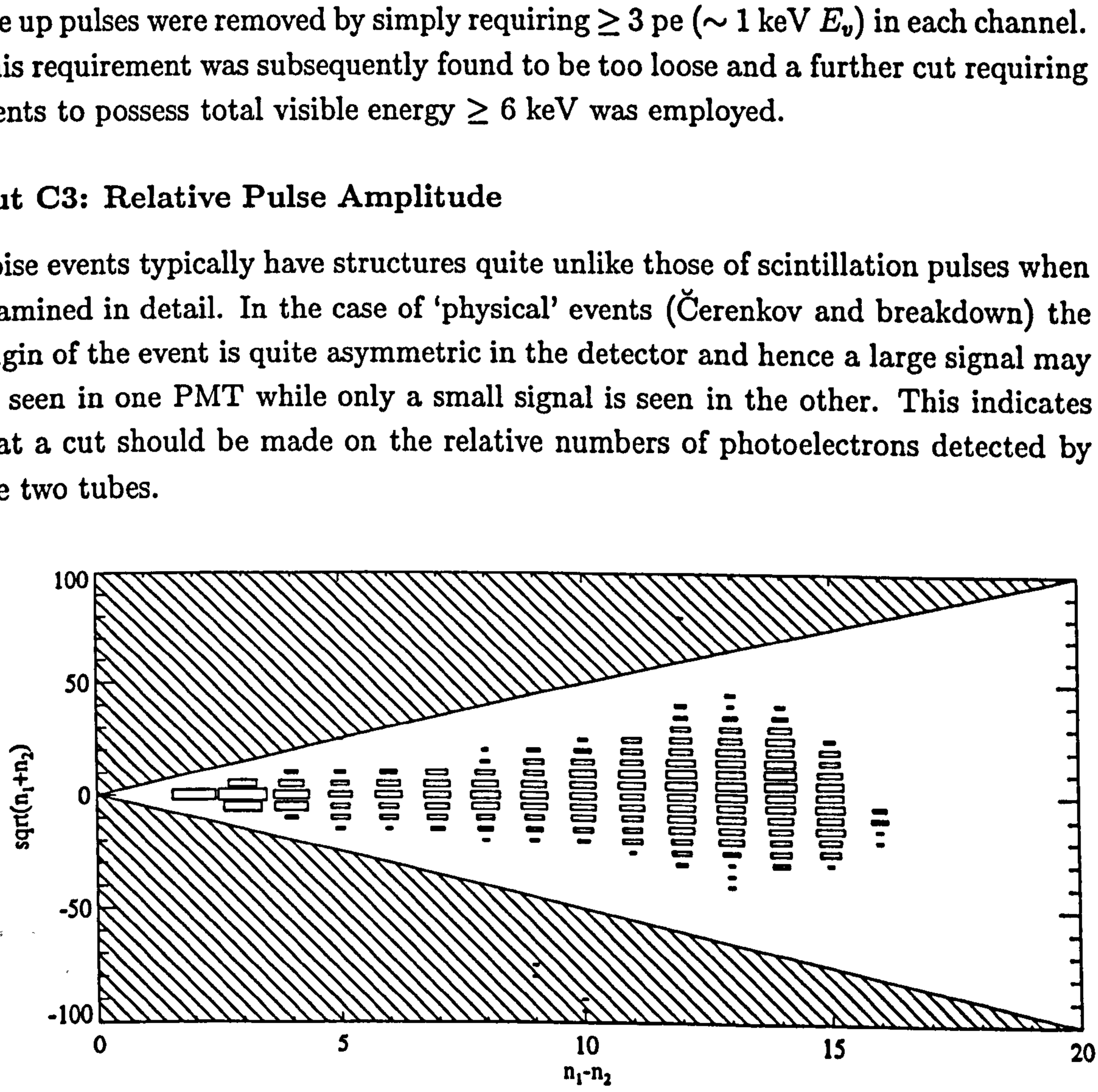

Figure 8.2: *Cut C3. The difference in numbers of photoelectrons in each PMT plotted against the theoretical standard deviation. The events in the hatched regions were rejected by the cut. The data is from the DM46 detector.*

The relative photoelectron number cut was based upon the binomial statistics of

the photoelectron distribution between the two tubes. The standard deviation in the number of photoelectrons n seen by a given PMT for repeated identical recoil events is $\sqrt{n}$. The total standard deviation for two PMTs may then be approximated by $\sqrt{n_1 + n_2}$ for n_1 and n_2 photoelectrons seen in each PMT for a given event. Choosing to cut loosely at 5 standard deviations away from the mean then implies for valid events

$$|n_1 - n_2| < 5\sqrt{n_1 + n_2}. \tag{8.3}$$

This cut is displayed graphically in Fig. 8.2.

Cut C4: Relative Pulse Start Time

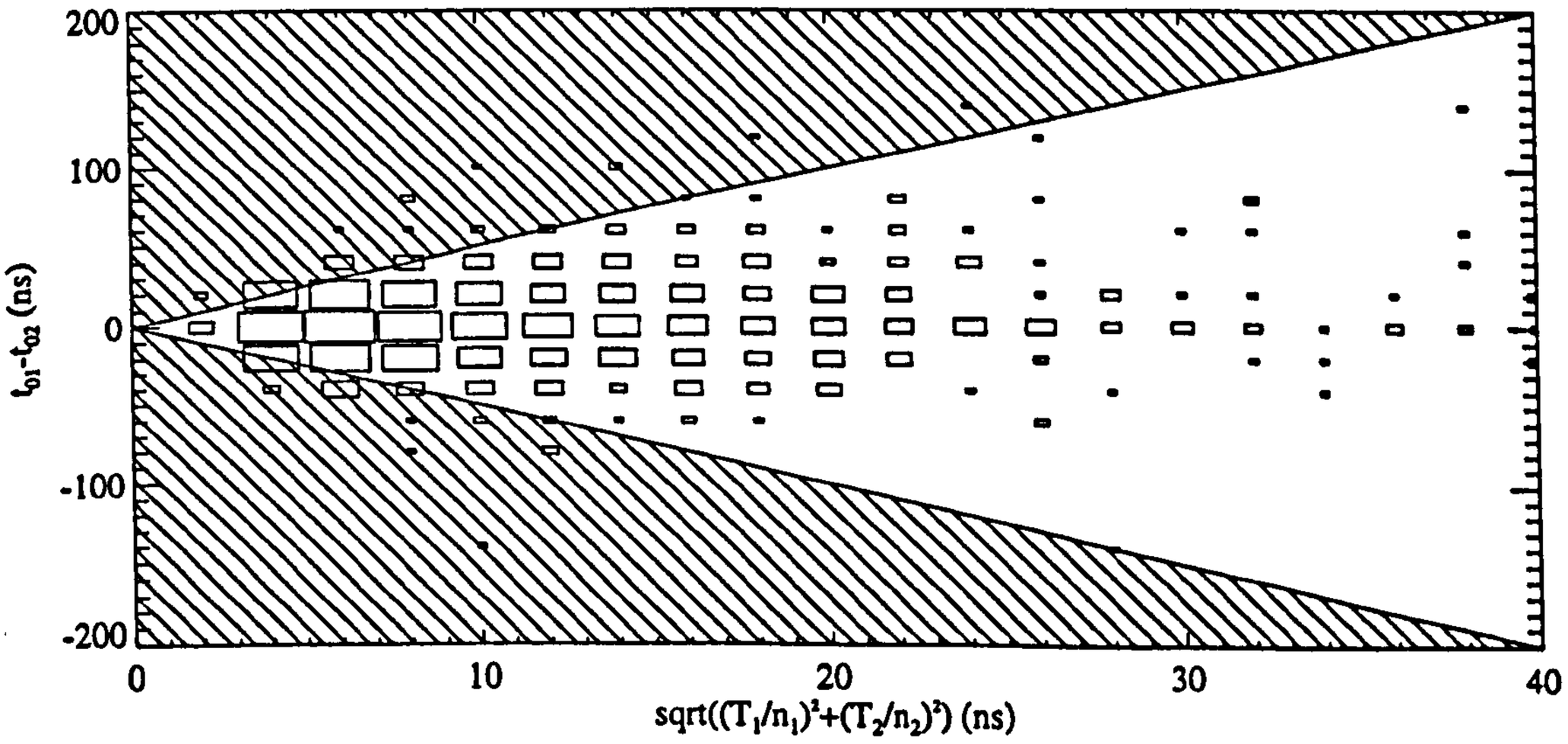

Figure 8.3: *Cut C4. The difference in pulse start time for each PMT plotted against* $\sqrt{(T_1/n_1)^2 + (T_2/n_2)^2}$. *The events in the hatched regions were rejected by the cut. The data is from the DM46 detector.*

A further consequence of asymmetry for noise events is that the pulses do not begin at the same time in the two PMTs. The measurement of this time difference was complicated by low photoelectron statistics, because for progressively smaller numbers of photoelectrons the first photoelectron occurs on average further from the start of the pulse (§6.4.2). In fact by considering $P(t_0 = t \cap t_{i\geq 1} > t)$ it may be shown that for an n photoelectron exponential pulse the mean arrival time t_0 of the first photoelectron is τ/n after the start of the pulse. The variance in this value is

τ^2/n^2. A cut was defined for valid events by

$$|t_{01} - t_{02}| < 5\sqrt{\frac{T_1^2}{n_1^2} + \frac{T_2^2}{n_2^2}}, \tag{8.4}$$

for first photoelectron arrival times in each PMT t_{01} and t_{02} and mean times T_1 and T_2 respectively (equating T with τ). This cut is displayed graphically in Fig. 8.3.

Cut C5: Relative Pulse Mean Time

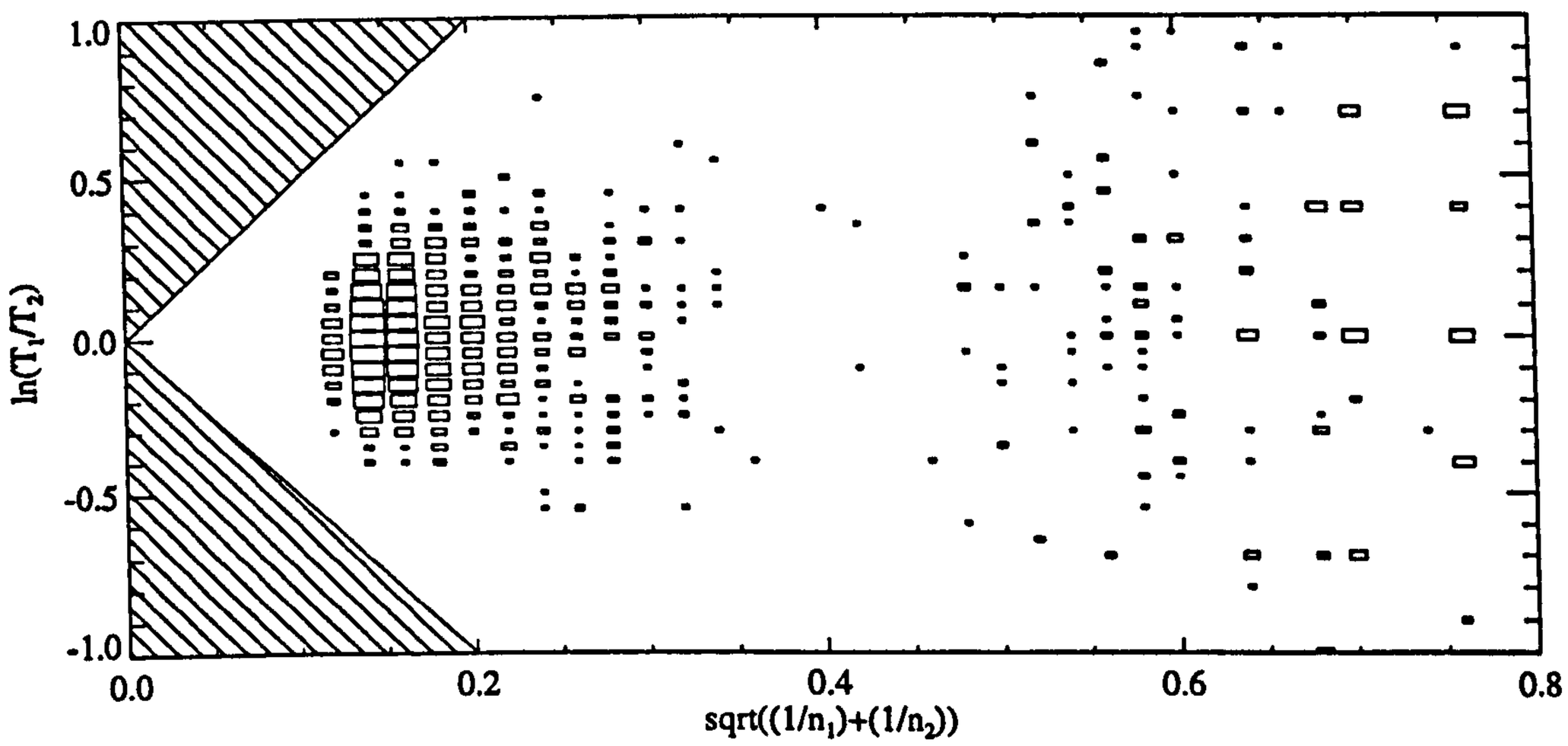

Figure 8.4: *Cut C5. The difference in natural logs of pulse mean times for each PMT plotted against the theoretical standard deviation. The events in the hatched regions were rejected by the cut. The diffuse cluster of events on the right are small noise pulses (rejected by cut C2). The data is from the DM46 detector.*

Noise events can occur in which slow pulses are seen in one PMT while fast pulses are seen in the other [173]. These events were removed by cutting on the ratio of the decay time constants of the two PMT pulses (here approximated by the mean photoelectron arrival times). For genuine scintillation pulses the mean times are distributed according to Eqn. 4.9. This is a normal distribution in $\ln(T)$ with the standard deviation in $\ln(T_0)$ proportional to $1/\sqrt{n}$. A cut was hence defined for valid events by

$$|\ln(T_1) - \ln(T_2)| < 5\sqrt{\frac{1}{n_1} + \frac{1}{n_2}}. \tag{8.5}$$

This was equivalent to cutting on the ratio of mean times T_1/T_2. The cut is displayed graphically in Fig. 8.4.

Cut C6: Absolute Pulse Goodness of Fit

In the previous cuts the event pulse shape was assumed to be exponential in form but for noise events this may not be the case. When fitting to the full two dimensional digitised pulse shape (§4.2.2) this fact can be used to advantage by cutting on the χ^2 of the exponential fit. Here however the more correct one dimensional treatment was used and the absence of a pulse shape fit meant that there was no χ^2 on which to cut. This problem was solved by defining a variable X_2 on the time axis:

$$X_2 = \sum_{i=0}^{n-1} (t_i - t_i')^2, \tag{8.6}$$

where t_i is the arrival time of the i^{th} photoelectron and t_i' is the equivalent time calculated from an exponential function of decay time constant $\tau = T$, photoelectron amplitude n and start time t_0. Following extensive event scanning a value of 10^{-12} was taken as the maximum allowable for this variable before the event was rejected. This appeared to be effective in removing the majority of non-exponential noise events. The cut is displayed graphically in Fig. 8.5.

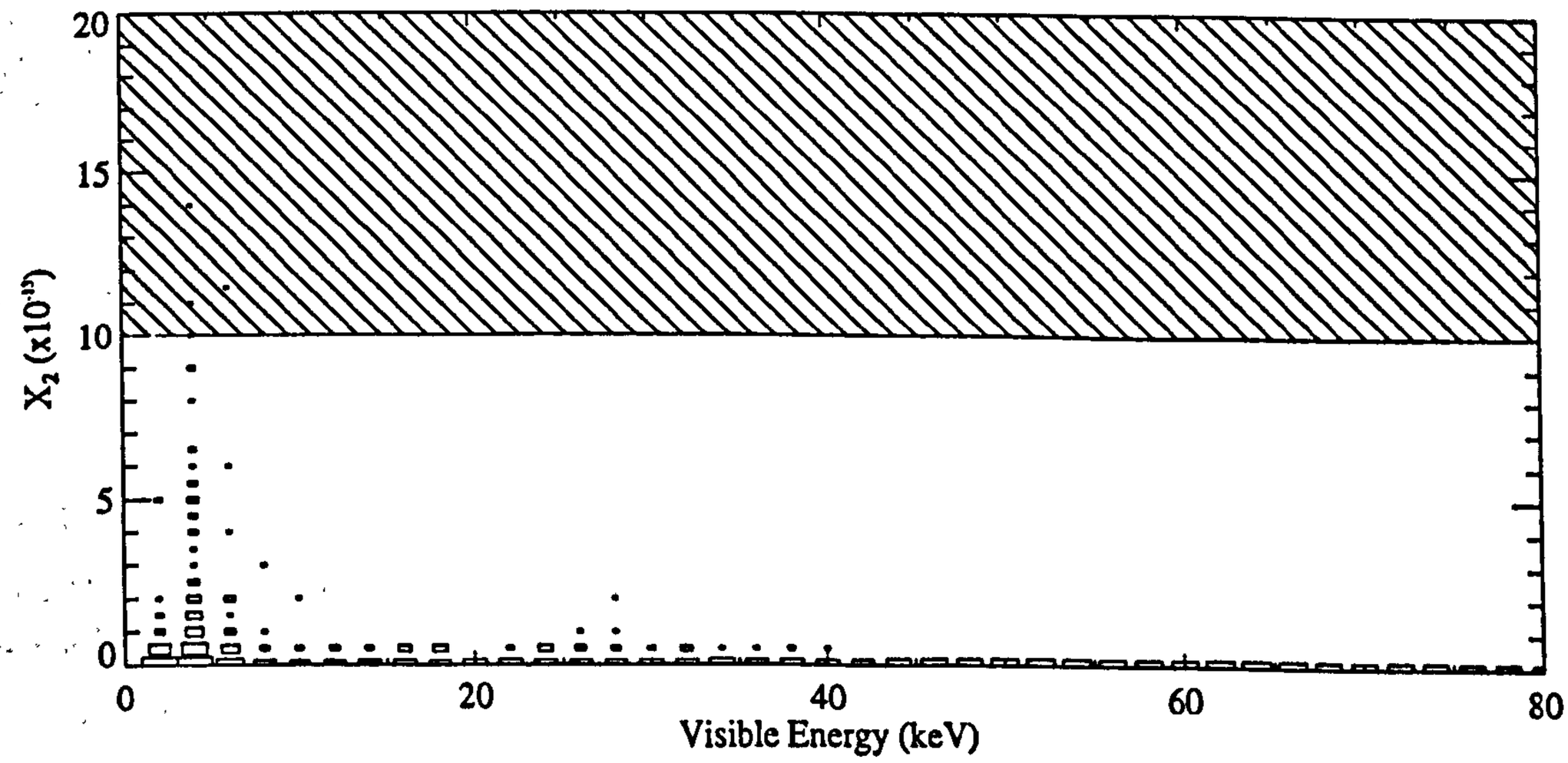

Figure 8.5: *Cut C6. Overall Pulse X_2 variable (defined in text) plotted against visible energy. The events in the hatched region were rejected by the cut. The cut was also performed on X_2 values for individual PMTs. Photoelectron statistics cause low energy events to possess large values of X_2. The data is from the DM46 detector.*

Cut	*Variable*	*Fraction of Events Rejected*
C1	T	29%
C2	n	0.7%
C3	$n_1 - n_2$	1.1%
C4	$t_{01} - t_{02}$	2.7%
C5	$\ln(T_1) - \ln(T_2)$	4.6%
C6	X_2	4.6%
Total		31%

Table 8.2: *Fractions of data events rejected by noise cuts. The total fraction does not equal the sum of the individual contributions because some events failed more than one cut.*

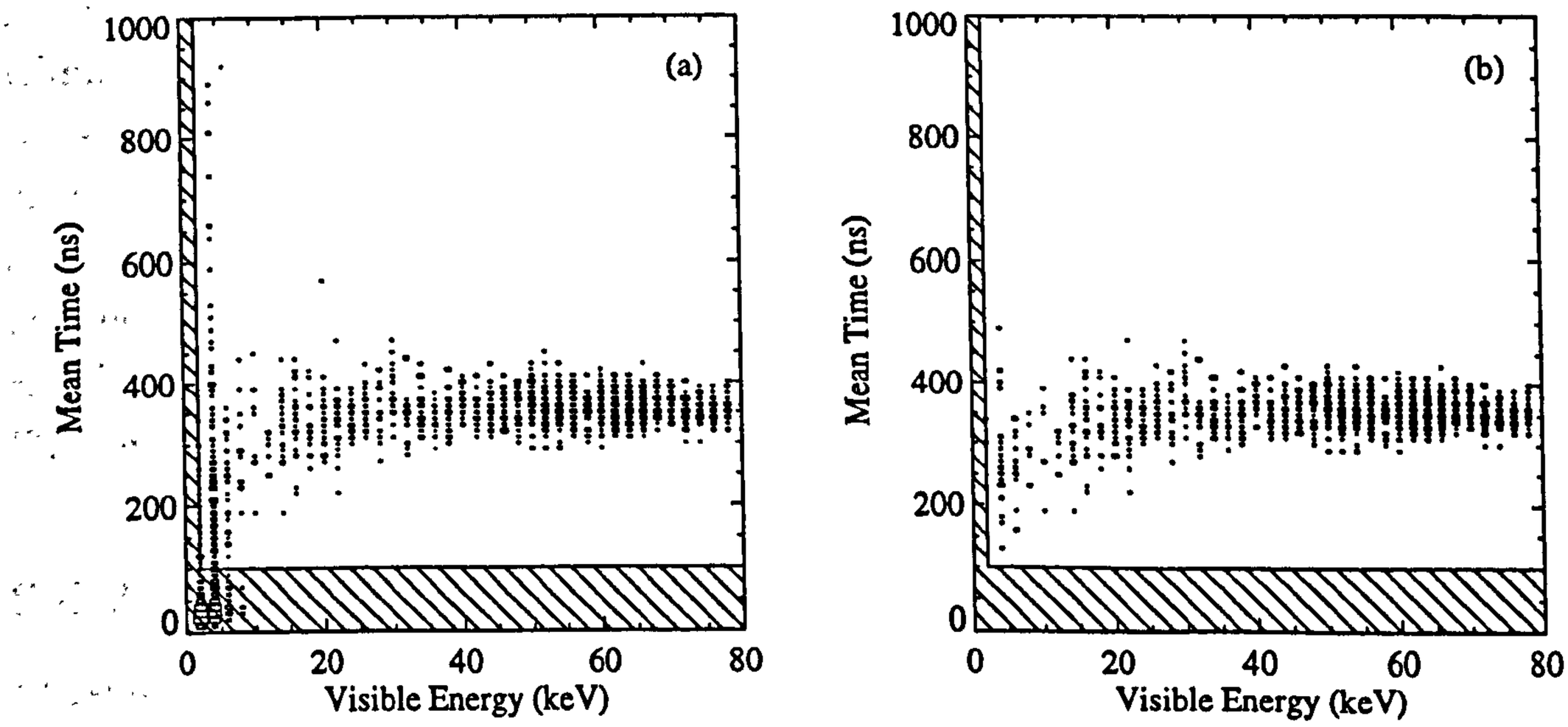

Figure 8.6: *The overall effect of cuts on data. Figure (a) shows the distribution in E_v-T space of 2936 raw triggers. Events lying within the hatched regions were rejected on the basis of cuts C1 and C2. Figure (b) shows the equivalent distribution of the 2021 events passing all cuts.*

Summary of Cuts

The preselection cuts are listed in Table 8.2. By manually scanning 5000 events it was found that < 0.05 % of accepted events possessed pulse shapes unlike typical scintillation events[1] such as Fig. 8.1(a). The reduction in signal efficiency which

[1] no 'noise' events were accepted in the 2773 valid events scanned

these cuts introduce was quantified through the use of the detector response matrix described in §8.7.2. The distribution of events in E_v-T space before and after cuts is shown in Fig. 8.6.

8.4 Pulse Shape Discrimination

8.4.1 Introduction

Two PSA techniques were used for discrimination: that using the mean photoelectron arrival time (MT - §4.3.3) defined as $T = 1/n \sum_{i=1}^{n-1}(t_i - t_0)$ for n photoelectron arrival times t_i, and that using the likelihood ratio (LR - §4.3.3) defined as $\Re = \ln(\mathcal{L}_e/\mathcal{L}_n)$ for electron and nuclear recoil pulse shape probabilities $\mathcal{L}_e$ and $\mathcal{L}_n$ respectively. The former technique is best suited to an approximately single exponential NaI(Tl) pulse shape and benefits from a well understood T distribution (Eqn. 4.9), while the latter seeks to make better use of the possible 'flattening' of the electron recoil pulse shape discussed in §4.2.2. The LR technique made use of mean scintillation pulse shapes (photoelectron histograms) determined from **CCAL** and neutron beam data. Nuclear and electron recoil reference distributions for both techniques were provided by **CCAL** and **NCAL** data while values for the nuclear recoil signal rate $S_f(E_v)$ and its error $\sigma(S_f)$ were determined by using χ^2 fits to the **DATA** event sample (§3.7.1).

8.4.2 Mean Pulse Shapes

Nuclear Recoils

The LR technique requires the use of mean scintillation pulse shapes for nuclear and electron recoils (§4.3.3). Due to the poor statistics and heavy electron recoil contamination of the **NCAL** event sample it proved to be impossible to use this data to obtain a measurement of the true nuclear recoil pulse shape. As a result it was decided to use instead the neutron beam Na recoil data from §6.4.2 in the subsequent analysis. Although this data was taken with a different crystal (DM47) the electron recoil T distribution was similar to that for DM46 and hence nuclear recoil pulse shape differences were assumed to be small. There is no evidence from the results of §6.4.2 that the nuclear recoil pulse shape varies significantly with energy and so a single pulse shape was assumed for all energy bins. This pulse shape was derived from that shown in Fig. 6.17(a), with adjacent time bins being summed to give a 20 ns bin width compatible with the digitisation interval of the DM46 DAQ system.

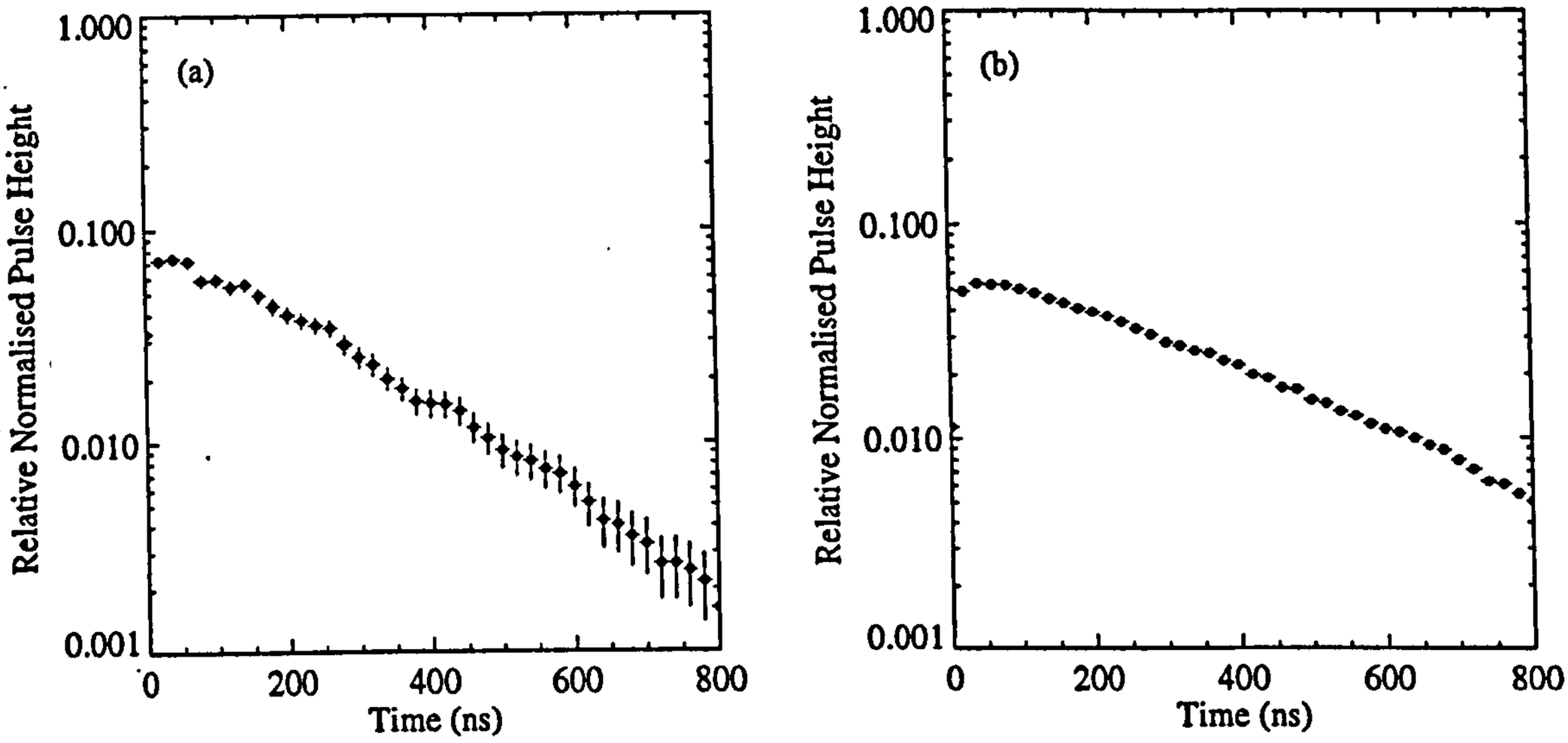

Figure 8.7: *Mean scintillation pulse shapes used in conjunction with the LR technique for analysing DM46 data. Figure (a) shows the nuclear recoil pulse shape while Figure (b) shows the electron recoil pulse shape in the visible energy range 10 - 20 keV.*

The distribution was also smoothed by summing adjacent time bins and using linear interpolation in order to lessen the effects of photoelectron statistics. The similar temperatures of the DM46 and DM47 crystals at the time of data taking ($\sim$ 10 °C and $\sim$ 11 °C respectively) removed the need for temperature correction of the pulse shape. The calculated mean nuclear recoil pulse shape is plotted in Fig. 8.7(a).

Electron Recoils

The mean electron recoil pulse shape was determined by analysing 100 000 valid **CCAL** events. The events were binned in 1 keV visible energy bins over the range 2 - 80 keV and the normalised photoelectron distributions calculated from the arrival times of all photoelectrons in each event. A representative distribution from the 10 - 20 keV visible energy bin is plotted in Fig. 8.7(b). Afterpulsing in the PMTs at photoelectron arrival times $\sim 1\mu$s led to the use of only those photoelectrons with $t_i < 800$ ns when calculating both the mean pulse shape and the LR. Such afterpulsing was not seen in the neutron beam data due to the use of a different PMT. Mean pulse shapes for both nuclear and electron recoil events were renormalised to unity in the 0 - 800 ns time interval in order to properly calculate the probability of a given t_i under each hypothesis.

8.4.3 Analysis

Pulse Shape Analysis (PSA) was performed on all data (**DATA**, **CCAL** and **NCAL**) using both the mean time and likelihood ratio techniques. Following PSA the energies, mean times, likelihood ratios and Julian dates of all valid events were output to Data Summary Files (DSF) for subsequent interpretation (Fig. 8.8). This allowed the analysis procedure to be refined without repetition of the time consuming initial stages of data processing.

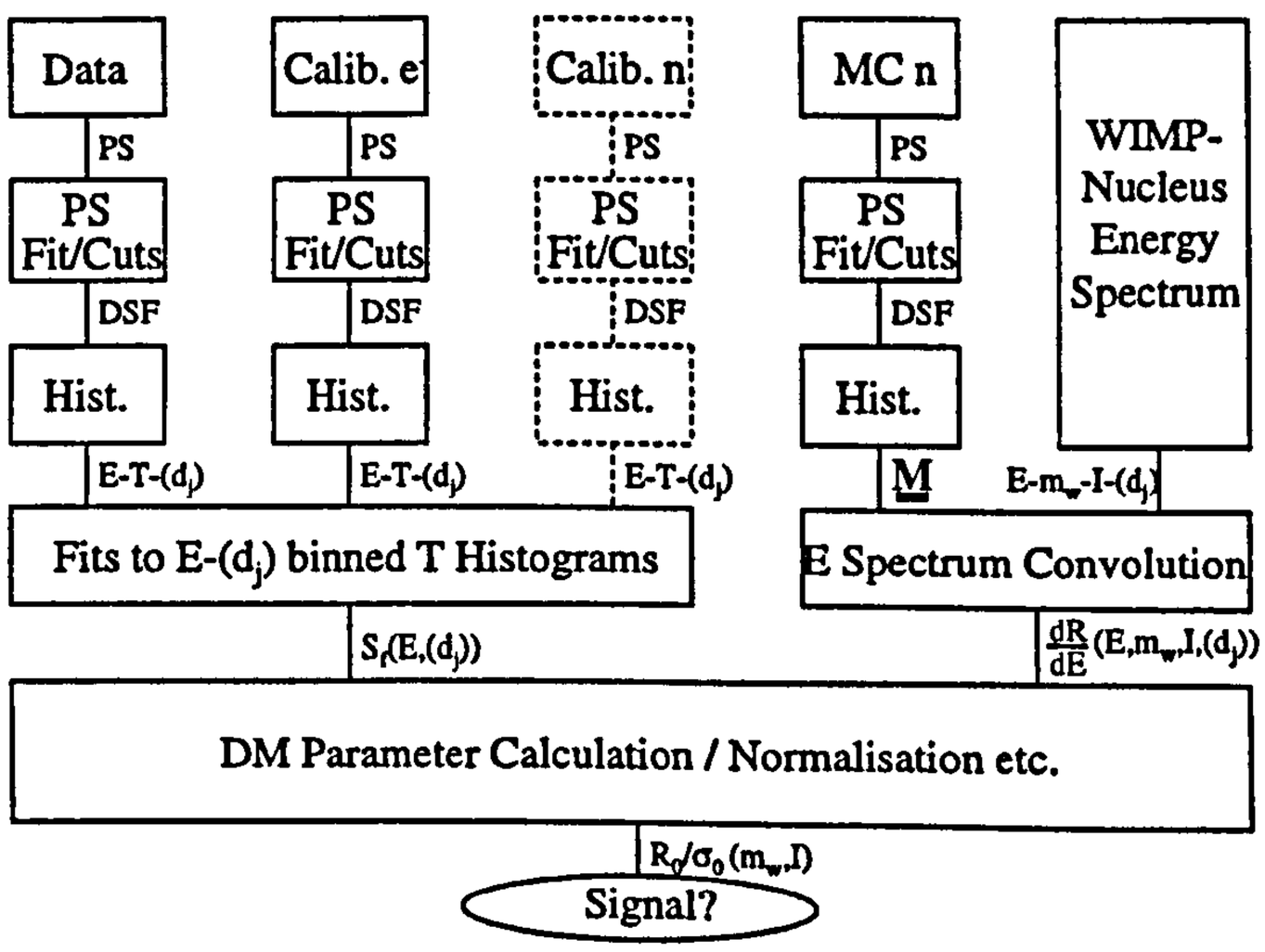

Figure 8.8: *A flow chart of the analysis procedure.*

The DSFs were analysed by code which read in the event parameters and used them to construct histograms (Fig. 8.8). For **CCAL**, **NCAL** and **DATA** event samples histograms of both mean time (10 ns bin width) and likelihood ratio (bin width 1.0) against visible energy (4 keV bin width) were constructed. Histograms of these quantities were also created for **DATA** events with an additional 91 Julian day ($\sim$ 3 month) event time binning in order to search for evidence of annual modulation. These histograms used a more coarse 12 keV visible energy binning in order to increase the statistics in each event time bin.

Also calculated was the detector live time both in total and for each 3 month time bin (required for the annual modulation analysis). The procedure adopted was to sum the time differences between **DATA** events, providing the time differences were less than 0.01 Julian days ($\sim$ 14 minutes). This time cut off was sufficient to resolve breaks in data taking due to Compton and energy calibration (durations $\sim$ 0.2 and 0.04 Julian days respectively) but using the properties of the exponential probability distribution can be shown to be $\sim$ 22 standard deviations greater than

the mean time interval between events ($\sim$ 39 seconds). Thus there is expected to be a negligible error in the calculated live time due to statistical fluctuations in the counting rate. The live time as a function of time is plotted in Fig. 8.9. For the annual modulation analysis the mean Julian date for each 3 month time bin was also calculated to enable later comparison with theory.

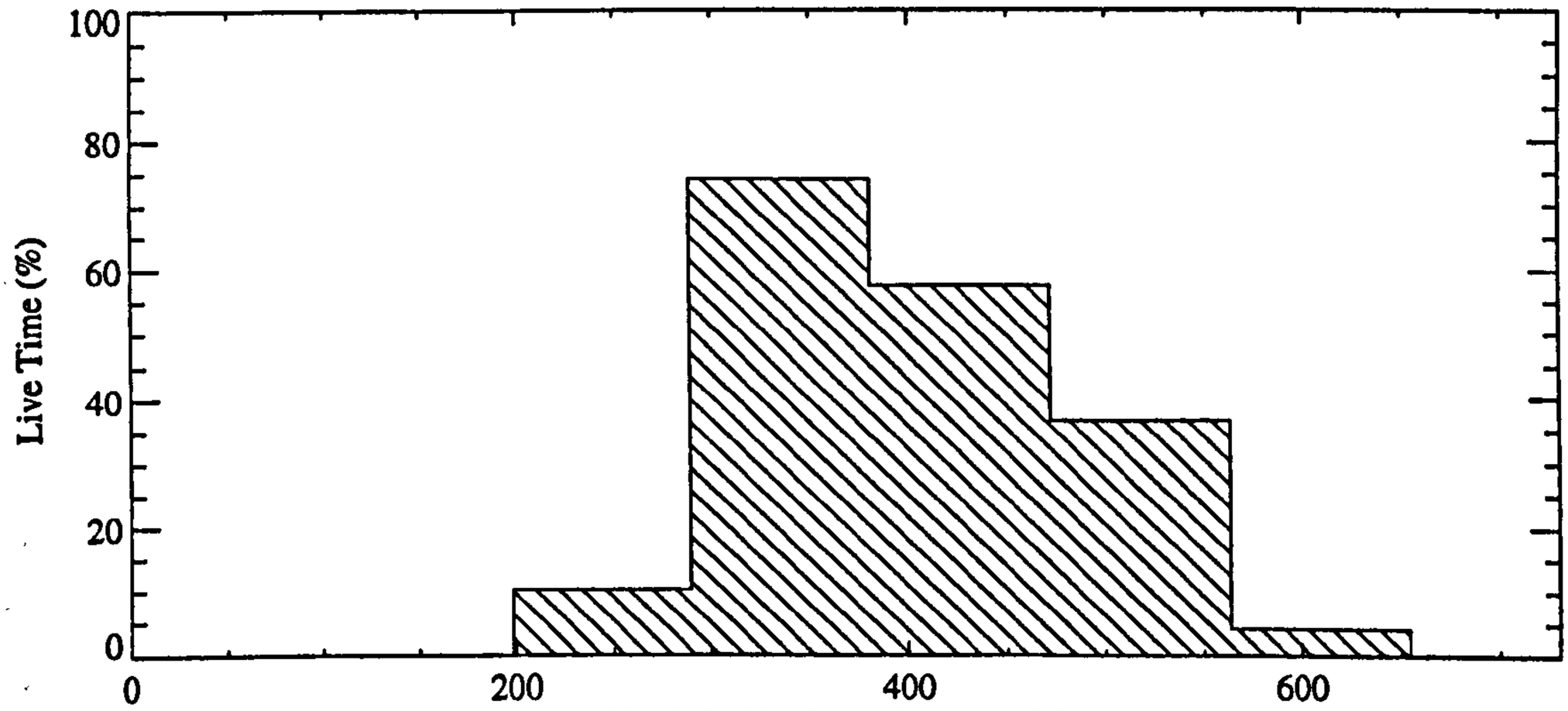

Figure 8.9: *The live time distribution for the data from the DM46 detector analysed in this thesis. The x axis is scaled in days after 1st January 1996. The data is binned in 91 Julian day intervals.*

The discrimination process itself was performed by fitting to the MT and LR histograms using a weighted χ^2 technique. For this purpose the IDL [143] fitting routine 'Curvefit', adapted from an algorithm described in [176], was used. For **DATA** and **CCAL** events fits were performed on each histogram separately. For **NCAL** data however the low statistics required energy bins to be combined to give one energy bin in the visible energy range 14 - 30 keV, where the ratio of nuclear recoil to electron recoil and noise events was expected to be largest. A larger energy bin width was not used because the systematic variation in the electron recoil T_0 with energy could cause the number and T_0 of nuclear recoil events to be overestimated.

In the weighted χ^2 fitting technique the weight associated with each histogram bin corresponds to the reciprocal of the variance of the number of events in that bin. For a Poisson process (as here) this is just the reciprocal of the bin content. The technique is only rigorously defined however for Gaussian errors and this in turn requires that the bin content be $\gtrsim 5$ for all bins [177]. In order to account for this

adjacent bins were summed prior to fitting until all bins contained either 0 or ≥ 5 events. Fitting was then performed using only those bins with non-zero contents.

The majority of signal events possess mean times and likelihood ratios less than those of electron recoil and noise events. Consequently in the high tails of the distributions there are unlikely to be significant numbers of signal events, but possibly a large proportion of the background and noise events. A further requirement was therefore that bins corresponding to these tails (mean times > 500 ns or likelihood ratios > 50) be discarded.

The fits to MT data are plotted in Figs. 8.10, 8.11 and 8.12, while the fits to LR data are plotted in Figs. 8.13, 8.14 and 8.15. The fits to **CCAL** data were performed assuming log-normal distributions for T and normal distributions for $\Re$. The latter assumption was not well motivated theoretically but was simpler from the point of view of fitting than Eqn. 4.11, which in any case is only valid for pure exponential pulses. As required by the central limit theorem the LR distributions may be approximated by normal curves in the region of their peaks although the agreement is less good in their tails. Investigation of the optimum assumed distribution from the perspective of both ease of fitting and quality of fit will require further work.

The **CCAL** fits were performed by allowing the widths, means and overall normalisations of the assumed distributions to vary. Similar distributions were assumed for nuclear recoil events in the **DATA** and **NCAL** samples, with the means and normalisations acting as free parameters. Empirically the widths of nuclear and electron recoil distributions of a given visible energy are similar, being governed by the similar decay components and photoelectron statistics of the two pulses (§4.2.2). Consequently the widths of the nuclear recoil distributions were fixed to the values determined from the **CCAL** data.

The distributions assumed for electron recoil events contaminating the **DATA** and **NCAL** MT data were again normal, with freely varying normalisations and means, and widths fixed at the **CCAL** values. The means were allowed to vary so as to account for systematic variation in T_0 over the course of data taking due to changes in the target value of the temperature control system in the range 8°C - 12 °C. Such fluctuations were small and to first order can be taken into account by merely assuming a linear shift in the mean of the electron recoil distribution [88].

In the likelihood ratio treatment the only major difference in addition to the functional form of the distributions (normal rather than log-normal) was the fitted form of the **DATA** and **NCAL** electron recoil distributions. Departures of the observed distributions from either those expected for a pure exponential pulse shape (Eqn. 4.11) or normal distributions led to the use instead of the empirical **CCAL**

distributions. These distributions were first normalised to unity and then the renormalisation factor, equivalent to the fitted number of electron recoil events in the data, was used as a free parameter. This approach did not permit the effects of systematic temperature variation to be taken into account and this problem remains unresolved.

The fits to MT data are plotted in Figs. 8.10, 8.11 and 8.12, while the fits to LR data are plotted in Figs. 8.13, 8.14 and 8.15. The data and fits will be discussed in the next section.

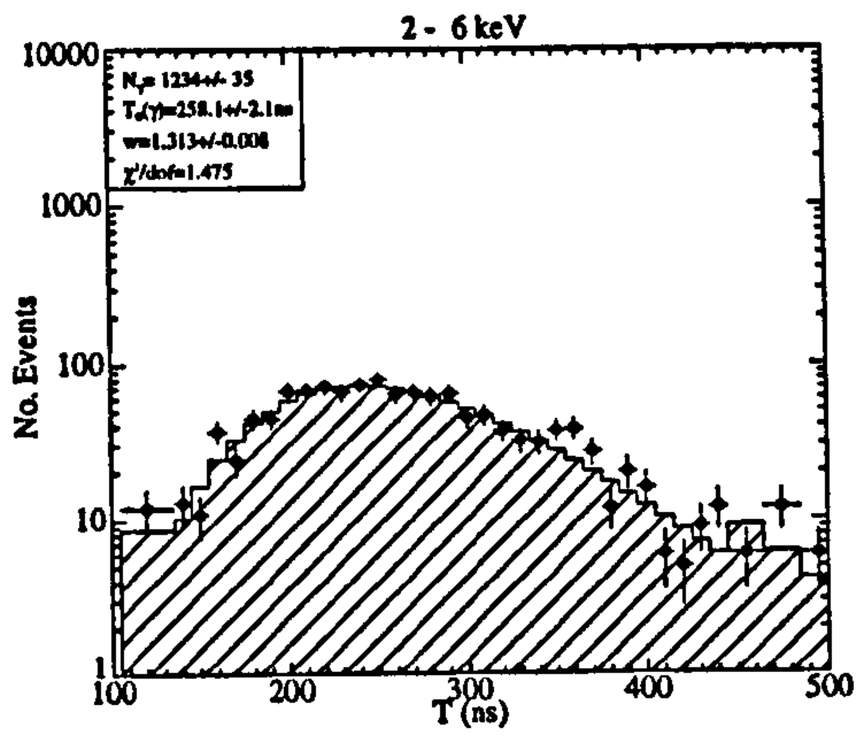

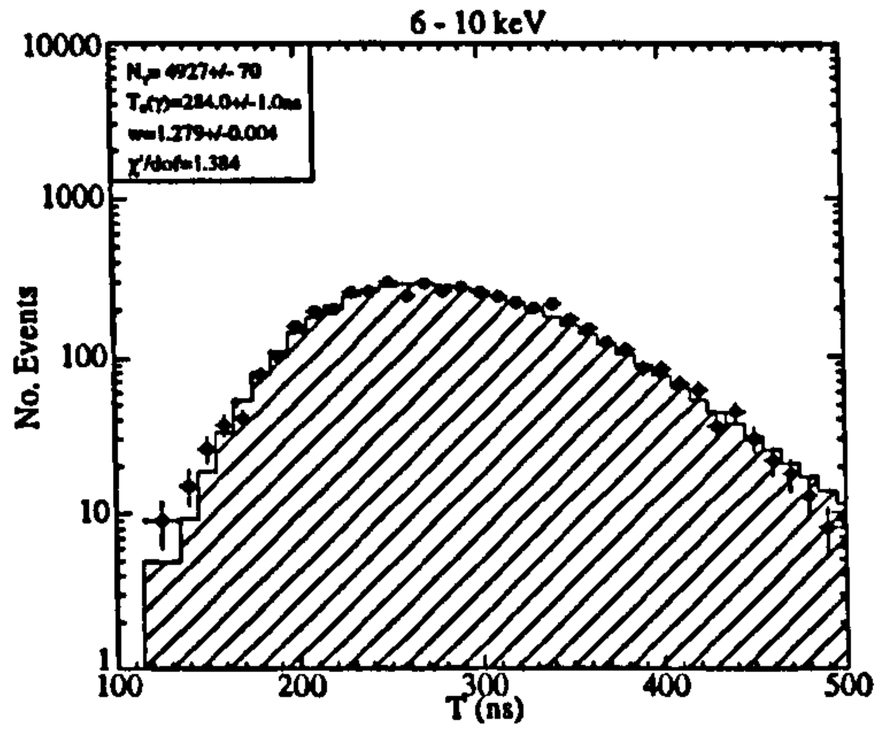

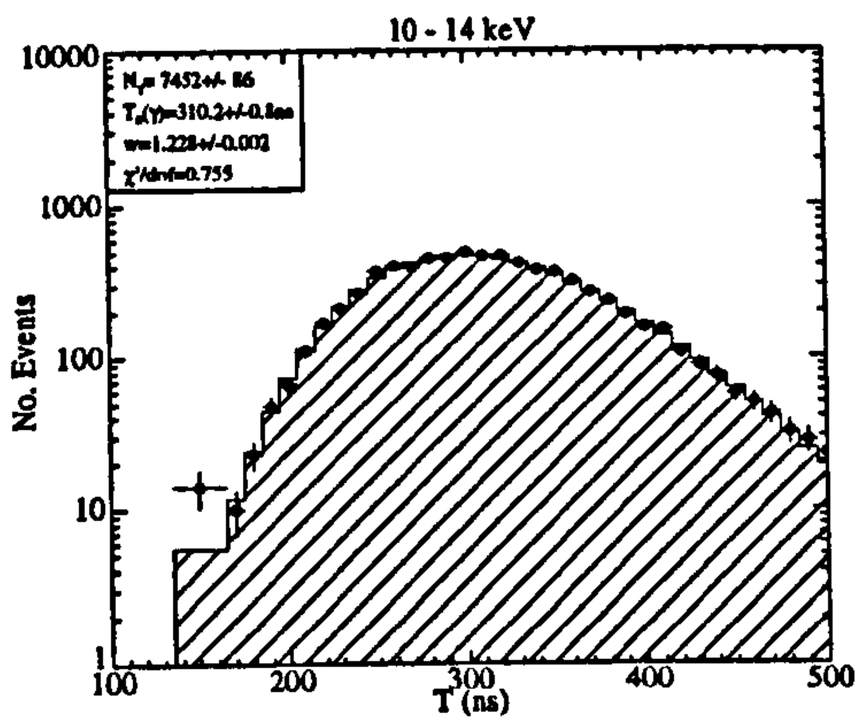

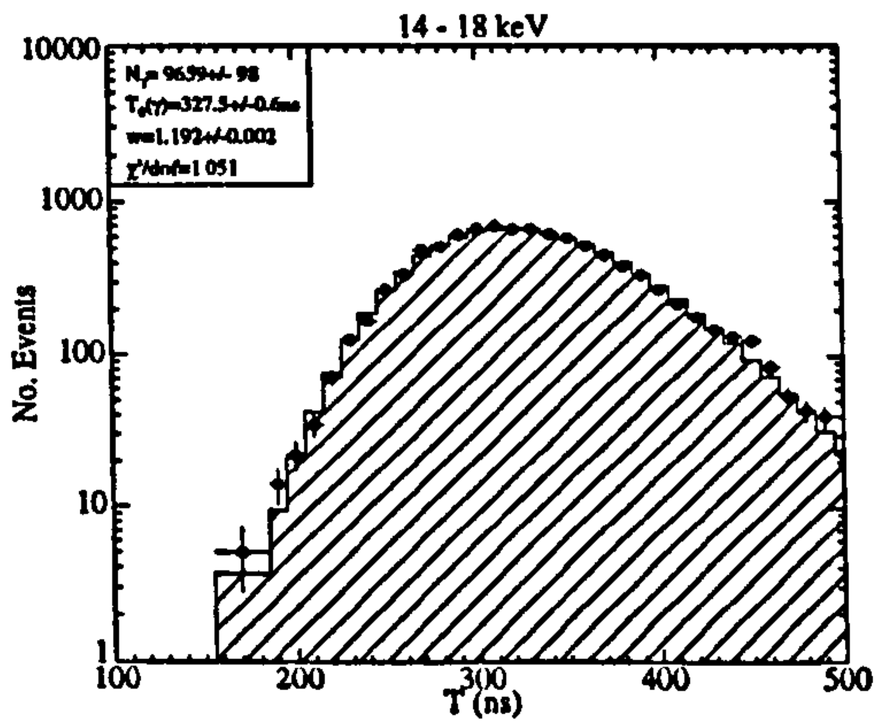

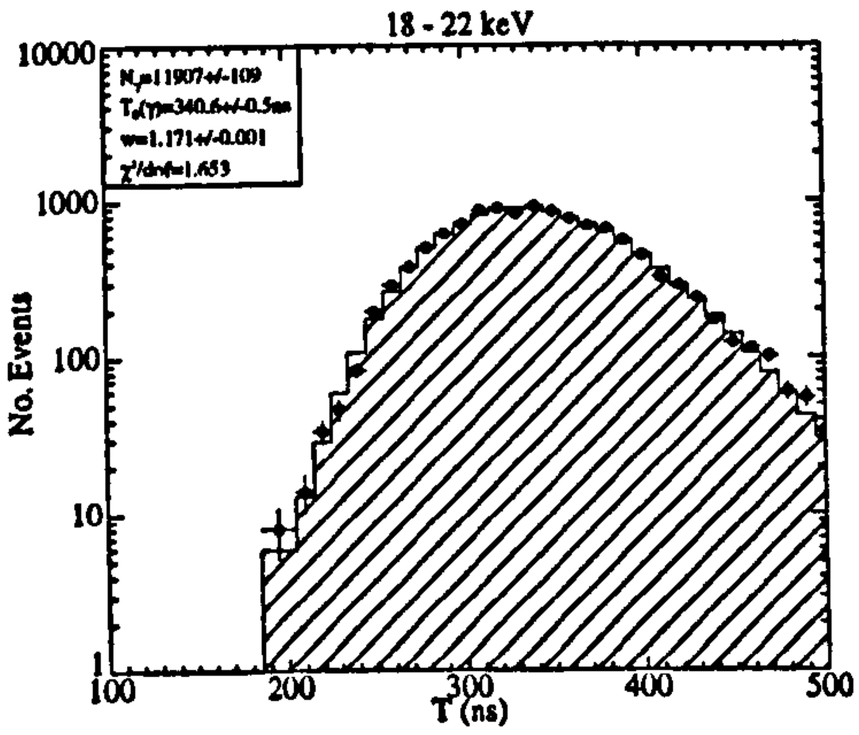

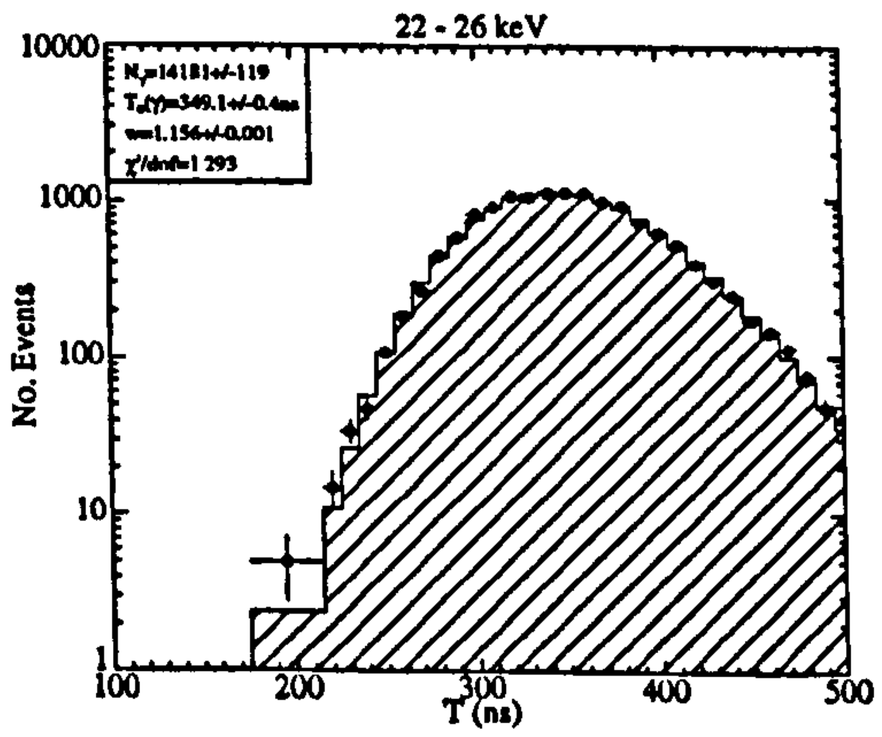

Figure 8.10: *T distributions for* **CCAL** *events in 4 keV visible energy bins. The hatched areas represent fits to log-normal distributions with free parameters w ($w = \exp(\sigma)$ with σ defined by Eqn. 4.9), T_0 and N_γ (normalisation). These distributions are included for comparison with Fig. 8.11.*

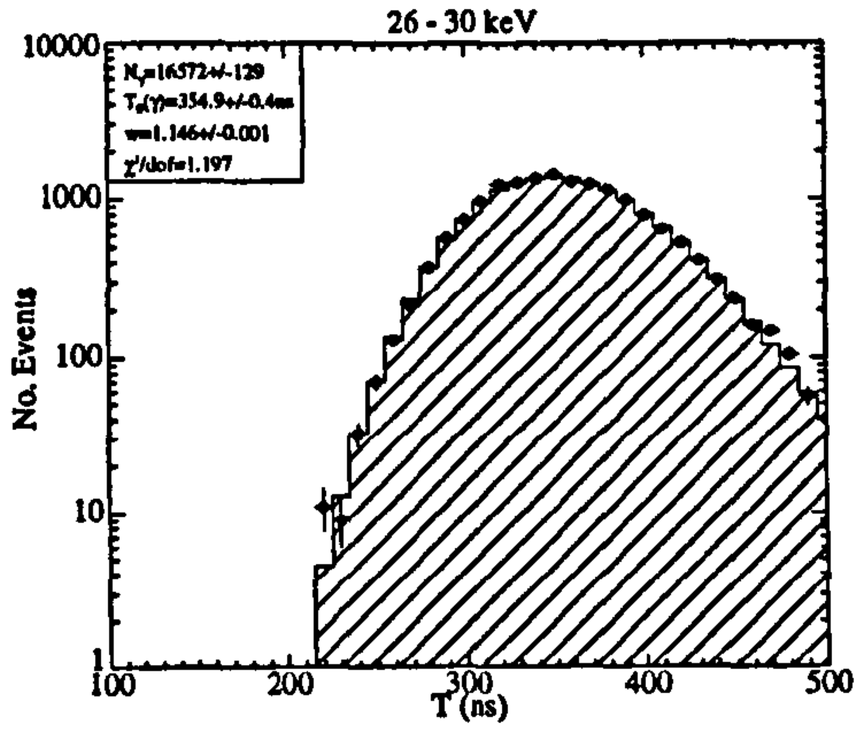

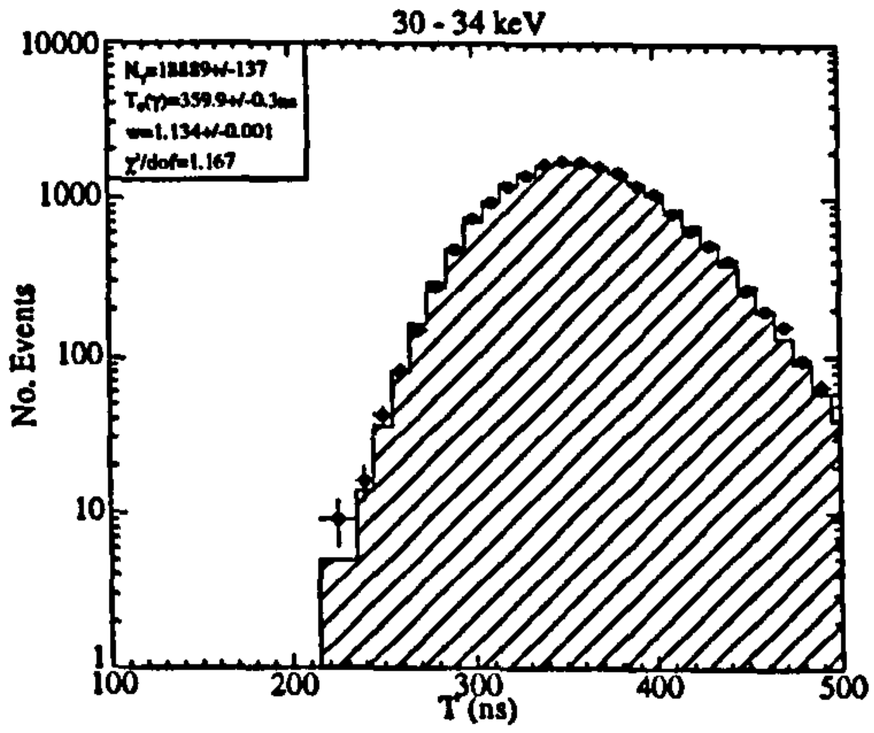

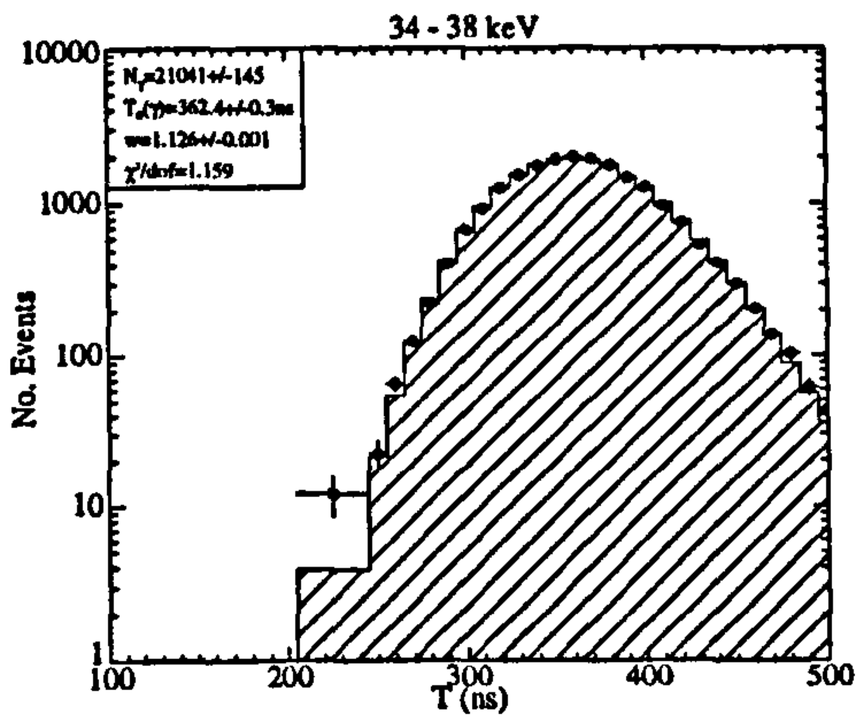

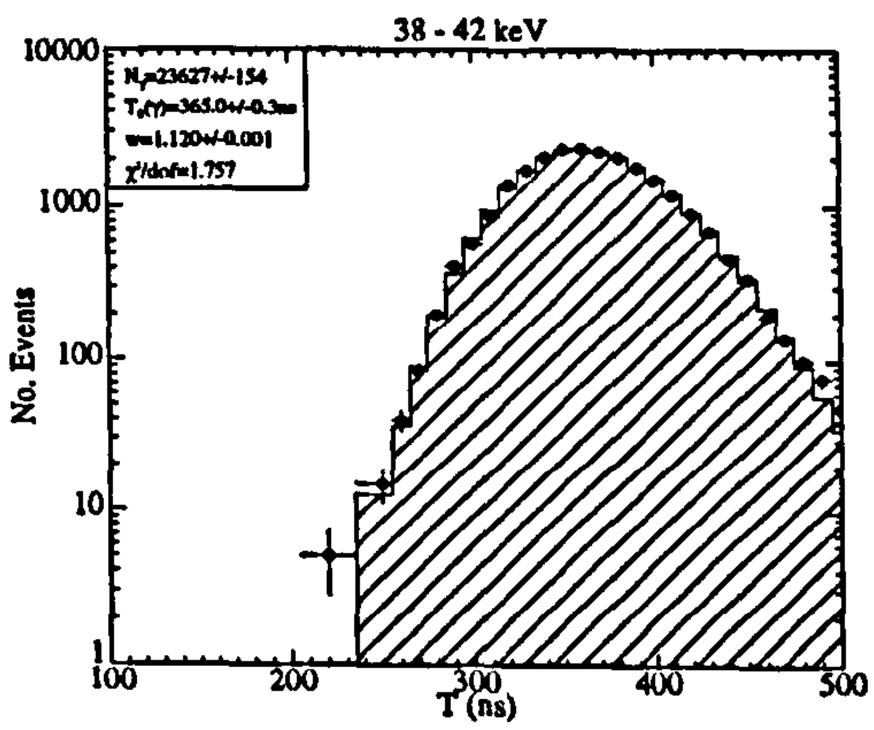

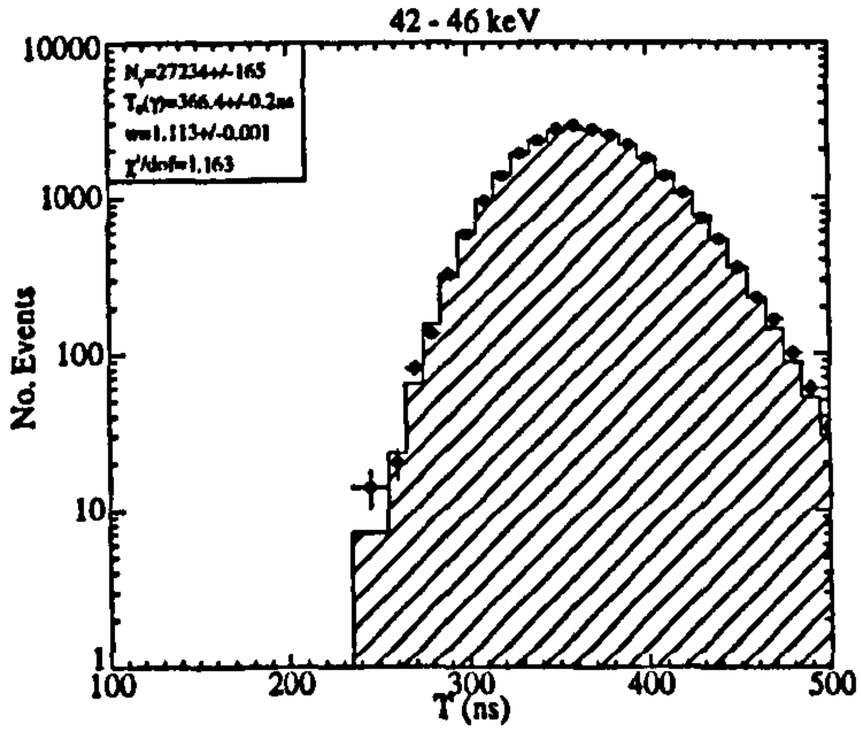

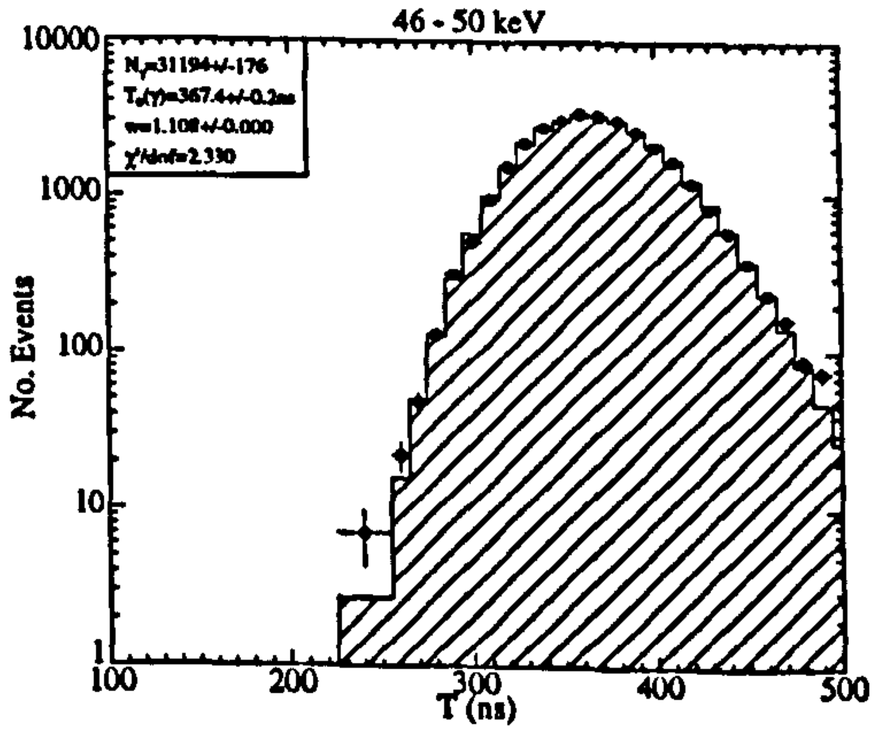

Figure 8.10 (continued).

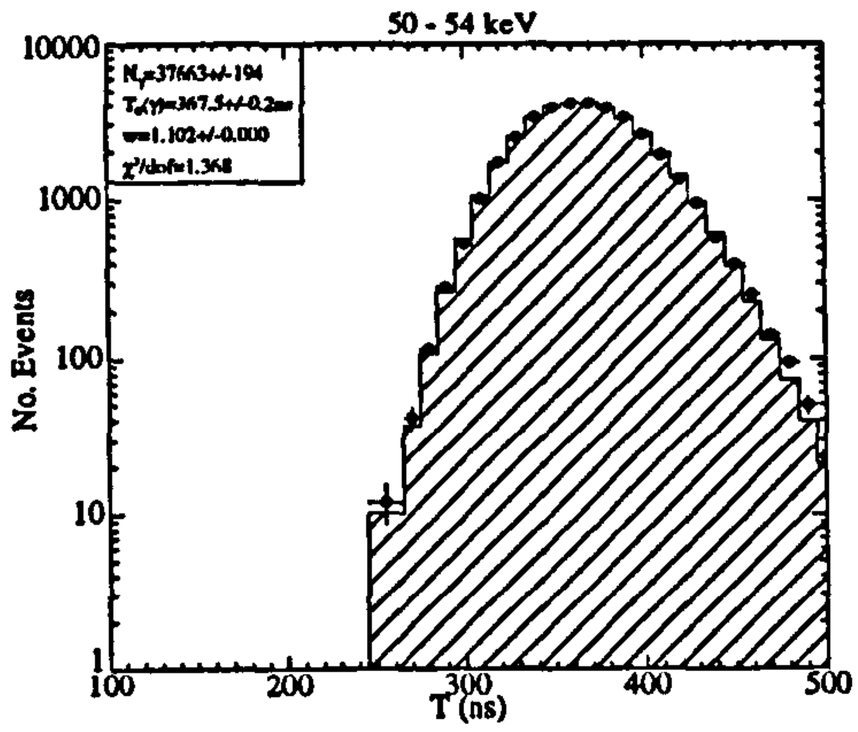

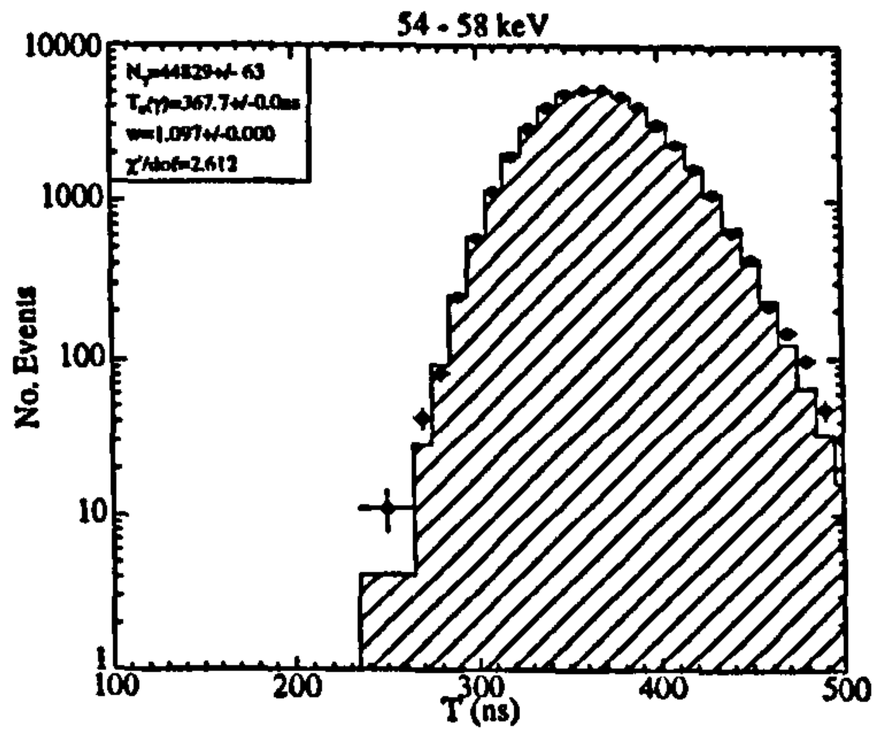

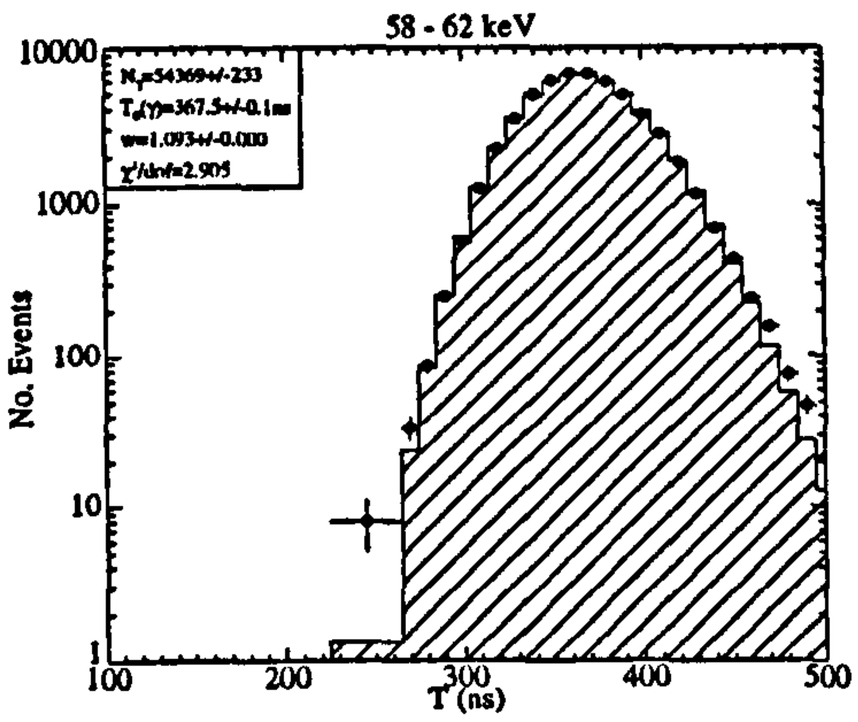

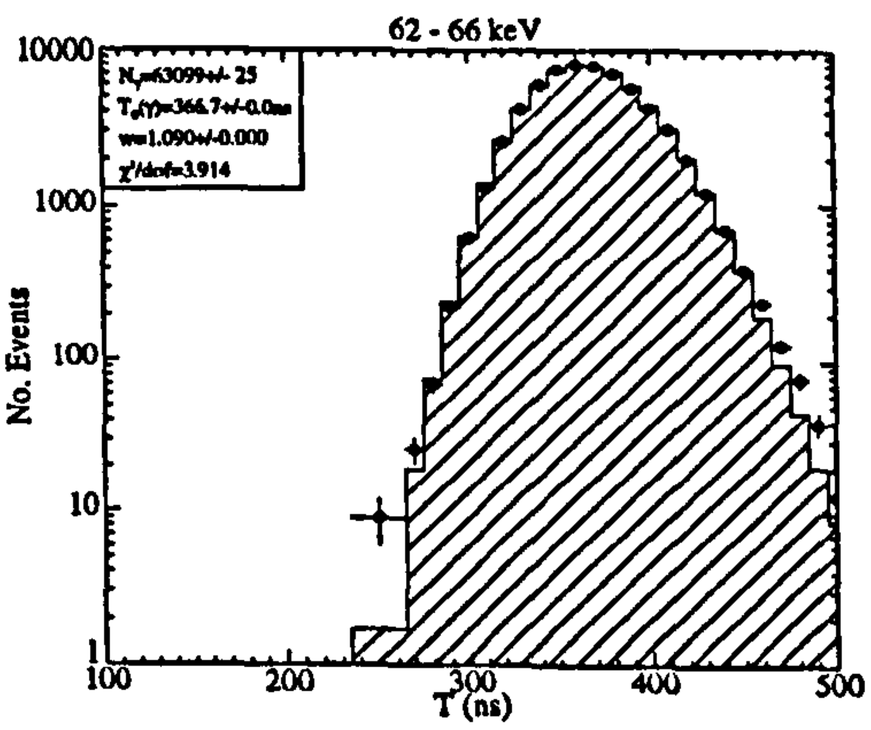

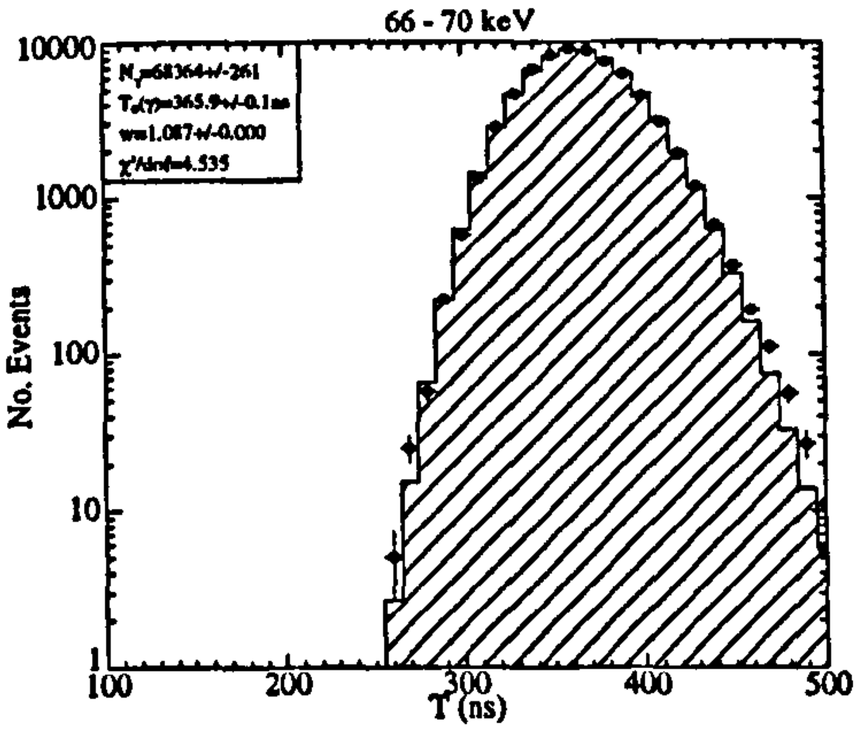

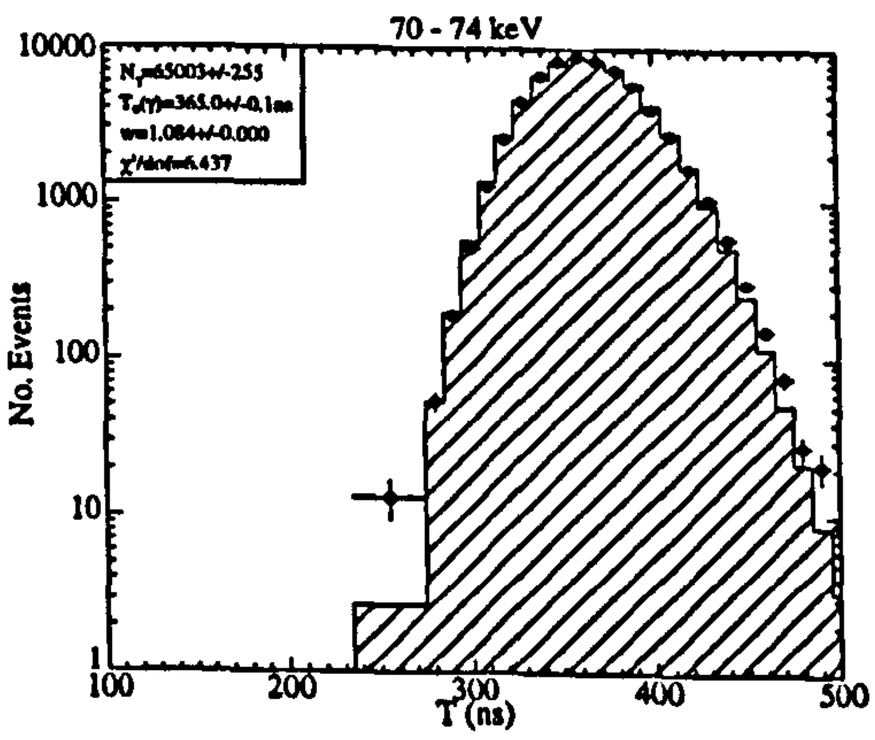

Figure 8.10 (continued).

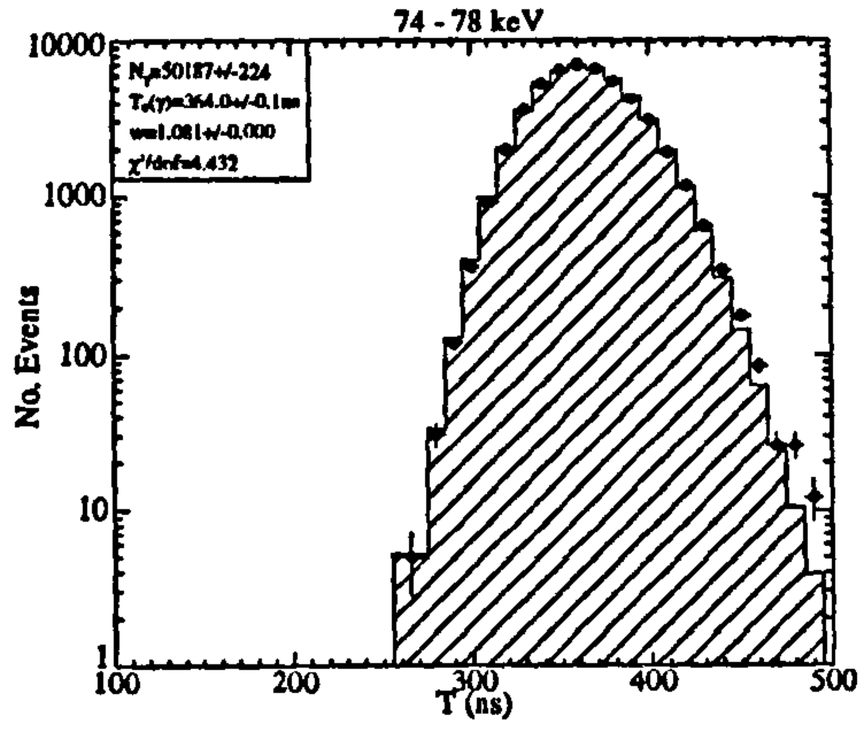

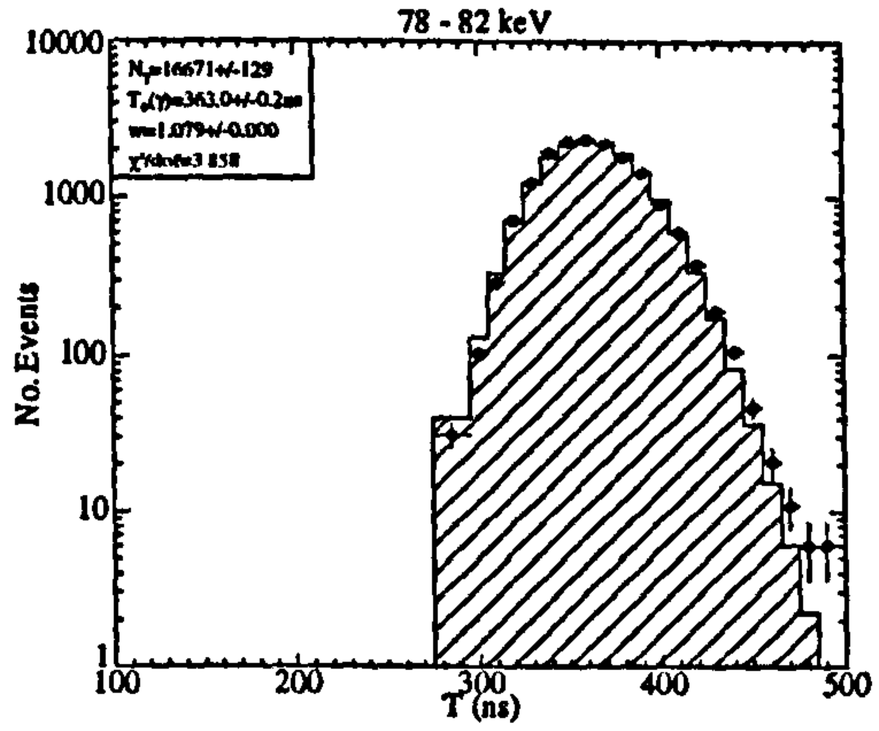

Figure 8.10 (continued).

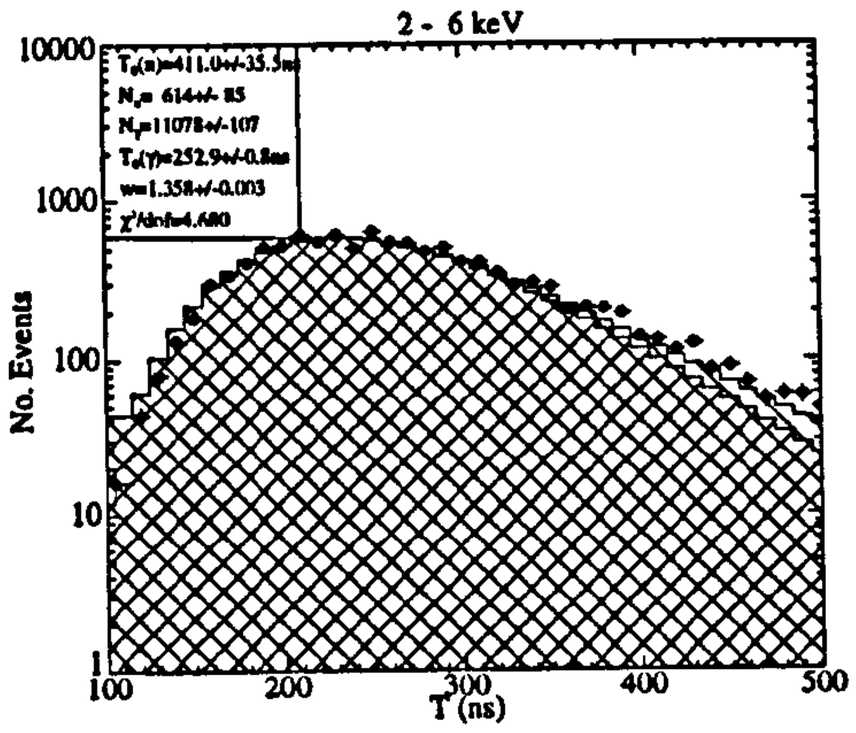

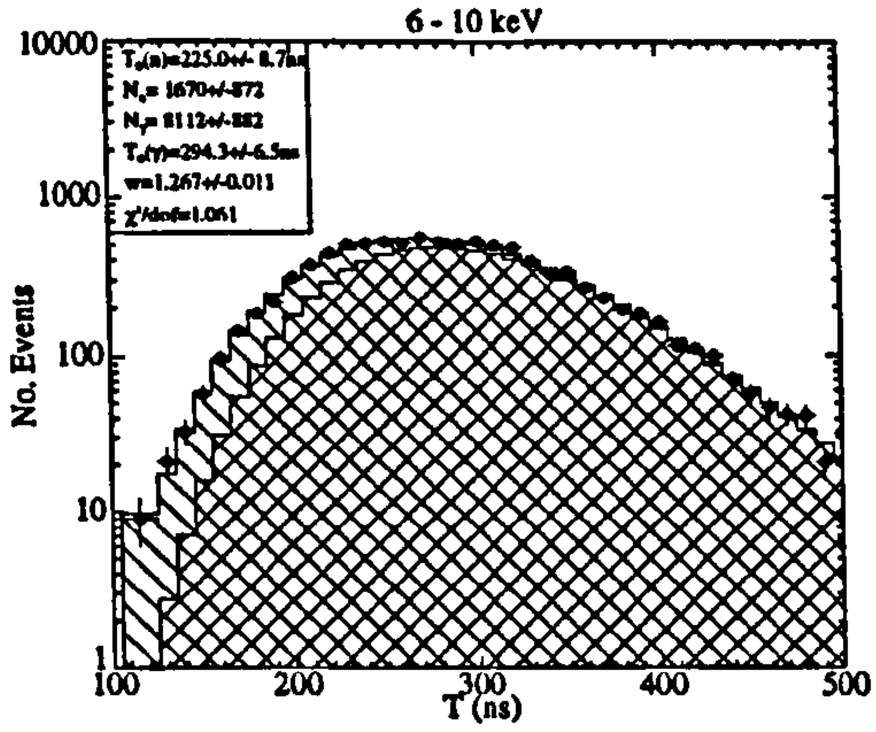

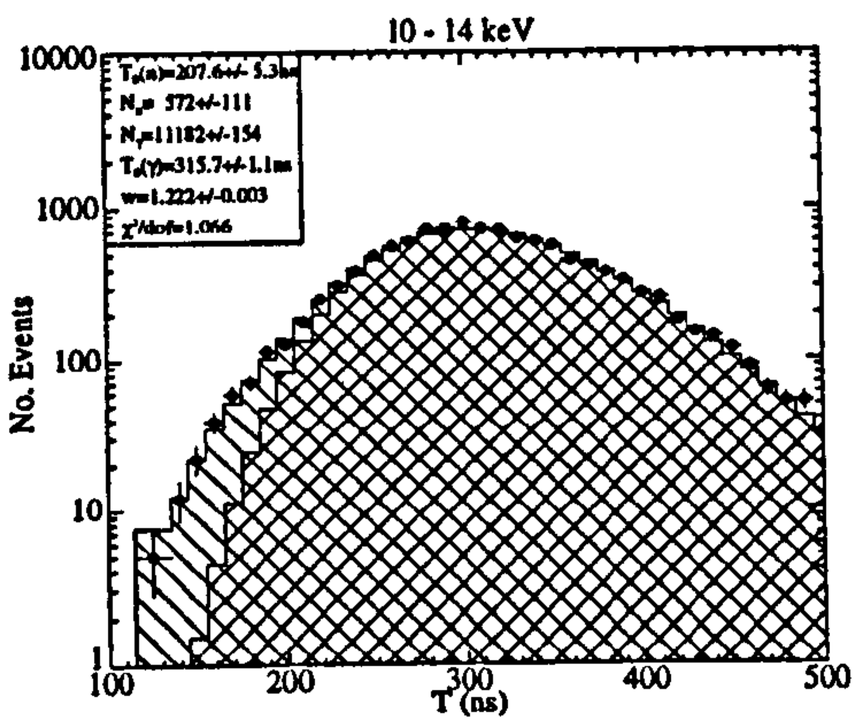

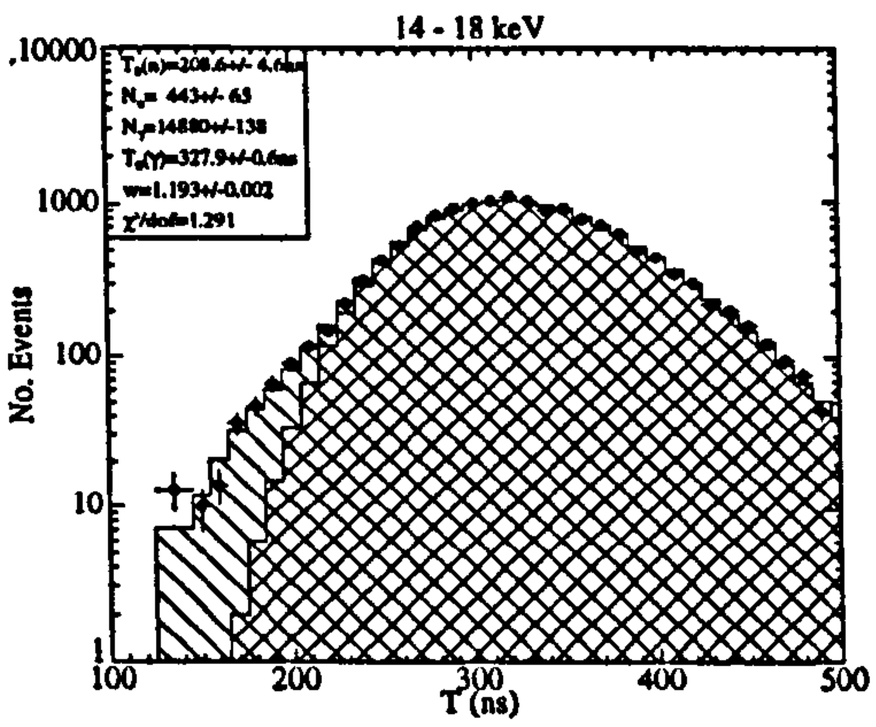

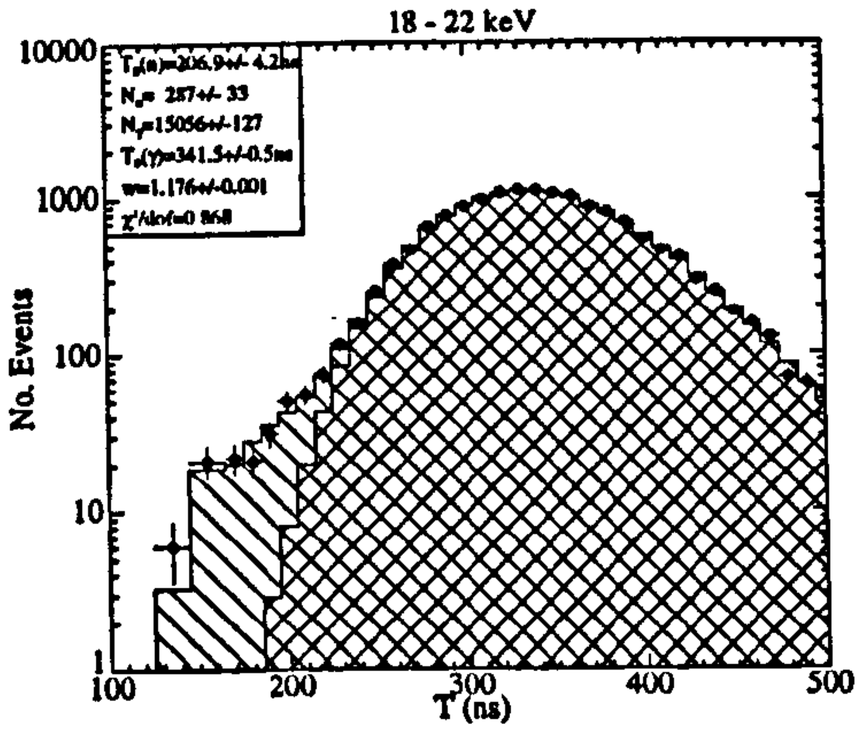

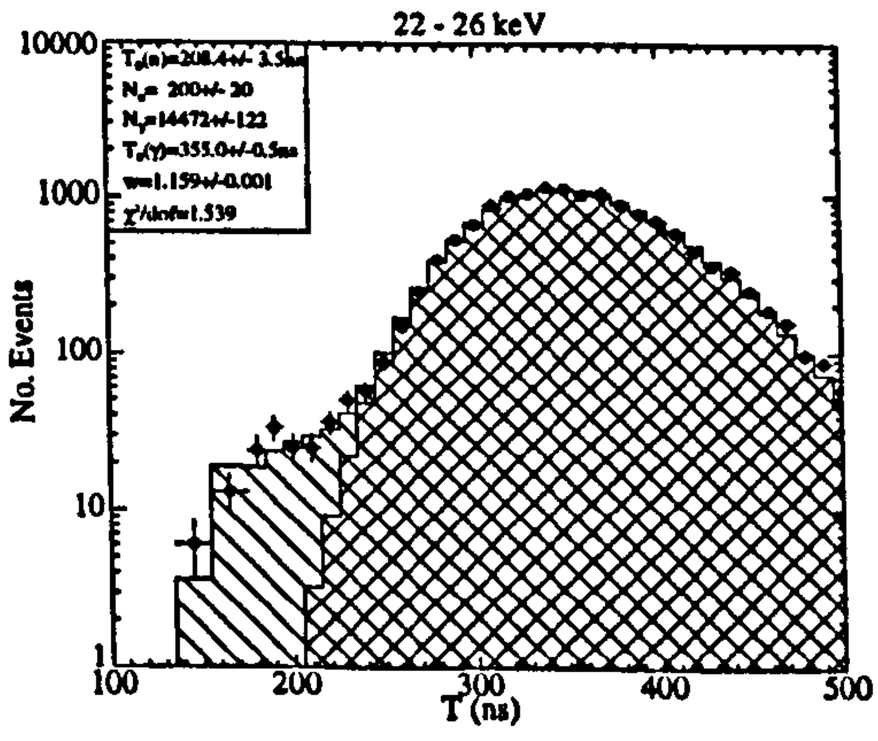

Figure 8.11: *T distributions for* **DATA** *events in 4 keV visible energy bins. The histograms represent fits to sums of two log-normal distributions representing nuclear and electron recoil populations. The cross hatched areas represent the contributions from the electron recoil distributions. The free parameters are* $T_0(n)$ *and* $T_0(\gamma)$, N_n *and* N_γ *(nuclear and electron recoil distribution normalisations) and* w *(*$w = \exp(\sigma)$ *with* σ *defined by Eqn. 4.9). Relevant fitted parameter values can be found in Table 8.3.*

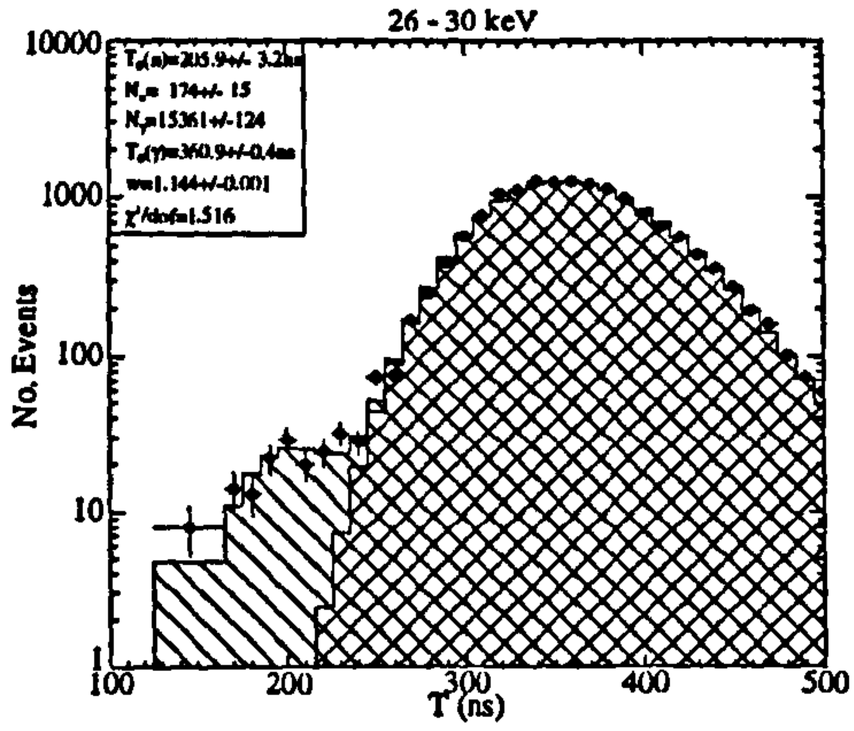

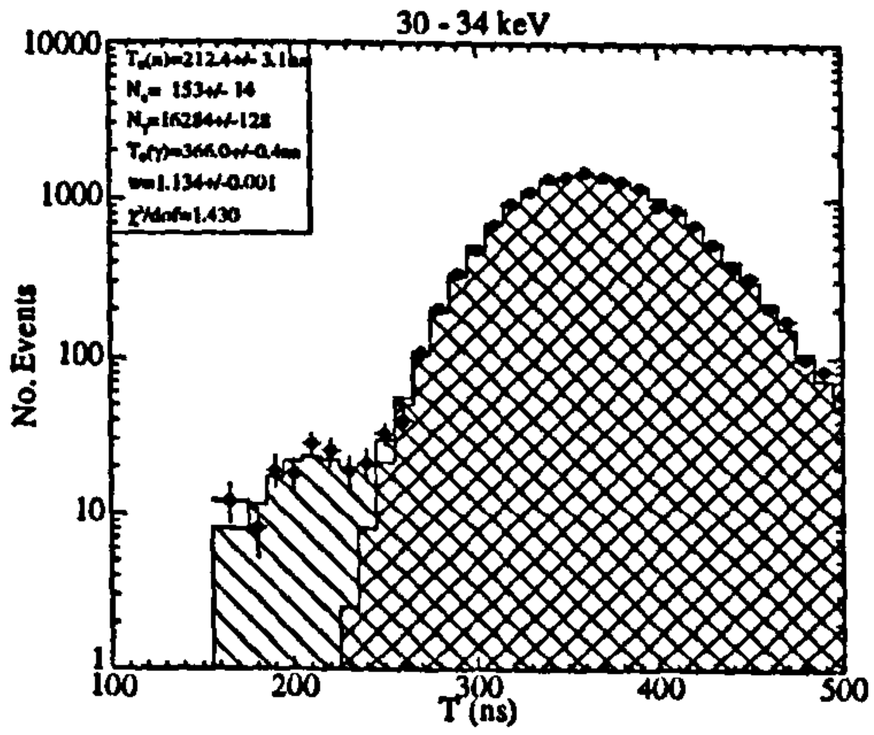

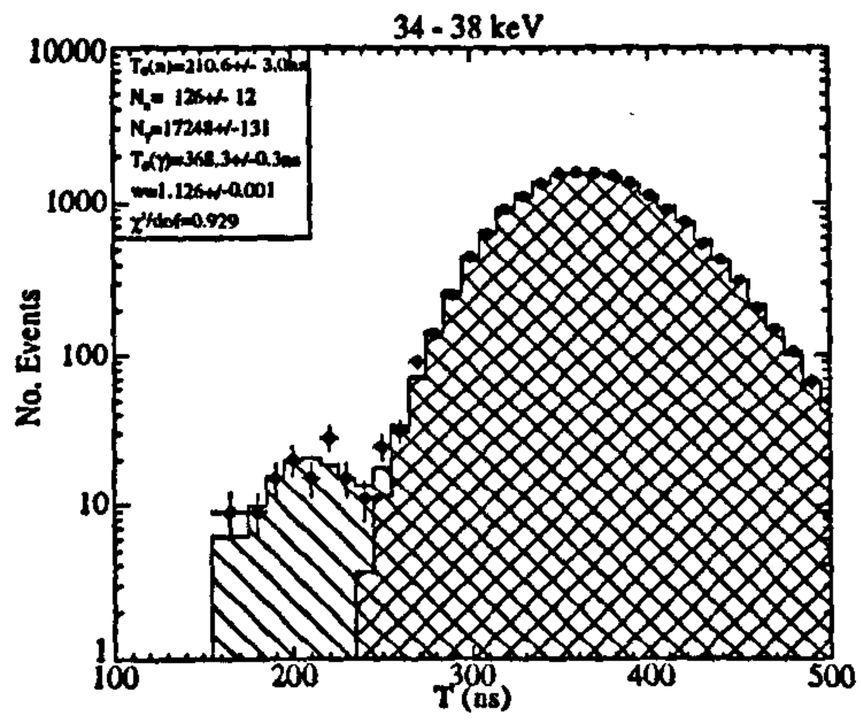

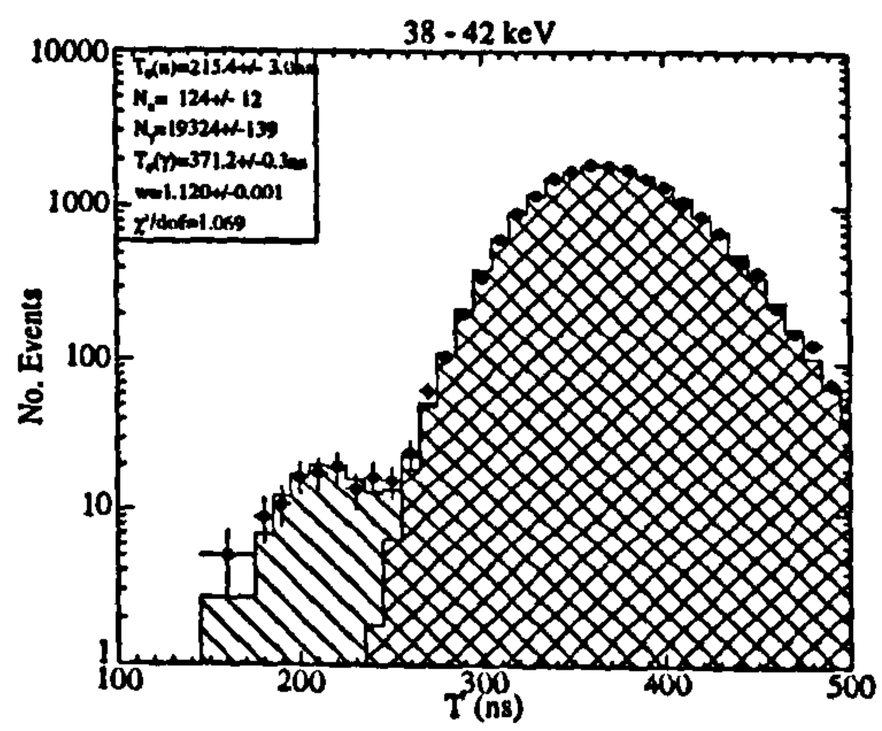

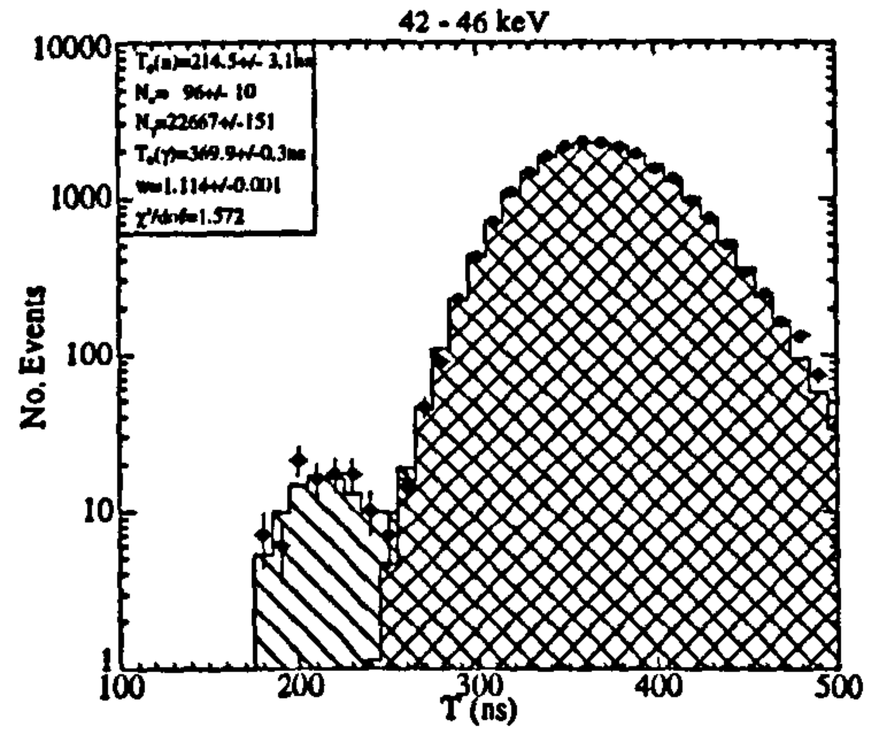

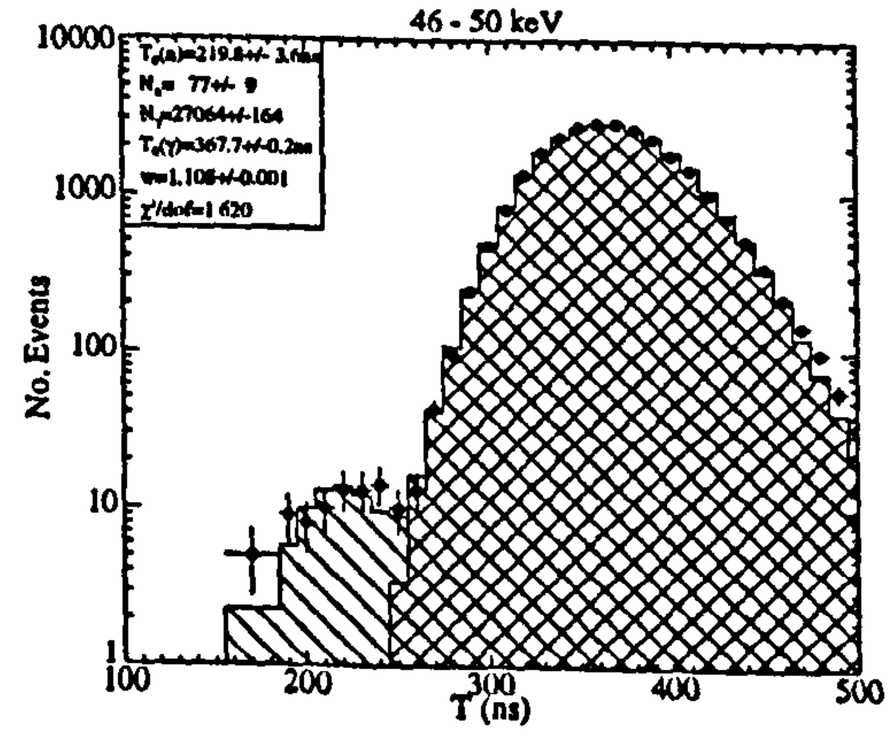

Figure 8.11 (continued).

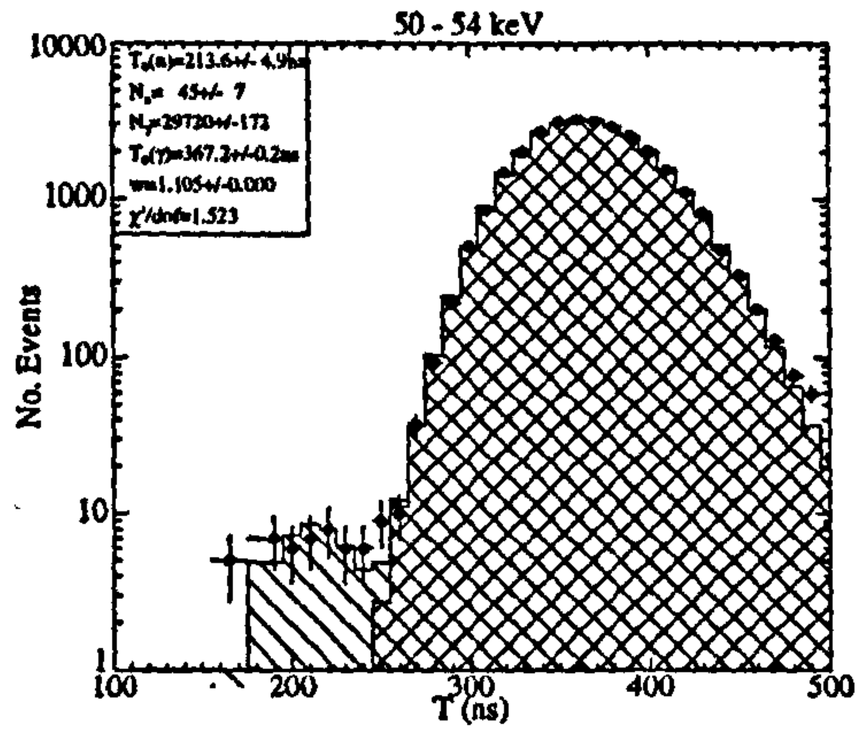

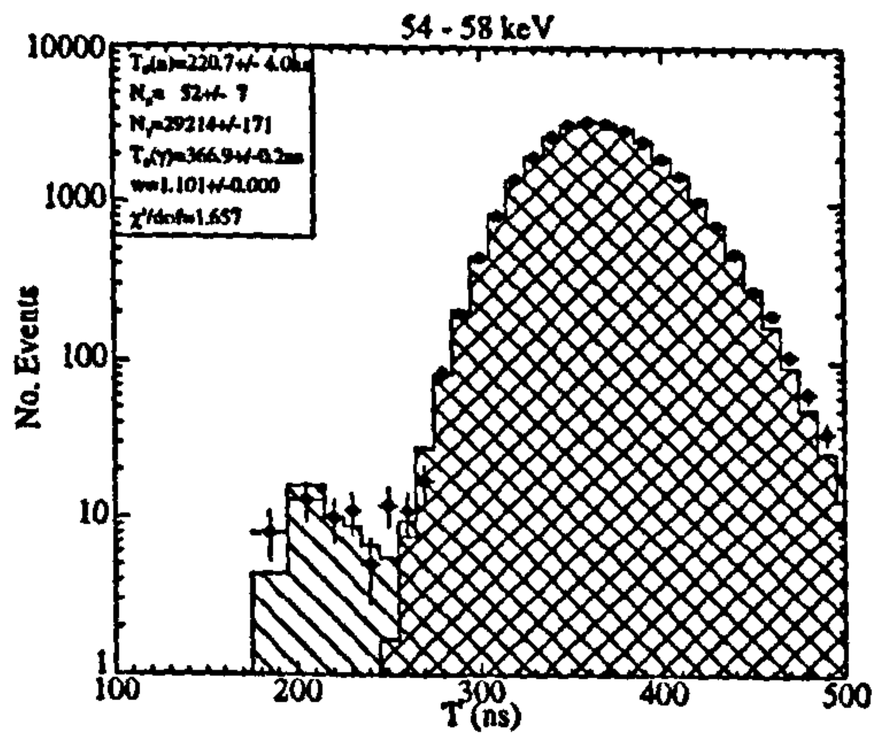

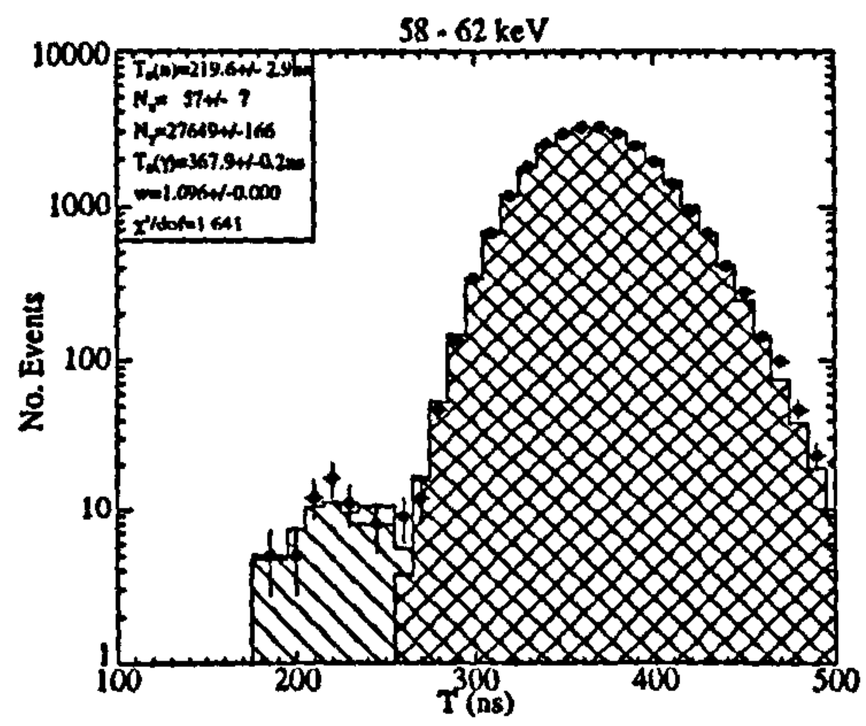

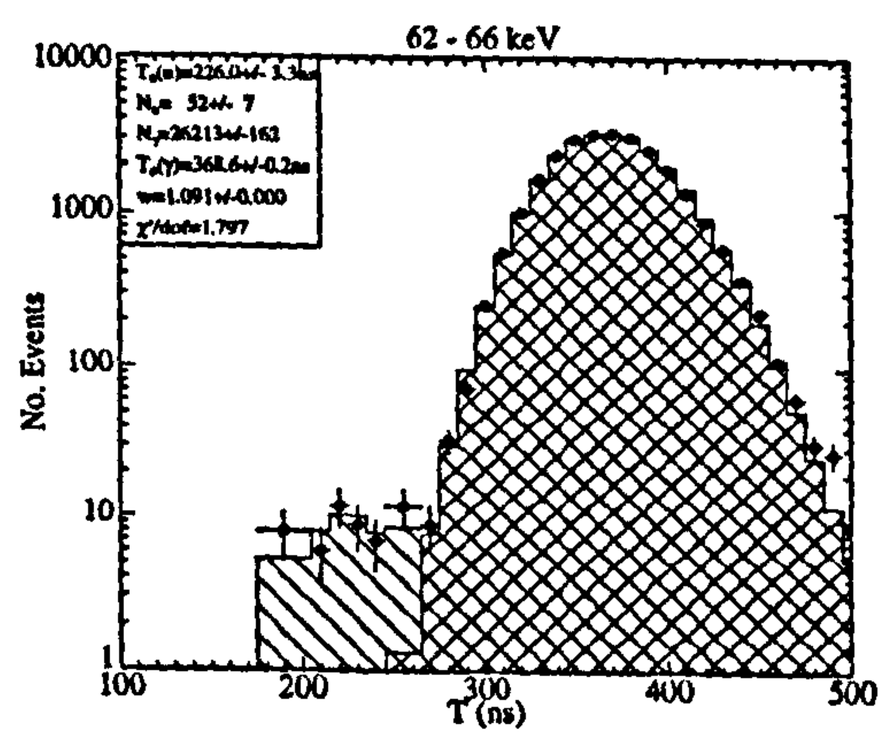

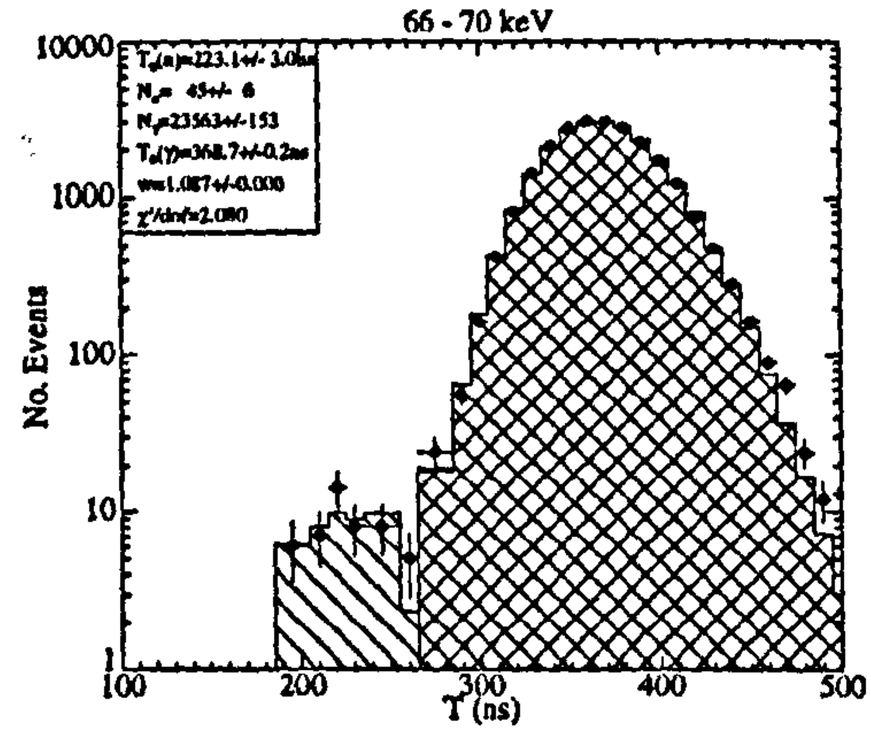

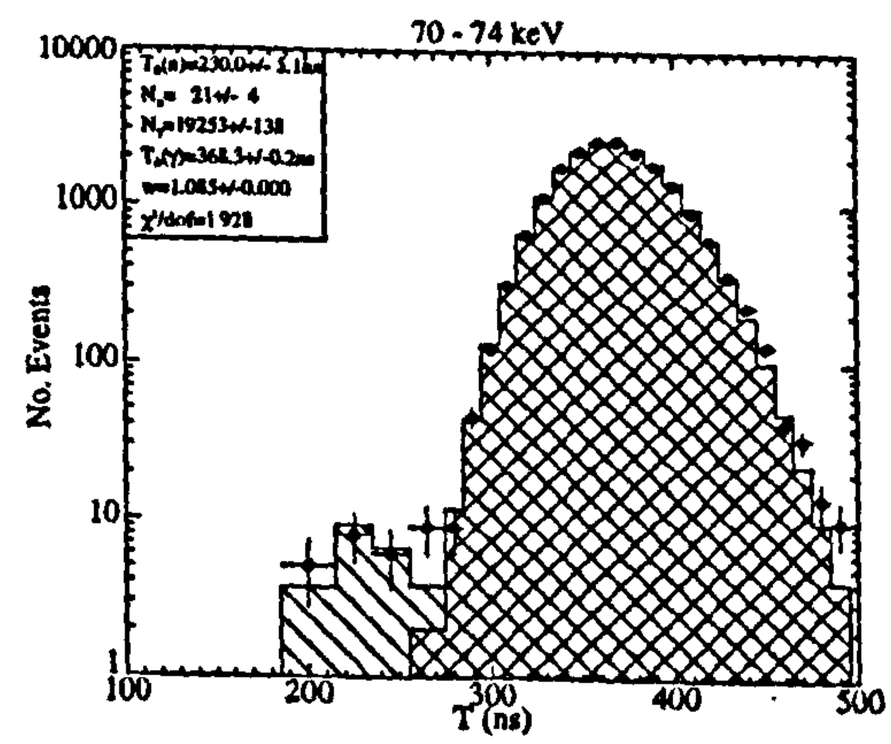

Figure 8.11 (continued).

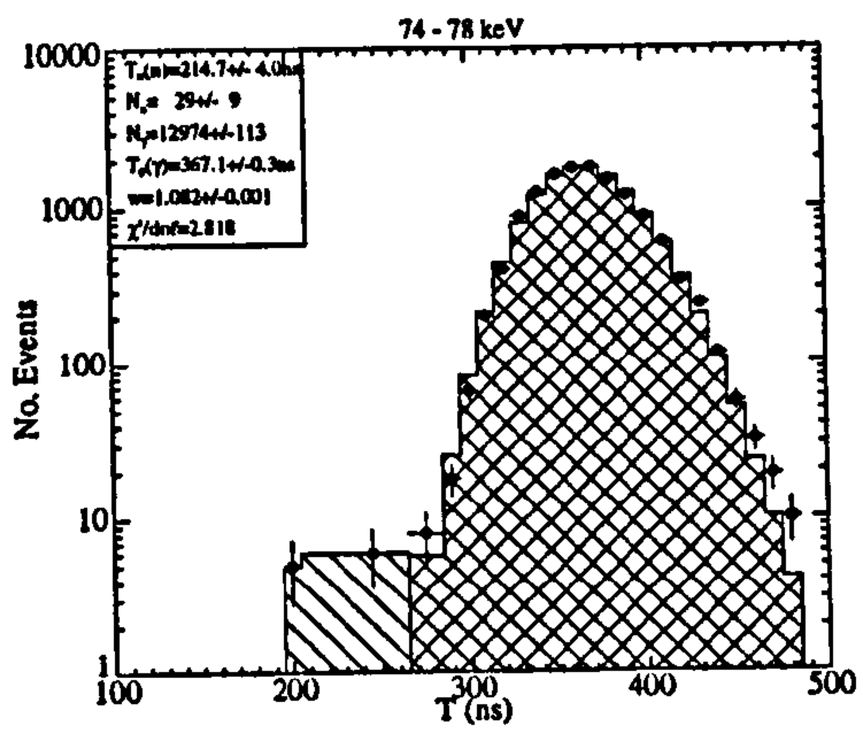

Figure 8.11 (continued).

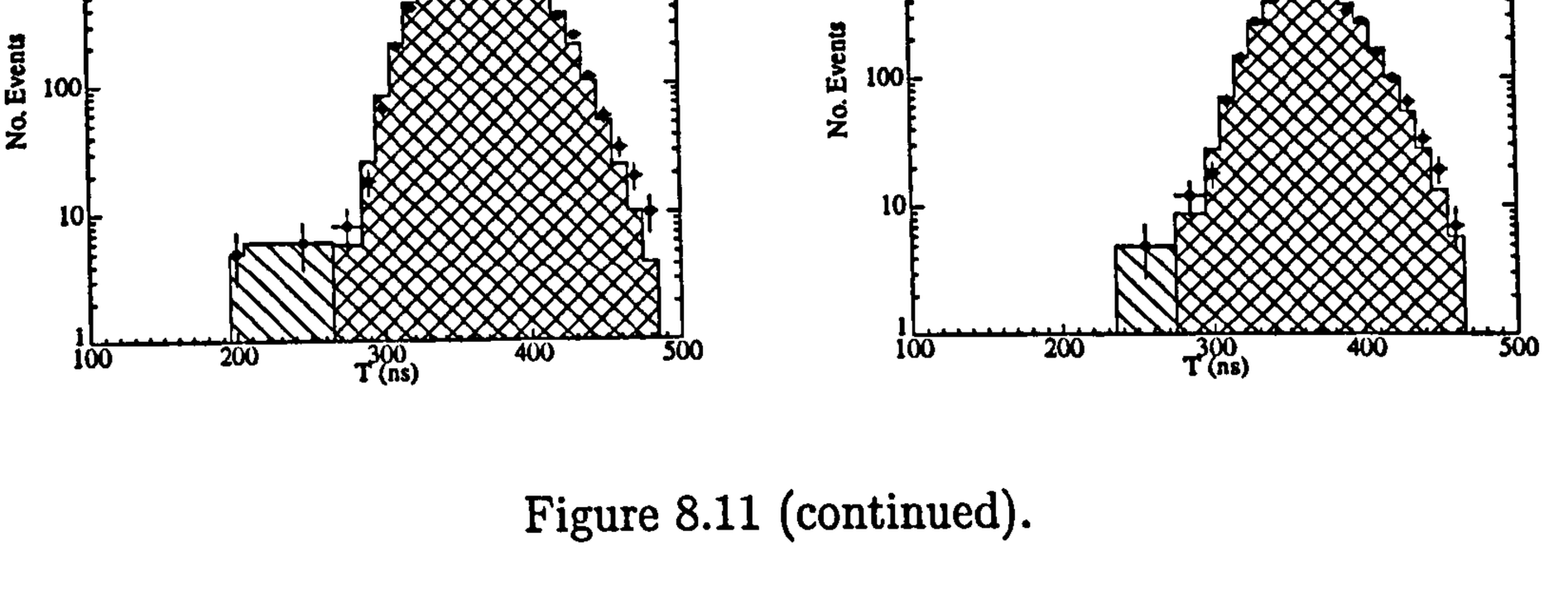

Figure 8.12: *T distributions for* **CCAL** *and* **NCAL** *events in the 14 - 30 keV visible energy bin. In the lefthand figure the histogram is a fit to* **CCAL** *data with a log-normal distribution as in Fig. 8.10. In the righthand figure the histogram is a fit to* **NCAL** *data with the sum of two log-normal distributions representing nuclear and electron recoil populations. The cross hatched area represents the contribution from the electron recoil distribution, as in Fig. 8.11. The free parameters are as before.*

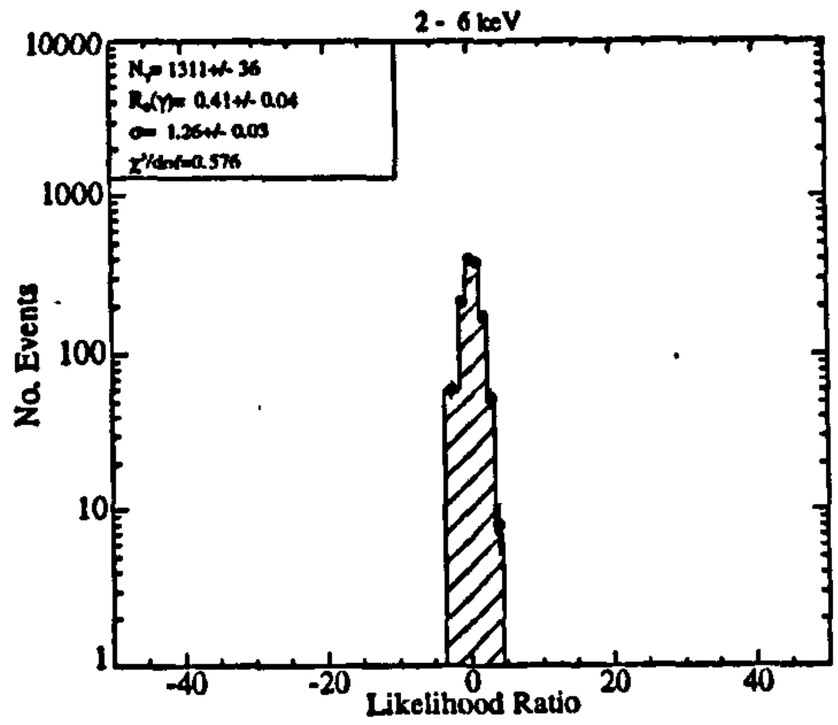

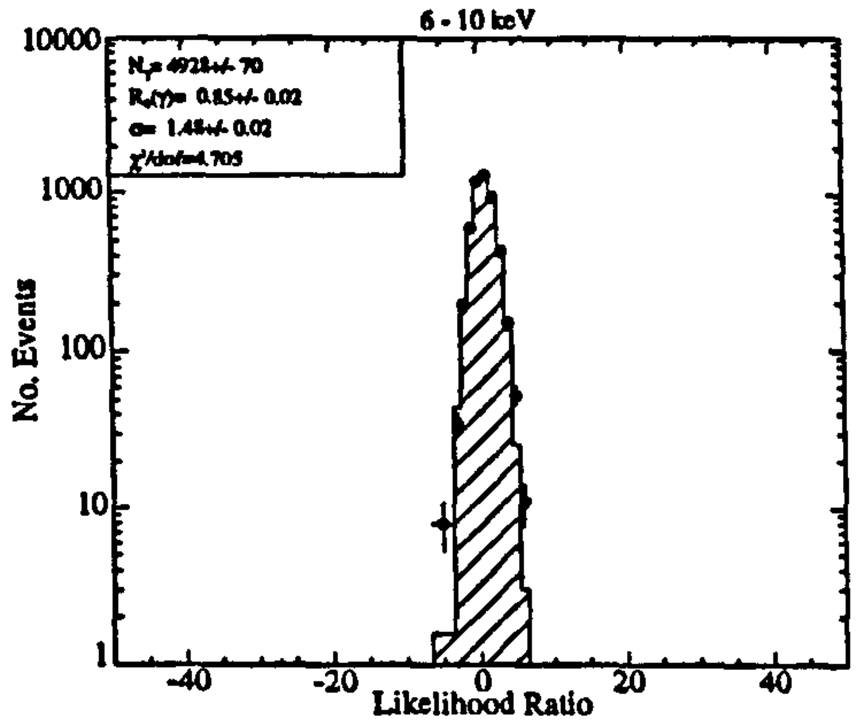

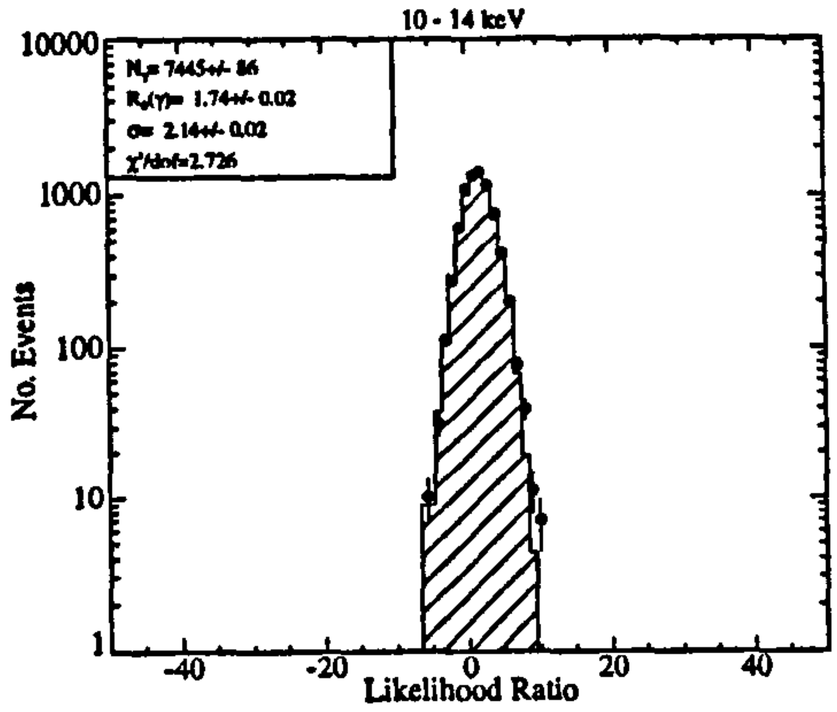

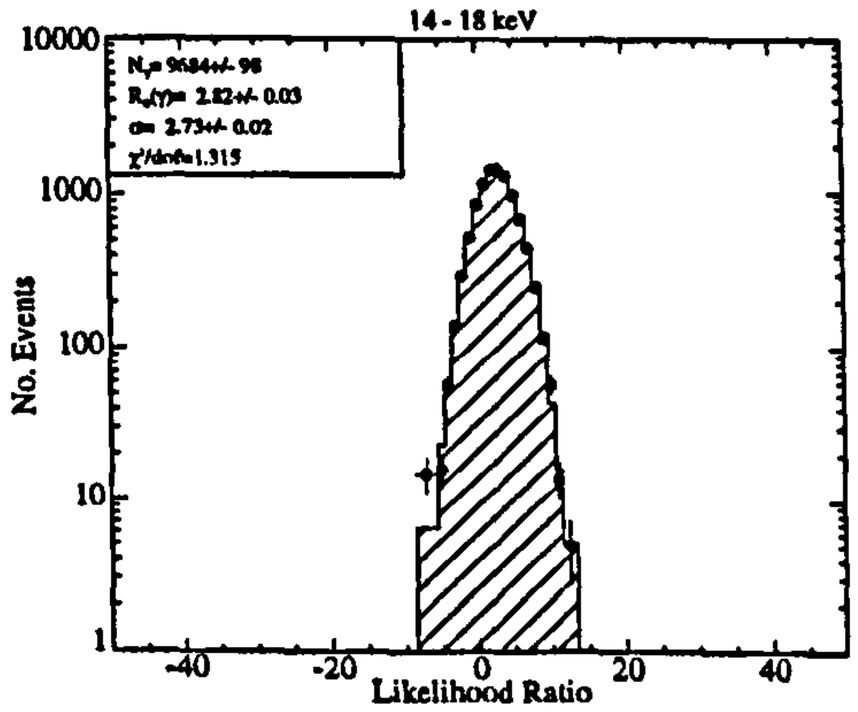

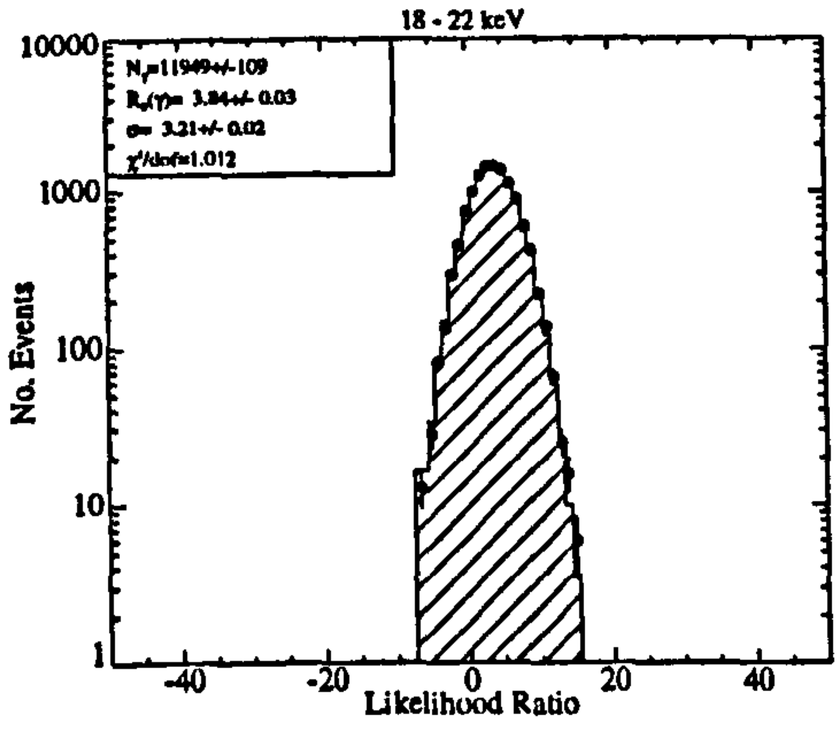

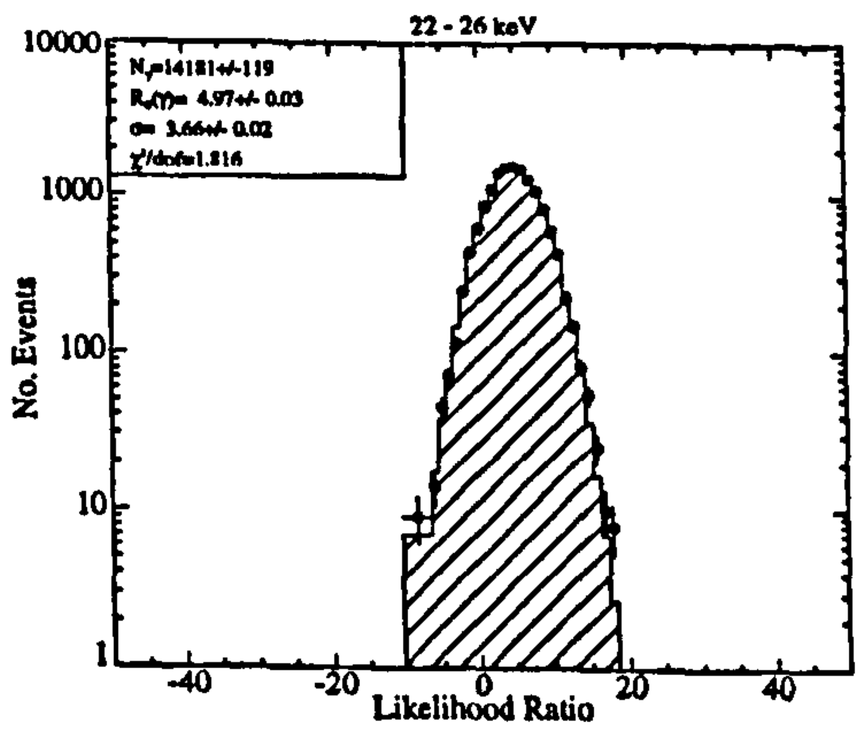

Figure 8.13: $\Re$ *distributions for* **CCAL** *events in 4 keV visible energy bins. The histograms represent fits to normal distributions with free parameters* σ, $\Re_0(\gamma)$ *(mean) and* N_γ *(normalisation). These distributions are included for comparison with Fig. 8.14.*

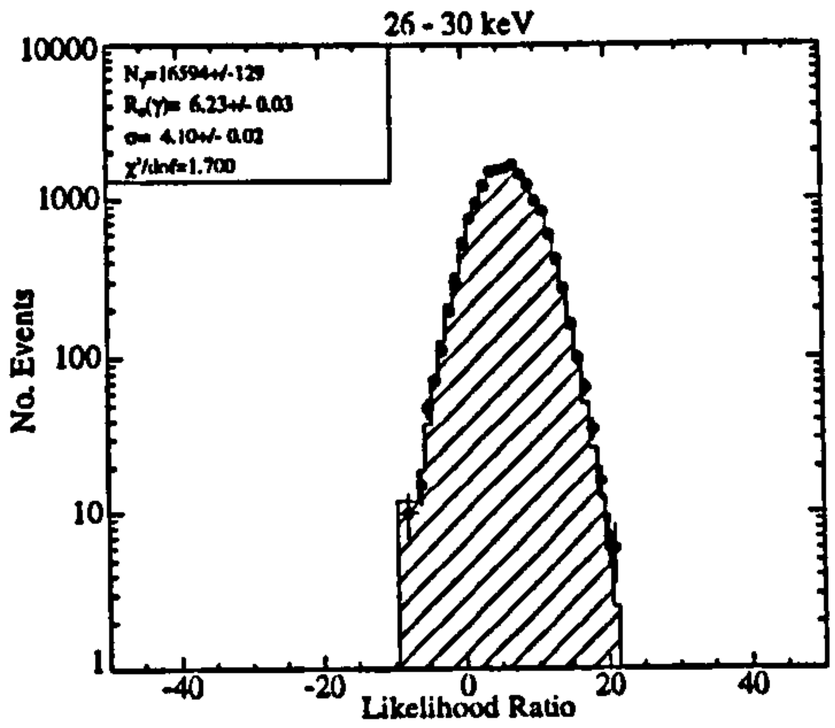

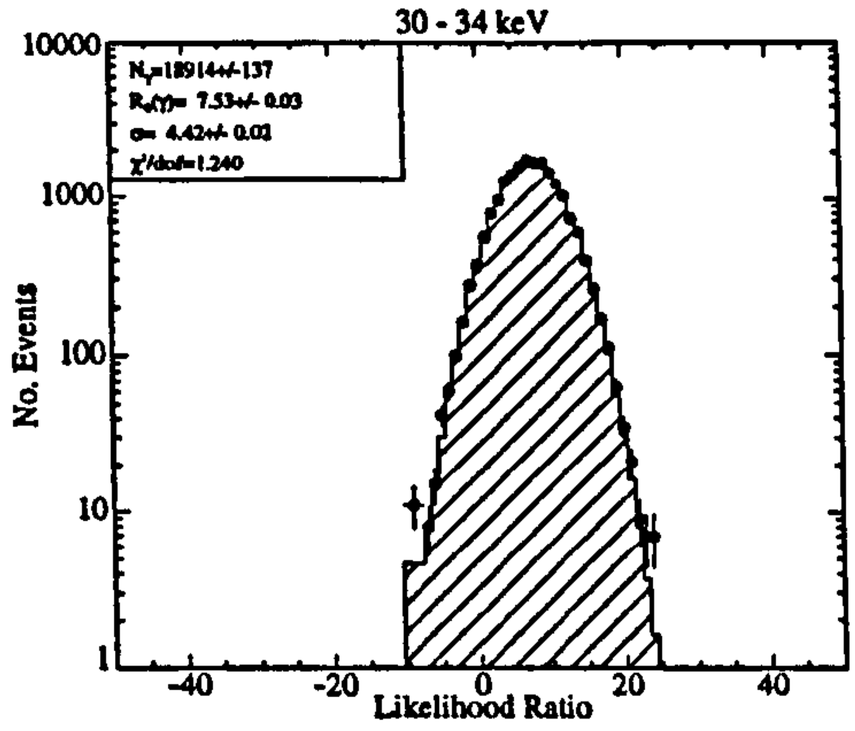

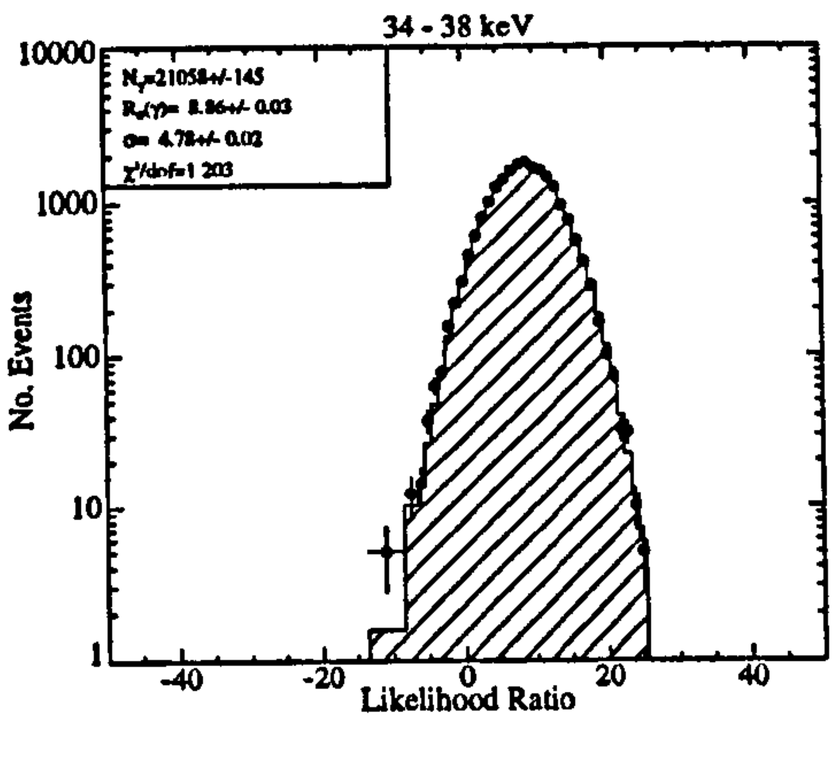

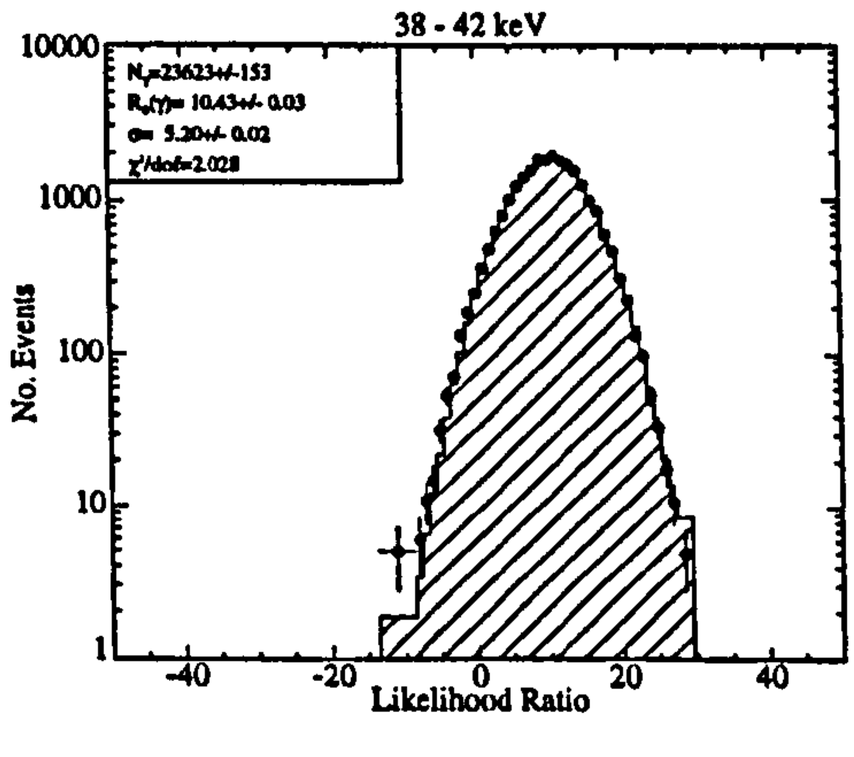

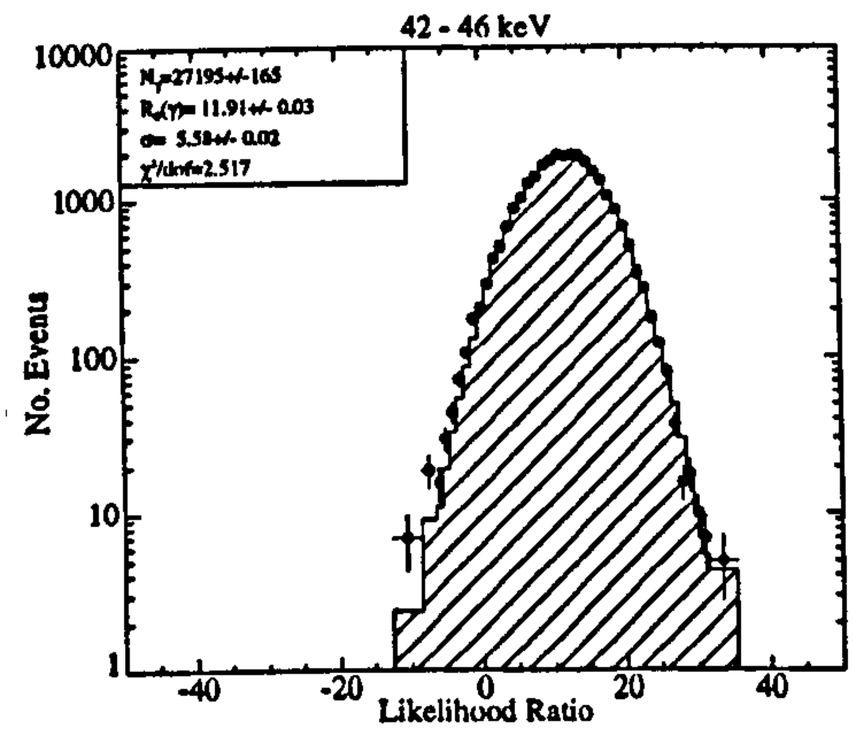

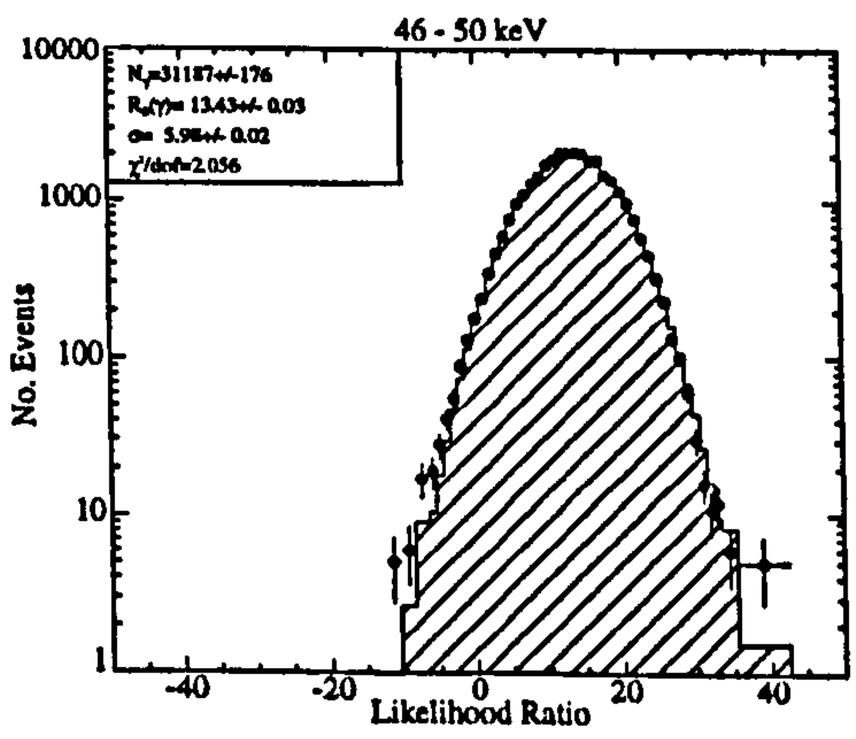

Figure 8.13 (continued).

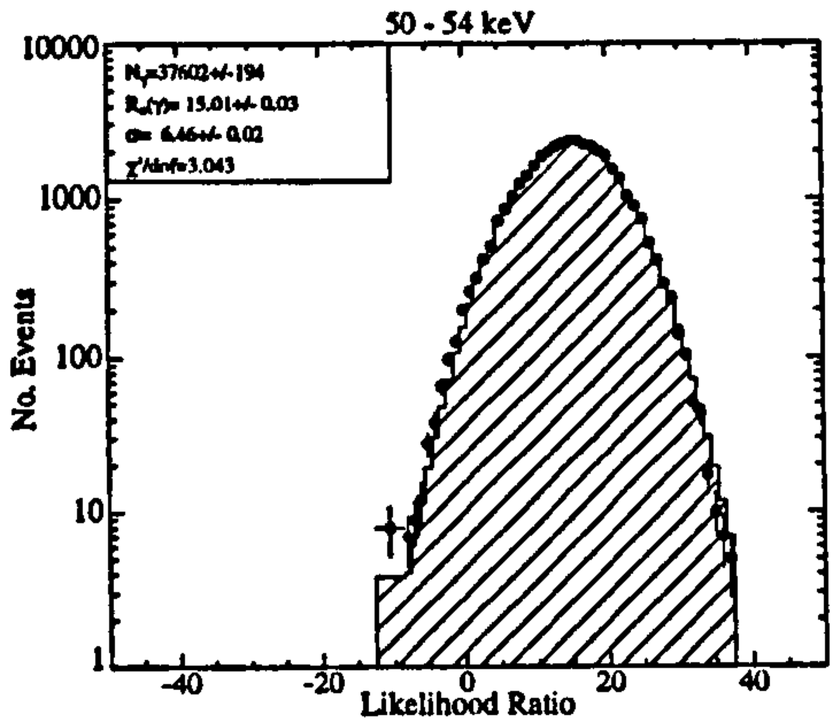

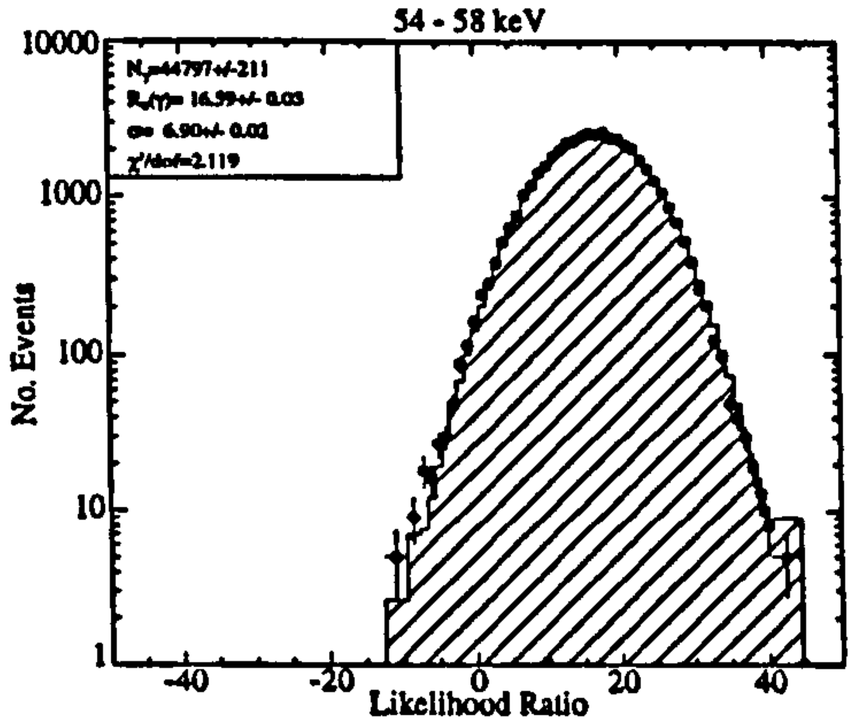

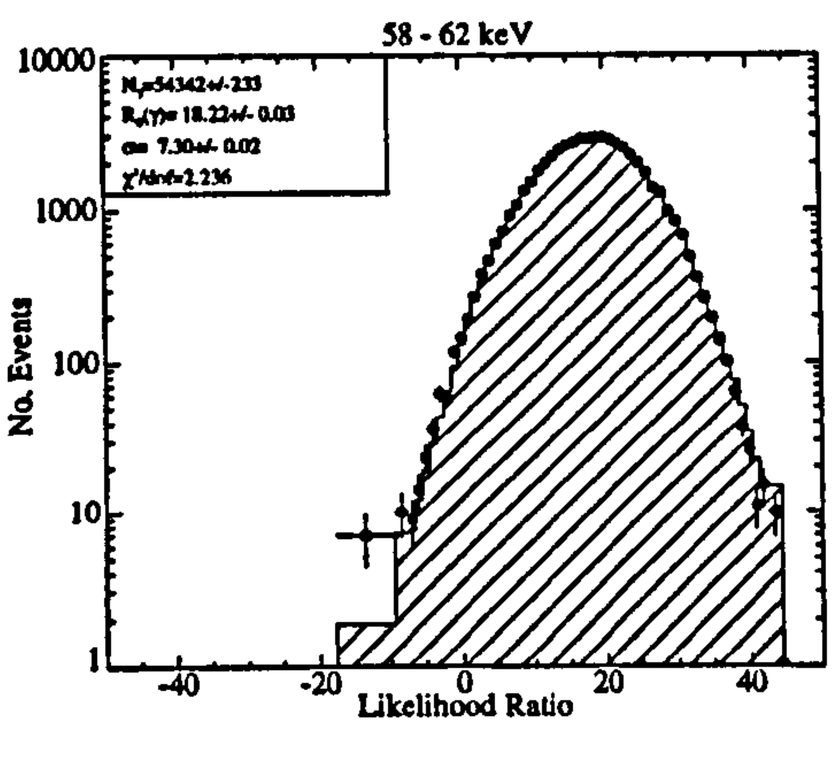

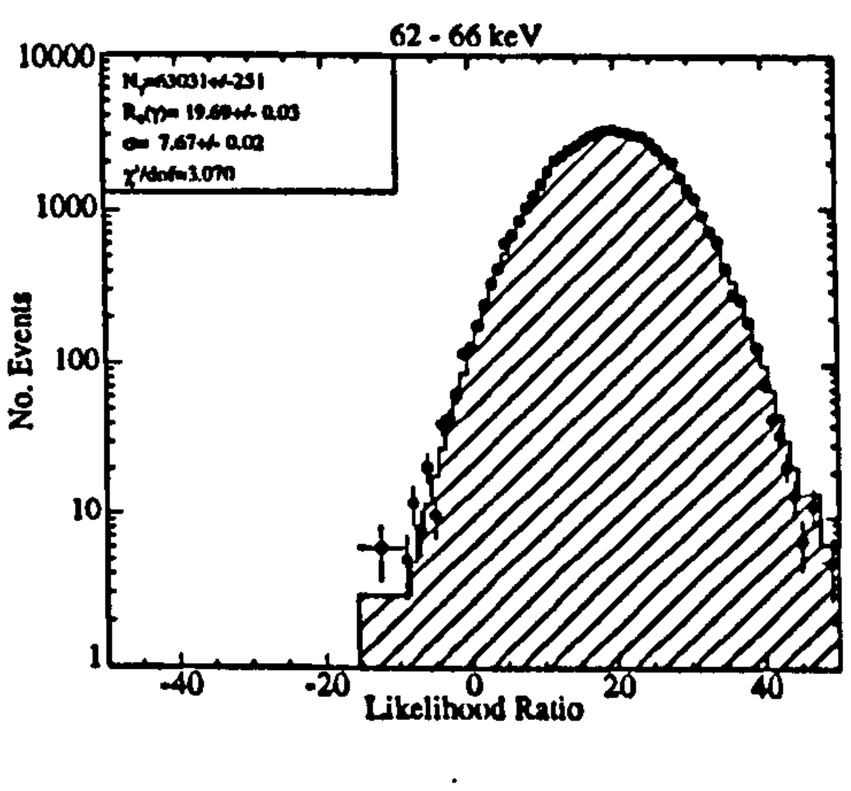

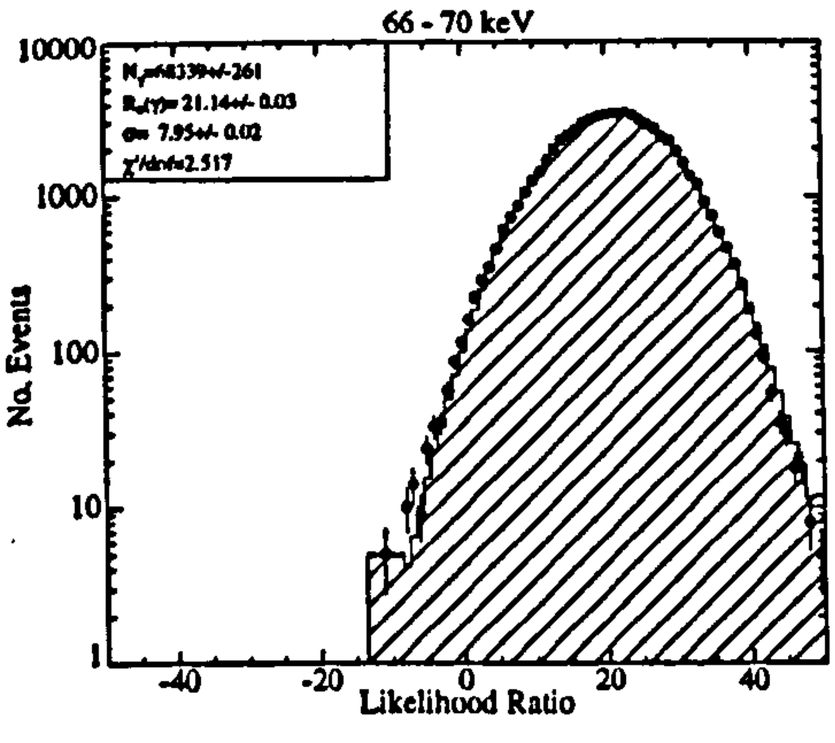

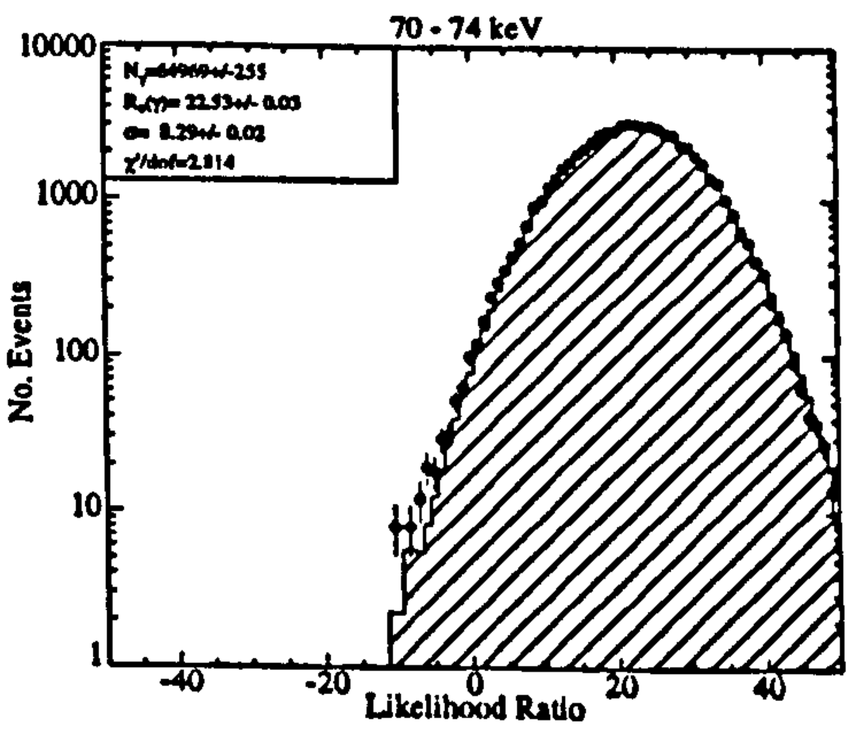

Figure 8.13 (continued).

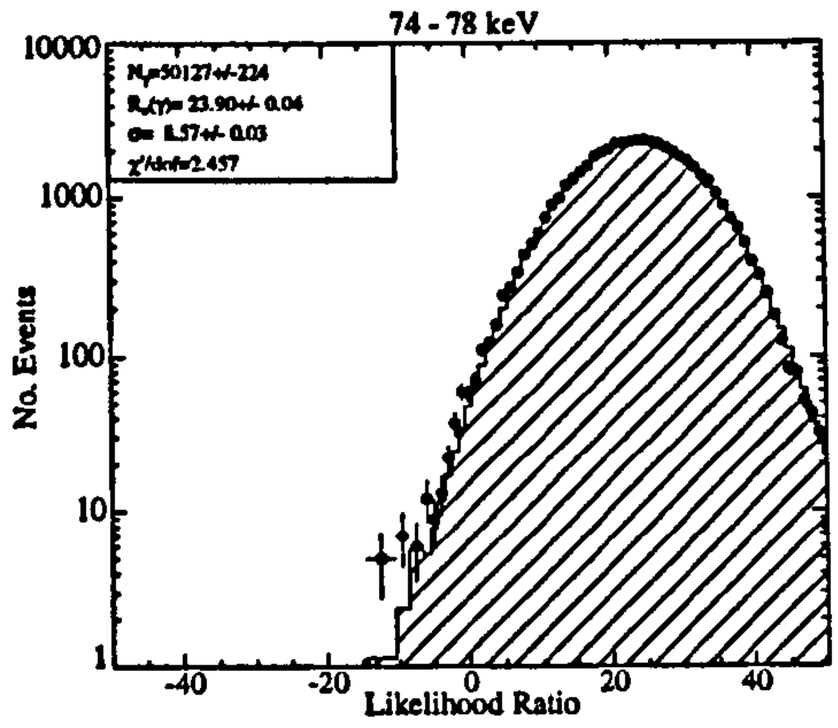

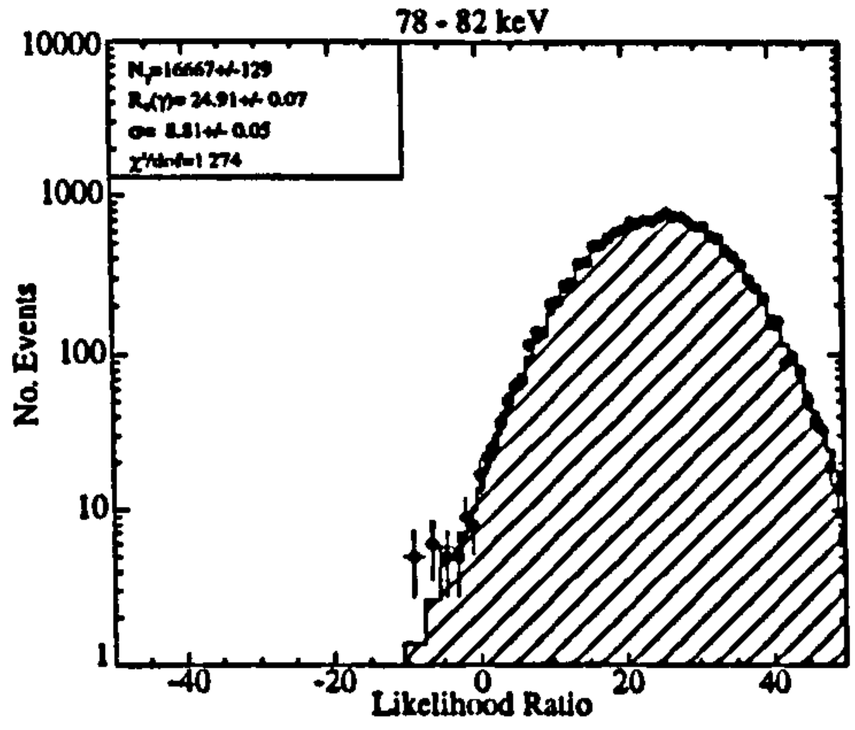

Figure 8.13 (continued).

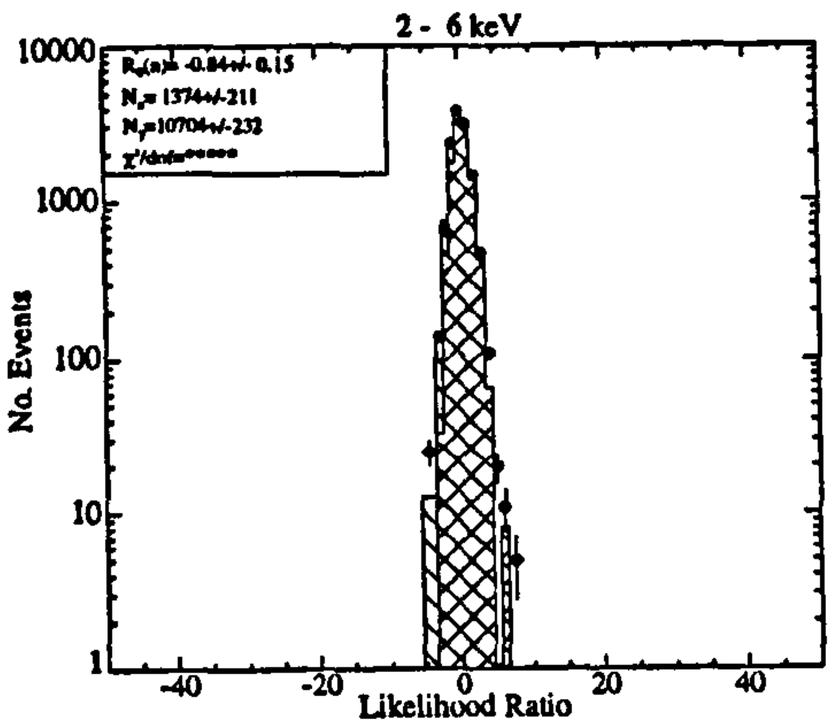

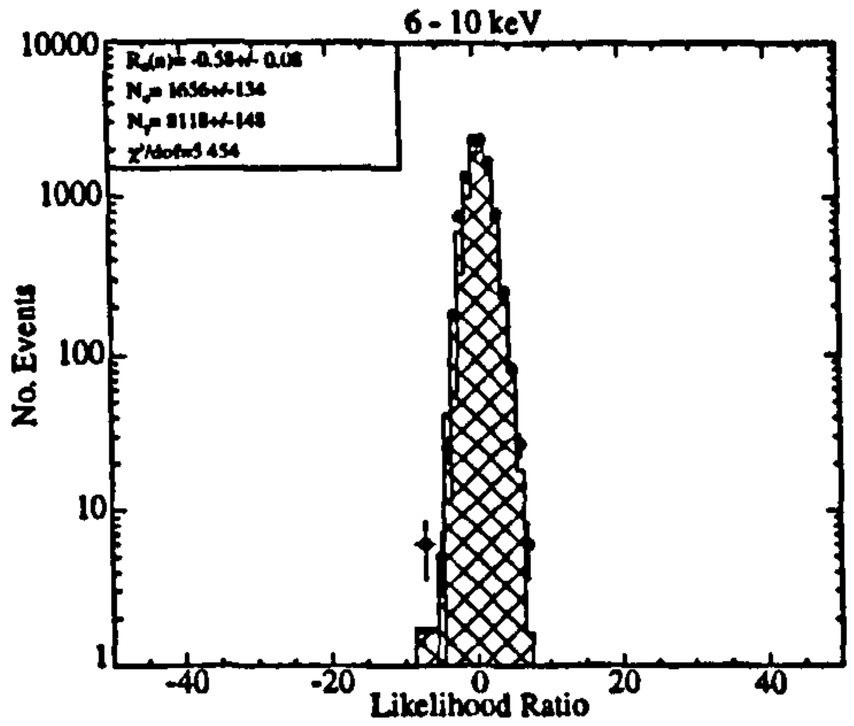

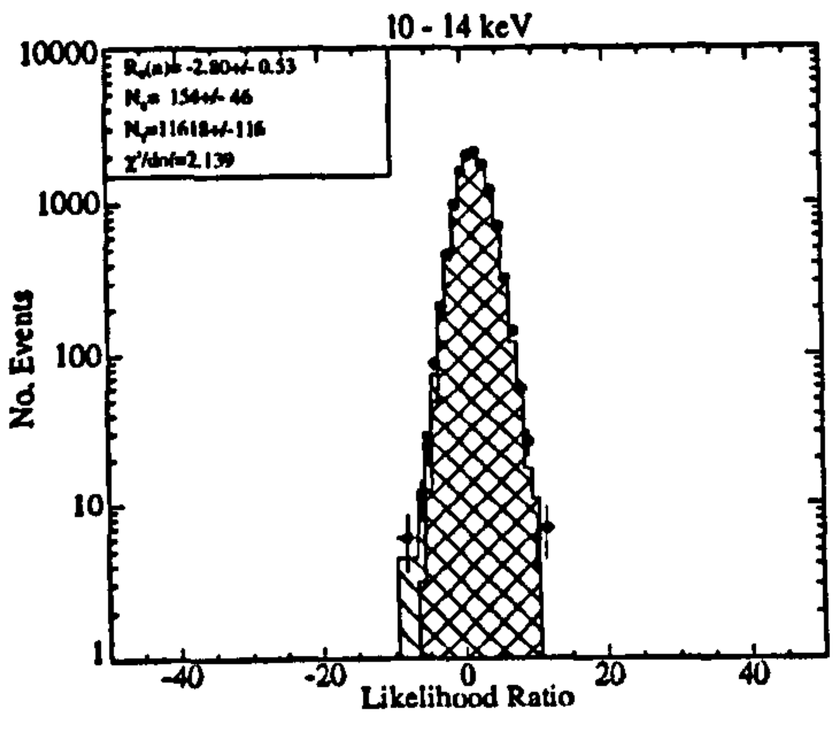

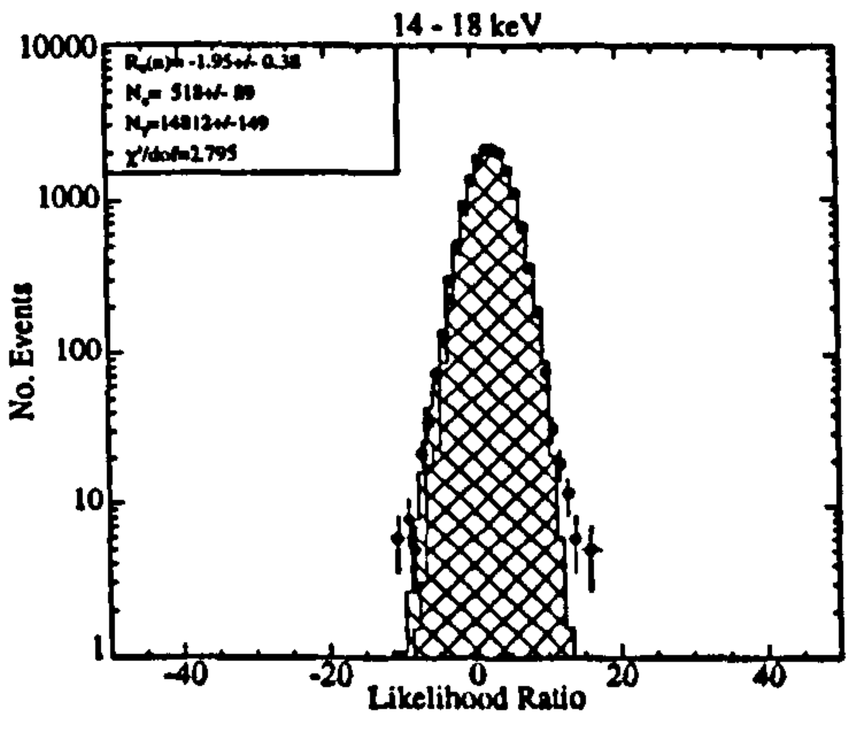

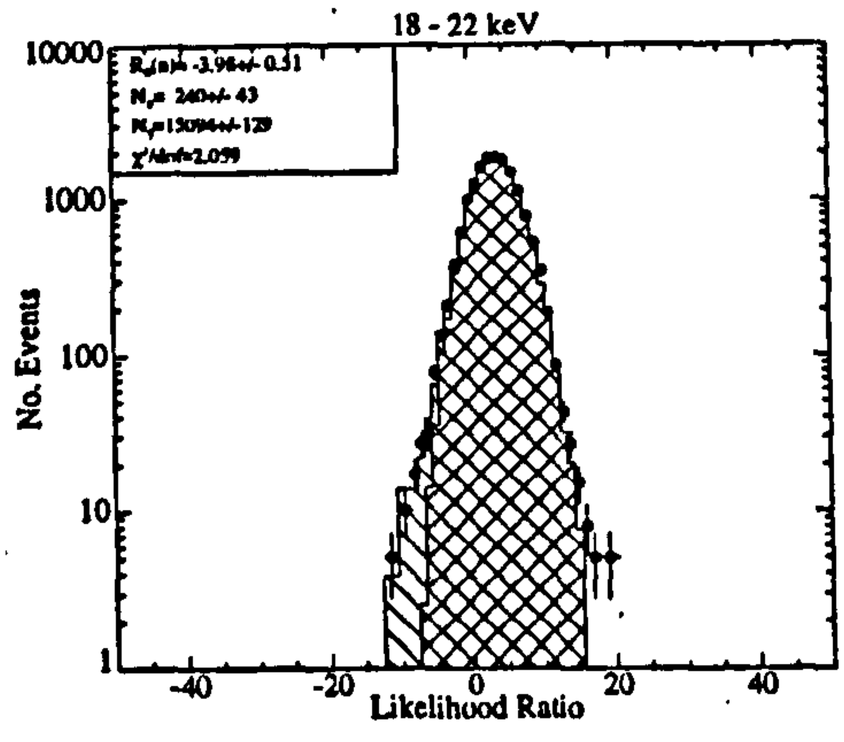

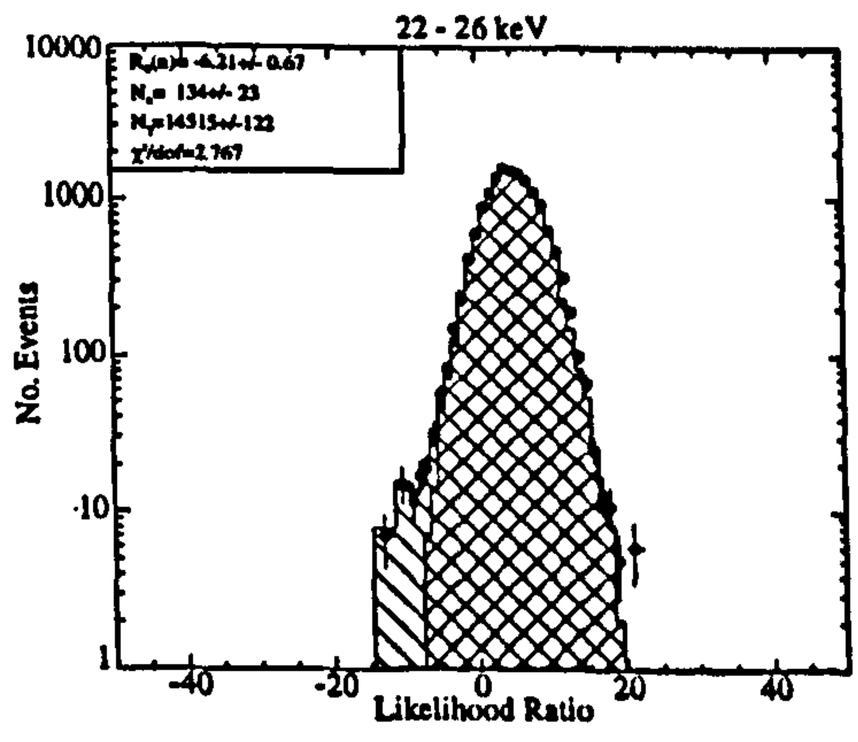

Figure 8.14: $\Re$ *distributions for* **DATA** *events in 4 keV visible energy bins. The histograms represent fits to sums of a normal distribution and the corresponding normalised* **CCAL** *distribution representing the nuclear and electron recoil populations respectively. The cross hatched areas represent the contributions from the electron recoil distributions. The free parameters are* $\Re_0(n)$ *(nuclear recoil distribution mean) and* N_n *and* N_γ *(nuclear and electron recoil distribution normalisations). Relevant fitted parameter values can be found in Table 8.4.*

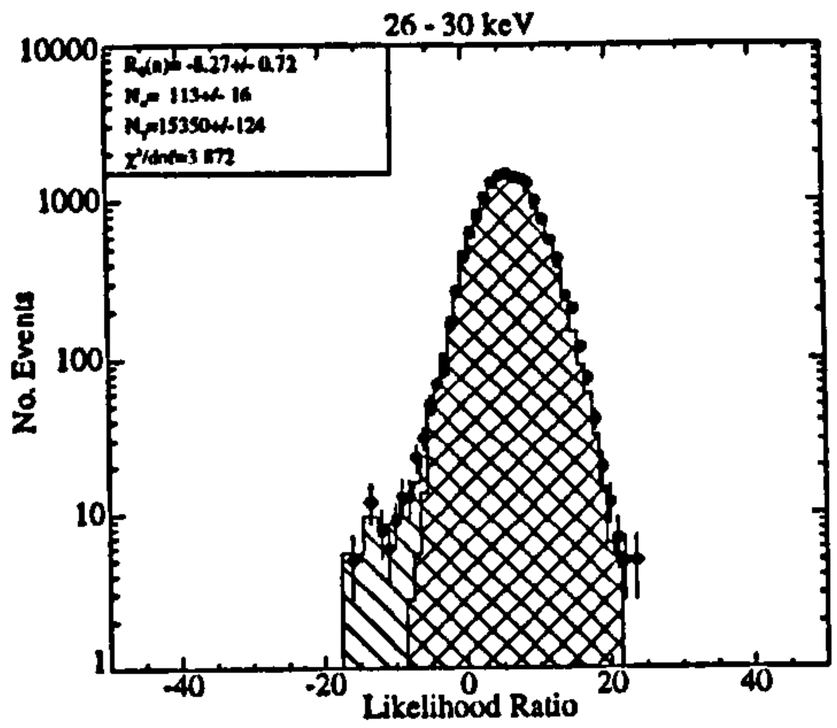

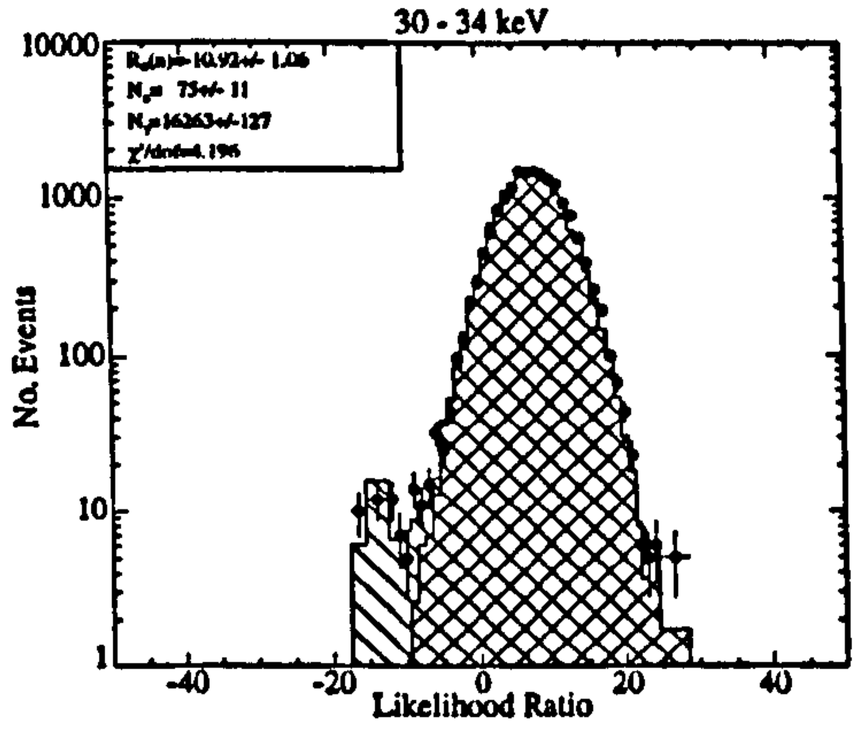

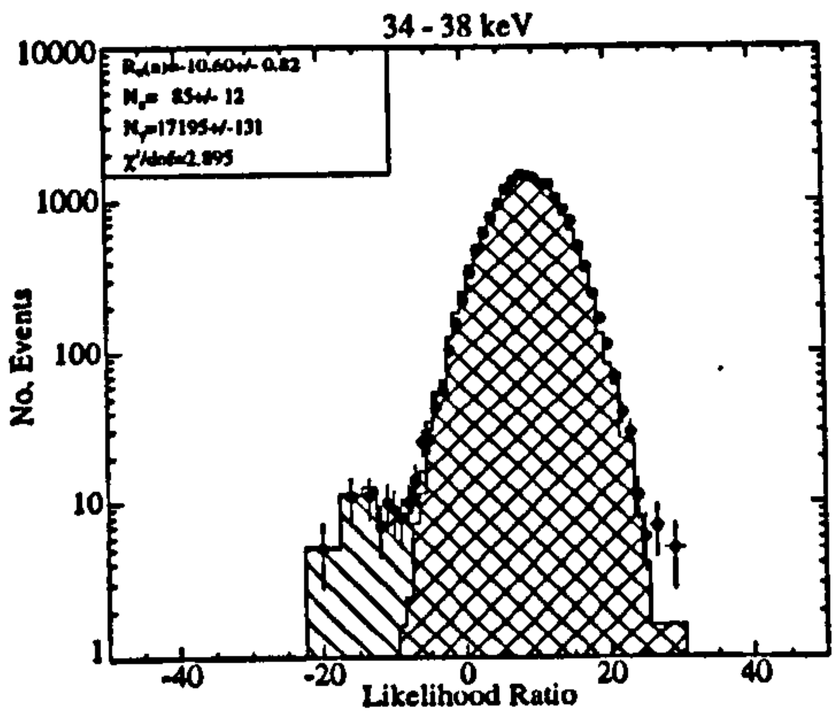

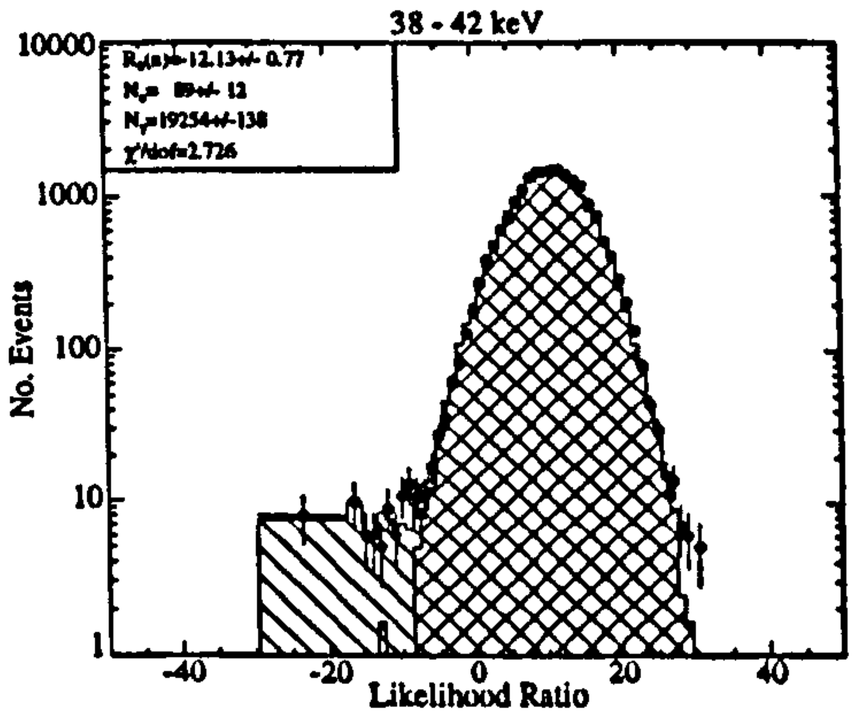

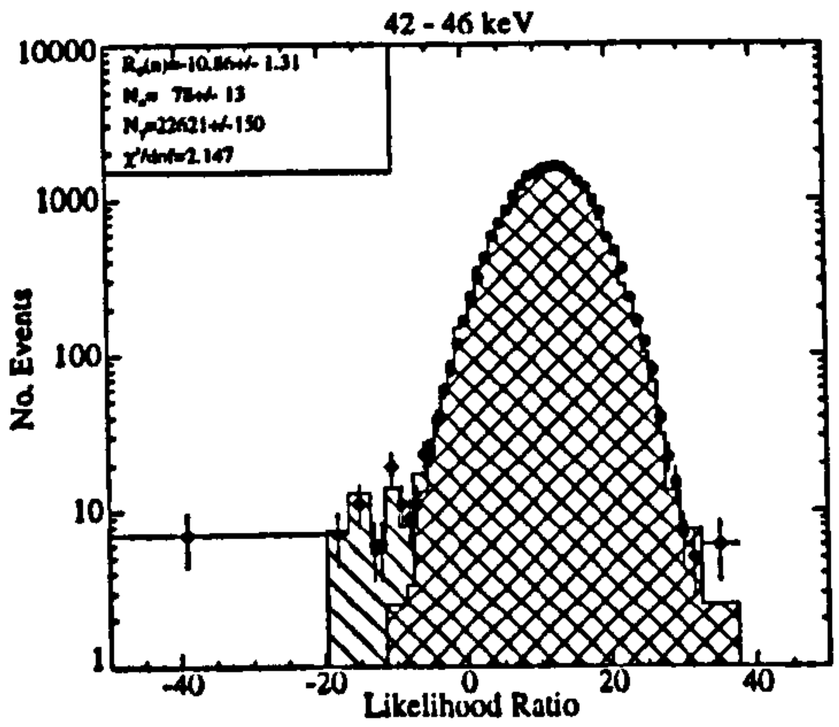

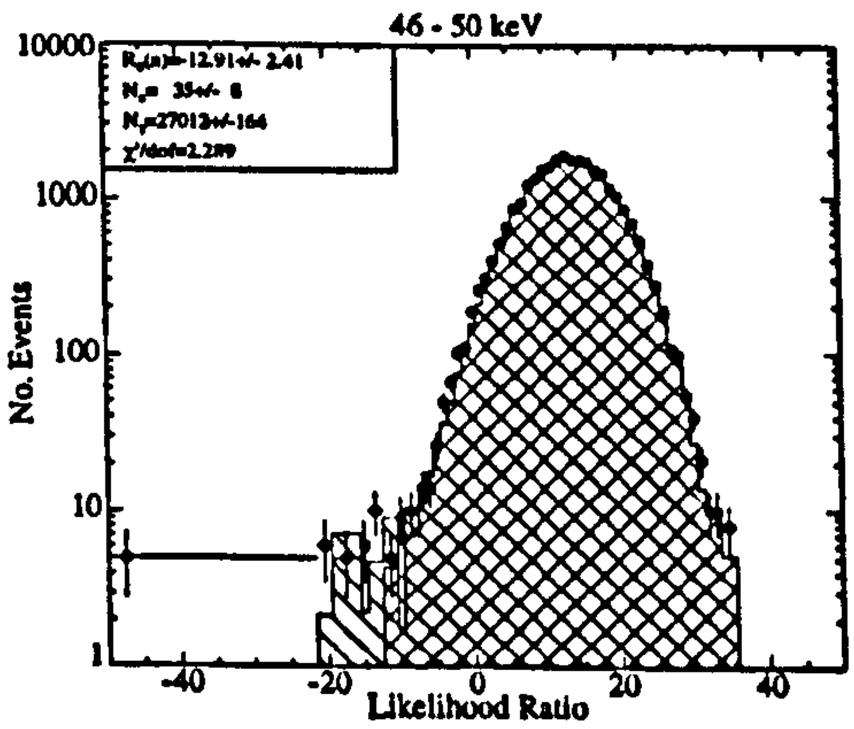

Figure 8.14 (continued).

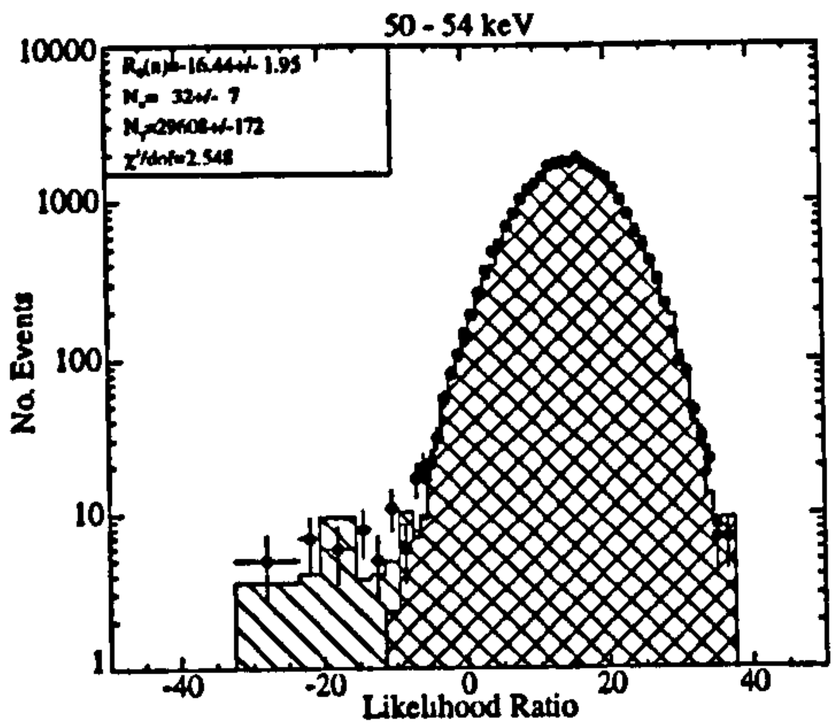

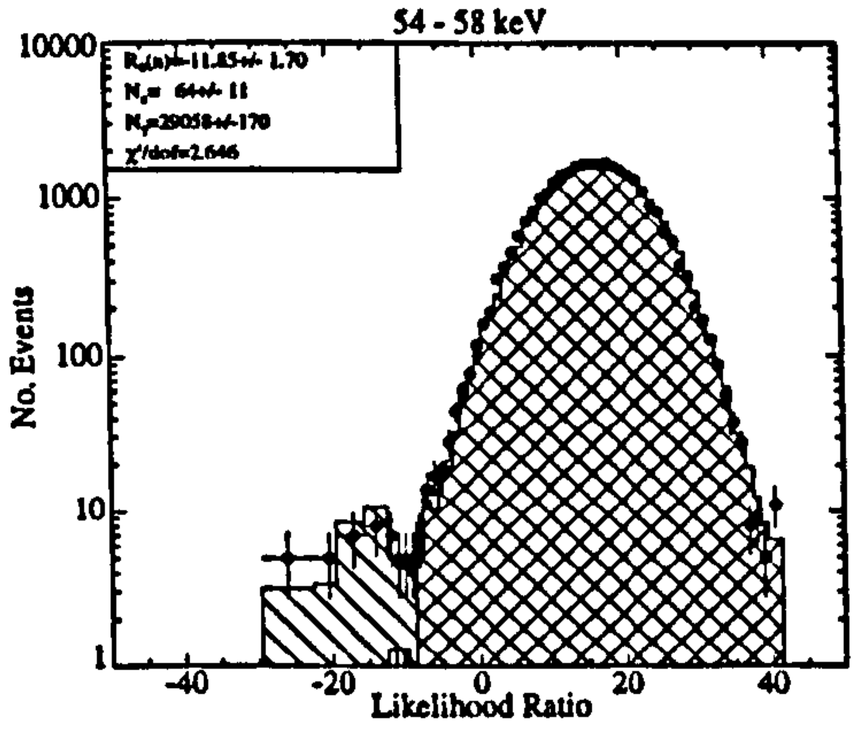

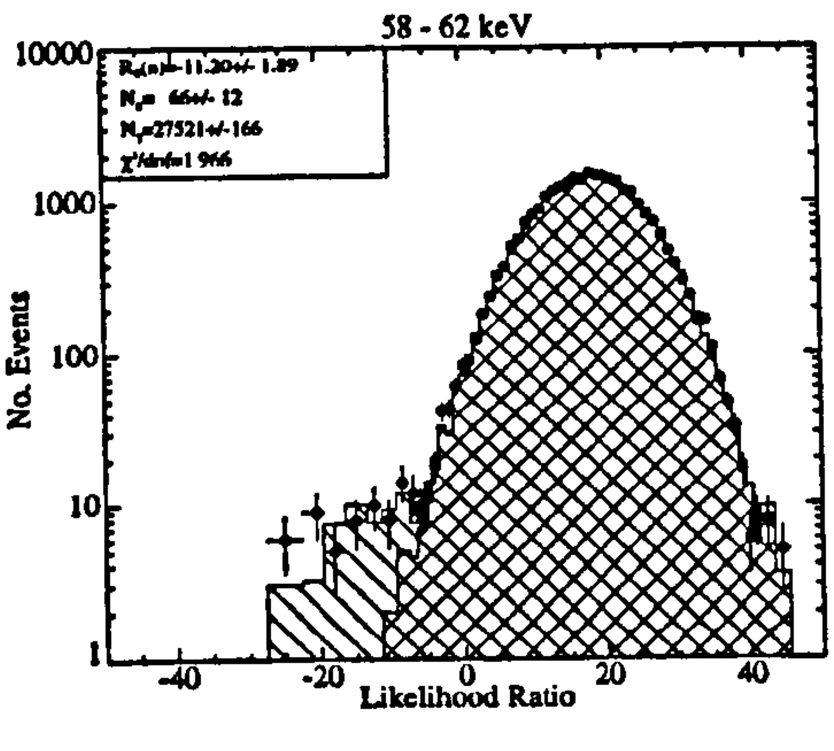

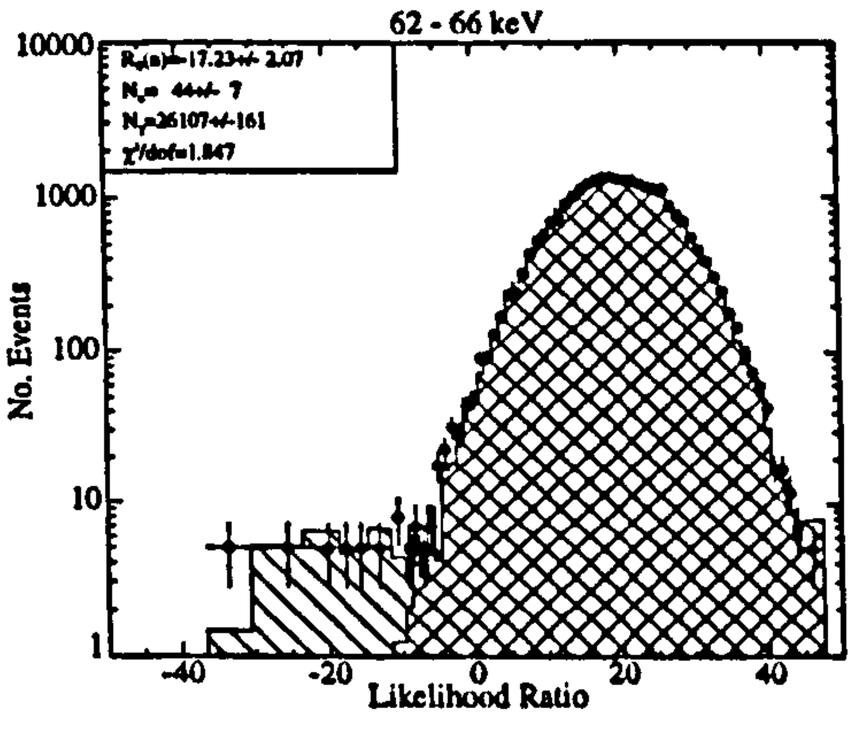

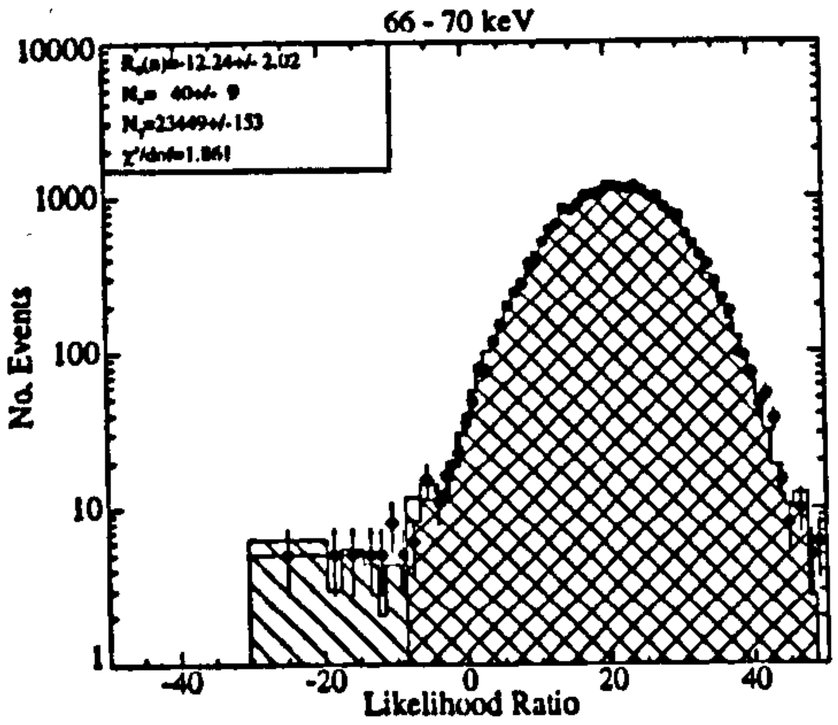

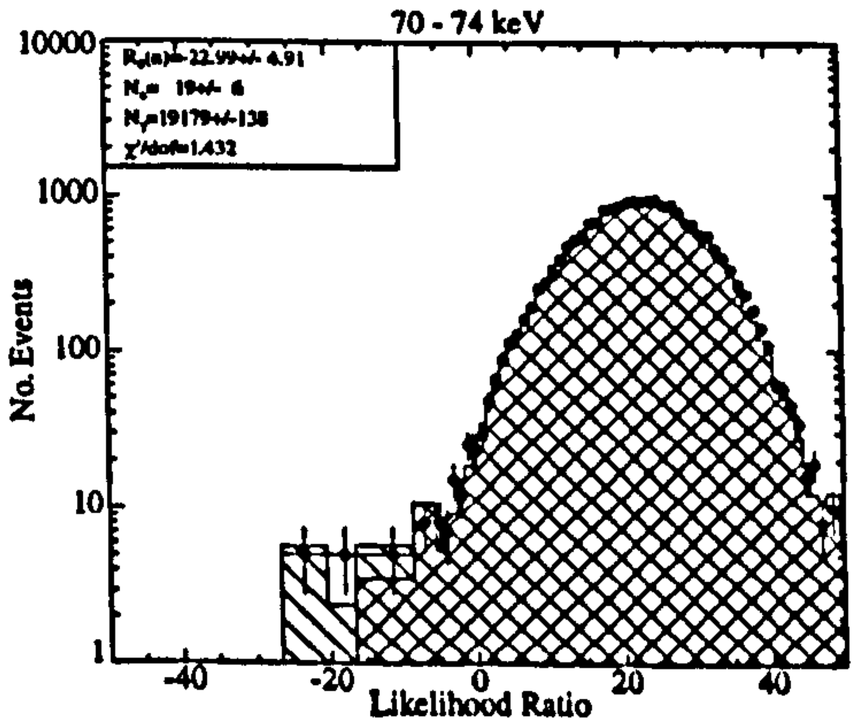

Figure 8.14 (continued).

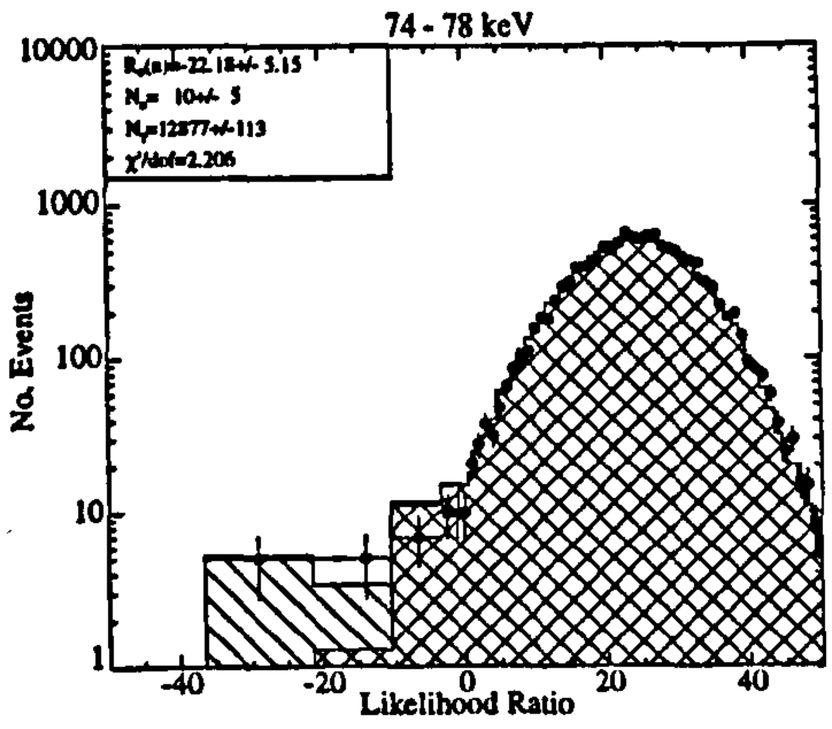

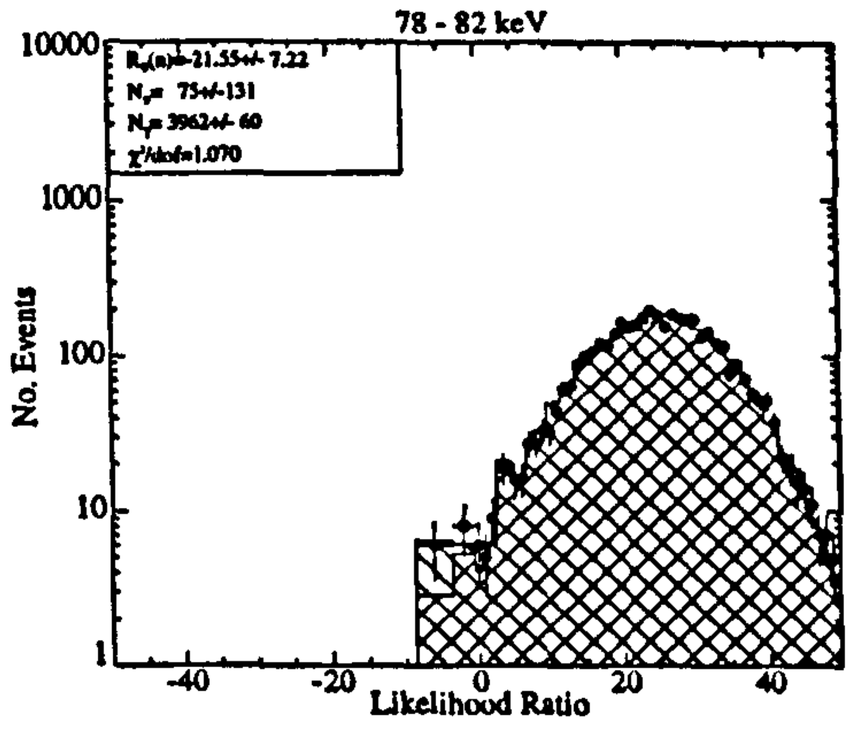

Figure 8.14 (continued).

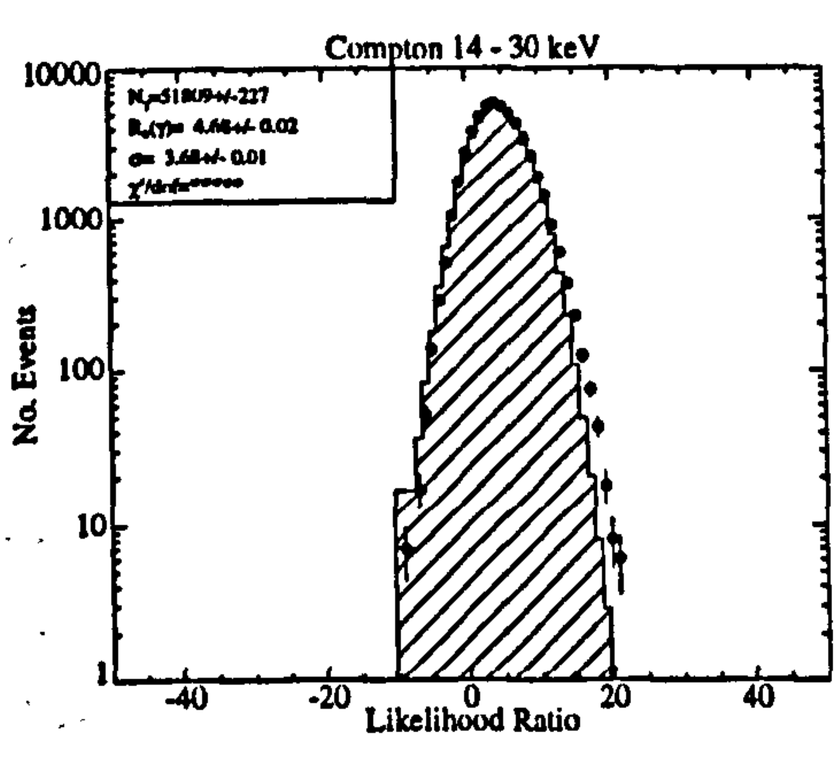

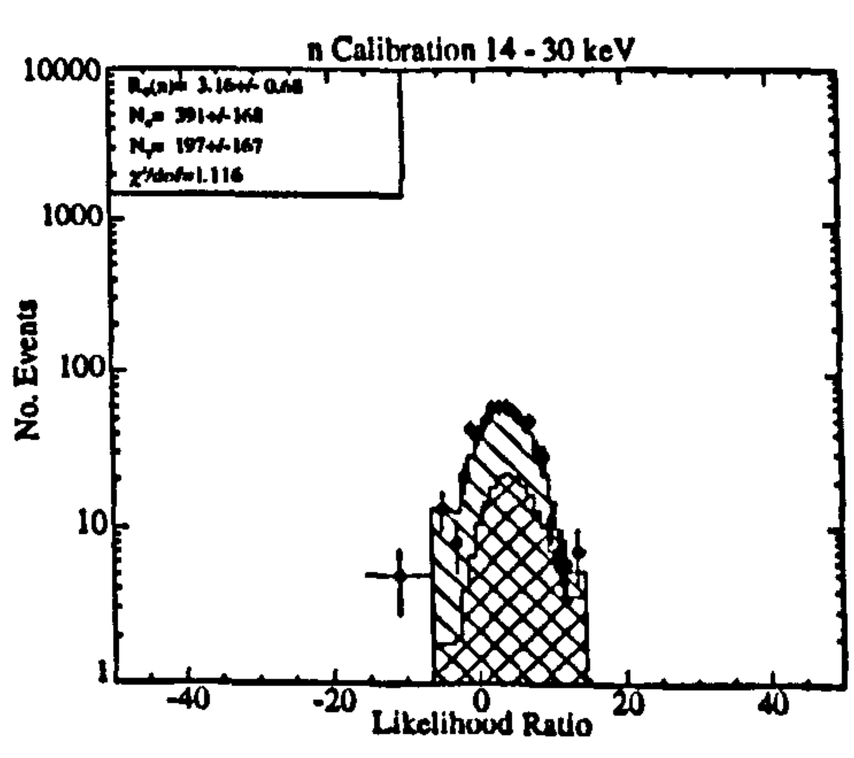

Figure 8.15: $\Re$ *distributions for* **CCAL** *and* **NCAL** *events in the 14 - 30 keV visible energy bin. In the lefthand figure the histogram is a fit to* **CCAL** *data with a normal distribution as in Fig. 8.13. In the righthand figure the histogram is a fit to* **NCAL** *data with the sum of a normal distribution and the corresponding normalised* **CCAL** *distribution representing nuclear and electron recoil populations respectively. The cross hatched area represents the contribution from the electron recoil distribution, as in Fig. 8.14. The free parameters are as before.*

8.5 Results

8.5.1 Fit Results

The results of the MT and LR fits are presented in Tables 8.3 and 8.4 respectively (overleaf). There is evidence in Figs. 8.11 and 8.14 for an anomalous population of events in all energy bins, situated at $T < 220$ ns and $\Re < 0$. Both the MT and LR fits confirm this hypothesis with the best fits obtained for nuclear recoil signal rates S_f many standard deviations from zero. This hypothesis and the data in general will now be considered in more detail.

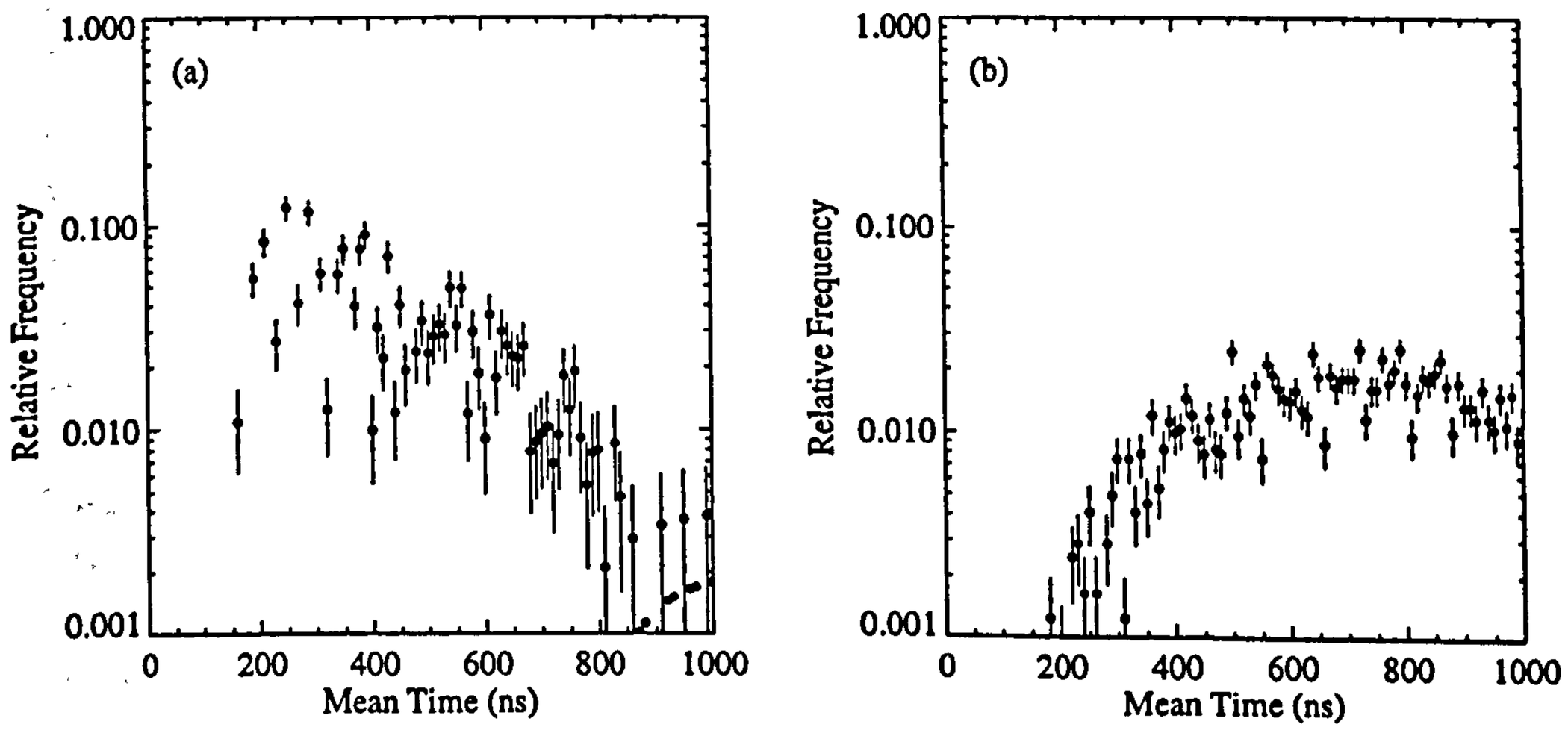

Figure 8.16: *The mean time distributions of noise events in the 2 - 6 keV visible energy bin. Figure (a) shows the residuals from the fit to* **DATA** *events. Figure (b) shows Monte Carlo data.*

Consider first the 2 - 6 keV visible energy bin of the MT **DATA** events (Fig. 8.11). The fit in this first bin is particularly poor ($\chi^2/\text{dof} = 4.68$) relative to those in subsequent bins. The reason for this poor fit is a long tail of events at high T (relative to the majority of the **CCAL** data), which does not occur at higher energies. The residuals from the fit are plotted in Fig. 8.16(a). It was postulated that these events were due to stochastic pile up of single thermal photoelectrons and this hypothesis was tested with a Monte Carlo simulation (Fig. 8.16(b)). The simulation was performed by assuming a realistic single photoelectron dark count (10 kHz) and trigger requirement (> 2 pe in 5μs) for each PMT. The simulation indicated that 99.5 % of such events should be rejected by the preselection cuts and that of the 535 events

E_v	S_f	$\sigma(S_f)$	G_f	$\sigma(G_f)$	$T_0(n)$	$\sigma(T_0)$	$T_0(\gamma)$	$\sigma(T_0)$	χ^2/dof
2-6	0.177	0.025	3.19	0.03	411.0	35.5	252.9	0.8	4.680
6-10	0.482	0.252	2.34	0.25	225.0	8.7	294.3	6.5	1.061
10-14	0.165	0.032	3.22	0.04	207.6	5.3	315.7	1.1	1.066
14-18	0.128	0.019	4.29	0.04	208.6	4.6	327.9	0.6	1.291
18-22	0.083	0.010	4.34	0.04	206.9	4.2	341.5	0.5	0.868
22-26	0.058	0.006	4.17	0.04	208.4	3.5	355.0	0.5	1.539
26-30	0.050	0.005	4.43	0.04	205.9	3.2	360.9	0.4	1.516
30-34	0.044	0.004	4.70	0.04	212.4	3.1	366.0	0.4	1.430
34-38	0.037	0.004	4.97	0.04	210.6	3.0	368.3	0.3	0.929
38-42	0.036	0.003	5.57	0.04	215.4	3.0	371.2	0.3	1.069
42-46	0.028	0.003	6.54	0.04	214.5	3.1	369.9	0.3	1.572
46-50	0.022	0.003	7.80	0.05	219.8	3.6	367.7	0.2	1.620
50-54	0.013	0.002	8.57	0.05	213.6	4.9	367.2	0.2	1.523
54-58	0.015	0.002	8.42	0.05	220.7	4.0	366.9	0.2	1.657
58-62	0.016	0.002	7.97	0.05	219.6	2.9	367.9	0.2	1.641
62-66	0.015	0.002	7.56	0.05	226.0	3.3	368.6	0.2	1.797
66-70	0.013	0.002	6.79	0.04	223.1	3.0	368.7	0.2	2.080
70-74	0.006	0.001	5.55	0.04	230.0	5.1	368.3	0.2	1.928
74-78	0.009	0.003	3.74	0.03	214.7	4.0	367.1	0.3	2.818
78-82	0.097	1.139	1.16	0.02	204.4	54.6	365.6	0.5	1.552

Table 8.3: *The results of fits to mean time distributions of* **DATA** *events. S_f is the fitted nuclear recoil signal rate (/keV/kg/day), G_f is the fitted electron recoil rate (/keV/kg/day), $T_0(n)$ is the fitted nuclear recoil mean time parameter (ns) and $T_0(\gamma)$ is the fitted electron recoil mean time parameter (ns). E_v is measured in keV. The fitted values of the common width parameter w have been omitted for brevity. All parameters can also be found on the relevant figures.*

E_v(keV)	S_f	$\sigma(S_f)$	G_f	$\sigma(G_f)$	$\Re_0(n)$	$\sigma(\Re_0(n))$	χ^2/dof
2-6	0.396	0.061	3.087	0.067	-0.84	0.15	10.283
6-10	0.478	0.039	2.341	0.043	-0.58	0.08	5.454
10-14	0.045	0.014	3.350	0.034	-2.80	0.53	2.139
14-18	0.149	0.026	4.271	0.043	-1.95	0.38	2.795
18-22	0.069	0.012	4.352	0.037	-3.98	0.51	2.059
22-26	0.039	0.007	4.185	0.035	-6.21	0.67	2.767
26-30	0.033	0.005	4.426	0.036	-8.27	0.72	3.872
30-34	0.022	0.003	4.690	0.037	-10.92	1.06	4.196
34-38	0.025	0.004	4.958	0.038	-10.60	0.82	2.895
38-42	0.026	0.004	5.552	0.040	-12.13	0.77	2.726
42-46	0.023	0.004	6.523	0.043	-10.86	1.31	2.147
46-50	0.010	0.003	7.789	0.047	-12.91	2.41	2.289
50-54	0.009	0.002	8.537	0.050	-16.44	1.95	2.548
54-58	0.019	0.003	8.379	0.049	-11.85	1.70	2.646
58-62	0.019	0.004	7.936	0.048	-11.20	1.89	1.966
62-66	0.013	0.002	7.528	0.047	-17.23	2.07	1.847
66-70	0.012	0.003	6.762	0.044	-12.24	2.02	1.861
70-74	0.006	0.002	5.530	0.040	-22.99	4.91	1.432
74-78	0.003	0.002	3.713	0.033	-22.18	5.15	2.206
78-82	0.022	0.038	1.142	0.017	-21.55	7.22	1.070

Table 8.4: *The results of fits to likelihood ratio distributions of* DATA *events.* S_f *is the fitted nuclear recoil signal rate (/keV/kg/day),* G_f *is the fitted electron recoil rate (/keV/kg/day) and* $\Re_0(n)$ *is the fitted nuclear recoil LR. All parameters can also be found on the relevant figures.*

remaining out of 100 000 generated, all were placed in the 2 - 6 keV visible energy bin. Given that this contamination thus appears both experimentally and theoretically to be confined to this energy bin only, one approach would be to add to the fit a suitably normalised contribution from the simulated distribution of noise events. The Monte Carlo distribution is not sufficiently accurate to enable this however. This is probably due to non-Poissonian effects in the data and complications in the trigger requirement introduced by the slow recovery time of the buffer. It was decided instead therefore to adopt the conservative approach of discarding the 2 - 6 keV energy bin altogether in both the MT and LR analyses.

The fit to the MT histogram in the next (6 - 10 keV visible energy) bin is good (χ^2/dof = 1.061) however the LR fit in the same bin is less satisfactory (χ^2/dof = 5.454). This general behaviour is repeated for most of the subsequent energy bins and probably originates from poor quantification of the form of the parent LR distribution (§8.4.3). The large fluctuations in the fitted S_f and $\Re_0(n)$ values from the LR technique, on a scale larger than that expected from the errors or the detector energy resolution[2], also indicates that this technique suffers from badly understood systematics. More accurate parameterisation of the LR distribution is clearly needed. Nevertheless the S_f values are in qualitative agreement with those obtained from the MT technique.

The MT and LR fits to the **NCAL** data are also worthy of discussion. The fitted value of the nuclear recoil mean time (202 $\pm$ 28 ns) is consistent within errors with that of the population of anomalous events. The limited statistics of this sample however prevents a definitive statement from being made about the origin of the anomalous events. The equivalent fit using the LR technique is not consistent with the $\Re$ distribution of anomalous events in the **DATA** sample in the same energy region. While this may be due to the presence of systematics in this technique this fact does indicate that it is indeed difficult to come to a firm conclusion about the nuclear recoil T_0 from the **NCAL** data alone.

8.5.2 Error Analysis

In order to properly investigate the parameters of the population of anomalous events a systematic study was carried out of errors introduced by the fitting procedure. The fitted parameters were used to construct theoretical MT and LR distributions for each energy bin (log-normal for the MT technique, normal for the LR technique), and a number of events was sampled from the distributions equal in number to the

[2] $\sigma/E = 1.66/\sqrt{E}$ at 662 keV ee

normalisations determined from the DATA fits. Fits to the generated event distributions were then performed in the same manner as to the DATA events. This process was repeated for 100 simulated experiments and the fitted signal parameters histogrammed and χ^2 fitted with normal distributions such that the widths σ represented the statistical errors and the means the systematics. These systematics were subsequently subtracted from the DATA values. It should be emphasised that this process was only capable of accounting for systematics arising from the fitting process itself, as the forms of the MT and LR distributions are not perfectly represented by the assumed distributions[3].

The fitted S_f distributions determined from the MT and LR techniques are plotted in Figs. 8.17 and 8.18. Similar distributions were also constructed for $T_0(n)$ and $\Re_0(n)$. The corrected (systematic subtracted) parameter values and statistical errors determined from these distributions are presented in Tables 8.5 and 8.6. These tables also contain estimates of the small systematic error in S_f coming from uncertainties in the detector live time and mass (~ 0.01 S_f in both cases). Not listed is the residual systematic variation in T_0 due to temperature fluctuations, which was conservatively estimated at $\pm$ 6 ns for a $\pm$ 2 ^{o}C fluctuation [88].

The results of these studies indicate that on average the simulated statistical errors are in agreement with the 'Curvefit' values. In most energy bins the errors are Gaussian to a good approximation, the one exception being the 6 - 10 keV visible energy bin in the MT analysis. The distribution of S_f in this bin is slightly asymmetric (the first point is ~ 5 standard deviations above the expectation) however even here the assumption of Gaussian errors does appear to be a reasonable approximation. In this same one energy bin 'Curvefit' significantly underestimated the statistical error, possibly for this reason. Systematic bias in all bins was found to be introduced by the χ^2 fitting process but only at the 10 % level. The systematic corrected values of the parameters of the distribution of anomalous events are used throughout the rest of this chapter.

[3] χ^2/dof > 1 for most visible energy bins

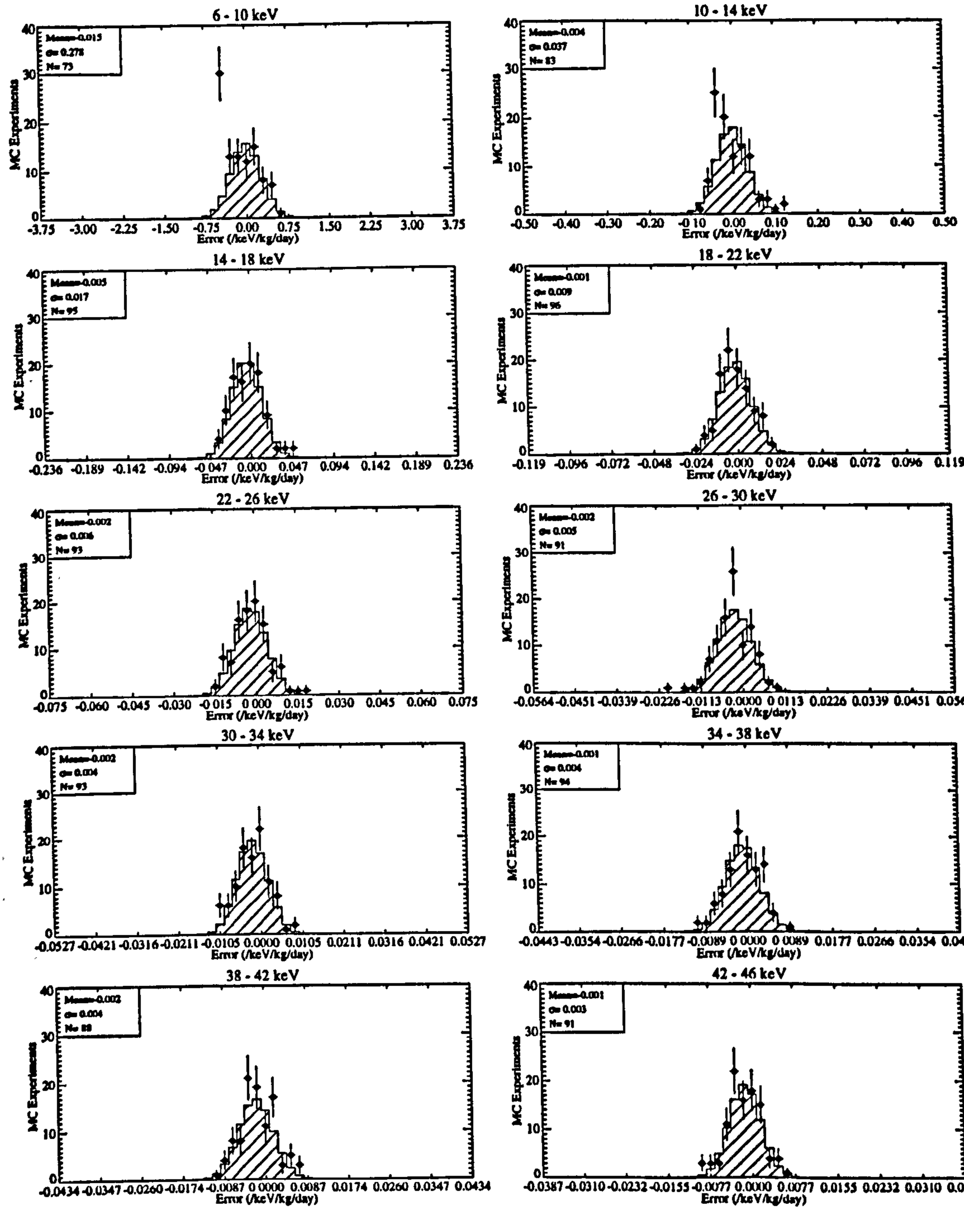

Figure 8.17: *The distribution of S_f values for Monte Carlo MT data. The histograms are fits to normal distributions.*

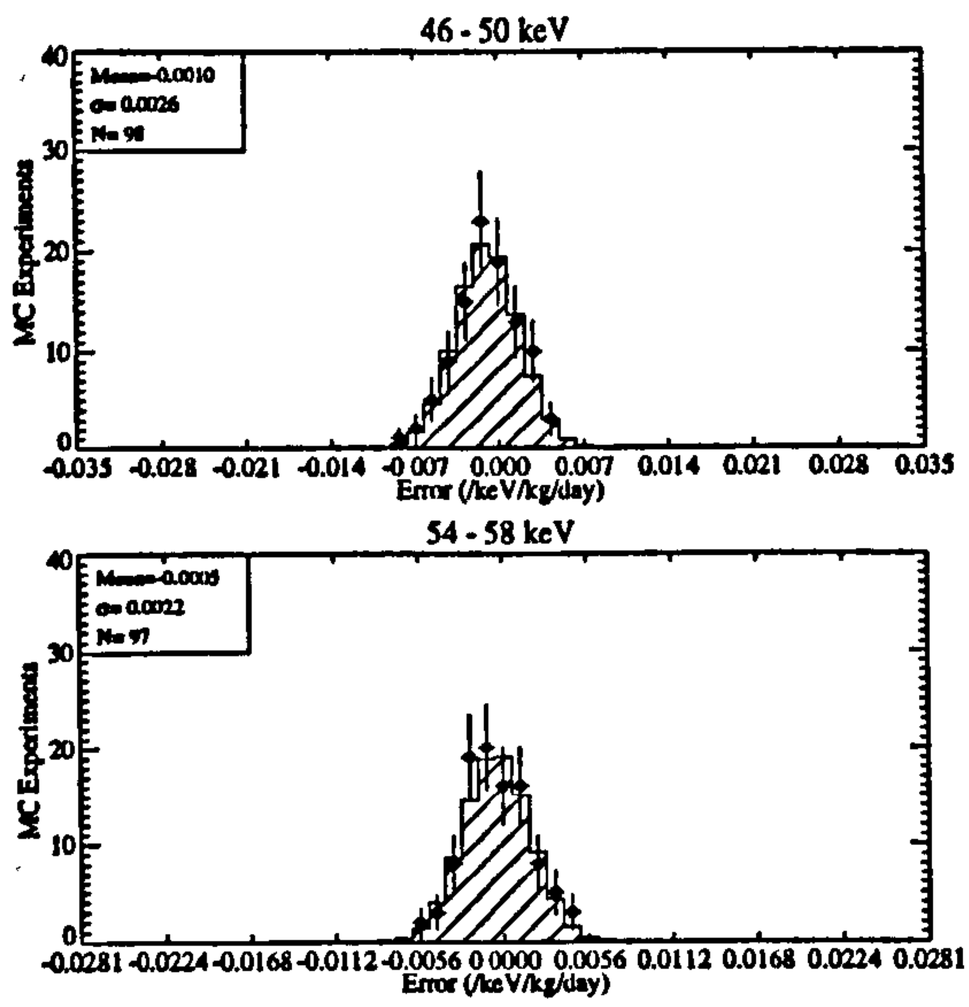

Figure 8.17 (continued).

E_v(keV)	$S_f(obs)$	$S_f(cor)$	$\sigma_{syst}(S_f)$	$\sigma_{stat}(S_f)$	$T_0(obs)$	$T_0(cor)$	$\sigma_{stat}(T_0)$
6-10	0.4817	0.4964	0.0067	0.2781	225.0	236.6	17.3
10-14	0.1651	0.1695	0.0023	0.0370	207.6	209.6	6.5
14-18	0.1279	0.1325	0.0018	0.0172	208.6	209.3	4.8
18-22	0.0828	0.0840	0.0011	0.0093	206.9	207.7	3.8
22-26	0.0578	0.0598	0.0008	0.0060	208.4	209.0	3.7
26-30	0.0503	0.0526	0.0007	0.0046	205.9	207.8	3.4
30-34	0.0444	0.0465	0.0006	0.0040	212.4	213.3	3.6
34-38	0.0366	0.0377	0.0005	0.0036	210.6	211.3	3.4
38-42	0.0358	0.0378	0.0005	0.0037	215.4	216.7	3.2
42-46	0.0278	0.0292	0.0004	0.0029	214.5	215.8	2.8
46-50	0.0223	0.0233	0.0003	0.0026	219.8	221.0	3.9
50-54	0.0133	0.0133	0.0002	0.0020	213.6	215.4	3.7
54-58	0.0153	0.0158	0.0002	0.0022	220.7	222.0	2.9
58-62	0.0165	0.0166	0.0002	0.0020	219.6	220.7	3.4
62-66	0.0152	0.0154	0.0002	0.0019	226.0	226.7	3.1
66-70	0.0132	0.0139	0.0002	0.0018	223.1	224.3	3.3
70-74	0.0063	0.0060	0.0001	0.0014	230.0	230.4	4.9
74-78	0.0085	0.0079	0.0001	0.0019	214.7	214.1	4.7

Table 8.5: *The results of the Monte Carlo study of the parameters of the anomalous events. S_f is measured in units of /keV/kg/day, T_0 in units of ns. 'obs' indicates the observed values of the parameters. 'cor' indicates the corrected values of the same parameters. Statistical errors are determined from the widths of the Monte Carlo parameter distributions. Residual systematic errors in S_f are determined from uncertainties in detector exposure. An additional systematic error in T_0 due to fluctuation in the detector temperature in the range $10 \pm 2\,^{\circ}C$ is accounted for by a uniform residual systematic of $\pm$ 6 ns [88] (not shown here).*

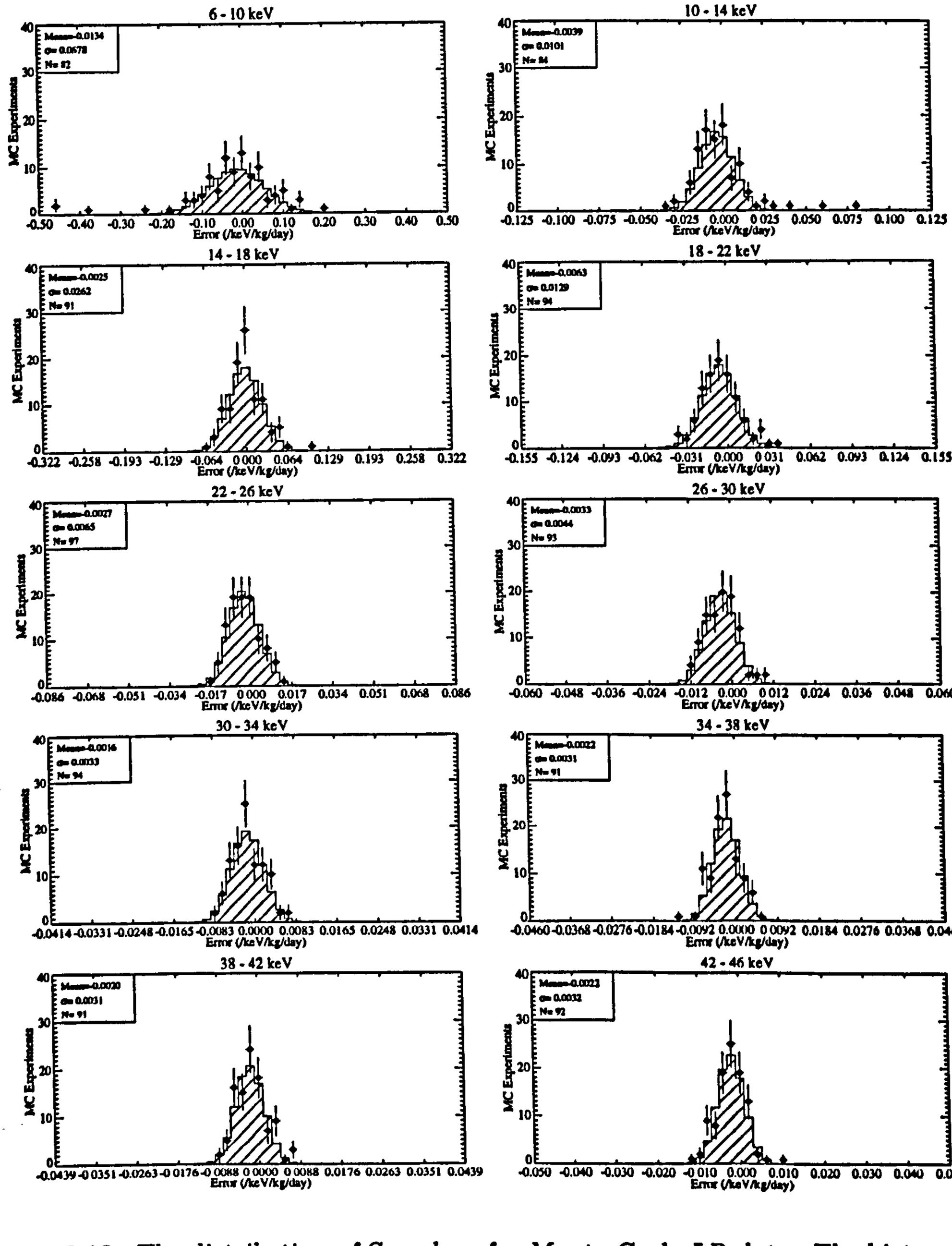

Figure 8.18: *The distribution of S_f values for Monte Carlo LR data. The histograms are fits to normal distributions.*

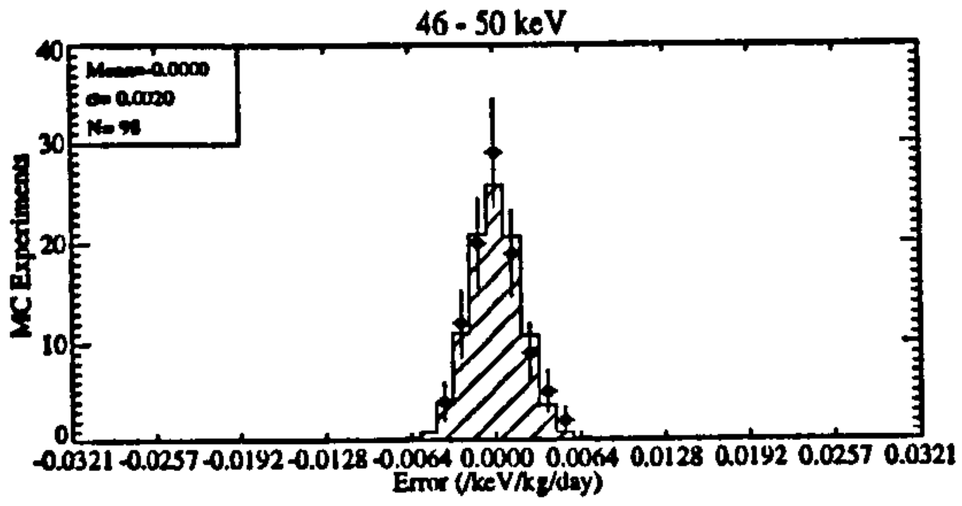

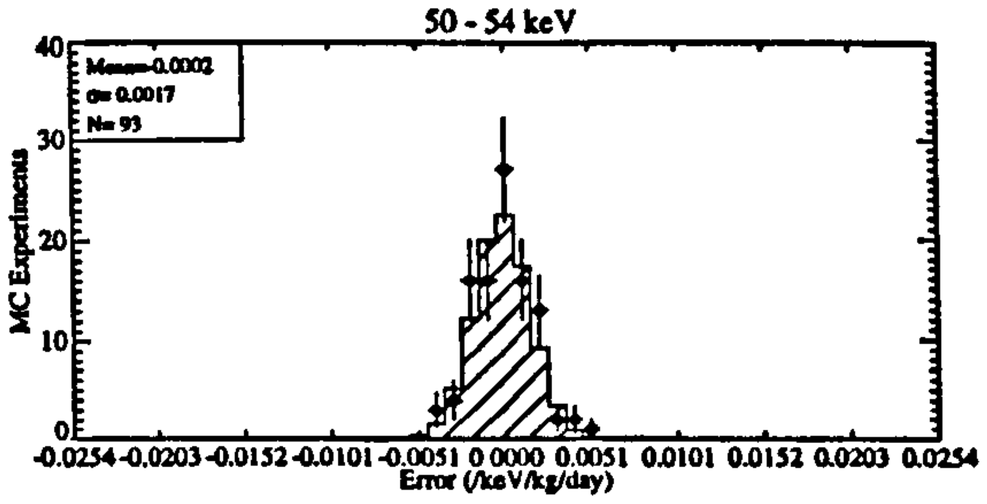

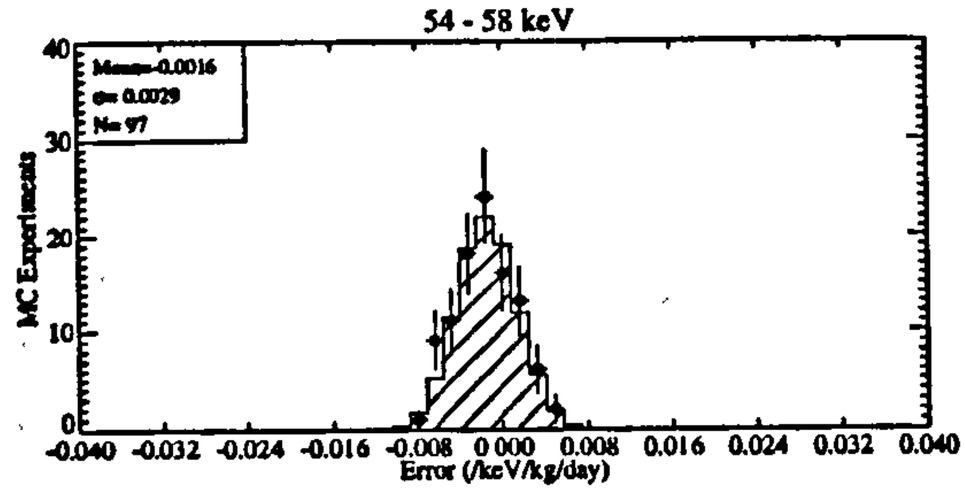

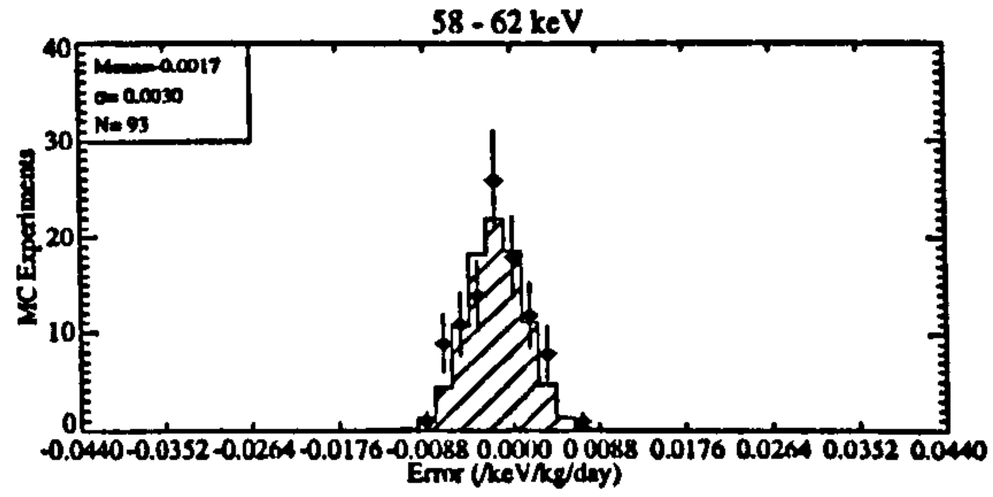

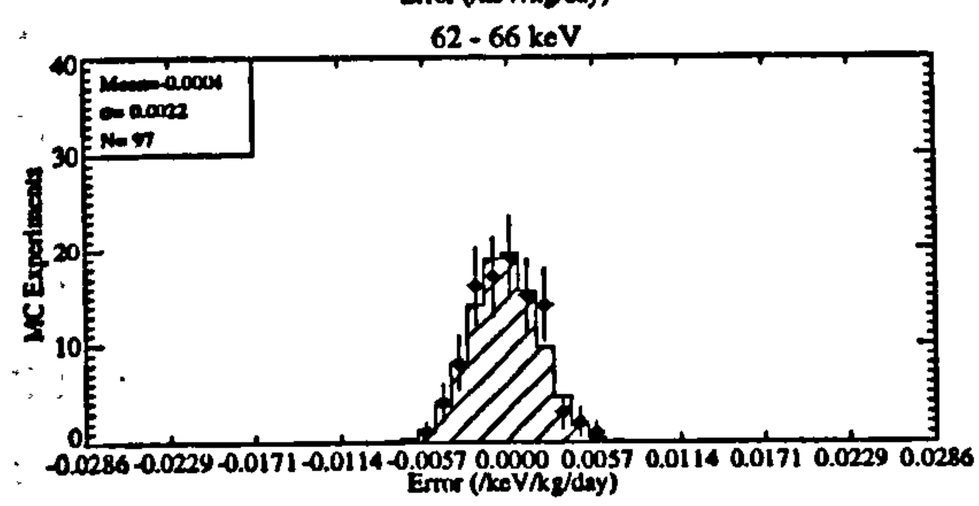

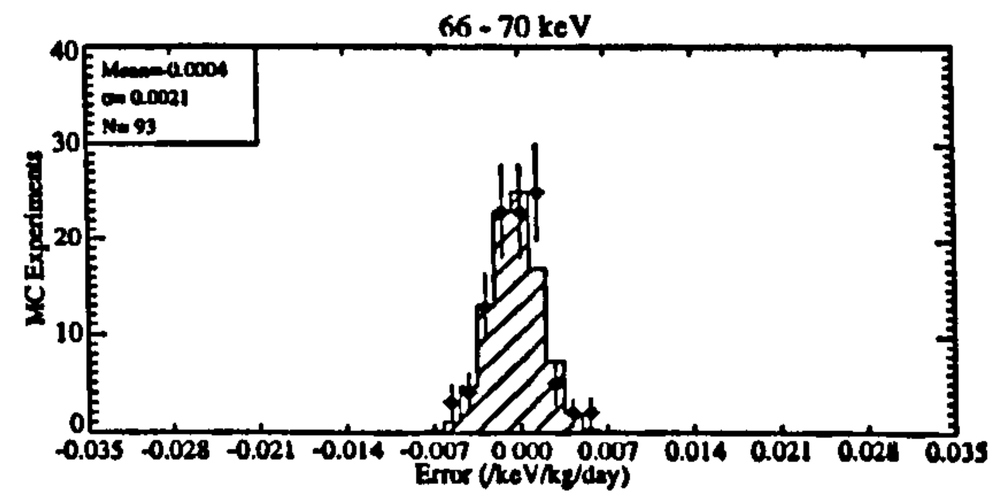

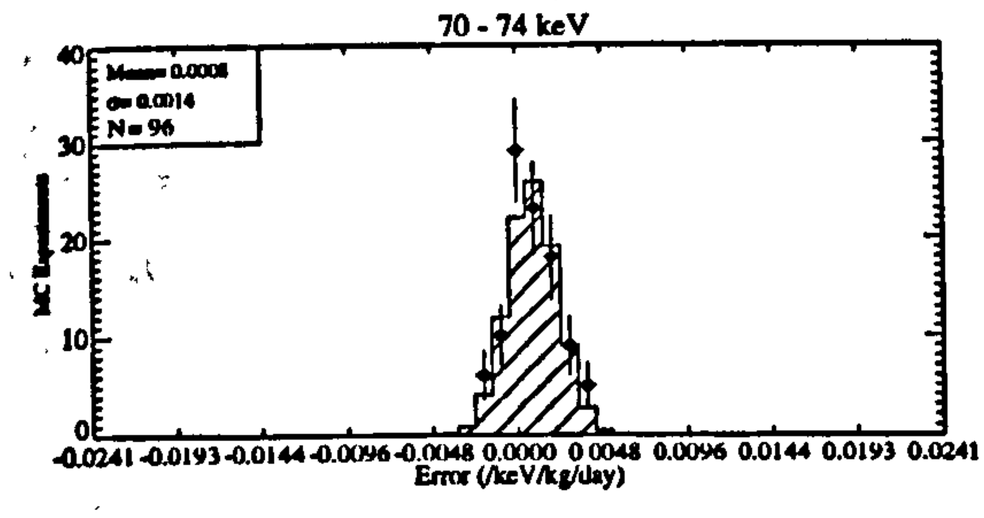

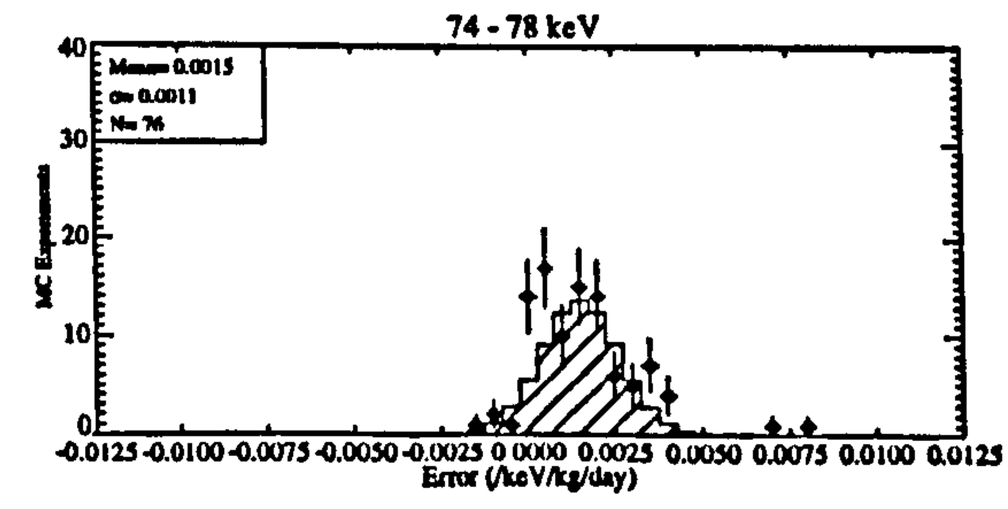

Figure 8.18 (continued).

E_v(keV)	$S_f(obs)$	$S_f(act)$	$\sigma_{syst}(S_f)$	$\sigma_{stat}(S_f)$	$\Re_0(obs)$	$\Re_0(act)$	$\sigma_{stat}(\Re_0)$
6-10	0.4776	0.4909	0.0066	0.0678	-0.6	-0.6	0.1
10-14	0.0447	0.0485	0.0006	0.0101	-2.8	-2.5	0.6
14-18	0.1494	0.1519	0.0021	0.0262	-1.9	-1.9	0.4
18-22	0.0693	0.0756	0.0010	0.0129	-4.0	-3.8	0.6
22-26	0.0389	0.0416	0.0005	0.0065	-6.2	-6.0	0.6
26-30	0.0326	0.0359	0.0005	0.0044	-8.3	-8.0	0.6
30-34	0.0216	0.0232	0.0003	0.0033	-10.9	-10.4	0.8
34-38	0.0247	0.0268	0.0003	0.0031	-10.6	-10.0	0.8
38-42	0.0258	0.0278	0.0004	0.0031	-12.1	-11.6	0.9
42-46	0.0228	0.0250	0.0003	0.0032	-10.9	-10.1	1.1
46-50	0.0103	0.0103	0.0001	0.0020	-12.9	-11.6	1.6
50-54	0.0093	0.0095	0.0001	0.0017	-16.4	-15.5	1.5
54-58	0.0186	0.0201	0.0003	0.0029	-11.8	-11.1	1.4
58-62	0.0193	0.0210	0.0003	0.0030	-11.2	-9.8	1.6
62-66	0.0128	0.0132	0.0002	0.0022	-17.2	-16.6	1.7
66-70	0.0117	0.0121	0.0002	0.0021	-12.2	-10.7	1.9
70-74	0.0056	0.0048	0.0001	0.0014	-23.0	-22.8	2.4
74-78	0.0030	0.0015	0.0000	0.0011	-22.2	-23.7	4.1

Table 8.6: *The results of the Monte Carlo study of the parameters of the anomalous events. S_f is measured in units of /keV/kg/day. 'obs' indicates the observed values of the parameters. 'cor' indicates the corrected values of the same parameters. Statistical errors are determined from the widths of the Monte Carlo parameter distributions. Residual systematic errors are determined from uncertainties in detector exposure.*

The final values of S_f (anomaly event rate), T_0, $\Re_0$ and G_f (electron recoil event rate) determined from this data using the MT and LR techniques are plotted in Figs. 8.19, 8.20 and 8.21. The error bars in these plots represent total errors determined by adding systematic and statistical (dominant) errors in quadrature. In Fig. 8.20(a) the electron recoil T_0 values determined from the **CCAL** data have been plotted in addition to the values determined from the **DATA** event sample and the values of $T_0(n)$. In Fig. 8.20(b) just the **CCAL** electron recoil $\Re_0(\gamma)$ and the **DATA** $\Re_0(n)$ have been plotted.

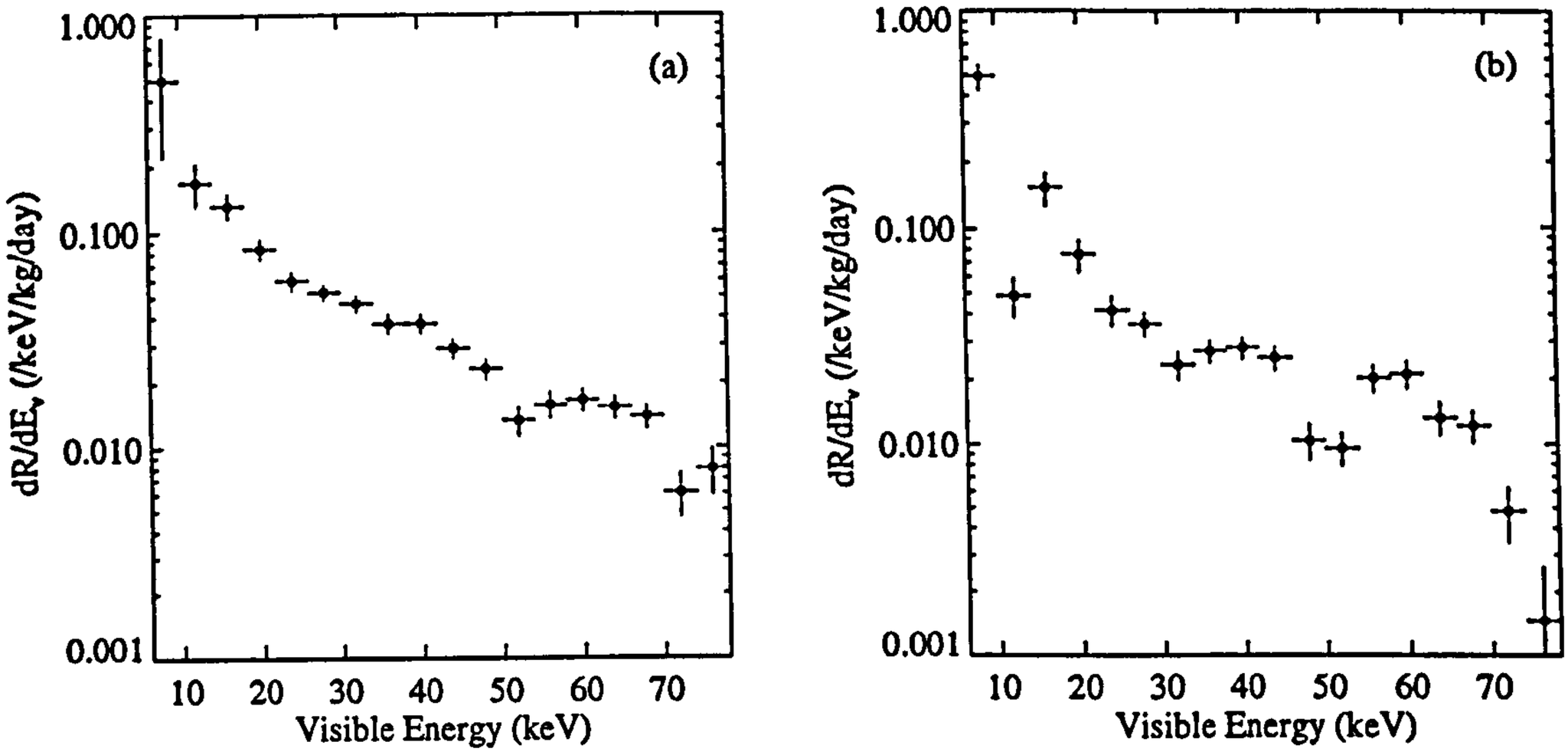

Figure 8.19: *Corrected S_f (anomaly event rate) values determined using (a) the MT technique and (b) the LR technique.*

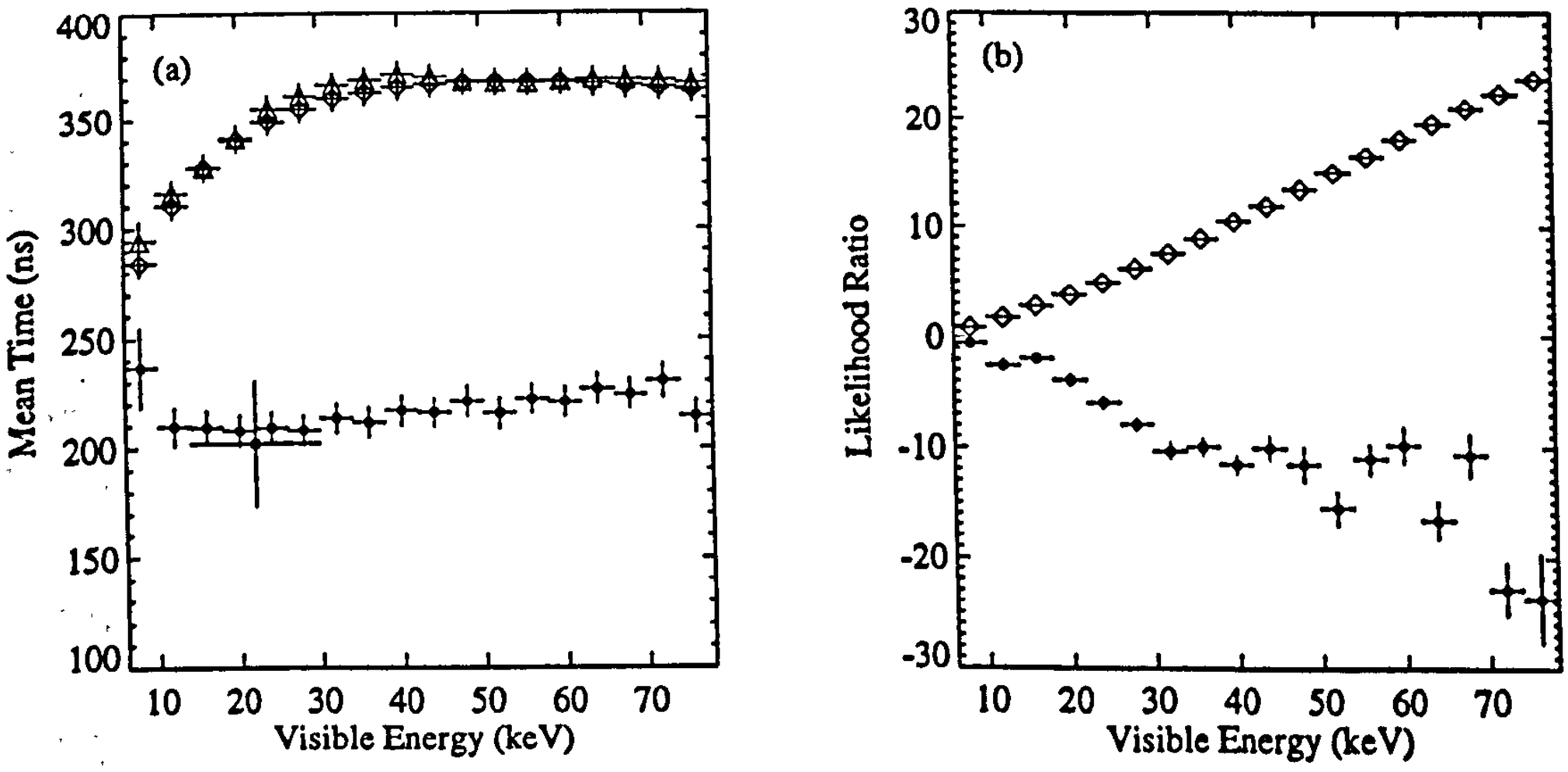

Figure 8.20: *Values of (a) T_0 and (b) $\Re_0$. The filled circles represent $T_0(n)$ and $\Re_0(n)$, the diamonds $T_0(\gamma)$ and $\Re_0(\gamma)$ determined from* **CCAL** *data, and the triangles $T_0(\gamma)$ determined from* **DATA** *events (MT only). The open circle in Figure (a) represents the measured* **NCAL** *T_0 value. Parameter values have been corrected for systematic bias from the fitting process. T_0 errors include a conservative 6 ns systematic error due to temperature fluctuation.*

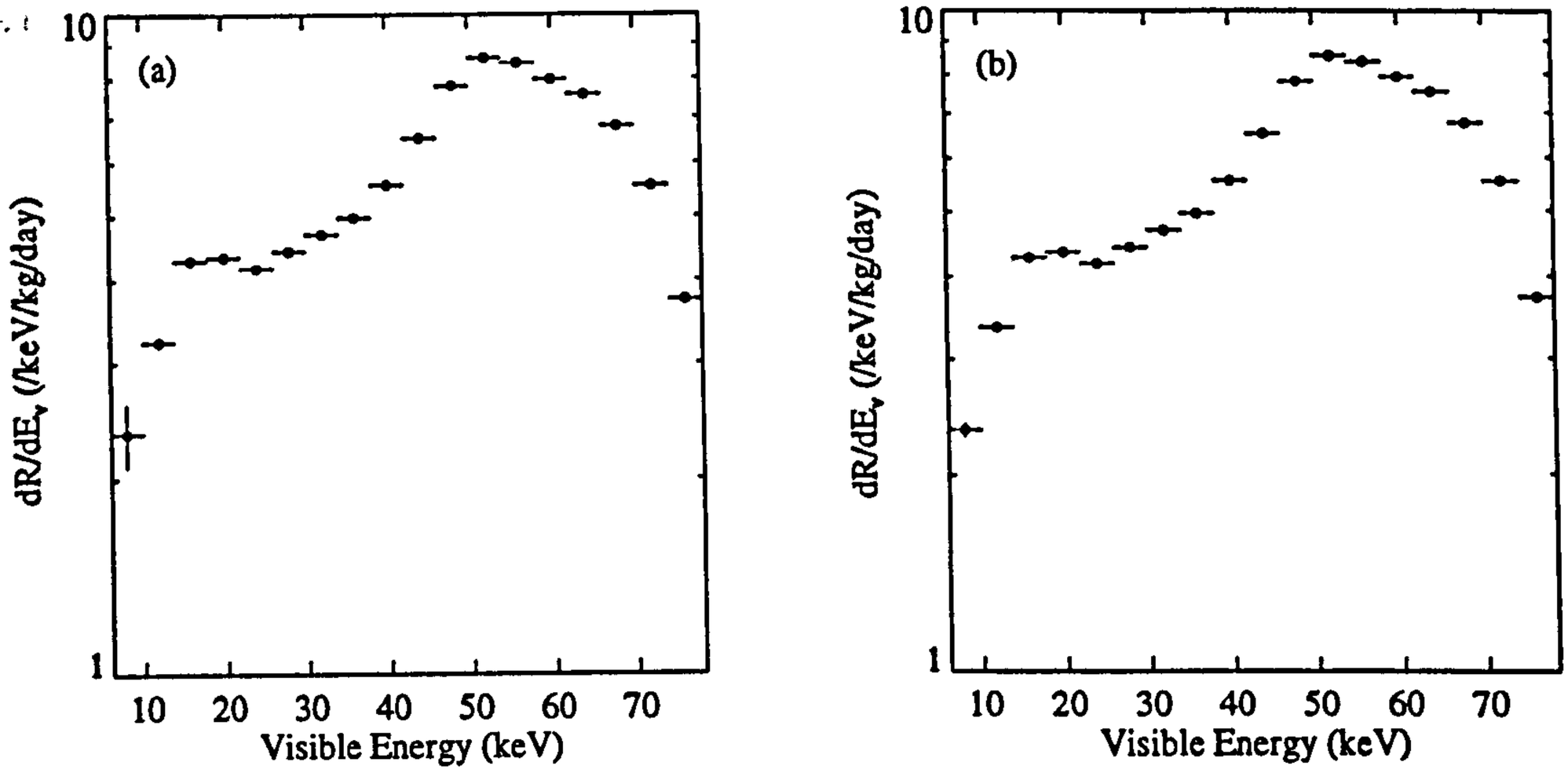

Figure 8.21: *Values of G_f (electron recoil event rate) determined using (a) the MT technique and (b) the LR technique.*

8.5.3 Discussion

The data presented above provides strong evidence for the existence of an additional component to the **DATA** MT and LR distributions in addition to that due to electron recoils. The origin of this component is however unknown. The T_0 distribution of these events remains roughly constant with increasing E_v (Fig. 8.20(a)) in contrast to that of the electron recoil distribution. This behaviour is similar to that observed for nuclear (Na) recoils in the neutron beam data (§6.4.2) although this in itself does not prove the existence of a nuclear recoil signal. The absolute magnitude of the T_0 of the anomalous events ($\sim$ 210 ns) is considerably lower than that observed in the neutron beam data ($\sim$ 280 ns) however this may have come from the use of different crystals in each case. The results from the neutron calibration (Fig. 8.12) appear to be consistent with the identification of the anomalous events with nuclear recoils, however the poor statistics of that data make any firm link difficult to establish.

The LR technique was unable to make use of additional pulse shape differences such as may exist for nuclear and electron recoils (Fig. 6.17(a)) between the anomalous events and electron recoils. This is demonstrated by the larger errors on S_f as measured by this technique. Samples of anomalous events and **CCAL** electron recoil events of similar energy (E_v in the range 10 - 20 keV) were assembled to test this hypothesis. The mean pulse shapes of these events are plotted in Fig. 8.22.

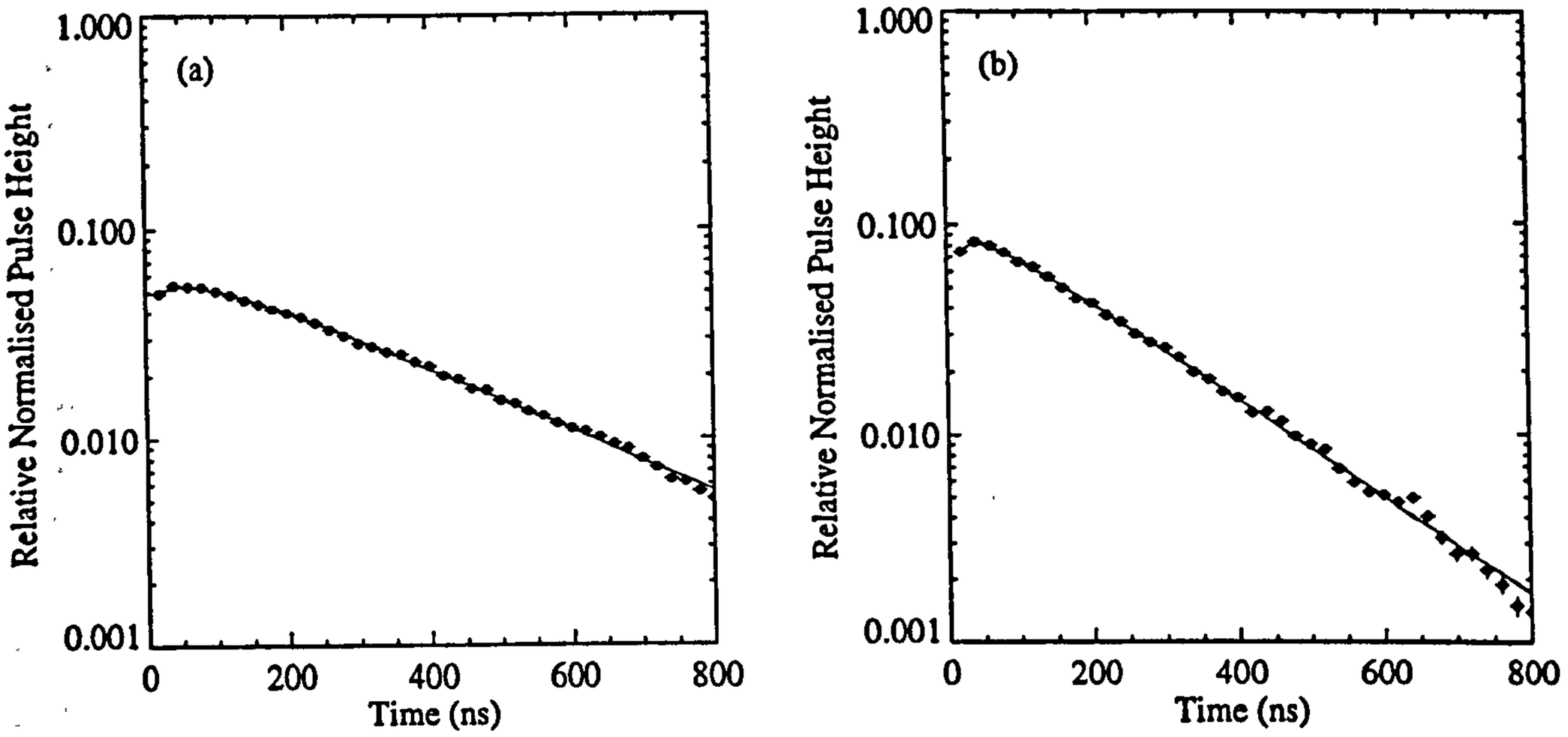

Figure 8.22: *Mean pulse shapes of (a) electron recoil and (b) anomalous events. The full curves are from fits to gamma distributions (§4.2.2).*

Parameter	*Electrons*	*Anomaly*
t_0(ns)	1.6 ± 0.5	18 ± 1
τ(ns)	319.3 ± 0.5	197 ± 1
b	1.182 ± 0.002	1.09 ± 0.01
χ^2/dof	5.46	1.643

Table 8.7: *Results of gamma distribution fits to the mean pulse shapes for electron recoil and anomalous events. The anomalous events were selected from* **DATA** *events by requiring $T < 220$ ns.*

Fits of Eqn. 4.3 to both pulse shapes are also plotted in Fig. 8.22 and these yield the parameterisations in Table 8.7. These results confirm that only minor additional differences in pulse shape [4] beyond those due to the exponential decay time constant were observable. This is however in agreement with the results from neutron beam tests in Table 6.3.

The results of this analysis would appear to indicate that the LR technique was inferior to the MT technique when used with this data set, both in terms of quantified errors and the presence of uncontrolled systematic bias. With more work aimed at understanding the underlying distribution of events this technique may

[4] i.e. differences in b

become competitive with the former technique however. At the very least the LR technique has been demonstrated to be feasible and to produce results which agree qualitatively with those obtained from the MT technique.

8.6 Annual Modulation

Given the presence of an additional anomalous component to the DATA MT and LR distributions the question may be asked as to whether these events display an annual modulation signature characteristic of a WIMP induced nuclear recoil signal (Eqn. 3.43). This question was addressed by performing χ^2 fits to the 91 Julian day time binned CCAL and DATA MT distributions described in §8.4.3. The LR data was not used due to the larger errors associated with that technique. The fitted rates associated with the anomalous and electron recoil event populations, together with estimates of the systematic and statistical errors on these parameters are listed in Table 8.8 and plotted in Fig. 8.23 (overleaf).

The results from this analysis are relatively inconclusive. The time binning was arranged such that the second bin (335.4 Julian days) lay roughly at the expected turning point in a WIMP signal (2nd December [84]). Thus the signature of a WIMP signal should be a rate which steadily rises (falls) through the year from a minimum (maximum) in this bin, depending upon the WIMP mass. Furthermore there should be no similar modulation to the electron recoil background rate. In three of the six 12 keV visible energy bins there is indeed a minimum rate of anomalous events in the second Julian day bin which is not matched by a similar modulation of the same fractional magnitude in the electron recoil rate. It is difficult to assign the cause of such a fluctuation to WIMP induced annual modulation however, in particular in view of the fact that this is expected to have an amplitude in the region of 3 - 6 % [84], which is considerably smaller than both the observed fluctuation and the magnitude of the statistical errors. More statistics are required to make a conclusive statement and in particular a full year's worth of data is needed in order to observe the complete modulation effect.

Day	E_v(keV)	S_f	σ_{syst}	σ_{stat}	G_f	σ_{syst}	σ_{stat}	χ^2/dof
283.9	6-18	0.4761	0.0066	0.0859	2.92	0.04	0.11	0.631
	18-30	0.0811	0.0011	0.0211	4.06	0.06	0.09	0.833
	30-42	0.0452	0.0006	0.0098	4.76	0.07	0.09	0.421
	42-54	0.0288	0.0004	0.0097	7.06	0.10	0.11	2.041
	54-66	0.0214	0.0003	0.0062	8.01	0.11	0.12	0.927
	66-78	0.0086	0.0001	0.3659	6.39	0.09	0.11	1.150
335.4	6-18	0.2579	0.0036	0.0317	3.28	0.05	0.04	1.175
	18-30	0.0812	0.0011	0.0075	4.35	0.06	0.03	1.421
	30-42	0.0412	0.0006	0.0035	5.09	0.07	0.03	1.486
	42-54	0.0186	0.0003	0.0022	7.65	0.11	0.04	1.854
	54-66	0.0143	0.0002	0.0019	8.14	0.11	0.04	3.585
	66-78	0.0080	0.0001	0.0014	5.69	0.08	0.04	6.063
421.4	6-18	0.3467	0.0048	0.0387	3.32	0.05	0.05	1.998
	18-30	0.0644	0.0009	0.0062	4.26	0.06	0.04	1.746
	30-42	0.0364	0.0005	0.0038	5.03	0.07	0.04	1.475
	42-54	0.0201	0.0003	0.0027	7.56	0.10	0.05	1.858
	54-66	0.0160	0.0002	0.0023	7.94	0.11	0.05	1.150
	66-78	0.0081	0.0001	0.0016	5.42	0.08	0.04	1.899
534.1	6-18	0.3101	0.0043	0.0456	3.22	0.04	0.06	0.978
	18-30	0.0910	0.0013	0.0093	4.47	0.06	0.05	1.065
	30-42	0.0362	0.0005	0.0046	5.38	0.07	0.05	1.174
	42-54	0.0259	0.0004	0.0038	8.09	0.11	0.06	1.146
	54-66	0.0172	0.0002	0.0030	8.00	0.11	0.06	0.914
	66-78	0.0060	0.0001	0.0018	4.54	0.06	0.05	2.043
565.8	6-18	0.0236	0.0003	0.0446	2.31	0.03	0.10	1.579
	18-30	0.0949	0.0013	0.0577	3.15	0.04	0.12	0.493
	30-42	0.0516	0.0007	0.0158	3.68	0.05	0.12	0.418
	42-54	0.0482	0.0007	0.0159	5.57	0.08	0.15	1.129
	54-66	0.0126	0.0002	0.0386	5.48	0.08	0.15	1.226
	66-78	0.0282	0.0004	0.2964	3.05	0.04	0.11	1.308

Table 8.8: *The results of fits to the time binned MT data. The 'day' column refers to days after 1st January 1996. All rates are measured in units of /keV/kg/day. The bin centred on 335.4 Julian days corresponds roughly to the expected turning point in a WIMP signal (2nd December). The statistical errors are from 'Curvefit'.*

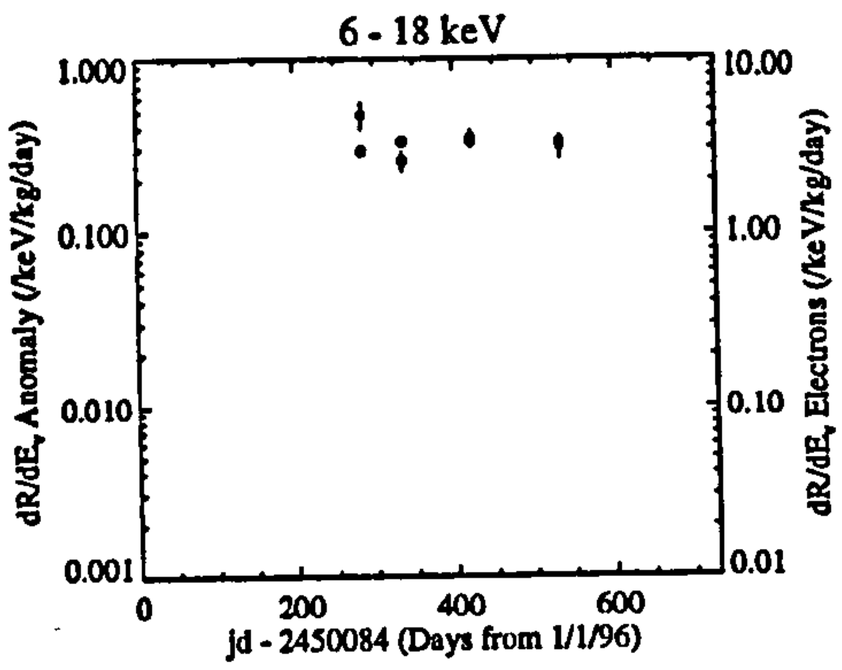

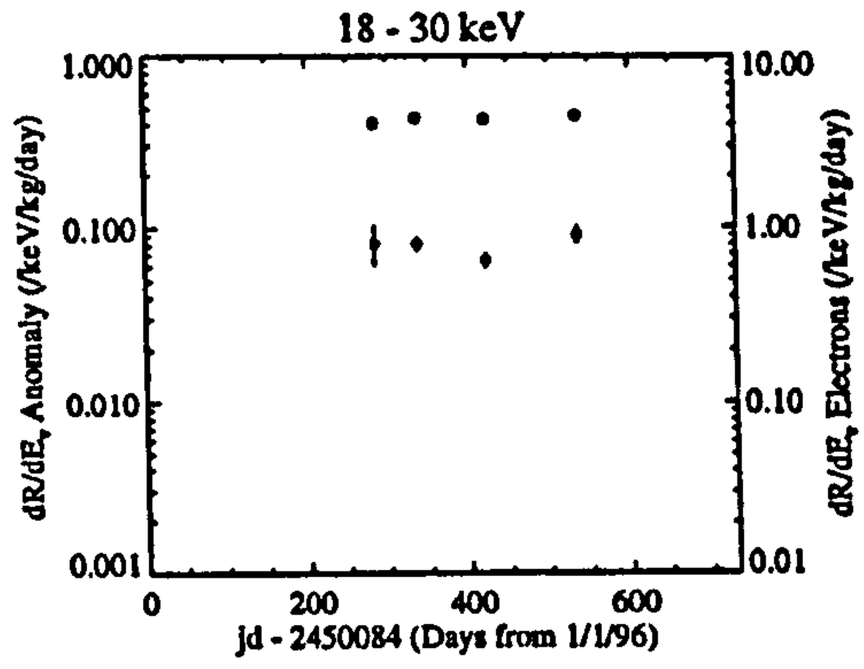

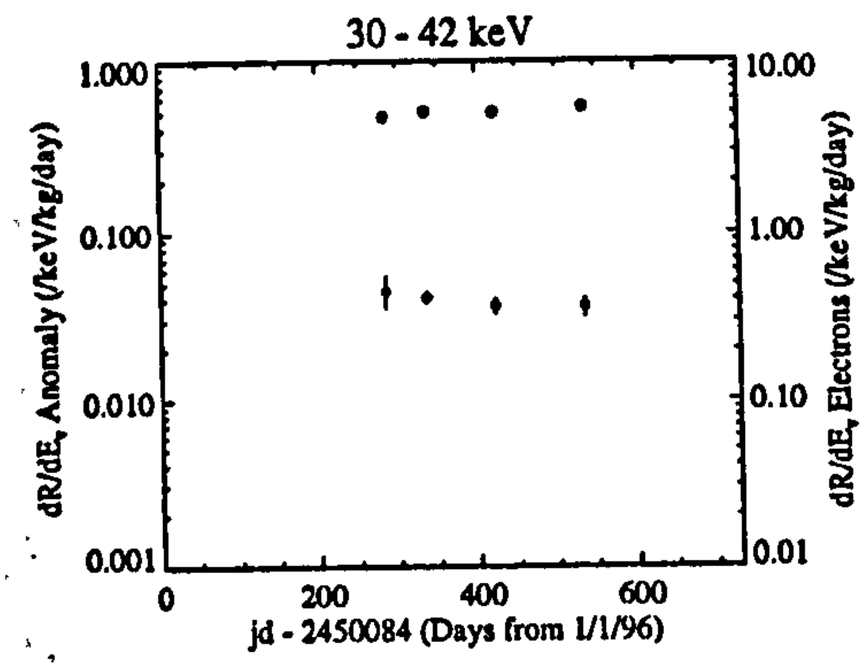

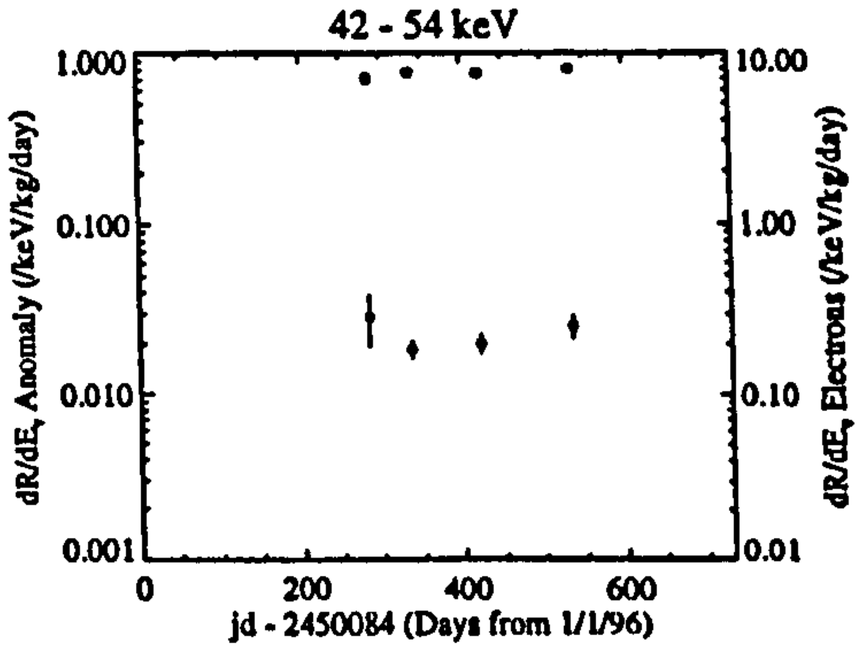

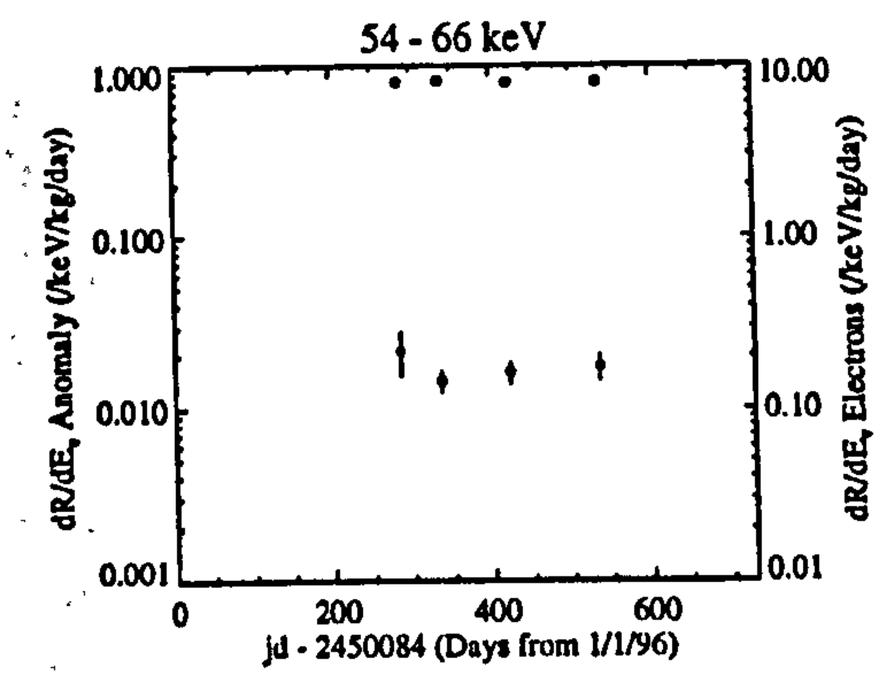

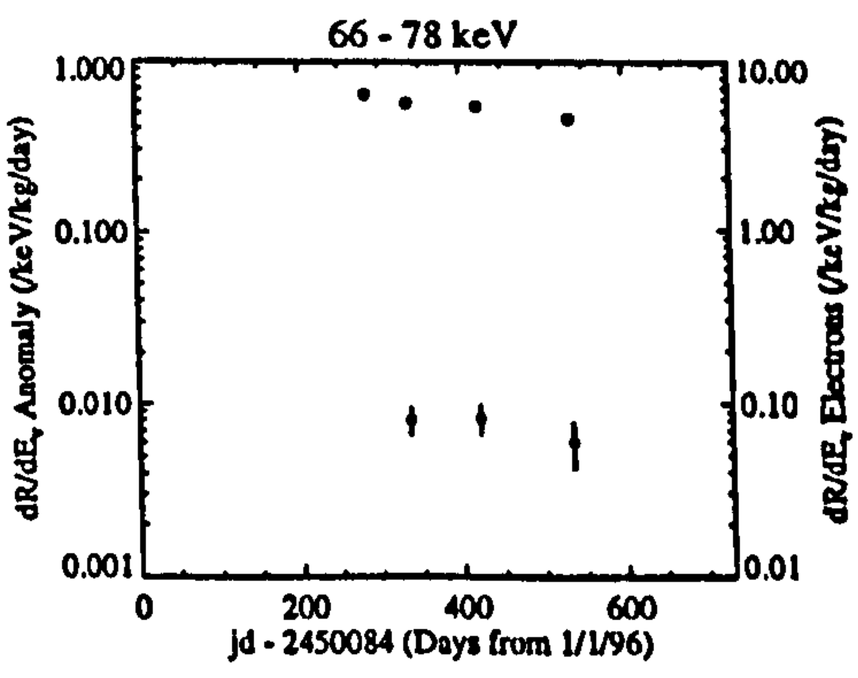

Figure 8.23: *The results of fits to the time binned MT data. The time axis is scaled in terms of days after 1st January 1996. The filled circles represent rates of anomalous events. The open circles represent rates of electron recoils. Note that the latter are plotted on a vertical scale ten times that of the former. The bin centred on 335.4 Julian days corresponds roughly to the expected turning point in a WIMP signal (2nd December). The points lie at the live time means of each 91 Julian day bin rather than the bin centres.*

8.7 Interpretation

8.7.1 Background Interpretations

Interpretation of the results presented here is difficult. Assuming for the moment that the anomalous events are not due to a WIMP signal several problems become apparent. The events cannot be due to electron recoils because in this case they would have been observed in the **CCAL** data. It might be asked why they are not observed in this data even if they are not caused by electron recoils given that the **CCAL** live time is of order one quarter of that for the **DATA** sample. The very high rate of **CCAL** events acts to swamp the DAQ system however and the dead time thus introduced causes very few background events, anomalous or otherwise, to be observed during this period.

Another interpretation is that the anomalous events are due to α particles recoiling through the crystal. High energy α events from the decay of radioactive impurities certainly have very different decay time constants to electron recoils in NaI(Tl) [100] and hence could explain the MT distributions of the anomalous events. α decays are two body processes however and typically generate recoils in the MeV energy range. Thus α events are expected to be monoenergetic and occur at visible energies far in excess of those considered here. A method of avoiding this problem is to postulate the existence of a dead layer on the surface of the crystal covered by a layer of α emitters [175]. α particles would then recoil through the dead layer dumping most of their energy in an invisible form before ranging out in the active part of the crystal to create small scintillation events. This hypothesis can explain the energy spectrum of the anomalous events qualitatively however more detailed Monte Carlo simulations indicate that rather improbable assumptions (e.g. $\gtrsim 1$ ppm concentration of α emitters) are required to provide quantitative agreement [175]. Further work on this interpretation is in progress.

A further possibility which has been considered is that the anomalous events are due to photodisintegration of nuclei to α particles or protons. This interpretation could possibly explain the shape of both the MT distributions and the anomalous event energy spectrum however given the observed rate of gamma (electron recoil) events in the crystal it is estimated that the total event rate is too low [175].

The next interpretation is that the anomalous events are due to nuclear recoils caused by background neutrons, however there are several problems with this hypothesis too. Firstly and most importantly the crystal was shielded from sources of neutrons external to the detector by 200 tonnes of high purity water. This reduces the neutron flux at the position of the detector by a factor 10^6 relative to that in the

cavern, making such an interpretation incompatible with the estimated unshielded interaction rate of 100 /kg/day [120]. Were the neutrons to originate within the detector itself from fission or α knockout processes at least 10^5 times as many gammas would be produced [120] and this is inconsistent with the observed electron recoil rate.

8.7.2 Other Data Sets

An interpretation of these results should also take into account results obtained from other data sets. A substantial amount of neutron calibration data was obtained in March 1998 from the DM46 detector and this suggests unambiguously that the neutron induced nuclear recoil MT distribution has a mean $\sim 280 \pm 10$ ns [175]. Despite changes in detector characteristics due to the replacement of a PMT (§8.2) this data is consistent with the results of the neutron beam tests [175] and inconsistent with the T_0 of the anomalous events. This makes a neutron background interpretation of these events unlikely. A WIMP interpretation is also more difficult in the light of this data. However it may be that effects such as multiple neutron scattering cause the T_0 determined in this way to differ from that for WIMP induced nuclear recoil events. This scenario has been investigated extensively [174] but it has nevertheless not been possible to recreate the T_0 of the anomalous events [174].

Another consideration is that neutron source tests create predominantly Na recoil events and so if there is a difference between the T_0 of Na and I events then this may allow the anomalous events to be interpreted as WIMP induced I recoils. The neutron beam results of §6.4.2 suggest that at low energies there is little difference between the Na and I T_0 values but these results do not extend up into the visible energy range considered here (> 6 keV).

Further relevant data has come from other NaI(Tl) detectors operated at Boulby Mine by the UKDMC. The results from these detectors also provide evidence for an anomalous population of events at low values of T at rates apparently consistent with those seen in DM46 [175]. These detectors are situated in different locations within the mine and are shielded in a different way (Pb-Cu castles rather than water shielding), and yet the observed rates of anomalous events are nevertheless similar. These results indicate that the WIMP interpretation should be considered in more detail.

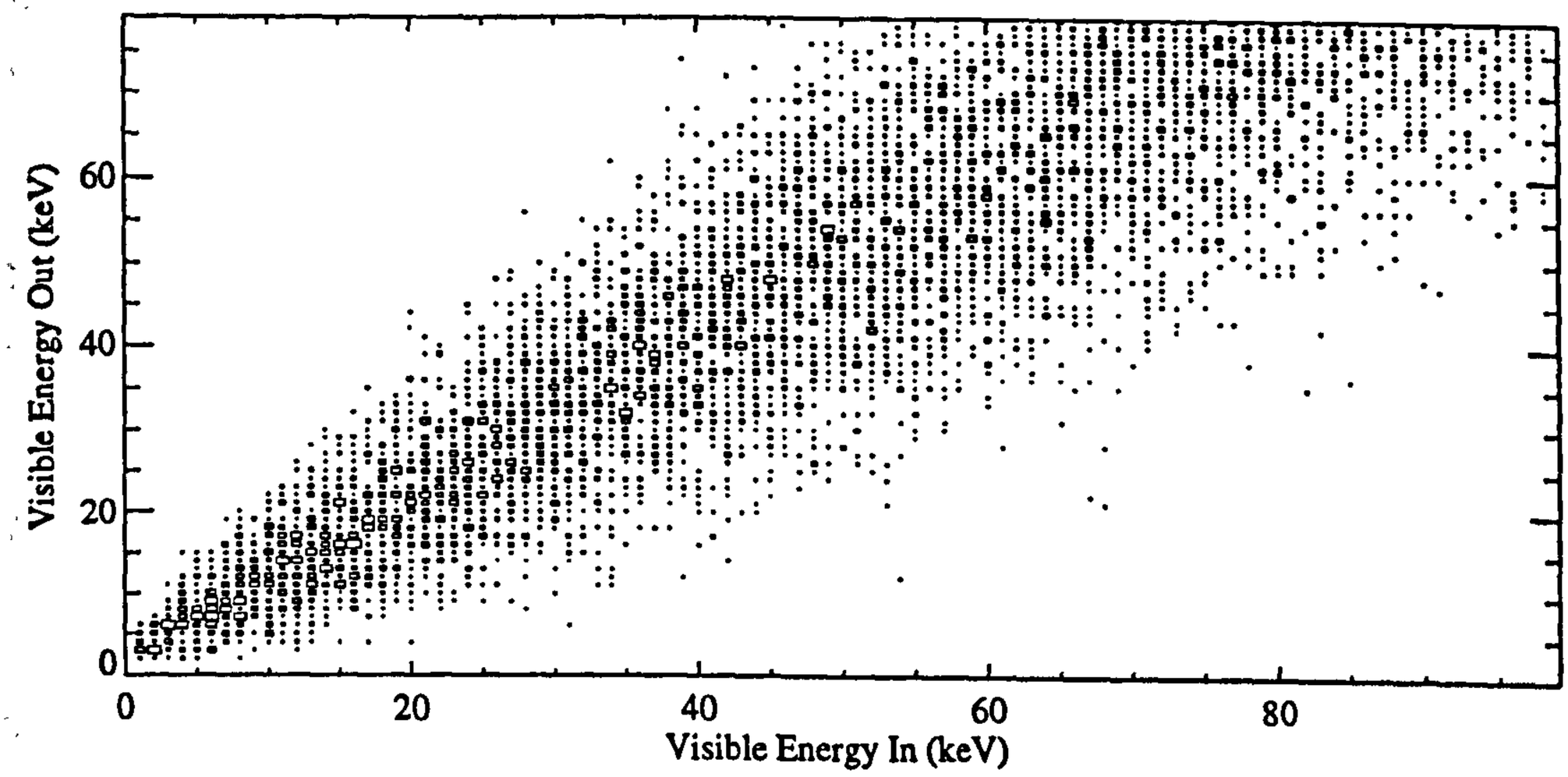

Figure 8.24: *The response matrix for the DM46 detector.*

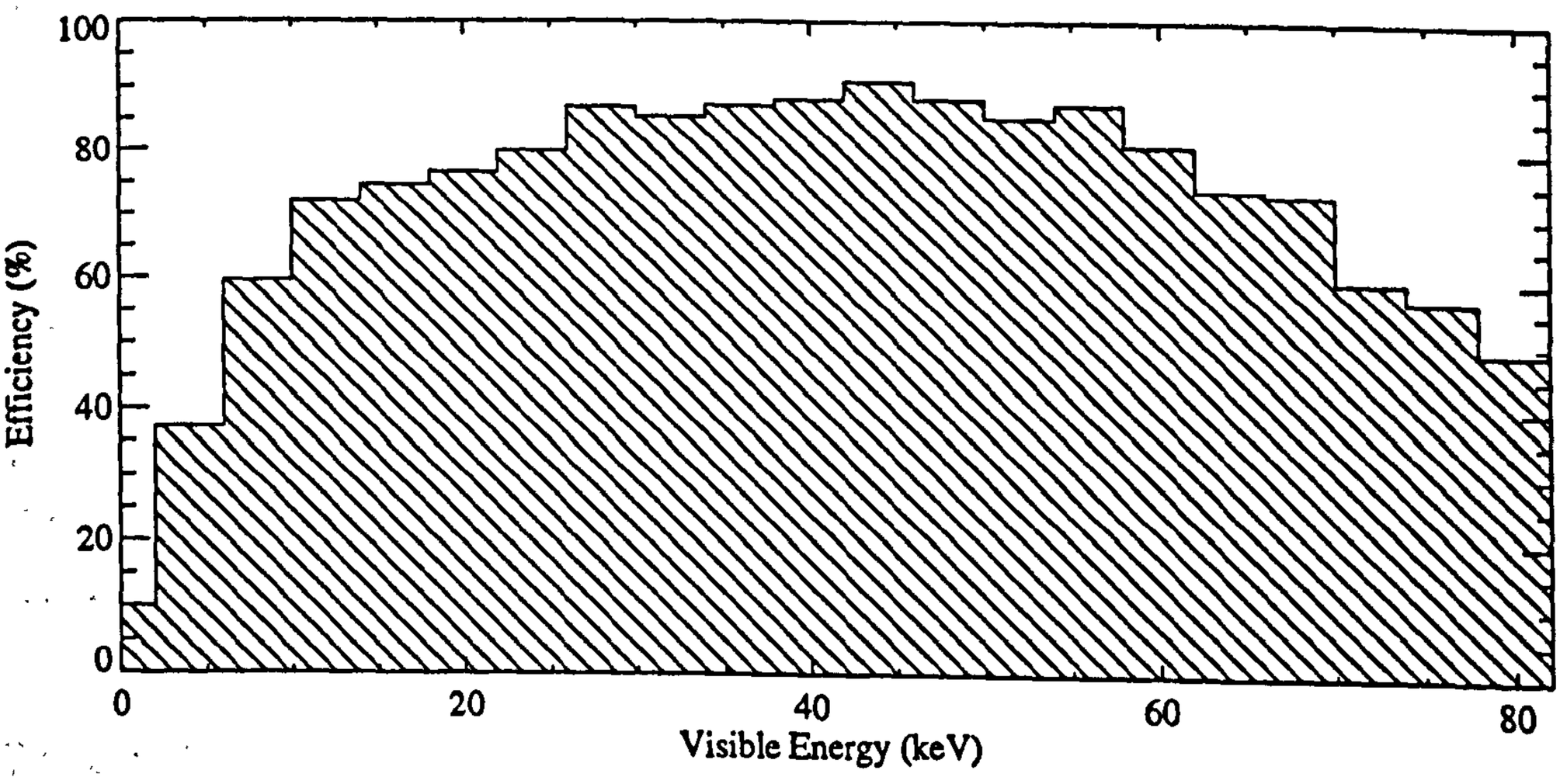

Figure 8.25: *Event identification efficiencies derived from the response matrix of Fig. 8.24. The x axis is scaled in terms of visible energy input to* M *in the analysis. A 4 keV visible energy binning has been used to aid comparison with observed energy spectra.*

8.7.3 The WIMP Interpretation

If the anomalous events are WIMP induced nuclear recoils then it should be possible to model the observed energy spectrum (hereafter that determined using the MT

technique) using Eqn. 3.65, as described in §3.7.3. For this purpose a detector response matrix M was constructed using Monte Carlo simulation. This Monte Carlo was similar to that used in §7.4.3 to generate the CASPAR response matrix, however the pulse shape distribution from which photoelectron arrival times were sampled was here that used in the DM46 LR technique to represent nuclear recoils. Measured PMT light collection asymmetries were incorporated into the simulation as were the effects of the detector energy resolution. The response matrix is plotted in Fig. 8.24 while the equivalent event identification efficiency is plotted in Fig. 8.25.

Three sets of WIMP halo velocity parameters (v_0 and v_{esc}) were chosen for use in the analysis; a set of extreme low values (set I), a median set (set II) and a set of extreme high values (set III). These parameter sets are listed in Table 8.9. For each of these parameter sets the χ^2 surface in $\sigma_{w-N} - m_w$ (WIMP-nucleon cross section - WIMP mass) space was calculated from Eqn. 3.65, in addition to the minimum value of χ^2/dof and the coupling with which this was obtained. These latter values are also listed in Table 8.9.

Set	v_0	v_{esc}	χ^2/dof	*Coupling*
I	200	450	31.12	*s.d.*
II	270	650	9.76	*s.d.*
III	340	850	2.78	*s.d.*

Table 8.9: *The sets of halo velocity parameters used in the WIMP analysis. All velocities are in* kms^{-1}. *The values of* χ^2/dof *are asymptotic minimum values obtained in the infinite mass limit of Eqn. 3.65 (see text). 'Coupling' is the WIMP-nucleon coupling, spin dependent (s.d.) or spin independent, with which the minimum* χ^2/dof *was obtained.*

The best fit visible energy spectra for each parameter set are plotted in Fig. 8.26 (overleaf). The most striking feature of this analysis is that in order to adequately fit the data an extreme set of halo velocity parameters (set III) is required, in addition to an extremely high WIMP mass and a predominantly spin dependent WIMP-nucleon coupling. Because of the asymptotic form of Eqn. 3.65 it proved impossible to fit to the observed spectrum with even an infinitely heavy WIMP without resorting to the extreme parameter values, although the best fits were obtained with infinite WIMP masses. Consequently minimum χ^2/dof values are quoted in the infinite mass limit. The best fit χ^2/dof value (2.78) is still rather improbable, however this may be ascribed to systematic uncertainty in the theoretical model (form factors or halo model) rather than the data itself. Nevertheless the need for improbably high

values of v_0 and v_{esc} in order to ensure a good fit causes doubt to be cast on this interpretation. Non-standard halo models [98] may be required in order to fit the data with reasonable astrophysical assumptions.

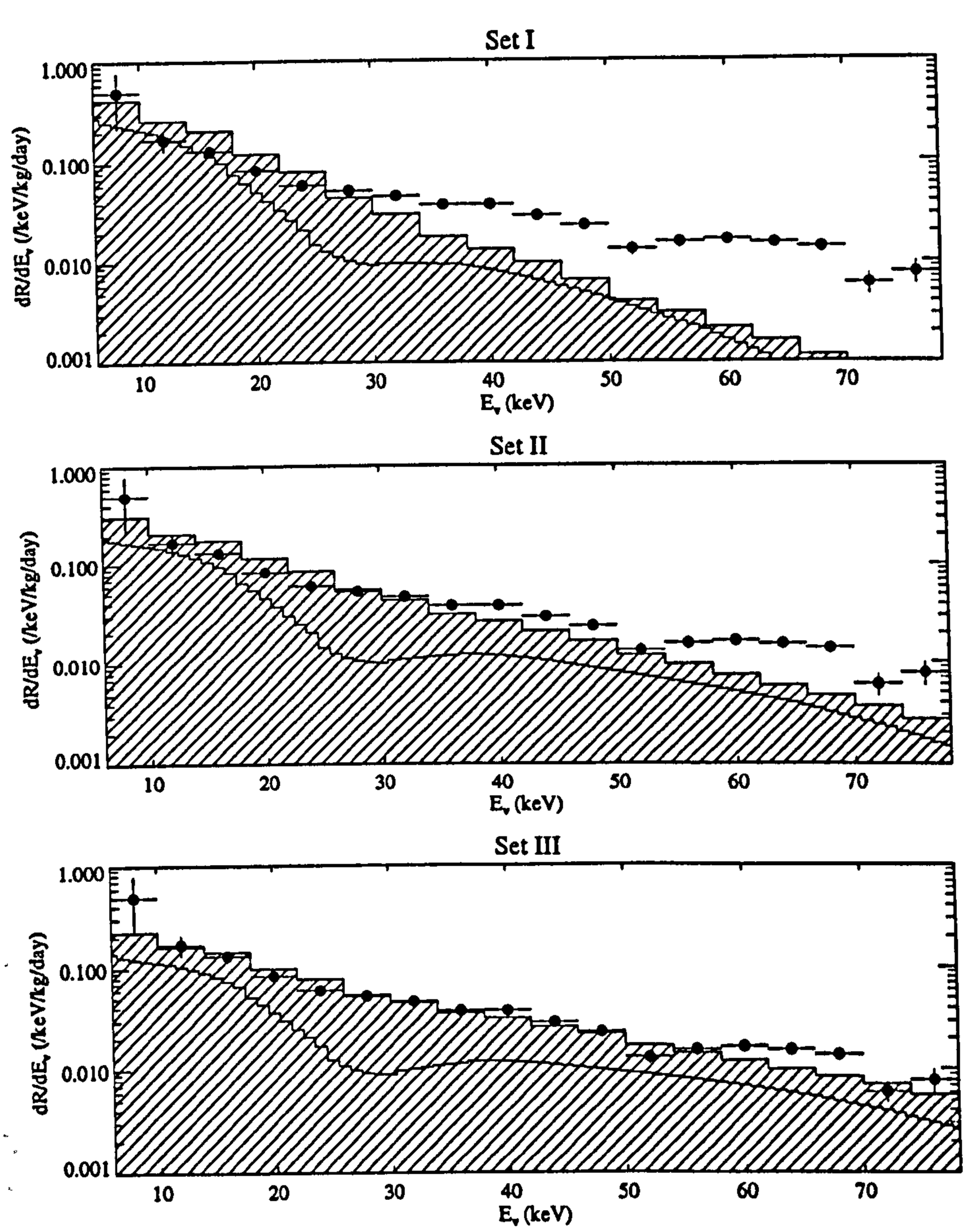

Figure 8.26: *The best fit energy spectra for three different sets of halo velocity parameters. The points represent the data from the MT technique, the filled histograms the best fit theoretical curves and the open histograms the best fit theoretical curves prior to convolution with the detector energy response.*

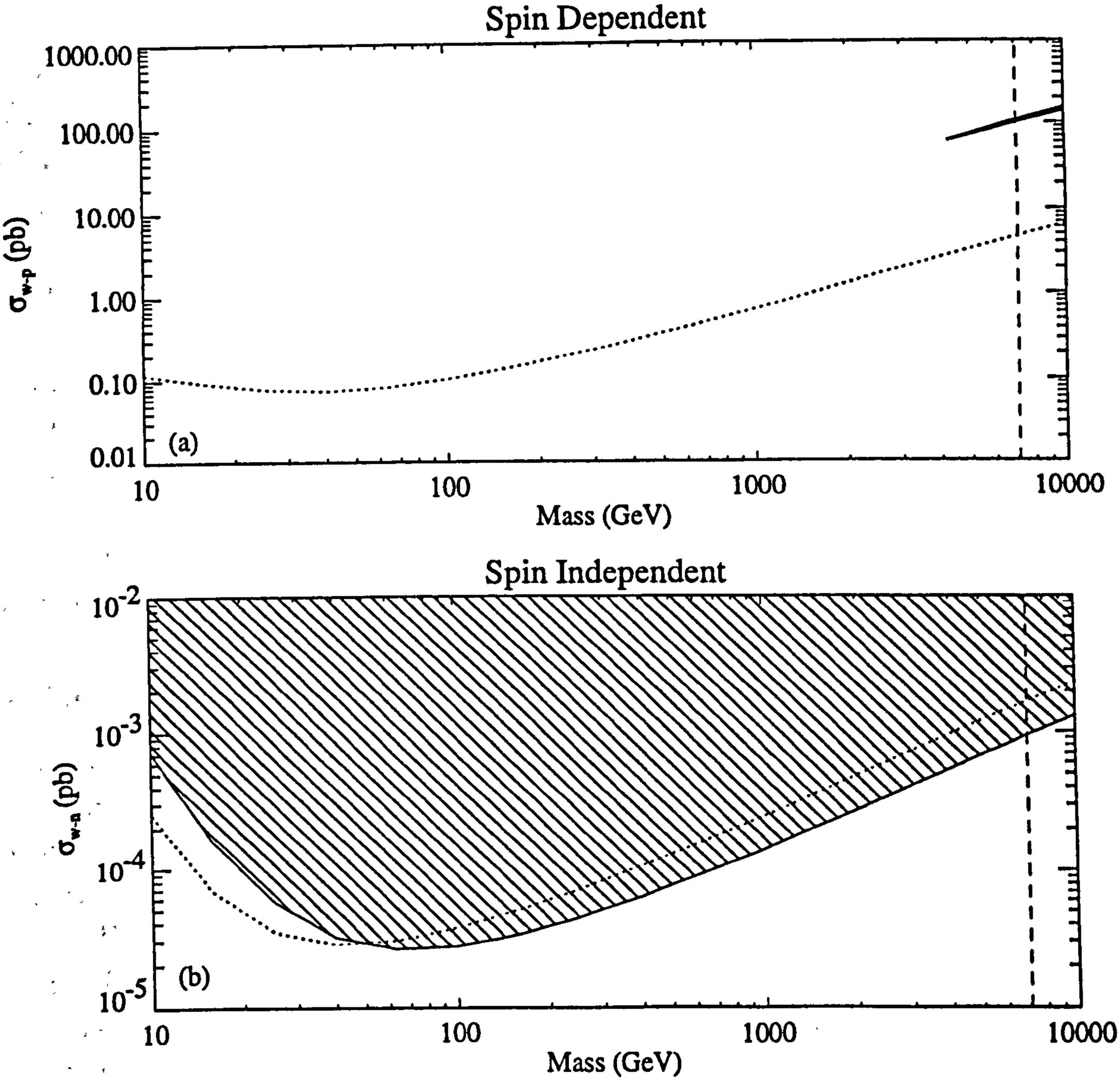

Figure 8.27: *Regions of $\sigma_{w-N} - m_w$ (WIMP-nucleon cross section - WIMP mass) parameter space favoured and excluded by the DM46 data. The shaded slice on the right of Figure (a) is the 90 % allowed region for spin dependent interactions determined from this data. The hatched region in Figure (b) (spin independent cross section) is excluded by this data under the hypothesis of a spin dependent WIMP-nucleon origin for the anomalous events. The dashed lines indicate the 90 % C.L. lower limit on the WIMP mass alone under this hypothesis (7.1 TeV/c^2). The dotted lines represent the limits obtainable with a 120 g $CaF_2(Eu)$ CASPAR detector running for one year.*

The region of $\sigma_{w-p}-m_w$ parameter space favoured by this data under the hypothesis of a halo with velocity parameters described by set III is plotted in Fig. 8.27(a). The 90 % allowed region lies inside that predicted to be excludable (in the absence of a signal) by a 120 g CaF_2(Eu) CASPAR detector running for one year (§7.4.3). The spin dependent WIMP-nucleon coupling hypothesis should thus be testable in the near future with a completely different class of detector.

If the WIMP hypothesis is adopted then the absence of an observable spin independent signal[5] also allows *limits* to be set on the spin independent cross section. These limits are plotted in Fig. 8.27(b) and extend beyond those predicted to be set by CASPAR (§7.4.3). In the figure CASPAR exclusion curves have been recalculated using the halo velocity parameters of set III in order to aid comparison. Previously published UKDMC NaI(Tl) limits [88] are not plotted in the figure as they are not directly comparable. This is because the technique used for the analysis of that data was less sensitive to signal events with fast decay time constants [174].

8.7.4 Further Investigation of the WIMP Hypothesis

The question of whether the allowed and excluded regions of parameter space are compatible with the predictions of supersymmetry was addressed using the neutdriver package of G. Jungman *et al.* [46]. A 'practical' version of the MSSM (§2.3.2) was chosen which was described by five free parameters: M_2 (a gaugino mass parameter), μ (the Higgsino mass parameter), $\tan\beta$ (the ratio of the Higgs v.e.v.s), m_A (the mass of the CP odd Higgs) and m_s^2 (a common scalar mass squared parameter). GUT parameter relations including Eqn. 2.5 were assumed throughout. M_2 was allowed to scan through the range 1000 - 20000 GeV/c^2 while μ was allowed to take values in the same range and also in the range -20000 - -1000 GeV/c^2 in order to provide a high mass for the lightest neutralino. m_A was allowed to take low and high values of 170 GeV/c^2 and 10000 GeV/c^2 respectively while $\tan\beta$ was set to 1.2 or 60. m_s was set to 4×10^8 (GeV/c^2)^2 to ensure that the neutralino was lighter than the sfermions. The resulting WIMP-nucleon cross sections were then compared with the data. The maximum values of σ_{w-p} obtained in this way for physically acceptable models ($0.025 < \Omega h^2 < 1$ [46]) were in excess of 10^8 times smaller than the values allowed by the data.

Physically this conclusion is motivated by considering the squark propagator in Fig. 3.4, which must have a mass greater than that of the neutralino. In the limit of zero momentum transfer this contribution to the matrix element for spin

[5] the best fit spin dependent curve is consistent with the errors in the first (2 - 6 keV) visible energy bin where the spin independent contribution is expected to be largest

dependent interactions is suppressed by a factor $1/m_{\tilde{q}}^2$. High neutralino masses thus give comparatively low scattering cross sections.

These considerations indicate that it is unlikely that the anomalous events can be explained by the scattering of neutralino dark matter described by the MSSM. Other non-minimal models or indeed non-SUSY WIMPs such as massive righthanded neutrinos may give better fits to the data however, although such hypotheses have yet to be tested.

8.8 Conclusions

Data from an operational 5.2 kg NaI(Tl) detector has been analysed using pulse shape discrimination techniques. The presence of an anomalous population of events inconsistent with an electron recoil hypothesis has been identified using both the mean time and likelihood ratio techniques. A time binned analysis has demonstrated the presence of a *fluctuation* in the rate of these events over the course of data taking however it was impossible to determine whether this was due to an annual *modulation*. The energy spectrum of these events is consistent with a heavy (> 7.1 TeV/c^2 90 % C.L.) WIMP hypothesis, but only at the expense of assuming a rather improbable set of halo velocity parameters. The allowed region of parameter space delimited under this assumption appears to be incompatible with supersymmetric dark matter within the minimal supersymmetric extension of the standard model.

Chapter 9

Conclusions

The work presented in this thesis has demonstrated the power of pulse shape discrimination to improve the sensitivity of scintillator dark matter detectors. The results of photoluminescence tests, neutron beam scattering experiments and Monte Carlo simulations show that the CASPAR technique in particular has the potential to significantly improve sensitivity. This may well be of crucial importance when attempting to investigate further the source of the anomalous events discovered during the analysis of data from the operational NaI(Tl) detector DM46. Although apparently incompatible with a supersymmetric dark matter interpretation the origin of these events is nevertheless intriguing and could be tested with a prototype CASPAR detector. In the longer term UKDMC liquid xenon and double phase xenon detectors should push dark matter limits deep into favoured regions of SUSY parameter space if these events are not in fact the first evidence for the existence of WIMPs.

Appendix A

Chemical Synthesis of CASPAR $CaF_2(Eu^{+2})$ Powder

The following is a step by step guide to synthesising sub-micron radiopure CaF_2 powder doped with Eu^{+2} ions (§5.3.2). The process was developed by the author and refined by C.J. Martoff.

A.1 DIPHONIX Purification

(i) Prepare a 5M solution of $CaCl_2$ in deionised low tritium water. High purity $CaCl_2.6H_2O$ crystals for this purpose can be purchased from Fluka [148]. The beaker should be made from PTFE (e.g. as purchased from Cowie Ltd. [178]) and **NOT** glass (radioimpurities). The reaction is endothermic and so the beaker may need to be heated on a hot plate while being stirred with a PTFE flea [178].

(ii) Fill a PTFE chromatography column with DIPHONIX [149] resin. Prime the column by passing 2 column volumes of conc. HCl through first (HNO_3 if purifying NaI solution). The DIPHONIX will shrink considerably; do **NOT** top up as it will expand again later. Next pass ~ 4 column volumes of 5M $CaCl_2$ solution through the column and discard. Finally pass the remaining $CaCl_2$ through the column at a rate ~ 1 drop/s and store for synthesis. A large head of pressure helps the solution to pass through the column and so a header tank may be needed. Suitable apparatus is sketched in Fig. A.1.

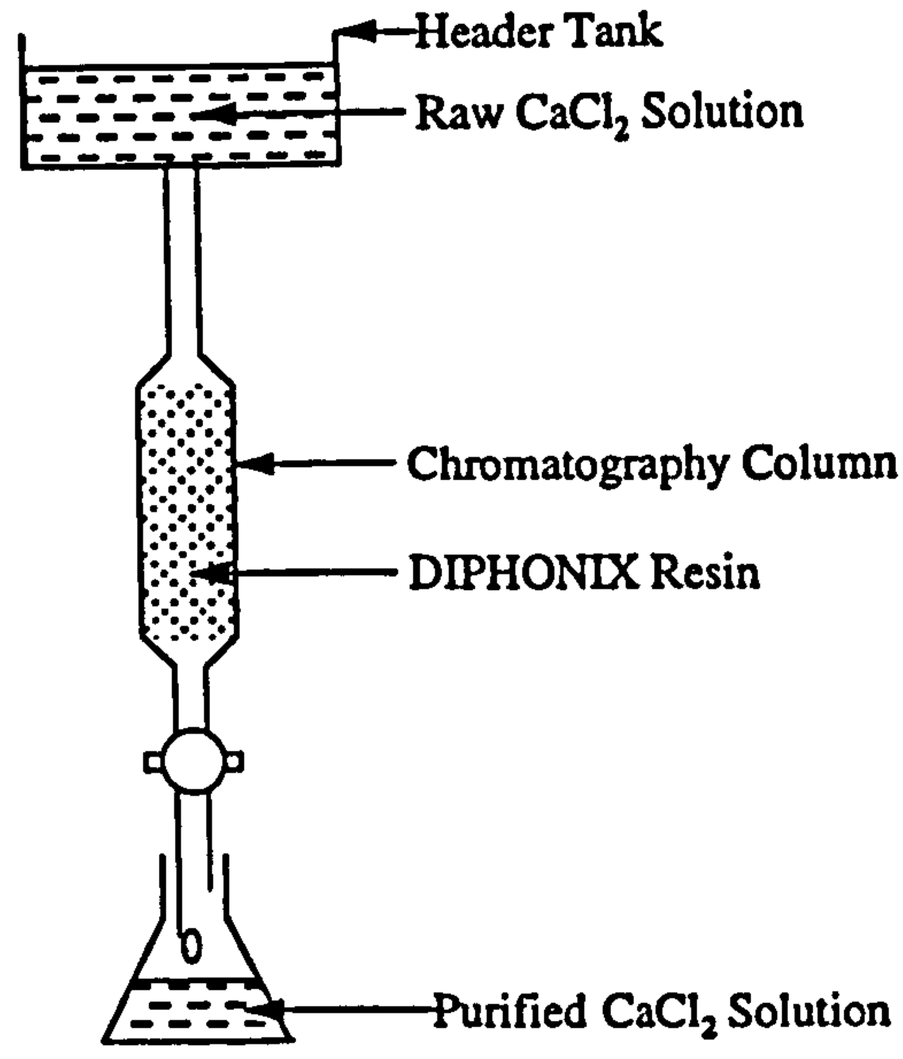

Figure A.1: *The DIPHONIX apparatus for the purification of $CaCl_2$ soln.*

A.2 Chemical Synthesis

The main steps in the synthesis process are outlined in Fig. A.2 (overleaf).

(iii) Assemble the following: 3 PTFE beakers (2 x 2000 ml, 250 ml Cowie [178]), measuring cylinder, ultrasonic bath, centrifuge, plastic seed tray, plastic bucket, balance, PTFE stirring rod (Cowie [178]), dropper, ammonium carbonate powder, large beaker of 880 ammonia soln., purified $CaCl_2$ soln., 48 % HF soln. (Fluka [148]), glacial acetic acid (Fluka [148]), $EuCl_2$ powder (Aldrich [153]), acetone, heptane, deionised water, safety gear (full length face mask, PVC gloves, PVC apron). Place all except the safety gear in a fume cupboard.

(iv) Dissolve the ammonium carbonate powder in warm water in the bucket and have it and paper wipes easily to hand. Keep the ammonia soln. nearby to remove HF fumes from the atmosphere. Leak test the gloves and don the safety gear.

(v) Place the required amount of $EuCl_2$ (§5.3.2) in the small PTFE beaker. Add $\sim$ 3 cm^3 of water per gram of $EuCl_2$. Add $\sim$ 1 cm^3 acetic acid

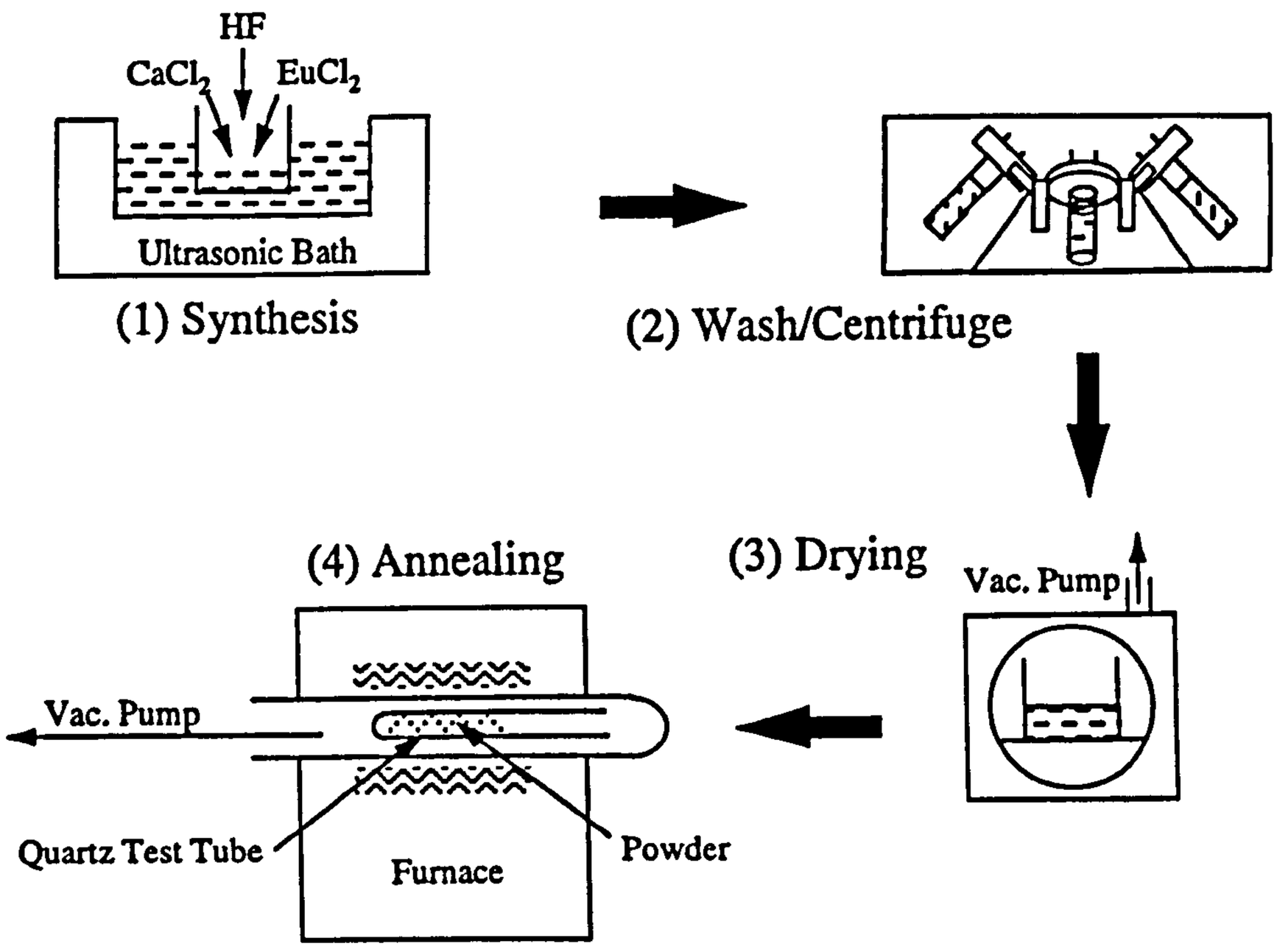

Figure A.2: *The CASPAR $CaF_2(Eu)$ synthesis procedure.*

per gram of $EuCl_2$. Stir vigorously until the powder dissolves and a transparent yellow solution is formed.

(vi) Add the $EuCl_2$ solution and some excess acetic acid to the $CaCl_2$ solution contained in one of the large PTFE beakers. The beaker should be clamped in the ultrasonic bath (filled with water).

(vii) Measure a stoichiometric quantity of HF into the second large PTFE beaker with care, using a measuring cylinder or balance standing in the seed tray (to contain leaks).

(viii) Turn on the ultrasonic bath. Rapidly add the HF to the $CaCl_2 + EuCl_2$ solution while stirring vigorously with the PTFE rod. Stirring may alternatively be performed with a mechanical stirrer. The reaction is mildly exothermic. $CaF_2(Eu^{+2})$ precipitates out of solution as an opalescent gelatinous mass.

(ix) After a few minutes turn off the ultrasound and cease stirring. Remove the beaker from the bath. Place all HF contaminated materials in the ammonium carbonate solution overnight for decontamination. Sluice down

the HF container and all HF spills with wipes soaked in ammonium carbonate solution followed by water.

(x) Place the solution containing the $CaF_2(Eu^{+2})$ powder in the plastic buckets of a centrifuge. Centrifuge the solution for $\sim$ 15 minutes at $\sim$ 3000 rpm. Pour off the liquor and discard. Refill the buckets with deionised water.

(xi) Repeat step (x) until the pH of the liquid is > 3. Pour off the liquor and discard. Refill the buckets with acetone.

(xii) Centrifuge the solution for $\sim$ 30 minutes at $\sim$ 4000 rpm. Pour off the liquor and discard. Refill the buckets with acetone.

(xiii) Repeat step (xii) $\sim$ 5 times. Then repeat step (xii) another 5 times but substituting heptane for acetone.

(xiv) Dry the precipitate under vacuum at $\sim$ 100 °C overnight. The resulting dry powder should break up easily with shaking and have the consistency of talc.

A.3 Annealing

(xv) Place the powder in a quartz tube suitable for use in a tube furnace. Pump the tube down slowly taking care not to disturb the powder. Once under a good vacuum raise the temperature of the furnace to $\sim$ 100 °C and hold for several hours to drive off any water vapour.

(xvi) Ramp the temperature rapidly up to $\sim$ 900°C and hold for $\sim$ 10 minutes. Turn off the furnace and let the powder cool naturally ($\sim$ 300 °C/hr. is acceptable).

A.4 Variations in Technique

If dopants other than Eu^{+2} are required then step (v) above will be different. The required ionisation state of the required dopant must be soluble in water and not readily oxidised in aqueous solution. A solution should be made of a salt of the required ion (e.g. $EuCl_3$ for the Eu^{+3} ion), using heat if necessary. Other possible dopants include Tb^{+3} ions for a green phosphor and other lanthanides. Mixed dopings may be created by adding several different doping ions to the starting solution. Alternatively different ions of the same doping element may be obtained by

initially performing step (v) with the most oxidised ion required. Prolonged heating at step (xvi) ($\sim$ several days) at high temperatures ($\sim$ 1000 °C) reduces these ions to lower valency states. Depending on temperature and time several different ionisation states can be present simultaneously giving a mixed emission (e.g. as in Fig. 5.17). The grain size of the powder may be altered by changing the rate of reaction and the concentration of reactants and by removing the ultrasonic field.

Appendix B

Refractive Index Matching for CASPAR

There follows a description of the technique for matching the refractive index of dioxan scintillator to that of CaF_2(Eu) powder.

(i) Obtain fine, dry CaF_2(Eu) powder with the consistency of talc. This may necessitate ultrasonic processing or grinding after annealing the powder. In this case the precipitate (with the consistency of emulsion paint if it is correctly dispersed) should be dried thoroughly using steps (x) to (xiv) of Appendix A.

(ii) Using a Cu nozzle bubble dry N_2 gas through naphthalene free dioxan scintillator (Zinsser Analytic (UK) Ltd. [161]) for $\sim$ 3 hours at a rate $\sim$ 1 bubble per second.

(iii) Place the required amount of liquid scintillator in a mixing vessel and add the CaF_2(Eu) powder. The powder should disperse to give a gelatinous precipitate after vigorous stirring. If this does not happen the subsequent steps will not be successful.

(iv) Slowly add small amounts of scintillation grade naphthalene crystals while stirring vigorously. The process is endothermic and so the mixing vessel may need to be placed in a bath of warm water. As the correct refractive index is approached the solution will go from cloudy to clear. It is difficult to get the correct refractive index immediately (because the crystals quantise the amount of naphthalene added). It is thus preferable to go slightly over and then add methanol one drop at a time with a plastic dropper. At precisely the correct amount of methanol it should

be possible to see a good quality image through at least 50 mm of the mixture.

(v) Fill the desired liquid scintillator cell with CAB-O-SIL [165] and then pour in the CaF_2(Eu) mixture while stirring. A transparent thixotropic gel should be formed. If the cell has a narrow neck it may be preferable to add the CAB-O-SIL in the mixing vessel and then shake or stir the gel sufficiently to permit pouring.

(vi) Cover the mixture with a blanket of dry N_2 and then stopper the cell, sealing with PTFE tape or vacuum grease.

At all times contact with glass (poor radiopurity), water or oxygen (quenches scintillation) should be minimised. The majority of the refractive index matching should be performed with the naphthalene and as little methanol as possible should be used. The entire procedure should be performed in a fume cupboard in order to avoid contact with toxic dioxan vapour.

Bibliography

[1] E. Hubble. *Proceedings of the National Astronomical Society*, 15:168, 1929.

[2] E.W. Kolb and M.S. Turner. *The Early Universe.* Frontiers in Physics. Addison-Wesley Publishing Company, Redwood City, 1990.

[3] R.J. Tayler. *The Hidden Universe.* Ellis Horwood Library of Space Science and Space Technology. Ellis Horwood, Chichester, 1991.

[4] P.J.E. Peebles. *Principles of Physical Cosmology.* Princeton Series in Physics. Princeton University Press, Princeton, 1993.

[5] M. Roos. *Introduction to Cosmology.* John Wiley & Sons, New York, 1997.

[6] A. Einstein. *S.-B. Preuss. Akad. Wiss.*, 142, 1917.

[7] A. Friedmann. *Zeitung für Physik*, 10:377, 1929.

[8] S.M. Carroll. Lecture Notes on General Relativity. gr-qc/9712019.

[9] F. Zwicky. *Helvetica Physica Acta*, 6:110, 1933.

[10] A. Dekel *et al.* Measuring Ω. In N. Turok, editor, *Critical Dialogues in Cosmology*, page 97. World Scientific, 1997.

[11] J.A. Tyson *et al.* Detailed Mass Map of CL0024+1654 from Strong Lensing. *Astrophysical Journal*, 498:L107, 1998.

[12] K.G. Begeman *et al.* *Monthly Notices of the Royal Astronomical Society*, 249:523, 1991.

[13] M. Fich and S. Tremaine. *Annual Review of Astronomy and Astrophysics*, 29:409, 1991.

[14] J. Brand and L. Blitz. The velocity field of the outer galaxy. *Astronomy and Astrophysics*, 275:67, 1993.

[15] G. Raffelt. Dark Matter : Candidates, Motivations and Searches. In N. Ellis and M. Neubert, editors, *Proceedings of the 1997 European School of High-Energy Physics*, page 235. CERN, 1998.

[16] W.L. Freedman. Measuring Cosmological Parameters. In J.A. Frieman A.V. Olinto and D.N. Schramm, editors, *18th Texas Symposium on Relativistic Astrophysics and Cosmology*, page 188. World Scientific, 1998.

[17] J.R. Primack. Current Status of the Cosmological Parameters: $\Omega_0 = 1$ vs. 0.3. In H.V. Klapdor-Kleingrothaus and Y. Ramachers, editors, *Dark Matter in Astro- and Particle Physics*, page 97. World Scientific, 1997.

[18] A. Guth. *Physical Review*, **D23**:347, 1981.

[19] A.D. Linde. A New Inflationary Universe Scenario - A Possible Solution of the Horizon, Homogeneity, Isotropy and Primordial Monopole Problems. *Physics Letters*, **B108**:389, 1982.

[20] A.D. Linde. Chaotic Inflation. *Physics Letters*, **B129**:177, 1983.

[21] J. Silk. The Cosmic Microwave Background. In N.J.C. Spooner, editor, *The Identification of Dark Matter*, page 13. World Scientific, 1997.

[22] C.H. Lineweaver *et al.* Constraints on h, Ω_b and λ_0 from Cosmic Microwave Background Observations. *Astronomy and Astrophysics*, **322**:365, 1997.

[23] S. Perlmutter *et al.* Discovery of a Supernova Explosion at Half the Age of the Universe and its Cosmological Implications. *Nature*, **392**:311, 1998.

[24] S. Perlmutter. Measurements of Ω and Λ from Supernovae. Talk given at 3^{rd} International Symposium on 'Sources and Detection of Dark Matter in the Universe', Santa Monica, California, February, 1998.

[25] M. Drees. Particle Dark Matter Physics: an Update. hep-ph/9804231. Submitted to *Proc. WHEPP5*, Pune, India, January, 1998.

[26] A.G. Kim. A Review of the High-Redshift Supernova Searches. astro-ph/9805196.

[27] M.S. Turner. Cosmology 1996. In N.J.C. Spooner, editor, *The Identification of Dark Matter*, page 43. World Scientific, 1997.

[28] S. Sarkar. Primordial Nucleosynthesis and Dark Matter. In H.V. Klapdor-Kleingrothaus and Y. Ramachers, editors, *Dark Matter in Astro- and Particle Physics*, page 235. World Scientific, 1997.

[29] L.M. Krauss. Baryons or Nothing? Results from BBN. In N.J.C. Spooner, editor, *The Identification of Dark Matter*, page 3. World Scientific, 1997.

[30] B.J. Carr. Baryons as Dark Matter. In N.J.C. Spooner, editor, *The Identification of Dark Matter*, page 135. World Scientific, 1997.

[31] C. Renault *et al.* Results from EROS. In N.J.C. Spooner, editor, *The Identification of Dark Matter*, page 212. World Scientific, 1997.

[32] D. Pfenniger. Cold Molecular Gas as Dark Matter Component. In H.V. Klapdor-Kleingrothaus and Y. Ramachers, editors, *Dark Matter in Astro- and Particle Physics*, page 54. World Scientific, 1997.

[33] W. Sutherland *et al.* Gravitational Micro-lensing Results from MACHO. In N.J.C. Spooner, editor, *The Identification of Dark Matter*, page 200. World Scientific, 1997.

[34] C. Renault *et al.* Observational Limits on Machos in the Galactic Halo. *Astronomy and Astrophysics*, **324**:L69, 1997.

[35] R.S. Somerville and J.R. Primack. Favoured Variants of Cold Dark Matter Cosmologies. In N.J.C. Spooner, editor, *The Identification of Dark Matter*, page 32. World Scientific, 1997.

[36] J.R. Primack. Cold + Hot and Other Dark Matter Cosmological Models vs. Observations. In H.V. Klapdor-Kleingrothaus and Y. Ramachers, editors, *Dark Matter in Astro- and Particle Physics*, page 127. World Scientific, 1997.

[37] B. Fuchs *et al.* Massive Black Holes in the Dark Halos of Dwarf Spirals. In N.J.C. Spooner, editor, *The Identification of Dark Matter*, page 67. World Scientific, 1997.

[38] W. Saunders *et al.* The Density Field of the Local Universe. *Nature*, **349**:32, 1991.

[39] G. Smoot *et al.* A Measurement of the Cosmic Microwave Background Temperature at 7.5 GHz. *Astrophysical Journal Letters*, 396:L1, 1992.

[40] J. Peacock and S.Dodds. *Monthly Notices of the Royal Astronomical Society*, **267**:1020, 1994.

[41] M.S. Turner. Cosmology. In Z.P. Zheng and H.S. Chen, editors, *Proceedings of the 17th International Symposium on Lepton-Photon Interactions : LP '95 Beijing*, page 693. World Scientific, 1997.

[42] R. Cowsik and J. McClelland. *Astrophysical Journal*, **180**:7, 1973.

[43] L. Di Lella. Neutrino Oscillations. In N. Ellis and M. Neubert, editors, *Proceedings of the 1995 European School of High-Energy Physics*, page 201. CERN, 1996.

[44] B.W. Lee and S. Weinberg. *Physical Review Letters*, **39**:165, 1977.

[45] M. Spiro. Desperately Seeking Dark Matter. In N. Ellis and M. Neubert, editors, *Proceedings of the 1995 European School of High-Energy Physics*, page 201. CERN, 1996.

[46] G. Jungman *et al.* Supersymmetric Dark Matter. *Physics Reports*, **267**:195, 1996.

[47] P. F. Smith and J.D. Lewin. Dark Matter Detection. *Physics Reports*, **187**:203, 1990.

[48] Y. Fukuda *et al.* Evidence for Oscillation of Atmospheric Neutrinos. hep-ex/9807003. Submitted to *Physical Review Letters.*

[49] L. Wolfenstein. *Physical Review*, **D17**:2369, 1978.

[50] S.P. Mikheyev and A.Yu. Smirnov. *Nuovo Cimento*, **9C**:17, 1986.

[51] H.H. Chen. Direct Approach to Resolve the Solar Neutrino Problem. *Physical Review Letters*, **55**:1534, 1985.

[52] C. Athanassopoulos *et al.* Candidate Events in a Search for $\bar{\nu}_\mu - \bar{\nu}_e$ Oscillations. *Physical Review Letters*, **75**:2650, 1995.

[53] J. Kleinfeller. New Results from the Karmen2 Neutrino Oscillation Search. Talk given at conference 'SUSY'98', Oxford, July 1998.

[54] D.S. Ayres *et al.* Detectors for the MINOS Long-Baseline Neutrino Oscillation Experiment. *Nuclear Physics (Proc. Suppl.)*, **B61**:12, 1998.

[55] P. Sikivie. Dark Matter Axions '96. In H.V. Klapdor-Kleingrothaus and Y. Ramachers, editors, *Dark Matter in Astro- and Particle Physics*, page 543. World Scientific, 1997.

[56] G. Raffelt. Axion Hunting at the Turn of the Millenium. hep-ex/9806506.

[57] P. F. Smith and J.R.J. Bennett. *Nuclear Physics*, **B149**:525, 1979.

[58] S. Sarkar and M. Birkel. Extremely High Energy Cosmic Rays from Relic Particle Decays. hep-ph/9804285. Submitted to *Astroparticle Physics.*

[59] G.G. Ross. Beyond the Standard Model. In N. Ellis and M.B. Gavela, editors, *Proceedings of the 1994 European School of High-Energy Physics*, page 119. CERN, 1995.

[60] M.M. Boliev *et al.* Search for Supersymmetric Dark Matter with Baksan Underground Telescope. *Nuclear Physics (Proc. Suppl.)*, **B 48**:83, 1996.

[61] M. Mori *et al.* Search for Neutralino Dark Matter Heavier than the W-Boson at Kamiokande. *Physical Review*, **D48**:5505, 1979.

[62] M. Spiro. Experimental Particle Astrophysics. In N. Ellis and M. Neubert, editors, *Proceedings of the 1996 European School of High-Energy Physics*, page 239. CERN, 1997.

[63] D.H. Perkins. *Introduction to High Energy Physics.* The Advanced Book Programme. Addison-Wesley Publishing Company, Menlo Park, 1987.

[64] I.J.R. Aitchison and A.J.G. Hey. *Gauge Theories in Particle Physics.* Graduate Student Series in Physics. Adam Hilger, Bristol, 1989.

[65] F. Halzen and A.D. Martin. *Quarks and Leptons: An Introductory Course in Modern Particle Physics.* John Wiley & Sons, New York, 1984.

[66] M. Kaku. *Quantum Field Theory: A Modern Introduction.* Oxford University Press, New York, 1993.

[67] D.V. Nanopoulos. Grand Unification and Physical Supersymmetry. In J.A. Grifols A. Ferrando and A. Méndez, editors, $SU(3) \times SU(2) \times U(1)$ *and Beyond*, page 156. World Scientific, 1983.

[68] H.E. Haber and G.L. Kane. The Search for Supersymmetry: Probing Physics Beyong the Standard Model. *Physics Reports*, **117**:75, 1985.

[69] J.H. Schwarz and N. Seiberg. String Theory, Supersymmetry, Unification and All That. hep-th/9803179. To appear in *Reviews of Modern Physics*, March, 1999.

[70] T.R. Morris. The Standard Model. In S.L. Lloyd, editor, *Proceedings of the 1996 School for Young High Energy Physicists (RAL-TR-97-013)*, page 105. CLRC, 1997.

[71] G.M. Shore. The Standard Model. In K.J. Peach, editor, *Proceedings of the 1995 School for Young High Energy Physicists (RAL-TR-96-018)*, page 101. CLRC, 1996.

[72] G.F. Giudice. Beyond the Standard Model. In N. Ellis and M. Neubert, editors, *Proceedings of the 1995 European School of High-Energy Physics*, page 183. CERN, 1996.

[73] M.W. Grunewald. Combined Analysis of Precision Electroweak Results. Talk given at ICHEP'98, Vancouver, Canada, July, 1998.

[74] S.P. Martin. A Supersymmetry Primer. hep-ph/9709356. To appear in Gordon L. Kane, editor, *Perspectives in Supersymmetry*, World Scientific, 1997.

[75] P.P.O. Morawitz. *The Zeus First Level Tracking Trigger and Studies of Supersymmetry at HERA*. PhD thesis, University of Oxford, 1993.

[76] H. Dreiner. An Introduction to Explicit R-parity Violation. hep-ph/9707435. To appear in Gordon L. Kane, editor, *Perspectives in Supersymmetry*, World Scientific, 1997.

[77] J. Adams *et al.* Search for Light Gluinos via the Spontaneous Appearance of $\pi^+\pi^-$ pairs with an 800 GeV/c Proton Beam at Fermilab. *Physical Review Letters*, **79**:4083, 1997.

[78] M.S. Kelly. *Searches for Gauge Mediated Supersymmetry Breaking using the Signal* $e^+e^- \longrightarrow \tilde{l}^+\tilde{l}^- \longrightarrow l^+l^-\tilde{\chi}_1^0\tilde{\chi}_1^0 \longrightarrow l^+l^-\tilde{G}\tilde{G}\gamma\gamma$. PhD thesis, University of Sheffield, 1998.

[79] D. Toback *et al.* CDF Searches for New Phenomena. hep-ph/9801445.

[80] R. Barate *et al.* Single- and Multi-Photon Production in e^+e^- Collisions at a Centre-of-Mass Energy of 183 GeV. cern/ep-98-053. Submitted to *Physics Letters* **B**.

[81] J. Ellis *et al.* Charginos and Neutralinos in the Light of Radiative Corrections Sealing the Fate of Higgsino Dark Matter. hep-ph/9801445. Submitted to *Physical Review* D.

[82] H. Baer and M. Brhlik. Neutralino Dark Matter in Minimal Supergravity: Direct Detection vs. Collider Searches. *Physical Review*, **D57**:567, 1998.

[83] M. Acciarri *et al.* Search for Neutral Higgs Bosons of the Minimal Supersymmetric Standard Model in e^+e^- Interactions at $\sqrt{s} = 130$ -183 GeV. CERN-EP-98-072. Submitted to *Physics Letters* B.

[84] J.D. Lewin and P.F. Smith. Review of Mathematics, Numerical Factors, and Corrections for Dark Matter Experiments Based on Elastic Nuclear Recoil. *Astroparticle Physics*, **6**:87, 1996.

[85] W.R. Leo. *Techniques for Nuclear and Particle Physics Experiments. A How To Approach.* Springer-Verlag, Berlin, 1994.

[86] In N.J.C. Spooner, editor, *The Identification of Dark Matter.* World Scientific, 1997.

[87] In H.V. Klapdor-Kleingrothaus and Y. Ramachers, editors, *Dark Matter in Astro- and Particle Physics.* World Scientific, 1997.

[88] P. F. Smith *et al.* Improved Dark Matter Limits from Pulse-Shape Discrimination in a Low Background Sodium-Iodide Detector at the Boulby Mine. *Physics Letters*, **B379**:299, 1996.

[89] R. Bernabei *et al.* WIMPs Search by Scintillators: Possible Strategy for Annual Modulation Search with Large-Mass Highly-Radiopure NaI(Tl). *Nuclear Physics (Proc. Suppl.)*, **B70**:79, 1999.

[90] G. Gerbier *et al.* Note on a "Hint" for an Annual Modulation Signature of a 60 GeV WIMP. astro-ph/9710181.

[91] M.W. Goodman and E. Witten. Detectability of Certain Dark Matter Candidates. *Physical Review*, **D31**:3059, 1985.

[92] J. Ellis and R.A. Flores. Realistic Predictions for the Detection of Supersymmetric Dark Matter. *Nuclear Physics*, **B307**:883, 1988.

[93] J.D. Lewin. *Private Communication.*

[94] M.T. Ressell and D.J. Dean. Spin-Dependent Neutralino-Nucleus Scattering for A Similar to 127 Nuclei. *Physical Review*, **C56**:535, 1997.

[95] G. Fricke *et al.* Nuclear Ground-State Charge Radii from Electromagnetic-Interactions. *Atomic Data and Nuclear Data Tables*, 60:177, 1995.

[96] R.H. Helm. *Physical Review*, **104**:1466, 1956.

[97] M. Kamionkowski and A. Kinkhabwala. Galactic Halo Models and Particle Dark Matter Detection. *Physical Review*, **D57**:3256, 1998.

[98] P. Sikivie *et al.* Secondary Infall Model of Galactic Halo Formation and the Spectrum of Cold Dark Matter Particles on the Earth. *Physical Review*, **D56**:1863, 1997.

[99] A.K. Drukier *et al.* Detecting Cold Dark Matter Candidates. *Physical Review*, **D33**:3495, 1986.

[100] J.B. Birks. *The Theory and Practice of Scintillation Counting.* Pergamon Press, Oxford, 1964.

[101] G.J. Davies. *Development of a Liquid Xenon Detector for use in Dark Matter Searches.* PhD thesis, Imperial College, London, 1994.

[102] G.F. Knoll. *Radiation Detection and Measurement.* John Wiley & Sons, New York, 1989.

[103] The Particle Data Group. Review of Particle Physics. *Physical Review*, **D54**:1, 1996.

[104] N.J.C. Spooner *et al.* Measurement of Na and I Recoil Discrimination and Detection Efficiency in a Cooled 'UVIS' NaI Crystal for Dark Matter Searches. *Astroparticle Physics*, 5:299, 1996.

[105] C.H. Lally. *Development of a Cooled Sodium Iodide Scintillation Detector and its use in a Search for Dark Matter.* PhD thesis, Imperial College, London, 1995.

[106] C. Kittel. *Introduction to Solid State Physics.* John Wiley & Sons, New York, 1996.

[107] N.J.T. Smith. *Private Communication.*

[108] J. Telfer. *Private Communication.*

[109] Bicron Corporation. Product Catalogue, 1991.

[110] R.C. Weast and M.J. Astle (eds.). *CRC Handbook of Chemistry and Physics 62nd Edition.* CRC Press, Boca Raton, 1981.

[111] W.T. Eadie *et al. Statistical Methods in Experimental Physics.* North-Holland Publishing Company, Amsterdam, 1971.

[112] G.D. Cowan. *Statistical Data Analysis.* Oxford University Press, Oxford, 1998.

[113] W.J. van Sciver and L. Bogart. *I.R.E. Transactions on Nuclear Science*, NS-**3**:90, 1958.

[114] N.J.C. Spooner and P.F. Smith. The UVIS Scintillation Detector. A Proposed Method of Nuclear Recoil Discrimination for Dark Matter Searches. *Physics Letters*, **B314**:430, 1993.

[115] R. Bernabei *et al.* Improved Limits on WIMP F-19 Elastic Scattering and First Limit on the 2EC2 Nu Ca-40 Decay by Using a Low Radioactive CaF2(Eu) Scintillator. *Astroparticle Physics*, **7**:73, 1997.

[116] N.J.C. Spooner *et al.* In *Proceedings of the XXIII Cosmic Ray Conference*, volume 4, page 760, 1993.

[117] D.R. Tovey *et al.* Pulse-Shape Discrimination in a Mixed Scintillator Dark Matter Detector. In N.J.C. Spooner, editor, *The Identification of Dark Matter*, page 551. World Scientific, 1997.

[118] N.J.C. Spooner *et al.* Demonstration of Nuclear Recoil Discrimination Using Recoil Range in a Mixed CaF_2 plus Liquid Scintillator Gel Detector for Dark Matter. *Astroparticle Physics*, 8:13, 1997.

[119] P.F. Smith. OMNIS - An Improved Low-Cost Detector to Measure Mass and Mixing of Mu/Tau Neutrinos from a Galactic Supernova. *Astroparticle Physics*, 8:27, 1997.

[120] U.K. Dark Matter Collaboration. Galactic Dark Matter Search Proposal (1997-2001), 1996.

[121] P. Belli *et al.* Search for WIMPs with Enriched Xenon at Gran Sasso. *Nuovo Cimento*, **C19**:537, 1996.

[122] H. Wang. WIMP Detection Using Double Phase TEA Doped Xenon. Talk given at conference 'COSMO '97', Ambleside, September 1997.

[123] U.K. Dark Matter Collaboration. Galactic Dark Matter Search Proposal (1999-2003), 1998.

[124] C.D. Peak. *Private Communication.*

[125] J.E. McMillan. *Private Communication.*

[126] J.W. Roberts. *Private Communication.*

[127] Electron Tubes Ltd., Bury Street, Ruislip, Middlesex HA4 7TA, U.K..

[128] Thorn EMI Electron Tubes Ltd. Photomultipliers and Accessories, 1993. *Product Catalogue.*

[129] H. Vine. *Private Communication.*

[130] T.J. Sumner and T. Ali. Dark Matter Scintillator Experiments with Avalanche Photodiodes. In N.J.C. Spooner, editor, *The Identification of Dark Matter*, page 557. World Scientific, 1997.

[131] N.J.C. Spooner. *Private Communication.*

[132] LeCroy Research Systems, 700 Chestnut Ridge Rd., NY 10977-6499, U.S.A..

[133] P. Horowitz and W. Hill. *The Art of Electronics.* Cambridge University Press, Cambridge, 1989.

[134] N.J.C. Spooner *et al.* Measurements of Carbon Recoil Scintillation Efficiency and Anisotropy in Stilbene for WIMP Searches with Direction Sensitivity. In N.J.C. Spooner, editor, *The Identification of Dark Matter*, page 481. World Scientific, 1997.

[135] C.J. Martoff. The DRIFT Concept: Can Gas Detectors Improve Overall WIMP Sensitivity? Talk given at conference 'IDM'98', Buxton, September 1998.

[136] K.N. Buckland *et al.* Low Pressure Gaseous Detector for Particle Dark Matter. *Physical Review Letters*, **73**:1067, 1994.

[137] C.J. Martoff. *Private Communication.*

[138] R.C. Ropp. *Luminescence and the Solid State.* Studies in Inorganic Chemistry. Elsevier, Amsterdam, 1991.

[139] Hilger Analytical Ltd., Westwood, Margate, Kent, CT9 4JL. U.K..

[140] Omega Technologies Inc., 725 Via Alondra, Camarillo, CA 93012, U.S.A..

[141] Edwards High Vacuum International, 16 Dalton Court, Astmoor, Runcorn, WA7 1PU, U.K..

[142] BDH Laboratory Supplies, Poole, BH15 1TD, U.K..

[143] Research Systems Inc., 2995 Wilderness Place, Suite 203, Boulder, CO 80301, U.S.A..

[144] G.C. Tyrrell. *Private Communication.*

[145] J.D. Lewin. UK Dark Matter Project: Radioactivity Test Results. *UKDMC Internal Note.*

[146] Sorby Centre for Electron Microscopy and Microanalysis, Department of Engineering Materials, University of Sheffield, Sir. Robert Hadfield Building, Mappin Street, Sheffield S1 3JD, U.K..

[147] J.W. Mellor. *A Comprehensive Treatise on Inorganic and Theoretical Chemistry*, volume 3. Longman.

[148] Fluka Chemie AG, Industriestrasse 25, CH-9471 Buchs, Switzerland.

[149] Eichrom Industries Inc., 107/8205 S. Cass Ave., Darien, IL 60561, U.S.A..

[150] I.M. Blair *et al.* Radiopurification of NaI and its Application to Dark Matter and Neutrino Experiments. In R. Bernabei and A. Incicchitti, editors, *The Dark Side of the Universe*, page 128. World Scientific, 1996.

[151] T.J. Mason (ed.). *Chemistry with Ultrasound*, volume 28. Elsevier Applied.

[152] X.M. Fang *et al.* Eu-Doped CaF_2 Grown on Si(100) Substrates by Molecular Beam Epitaxy. *Applied Physics Letters*, **67**:1891, 1995.

[153] Aldrich Chemical Company, The Old Brickyard, New Road, Gillingham, Dorset SP8 4XT, U.K..

[154] K. Aono *et al.* Ion Beam Induced White Luminescence of CaF2 Implanted with both Eu and Tb Ions. *Japanese Journal of Applied Physics - Part 1*, **32**:3851, 1993.

[155] U.G. Caldino *et al.* Energy Transfer in CaCl2-Eu-Mn Crystals. *Journal of Physics - Condensed Matter*, **5**:2195, 1993.

[156] A. Yates. *Private Communication.*

[157] Sonic and Materials Inc., Kenosia Avenue, Danbury, CT, U.S.A..

[158] NE Technology Ltd., Bath Road, Beenham, Reading, Berkshire RG7 5PR, U.K. Now owned by Bicron Corp.

[159] J.B. Birks. *An Introduction to Liquid Scintillation Counting and Solutes and Solvents for Liquid Scintillation Counting.* Koch-Light Laboratories Ltd., Colnbrook, 1975.

[160] Bicron Newbury, 12345 Kinsman Road, Newbury, Ohio 44065-9577, U.S.A..

[161] Zinsser Analytic (UK) Ltd., Howarth Road, Maidenhead, Berkshire SL6 1AP, U.K..

[162] Lightpath Optical Co. Ltd., No. 3 Factory, Elm Industrial Estate, Church Road, Harold Wood, Romford, Essex RM7 9LH, U.K..

[163] National Instruments, 6504 Bridge Point Parkway, Austin, TX 78730-5039, U.S.A..

[164] R. Huggett. *Private Communication.*

[165] Cabot Carbon Ltd., Barry Site, Sully Moors Rd., Sully, South Glamorgan CF64 5RP, Wales, U.K..

[166] J.D. Lewin. *Private Communication.*

[167] N.J.C. Spooner *et al.* The Scintillation Efficiency of Sodium and Iodine Recoils in a NaI(Tl) Detector for Dark Matter Searches. *Physics Letters*, **B321**:156, 1994.

[168] G.J. Davies *et al.* The Scintillation Efficiency for Calcium and Fluorine Recoils in CaF_2 and Carbon and Fluorine Recoils in C_6F_6 for Dark Matter Searches. *Physics Letters*, **B322**:159, 1994.

[169] ITT Systems & Sciences Corp., 4410 East Fountain Blvd., PO Box 15012, Colorado Springs, CO 80916, U.S.A..

[170] R. Hazama *et al.* Search for Dark Matters by Means of CaF_2 Detector. In N.J.C. Spooner, editor, *The Identification of Dark Matter*, page 397. World Scientific, 1997.

[171] G. Gerbier *et al.* WIMPs Search: the Saclay Programme. In J. Tran Thanh Van, editor, *25th Rencontre de Moriond: 10th Moriond Workshop on New and Exotic Phenomena*, page 469. Editions Frontieres, 1990.

[172] J.D. Lewin. Range-Energy Relations for Hypothetical Charged Particles. *Rutherford Lab. Technical Note (RL-77 126/A).*

[173] J.W. Roberts *et al.* Investigation of Background Signals in Photomultiplier based Scintillator Dark Matter Detectors at the Boulby Underground Facility. To be submitted to *Nuclear Instruments and Methods.*

[174] P.F. Smith. *Private Communication.*

[175] V. Kudryavtsev. *Private Communication.*

[176] W.H. Press (ed.). *Numerical Recipes in FORTRAN : the Art of Scientific Computing.* Cambridge University Press, Cambridge, 1992.

[177] R. Barlow. *Statistics : a Guide to the use of Statistical Methods in the Physical Sciences.* The Manchester Physics Series. John Wiley & Sons, Chichester, 1989.

[178] Cowie Technology Group Ltd., Ridgeway, Coulby Newham, Middlesborough, Cleveland TS8 0TQ, U.K..